



HAL
open science

Elaboration in silico of molecular systems for the fabrication of nano- and optoelectronic devices

Vincent Delmas

► **To cite this version:**

Vincent Delmas. Elaboration in silico of molecular systems for the fabrication of nano- and optoelectronic devices. Coordination chemistry. Université Rennes 1, 2021. English. NNT : 2021REN1S107 . tel-03682678

HAL Id: tel-03682678

<https://theses.hal.science/tel-03682678v1>

Submitted on 31 May 2022

HAL is a multi-disciplinary open access archive for the deposit and dissemination of scientific research documents, whether they are published or not. The documents may come from teaching and research institutions in France or abroad, or from public or private research centers.

L'archive ouverte pluridisciplinaire **HAL**, est destinée au dépôt et à la diffusion de documents scientifiques de niveau recherche, publiés ou non, émanant des établissements d'enseignement et de recherche français ou étrangers, des laboratoires publics ou privés.

THESE DE DOCTORAT DE

L'UNIVERSITE DE RENNES 1

ÉCOLE DOCTORALE N° 596

Matière, Molécules, Matériaux

Spécialité : Chimie Physique, Chimie Théorique

Par

Vincent DELMAS

Élaboration *in silico* de systèmes moléculaires pour la fabrication de dispositifs en nano- et opto-électronique

Thèse présentée et soutenue à Rennes, le 30 septembre 2021

Unité de recherche : Institut des sciences chimiques de Rennes

Thèse N° :

Rapporteurs avant soutenance :

Hélène JAMET Maître de conférences HDR, Université Grenoble Alpes
Alain ROCHEFORT Professeur des universités, Polytechnique Montréal

Composition du Jury :

Président :

Stéphane RIGAUT Professeur des universités, Université de Rennes 1

Examineurs :

Alain ROCHEFORT Professeur des universités, Polytechnique Montréal

Colin VAN DYCK Chargé de cours, Université de Mons

Hélène JAMET Maîtresse de conférences HDR, Université Grenoble Alpes

Dominique VUILLAUME Directeur de recherche, CNRS, Institut d'électronique de micro-électronique et de nanotechnologie

Directrice de thèse :

Karine COSTUAS Directrice de recherche, CNRS, Institut des Sciences Chimiques de Rennes

Co-directeur de thèse :

Jérôme CORNIL Directeur de recherche, FNRS, Université de Mons

Table of contents

| | |
|---|------------|
| GLOSSARY..... | 5 |
| CONTEXT AND OBJECTIVES | 7 |
| PART I – COMPUTATIONAL STUDY OF POLYMETALLIC COPPER (I) LUMINESCENT COMPLEXES | 13 |
| CHAPTER I – STATE OF THE ART AND METHODOLOGY | 13 |
| <i>I – Introduction.....</i> | <i>13</i> |
| <i>II – Concepts of luminescence.....</i> | <i>14</i> |
| <i>III – Cu(I) complexes.....</i> | <i>21</i> |
| <i>IV – Coordination-driven supramolecular chemistry (CDS).....</i> | <i>22</i> |
| <i>V – Computational studies of copper molecules</i> | <i>24</i> |
| <i>VI – Methodology and software</i> | <i>27</i> |
| CHAPTER II – STUDY OF DIPHOSPHINO-CU ₂ COORDINATION COMPLEXES..... | 37 |
| <i>I – Introduction.....</i> | <i>37</i> |
| <i>II – Experimental data obtained by Lescop and coworkers.....</i> | <i>38</i> |
| <i>III – Theoretical study.....</i> | <i>47</i> |
| <i>IV – Conclusion.....</i> | <i>65</i> |
| CHAPTER III – STUDY OF CU ₆ CN ₄ AND CU ₈ CN ₄ COORDINATION COMPLEXES | 69 |
| <i>I – Introduction.....</i> | <i>69</i> |
| <i>II – Experimental and computational study of a Cu₆(CN)₄-based metallacycle.....</i> | <i>70</i> |
| <i>III – Experimental and computational study of a Cu₈(CN)₄-based metallacycle</i> | <i>76</i> |
| <i>IV – Conclusion.....</i> | <i>81</i> |
| PART II – MOLECULAR JUNCTIONS | 83 |
| CHAPTER I – STATE OF THE ART AND THEORETICAL BACKGROUND..... | 83 |
| <i>I – Introduction.....</i> | <i>83</i> |
| <i>II – Most common experimental molecular junction setups</i> | <i>85</i> |
| <i>III – Theoretical background</i> | <i>90</i> |
| <i>IV – Thermoelectric properties</i> | <i>104</i> |
| <i>V – Thermoelectricity in molecular junctions</i> | <i>109</i> |
| CHAPTER II – ANALYSIS OF MOLECULAR JUNCTION CHARACTERISTICS | 125 |
| <i>I – Introduction.....</i> | <i>125</i> |
| <i>II – Methods to extract the key molecular parameters ϵ_0 and Γ</i> | <i>125</i> |

| | |
|--|-----|
| III – Transmission and thermoelectric junctions | 145 |
| IV – Transmission study: an overview on OPE molecules..... | 150 |
| CHAPTER III – STUDY OF OPAN MOLECULAR JUNCTIONS | 163 |
| I – Introduction..... | 163 |
| II – Experimental data and characterizations by Rigaut's and Scheer's groups | 164 |
| III – Results and analysis | 165 |
| IV – Computational study..... | 169 |
| V – Conclusions..... | 179 |
| CHAPTER IV – ORGANOMETALLIC SYSTEMS TO IMPROVE THERMOELECTRIC PROPERTIES .. | 183 |
| I – Introduction..... | 183 |
| II – Functionalization of the $Fe^{II}(\text{cyclam})(C_2Ph-S)_2$ system | 187 |
| III – Influence of meta/para thiol coordination on transmission properties..... | 194 |
| IV – Screening of organometallic systems and their transmission | 197 |
| CHAPTER V – ORGANOMETALLIC $Fe(\text{CYCLAM})$ AND $Ru(\text{DPPE})$ SYSTEMS | 219 |
| I – Introduction..... | 219 |
| II – Ru-dppe experimental data..... | 220 |
| III – Fe-cyclam experimental data | 230 |
| IV – I-V characteristics between the two sets of experimental data | 235 |
| V – Computational study of the Ru-dppe and Fe-cyclam junctions..... | 236 |
| VI – Conclusions | 248 |
| CHAPTER VI – TIGHT BINDING AS A PROSPECTIVE METHOD..... | 251 |
| I – Introduction..... | 251 |
| II – Tight-binding methods..... | 251 |
| III – Application on transition metal complexes | 258 |
| III – General statistics on the performance of the TB methods | 266 |
| IV – Conclusions and perspectives..... | 270 |
| CONCLUSION AND PERSPECTIVES | 279 |
| ANNEXES | 285 |

Glossary

| | |
|----------------------------------|--|
| AFM | Atomic Force Microscopy |
| CDS | Coordination-driven Supramolecular Chemistry |
| CP-AFM | Conductive Probe Atomic Force Microscopy |
| CT | Charge Transfer |
| DCM | Dichloromethane |
| DF | Density functional |
| DFT | Density Functional Theory |
| DFTB | Tight binding DFT |
| DFT-D(3) | DFT + dispersion (3) |
| DFT + Σ | DFT + self-energy correction |
| DH-GGA | Double Hybrid GGA |
| DNA | Deoxyribonucleic acid |
| dppa | diphenylphosphino-amine |
| dppm | diphenylphosphino-methyl |
| dppe | diphenylphosphino-ethyl |
| FMO | Frontier molecular orbital |
| F-N | Fowler-Nordheim |
| FWHM | Full width at half maximum |
| GGA | Generalized Gradient Approximation |
| HF | Hartree-Fock |
| HL gap | HOMO-LUMO gap |
| HM-GGA | Hybrid Meta GGA |
| HOMO | Highest Occupied Molecular Orbital |
| IC | Internal Conversion |
| IETS | Inelastic Electron Tunneling Spectroscopy |
| IPES | Inverse Photoemission Spectroscopy |
| ISC | Intersystem Crossing |
| I-V | Current – Voltage curve |
| LC-H-GGA | Long Range Corrected Hybrid GGA |
| LED | Light Emitting Diodes |
| LLCT | Ligand to Ligand Charge Transfer |
| LMCT | Ligand to Metal Charge Transfer |
| LUMO | Lowest Unoccupied Molecular Orbital |
| MBPT | Many Body Perturbation Theory |
| MC | Metal-Centered |
| MCBJ | Mechanically Controllable Break Junction |
| M-GGA | Meta GGA |

| | |
|----------------------|---|
| MLCT | Metal to Ligand Charge Transfer |
| MO | Molecular Orbital |
| MOSFET | Metal Oxide Semiconductor Field Effect Transistor |
| MSE | Mean Signed Error |
| NEGF | Non-Equilibrium Green's Functions |
| NTO | Natural Transition Orbitals |
| OLED | Organic Light Emitting Diode |
| PES | Potential Energy Surface |
| QC | Quantum Chemistry |
| QI | Quantum Interference |
| RISC | Reverse Inter-System Crossing |
| RT | Room Temperature |
| SAM | Self-Assembled Monolayer |
| SCC | Self-Consistent Charge |
| SLM | Single Level Model |
| S_n | Singlet excited state <i>n</i> |
| SO | Spin Orbitals |
| SOC | Spin-Orbit Coupling |
| SOPERT | Spin-Orbit PERTurbative method |
| STM | Scanning Tunneling Microscope |
| STS | Scanning Tunneling Spectroscopy |
| SVP | Split Valence Polarization |
| TADF | Thermally Activated Delayed Fluorescence |
| TBAF | Tetra- <i>n</i> -Butyl Ammonium Fluoride |
| TDA | Tamm-Dancoff Approximation |
| TD-DFT | Time-Dependent DFT |
| TE | Thermoelectric |
| THF | Tetrahydrofuran |
| TM | Transition Metal |
| TMSE | Trimethylsilane |
| T_n | Triplet excited state <i>n</i> |
| TVS | Transition Voltage Spectroscopy |
| TZ2P | Triple- ξ Double Polarization |
| UPS | Ultraviolet photo-electron spectroscopy |
| UV-VIS | Ultraviolet - Visible |
| WFT | Wave Function Theory |
| ZORA | Zero Order Regular Approximation |

Context and objectives

The team of Theoretical Inorganic Chemistry (CTI) at the Institute of Chemical Sciences in Rennes (ISCR) is a research group gathering 14 researchers of the CNRS, the University of Rennes 1 and the Engineering School of Chemistry of Rennes.¹ The research group makes use of computational chemistry tools to unravel structural and physical properties of molecules and solid-state systems. Its research topics are more specifically dealing with the rationalization using quantum chemical tools of chemical structures and physical properties of: i) complex architectures (i.e., large clusters, glasses) (axis 1), ii) solid-state materials for energy (axis 2), and iii) multifunctional molecular systems for opto-electronics or spintronics (axis 3).

The present project is part of the research axis 3 and aims at contributing to the development of technologies in molecular electronics, opto-electronics or spintronics using a computational approach. The main interest of these devices is to provide high efficiency at the nanometric scale (with a small number of atoms and low energy use) that is fully in line with nowadays environmental challenges. Molecular materials have demonstrated their potential applications in a wide group of sectors like data storage, information technologies, medicine, food, sensing, energy (solar energy harvesting, lighting...). The recent achievements of the CTI group performed in collaboration with experimentalists of the ISCR and with several foreign research teams clearly demonstrate that quantum chemical studies provide a clear added value to the understanding of physico-chemical properties in such systems and strongly help in the design of functional inorganic and organometallic molecular compounds for molecular (opto)-electronics and spintronics.^{2,3,4,5,6,7}

The CTI group aims at contributing to these research efforts using computational chemistry both as a comprehensive tool to understand physical properties, and as a molecular screening tool to access specific functionalities in the aim of conceiving efficient molecular-based devices. The thesis research project presented in this manuscript is devoted to two applications that take advantage of transition metal-containing molecules: low-cost lighting and (thermal) energy harvesting at the nanoscale (more specifically thermoelectricity at the nanoscale).

For the first objective, our effort has been driven toward copper containing molecules which are appealing systems because of the availability, low-toxicity and low cost of copper. The

general objective of this research is to provide an alternative to heavy metal and lanthanide systems which are the most commonly developed molecular systems for phosphorescent light emitting diodes (PhOLED) or lighting applications which are usually more toxic, rare and therefore relatively expensive. The use of heavy metal and lanthanide containing compounds is rationalized by their capacity to facilitate phosphorescence or late fluorescence and thus to lead to emission properties usually much more interesting than those of most of the pure organic materials. The group of Lescop at the ISCR has recently shown that, by a careful choice of its ligand sphere and an innovative synthesis procedure, highly interesting luminescent copper-containing compounds can be obtained. The computational study which is presented in this manuscript consists in the rationalization of the optical properties of different copper (I) complexes systems by employing a carefully selected theoretical approach.

A similar research approach will be applied to the *in-silico* design of molecular systems for nano-thermoelectric applications with the aim of harvesting and converting wasted energy (heat) in nano-devices into electricity (and to prevent over-heating damages as well). This project is developed together with the laboratory of "Chemistry of Novel Materials" at the University of Mons in Belgium for the computational aspects and different experimental partners:

- the research team of Rigaut at the ISCR, specialist in the synthesis of coordination systems containing transition metals or rare earth atoms mainly for molecular design for targeted applications and switchable molecules.
- the research team of Scheer of the Department of Physics of the University of Konstanz, specialist in mesoscopic physics with an accent on the field of nanoelectronics in which charge transport phenomena are explored, notably with the physical characterization of single molecule systems using the Mechanically Controlled Break Junctions (MCBJ) technique.
- the research team of Vuillaume at the Institute for Electronics, Microelectronics and Nanotechnology, specialist in the design and characterization of self-assembled monolayers and molecular-based nano-electronic devices using different scanning probe microscopy techniques (e.g., CP-AFM).

Based on our objectives, the manuscript is split in two parts as follows:

Part I: Computational study of multi-nuclear copper (I) luminescent complexes

The first chapter aims at developing the different terms and basic concepts that define the luminescence of molecules, notably the thermally activated delayed fluorescence (TADF) mechanism and the interest for molecules containing transition metals in that domain, more particularly copper-containing systems. This description is followed by a presentation of the coordination driven supramolecular chemistry developed by Lescop and coworkers to synthesize innovative multi-nuclear copper (I) complexes presenting interesting luminescent properties for some of them which are studied in the next chapters. To date, Density Functional Theory (DFT) is the only first-principles computational tool that is able to treat molecules containing several hundreds of atoms; consequently, this technique has been employed in these studies. The choice of the computational procedure, particularly the functional and the atomic basis set, is explained on the basis of literature. The second chapter is dedicated to the study of two di-nuclear complexes, $[\text{Cu}_2(\text{X})_3]^{2+}$ with X corresponding to bridging diphosphine ligands. The relatively small size of these systems was interesting to evaluate the precision of the computational methodology when increasing the atomic basis set and when adding the treatment of relativistic effects in comparison to the experimental data. The third chapter aims at rationalizing the photo-physical properties of two much larger copper (I) complexes, a hexa-nuclear and an octa-nuclear complex using the same computational methodology as in the previous chapter.

Part II: Study of metal-containing molecular junctions

The second part of the manuscript aims at developing a computational protocol to evaluate the thermoelectric properties of coordination compounds in molecular junction configurations and ultimately at performing a molecular design to enhance these properties. The thermoelectric ability of a system describes its potential to convert a thermal gradient into an electrical current (Seebeck effect), or reversely to cool down a device by applying an electrical potential (Peltier effect). The first chapter reports an introduction to the field of molecular electronics and the main experimental equipment used to characterize molecular junctions: Scanning Tunneling Microscope (STM), CP-AFM and MCBJ. This section is followed by a basic development of the theoretical background of molecular junctions for electronic transport as well as of the computational tools and details necessary to compute and rationalize the properties of the molecular systems studied in the next chapters. This chapter is concluded with the introduction

of theoretical concepts of thermoelectric transport in molecular junctions. The second chapter introduces elements and parameters to allow for the comparison between experimental data obtained from current-voltage curves (I-V curves) of molecular junction using different models (Single Level Model, Transition Voltage Spectroscopy) and additional measurements (Ultraviolet Photoelectron Spectroscopy). An overview of both theoretical and experimental values of the thermal phonon conductance κ_{ph} in a molecular junction involved in the thermoelectric effects is also given. Finally, the calculation of electronic transmissions is achieved to study the influence of the electrode geometries. The main aim of the third chapter is to computationally evaluate the thermoelectric ability of organometallic systems inserted in a junction and to determine the factors which could enhance it. This domain of research is an emerging field in the group of CTI that is triggered by the early results obtained by the consortium about a molecular junction showing photo-switchable electronic transport.⁸ The chapter four gathers experimental data obtained by our collaborators on organometallic junctions in different configurations and experimental conditions. They are analyzed by applying the different models described in chapter two. A computational analysis of the conducting properties of the corresponding model junctions and a comparison with the experimental data are reported. This analysis reveals the need of faster computational tools able to better take into consideration the diversity of geometries revealed by the dispersion observed in the experimental measurements. The increase in the speed of the calculations would also be beneficial for molecular design purpose. The chapter five also gathers experimental data obtained by the group of Scheer on organic systems, namely the gold / oligophenyl-diethynyl / gold junctions which anchoring groups are molecules alkynyl units (Au-C anchoring) - OPAn ($n = 2, 3, 4$), where n is the number of phenyl units. A computational approach based on DFT/NEGF and DFTB was performed to understand and rationalize the electrical properties of such systems and analyze the potential of direct bonding between carbon atoms and electrodes. Finally, as mentioned in the previous chapters, we also reach the conclusion that there is a need to address a large number of contact geometries in order to better compare the computational results to the experimental measurements which show usually important dispersion. The cost of the DFT/NEGF method is for the moment prohibitive for such studies. This issue is addressed preliminarily in the last chapter by using a tight-binding Density Functional Theory (DFTB) method which has been used successfully in organic systems and is evaluated there in the domain of organometallics and coordination chemistry.

¹ <https://iscr.univ-rennes1.fr/cti/>

² Gendron, F.; Di Pietro, S.; Abad Galán, L.; Riobé, F.; Placide, V.; Guy, L.; Zinna, F.; Di Bari, L.; Bensalah-Ledoux, A.; Guyot, Y.; Pilet, G.; Pointillart, F.; Baguenard, B.; Guy, S.; Cador, O.; Maury, O.; Le Guennic, B. Luminescence, Chiroptical, Magnetic and Ab Initio Crystal-Field Characterizations of an Enantiopure Helicoidal Yb(III) Complex. *Inorg. Chem. Front.* 2021, 8, 914–926. doi:10.1039/d0qi01194k.

³ Flores Gonzalez, J.; Douib, H.; Le Guennic, B.; Pointillart, F.; Cador, O. Ytterbium-Centered Isotopic Enrichment Leading to a Zero-Field Single-Molecule Magnet. *Inorg. Chem.* 2021, 60, 540–544. doi:10.1021/acs.inorgchem.0c02652.

⁴ Wilmet, M.; Lebastard, C.; Sciortino, F.; Comby-Zerbino, C.; MacAleese, L.; Chirot, F.; Dugourd, P.; Grasset, F.; Matsushita, Y.; Uchikoshi, T.; Ariga, K.; Lemoine, P.; Renaud, A.; Costuas, K.; Cordier, S. Revisiting Properties of Edge-Bridged Bromide Tantalum Clusters in the Solid-State, in Solution and Vice Versa: An Intertwined Experimental and Modelling Approach. *Dalton Trans.* 2021, 50, 8002–8016. doi:10.1039/d0dt04200e.

⁵ Evariste, S.; Khalil, A. M.; Kerneis, S.; Xu, C.; Calvez, G.; Costuas, K.; Lescop, C. Luminescent Vapochromic Single Crystal to Single Crystal Transition in One-Dimensional Coordination Polymer Featuring the First Cu(I) Dimer Bridged by an Aqua Ligand. *Inorg. Chem. Front.* 2020, 7, 3402–3411. doi:10.1039/d0qi00691b.

⁶ Kepenekian, M.; Molard, Y.; Costuas, K.; Lemoine, P.; Gautier, R.; Ababou Girard, S.; Fabre, B.; Turban, P.; Cordier, S. Red-NIR Luminescence of Mo 6 Monolayered Assembly Directly Anchored on Au(001). *Mater. Horiz.* 2019, 6, 1828–1833. doi:10.1039/c9mh00724e.

⁷ Groizard, T.; Papior, N.; Le Guennic, B.; Robert, V.; Kepenekian, M. Enhanced Cooperativity in Supported Spin-Crossover Metal–Organic Frameworks. *J. Phys. Chem. Lett.* 2017, 8, 3415–3420. doi:10.1021/acs.jpcllett.7b01248.

⁸ Meng, F.; Hervault, Y.-M.; Norel, L.; Costuas, K.; Van Dyck, C.; Geskin, V.; Cornil, J.; Hng, H. H.; Rigaut, S.; Chen, X. Photo-Modulable Molecular Transport Junctions Based on Organometallic Molecular Wires. *Chemical Science* 2012, 3, 3113. doi:10.1039/c2sc20323e.

Chapter I – State of the art and methodology

I – Introduction

The relationship between the black-body radiation, fluorescent lamps, light emitting diodes (LEDs) and more and more applications (sensors, biomedical imaging...) is that all take advantage of the luminescent properties of materials. The research of new luminescent constituents has been growing exponentially since the early 60s to reach more than 23 000 articles containing the words “luminescent materials” in the article in 2020 (Figure 1). This growing interest is related to the global warming issues that drive innovation toward sustainable energy in which luminescent materials are particularly attractive.

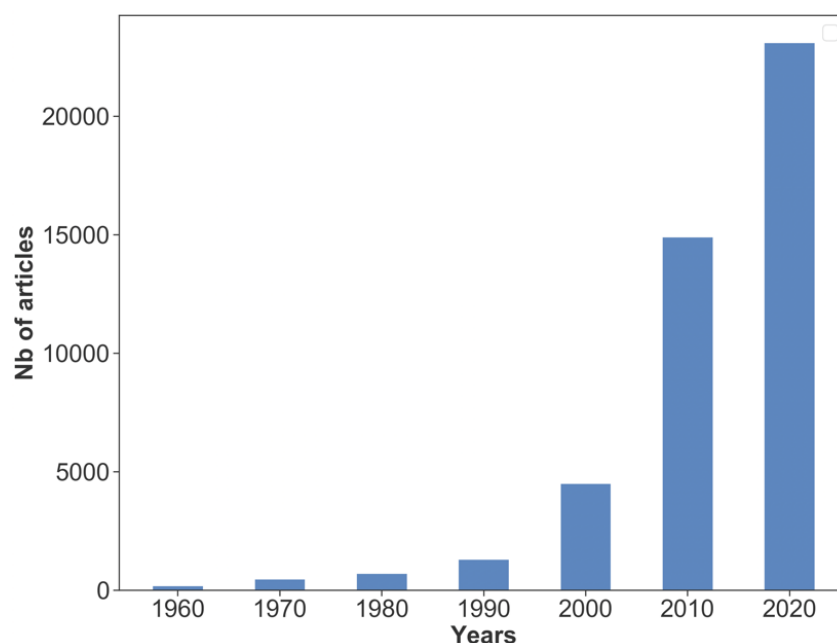


Figure 1 – Evolution of the number of articles by selected years containing the word “luminescent materials”. *Source:* Google Scholar.

Different means of excitation are generating luminescence of systems of large diversity (bulk, molecules, atoms), allowing for a wide range of applications (Table 1). Here, we will focus on lighting applications for which copper (I) complexes are particularly attractive as discussed below. Our interest will be essentially focused on the photoluminescence properties of those systems in the context of a close collaboration with the experimental team of Lescop, INSA, Rennes.

Table 1 – Typical applications and usual luminous efficiency (order of magnitude) of selected luminescence types.¹

| Luminescence type | Typical application | Efficiency |
|----------------------|---|--------------|
| Black-body radiation | Tungsten filament lamp | ≈ 5 % |
| Photoluminescence | Fluorescence lamps and phosphorescent devices | ≈ 20 % |
| Cathodoluminescence | Cathodic television screen | ≈ 10 % |
| Electroluminescence | Light-emitting diode (LED), flat TV screen panels | ≈ 0.1 – 50 % |

II – Concepts of luminescence

II.1 – General notions of luminescence

The luminescence is a general term used to describe an electromagnetic radiation – photon emission from a material which is not induced by a thermal process. The phenomenon is triggered by the de-excitation of a system from an excited state to a more stable state.² The word “luminescence” is attributed to the physicist Wiedemann in 1888. It is derived from the Latin word “lumen” which means “the light”.³ As said previously, our research will be focused on photoluminescence, which is the emission of light induced by photo-excitation. Indeed, upon light absorption (energy of the photons $h\nu$; h = Planck constant; ν = frequency), a molecule can undergo a change in its electronic configuration leading to the promotion of an electron to a higher-lying unoccupied electronic level. The energy gap between these two states matches the photon energy. From this excited state, several de-excitation processes exist to return to the ground state, such as typically internal conversion (IC) (loss of energy by phonon emission/vibration), or photon emission i.e. luminescent de-excitation.²

Photoluminescence is usually divided in two categories: fluorescence and phosphorescence. The differentiation is based on the nature of the electronic properties of the excited state from which the emission occurs.⁴ In the case of a system whose ground state is a closed-shell singlet state, the emission which arises from a singlet excited state is called fluorescence. In certain cases, a non-radiative intersystem crossing (ISC) between two different spin states, typically between a singlet excited state (S_n) and a triplet excited state (T_n), can be non-negligible as shown in Figure 2. For numerous organic molecules in which the spin-orbit coupling (SOC) energies are negligible, ISC does not occur. The selection rules^{1,5} which state that a change of

spin multiplicity is prohibited during optical transitions are indeed based on this hypothesis. The SOC corresponds to relativistic interactions that are usually found in non-planar aromatic molecules and/or heavy atom-containing systems. A second consequence of the SOC is that the lifetime of a triplet state is longer than that of a singlet state. In that context, nuclear relaxation can occur, leading to a modification of the excited state geometry. Spontaneous emission of photons from the triplet excited state to the local ground state (constant geometry) eventually occurs after a certain lifetime determined by SOC. This corresponds to the second type of luminescent process which is called phosphorescence.

Experimentally, considering a continuous excitation, a main observable difference between fluorescence and phosphorescence is the characteristic time scale for the light emission to decay. It should be noted that for some metal-containing complexes, the time decay does not provide a clear distinction between fluorescence and phosphorescence. The various electronic processes induced by the absorption of light by a luminescent material (also called luminophore or luminochrome) can be, in a first approximation, represented by a Jablonski-type diagram (Figure 2). The fundamental singlet state, S_0 , the first excited states S_1 and T_1 , and higher excited states S_A and T_B are represented. Each of these states includes several vibrational energy sublevels. At room temperature (RT) the thermal energy ($k_B T \approx 25$ meV) is in most of the cases not sufficient to populate the first excited states. The absorption of light can promote the system from the ground state to an excited state S_A if the incoming photon energy $h\nu$ matches the energy gap between the two states. The absorption usually takes place from the lowest vibrational sub-level of the ground state S_0 because it is the most occupied vibrational state. After absorption, the excited molecule can:

- follow Kasha's rule⁶, and rapidly relax by IC from the S_A excited state to the S_1 state before: i) emitting a photon (fluorescence); ii) non-radiative vibrational de-excitation (exothermic processes) or iii) undergoing an ISC to a triplet state if the SOC is substantial and emit a photon from the T_1 state (after nuclear geometry relaxation).
- emit a photon from the S_A excited state or from a lower-energy S_{A-x} state above S_1 that is populated upon IC. This does not follow Kasha's rule and usually occurs when the S_1 state is largely separated from the rest of the excited states.
- follow an alternative route: the system can undergo ISC from the populated S_{A-x} to a triplet T_B excited state whose lifetime usually allows geometrical relaxation and/or IC. Eventually, emission of light (phosphorescence) followed by non-radiative relaxation to the ground state geometry will follow.

Those different relaxation routes can be competing and thermal population of a state can also occur (Figure 2). Other external competing phenomena such as energy transfer between fluorophores or other molecules (fluorescence inhibitors) may also take place in the excited state. This competition between processes can reduce the number of emitted photons compared to the number of absorbed photons (quenching of the luminescence). Since the excited triplet state is stabilized by additional exchange energy compared to the excited singlet state, the energy released by phosphorescence is lower than in the fluorescence process when the emission occurs from the lowest excited state. The phosphorescence emission is in that case shifted towards longer wavelengths relative to the fluorescence emission (bathochromic shift). Furthermore, the phosphorescent decay ranges between 10^{-6} s and 10 s, while a decay of 10^{-10} s to 10^{-7} s is measured for the fluorescence.²² Because of this decay time, phosphorescence has the characteristic to be eye-perceived upon extinction of the light source if the wavelength is in the visible region.

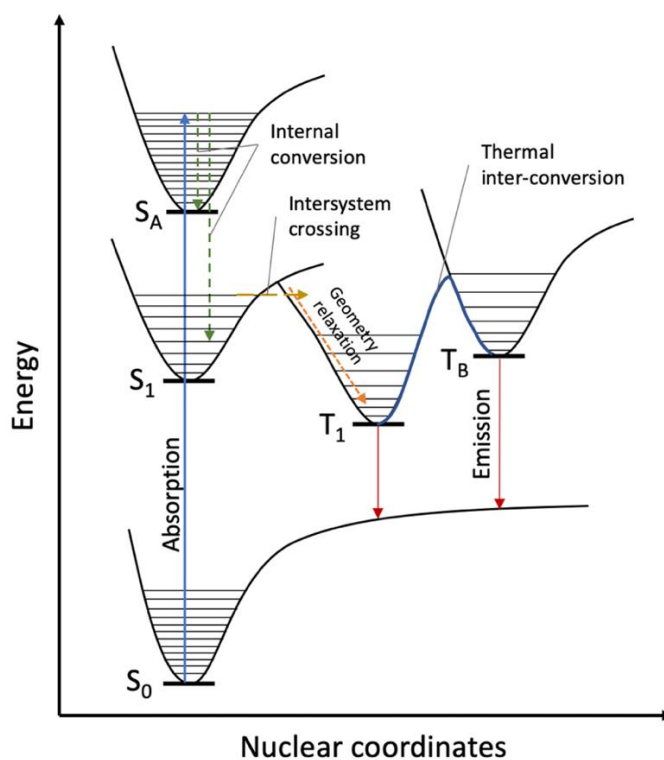


Figure 2 – Jablonski-type schematic energy diagram of a closed-shell molecule with a singlet ground state S_0 . The singlet and triplet excited states, S_n and T_n , with $n = 1, 2, \dots$ are represented by bold lines. The thin lines represent the lower lying vibrational sub-levels of each state. The potential energy surfaces are given as a function of nuclear coordinate modifications.

The second and third row transition metal containing systems have been intensively studied. The heavy atom effect is indeed rendering those compounds really attractive for emission properties.^{7,8} They have the advantage, compared to organic phosphors, that the efficiency of the phosphorescence is increased. The lower-lying triplet excited states of a coordination complex have in most of the cases half-life times several orders of magnitude shorter than in organic molecules due to the much higher rate of spontaneous emission. For example, the emissive triplet state of naphthalene has a half-life duration of 2 s, while that of the organometallic $[\text{Ru}(\text{bpy})_3]^{2+}$ complex is approximately 1 μs .⁹ They do offer a variety of excited states in which the ligands play an important role. The electronic transitions that can occur can be classified into three major families:

- Metal-centered transitions (MC). These transitions are occurring between metal-centered levels (d orbitals). They are called d-d transitions and often result in low intensity bands because of the selection rules. They are located in the visible or near-IR ($12000 - 28000 \text{ cm}^{-1} / 1.5 - 3.5 \text{ eV}$).
- Transitions with a large charge transfer character (CT) which include:
 - Ligand to metal charge transfer (LMCT) or metal to ligand charge transfer (MLCT). The corresponding absorption bands can be strong in intensity and are also localized in the UV or in the visible region of the spectra. MLCT are often observed in transition metals whose electronic configurations are d^6 , d^8 or d^{10} , with metals having a large reducing character and when ligands have low energy orbitals with σ^* or π^* -acceptor character such as poly-pyridine ligands.
 - Ligand to ligand charge transfer (LLCT) or ligand to another type of ligand charge transfer (LL'CT).

In general, the electronic transitions in a metallic complex containing conjugated or aromatic ligands are enlarged to:

- Transitions between levels mainly localized on ligands. These are the $n \rightarrow \pi^*$ or $\pi \rightarrow \pi^*$ transitions. The absorption bands corresponding to the $\pi \rightarrow \pi^*$ transitions are relatively intense. They are generally located in the UV range.

Metal complexes with $4d^6$, $5d^6$ or $5d^8$ electronic configurations are extensively used for optoelectronic applications (with Ru, Re, Os, Ir, Pt or Au).¹⁰ The efficiency of the singlet-triplet ISC is the key mechanism in photophysical properties. It is due to the heavy atom effects fostered by the important atomic SOC constant of those metals (between 400 to 4000 cm^{-1} depending on the metal ion and its electronic state).¹¹ The resulting triplet emissive states, most

of the time $^3\text{MLCT}$ states, are usually highly emissive for the same reason. It makes these systems attractive for several types of applications such as organic light-emitting diodes (OLEDs), light-emitting electrochemical cells, photovoltaic cells, chemical sensors, or bio-imaging.^{12,13} The disadvantage of these compounds is that they are composed of metals with low to very low abundance in the Earth's crust and are thus really expensive and generate geopolitical tensions (Table 2). For this reason, creating photoactive molecular complexes composed of abundant elements instead (like Cu, Fe or Cr) is an appealing solution. Cu(I) containing systems are for some of them MLCT emitters with an absence of d-d excitations due to the $3d^{10}$ electronic configuration. The quite low atomic SOC (between 200 to 900 cm^{-1} depending on the electronic structure)^{14,15} that decreases the ISC and the spontaneous emission probability has some advantages since it allows for a competition between different processes like ISC, reverse inter-system-crossing (RISC) or thermal activation thanks to the longer life lifetime of the excited states.

Table 2 – Typical abundance, in mass percent, of transition metals available in the earth's crust.^{10,16}

| | |
|---|--------------------------|
| Fe | 4.7 % |
| Cr | 0.01 % |
| Ni | 7.10^{-3} % |
| Zn | 7.10^{-3} % |
| Ce | 6.10^{-3} % |
| Cu | 5.10^{-3} % |
| Co | 2.10^{-3} % |
| Gd, Dy, Er, Yb, U, Eu, W, Mo, Tb, Tl, Lu, Tm | $> 10^{-3}; < 10^{-5}$ % |
| Ag, Pd, Pt, Au, Os, Ru, Ir, Re | $> 10^{-5}$ % |

II.2 – Thermally Activated Delayed Fluorescence - TADF

Among all possible de-excitation schemes, a competition between several paths can occur. This is the case in thermally activated delayed fluorescence (TADF). Intense research has been conducted on TADF, both in organic and in coordination chemistry. It offers a large range of emission properties.¹⁷ The concept of TADF is not new, as it has been reported for the first time by Perrin et al. in 1929,¹⁸ and was studied by a few others during the 20th century.¹⁹ In 2012,

Adachi and coworkers²⁰ used the TADF mechanism to create an efficient OLED without phosphorescence signal, which generated an extensive attention in this competitive domain. This topic is currently studied by several research groups around the world.

A simplified description of the TADF mechanism is given in Figure 3. In a TADF emitter, the S_A and T_B energy levels which are usually S_1 and T_1 are sufficiently coupled to allow an ISC between the two states. If the SOC is sufficient, the ISC time scale to populate T_B will become competitive with the reverse thermal ISC process, i.e., repopulation of S_A from T_B and eventually fluorescence. The TADF occurs when the energy separation (ΔE_{ST}) and the associated thermal energy barrier are sufficiently small. Nevertheless, to obtain interesting TADF properties at room temperature, ΔE_{ST} should be lower than $\sim 1000 \text{ cm}^{-1}$ (125 meV).²² This small energy gap allows for a RISC from the T_A state to the S_B state in a thermally activated process. Once in the S_A state, the de-excitation to the ground state eventually occurs via fluorescence and associated non-radiative relaxation paths. Since RISC is a slow process, the fluorescence from harvested triplet excitons occurs with a latency compared to direct fluorescence. Therefore, this fluorescence is called thermally-activated delayed fluorescence. At room temperature, the compounds exhibiting such a property are leading to a high quantum yield of emission and emission decay time of the order of few microseconds (Figure 3). For organic systems exhibiting TADF, no direct fluorescence is generally observed.²¹ Since the SOC is small in organic molecules, phosphorescence from the triplet states are also rarely observed. In metal-containing complexes, phosphorescence can also take place when the temperature is too small to induce RISC. Indeed, at low temperature, the system is trapped in the triplet excited state and undergoes phosphorescence only if the SOC is sufficient. It becomes a competing deactivation process to TADF at higher temperature. The emission lifetime is thus strongly influenced by the temperature, ranging from a few microseconds when the TADF process dominates to hundreds of microseconds up to milliseconds at low temperature. The reduction of ΔE_{ST} has a leading effect on the TADF lifetime decay. However, this is no more the case when ΔE_{ST} is lower than 25-40 meV ($\approx 200 - 300 \text{ cm}^{-1}$); in this situation, the El Sayed's rule^{22,23} shows that the singlet excited state and the triplet excited state have very similar charge transfer/local exciton character leading to the reduction of the RISC coupling. Depending on the targeted applications, the radiative decay should be fast as for OLED applications or slow as for lighting and sensing.

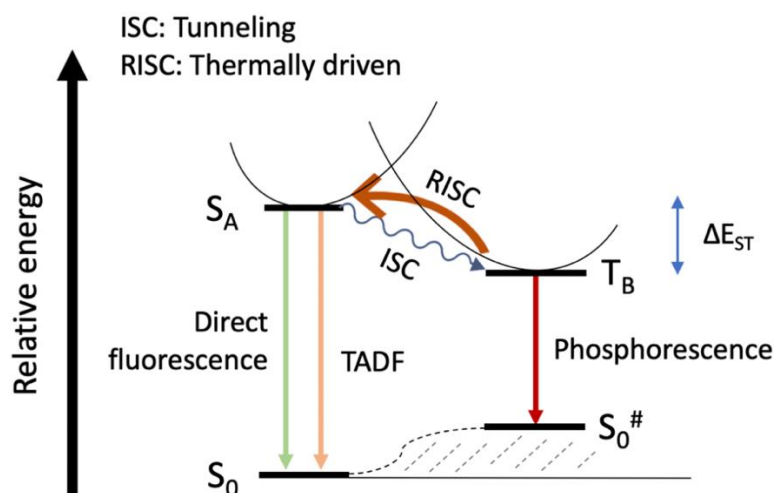


Figure 3 – Simplified mechanism of a phosphorescent/TADF emitter. The energy ΔE_{ST} is the barrier between the coupled triplet and singlet states. The ISC rate increases with SOC, which induces a competition between ISC and fluorescence (in green). For moderate SOC, RISC can be thermally driven leading to TADF (in orange). RISC is in competition with phosphorescence (red). $S_0^\#$ represents the transient state on the potential energy surface (PES) of S_0 at the triplet state T_B geometry. The system relaxes by non-radiative means from $S_0^\# \rightarrow S_0$.

Within this TADF framework, the lifetime variation as a function of the temperature follows the relation:²²

$$\tau(obs) = \frac{3 + \exp\left(-\frac{\Delta E_{ST}}{k_B T}\right)}{3k(T_A) + k(S_B) \exp\left(-\frac{\Delta E_{ST}}{k_B T}\right)} \quad \text{Eq. 1}$$

where $\tau(obs)$ is the observed lifetime at a given temperature, $k(T_A)$ and $k(S_B)$ the decay rates of the excited state T_A and S_B , respectively. k_B , the Boltzmann constant, T the temperature of the system and ΔE_{ST} the energy difference between the T_A and S_B state.

The lifetime of the S_A and T_B states are directly related to their decay rate by $k(T_A) = 1/\tau(T_A)$ and $k(S_B) = 1/\tau(S_B)$. TADF is observed for organic molecular systems²⁴ and for coordination complexes. An example of TADF-related photophysical properties of a Cu(I) complex is depicted in Figure 4.²⁵

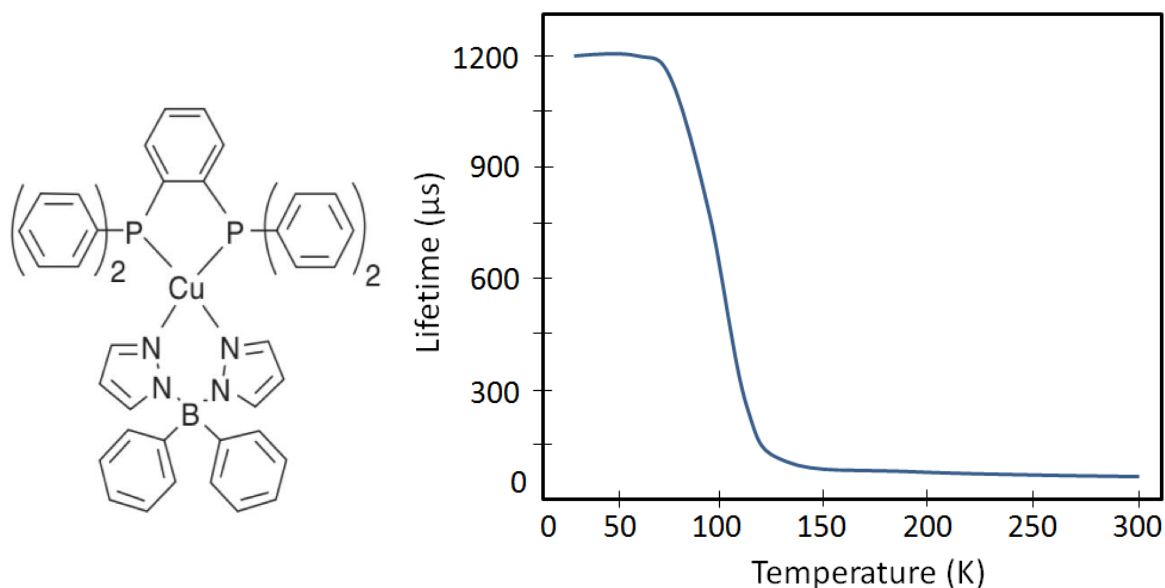


Figure 4 – Left: molecular representation of the Cu(dppb)(pz₂Bph₂) complex. Right: emission lifetime $\tau(\text{obs})$ versus temperature. Adapted from reference 26.

III – Cu(I) complexes

Copper is a transition metal naturally present and abundant in earth's crust (see Table 2).²⁷ In solution, it is generally found in two oxidation degrees: +I and +II. Due to a special combination of electronic and structural characteristics (e.g. flexible geometric structure, chromophoric character, luminescence, electrochemical behavior), Cu(I) complexes have stimulated a great interest in several fields such as supramolecular chemistry, molecular machinery, catalysis, ultrafast spectroscopy, solar energy conversion, opto-electronics and luminescence.^{25-a)} As stated before, the optical properties of Cu(I) complexes are directly related to their d¹⁰ electronic configuration. This configuration favors an electronic transition from the metal to ligands (MLCT), the formally populated ligand orbitals being often π anti-bonding orbitals (π^*). The Cu(I) ionic metal center is thus used to build coordination complexes. Several series of complexes are presenting small singlet-triplet energy gap (ΔE_{ST}) often leading to TADF emission upon harvesting of the triplet excitons, which is of great interest in OLED applications. These emission properties that are function of temperature have also other applications like lighting, optical thermometry, sensing and imaging for instance.

Commonly, copper complexes adopt a (distorted-)tetrahedral geometry around the Cu(I) atom (Figure 5). Unfortunately, pseudo-tetrahedral assemblies often exhibit low luminescence due to the important non-radiative de-excitation mechanisms produced by the geometrical distortion

that can occur in the excited states. To overcome this problem, an interesting way to design highly luminescent Cu(I) complexes using a TADF mechanism is to introduce bulky chromophoric ligands around the Cu(I), thus, limiting the possibilities of geometric reorganization and protecting the metallic center from its environment. Other possible ways include the preparation of coordination complexes where the Cu(I) metal center exhibits a trigonal-planar or a linear geometry with rigid ligands to hamper the geometric distortion in the excited states. It is also possible to build complex polynuclear structures of Cu(I) where the metal centers are introduced in complex polycyclic and geometrically constrained supramolecular structures.

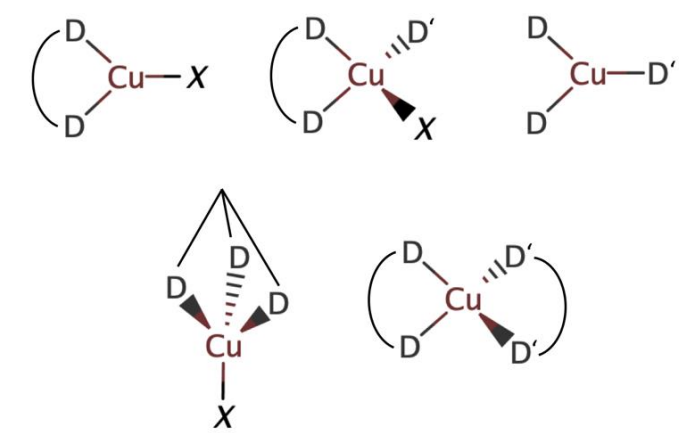


Figure 5 – Usual coordination modes for a Cu(I) complex. Here X corresponds to a halide atom and D, D' refer to poly- and mono-dentate ligand, respectively. A non-halide Cu(I) complex can either be cationic or neutral depending on the coordinating ligands. Adapted from reference 28.

IV – Coordination-driven supramolecular chemistry (CDS)

Among all possible synthetic routes, supramolecular chemistry consisting in the association of precursor molecules to create new assemblies has emerged recently. It involves the creation of weak interactions like electrostatic forces, hydrogen bonds, van der Waals forces or hydrophobic interactions between molecules. These interactions play an important role in various fields. They are for example the reason of the double helix shape of DNA (deoxyribonucleic acid). These interactions were theorized by the chemist Fischer in the 19th century.²⁹ The first statement of supramolecular chemistry was found in the Webster dictionary in 1903,³⁰ and it was then redefined in 1978 by the chemist Lehn (Figure 6).³¹ Nowadays, supramolecular chemistry is widely explored in various fields like molecular machines,³²

molecular sensors,³³ gas adsorption,³⁴ nanoreactors,³⁵ chemical catalysis³⁶ and many others. It can be seen as a cross-disciplinary science, which relies on organic chemistry, coordination chemistry, polymer chemistry, material science, and biological sciences.³⁷

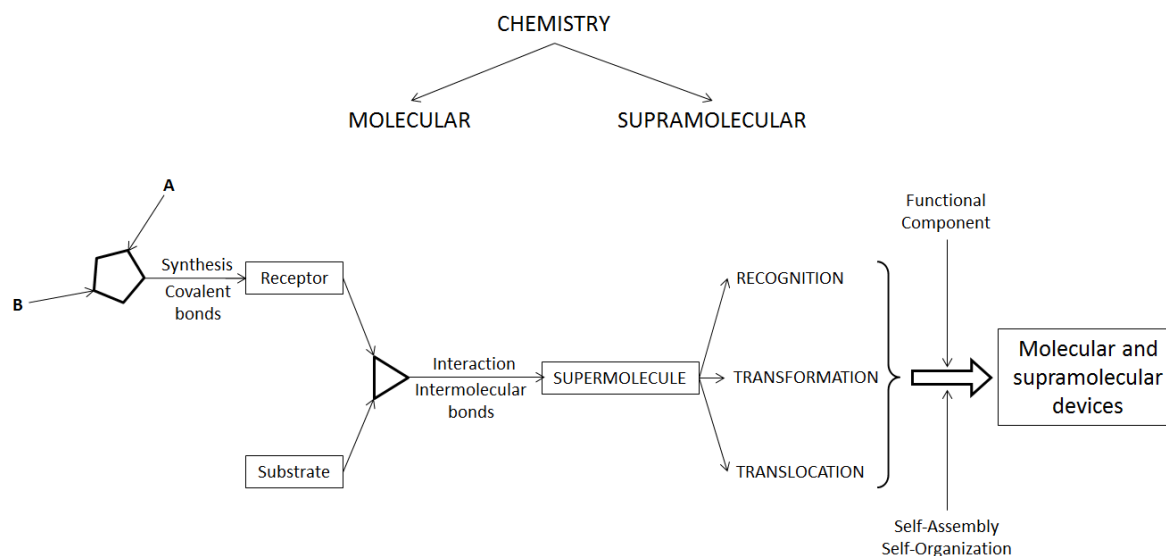


Figure 6 – From molecular chemistry to supramolecular chemistry with molecules, supermolecules, and (supra)molecular devices according to Lehn.³⁸

One of the important concepts of supramolecular chemistry is the auto-assembly faculty,³⁹ which is the ability of individual components to establish, *via* intermolecular interactions the generation of functional assemblies. In that context, Cu(I) copper complexes used in supramolecular chemistry are generally performing poorly, notably because of the insufficient rigidity of the molecular clips and precursors.

Supramolecular chemistry based on coordination (coordination-driven supramolecular chemistry, CDS) is based on a similar synthetic scheme but the association of molecular elements is done in that case *via* coordination bonds between pre-defined building-blocks. It is the molecular recognition which is the driving force in the synthetic mechanism.⁴⁰ Yields are usually quite high for this one-pot synthesis in which the precursors have a pre-determined connectivity. In this field, the work of Stang,⁴¹ Fujita,⁴² Scheer,⁴³ Nitschke,⁴⁴ Lehn,⁴⁵ Severin,⁴⁶ Ward,⁴⁷ Raymond,⁴⁸ Clever,⁴⁹ and others⁵⁰ showed, in an independent manner, that a huge variety of metallic complexes and connecting ligands can be assembled to create supramolecular architectures. A number of supramolecular derivatives have been synthesized from “molecular clips” based on metal ions such as Pt(II)⁵¹, Pd(II)⁵², Au(I)⁵³ and Ag(I)⁵⁴ with

rigid ligands. Interestingly, a limited number of supramolecular derivatives based on the Cu(I) ion has been developed.⁵⁵ Indeed, the Cu(I) ion is, *a priori*, not really suitable to be included in a supramolecular association process guided by coordination chemistry. The main reasons are that Cu(I)-ligand bonds are usually quite labile in solution and that the coordination sphere of Cu(I) shows usually a conformational flexibility that prevents directional interactions.

However, the work carried out in the group of Lescop, at INSA Rennes, has shown that it is possible to circumvent this limitation by using dimeric Cu(I) precursors based on phosphol assembler ligands in which the inter-metallic distances are relatively small. This type of pre-organized and stable copper(I) precursor complexes have been successfully used to synthesize supramolecular complexes.^{39-f,56} The group has enlarged the concept to polyphosphinyl compounds to conceive large assemblies by supramolecular chemistry guided by coordination. Interestingly, contrarily to the organophosphate series, most of the phosphinyl-based supramolecular systems synthesized by Lescop and coworkers are luminescent. Among them, some are presenting thermochromic and mechanochromic luminescent properties. These interesting optical properties which are attributed to TADF in some cases are due to a combination of factors for which computational studies are highly valuable to understand the electronic features which are driving such behaviors.

V – Computational studies of copper molecules

The Density Functional Theory (DFT) and Time-Dependent DFT (TD-DFT) methods have currently become universal tools to apprehend and predict the behavior of an extensive variety of chemical, physical, and biological phenomena, including in the coordination chemistry field.⁵⁷ The DFT formalism describes the different electronic states of atoms and molecules from the three-dimensional electron density. Such a paradigm allows DFT to be several orders of magnitude faster than the wave function theory (WFT) for a reasonable accuracy level. Indeed, the WFT methods which are providing more quantitative results are not affordable to treat large (poly-) metallic systems (geometry optimization, description of excited states, excited state relaxation...).

Nowadays, a large number of papers with DFT calculations dealing with copper systems have been devoted to the study of a wide range of properties. They offer reliable information on the geometric and electronic structures, the electronic absorption and emission spectra, and

vibrational spectra of copper coordination complexes. Several benchmark articles deal with DFT computational protocols applied to Cu(I) and Cu(II) containing systems. The density functional (DF) and basis set combination is the key factor to acquire an overall satisfactory comprehension of the properties of Cu(I) and Cu(II) centers for a reasonable computational cost.⁵⁸ The size of the studied complexes is the element which will drive the choice of the theoretical methodology.

In the paper of Sousa in reference 58, 18 Density Functionals (DFs) and 14 different basis sets were tested (selection of DFs and basis sets in Table 3) for a total of 119 combinations of functional/basis set to determine the geometric properties of a set of 50 copper complexes. 24 Cu(I) and 26 Cu(II) systems were investigated. Globally, as the complexity of the DFT method increases, the better is the description of the systems compared to experimental data. Certain DFs stand out:

- double Hybrid-Generalized Gradient Approximation (DH-GGA), notably the mPW2PLYPD density functional associated with the 6-31+G(d) basis set.
- long range Corrected-Hybrid-GGA (LC-H-GGA), like the LC-wPBE similarly coupled with the 6-31+G(d) basis set.

They are both providing the finest description of the complexes. It is important to highlight that the PBE density functional, which lies in the pure-GGA formalism is also giving interesting results. The same remark goes for the hybrid-GGA (H-GGA) B3LYP. With the dataset used, the DFs with added dispersion correction such as the DFT-D and DFT-D3 (from S. Grimme and co-workers⁵⁹) does not enhance the precision of the computational results. Here, we present some examples of copper-ligand distances compared to experimental data (mean signed error – MSE –, compared to the Cambridge database) as a function of the functional, as averaged over the whole basis set from reference 58:

- Cu-ligand bond (average):
 - GGA-BLYP: +0.058 Å
 - H-GGA-B3LYP: +0.044 Å
 - HM-GGA-M06: +0.016 Å
- Cu-N bond specifically:
 - GGA-BLYP: +0.052 Å
 - H-GGA-B3LYP: +0.040 Å
 - HM-GGA-M06: +0.029 Å

Selected MSE in the ligand-Cu-ligand angles ($^{\circ}$) for copper(I) complexes are:

- Ligand-Cu-ligand angle (average):
 - GGA-BLYP: +4.4 $^{\circ}$
 - H-GGA-B3LYP: +4.4 $^{\circ}$
 - HM-GGA-M06: +4.0 $^{\circ}$

Table 3 – Description of selected density functionals and basis sets involved in reference 58.

| Functional | Year | Type | Basis set | Type |
|------------|------|----------|--------------|-----------------|
| BLYP | 1988 | GGA | 6-31G(d) | All electron |
| BP86 | 1986 | GGA | 6-31G(d,p) | All electron |
| PBE | 1996 | GGA | 6-31+G(d) | All electron |
| B3LYP | 1994 | M-GGA | 6-31+G(d,p) | All electron |
| B3LYP-D3 | 2010 | M-GGA | SDD | Small core |
| M06 | 2007 | HM-GGA | TZV | Triple- ζ |
| TPSSH | 2003 | HM-GGA | TZVP | Triple- ζ |
| B2PLYP | 2006 | DH-GGA | cc-pVTZ | Triple- ζ |
| mPW2PLYP | 2006 | DH-GGA | aug-cc-pVTZ | Triple- ζ |
| CAM-B3LYP | 2004 | LC-H-GGA | 6-311G(d,p) | Triple- ζ |
| wB97XD | 2008 | LC-H-GGA | 6-311+G(d,p) | Triple- ζ |

In another work of Ansbacher *et al.* in reference 60, several copper (I) coordination complexes with thiophenyl ligands were calculated with several types of basis sets with the objective to establish a consistent level of prediction for Cu(I) complexes using PBE0, a hybrid-GGA functional.

From the work of Quintal *et al.* in reference 61, the performance and accuracy of a large selection of DFT functionals for transition metal reaction profiles were evaluated. From their point of view, there is not a single “best functional” for the transition-metal reactions, but there is a group of several hybrid-GGA functionals like PBE0, B1B95 or PW6B95 that can globally achieve the same precision. The optimal Hartree-Fock exact exchange percentages needed in

hybrid functionals depends on the class of systems considered. The use of hybrid-GGA density functionals appears to be suitable, notably PBE0.

Regarding TD-DFT calculations and optical simulations, the paper of Herres-Pawlis and coworkers, reference 57, reports a computational benchmarking for the structural and the optical properties for a bis(chelate)copper(I)guanidine–quinoline complex. They found that the exact Hartree-Fock exchange quantity used in the functionals and the nature of the basis set have a huge influence on their results. A shift of the metal-to-ligand bands up to 1.0 eV is calculated in the absorption spectrum depending on the quantity of exact exchange used. The DF/basis set combination that better fits the experimental data is the BP86/6-311G(d) and B3LYP/def2-TZVP. Moreover, their TD-DFT excitation energies diverge from the Many Body Perturbation Theory (MBPT) results by about 0.5 eV. Selected results are collected in Table 4.

Table 4 – Percentage difference of selected distances between experimental and theoretical results for Cu(I)-N bonds from reference 57.

| Functional | Basis set | Cu-N _{imine, guanine} | Cu-N _{quinine} | Cu-N _{amine} |
|-------------|-----------|--------------------------------|-------------------------|-----------------------|
| GGA BP86 | | 1.1 % | 1.3 % | 1.4 % |
| GGA BLYP | def2-SVP | 3.2 % | 2.4 % | 1.8 % |
| H-GGA B3LYP | | 3.1 % | 3.6 % | 0.9 % |

VI – Methodology and software

On the basis of these computational benchmarking and tests performed on a first series of large systems, the best DF/basis set combination that could be afforded to treat the ground and excited states is PBE0/SVP. For sake of comparison, all studied copper compounds will be treated at this level of theory as a first step. The Gaussian 2016 software⁶² A.03 revision was used for all geometry optimizations and the TD-DFT calculations. The Amsterdam Density Functional (ADF 2019) software from Software for Chemistry & Materials B.V. (SCM) has been used for the SOC calculations.⁶³ The PBE0 has been settled on the basis of the pure-GGA functional proposed by Perdew, Burke and Ernzerhof (PBE) in 1994 and adapted into a hybrid functional by Adamo (H-GGA).⁶⁴ This functional integrates 25% of Hartree-Fock exact exchange and 75% of DFT exchange. The basis set used for all systems is the Split Valence Polarization (SVP) from Ahlrichs et al.⁶⁵ Unfortunately, it was not conceivable to use a higher level of DFT, using LC-H-GGA or DH-GGA functionals as proposed in reference 58 or larger basis sets (reference 61) because of the large size of the studied copper complexes.

The protocol employed for the upcoming computational studies is the following:

- Geometry optimization in the ground state.
- Calculations of the absorption spectra (vertical TD-DFT), and vertical triplet states.
- Geometry optimization in the excited states (TD-DFT).
- Rationalization of the electronic and geometric properties.

The simulated absorption spectra were convoluted by using the GaussView software. The calculation of the molar attenuation coefficients is achieved as follows:

$$\epsilon(\tilde{\nu}) = \sum_{i=1}^n \epsilon_i(\tilde{\nu}) = \sum_{i=1}^n \left(1.3063 \cdot 10^8 \frac{f_i}{\sigma} \exp \left[- \left(\frac{\tilde{\nu} - \tilde{\nu}_i}{\sigma} \right)^2 \right] \right) \quad \text{Eq. 2}$$

where i runs from the first to the n^{th} electronic excitation. f is the dimensionless oscillator strength, σ the Full-Width at Half Maximum (FWHM), $\tilde{\nu}_i$ the excitation energy corresponding to the electronic excitation of interest, and ϵ_i the molar attenuation coefficient.

The evaluation of the atomic percentage contribution on each molecular orbital was performed with the method proposed by Ros and Schuit.⁶⁶

-
- ¹ Kitai, A. *Luminescent Materials and Applications*; Wiley series in materials for electronic and optoelectronic applications. John Wiley: Chichester, England; Hoboken, NJ, 2008.
- ² Rendell, D. *Fluorescence and Phosphorescence Spectroscopy*. Wiley, 1997.
- ³ Luminescence, fluorescence et phosphorescence des minéraux : <http://www.fluomin.org/histoire/XIX.php>
- ⁴ Brouwer, A. M. Standards for Photoluminescence Quantum Yield Measurements in Solution. *Pure Appl. Chem.* 2011, 83, 2213–2228. doi:10.1351/PAC-REP-10-09-31.
- ⁵ [https://chem.libretexts.org/Bookshelves/Physical_and_Theoretical_Chemistry_Textbook_Maps/Supplemental_Modules_\(Physical_and_Theoretical_Chemistry\)/Spectroscopy/Fundamentals_of_Spectroscopy/Selection_Rules](https://chem.libretexts.org/Bookshelves/Physical_and_Theoretical_Chemistry_Textbook_Maps/Supplemental_Modules_(Physical_and_Theoretical_Chemistry)/Spectroscopy/Fundamentals_of_Spectroscopy/Selection_Rules)
- ⁶ Kasha, M. Characterization of Electronic Transitions in Complex Molecules. *Discuss. Faraday Soc.* 1950, 9, 14–19.
- ⁷ Yam, V. W.-W.; Wong, K. M.-C. Luminescent metal complexes of d⁶, d⁸ and d¹⁰ transition metal centers. *Chem. Comm.* 2011, 47, 11579. doi:10.1039/c1cc13767k.
- ⁸ Gareth Williams, J. A.; Develay, S.; Rochester, D. L.; Murphy, L. Optimizing the Luminescence of Platinum (II) Complexes and Their Application in Organic Light Emitting Devices (OLEDs). *Coord. Chem. Rev.* 2008, 252, 2596–2611. doi: 10.1016/j.ccr.2008.03.014.
- ⁹ Montalti, M.; Credi, A.; Prodi, L.; Gandolfi, M. T.; Credi, A.; Prodi, L.; Gandolfi, M. T. *Handbook of Photochemistry*; CRC Press, 2006. doi:10.1201/9781420015195.
- ¹⁰ Wenger, O. S. Photoactive Complexes with Earth-Abundant Metals. *J. Am. Chem. Soc.* 2018, 140, 13522–13533. doi:10.1021/jacs.8b08822.
- ¹¹ Clancy, J. P.; Chen, N.; Kim, C. Y.; Chen, W. F.; Plumb, K. W.; Jeon, B. C.; Noh, T. W.; Kim, Y.-J. Spin-Orbit Coupling in Iridium-Based 5 d Compounds Probed by x-Ray Absorption Spectroscopy. *Phys. Rev. B* 2012, 86, 195131. doi:10.1103/PhysRevB.86.195131.
- ¹² Zhi, J.; Zhou, Q.; Shi, H.; An, Z.; Huang, W. Organic Room Temperature Phosphorescence Materials for Biomedical Applications. *Chem. Asian J.* 2020, 15, 947–957. doi:10.1002/asia.201901658.
- ¹³ He, Z.; Gao, H.; Zhang, S.; Zheng, S.; Wang, Y.; Zhao, Z.; Ding, D.; Yang, B.; Zhang, Y.; Yuan, W. Z. Achieving Persistent, Efficient, and Robust Room-Temperature Phosphorescence from Pure Organics for Versatile Applications. *Adv. Mater.* 2019, 31, 1807222. doi:10.1002/adma.201807222.
- ¹⁴ Lewis, W. B.; Mann, J. B.; Liberman, D. A.; Cromer, D. T. Calculation of Spin–Orbit Coupling Constants and Other Radial Parameters for the Actinide Ions Using Relativistic Wavefunctions. *J. Chem. Phys.* 1970, 53, 809–820. doi:10.1063/1.1674064.
- ¹⁵ Koseki, S.; Matsunaga, N.; Asada, T.; Schmidt, M. W.; Gordon, M. S. Spin–Orbit Coupling Constants in Atoms and Ions of Transition Elements: Comparison of Effective Core Potentials, Model Core Potentials, and All-Electron Methods. *J. Phys. Chem. A* 2019, 123, 2325–2339. doi:10.1021/acs.jpca.8b09218.
- ¹⁶ Holleman, A. F.; Wiberg, N. *Lehrbuch der Anorganischen Chemie*. Walter de Gruyter, Berlin, 2007. doi:10.1515/9783110206845.
- ¹⁷ Dias, F. B.; Penfold, T. J.; Monkman, A. P. Photophysics of Thermally Activated Delayed Fluorescence Molecules. *Methods Appl. Fluoresc.* 2017, 5, 012001. doi:10.1088/2050-6120/aa537e.

- ¹⁸ Delorme, R.; Perrin, F. Durées de fluorescence des sels d'uranyle solides et de leurs solutions. *J. Phys. Radium* 1929, 10, 177–186. doi:10.1051/jphysrad:01929001 005017700.
- ¹⁹ a) Lewis, G. N.; Lipkin, D.; Magel, T. T. Reversible Photochemical Processes in Rigid Media. A Study of the Phosphorescent State. *J. Am. Chem. Soc.* 1941, 63, 3005–3018. doi:10.1021/ja01856a043. b) Parker, C. A.; Hatchard, C. G. Triplet-Singlet Emission in Fluid Solutions. Phosphorescence of Eosin. *Trans. Farad. Soc.* 1961, 57, 1894. doi:10.1039/TF9615701894.
- ²⁰ Uoyama, H.; Goushi, K.; Shizu, K.; Nomura, H.; Adachi, C. Highly Efficient Organic Light-Emitting Diodes from Delayed Fluorescence. *Nature* 2012, 492, 234–238. doi:10.1038/nature11687.
- ²¹ Penfold, T. J.; Dias, F. B.; Monkman, A. P. The Theory of Thermally Activated Delayed Fluorescence for Organic Light Emitting Diodes. *Chem. Comm.* 2018, 54, 3926–3935. doi:10.1039/C7CC09612G.
- ²² Yersin, H. Highly Efficient OLEDs: Materials Based on Thermally Activated Delayed Fluorescence. Wiley-VCH Verlag GmbH & Co. KGaA, Germany, 2018. doi:10.1002/9783527691722.
- ²³ El-Sayed, M. A. Spin-Orbit Coupling and the Radiationless Processes in Nitrogen Heterocyclics. *J. Chem. Phys.* 1963, 38, 2834–2838. doi:10.1063/1.1733610.
- ²⁴ Wong, M. Y.; Zysman-Colman, E. Purely Organic Thermally Activated Delayed Fluorescence Materials for Organic Light-Emitting Diodes. *Adv. Mater.* 2017, 29, 1605444. doi:10.1002/adma.201605444.
- ²⁵ a) Czerwieńiec, R.; Leitl, M. J.; Homeier, H. H. H.; Yersin, H. Cu(I) Complexes – Thermally Activated Delayed Fluorescence. Photophysical Approach and Material Design. *Coord. Chem. Rev.* 2016, 325, 2–28. doi:10.1016/j.ccr.2016.06.016. b) Hamze, R.; Peltier, J. L.; Sylvinson, D.; Jung, M.; Cardenas, J.; Haiges, R.; Soleilhavoup, M.; Jazzar, R.; Djurovich, P. I.; Bertrand, G.; et al. Eliminating Nonradiative Decay in Cu(I) Emitters: 99% Quantum Efficiency and Microsecond Lifetime. *Science* 2019, 363, 601–606. doi:10.1126/science.aav2865. c) Li, X.; Zhang, J.; Zhao, Z.; Yu, X.; Li, P.; Yao, Y.; Liu, Z.; Jin, Q.; Bian, Z.; Lu, Z.; et al. Bluish-Green Cu(I) Dimers Chelated with Thiophene Ring-Introduced Diphosphine Ligands for Both Singlet and Triplet Harvesting in OLEDs. *ACS Appl. Mater. Interfaces* 2019, 11, 3262–3270. doi:10.1021/acsami.8b15897.
- ²⁶ Czerwieńiec, R.; Yersin, H. Diversity of Copper(I) Complexes Showing Thermally Activated Delayed Fluorescence: Basic Photophysical Analysis. *Inorg. Chem.* 2015, 54, 4322–4327. doi:10.1021/ic503072u
- ²⁷ Hanson, B. Geology: Copper in the Crust. *Science* 2008, 319, 1737c–1737c. doi:10.1126/science.319.5871.1737c.
- ²⁸ Bergmann, L.; Braun, C.; Nieger, M.; Bräse, S. The coordination- and photochemistry of copper(I) complexes: variation of N^N ligands from imidazole to tetrazole. *Dalton Trans.* 2018, 47, 608–621. doi:10.1039/c7dt03682e.
- ²⁹ Fischer, E. Influence of configuration on the action of enzymes. *Berichte der Deutschen Chemischen Gesellschaft zu Berlin* 1894, 27, 2985–93. doi:10.1002/cber.18940270364.
- ³⁰ Neilson, W. A.; Knott, T. A.; Carhart, P. W. Webster's New International Dictionary - Second Edition Unabridged. G. & C. Merriam Company, Springfield, Mass, 1937.
- ³¹ a) Lehn, J. M. Cryptates: Inclusion Complexes of Macropolycyclic Receptor Molecules. *Pure Appl. Chem., PAC* 1978, 50, 871–892. doi:10.1351/pac197850090871. b) Lehn, J.-M. Supramolecular Chemistry - Scope and Perspectives Molecules, Supermolecules, and Molecular Devices (Nobel Lecture). *Angewandte Chem. Int. Ed.* 1988, 27, 89–112. doi:10.1002/anie.198800891.

- ³² a) Warnan, J.; Pellegrin, Y.; Blart, E.; Odobel, F. Supramolecular Light Harvesting Antennas to Enhance Absorption Cross-Section in Dye-Sensitized Solar Cells. *Chem. Comm.* 2011, 48, 75–677. doi:10.1039/C1CC16066D. b) Sauvage, J.-P. From Chemical Topology to Molecular Machines (Nobel Lecture). *Angewandte Chem. Int. Ed.* 2017, 56, 11080–11093. doi:10.1002/anie.201702992.
- ³³ a) Palacios, M. A.; Nishiyabu, R.; Marquez, M.; Anzenbacher, P. Supramolecular Chemistry Approach to the Design of a High-Resolution Sensor Array for Multianion Detection in Water. *J. Am. Chem. Soc.* 2007, 129, 7538–7544. doi:10.1021/ja0704784. b) Resendiz, M. J. E.; Noveron, J. C.; Disteldorf, H.; Fischer, S.; Stang, P. J. A Self-Assembled Supramolecular Optical Sensor for NiII, CdII, and CrIII. *Org. Lett.* 2004, 6, 51–653. doi:10.1021/ol035587b. c) Ermakova, E. V.; Bessmertnykh-Lemeune, A. G.; Meyer, M.; Ermakova, L. V.; Tsvadze, A. Yu.; Arslanov, V. V. Supramolecular Assembly of Planar Systems from Modular Molecules with a Given Hydrophilic–Lipophilic Balance: Film Sensors with an Anthraquinone Signal Group. *Prot. Met. Phys. Chem. Surf.* 2018, 54, 6–18. doi:10.1134/S2070205118010057. d) Zhang, P.; Gao, X.; Liu, M.; Liang, L.; Wang, J.; Cui, L.; Zhang, M.; Li, H.; Wang, Y. A New Cucurbit Uril Based Supramolecular Assembly for Sensing Small Organic Solvents and Rapid Adsorption of Reactive Blue 19 Dye. *Inor. Chem. Comm.* 2018, 90, 78–81. doi:10.1016/j.inoche.2018.02.016.
- ³⁴ Rudkevich, D. M. Progress in Supramolecular Chemistry of Gases. *Euro. J. Orga. Chem.* 2007, 2007, 3255–3270. doi:10.1002/ejoc.200700165.
- ³⁵ Cacciapaglia, R.; Di Stefano, S.; Mandolini, L. Effective Molarities in Supramolecular Catalysis of Two-Substrate Reactions. *Acc. Chem. Res.* 2004, 37, 113–122. doi:10.1021/ar020076v.
- ³⁶ a) Hong, C. M.; Bergman, R. G.; Raymond, K. N.; Toste, F. D. Self-Assembled Tetrahedral Hosts as Supramolecular Catalysts. *Acc. Chem. Res.* 2018, 51, 2447–2455. doi:10.1021/acs.accounts.8b00328. b) Meeuwissen, J.; Reek, J. N. H. Supramolecular Catalysis beyond Enzyme Mimics. *Nature Chem.* 2010, 2, 615–621. doi:10.1038/nchem.744. c) Raynal, M.; Ballester, P.; Vidal-Ferran, A.; Leeuwen, P. W. N. M. van. Supramolecular Catalysis. Part 1: Non-Covalent Interactions as a Tool for Building and Modifying Homogeneous Catalysts. *Chem. Soc. Rev.* 2014, 43, 1660–1733. doi:10.1039/C3CS60027K. d) Brown, C. J.; Toste, F. D.; Bergman, R. G.; Raymond, K. N. Supramolecular Catalysis in Metal-Ligand Cluster Hosts. *Chem. Rev.* 2015, 115, 3012–3035. doi:10.1021/cr4001226. e) Kaphan, D. M.; Levin, M. D.; Bergman, R. G.; Raymond, K. N.; Toste, F. D. A Supramolecular Microenvironment Strategy for Transition Metal Catalysis. *Science* 2015, 350, 1235–1238. doi:10.1126/science.aad3087.
- ³⁷ Gale, P. A.; Steed, J. W. *Supramolecular Chemistry: From Molecules to Nanomaterials*. Wiley 2012: Chichester. ISBN: 978-0-470-74640-0.
- ³⁸ Lehn, J.-M. *Supramolecular Chemistry: Concepts and Perspectives: A Personal Account Built upon the George Fisher Baker Lectures in Chemistry at Cornell University and Lezioni Lincee, Accademia Nazionale Dei Lincei* 1995, Roma, Weinheim, New York.
- ³⁹ a) Scheer, M. The Coordination Chemistry of Group 15 Element Ligand Complexes—a Developing Area. *Dalton Trans.* 2008, 33, 4372–4386. doi:10.1039/b718179p. b) Harris, K.; Fujita, D.; Fujita, M. Giant Hollow MnL₂n Spherical Complexes: Structure, Functionalization and Applications. *Chem. Comm.* 2013, 49, 6703–6712. doi:10.1039/C3CC43191F. c) Cook, T. R.; Stang, P. J. Recent Developments in the Preparation and Chemistry of Metallacycles and Metallacages via Coordination. *Chem. Rev.* 2015, 115, 7001–7045. doi:10.1021/cr5005666. d) Xu, L.; Wang, Y.-X.; Chen, L.-J.; Yang, H.-B. Construction of Multiferoceanyl Metallacycles and Metallacages

via Coordination-Driven Self-Assembly: From Structure to Functions. *Chem. Soc. Rev.* 2015, 44, 2148–2167. doi:10.1039/C5CS00022J. d) Yam, V. W.-W.; Au, V. K.-M.; Leung, S. Y.-L. Light-Emitting Self-Assembled Materials Based on D8 and D10 Transition Metal Complexes. *Chem. Rev.* 2015, 115, 7589–7728. doi:10.1021/acs.Chemrev.5b00074. e) Newkome, G. R.; Moorefield, C. N. From 1 → 3 Dendritic Designs to Fractal Supramacromolecular Constructs: Understanding the Pathway to the Sierpiński Gasket. *Chem. Soc. Rev.* 2015, 44, 3954–3967. doi:10.1039/C4CS00234B. f) Lescop, C. Coordination-Driven Syntheses of Compact Supramolecular Metallacycles toward Extended Metallo-Organic Stacked Supramolecular Assemblies. *Acc. Chem. Res.* 2017, 50, 885–894. doi:10.1021/acs.accounts.6b00624. g) Ryu, J. Y.; Lee, J. M.; Van Nghia, N.; Lee, K. M.; Lee, S.; Lee, M. H.; Stang, P. J.; Lee, J. Supramolecular Pt(II) and Ru(II) Trigonal Prismatic Cages Constructed with a Tris(Pyridyl)Borane Donor. *Inorg. Chem.* 2018, 57, 11696–11703. doi:10.1021/acs.inorgchem.8b01830. h) Song, B.; Kandapal, S.; Gu, J.; Zhang, K.; Reese, A.; Ying, Y.; Wang, L.; Wang, H.; Li, Y.; Wang, M.; et al. Self-Assembly of Polycyclic Supramolecules Using Linear Metal-Organic Ligands. *Nature Comm.* 2018, 9, 4575. doi:10.1038/s41467-018-07045-9.

⁴⁰ Gellman, S. H. Introduction: Molecular Recognition. *Chem. Rev.* 1997, 97, 1231–1232. doi:10.1021/cr970328j.

⁴¹ Saha, M. L.; Yan, X.; Stang, P. J. Photophysical Properties of Organoplatinum (II) Compounds and Derived Self-Assembled Metallacycles and Metallacages: Fluorescence and Its Applications. *Acc. Chem. Res.* 2016, 49, 2527–2539. doi:10.1021/acs.accounts.6b00416.

⁴² a) Fujita, M. Metal-Directed Self-Assembly of Two- and Three-Dimensional Synthetic Receptors. *Chem. Soc. Rev.* 1998, 27, 417–425. doi:10.1039/A827417Z. b) Yoshizawa, M.; Ono, K.; Kumazawa, K.; Kato, T.; Fujita, M. Metal-Metal d-d Interaction through the Discrete Stacking of Mononuclear M(II) Complexes (M = Pt, Pd, and Cu) within an Organic-Pillared Coordination Cage. *J. Am. Chem. Soc.* 2005, 127, 10800–10801. doi:10.1021/ja053009f. c) Yoshizawa, M.; Klosterman, J. K.; Fujita, M. Functional Molecular Flasks: New Properties and Reactions within Discrete, Self-Assembled Hosts. *Angew. Chem. Int. Ed.* 2009, 48, 3418–3438. doi:10.1002/anie.200805340. d) Ikemi, M.; Kikuchi, T.; Matsumura, S.; Shiba, K.; Sato, S.; Fujita, M. Peptide-Coated, Self-Assembled M12L24 Coordination Spheres and Their Immobilization onto an Inorganic Surface. *Chem. Sci.* 2010, 1, 68–71. doi:10.1039/C0SC00198H. e) Yamauchi, Y.; Fujita, M. Self-Assembled Cage as an Endo-Template for Cyclophane Synthesis. *Chem. Comm.* 2010, 46, 5897–5899. doi:10.1039/C0CC00963F.

⁴³ a) Fleischmann, M.; Dütsch, L.; Moussa, M. E.; Schindler, A.; Balázs, G.; Lescop, C.; Scheer, M. Organometallic Polyphosphorus and -Arsenic Ligands as Linkers between Pre-Assembled Linear Cu(I) Fragments. *Chem. Comm.* 2015, 51, 2893–2895. doi:10.1039/C4CC09845E. b) Attenberger, B.; El Sayed Moussa, M.; Brietzke, T.; Vreshch, V.; Holdt, H.-J.; Lescop, C.; Scheer, M. Discrete Polymetallic Arrangements of Ag(I) and Cu(I) Ions Based on Multiple Bridging Phosphane Ligands and π - π Interactions. *Euro. J. Inorg. Chem.* 2015, 2015, 2934–2938. doi:10.1002/ejic.201500445. c) Fleischmann, M.; Dütsch, L.; Elsayed Moussa, M.; Balázs, G.; Kremer, W.; Lescop, C.; Scheer, M. Self-Assembly of Reactive Linear Cu₃ Building Blocks for Supramolecular Coordination Chemistry and Their Reactivity toward En Ligand Complexes. *Inorg. Chem.* 2016, 55, 2840–2854. doi:10.1021/acs.inorgchem.5b02641. d) Elsayed Moussa, M.; Evariste, S.; Krämer, B.; Réau, R.; Scheer, M.; Lescop, C. Can Coordination-Driven Supramolecular Self-Assembly Reactions Be Conducted from Fully Aliphatic Linkers? *Angew. Chem. Int. Ed.* 2018, 57, 795–799. doi:10.1002/anie.201709119.

- ⁴⁴ a) Nitschke, J. R. Construction, Substitution, and Sorting of Metallo-Organic Structures via Subcomponent Self-Assembly. *Acc. Chem. Res.* 2007, 40, 103–112. doi:10.1021/ar068185n. b) Smulders, M. M. J.; Riddell, I. A.; Browne, C.; Nitschke, J. R. Building on Architectural Principles for Three-Dimensional Metallo-supramolecular Construction. *Chem. Soc. Rev.* 2013, 42, 1728–1754. doi:10.1039/C2CS35254K. c) Ronson, T. K.; Pilgrim, B. S.; Nitschke, J. R. Pathway-Dependent Post-Assembly Modification of an Anthracene-Edged MII4L6 Tetrahedron. *J. Am. Chem. Soc.* 2016, 138, 10417–10420. doi:10.1021/jacs.6b06710. d) Rizzuto, F. J.; Ramsay, W. J.; Nitschke, J. R. Otherwise Unstable Structures Self- Assemble in the Cavities of Cuboctahedral Coordination Cages. *J. Am. Chem. Soc.* 2018, 140, 11502–11509. doi:10.1021/jacs.8b07494. e) Greenfield, J. L.; Rizzuto, F. J.; Goldberga, I.; Nitschke, J. R. Self-Assembly of Conjugated Metallopolymers with Tunable Length and Controlled Regio-chemistry. *Angew. Chem Int. Ed.* 2017, 56, 7541–7545. doi:10.1002/anie.201702320. f) Greenfield, J. L.; Evans, E. W.; Di Nuzzo, D.; Di Antonio, M.; Friend, R. H.; Nitschke, J. R. Unraveling Mechanisms of Chiral Induction in Double-Helical Metallopolymers. *J. Am. Chem. Soc.* 2018, 140, 10344–10353. doi:10.1021/jacs.8b06195.
- ⁴⁵ Ruben, M.; Lehn, J.-M.; Müller, P. Addressing Metal Centres in Supramolecular Assemblies. *Chem. Soc. Rev.* 2006, 35, 1056–1067. doi:10.1039/b517267p.
- ⁴⁶ a) Jansze, S. M.; Wise, M. D.; Vologzhanina, A. V.; Scopelliti, R.; Severin, K. PdII2L4- Type Coordination Cages up to Three Nanometers in Size. *Chem. Sci.* 2017, 8, 1901–1908. doi:10.1039/C6SC04732G. b) Jansze, S. M.; Ortiz, D.; Tirani, F. F.; Scopelliti, R.; Menin, L.; Severin, K. Inflating Face-Capped Pd6L8 Coordination Cages. *Chem. Comm.* 2018, 54, 9529–9532. doi:10.1039/C8CC04870C.
- ⁴⁷ Ward, M. D.; McCleverty, J. A.; Jeffery, J. C. Coordination and Supramolecular Chemistry of Multi-nucleating Ligands Containing Two or More Pyrazolyl-Pyridine ‘Arms.’ *Coord. Chem. Rev.* 2001, 222, 251–272. doi:10.1016/S0010-8545(01)00301-0.
- ⁴⁸ a) Pluth, M. D.; Raymond, K. N. Reversible Guest Exchange Mechanisms in Supramolecular Host-Guest Assemblies. *Chem. Soc. Rev.* 2007, 36, 161–171. doi:10.1039/b603168b. b) Levin, M. D.; Kaphan, D. M.; Hong, C. M.; Bergman, R. G.; Raymond, K. N.; Toste, F. D. Scope and Mechanism of Cooperativity at the Intersection of Organometallic and Supramolecular Catalysis. *J. Am. Chem. Soc.* 2016, 138, 9682–9693. doi:10.1021/jacs.6b05442.
- ⁴⁹ a) Clever, G. H.; Kawamura, W.; Tashiro, S.; Shiro, M.; Shionoya, M. Stacked Platinum Complexes of the Magnus’ Salt Type Inside a Coordination Cage. *Angew. Chem. Int. Ed.* 2012, 51, 2606–2609. doi:10.1002/anie.201108197. b) Han, M.; Engelhard, D.; Clever, G. Self-Assembled Coordination Cages Based on Banana-Shaped Ligands. *Chem. Soc. Rev.* 2014, 43, 1848–1860. doi:10.1039/C3CS60473J. c) Käseborn, M.; Holstein, J. J.; Clever, G. H.; Lützen, A. A Rotaxane-like Cage-in-Ring Structural Motif for a Metallo-supramolecular Pd₆L₁₂ Aggregate. *Angew. Chem. Int. Ed.* 2018, 57, 12171–12175. doi:10.1002/anie.201806814
- ⁵⁰ a) Yam, V. W.-W.; Lo, K. K.-W. Luminescent Polynuclear d 10 Metal Complexes. *Chemical Society Reviews* 1999, 28, 323–334. doi:10.1039/A804249G. b) Chen, X.; Gerger, T. M.; Räuber, C.; Raabe, G.; Göb, C.; Oppel, I. M.; Albrecht, M. A Helicate-Based Three-State Molecular Switch. *Angew. Chem. Int. Ed.* 2018, 57, 11817–11820. doi:10.1002/anie.201806607. c) Kim, Y.; Koo, J.; Hwang, I.-C.; Mukhopadhyay, R. D.; Hong, S.; Yoo, J.; Dar, A. A.; Kim, I.; Moon, D.; Shin, T. J.; et al. Rational Design and Construction of Hierarchical Superstructures

Using Shape-Persistent Organic Cages: Porphyrin Box-Based Metallo-supramolecular Assemblies. *J. Am. Chem. Soc.* 2018, 140, 14547–14551. doi:10.1021/jacs.8b08030.

⁵¹ Kuehl, C. J.; Huang, S. D.; Stang, P. J. Self-Assembly with Postmodification: Kinetically Stabilized Metallasupramolecular Rectangles. *J. Am. Chem. Soc.* 2001, 123, 9634–9641. doi:10.1021/ja0114355.

⁵² Sommer, R. D.; Rheingold, A. L.; Goshe, A. J.; Bosnich, B. Supramolecular Chemistry: Molecular Recognition and Self-Assembly Using Rigid Spacer-Chelators Bearing Co-facial Terpyridyl Palladium (II) Complexes Separated by 7 Å. *J. Am. Chem. Soc.* 2001, 123, 3940–3952. doi:10.1021/ja004279v.

⁵³ a) Tang, H.-S.; Zhu, N.; Yam, V. W.-W. Tetranuclear Macrocyclic Gold(I) Alkynyl Phosphine Complex Containing Azobenzene Functionalities: A Dual-Input Molecular Logic with Photoswitching Behavior Controllable via Silver (I) Coordination/Decoordination. *Organometallics* 2007, 26, 22–25. doi:10.1021/om0609719. b) Yam, V. W.-W.; Cheng, E. C.-C. Highlights on the Recent Advances in Gold Chemistry - a Photophysical Perspective. *Chem. Soc. Rev.* 2008, 37, 1806–1813. doi:10.1039/B708615F. c) He, X.; Chung-Chin Cheng, E.; Zhu, N.; Wing-Wah Yam, V. Selective Ion Probe for Mg 2+ Based on Au(I)⋯Au(I) Interactions in a Tripodal Alkynylgold(I) Complex with Oligoether Pendant. *Chem. Comm.* 2009, 27, 4016–4018. doi:10.1039/B902690H. d) Lee, T. K.-M.; Zhu, N.; Yam, V. W.-W. An Unprecedented Luminescent Polynuclear Gold(I) M₃-Sulfido Cluster with a Thiocrown-like Architecture. *J. Am. Chem. Soc.* 2010, 132, 17646–17648. doi:10.1021/ja1055017. e) Shakirova, J. R.; Grachova, E. V.; Gurzhiy, V. V.; Koshevoy, I. O.; Melnikov, A. S.; Sizova, O. V.; Tunik, S. P.; Laguna, A. Luminescent Heterometallic Gold–Copper Alkynyl Complexes Stabilized by Tridentate Phosphine. *Dalton Trans.* 2012, 41, 2941–2949. doi:10.1039/C2DT11710J.

⁵⁴ a) Shafikov, M. Z.; Suleymanova, A. F.; Czerwieniec, R.; Yersin, H. Thermally Activated Delayed Fluorescence from Ag(I) Complexes: A Route to 100% Quantum Yield at Unprecedentedly Short Decay Time. *Inorg. Chem.* 2017, 56, 13274–13285. doi:10.1021/acs.inorgchem.7b02002. b) Shafikov, M. Z.; Suleymanova, A. F.; Czerwieniec, R.; Yersin, H. Design Strategy for Ag(I)-Based Thermally Activated Delayed Fluorescence Reaching an Efficiency Breakthrough. *Chem. Mater.* 2017, 29, 1708–1715. doi:10.1021/acs.chemmater.6b05175. c) Moussa, M. E.; Welsch, S.; Gregoriades, L. J.; Balázs, G.; Seidl, M.; Scheer, M. The Diphosphorus Complex [Cp₂Cr₂(CO)₄(H₂-P₂)] as a Building Block in the Coordination Chemistry of Silver. *Euro. J. Inorg Chem.* 2018, 2018, 1683–1687. doi:10.1002/ejic.201800141. d) Shafikov, M. Z.; Suleymanova, A. F.; Schinabeck, A.; Yersin, H. Dinuclear Ag(I) Complex Designed for Highly Efficient Thermally Activated Delayed Fluorescence. *J. Phys. Chem. Lett.* 2018, 9, 702–709. doi:10.1021/acs.jpcclett.7b03160.

⁵⁵ Chakrabarty, R.; Mukherjee, P. S.; Stang, P. J. Supramolecular Coordination: Self-Assembly of Finite Two- and Three-Dimensional Ensembles. *Chem. Rev.* 2011, 111, 6810–6918. doi:10.1021/cr200077m.

⁵⁶ Lescop, C. Coordination-driven Supramolecular Synthesis based on Bimetallic Cu(I) Precursors: Adaptive Behavior and Luminescence. *The Chemical Record* 2020. doi:10.1002/tcr.202000144

⁵⁷ Tsipis, A. C. DFT/TDDFT insights into the chemistry, biochemistry and photo-physics of copper coordination compounds. *Royal Chem. Soc. Adv.* 2014, 4, 32504–32529. doi:10.1039/c4ra04921g.

⁵⁸ Sousa, S. F.; Pinto, G. R. P.; Ribeiro, A. J. M.; Coimbra, J. T. S.; Fernandes, P. A.; Ramos, M. J. Comparative analysis of the performance of commonly available density functionals in the determination of geometrical parameters for copper complexes. *J. Comput. Chem.* 2013, 34, 2079.

-
- ⁵⁹ Grimme, S.; Antony, J.; Ehrlich, S.; Krieg, H.; consistent and accurate ab initio parametrization of density functional dispersion correction (DFT-D) for the 94 elements H-Pu. *J. Chem. Phys.* 2010, 132, 154104; doi:10.1063/1.3382344.
- ⁶⁰ Ansbacher, T.; Srivastava, H. K.; Martin, J. M. L.; Shurki, A. Can DFT methods correctly and efficiently predict the coordination number of copper(I) complexes? A case study. *J. Comput. Chem.* 2009, 131, 75-83. doi: 10.1002/jcc.21277.
- ⁶¹ Quintal, M. M.; Karton, A.; Iron, M. A.; Boese, A. D.; Martin, J. M.L. Benchmark Study of DFT Functionals for Late-Transition-Metal Reactions. *J. Phys. Chem. A* 2006, 110, 709. doi:10.1021/jp054449w.
- ⁶² Frisch, M. J.; Trucks, G. W.; Schlegel, H. B.; Scuseria, G. E.; Robb, M. A.; Cheeseman, J. R.; Scalmani, G.; Barone, V.; Petersson, G. A.; Nakatsuji, H.; Li, X.; Caricato, M.; Marenich, A. V.; Bloino, J.; Janesko, B. G.; Gomperts, R.; Mennucci, B.; Hratchian, H. P.; Ortiz, J. V.; Izmaylov, A. F.; Sonnenberg, J. L.; Williams-Young, D.; Ding, F.; Lipparini, F.; Egidi, F.; Goings, J.; Peng, B.; Petrone, A.; Henderson, T.; Ranasinghe, D.; Zakrzewski, V. G.; Gao, J.; Rega, N.; Zheng, G.; Liang, W.; Hada, M.; Ehara, M.; Toyota, K.; Fukuda, R.; Hasegawa, J.; Ishida, M.; Nakajima, T.; Honda, Y.; Kitao, O.; Nakai, H.; Vreven, T.; Throssell, K.; Montgomery, J. A., Jr.; Peralta, J. E.; Ogliaro, F.; Bearpark, M. J.; Heyd, J. J.; Brothers, E. N.; Kudin, K. N.; Staroverov, V. N.; Keith, T. A.; Kobayashi, R.; Normand, J.; Raghavachari, K.; Rendell, A. P.; Burant, J. C.; Iyengar, S. S.; Tomasi, J.; Cossi, M.; Millam, J. M.; Klene, M.; Adamo, C.; Cammi, R.; Ochterski, J. W.; Martin, R. L.; Morokuma, K.; Farkas, O.; Foresman, J. B.; Fox, D. J. *Gaussian 16 Revision A.03*. 2016.
- ⁶³ ADF 2019, SCM, Theoretical Chemistry, Vrije Universiteit, Amsterdam, The Netherlands, <http://www.scm.com>.
- ⁶⁴ Adamo, C.; Barone, V. Toward reliable density functional methods without adjustable parameters: The PBE0 model. *J. Chem. Phys.* 1999, 110, 6158–6170. doi:10.1063/1.478522.
- ⁶⁵ Schaefer, A.; Huber, C.; Ahlrichs, R. Fully optimized contracted Gaussian-basis sets of triple zeta valence quality for atoms Li to Kr. *J. Chem. Phys.* 1994, 100, 5829-5835. doi:10.1063/1.467146.
- ⁶⁶ Ros, P.; Schuit, G. C. A. *Theo. Chim. Acta* 1966, 4, 1-12. doi:10.1007/BF00526005.

Chapter II – Study of diphosphino-Cu₂ coordination complexes

I – Introduction

As previously detailed, Cu(I)-based systems are attractive candidates to conceive cheap and efficient lighting devices. Our research is specifically devoted to the understanding of the unusual photophysical properties of Cu(I) polymetallic arrangements that are synthesized via the “one-pot” CDS protocols developed by Lescop and coworkers. For these systems, a subtle balance is found between the different processes and a computational study allows to better understand them. Our collaborators intentionally develop their research toward accessible and cheap molecular building blocks. The bidentate diphosphine bridging ligand has been one of the chosen ligands. This choice was driven because of their short-bite angle which confers a relatively short Cu–Cu distance in the complex and often promotes enhanced spin-orbit coupling. Additionally, most of those ligands like the diphenyl-diphosphino-methane (dppm) present a good compromise in rigidity and fluxionality (bridging or chelating coordination modes) that is necessary for CDS assembling.¹ The di-phosphine Cu(I) complexes have been extensively studied and a variety of coordination sphere around the metal has been identified from tetrahedral to linear conformations with a variety of luminescent properties.^{2,3,4,5,6,7,8} Interestingly, no full characterization of the dimer systems with diphosphinyl-only bridging ligands have been published to date. These systems are interesting compounds since they are the smallest systems of the target series in which several Cu–Cu dimers will be present. A combined experimental and computational study is thus of high interest for later comparisons. This chapter is devoted to the theoretical investigations of [Cu(dppm)₃]²⁺ and [Cu(dppa)₃]²⁺ (dppa = diphenyl-diphosphino-amine) in which the CH₂ unit is replaced by a NH group. The experimental characterizations of the solid-state compounds containing these cations are reported and discussed in light of our computational results.

II – Experimental data obtained by Lescop and coworkers

The permission of reporting the following unpublished results has been obtained from the research team which has obtained them: Lescop, Xu, Moutier and Calvez from the ISCR – INSA, Rennes. The synthetic protocol employed was to react a Cu^+ ionic source with a corresponding phosphine in a dichloromethane (DCM) solution under air. The TEF^- ($[\text{Al}(\text{OC}(\text{CF}_3)_3)_4]^-$), PF_6^- and BF_4^- anions have been used as counter anions. Monocrystals were obtained upon solvent evaporation. X-ray crystallography was employed to characterize their solid-state structural arrangements.

II.1 – The $[\text{Cu}_2(\text{dppm})_3]^{2+}$ system

II.1.1 – X-ray crystallographic geometries of the $[\text{Cu}_2(\text{dppm})_3]^{2+}$ solid-state system

The $[\text{Cu}_2(\text{dppm})_3]^{2+}$ cations were crystallized with two TEF^- counter ions giving rise to $\mathbf{A}_{\text{TEF}} = [\text{Cu}_2(\text{dppm})_3][\text{TEF}]_2 \cdot \text{DCM}$. This solid-state compound contains also DCM solvent molecules (Figure 1). The main experimental angles and distances obtained by single-crystal X-ray diffraction analysis are reported Table 1.

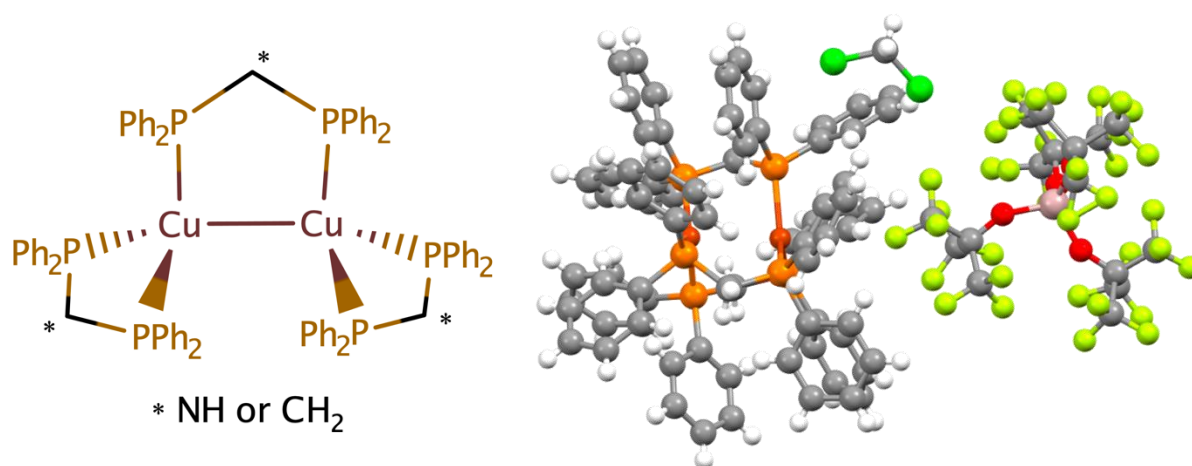
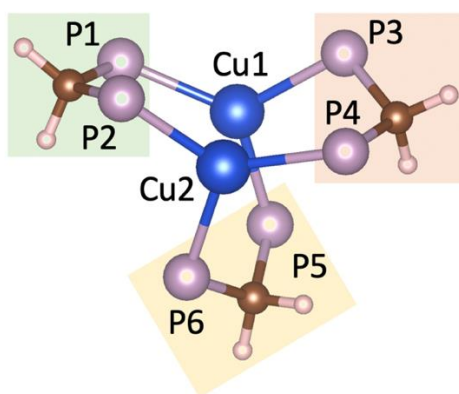


Figure 1 – Left: 2-D structures of $[\text{Cu}(\text{dppm})_3]^{2+}$ and $[\text{Cu}(\text{dppa})_3]^{2+}$. Right: representation of the X-ray structural arrangement of \mathbf{A}_{TEF} . The orientation corresponds to the alignment of the Cu-Cu axis parallel to the sketch plane. Only one TEF^- and DCM is shown for clarity. By the courtesy of Lescop and coworkers.

The numbering of the atoms is indicated in Scheme 1. It was chosen in such way that the dppm arrangements between the phenyl groups are similar for all the considered geometries.



Scheme 1 – Numbering of the atoms for **A** (phenyl groups omitted for sake of clarity). The phenyl orientations of the dppm arrangements are determining the numbering, (similar for all geometries).

Table 1 – Main experimental geometrical data of the $[\text{Cu}_2(\text{dppm})_3]^{2+}$ **A**_{TEF} and the DFT optimized structure of $[\text{Cu}_2(\text{dppm})_3]^{2+}$ (**A**_{theo}) for sake of comparison. This will be discussed in the theoretical section. Distances are given in Å and angles in degree. For the numbering see Scheme 1.

| Compound | A _{TEF} | A _{theo} | Compound | A _{TEF} | A _{theo} |
|----------|-------------------------|--------------------------|-----------|-------------------------|--------------------------|
| Cu1-Cu2 | 2.913 | 2.799 | P1-Cu1-P3 | 129.2 | 125.9 |
| Cu1-P1 | 2.298 | 2.351 | P2-Cu2-P4 | 136.7 | 131.0 |
| Cu2-P2 | 2.283 | 2.348 | P3-Cu1-P5 | 109.0 | 107.3 |
| Cu1-P3 | 2.329 | 2.353 | P4-Cu2-P6 | 110.3 | 118.7 |
| Cu2-P4 | 2.294 | 2.348 | P5-Cu1-P1 | 121.8 | 126.4 |
| Cu1-P5 | 2.307 | 2.384 | P6-Cu2-P2 | 112.6 | 109.5 |
| Cu2-P6 | 2.311 | 2.377 | | | |

The Cu–Cu bond is compatible with a cuprophilic interaction, i.e., a distance shorter than about 3.00 Å.^{9,10} The close Cu–Cu distance could also result from the chelating effect of the dppm bridging ligands. The sum of the angles P–Cu–P for each copper is 360° reflecting a trigonal planar arrangement. This trigonal arrangement is importantly deviating from the D_{3h} highest symmetry with angles ranging from 107.3° to 136.7°.¹¹

II.1.2 – Experimental solid-state absorption and excitation spectra

The optical properties of **A**_{TEF} (solid-state) were investigated in Lescop's group. **A**_{TEF} absorption spectrum is represented in Figure 2a. A weak continuous absorption is measured between 750 to 400 nm followed by two main peaks situated at 350 nm and 280 nm.

The excitation spectrum in Figure 2b was recorded considering an emission wavelength (λ_{em}) of 478 nm. Absorption above 400 nm does not lead to emission. The lowest energy efficient excitation is situated near 340 nm at a wavelength slightly lower than the maximum absorption peak.

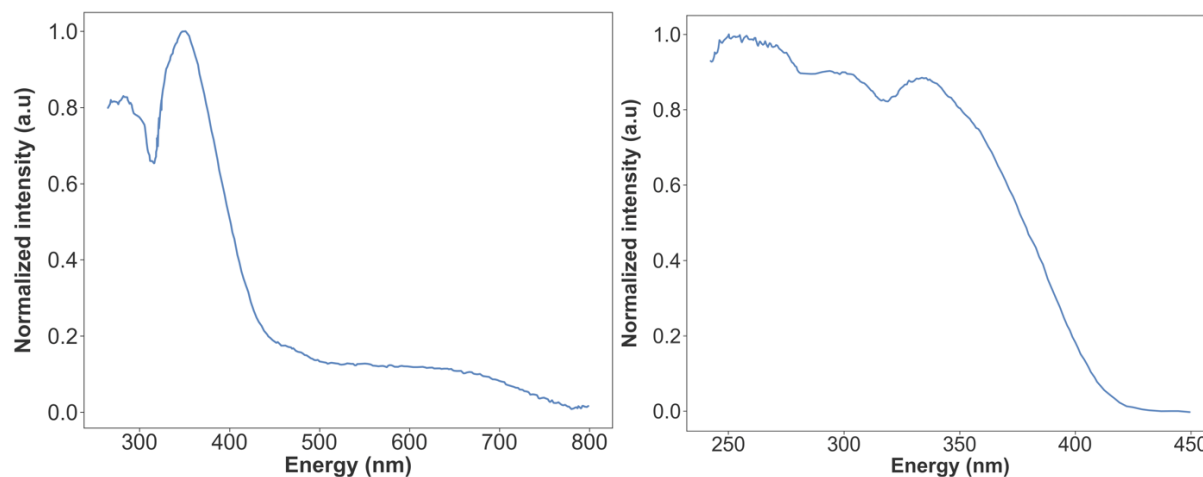


Figure 2 – a) Experimental solid-state absorption spectrum of A_{TEF} . b) Experimental excitation spectrum of A_{TEF} for an emission at $\lambda_{ex} = 478$ nm.

II.1.3 – Experimental solid-state emission spectra

The solid-state emission spectra of A_{TEF} were also recorded by the group of Lescop at several temperatures between 80 to 300 K ($\lambda_{ex} = 375$ nm). At RT, the maximum of emission is centered at 478 nm. The emission peak is shifted to lower wavelengths upon lowering of temperature. This global hypsochromic shift of emission upon temperature increase from 489 nm at 80 K to 479 nm at 300 K is not linear. Indeed, the maximum wavelength is measured between 160-170 K with a maximum of emission at 497 nm. Considering the literature of copper (I) emissive systems,¹² this behavior corresponds to a TADF mechanism associated with phosphorescence at low-temperature and a thermal activation of the RISC that populates the lowest singlet excited state at higher temperature. The study of the emission lifetimes is necessary to support this hypothesis.

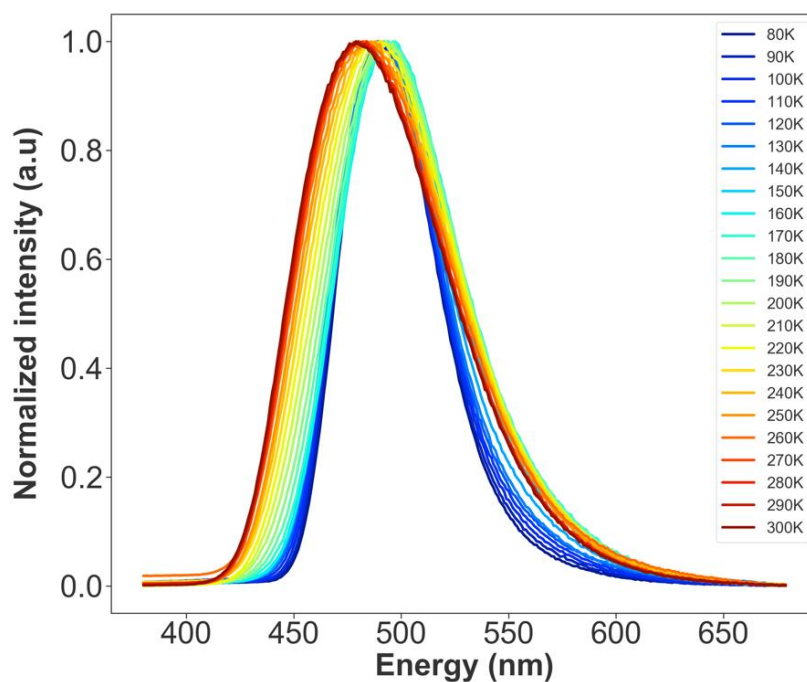


Figure 3 – Temperature-dependent experimental normalized solid-state emission spectrum of A_{TEF} in nm. Wavelength of excitation $\lambda_{ex} = 375$ nm.

II.1.4 – Temperature dependent lifetime

The lifetime evolution measured by the group of Lescop roughly follows the behavior expected in a TADF process associated with a changing phosphorescence at low temperature. The global lifetime at 80 K is a hundred of microseconds ($\tau = 443 \mu s$). It slightly decreases up to 130 K and then increases until around 160 K where a sudden drop of the decay time is observed. Due to technical issues, the measurements could not be performed above 370 K and the expected plateau was not reached. A fitting using the TADF equation (Eq. 1, chapter I, section II.2) was applied and provided a ΔE_{ST} of 0.129 eV (1040 cm^{-1}) between the S_1 and the T_1 and respective lifetimes of 350 ns and 428 μs ; however, the absence of a plateau surely leads to fairly imprecise values. Computational studies will be performed to give some more credits to this hypothesis.

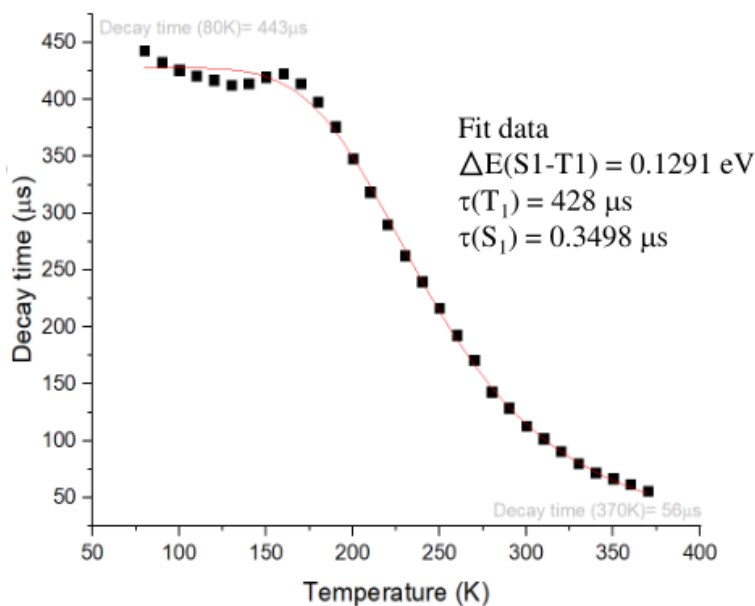


Figure 4 – Luminescence decay time of the solid-state emission spectrum of \mathbf{A}_{TEF} from 80 K to 370 K.

II.2 – The $[\text{Cu}_2(\text{dppa})^{2+}]$ system

II.2.1 – X-ray crystallographic geometries of the $[\text{Cu}_2(\text{dppa})_3]^{2+}$ solid-state system

A second bimetallic copper(I) compound was synthesized by Lescop and coworkers using dppa as chelating ligand. Two $[\text{Cu}_2(\text{dppa})_3]^{2+}$ containing solid-state compounds were crystallized with a BF_4^- counter anion for one and a PF_6^- for the other: $\mathbf{B}_{\text{BF}_4} = [\text{Cu}_2(\text{dppa})_3][\text{BF}_4]_2 \cdot \text{DCM}$, $\mathbf{B}_{\text{PF}_6} = [\text{Cu}_2(\text{dppa})_3][\text{PF}_6]_2 \cdot \text{DCM}$. Molecules of DCM solvent are included in these solid-state structures (Figure 5). A single crystal X-ray diffraction analysis could be performed for both. The main experimental angles and distances are reported in Table 2.

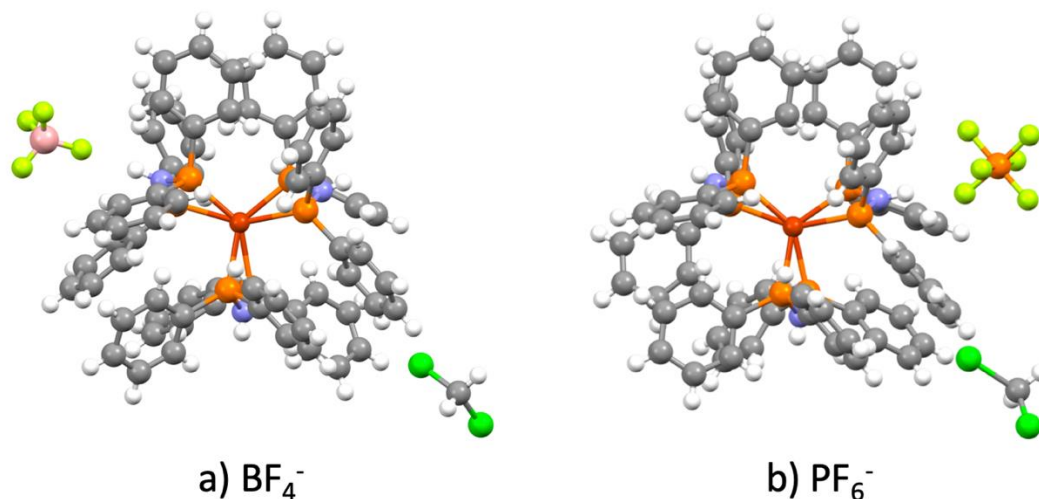
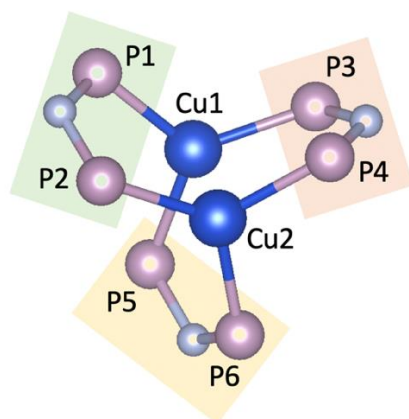


Figure 5 – Experimental X-ray structural arrangements of **B_{BF₄}** and **B_{PF₆}**. The chosen orientation corresponds to the alignment of the Cu–Cu axis normal to the sketch plane. Only one BF₄[−] and PF₆[−] counterion are shown for clarity. By the courtesy of Lescop and coworkers.

The numbering of the atoms is indicated in Scheme 2. It was chosen in such a way that the phenyl group arrangements between the dppa are similar in both views.



Scheme 2 – Numbering of the atoms for the **B** structures (phenyl groups omitted for sake of clarity). The phenyl orientations of the dppa arrangements are determining the numbering (similar for all geometries).

Table 2 – Main experimental geometrical data of [Cu₂(dppa)₃]²⁺. Distances are given in Å and angles in degree. Optimized structures of [Cu₂(dppa)₃]²⁺, **B_{theo}**; those for the mono and bis-deprotonated [Cu₂(dppa)₃]²⁺, **B_{theo/-H+}** and **B_{theo/-2H+}**, are given for sake of comparison. This will be discussed in the theoretical section. For numbering see Scheme 2. (*) dppa ligand whose amino group is interacting with a counteranion.

| Compound | B_{BF₄} | B_{PF₆} | B_{theo} | B_{theo/-H+} | B_{theo/-2H+} |
|----------|-----------------------------------|-----------------------------------|-------------------------|-----------------------------|------------------------------|
| Cu1-Cu2 | 2.606 | 2.635 | 2.643 | 2.632 | 2.664 |
| Cu1-P1 | 2.296 | 2.300 | 2.339 | 2.332 | 2.331 |
| Cu2-P2 | 2.269 | 2.290 | 2.344 | 2.318 | 2.345 |
| Cu1-P3 | 2.285 * | 2.286 | 2.344 | 2.347 | 2.320 |
| Cu2-P4 | 2.294 * | 2.284 | 2.339 | 2.324 | 2.331 |
| Cu1-P5 | 2.322 | 2.279 * | 2.372 | 2.373 | 2.323 |
| Cu2-P6 | 2.297 | 2.304 * | 2.372 | 2.329 | 2.347 |

| Compound | B_{BF4} | B_{PF6} | B_{theo} | B_{theo/-H+} | B_{theo/-2H+} |
|-----------|------------------------|------------------------|-------------------------|-----------------------------|------------------------------|
| P1-Cu1-P3 | 127.3 | 121.8 | 124.5 | 127.4 | 113.5 |
| P2-Cu2-P4 | 124.4 | 122.2 | 124.5 | 117.8 | 126.3 |
| P3-Cu1-P5 | 121.4 | 125.2 | 126.9 | 120.9 | 129.4 |
| P4-Cu2-P6 | 115.2 | 127.7 | 107.7 | 112.4 | 115.3 |
| P5-Cu1-P1 | 110.7 | 112.4 | 107.7 | 111.4 | 117.0 |
| P6-Cu2-P2 | 119.8 | 109.6 | 126.9 | 129.0 | 118.4 |

Interestingly, the geometries of the $[\text{Cu}_2(\text{dppa})_3]^{2+}$ ions are slightly different in the two compounds. Indeed, hydrogen interactions of different extent are found between the counterions and the protons of the bridging amine groups of the dppa ligands. The sum of the P-Cu-P angles around each copper atom is 359.4° , very close to a planar trigonal configuration, as already observed for the **A_{TEF}** system. The Cu–Cu distance is shorter in **B_{BF4}** than in **B_{PF6}** (2.606 Å vs. 2.635 Å). This difference could be attributed to crystal packing for the $[\text{Cu}_2(\text{dppa})_3]^{2+}$ ions or a reinforcement of the cuprophilic interactions. Steric hindrances are enforced to the phenyl groups due to hydrogen bonding interactions with the counterions and the presence of solvent. Hydrogen bonds are found for one of the three amino groups. Small modifications in the orientation of the indented phenyl groups can be detected but their extent is too small for further interpretation.

II.2.2 – Experimental solid-state absorption and excitation spectra

In order to evaluate the influence of the intermolecular interactions on the optical properties of the $[\text{Cu}_2(\text{dppa})_3]^{2+}$ systems, experimental measurements were performed on two different solid-state arrangements, **B_{BF4}** and **B_{PF6}**. The absorption spectra of both systems were conducted in the solid state and are shown in Figure 6. The first low-energy intense absorption peak is located around 400 nm for both systems but a noticeable absorption is observed at lower energy. This shoulder located around 500 nm is more marked for **B_{PF6}**. The system containing the BF_4^- counterion (**B_{BF4}**) has 2 peaks at 417 nm and 317 nm; in the other structure (**B_{PF6}**), two peaks are also present, but at 406 nm and 319 nm. It represents a difference of 80 meV (417 vs 406 nm) and 25 meV (319 vs 317 nm) depending on the counterion.

The absorption properties are slightly different depending on the counterion and solvent forming the crystals. The maximum of absorption is blue shifted compared to the parent **A_{TEF}** revealing either electronic modifications due to the substitution of the CH_2 of the dppm by NH and/or by geometrical modifications due to differences in the crystal packing.

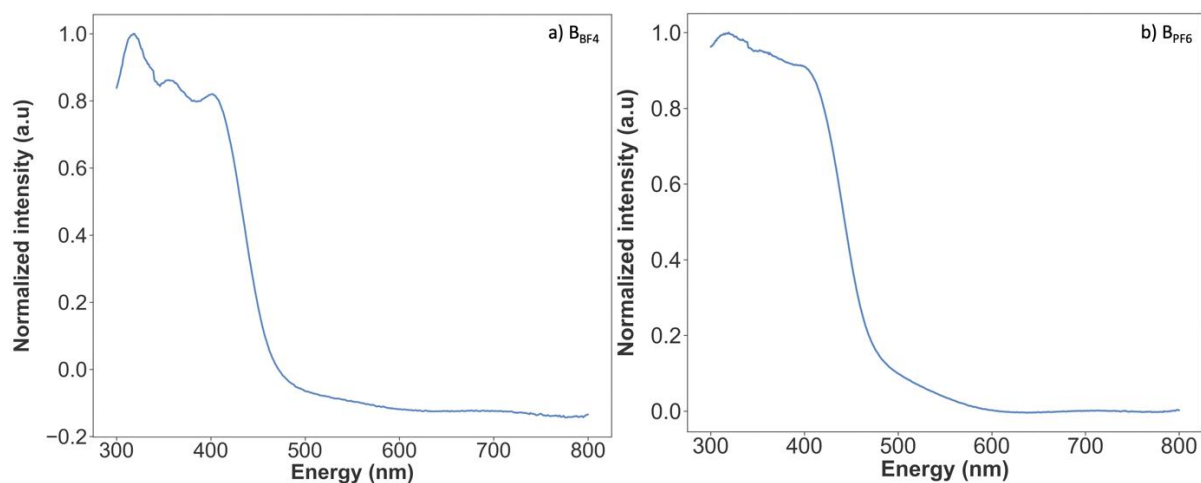


Figure 6 – Experimental solid-state absorption spectra of a) \mathbf{B}_{BF_4} and b) \mathbf{B}_{PF_6} .

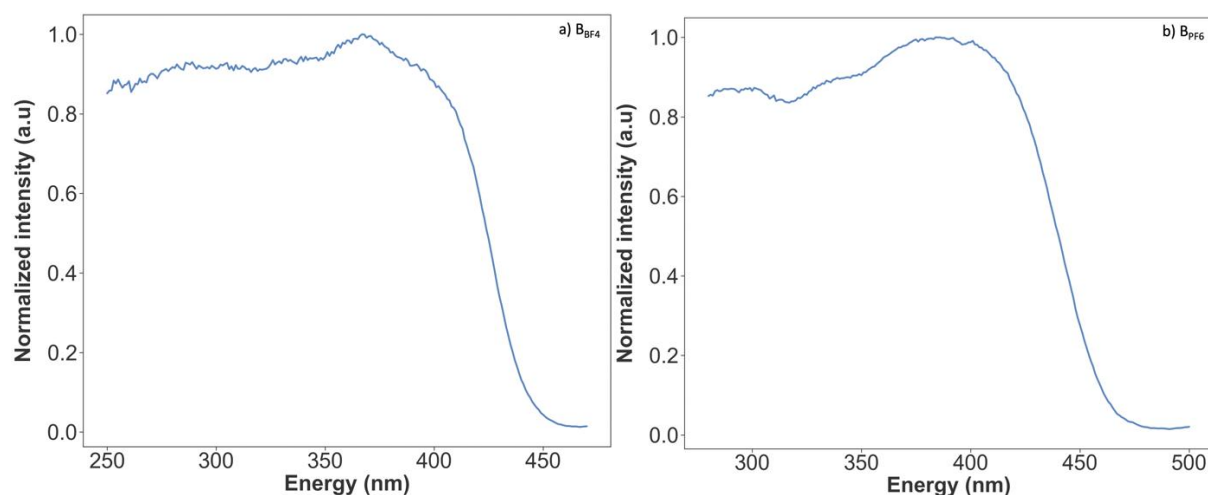


Figure 7 – Experimental excitation spectra of a) \mathbf{B}_{BF_4} , $\lambda_{\text{ex}} = 488$ nm and b) \mathbf{B}_{PF_6} , $\lambda_{\text{ex}} = 520$ nm.

II.2.3 – Experimental solid-state emission spectra

The maximum emission wavelengths of both compounds \mathbf{B}_{BF_4} and \mathbf{B}_{PF_6} change as the temperature rises. The maximum of emission decreases from 516 nm to 493 nm for \mathbf{B}_{BF_4} , and from 551 nm to 520 nm for \mathbf{B}_{PF_6} going from 80 K to 300 K. A probable explanation considering the previous results reported in the literature¹² and the experimental results obtained for the \mathbf{A}_{TEF} system is a combination of phosphorescence at low temperature followed by a TADF process at higher temperature. Here again, the study of the evolution of the emission lifetime is necessary to support this hypothesis.

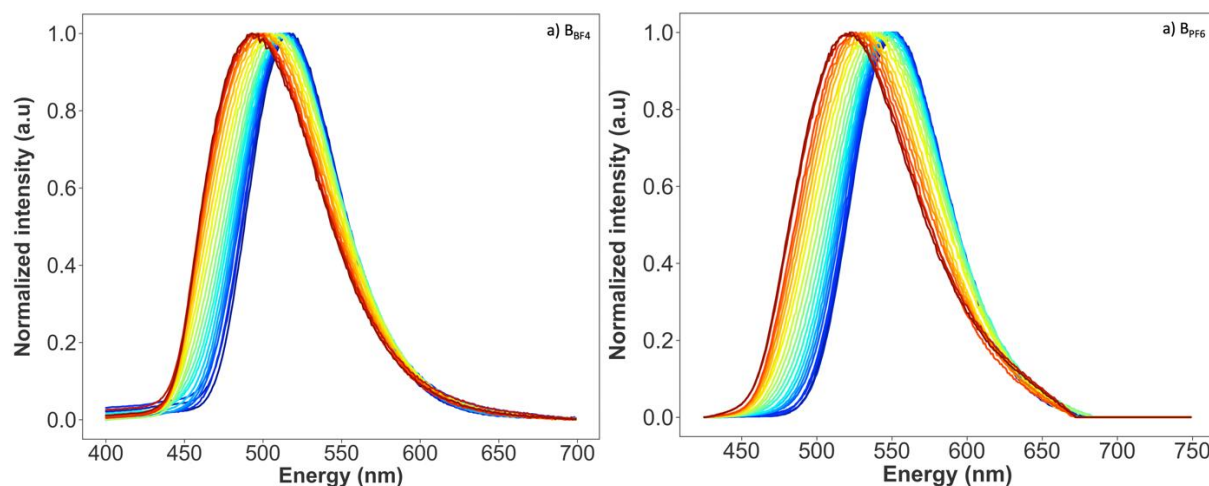


Figure 8 – Temperature-dependent experimental emission spectra of a) **B_{BF4}** with $\lambda_{\text{ex}} = 375$ nm and b) **B_{PF6}** with $\lambda_{\text{ex}} = 405$ nm (80 K in blue, 300 K in red). See Figure 3 for the details of the temperature coloring scale.

II.2.4 – Temperature dependent lifetime

The experimental temperature dependent decay time of the emission was measured in Figure 9 from 80 K to 370 K for the two compounds **B_{BF4}** and **B_{PF6}**. Both lifetimes follow a Boltzmann-type curve which can reveal a TADF process. As previously, using Eq. 1 (chapter I, section II.2) one can extract the lifetime of the excited triplet and singlet state involved, and ΔE_{ST} . Again, this fit could underestimate the ΔE_{ST} and overestimate the $\tau(S_1)$ value if, at high temperature, the lifetime plateau is not reached. This is the case for both system since the lifetime still decreases upon increase of the temperature up to 370 K.

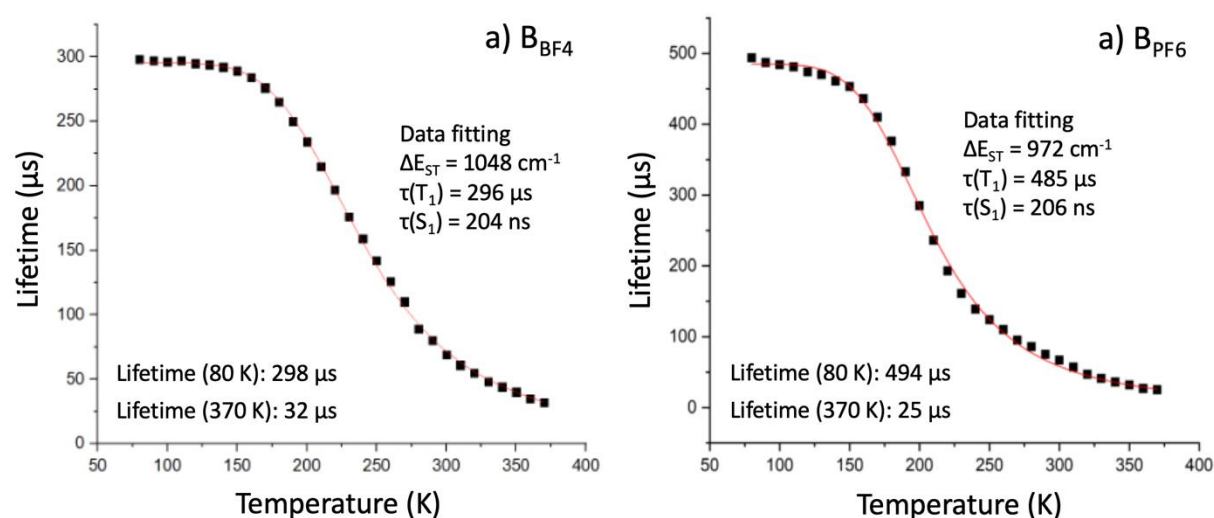


Figure 9 – Luminescence lifetime of the bi-nuclear copper systems a) **B_{BF4}** and b) **B_{PF6}** from 80 K to 370 K.

III – Theoretical study

A computational study at the DFT level was performed on both isolated ions $[\text{Cu}_2(\text{dppm})_3]^{2+}$ (\mathbf{A}_{theo}) and $[\text{Cu}_2(\text{dppa})_3]^{2+}$ (\mathbf{B}_{theo}) in order to get insights on the intrinsic emissive properties of the ions and possibly deduce information on the role of the solid-state environment. Indeed, the previous section reveals that the emission properties can be altered depending on the counterion (\mathbf{B}_{BF_4} and \mathbf{B}_{PF_6}).

III.1 – Geometry optimization

We first performed the geometry optimizations in the ground state of the \mathbf{A}_{theo} and \mathbf{B}_{theo} compounds in vacuum at 0 K using the DFT protocol detailed in the chapter I (Figure 10). The starting geometries were extracted from the crystallographic X-ray structures to keep the same arrangement between the phenyl groups for sake of comparison between systems and with experimental results (\mathbf{A}_{TEF} and \mathbf{B}_{BF_4}). It appears interesting to evaluate the influence of the deprotonation of the amine groups of the \mathbf{B} cation on the electronic and photophysical properties. X-Ray resolution does not provide sufficiently precise information to quantitatively calculate the strength of the hydrogen bonding that induces a weakening of the N-H bond by interaction with the fluorine atoms of the counterions. Thus, we choose to simulate the effect of the extreme case, i.e. deprotonation, on the electronic and photophysical properties.

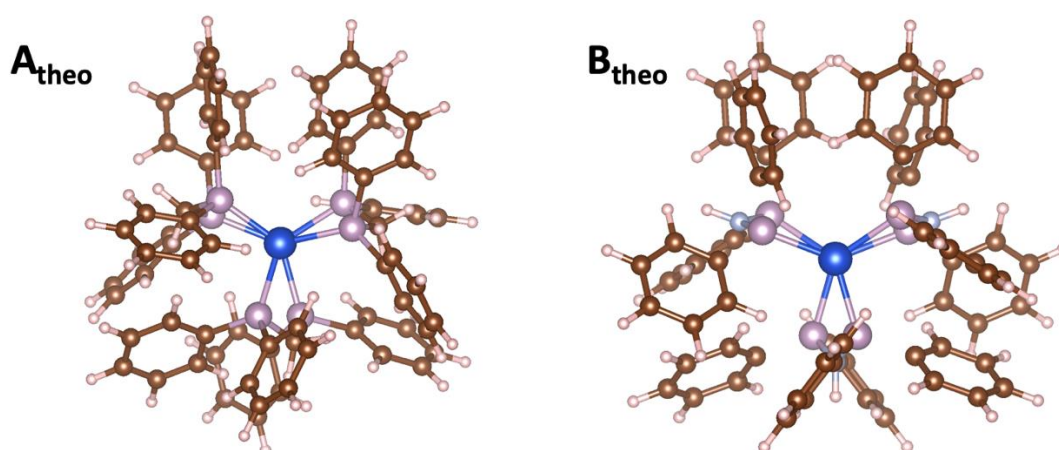


Figure 10 – Representation of the DFT optimized ground state geometries of the complexes \mathbf{A}_{theo} and \mathbf{B}_{theo} complex.

The main distances and angles are given in Table 3 and compared with the corresponding experimental data in Table 2. Comparing the \mathbf{A}_{theo} and \mathbf{B}_{theo} optimized structures, one of the

small differences is due to a different bite angle imposed by the dppm and dppa ligand, 63° and 64°, respectively, in a monometallic coordination.¹³ No study exists on the evaluation of the angle imposed by di-phosphine ligand in bimetallic bridging configuration but we can presume similar constraints for dppa and dppm. Nevertheless, the Cu–Cu distance is 2.643 Å in **B**_{theo} and 2.799 Å in **A**_{theo} revealing that electronic effects are to be considered. The Cu–P mean distance is slightly shorter in **B**_{theo} (2.351 Å vs. 2.360 Å), a feature also found in the X-ray experimental structures (2.294 Å vs. 2.304 Å). The Cu–P bond distance deviation between experimental and optimized structures are ranging from 1.5 % to 3.5 % which is in good agreement with the experimental structure considering that metal–P distances are always slightly underestimated in DFT (GGA and hybrid functionals).¹⁴ The experimental Cu–Cu bond is well reproduced by DFT calculations for both dppa-containing systems (**B**_{PF6} and **B**_{BF4}) with a difference of less than 2 %. It is less the case for the dppm system with an experimental value of 2.913 Å in **A**_{TEF} and 2.799 Å in **A**_{theo} (-3.9 %). In order to evaluate the impact of deprotonation of the amine groups on the electronic and optical properties, the mono and bis deprotonated systems [Cu₂(dppa)₂dppa-H₊]²⁺ (**B**_{theo/-H+}) and [Cu₂(dppa)(dppa-H₊)₂]²⁺ (**B**_{theo/-2H+}) were optimized. The impact on the Cu–P distances and angles is moderate. The mean Cu–P distances are only slightly shorter (-0.009 Å and -0.018 Å for dppa-H₊ and dppa-2H₊ respectively). The N–P distances are also affected by the deprotonation (-0.07 Å in both cases).

Table 3 – Comparison between the optimized geometrical data of **A**_{theo}, **B**_{theo}, **B**_{theo/-H+} and **B**_{theo/-2H+}. For numbering, see Scheme 1 and 2.

| Compound | A _{theo} | B _{theo} | B _{theo/-H+} | B _{theo/-2H+} |
|----------|--------------------------|--------------------------|------------------------------|-------------------------------|
| Cu1-Cu2 | 2.799 | 2.643 | 2.632 | 2.664 |
| Cu1-P1 | 2.351 | 2.339 | 2.332 | 2.331 |
| Cu2-P2 | 2.348 | 2.344 | 2.318 | 2.345 |
| Cu1-P3 | 2.353 | 2.344 | 2.347 | 2.320 |
| Cu2-P4 | 2.348 | 2.339 | 2.324 | 2.331 |
| Cu1-P5 | 2.384 | 2.372 | 2.373 | 2.323 |
| Cu2-P6 | 2.377 | 2.372 | 2.329 | 2.347 |

| Compound | A _{theo} | B _{theo} | B _{theo/-H+} | B _{theo/-2H+} |
|-----------|--------------------------|--------------------------|------------------------------|-------------------------------|
| P1-Cu1-P3 | 125.9 | 124.5 | 127.4 | 113.5 |
| P2-Cu2-P4 | 131.0 | 124.5 | 117.8 | 126.3 |
| P3-Cu1-P5 | 107.3 | 126.9 | 120.9 | 129.4 |
| P4-Cu2-P6 | 118.7 | 107.7 | 112.4 | 115.3 |
| P5-Cu1-P1 | 126.4 | 107.7 | 111.4 | 117.0 |
| P6-Cu2-P2 | 109.5 | 126.9 | 129.0 | 118.4 |

III.2 – Electronic structures

The electronic structures of \mathbf{A}_{theo} and \mathbf{B}_{theo} are given in Figure 11. Both systems are thermodynamically stable with a large energy gaps between the occupied and the virtual MOs (4.54 and 4.25 eV for \mathbf{A}_{theo} and \mathbf{B}_{theo} , respectively). In both cases, the LUMO electronic level is well separated from other unoccupied energy levels and shows a Cu–Cu bonding as main character. The HOMO is mainly localized on copper atoms and phosphorous atoms (~20 % Cu, ~35 % P), the rest being delocalized over the phenyl rings. Globally, the LUMO is mostly metal-centered but the LUMO of \mathbf{B}_{theo} presents a substantial participation of the amine group (23 % Cu, 18 % N, 15 % P). This can explain its stabilization compared to the LUMO of \mathbf{A}_{theo} . The HOMO-1 and the LUMO+1 of both systems are represented in Figure 12. The nature of the HOMO-1 is similar to the HOMO. In contrast, the LUMO+1 differs from the LUMO since it is π^* phenyl-centered. It is also holding true for the closeby LUMOs.

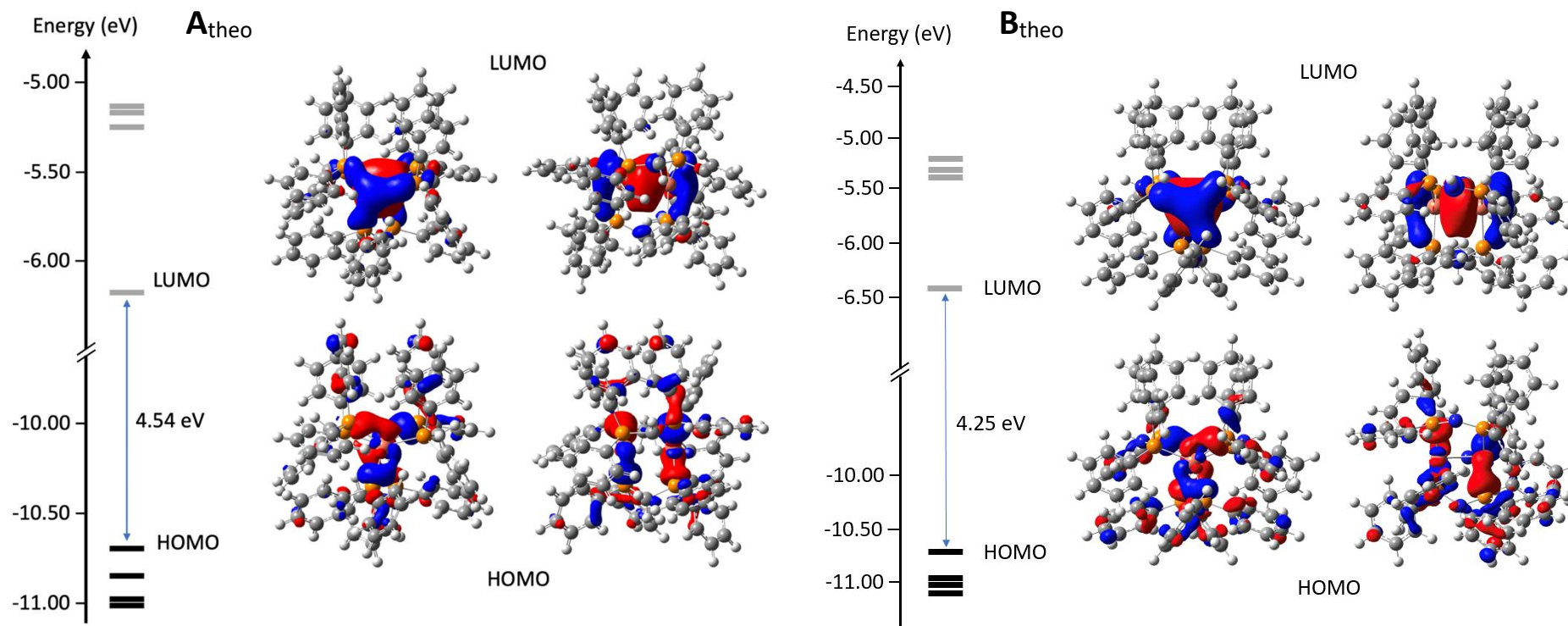


Figure 11 – **A_{theo}** and **B_{theo}** MOs energetic diagrams. The iso-values used for the representation of the orbitals is ± 0.03 (e/Bohr³)^{1/2}.

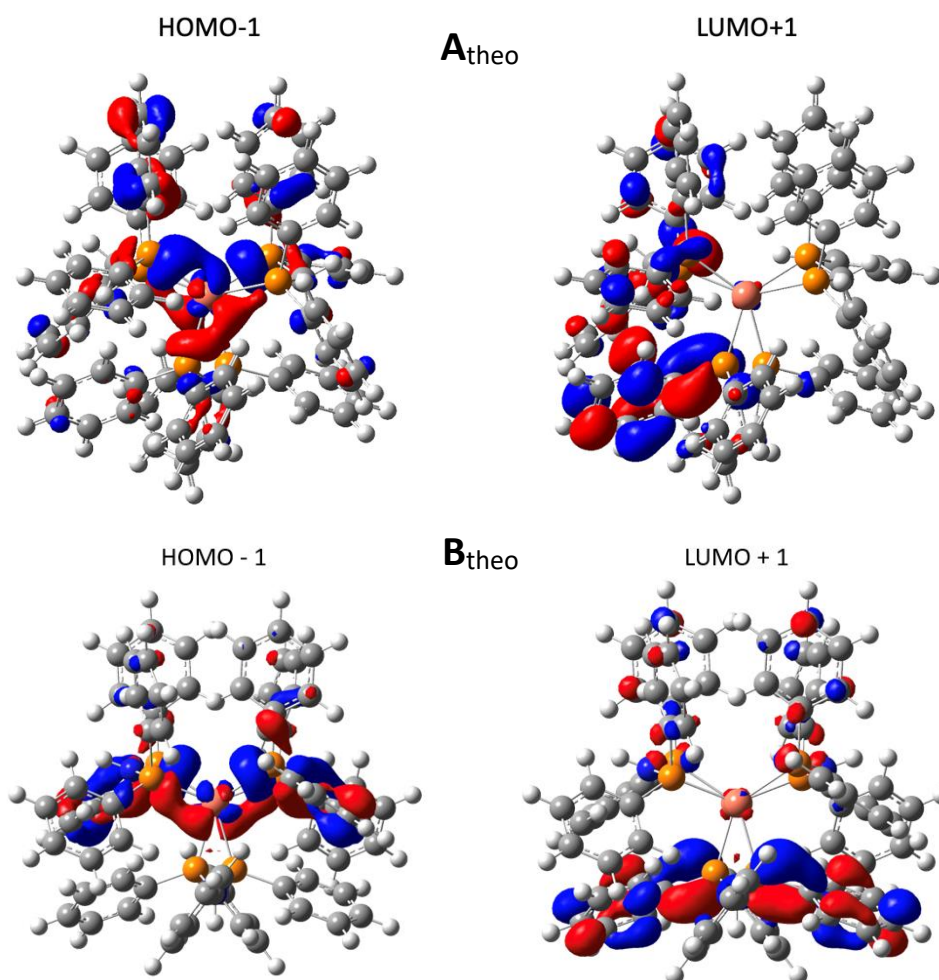


Figure 12 – MOs energetic diagram of \mathbf{A}_{theo} and \mathbf{B}_{theo} . The iso-values used for the representation of the orbitals is ± 0.03 (e/Bohr³)^{1/2}.

The MOs energetic diagram of the mono-deprotonated system $\mathbf{B}_{\text{theo/-H}^+}$ is represented in Figure 13. The deprotonation changes importantly the electronic structures. Indeed, the HOMO is significantly localized on the nitrogen non-bonding doublet of the amine group of the deprotonated dppa ligand ($\sim 20\%$) and not on the other amine groups. As for \mathbf{B}_{theo} , the HOMO has a substantial metallic character ($\sim 19\%$), the rest being localized on the phosphorus atoms (25%) and the phenyl groups of the dppa. The LUMO is highly similar to that of \mathbf{B}_{theo} with slightly more delocalization on the phenyl rings.

The HOMO-1 and LUMO+1 are localized on the $\text{Cu}_2\text{-dppa-}_{\text{H}^+}$ part for the former and on the two non-deprotonated dppa for the latter. The HOMO-LUMO gap is mainly decreased (3.57 for $\mathbf{B}_{\text{theo/-H}^+}$ vs 4.25 eV for \mathbf{B}_{theo}) because of the nitrogen lone-pair contribution in the HOMO. These electronic structure modifications will have an impact on the electronic excitation properties.

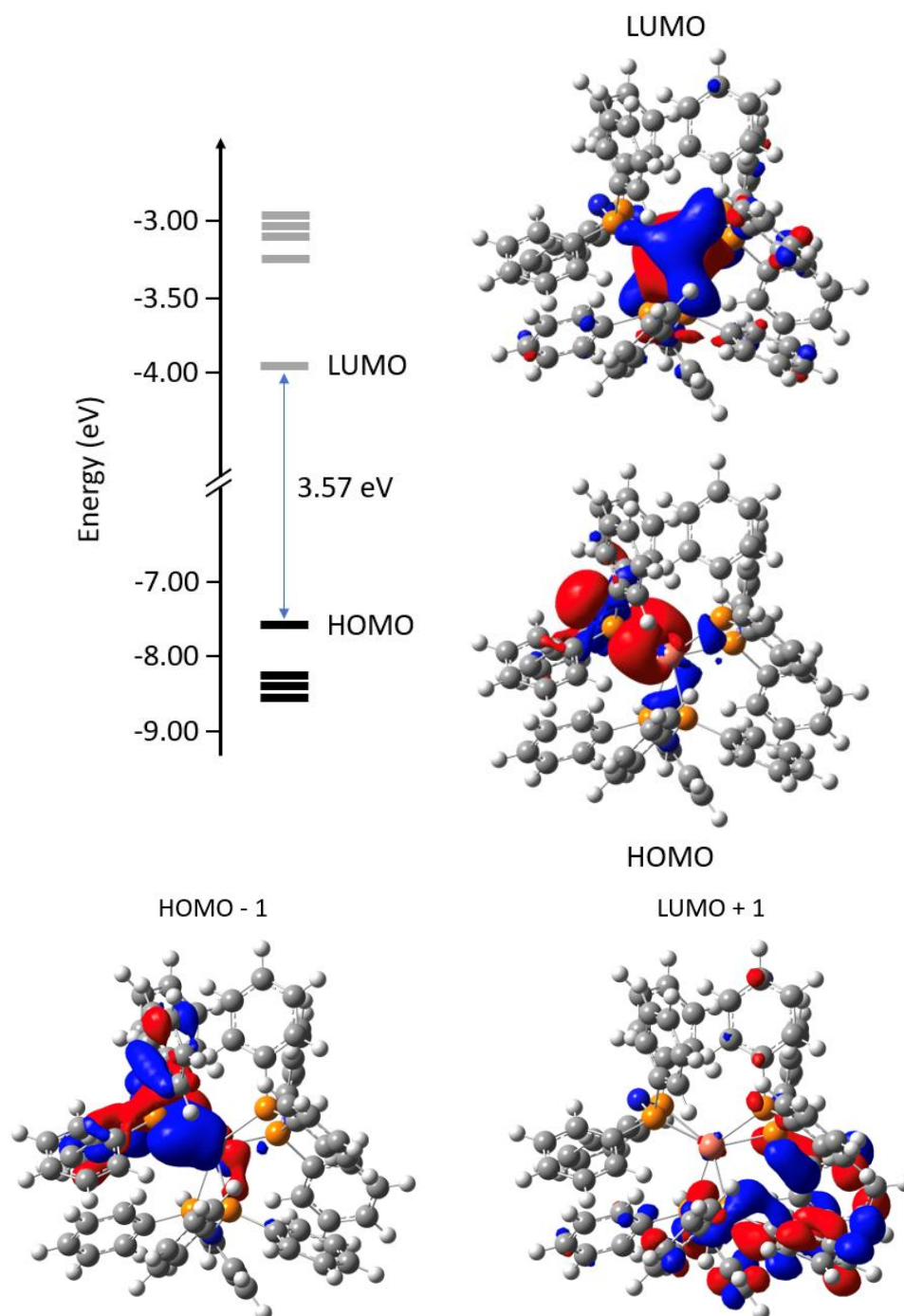


Figure 13 – MOs energetic diagram of the $\mathbf{B}_{\text{theo}}/\text{-H}^+$. The iso-values used for the representation of the orbitals are ± 0.03 (e/Bohr^3)^{1/2}.

III.3 – Electronic excitation energies, simulated UV-Vis absorption spectra

Computational details

The lowest 15 excitation energies were calculated using the Time-Dependent Tamm-Dancoff Approximation DFT (TDA-DFT)^{15,16} approach at the same level of theory as the geometry optimization (SVP atomic basis set, PBE0 functional), as implemented in Gaussian 16. This

level of calculation is called **level_{Gauss1}** next. The effect of the reduced SVP basis set was evaluated by expanding the basis to the 6-311G (3df, 3pd) atomic basis set as implemented in Gaussian (**level_{Gauss2}**). Since the bimetallic systems are much smaller than the CDS polymetallic compounds of the next chapter, more sophisticated calculations were manageable. We also shed light on additional processes such as the ISC notably, and the SOC influence for some systems. To date, SOC is not implemented for DFT in Gaussian 16; we thus used the ADF program of Amsterdam Modeling Suite.¹⁷ In this case, the calculations were performed using the hybrid PBE0 functional with a large atomic basis set (triple- ξ and two polarization functions (TZ2P, all electrons))¹⁸ at the scalar Zero Order Regular Approximation (ZORA).¹⁹ This computational method will be called **level_{ADF}**. We have tested for one system the influence of the scalar-ZORA correction by first removing it (**level_{ADF-w/o-ZORA}**). A better level of theory, effectively including SOC, was also tested in the case of **B_{theo}** (**level_{ADF-SOC}**). We have also calculated the SOC between excited states by the perturbative TDA-SOPERT approach (**level_{ADF-SOPERT}**),²⁰ at the same level of theory (basis set / functional). If unspecified, the geometry used is the optimized geometry at the **level_{Gauss1}**.

Vertical excited state energies and absorption spectra

The energies of the five first vertical singlet and triplet states were calculated for **A_{theo}** at the **level_{Gauss1}** and **level_{ADF}** relatively to the energy of the ground state S_0 . The oscillator strength of the first two singlet excited states are really small ($f < 0.01$) so that a comparison with the experimental absorption spectra is not possible. It appears interesting to us to evaluate the level of precision of the **Level_{Gauss1}** which will be used in the next chapter by comparing it with alternatives, i.e. larger basis set and relativistic effect corrections. The vertical energies of the singlet excited states are 0.15 eV smaller on average at the **Level_{ADF}**. Interestingly, the first two triplet excited states are a tiny less shifted (~ 0.11 eV).

A more complete study of the DFT level impact was performed for **B_{theo}**. These results are summarized in Table 5. The deviation between **Level_{Gauss1}** and **Level_{ADF}** is really similar to **A_{theo}** with a lowering by 0.16 eV on average of the energies of the first singlet states, and by 0.10 eV for the first three vertical triplet states. To better discriminate between the effects of the augmentation of the atomic basis set, the change between Gaussian function type to Slater function type, and the effect of relativistic corrections, we performed the same calculations with different levels of theory. First, an extension of the Gaussian-type function basis set from SVP to 6-311G (3df, 3pd) (**Level_{Gauss2}**) was performed (Table 5). The result on the excited state energies is really homogeneous with a lowering by 0.07 eV on average. Changing from

Gaussian type basis set to the triple-zeta Slater type basis set **Level_{ADF-w/o-ZORA}** leads to the same trend, with a lowering by 0.11 eV for the singlet excited states and 0.05 eV for the triplet states. The effect of the basis set can explain the main part of the changes between **Level_{Gauss1}** and **Level_{ADF}**. Yet, the relativistic effects are also playing a part since introducing a scalar ZORA correction (**Level_{ADF}**) weakens by 0.05 eV more on average all excited state energies.

Table 4 – Relative energies in eV of the first five singlet and triplet vertical excited states for **A_{theo}** at the **Level_{Gauss1}** and **level_{ADF}**. The energy of S₀ is taken as reference energy.

| x | Level_{Gauss1} | | Level_{ADF} | |
|---|-------------------------------|---------------------|----------------------------|---------------------|
| | S _{x-vert} | T _{x-vert} | S _{x-vert} | T _{x-vert} |
| 1 | 3.453 | 3.242 | 3.288 | 3.114 |
| 2 | 3.655 | 3.385 | 3.492 | 3.299 |
| 3 | 3.808 | 3.435 | 3.647 | 3.455 |
| 4 | 3.876 | 3.453 | 3.726 | 3.496 |
| 5 | 4.259 | 3.462 | 4.128 | 3.771 |

Table 5 – Relative energies in eV of the first five singlet and triplet vertical excited states for the **B_{theo}** at the **level_{Gauss1}**, **level_{Gauss2}**, **Level_{ADF-w/o-ZORA}**, **level_{ADF}**, **Level_{ASF-SOC}** (see text). The energy of S₀ is the reference energy.

| x | Level_{Gauss1} | | Level_{Gauss2} | | Level_{ADF-w/o-ZORA} | | Level_{ADF} | | Level_{ADF-SOC} |
|---|-------------------------------|---------------------|-------------------------------|---------------------|-------------------------------------|---------------------|----------------------------|---------------------|--------------------------------|
| | S _{x-vert} | T _{x-vert} | S _{x-vert} | T _{x-vert} | S _{x-vert} | T _{x-vert} | S _{x-vert} | T _{x-vert} | |
| 1 | 3.201 | 2.993 | 3.126 | 2.911 | 3.087 | 2.914 | 3.030 | 2.863 | 2.901 × 3 (~T ₁) |
| 2 | 3.515 | 3.259 | 3.444 | 3.188 | 3.405 | 3.214 | 3.345 | 3.159 | 3.067 (~S ₁) |
| 3 | 3.644 | 3.377 | 3.572 | 3.317 | 3.535 | 3.350 | 3.484 | 3.303 | 3.201 × 3 (~T ₂) |
| 4 | 3.812 | 3.394 | 3.741 | 3.355 | 3.704 | 3.505 | 3.654 | 3.459 | |
| 5 | 3.978 | 3.458 | 3.907 | 3.430 | 3.895 | 3.551 | 3.854 | 3.478 | |

The absorption spectra can be simulated on the basis of these excitation energies. They are given in Figure 14. The lowest absorption peak observed is at 359 nm and at 387 nm for **A_{theo}** and **B_{theo}** and is followed by several more intense peaks. The experimental solid-state absorption spectra are given in Figure 2 and Figure 6 for **A_{TEF}**, and **B_{BF4}** and **B_{PF6}** respectively. A direct comparison of the intensities is not possible but the comparison of the energies can be performed. For **A_{TEF}**, the onset of the absorption peak is in the same region as predicted by the

calculations (considering a calculation error of ~ 0.15 eV), while it is overestimated for \mathbf{B}_{BF_4} and \mathbf{B}_{PF_6} whose absorption peaks are roughly rising from 500 nm to lower wavelengths. This could be attributed to the difference in geometry between the optimized geometry \mathbf{B}_{theo} and the experimental one (for which the hydrogen atom positions are not available), as often stated in the literature. We also have simulated the absorption spectrum of the $[\text{Cu}_2(\text{dppa})_3]^{2+}$ geometry extracted from the X-Ray structure of \mathbf{B}_{PF_6} with the hydrogen atom positions optimized (blue curve in Figure 14). The most intense absorption peak is slightly shifted to lower wavelengths and a shoulder appears without improving the comparison with experimental observations. The origin of the discrepancies is thus different.

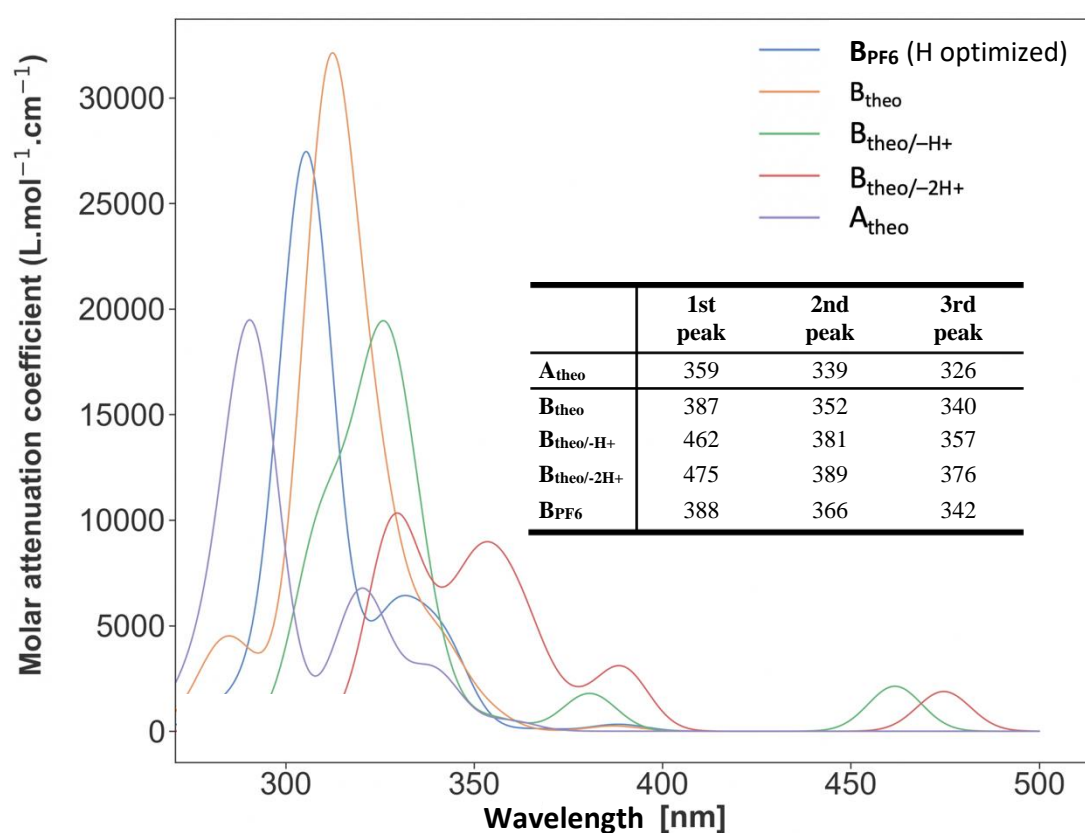


Figure 14 – Simulated UV-VIS absorption spectra of \mathbf{B}_{PF_6} with hydrogen atom positions optimized, \mathbf{B}_{theo} , $\mathbf{B}_{\text{theo/-H}^+}$, $\mathbf{B}_{\text{theo/-2H}^+}$, and \mathbf{A}_{theo} , as computed with a Gaussian smearing of 50 meV. Inset: summary table of the wavelengths of the lowest (energy) absorption peaks in nm.

The hydrogen interactions (partial hydrogen deprotonations) that are observed in the experimental X-Ray structures are detailed in the experimental section description. The studies of the deprotonated $\mathbf{B}_{\text{theo/-H}^+}$ and $\mathbf{B}_{\text{theo/-2H}^+}$ described previously show that the electronic structure is deeply modified, with the HOMO-LUMO gap getting smaller (3.57 eV ($\mathbf{B}_{\text{theo/-H}^+}$) vs 4.25 eV (\mathbf{B}_{theo}))

and the participation of the lone pair of the deprotonated nitrogen atom in the HOMO. The simulated absorption spectra of $\mathbf{B}_{\text{theo/-H}^+}$ and $\mathbf{B}_{\text{theo/-2H}^+}$ are given in Figure 14 (green and red curves, respectively). As expected from the study of the electronic structures, the first absorption bands are found at 462 and 475 nm, respectively, followed by several absorption bands from 400 nm to the UV region. These simulations allow to speculate that the hydrogen bonds present in the crystal are leading to partial deprotonations that lower the energies of the first excited states.

The nature of the first excited states is particularly important to understand the properties of the excited states, and hence the emission in the present case. Table 6 and Table 7 are gathering the description of the lowest singlet excited states for \mathbf{A}_{theo} and \mathbf{B}_{theo} at the $\text{level}_{\text{Gauss1}}$.

Table 6 – Calculated electronic vertical excitation energies of \mathbf{A}_{theo} ($\text{level}_{\text{Gauss1}}$). f corresponds to the dimensionless oscillator strength. The nature of the excitation in terms of the main MO transitions is given in the column “Main transition”.

| $\mathbf{A}_{\text{theo}} - \text{level}_{\text{Gauss1}}$ | | | | | |
|---|------|-----|--------|-----------------|----|
| State | eV | nm | f | Main transition | % |
| S _{1-vert} | 3.45 | 359 | 0.0038 | HOMO → LUMO | 91 |
| S _{2-vert} | 3.66 | 339 | 0.0218 | HOMO-1 → LUMO | 90 |
| S _{3-vert} | 3.81 | 325 | 0.0032 | HOMO-2 → LUMO | 86 |
| S _{4-vert} | 3.88 | 320 | 0.0489 | HOMO-3 → LUMO | 86 |
| S _{5-vert} | 4.26 | 291 | 0.1374 | HOMO-4 → LUMO | 72 |

The main MO transition in all cases lead to the population of the LUMO which has mainly Cu–Cu bonding character and the depopulation of one of the highest MOs with Cu-P bonding character. The natural transition orbitals (NTOs) describing these excitations are represented for S_{1-vert} (Figure 15 and 16). As expected, they highly resemble the HOMO and LUMO. The nature of the electronic transition which describes the T_{1-vert} excitation is similar to S_{1-vert} as shown in Figure 15 and 16. Another way of describing the nature of the excitations is to plot the difference between the total density of the considered excited state with respect to the ground state (Figure 17 for \mathbf{B}_{theo}). It allows to visualize the increase of density between the two copper atoms and the high similarities between S_{1-vert} and T_{1-vert} vertical excited states. The description of the emission properties necessitates to consider the relaxed excited states (see next section). A strengthening of the Cu–Cu interaction is expected in the relaxed geometries of S_{1-vert} and T_{1-vert} in all cases compared to the ground state.

Table 7 – Calculated electronic vertical excitation energies of B_{theo} , $B_{\text{theo}/\text{H}^+}$ and $B_{\text{theo}/\text{2H}^+}$ ($\text{level}_{\text{Gauss1}}$). f corresponds to the dimensionless oscillator strength. The nature of the excitation in terms of MO transitions is given in the column “Main transition”.

| $B_{\text{theo}} - \text{level}_{\text{Gauss1}}$ | | | | | |
|--|------|-----|--------|-----------------|----|
| State | eV | nm | f | Main transition | % |
| S ₁ -vert | 3.20 | 387 | 0.0019 | HOMO → LUMO | 93 |
| S ₂ -vert | 3.52 | 352 | 0.0073 | HOMO-1 → LUMO | 87 |
| S ₃ -vert | 3.65 | 340 | 0.0315 | HOMO-2 → LUMO | 89 |
| S ₄ -vert | 3.82 | 324 | 0.0742 | HOMO-3 → LUMO | 83 |
| S ₅ -vert | 3.98 | 311 | 0.2292 | HOMO-4 → LUMO | 84 |

| $B_{\text{theo}/\text{H}^+} - \text{level}_{\text{Gauss1}}$ | | | | | |
|---|------|-----|--------|-----------------|----|
| State | eV | nm | f | Main transition | % |
| S ₁ -vert | 2.69 | 462 | 0.0163 | HOMO → LUMO | 98 |
| S ₂ -vert | 3.26 | 381 | 0.0137 | HOMO-1 → LUMO | 92 |
| S ₃ -vert | 3.47 | 357 | 0.0023 | HOMO-2 → LUMO | 68 |
| S ₄ -vert | 3.52 | 353 | 0.0026 | HOMO-3 → LUMO | 64 |
| S ₅ -vert | 3.68 | 337 | 0.0242 | HOMO → LUMO+1 | 80 |

| $B_{\text{theo}/\text{2H}^+} - \text{level}_{\text{Gauss1}}$ | | | | | |
|--|------|-----|--------|-----------------|----|
| State | eV | nm | f | Main transition | % |
| S ₁ -vert | 2.61 | 475 | 0.0144 | HOMO → LUMO | 96 |
| S ₂ -vert | 3.18 | 389 | 0.0224 | HOMO-1 → LUMO | 85 |
| S ₃ -vert | 3.29 | 376 | 0.0062 | HOMO-2 → LUMO | 76 |
| S ₄ -vert | 3.39 | 366 | 0.0090 | HOMO → LUMO+1 | 88 |
| S ₅ -vert | 3.43 | 362 | 0.0221 | HOMO → LUMO+2 | 81 |

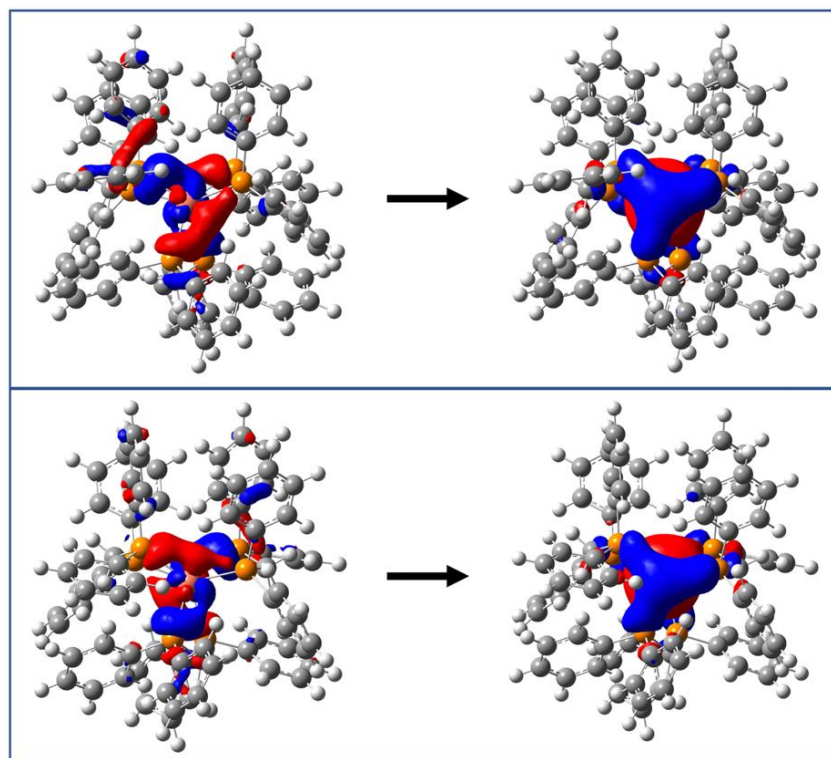


Figure 15 – Representation of the Natural Transition Orbitals (NTO) associated to the S_0 to $T_{1\text{-vert}}$ (top) and S_0 to $S_{1\text{-vert}}$ (bottom) excitations for \mathbf{A}_{theo} (`levelGauss1`).

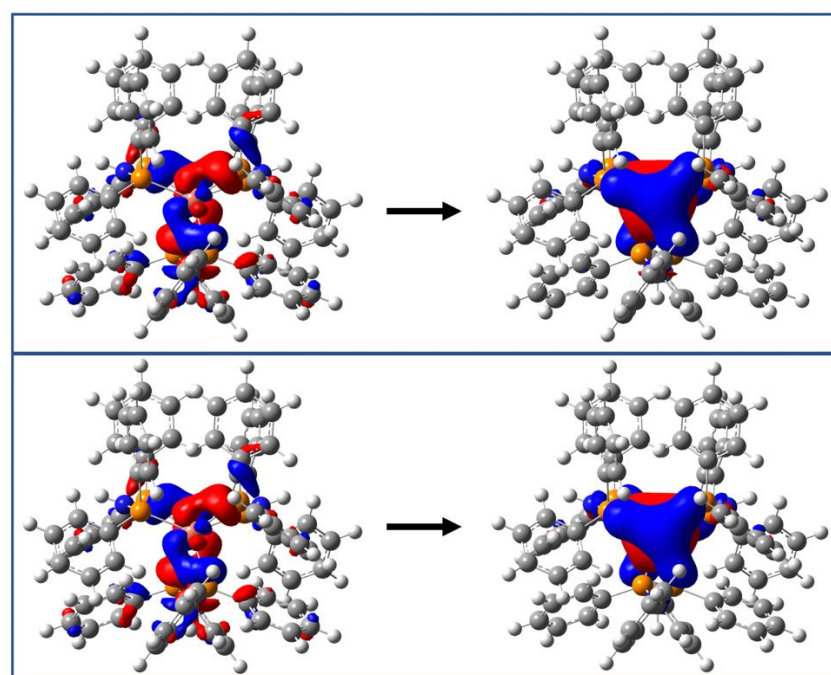


Figure 16 – Representation of the NTOs associated to the S_0 to $T_{1\text{-vert}}$ (top) and S_0 to $S_{1\text{-vert}}$ (bottom) excitations for \mathbf{B}_{theo} (`levelGauss1`).

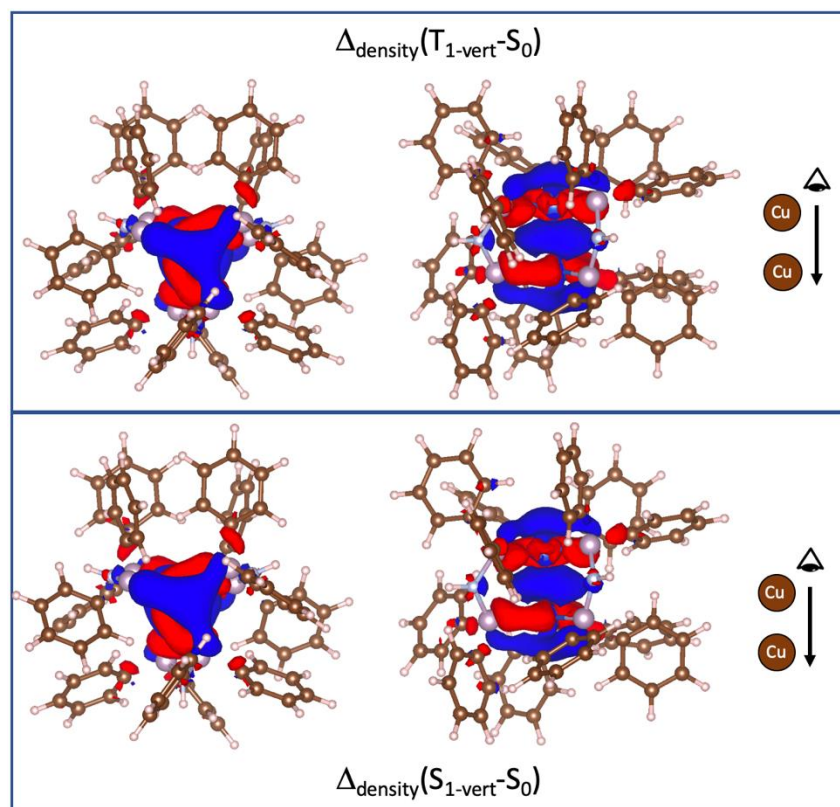


Figure 17 – One perpendicular (left) and one lateral (right) view of the isosurface description of the electronic charge-density difference between the first vertical triplet ($T_{1\text{-vert}}$, top) and singlet ($S_{1\text{-vert}}$, bottom) excited states, and the ground state (S_0) of \mathbf{B}_{theo} ($\text{level}_{\text{Gauss1}}$); red = density depletion; blue = density increase; the iso-density is 1.10^{-4} e/bohr³.

The fast-non-radiative de-excitation process which follows the excitation encompasses by IC between singlet excited states followed by an ISC to a triplet excited state. The Kasha's rule establishes that the IC processes should lead to the lowest excited state (S_1), and then the ISC occurs between $S_{1\text{-vert}}$ and $T_{1\text{-vert}}$. The ISC is favored by spin-orbit coupling. The SOC matrix elements between excited states were calculated at the $\text{level}_{\text{ADF-SOPERT}}$ for \mathbf{A}_{theo} and \mathbf{B}_{theo} in the S_0 geometry (considering that the geometry relaxation occurs at a slower time scale) and collected in Table 8. The $S_{1\text{-vert}}$ to $T_{1\text{-vert}}$ ISC is largely disfavored due to negligible SOC between the two states. For both, $S_{1\text{-vert}}$ to $T_{2\text{-vert}}$ ISC is not possible since $T_{2\text{-vert}}$ is higher in energy. For \mathbf{A}_{theo} , this difference in energy is small ($+88$ cm⁻¹), which is within the calculation precision at this level of theory. When increasing the level of calculation to $\text{level}_{\text{ADF-SO}}$, the $T_{2\text{-vert}}$ is even higher in energy ($+1081$ cm⁻¹) ruling out this possibility of ISC from $S_{1\text{-vert}}$ to $T_{2\text{-vert}}$. The most important SOC, in both compounds, is between $S_{2\text{-vert}}$ and $T_{1\text{-vert}}$ (112 and 143 cm⁻¹, respectively). However, their energy difference is more than 3000 cm⁻¹ which is a really high value and one would need to know about the superposition between vibrational states to be

conclusive. Considering this analysis, non-radiative de-excitation processes are competing but more accurate quantum methods are necessary to draw more precise descriptions. The $\mathbf{T}_{1\text{-vert}}$ is eventually populated and geometrical relaxations will occur modifying the energy ordering between excited states.

Table 8 – Spin-orbit coupling matrix elements between the lowest vertical singlet and triplet excited states in cm^{-1} and difference in energy between selected states for \mathbf{A}_{theo} and \mathbf{B}_{theo} ($\text{level}_{\text{ADF-SOPERT}}$) in cm^{-1} and eV. The crossed-out table cells are corresponding to cases for which the triplet states are higher in energy than the considered singlet states.

| $\mathbf{A}_{\text{theo}} - \text{level}_{\text{ADF-SOPERT}}$ | | | | | | |
|--|----------------|----------------|----------------|----------------|----------------|--|
| $\langle \mathbf{S} \mathbf{H}_{\text{so}} \mathbf{T} \rangle$ | \mathbf{T}_1 | \mathbf{T}_2 | \mathbf{T}_3 | \mathbf{T}_4 | \mathbf{T}_5 | $\Delta E / \text{cm}^{-1}$ (eV) |
| $\mathbf{S}_{1\text{-vert}}$ | 7 | 84 | 197 | 54 | 25 | $\mathbf{S}_{1\text{-vert}} - \mathbf{T}_{1\text{-vert}}$ 1403 (0.174) |
| $\mathbf{S}_{2\text{-vert}}$ | 112 | 5 | 42 | 190 | 64 | $\mathbf{S}_{1\text{-vert}} - \mathbf{T}_{2\text{-vert}}$ -88 (-0.011) |
| $\mathbf{S}_{3\text{-vert}}$ | 189 | 52 | 13 | 86 | 44 | $\mathbf{S}_{2\text{-vert}} - \mathbf{T}_{1\text{-vert}}$ 3049 (0.378) |

| $\mathbf{B}_{\text{theo}} - \text{level}_{\text{ADF-SOPERT}}$ | | | | | | |
|--|----------------|----------------|----------------|----------------|----------------|--|
| $\langle \mathbf{S} \mathbf{H}_{\text{so}} \mathbf{T} \rangle$ | \mathbf{T}_1 | \mathbf{T}_2 | \mathbf{T}_3 | \mathbf{T}_4 | \mathbf{T}_5 | $\Delta E / \text{cm}^{-1}$ (eV) |
| $\mathbf{S}_{1\text{-vert}}$ | 2 | 122 | 165 | 27 | 27 | $\mathbf{S}_{1\text{-vert}} - \mathbf{T}_{1\text{-vert}}$ 1347 (0.167) |
| $\mathbf{S}_{2\text{-vert}}$ | 143 | 4 | 56 | 142 | 92 | $\mathbf{S}_{2\text{-vert}} - \mathbf{T}_{1\text{-vert}}$ 3904 (0.484) |
| $\mathbf{S}_{3\text{-vert}}$ | 147 | 57 | 6 | 125 | 75 | $\mathbf{S}_{3\text{-vert}} - \mathbf{T}_{1\text{-vert}}$ 5018 (0.622) |

III.3 – Excited state geometry relaxation, emission properties

In order to study the emission properties, optimizations of the geometries of the first excited state of \mathbf{A}_{theo} and \mathbf{B}_{theo} were performed. Considering that the ISC should occur between $\mathbf{S}_{2\text{-vert}}$ and $\mathbf{T}_{1\text{-vert}}$ as established in the previous section, a relaxation of geometry at the \mathbf{T}_1 state is possible (the lifetime of triplet states is being much longer than that of singlet states). To have a full description of the process, other excited states should be considered. The optimized distances for each relevant state are given in Table for the \mathbf{B}_{theo} series. As expected from the description of the electronic density changes upon excitation, the Cu–Cu distances and Cu–P bond lengths are shorter in the first singlet and triplet excited states (-0.14 \AA to -0.24 \AA for Cu–Cu, and -0.02 \AA to -0.03 \AA for Cu–P), reorganization which occurs upon population of the LUMO. The metal electronic density is therefore involved in the excitation processes potentially reinforcing the SOC, and hence the RISC and the spontaneous emission. The geometries of \mathbf{S}_1 , \mathbf{S}_2 , \mathbf{T}_1 , \mathbf{T}_2 of \mathbf{B}_{theo} are displayed in Figure 18. The ground state \mathbf{S}_0 that is

represented as background image allows to visualize the small changes that occur in the geometry. This is similar in the A_{theo} series. This is beneficial to the RISC processes in which the difference in energy and the SOC also have to be considered.

Table 9 – Optimized distances of A_{theo} and B_{theo} in their different spin states S_1 , S_2 , T_1 , T_2 compared to S_0 . For numbering, refer to Scheme 1 and 2.

| A_{theo} state | S_0 | S_1 | S_2 | T_1 | T_2 |
|-------------------------|-------|-------|-------|-------|-------|
| Cu1-Cu2 | 2.799 | 2.574 | 2.658 | 2.556 | 2.634 |
| Cu1-P1 | 2.351 | 2.325 | 2.333 | 2.327 | 2.332 |
| Cu2-P2 | 2.348 | 2.351 | 2.382 | 2.363 | 2.375 |
| Cu1-P3 | 2.353 | 2.324 | 2.342 | 2.315 | 2.333 |
| Cu2-P4 | 2.348 | 2.316 | 2.366 | 2.319 | 2.376 |
| Cu1-P5 | 2.384 | 2.364 | 2.331 | 2.373 | 2.335 |
| Cu2-P6 | 2.377 | 2.335 | 2.311 | 2.340 | 2.314 |

| B_{theo} state | S_0 | S_1 | S_2 | T_1 | T_2 |
|-------------------------|-------|-------|-------|-------|-------|
| Cu1-Cu2 | 2.643 | 2.461 | 2.502 | 2.474 | 2.454 |
| Cu1-P1 | 2.339 | 2.305 | 2.306 | 2.301 | 2.310 |
| Cu2-P2 | 2.344 | 2.340 | 2.303 | 2.309 | 2.314 |
| Cu1-P3 | 2.344 | 2.338 | 2.371 | 2.379 | 2.314 |
| Cu2-P4 | 2.339 | 2.304 | 2.294 | 2.300 | 2.310 |
| Cu1-P5 | 2.372 | 2.336 | 2.345 | 2.342 | 2.360 |
| Cu2-P6 | 2.372 | 2.336 | 2.323 | 2.325 | 2.360 |

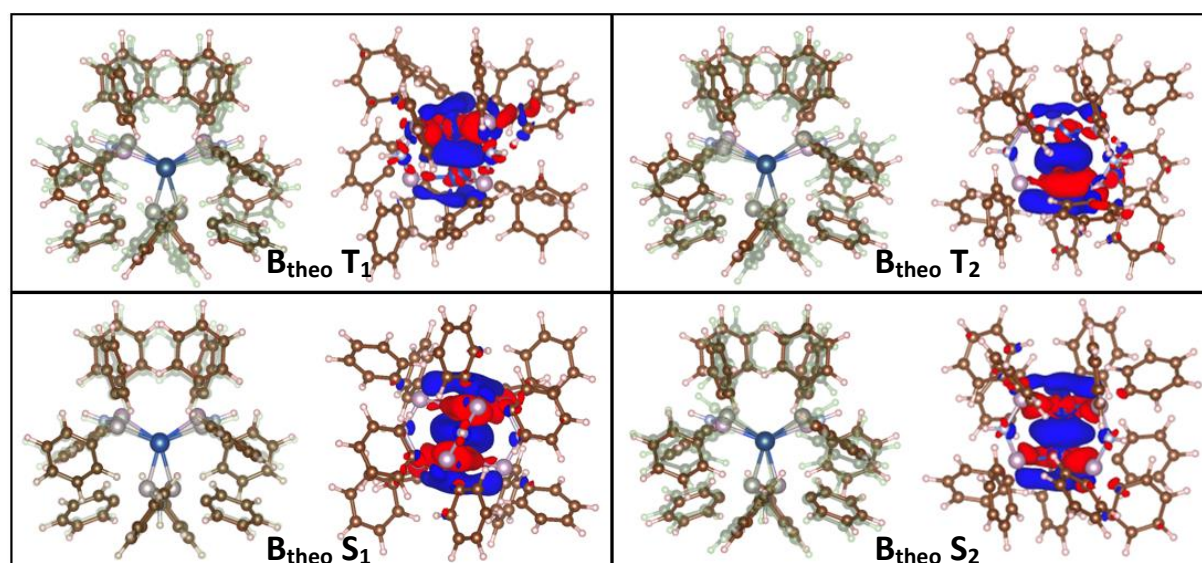


Figure 18 – For each table cell: (left) representations of optimized geometries of B_{theo} superimposed onto the S_0 B_{theo} optimized geometry in light green (T_1 , T_2 , S_1 or S_2); (right) and iso-surface representations of the electronic charge-density difference between the considered

excited state and the density of the closed shell singlet at the same geometry ($S_0^\#$) of \mathbf{B}_{theo} ($\text{level}_{\text{Gauss1}}$); red = density depletion; blue = density increase; the iso-surface is 1.10^{-4} e/bohr³.

The energy diagram of the relaxed states compared with the potential energy surface (PES) of the ground state for the two series \mathbf{A}_{theo} and \mathbf{B}_{theo} are represented in Figure 19. The numbering of the relaxed excited states is given as a function of their relative energies but the methodology used to relax the geometry of the excited states cannot confirm that they are kept in the same ordering as the vertical excited states (possibility of PES exchange).

The experimental study of the luminescent properties of \mathbf{A}_{TEF} shows that the maximum of emission which is 489 nm at 80 K, increases to 497 nm between 160 and 170 K, and then decreases to 479 nm at 300 K (Figure 3). The evolution of the lifetime also shows a decrease followed by an increase up to 160 K and then a usual TADF-like decay (Figure 4). This behavior cannot be explained by a simple TADF process. The energies of the excited states and the emission wavelengths of \mathbf{A}_{theo} states are given in Figure 19 (top). The T_1 relaxed state is low in energy and separated by 2073 cm^{-1} from the S_1 . The emission from the T_1 state is calculated at 593 nm, really far from the experimental values. The emission wavelengths of the relaxed T_2 and T_3 states of 522 nm and 452 nm better agree with the experimental emission wavelength below 170 K. Moreover, T_2 is rather close in energy to S_1 (1121 cm^{-1}) and T_3 to S_2 (2016 cm^{-1}). Several temperature-dependent non-radiative pathways involving both S_1 and S_2 can be invoked, associated with a dual combined phosphorescence. Additional experimental data with another counter-anion, study of the emission as the function of the excitation wavelength and time-resolved measurements for instance would be needed. The TADF behavior that appears to occur after 170 K should be studied differently by de-correlating the first process. Because the plateau at high temperature is not reached, a wavelength lower than 479 nm can be conjectured for the fluorescent species. Based on the computational results, the TADF process cannot involved the S_1 state whose emission wavelength is 512 nm and would more likely take place from the relaxed S_2 state.

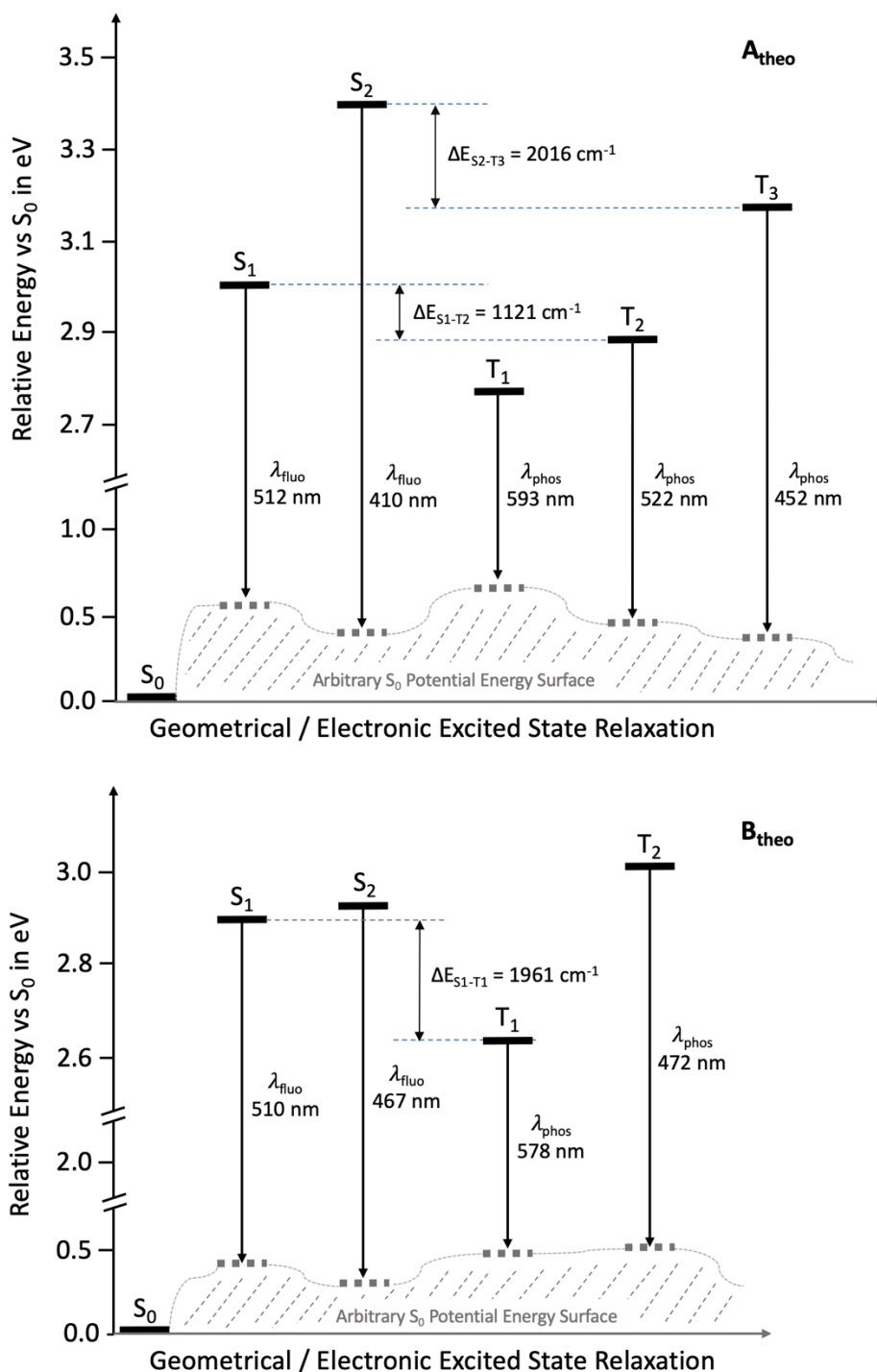


Figure 19 – Relative energy diagram of several lowest optimized excited states as calculated in the TD-DFT paradigm relative to S_0 in eV with their associated emission wavelengths in nm. Top: **A_{theo}**. Bottom: **B_{theo}**.

From the experimental results of Figure 8 (different excitation wavelengths used), the dppa-containing systems are showing an evolution of the maximum going from 516 nm to 493 nm for **B_{BF4}**, and from 551 nm to 520 nm for **B_{PF6}** upon the increase of temperature from 80 K to 300 K. The hydrogen interactions with the counter-ions play an important role, as detailed in

the experimental result section. To be able to reproduce these features, a study of the excited states should be done in the solid-state. Considering that $[\text{Cu}_2(\text{dppa})_3]^{2+}$ could be possibly co-crystallized with a non-interacting counter-ion, we performed a full study of the \mathbf{B}_{theo} which will be compared with these future results.

The energies of the excited states and emission wavelengths of \mathbf{B}_{theo} states are collected in Figure 19 (bottom). Contrarily to \mathbf{A}_{theo} , S_1 and S_2 states are close in energy (415 cm^{-1}) and only the triplet excited, T_1 , is found below. Once populated via ISC, from $S_{2\text{-vert}}$ to $T_{1\text{-vert}}$, two main processes can occur: RISC that can then lead to TADF and spontaneous emission. Calculations at the $\text{level}_{\text{ADF-SOPERT}}$ and $\text{level}_{\text{ADF-SO}}$ at the T_1 geometry were performed to evaluate their probabilities.

Modeling the RISC from T_1 to S_1 implies to calculate $|V_{\text{SOC}}|^2$. Because T_1 actually consists of three SO states, V_{SOC} can be considered as the average of the SOC matrix element. Considering that the RISC process occurs in a shorter timescale than the geometrical reorganization of the systems during the $T_1 \rightarrow S_1$ transition, the factor $|V_{\text{SOC}}|^2$ is computed at the optimized geometry of the T_1 state of \mathbf{B}_{theo} using $\text{level}_{\text{ADF-SOPERT}}$ and gives $V_{\text{SOC}}(T_1-S_1) = 2.5 \cdot 10^{-4} \text{ eV}$, thus, $|V_{\text{SOC}}|^2 = 6.25 \cdot 10^{-8} \text{ eV}^2$.

The other important factor to calculate the ρ_{FCWD} , the Frank-Condon-Weighted Density of States. Using the classical Marcus theory (CMT) to describe the thermo-kinetic barrier (Figure 20), the potential energy surface (PES) of both states around their respective minimum structures are described in terms of parabolic functions.

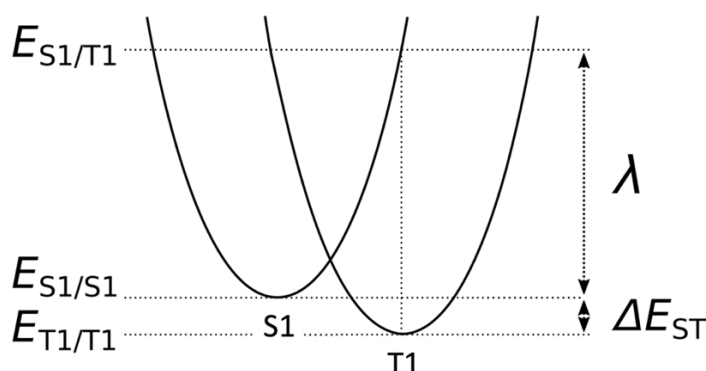


Figure 20 – PES of the S_1 and T_1 states described as quadratic functions centered at their respective minimum.

Using an Arrhenius-type expression for ρ_{FCWD} :

$$\rho_{FCWD} = \frac{1}{\sqrt{4\pi\lambda k_B T}} \exp\left(-\frac{(\Delta E_{ST} + \lambda)^2}{4\lambda k_B T}\right) \quad \text{Eq. 1}$$

with λ the reorganization energy considered as the energy required to bring the system in the S_1 state to the minimum structure of the T_1 state. Labeling the energy of the S_1 state at the S_1 geometry by E_{S_1/S_1} and the energy of the S_1 state at the T_1 geometry by E_{S_1/T_1} , leads to:

$$\lambda = E_{S_1/T_1} - E_{S_1/S_1} \quad \text{Eq. 2}$$

For \mathbf{B}_{theo} , at 300 K, the calculated $\lambda = 0.06$ eV and $\Delta E_{S_1-T_1} = 0.24$ eV which leads to $\rho_{FCWD} = 2.4 \cdot 10^{-6} \text{ eV}^{-1}$. Finally, using the Fermi's golden rule can be used to estimate k_{RISC} :²¹

$$k_{\text{RISC}} = \frac{2\pi}{\hbar} |V_{\text{SOC}}|^2 \cdot \rho_{FCWD} \quad \text{Eq. 3}$$

The theoretical T_1 to S_1 k_{RISC} for \mathbf{B}_{theo} is $4.7 \cdot 10^2 \text{ s}^{-1}$ ($1/k_{\text{RISC}} = 2.1 \cdot 10^{-3} \text{ s}$). This value has to be compared to the electric dipole spontaneous radiative lifetime of T_1 calculated using **level**_{ADF}-so. $\nu = 1.2 \cdot 10^2$ seconds. At RT, using simple expressions to estimate k_{RISC} , it appears that the RISC is favored compared to the spontaneous emission of the triplet state (one order of magnitude). Thus, our computational studies reveal that if the $[\text{Cu}_2(\text{dppa})_3]^{2+}$ could be crystallized without hydrogen bonding interactions with the counterions or included solvent, the TADF process should be operative.

IV – Conclusion

The study of fairly simple bimetallic copper(I) systems coordinated by diphosphinyl-only bridging ligands was performed initially to better evaluate the magnitude of uncertainty that is obtained by employing the **level**_{Gauss}. Indeed, the largest systems that have been studied in the group which are synthesized by our collaborator Lescop^{22,23,24,25} do not allow increasing the level of theory. Remarkably, their ground state and excited state properties are much complex than in the larger systems studied previously in the group. \mathbf{A}_{theo} emission properties are revealing at least two separate processes depending on the temperature. An unusual increase of the maximum of emission wavelength is observed upon increase of temperature from 80 K to 160 K, whose lifetime fits with phosphorescence, and a TADF like feature above 160 K. The computational studies show that the S_1 and T_1 states are low in energy and quite separated from the other excited states. Their emission wavelengths are higher compared to the experimental measurements; in this respect, we stress that in previous studies on much larger systems, the

differences between experimental and computational emission wavelengths were below 0.15 eV.²² The energy spectrum shown in Figure 19 is in favor of temperature dependency and most probably excitation wavelength dependency of the population for the T₂ and T₃ triplet states at low temperature, which would compete with a TADF process at higher temperature. A global explanation based on the computational results cannot be drawn and would necessitate to study conical intersections and the dynamic of the excited states. Additional experimental measurements are definitely required such as the study of the emission properties as the function of the excitation wavelength and time-resolved measurements.

The modification of the CH₂ group by NH in the diphosphine ligand in **A_{theo}** complicates the problem by introducing hydrogen bond interactions with the fluorine atoms of the counter-ions. Indeed, **B_{PF6}** and **B_{BF4}** have different absorption and emission properties which are attributed to the differences in the intermolecular interactions in the crystal. The weakening effect of the N-H bond due to hydrogen interactions has an effect on the absorption properties, as assessed theoretically by the electronic excitation properties of the deprotonated systems **B_{theo/-H+}** and **B_{theo/-2H+}**. This induces a red shifting of the absorption in agreement with experimental results. Unfortunately, a computational study of the excited states would need to be done in the solid-state to be comparable with the experimental results. Considering that [Cu₂(dppa)₃]²⁺ could be possibly crystallized with a non-interacting ligand, a study of the excited states of **B_{theo}** was done. Our simulations are indeed revealing that the TADF process would be operative in that configuration.

Overall, this theoretical study opens up interesting perspectives to study non-conventional emission properties of high interest at a fundamental point of view. The combination between experimental and computational results is highly desirable to tackle the problem.

-
- ¹ a) Ford, P.; Cariati, E.; Bourassa, J. Photoluminescence Properties of Multinuclear Copper(I) Compounds. *Chem. Rev.* 1999, 99, 3625–3648. doi:10.1021/cr960109i. b) Yam, V. W.-W.; Fung, W. K.-M.; Cheung, K.-K. Synthesis, Structure, Photophysics, and Excited-State Redox Properties of the Novel Luminescent Tetranuclear Acetylidocopper(I) Complex $[\text{Cu}_4(\mu\text{-dppm})_4(\mu_4\text{-}\eta^1, \eta^2\text{-C}\equiv\text{C})](\text{BF}_4)_2$. *Angew. Chem. Int. Ed.* 1996, 35, 1100–1102. doi:10.1002/anie.199611001.
- ² Zhang, Y.; Schulz, M.; Wächtler, M.; Karnahl, M.; Dietzek, B. Heteroleptic Diimine–Diphosphine Cu(I) Complexes as an Alternative towards Noble-Metal Based Photosensitizers: Design Strategies, Photophysical Properties and Perspective Applications. *Coord. Chem. Rev.* 2018, 356, 127–146. doi:10.1016/j.ccr.2017.10.016.
- ³ Cariati, E.; Lucenti, E.; Botta, C.; Giovanella, U.; Marinotto, D.; Righetto, S. Cu(I) Hybrid Inorganic–Organic Materials with Intriguing Stimuli Responsive and Optoelectronic Properties. *Coord. Chem. Rev.* 2016, 306, 566–614. doi:10.1016/j.ccr.2015.03.004.
- ⁴ Osawa, M. Highly Efficient Blue-Green Delayed Fluorescence from Copper(i) Thiolate Complexes: Luminescence Color Alteration by Orientation Change of the Aryl Ring. *Chem. Comm.* 2014, 50, 1801. doi:10.1039/c3cc47871h.
- ⁵ Lotito, K. J.; Peters, J. C. Efficient Luminescence from Easily Prepared Three-Coordinate Copper(i) Arylamidophosphines. *Chem. Comm.* 2010, 46, 3690. doi:10.1039/c000818d.
- ⁶ Lee, K.; Lai, P.-N.; Parveen, R.; Donahue, C. M.; Wymore, M. M.; Massman, B. A.; Vlasisavljevich, B.; Teets, T. S.; Daly, S. R. Modifying the Luminescent Properties of a Cu(i) Diphosphine Complex Using Ligand-Centered Reactions in Single Crystals. *Chem. Comm.* 2020, 56, 9110–9113. doi:10.1039/D0CC03427D.
- ⁷ Li, X.; Zhang, J.; Zhao, Z.; Yu, X.; Li, P.; Yao, Y.; Liu, Z.; Jin, Q.; Bian, Z.; Lu, Z.; Huang, C. Bluish-Green Cu(I) Dimers Chelated with Thiophene Ring-Introduced Diphosphine Ligands for Both Singlet and Triplet Harvesting in OLEDs. *ACS Appl. Mater. Interfaces* 2019, 11, 3262–3270. doi:10.1021/acsami.8b15897.
- ⁸ Yamazaki, Y.; Tsukuda, T.; Furukawa, S.; Dairiki, A.; Sawamura, S.; Tsubomura, T. A Series of Mixed-Ligand Cu(I) Complexes Comprising Diphosphine-Disulfide Ligands: Effects of Diphosphine Ligands on Luminescent Properties. *Inorg. Chem.* 2020, 59, 12375–12384. doi:10.1021/acs.inorgchem.0c01445.
- ⁹ Harisomayajula, N. V. S.; Makovetskyi, S.; Tsai, Y. Cuprophilic Interactions in and between Molecular Entities. *Chem. Eur. J.* 2019, 25, 8936–8954. doi:10.1002/chem.201900332.
- ¹⁰ Tsuboyama, A. Luminescent Dinuclear Copper(I) Complexes with Short Intramolecular Cu-Cu Distances. *Highly Efficient OLEDs* 2018, 93–118. doi:10.1002/9783527691722.ch3.
- ¹¹ Bergmann, L.; Braun, C.; Nieger, M.; Bräse, S. The coordination- and photochemistry of copper(i) complexes: variation of N^N ligands from imidazole to tetrazole. *Dalton Trans.* 2018, 47, 608–621. doi:10.1039/c7dt03682e.
- ¹² Yersin, H. *Highly Efficient OLEDs: Materials Based on Thermally Activated Delayed Fluorescence*. Wiley-VCH Verlag GmbH & Co. KGaA: Weinheim, Germany, 2018. doi:10.1002/9783527691722.
- ¹³ Fey, N.; Harvey, J. N.; Lloyd-Jones, G. C.; Murray, P.; Orpen, A. G.; Osborne, R.; Purdie, M. Computational Descriptors for Chelating P,P- and P,N-Donor Ligands. *Organometallics* 2008, 27, 1372–1383. doi:10.1021/om700840h.
- ¹⁴ Adamo, C.; Barone, V. Toward reliable density functional methods without adjustable parameters: The PBE0 model. *J. Chem. Phys.* 1999, 110, 6158–6170. doi:10.1063/1.478522.

-
- ¹⁵ Hirata, S.; Head-Gordon, M. Time-dependent density functional theory within the Tamm-Dancoff approximation, *Chem. Phys. Lett.* 1999, 314, 291.
- ¹⁶ Dhara, A. K., & Ghosh, S. K. (1987). Density-functional theory for time-dependent systems. *Physical Review A*, 35(1), 442–444. doi:10.1103/physreva.35.442
- ¹⁷ a) Te Velde, G.; Bickelhaupt, F. M.; Baerends, E. J.; Fonseca Guerra, C.; van Gisbergen, S. J. A.; Snijders, J. G.; Ziegler, T. Chemistry with ADF. *J. Comp. Chem.* 2001, 22, 931–967. doi:10.1002/jcc.1056. b) ADF2019, SCM, Theoretical Chemistry, Vrije Universiteit, Amsterdam, The Netherlands, <http://www.scm.com>.
- ¹⁸ Clementi, E.; Roetti, C. Roothaan-Hartree-Fock atomic wavefunctions: Basis functions and their coefficients for ground and certain excited states of neutral and ionized atoms, $Z \leq 54$, *Atomic Data and Nuclear Data Tables* 1974, 14, 177.
- ¹⁹ Van Lenthe, E.; van Leeuwen, R.; Baerends, E. J.; Snijders, J. G. Relativistic regular two-component Hamiltonians. *International J. Quantum Chem.* 1996, 57, 281–293. doi:10.1002/(sici)1097-461x(1996)57:3<281::aid-qua2>3.0.co;2-u.
- ²⁰ Wang, F.; Ziegler, T. A simplified relativistic time-dependent density-functional theory formalism for the calculations of excitation energies including spin-orbit coupling effect, *J. Chem. Phys.* 2005, 123, 154102.
- ²¹ Marian, C. M. Spin-Orbit Coupling and Intersystem Crossing in Molecules: Spin-Orbit Coupling. *WIREs Comput. Mol. Sci.* 2012, 2, 187–203. doi:10.1002/wcms.83.
- ²² El Sayed Moussa, M.; Evariste, S.; Wong, H.-L.; Le Bras, L.; Roiland, C.; Le Polles, L.; Le Guennic, B.; Costuas, K.; Yam, V. W.-W.; Lescop, C. A Solid State Highly Emissive Cu(I) Metallacycle: Promotion of Cuprophilic Interactions at the Excited States. *Chem. Comm.* 2016, 52, 11370–11373. doi:10.1039/C6CC06613E.
- ²³ Evariste, S.; Khalil, A. M.; Moussa, M. E.; Chan, A. K.-W.; Hong, E. Y.-H.; Wong, H.-L.; Le Guennic, B.; Calvez, G.; Costuas, K.; Yam, V. W.-W.; Lescop, C. Adaptive Coordination-Driven Supramolecular Syntheses toward New Polymetallic Cu(I) Luminescent Assemblies. *J. Am. Chem. Soc.* 2018, 140, 12521–12526. doi:10.1021/jacs.8b06901.
- ²⁴ El Sayed Moussa, M.; Khalil, A. M.; Evariste, S.; Wong, H.-L.; Delmas, V.; Le Guennic, B.; Calvez, G.; Costuas, K.; Yam, V. W.-W.; Lescop, C. Intramolecular Rearrangements Guided by Adaptive Coordination-Driven Reactions toward Highly Luminescent Polynuclear Cu(I) Assemblies. *Inorg. Chem. Front.* 2020, 7, 1334–1344. doi:10.1039/C9QI01595G.
- ²⁵ Evariste, S.; Khalil, A. M.; Kerneis, S.; Xu, C.; Calvez, G.; Costuas, K.; Lescop, C. Luminescent Vapochromic Single Crystal to Single Crystal Transition in One-Dimensional Coordination Polymer Featuring the First Cu(I) Dimer Bridged by an Aqua Ligand. *Inorg. Chem. Front.* 2020, 7, 3402–3411. doi:10.1039/D0QI00691B.

Chapter III – Study of Cu_6CN_4 and Cu_8CN_4 coordination complexes

I – Introduction

The use of polyatomic Cu(I) TADF luminescent precursors acting as pre-organized precursors to conduct general CDS toward emissive coordination-driven supramolecular assemblies has been recently reported by Lescop and coworkers.^{1,2} Cu(I) ion is usually described as a labile and non-directional coordination sphere that is *a priori* not sufficiently directional to allow to conduct selective CDS. Our collaborators from the INSA Rennes have recently shown that this limitation can be overcome using pre-assembled Cu(I) bimetallic molecular clips exhibiting short intermetallic distances, allowing general and versatile CDS preparation of a large family of stacked supramolecular assemblies.¹ They recently extended this CDS approach to the use of a pre-assembled TADF Cu(I) precursor, the tetrametallic metallacycle.³

The synthetic mechanism based on the adaptive CDS preparation of polyatomic Cu(I) supramolecular assembly **1** from the tetrametallic compound **A** is given in Figure 1. This methodology can afford much complex architectures which can include other metal ions and which present original solid-state luminescent properties.⁴

In this chapter, combined experimental (group of Lescop) and computational studies of the luminescent hexametalllic Cu(I) assembly **1** which results from the adaptive CDS reaction of **A** with CuCN, acting as an alternative cyano-based precursor, and of a $\text{Cu}_8(\text{CN})_4$ metallacycle which results from the reaction of **A** at RT with NaN_3 or $\text{KN}(\text{CN})_2$ are presented. The two systems are presenting interesting thermochromic luminescent properties.

II – Experimental and computational study of a [Cu₆(CN)₄]-based metallacycle

II.1 – Summary of the experimental study – Group of Lescop

Precursor **A** was reacted with CuCN in a 1:2 ratio (Figure 1). X-ray diffraction studies performed at low temperature by Lescop and coworkers on single crystals revealed two different crystals: one being a blue luminophore, corresponding to the non-reacted precursor **A** while the second is a green luminophore, the new hexa-metallic Cu(I) metallacycle **1** (Figure 1). In this Cu₆CN₄ metallacycle **1**, two peripheral [Cu₂(dppm)₂] fragments are connected by two almost linear NC-Cu-CN moieties (C-Cu_{inner}-C = 177.5°) leading to a planar Cu₆CN₄ diamond-shape metallacycle (maximum deviation from the mean plane of 0.05 Å, Figure 1). The [Cu₂(dppm)₂] unit metric parameters are very similar to those observed in the solid-state structure of **A** with a comparable peripheral intermetallic distance (2.881 Å in **1** and 2.867 Å in **A**) relevant for cuprophilic interactions. Conversely, Cu(I) metal centers belonging to the NC-Cu-CN connecting moieties are separated by 3.780 Å which is an intermetallic distance too large to engender cuprophilic interactions. In the crystal packing, neighboring metallacycles are imbricated with short contact interactions observed between the cyano fragments and phenyl rings of the next discrete assemblies ($d \leq 2.8$ Å, Figure 1b).

Crystalline samples of **1** display an intense green luminescence upon excitation at 365 nm (Figure 2) at 298 K. This corresponds to a broad emission band with an emission maximum λ_{em} at 490 nm and an emissive lifetime τ of 80 μ s. Upon cooling, the emission spectrum presents a gradual red-shift affording an intense yellowish luminescence at low temperature (Figure 2: $\lambda_{em} = 522$ nm at 80 K and $\tau = 365$ μ s). Upon heating up from RT to 363 K, very moderate thermal variations of both the emission spectrum and the lifetime are observed, and the luminescence maxima reach a plateau region at 330 K with $\lambda_{em} = 487$ nm ($\Delta\lambda_{em}$ 80 K / 363 K = 0.132 eV / 1065 cm^{-1}) and $\tau = 57$ μ s.

Such emission behavior is typical of Cu(I) derivatives showing TADF behavior.^{5,6} By fitting the thermal evolution of τ using Eq. 1 (chapter I), the values of $\Delta E(S_1-T_1) = 1023$ cm^{-1} ; $\tau(S_1) = 325$ ns and $\tau(T_1) = 352$ μ s could be obtained. Despite this set of values is significantly different from those obtained for the tetrametallic precursor **A** ($\Delta E(S_1-T_1) = 1560$ cm^{-1} , $\tau(S_1) =$

10 ns and $\tau(T_1) = 185 \mu\text{s}$) both account for TADF processes.³ In order to get more insights in the energetic and emission properties of **1**, we performed a DFT/TD-DFT computational study.

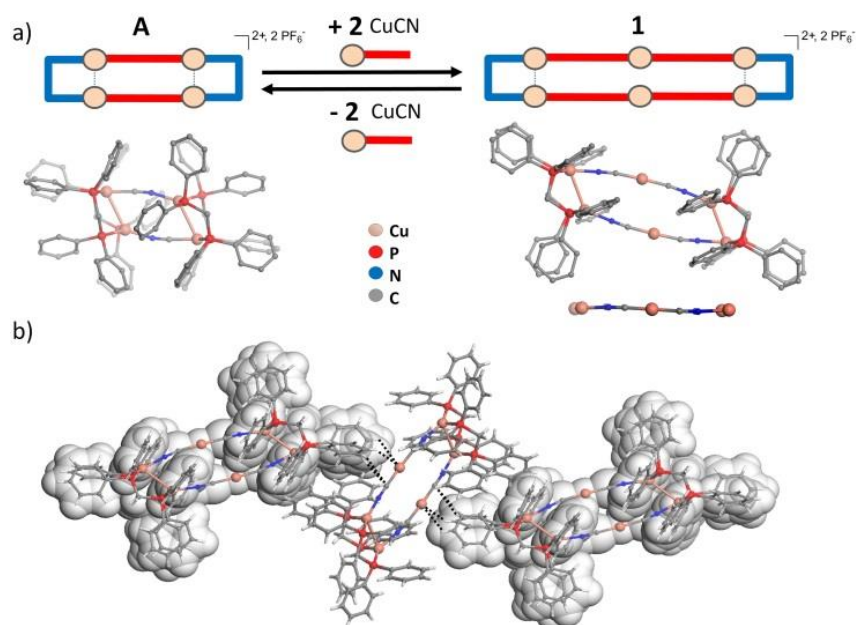


Figure 1 – a) Synthesis of **1** and comparative views of the X-ray crystal structures of **A** (top view) and **1** (top view and lateral simplified view; counter-anions, H atoms and solvent molecules have been omitted for clarity). b) View of the short contact inter-molecular interactions (shown with dotted lines) observed between neighboring imbricated metallacycles in the crystal structure.

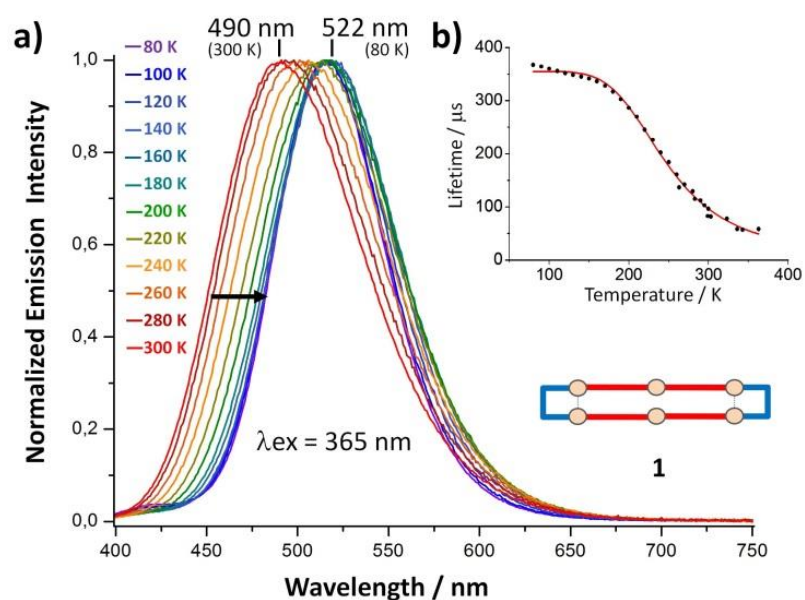


Figure 2 – a) Normalized solid-state emission spectra of **1** at temperatures between 80 K and 300 K upon excitation at 365 nm. The black arrow shows the direction of the thermochromic shift of the solid-state emission spectra observed upon cooling; b) plot of emission decay

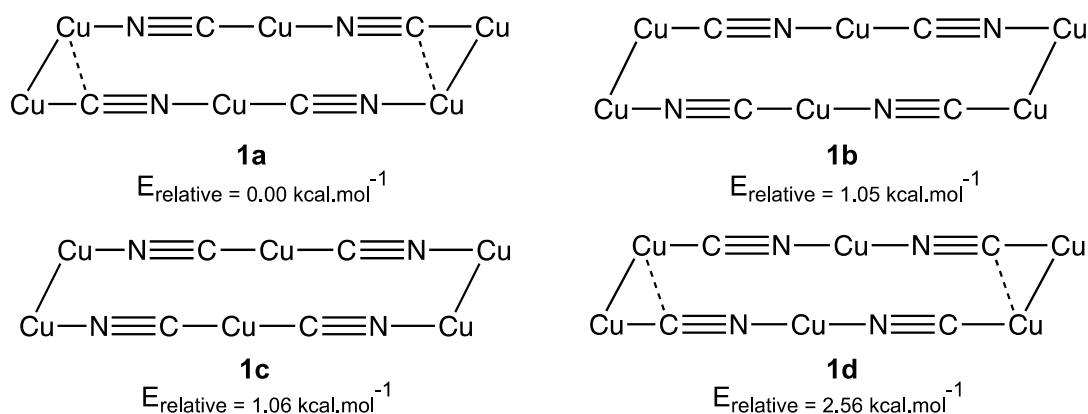
lifetime against temperature (80 K to 300 K); red line represents the fit according to the TADF equation (Eq. 1, chapter I).

II.2 – Computational study

Computational details

The DFT calculations were carried out using the Gaussian 16 program and using ADF for the SOC calculations. The different systems in their ground state configuration were fully optimized using the X-Ray data as guess geometries with the hybrid PBE0 functional and SVP atomic basis set. The high computational cost needed for full excited state investigations prevents us to increase the atomic basis set. A tight value of 10^{-10} u.a. was applied for energy convergence (vibrational frequency calculations could not be performed).

Several isomers are possible for **1**, as shown in Scheme 1, and the X-ray characterization does not allow to firmly choose between them. A computational study was thus performed to calculate the relative energies of each isomer. The arrangement **1a** presented in Scheme 1 is the most probable isomer according to DFT results. Nevertheless, the relative energies of those four isomers are small and do not exclude their existence on a thermodynamic point of view.



Scheme 1 – Isomers of Cu_6CN_4 configurations with their relative energies

Considering the massive computational cost that a complete excited state investigation of each isomer would generate, we have focused our efforts, at a first stage, on the study of the excited state properties of **1a**, the most stable isomer, and **1c**, which presents a nitrogen-only coordination sphere for the bridging bi-coordinated Cu atoms (most probable scenario from a synthetic mechanism point of view). In the most stable S_0 arrangement, **1a** is diverging more importantly from the experimental X-Ray geometry than **1c** (bent Cu-NC-Cu-CN-Cu chains ($167\text{-}174^\circ$) not experimentally observed). The first excited-state S_x and T_x ($x = 1, 2, 3$)

geometries of **1a** and **1c** were optimized using TD-DFT. At that stage, the isomer **1a** was excluded from the rest of the computational study since its first triplet excited state is higher in energy than the one of **1c** (+3.39 kcal.mol⁻¹ / +0.147 eV) and its associative emission energy at 478 nm diverges from the experimental measurements (~520 nm). Thus, only the **1c** isomer was considered for the rest of the study and the use of labelling **1** in the main text stands for this isomer.

The main results obtained for the ground state **1-S₀** and its lowest singlet and triplet relaxed excited states (**1-S₁** and **1-T₁**) are summarized in Figure 3 and Table 1. The DFT optimized geometry of **S₀** compares well with the X-Ray structure with intra-dimer Cu-Cu distances of 2.854 Å (exp. 2.881 Å, -0.9 % error) and Cu-Cu contact between the NC-Cu-CN connecting moieties of 3.840 Å (exp. 3.780 Å, 1.6 % error). The calculation of the first singlet-singlet excitation using TD-DFT reveals that this vertical excitation consists of an electronic density transfer mainly from the Cu-ligands to the interstitial Cu-Cu region. It induces a strengthening of the Cu-Cu interaction in each dimer, and, to a lesser extent, to the CN bridges (Figure 3). Interestingly, geometry relaxation following this excitation leads to a symmetry lowering in which only one of the Cu-Cu distance is shortened (2.592 Å) whereas the other one is lengthened (2.903 Å). These changes are associated with a translation between the Cu-NC-Cu-CN-Cu segments which lead to a more rectangular shape of the metallacycle. The central Cu...Cu separation is also distended (3.975 Å) with respect to 3.647 Å in the ground state.

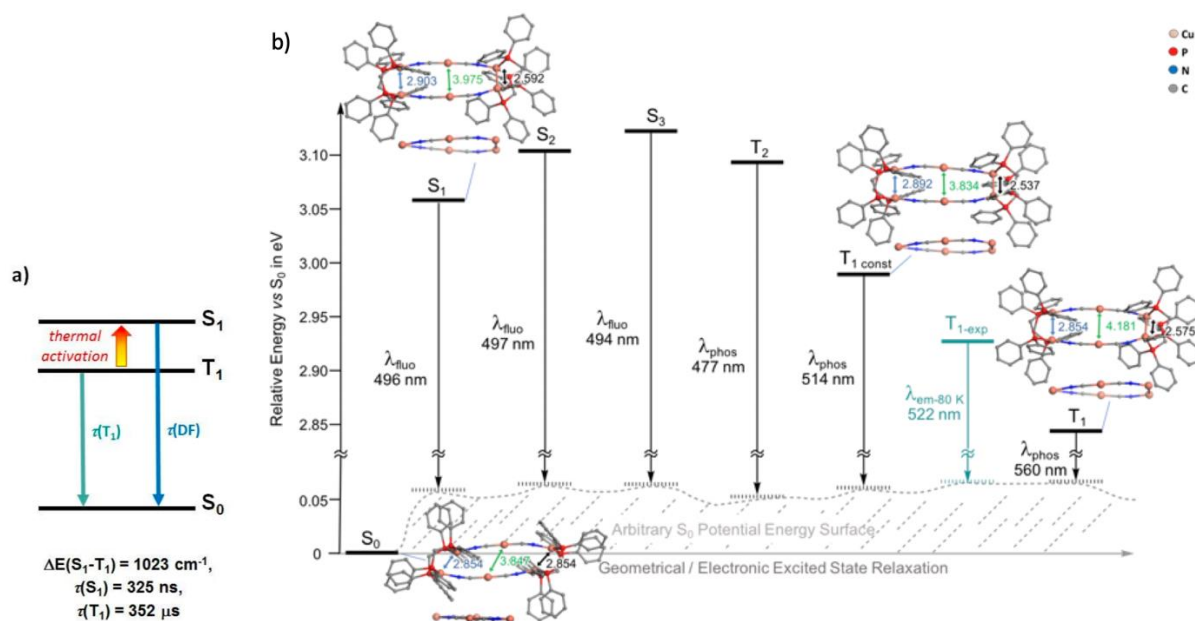


Figure 3 – a) Scheme of the TADF process and photophysical values experimentally obtained. b) Relative energy diagram of the first optimized excited states relative to S_0 in eV; associated emission wavelengths in nm; see Table 1 for a complete summary of the emission energies. Top view and lateral views of the optimized geometries of $\mathbf{1-S}_0$, $\mathbf{1-T}_1$, $\mathbf{1-T}_{1\text{-const}}$ and $\mathbf{1-S}_1$ (H atoms omitted); intermetallic Cu-Cu distances (in Å). Experimental T_1 level ($T_{1\text{-exp}}$) and associated experimental values in green for the sake of comparison.

Similar changes are calculated for the close energy-lying excited states $\mathbf{1-S}_2$, $\mathbf{1-S}_3$ and also for the first triplet states $\mathbf{1-T}_1$. For the latter, the metallacycle additionally show a swelling of the metallacycle with a Cu...Cu separation of 4.181 Å. Contrarily to the motion leading to a more rectangular metallacycle observed for the first singlet excited states, this swelling would importantly affect the crystal packing. Indeed, as shown in Figure 1b, short intermolecular contacts are observed between the cyano fragments and phenyl rings of the neighboring systems ($d \leq 2.8$ Å). To consider the solid-state environment, constrained geometry optimizations were performed for the first triplet state $\mathbf{1-T}_1$ restraining the Cu...Cu elongation to exceed the one found in $\mathbf{1-S}_1$. This constrained optimization gave rise to the system $\mathbf{1-T}_{1\text{-const}}$ (Figure 3 and Table 1).

Table 1 – Optimized excited states of $\mathbf{1}$: relative energies compare to S_0 and S_1 and emission energies. Experimental data are given for sake of comparison.

| States | E_{S_0} (eV) | E_{S_1} (cm ⁻¹) | E_{em} (eV) | E_{em} (nm) |
|--------------------------------------|----------------|-------------------------------|---------------|---------------|
| First relaxed singlet excited states | | | | |
| S_1 | 3.055 | 0 | 2.502 | 496 |
| S_2 | 3.100 | 364 | 2.492 | 497 |
| S_3 | 3.119 | 524 | 2.511 | 494 |
| First relaxed triplet excited states | | | | |
| T_1 | 2.843 | -1703 | 2.212 | 560 |
| $T_{1\text{-const}}$ | 2.988 | -533 | 2.412 | 514 |
| T_2 | 3.090 | 290 | 2.598 | 477 |
| Experimental data | | | | |
| S_1 | - | 0 | 2.546 | 487 |
| T_1 | - | -1023 | 2.375 | 522 |

The emission energies calculated from these relaxed excited state structures nicely explain the experimental optical measurements. Indeed, the calculated wavelength of fluorescence (from $\mathbf{1-S}_1$, 496 nm) agrees with the maximum of emission measured at 300 K (490 nm). At 80 K, the

experimental wavelength is 522 nm and its emission lifetime indicate a phosphorescence process. The calculated emission wavelength of **1**-T_{1-const} is 514 nm. The discrepancies between experimental and calculated emission energies is averaging 0.04 eV which is in line with the level of theory used. The calculated energy differences between (**1**-S₁, **1**-T₁) and (**1**-S₁, **1**-T_{1-const}) are 533 cm⁻¹ and 1703 cm⁻¹ respectively. An intermediate value of 1023 cm⁻¹ was extracted from the temperature dependent lifetime fit. This suggests that indeed the **1**-T₁ excited adopts a conformation in the solid state in which the metallacycle swollen moderately. This supports a TADF process for **1**. The moderate value of calculated SOC energies given in Table 2 agrees with a competition between ISC/RISC and thermal population of S₁ from T₁ which present both close geometries. DFT SOC calculations were performed with the ADF package on the optimized S_x and T_x structures. For these calculations, the same hybrid functional PBE0 was used, with an all-electron triple-zeta Slater basis set with two additional polarization functions (TZ2P). Calculations relying on the Tamm-Dancoff approximation (TDA) of the full TD-DFT equations were used to evaluate the lifetime of the excited states and the oscillator strengths.

Table 2 – Spin-orbit coupling energy (cm⁻¹) between states of **1** at the T₁, T_{1-const} and S₁ geometries.

| Geometry | S₀/T₁ | S₀/S₁ | S₁/T₁ |
|--------------------------------|------------------------------------|------------------------------------|------------------------------------|
| 1 -T ₁ | 26 | - | 6 |
| 1 -T _{1-const} | 34 | - | 34 |
| 1 -S ₁ | - | 26 | 5 |

III – Experimental and computational study of a $[\text{Cu}_8(\text{CN})_4]$ -based metallacycle

III.1 – Summary of the experimental study – Group of C. Lescop

The reaction of the precursor **A** at RT with NaN_3 or $\text{KN}(\text{CN})_2$ in, respectively, 1:2 and 1:1 ratio, was performed by Lescop and coworkers. It led to colorless solutions from which were obtained the **D** complex (Figure 4) as a polycrystalline powder. The same synthetic protocol can be used to synthesize a large variety of extended systems as shown in Figure 4, including heteropolyatomic structures in which another functionality coming from the included metal ion can be added (magnetism for instance). Our computational effort has been devoted to the study of **D** because of time limitation but the other systems will surely be studied in the group in the future. X-ray diffraction studies on single crystals obtained at RT revealed that **D** is a $\{\text{Cu}_8(\text{DCM})_2(\text{CN})_4\text{dppm}_8\}(\text{PF}_6)_2$ system. This octa-nuclear derivative can be described as resulting of the connection of four $[\text{Cu}_2(\text{dppm})_2]$ fragments with four ditopic cyano ligands forming a $\text{Cu}_8(\text{CN})_4$ metallacycle system with a slightly twisted rectangular shape (Figure 5). In each $[\text{Cu}_2(\text{dppm})_2]$ fragment, one of the metal centers has a distorted trigonal planar coordination sphere resulting from the coordination of two dppm ligands and a cyano ligand. The second Cu(I) metal center presents a distorted tetrahedral coordination sphere due to an additional coordination with the terminal atom of a DCM ligand. The two DCM ligands are located within the $\text{Cu}_8(\text{CN})_4$ metallacycle system, connecting two-by-two, two $\text{Cu}_2(\text{dppm})_2$ fragments ($d(\text{Cu}-\text{NDCM}) = 2.09 \text{ \AA}$). Intermetallic Cu(I) distances in the $[\text{Cu}_2(\text{dppm})_2]$ fragments ($d(\text{Cu}-\text{Cu}) = 3.43 \text{ \AA}$) exceed those recorded in the precursor **A** ($d(\text{Cu}-\text{Cu}) = 2.87 \text{ \AA}$) and are too large for cuprophilic interactions.

Crystalline samples of **D** also display at 300 K also a yellowish luminescence upon excitation at 365 nm (Figure 6). This corresponds to a RT emission band with an emission maximum λ_{em} at 500 nm associated with a bi-exponential emissive lifetime $\tau_1 = 52 \text{ \mu s}$ and $\tau_2 = 18 \text{ \mu s}$. Upon cooling to 80 K, the emission spectrum of **D** presents a gradual enhancement of its emission band associated with a moderate red-shift of the emission maximum ($\lambda_{\text{em}} = 512 \text{ nm}$ at 80 K). The detailed study of the temperature dependence of the emission lifetime (Figure 6) was conducted, revealing bi-exponential decay times all along the temperature range with a short-lived component having an almost linear and moderate progression upon cooling (at 80 K, $\tau_2 = 56 \text{ \mu s}$). Conversely, the long-lived component presents a larger amplitude variation (at 80 K, τ_1

= 238 μs) bearing a typical thermally activated delayed fluorescence (TADF) profile. By fitting the thermal variation of the τ_1 component to a Boltzmann-type equation, the values of $\Delta E(S_1-T_1) = 978 \text{ cm}^{-1}$, $\tau(S_1) = 229 \text{ ns}$ and $\tau(T_1) = 231 \mu\text{s}$ were obtained. This set of values ranges among those determined for the other Cu(I) CDS assemblies based on the $[\text{Cu}_2(\text{dppm})_2]$ fragment (including the precursor **A**) that were identified as TADF luminophores.

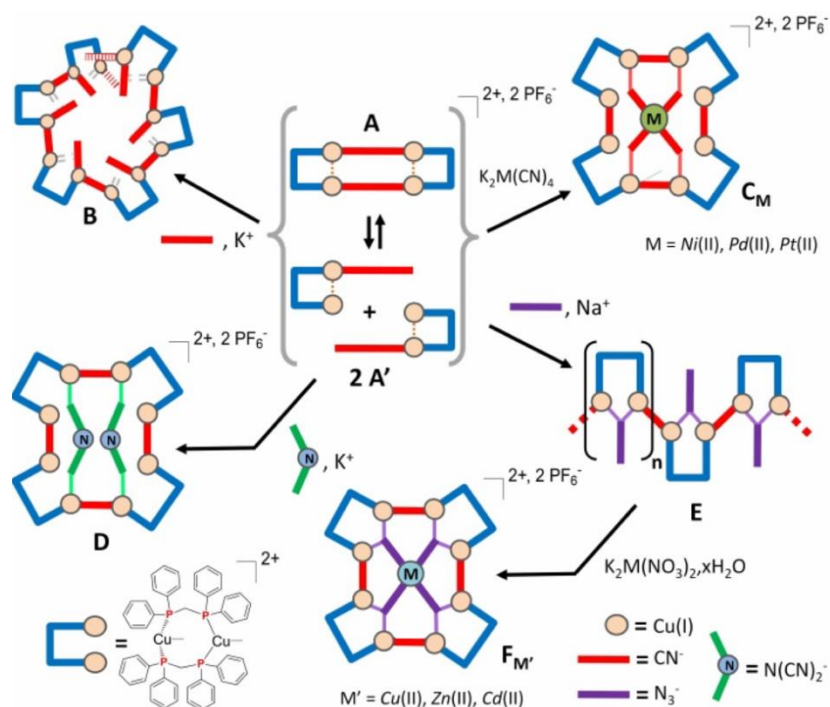


Figure 4 – Synthesis of several derivatives: **B**, **C_M**, **D**, **E** and **F_M**. Here, we focus only on the **D** system.

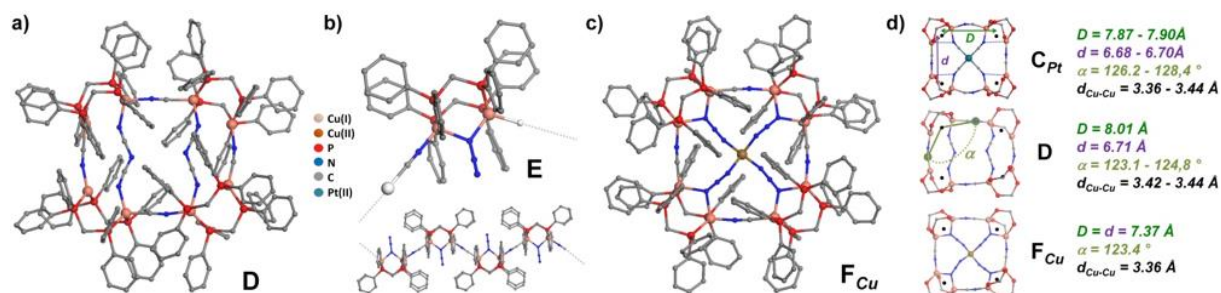


Figure 5 – Views of the molecular X-ray structures of **D**, **E** and **F_{Cu}** derivatives; Selected metric data. Counter-anions, H atoms and solvent molecules have been omitted for clarity; location of the C and N atoms of the cyano ligands has been chosen arbitrarily, black dots represent the central points of the Cu-Cu segments of each $[\text{Cu}_2(\text{dppm})_2]$ fragments.

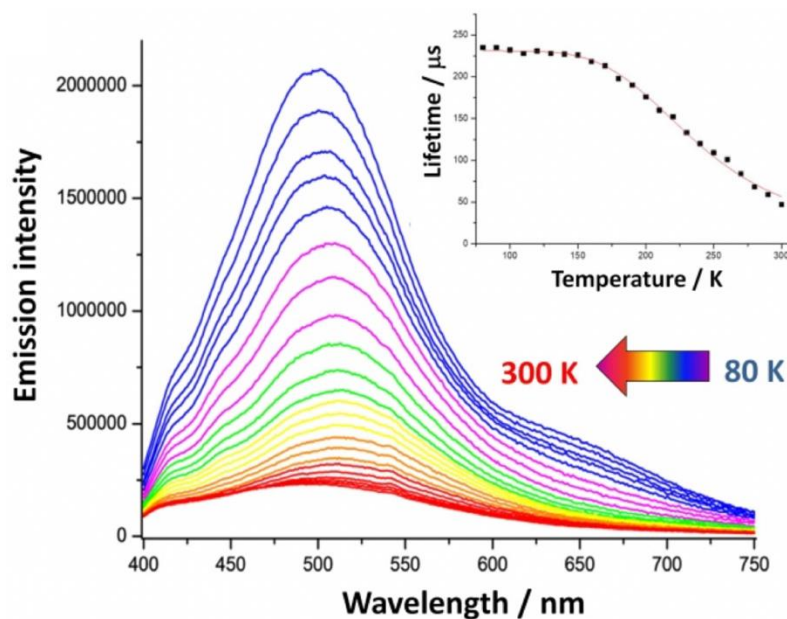


Figure 6 – Solid-state temperature dependent emission spectra of **D** ($\lambda_{\text{ex}} = 365 \text{ nm}$), inset: plot of emission decay lifetime against temperature (80 K to 300 K); the red line represents the fit according to the TADF Boltzmann-type (Eq.1, chapter I).

III.2 – Computational study

Quantum chemical calculations at the DFT level were performed for the compound **D** using the same methodology as for **1**. The geometry optimization of the ground state S_0 reveals that the metallacycle frame is preserved in vacuum which confirms the stability of such nanosized scaffold. The first vertical excitations of the lowest singlet and triplet excited states were calculated by TD-DFT (Table 3 and Table 4). Their electronic structures are highly similar (Figure 7) and correspond to electronic transitions from the metal-dppm centered molecular orbitals (MOs) to exclusively ligand-centered MOs involving both cyano and DCM ligands together with the phenyl rings of the dppm ligands. This demonstrates that introduction of different pseudo-halide ligands impacts not only the geometries and the self-assembling processes but also the photophysical properties of CDS Cu(I) assemblies. Figure 8 depicts the computationally optimized Cu_8CN_4 and the atom labeling used for the next tables. In Table 4 are presented the optimized Cu–Cu distances and angles. Compared to the experimental value $d_{\text{Cu-Cu}}(\text{exp})$ of 3.430 \AA , we found a mean intermetallic distance $d_{\text{Cu-Cu}}(\text{theo})$ of 3.395 \AA (-1.0 % error). The mean experimental $d_{\text{Cu-N}_{\text{DCM}}} = 2.090 \text{ \AA}$ is in excellent agreement with the computed value $d_{\text{Cu-N}_{\text{DCM}}}(\text{theo}) = 2.090 \text{ \AA}$.

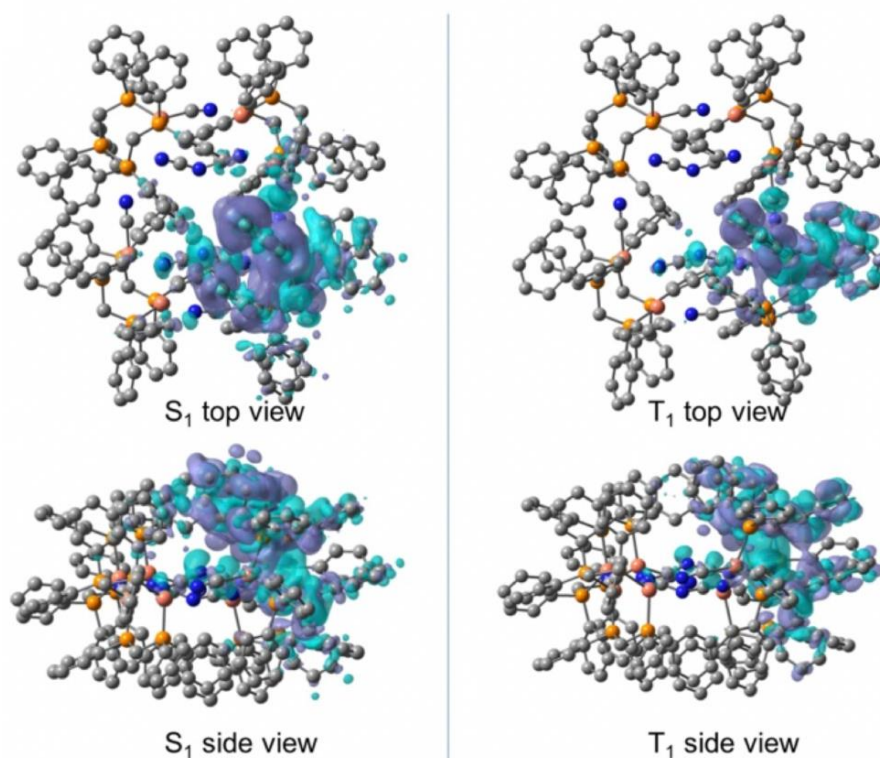


Figure 7 – Iso-surface ($\pm 1.10^{-4}$ e/bohr³) representations of the electronic charge-density difference between the first vertical singlet (S_1) or triplet (T_1) excited state, and the ground state (S_0) of **D** (violet = density depletion, cyan = density increase).

Table 3 – Calculated vertical singlet electronic excited state energies of **D** and associated oscillator strength f . The energy is given in eV and the wavelength λ in nm. The difference in the total density with S_0 is given in Figure 7 for the description of S_1 .

| State | Energy | λ | f | Description |
|-------|--------|-----------|-------|----------------------------------|
| S_1 | 3.91 | 317 | 0.003 | 39 % HOMO \rightarrow LUMO+1 |
| | | | | 35 % HOMO-2 \rightarrow LUMO+1 |
| S_2 | 3.98 | 311 | 0.008 | 51 % HOMO \rightarrow LUMO+3 |
| | | | | 16 % HOMO-3 \rightarrow LUMO+3 |
| S_3 | 3.99 | 310 | 0.005 | 11 % HOMO-2 \rightarrow LUMO+3 |
| | | | | 46 % HOMO-1 \rightarrow LUMO |
| S_4 | 4.05 | 306 | 0.011 | 18 % HOMO-3 \rightarrow LUMO |
| | | | | 13 % HOMO \rightarrow LUMO |
| | | | | 48 % HOMO-2 \rightarrow LUMO+6 |
| | | | | 34 % HOMO \rightarrow LUMO+6 |

Table 4 – Calculated vertical electronic triplet excited state energies of **D** (zero oscillator strength in the absence of SOC consideration). The description in terms of MO transition is not given since they are numerous for each state with participations by less than 10 %. The difference in the total density with S_0 is given in Figure 7 for the description of T_1 .

| State | Energy (eV) | λ (nm) |
|----------------|-------------|----------------|
| T ₁ | 3.75 | 330 |
| T ₂ | 3.78 | 328 |
| T ₃ | 3.79 | 327 |
| T ₄ | 3.80 | 326 |

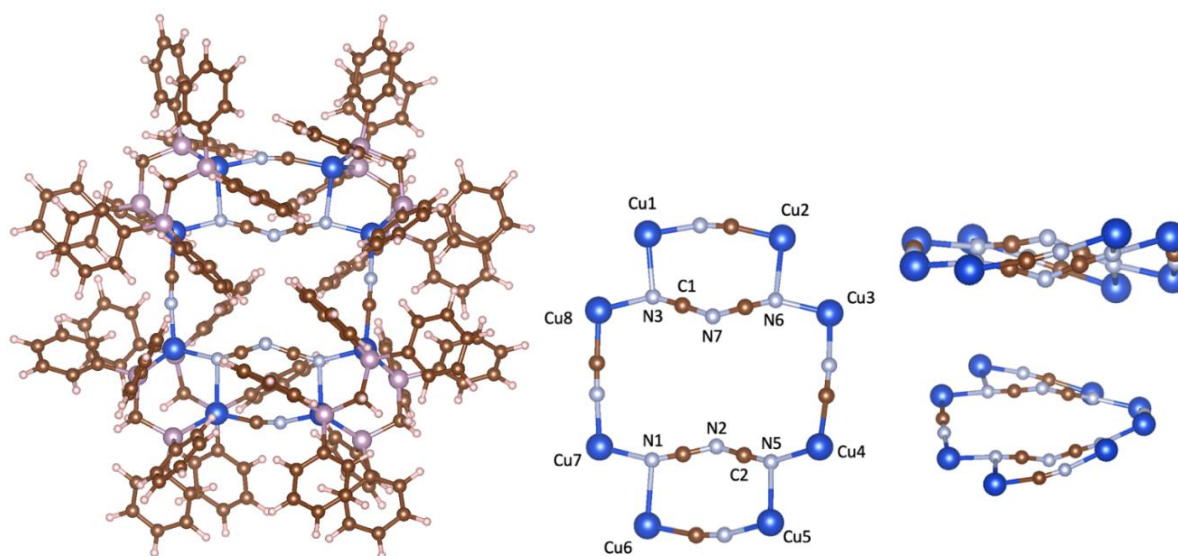


Figure 8 – Left: optimized geometry of the $\text{Cu}_8(\text{CN})_4$ complex at the DFT level. Right: backbone representation of the optimized system and the used labeling for Tables 5 and 6.

Table 5 – Cu–Cu distances in Å and main angles in degrees in the optimized geometry of the $\text{Cu}_8(\text{CN})_4$ complex.

| Cu–Cu | d | Cu–Cu | d | Pattern | Angles | Pattern | Angles |
|-----------|-------|-----------|--------|--------------------------------------|---------|--------------------------------------|---------|
| Cu1 - Cu2 | 5.054 | Cu7 - Cu8 | 5.158 | $\text{N}_1\text{-N}_2\text{-N}_5$ | 138.015 | $\text{Cu}_2\text{-N}_6\text{-Cu}_3$ | 96.492 |
| Cu2 - Cu3 | 3.372 | Cu8 - Cu1 | 3.409 | $\text{N}_3\text{-N}_7\text{-N}_6$ | 137.678 | $\text{Cu}_7\text{-N}_1\text{-Cu}_6$ | 97.766 |
| Cu3 - Cu4 | 5.156 | Cu8 - Cu3 | 8.627 | $\text{Cu}_4\text{-N}_5\text{-Cu}_5$ | 98.315 | $\text{C}_1\text{-N}_3\text{-Cu}_8$ | 149.198 |
| Cu4 - Cu5 | 3.370 | Cu7 - Cu4 | 8.593 | $\text{Cu}_8\text{-N}_3\text{-Cu}_1$ | 99.673 | $\text{C}_2\text{-N}_5\text{-Cu}_4$ | 152.111 |
| Cu5 - Cu6 | 5.051 | Cu1 - Cu6 | 10.907 | | | | |
| Cu6 - Cu7 | 3.430 | Cu2 - Cu5 | 10.731 | | | | |

IV – Conclusion

Adaptive CDS conducted from the Cu(I) bi-metallic precursors $[\text{Cu}_2(\text{dppm})_2]$ discovered by Lescop and coworkers gives a straightforward access to unprecedented polyatomic derivatives (**1** and **D**) bearing attractive solid-state luminescence properties. In the view of the originality and the complexity of the supramolecular architectures obtained in these one-step syntheses from simple and commercially available building blocks, this new and alternative approach opens appealing and general perspectives in the preparation of new multifunctional supramolecular objects embedded with luminescence properties.

The study of the luminescent properties of **1** and **D** reveals that the balance between the differences in energy between excited states, the importance of SOC and the crystal packing is crucial to evaluate and understand the evolution of luminescence with the temperature. Important perspectives are offered by these studies since a large number of compounds are accessible by the CDS procedure, as exemplified in Figure 4. The introduction of magnetic ions will provide multifunctionality to the systems. Computational studies will be of particular interest and are currently under investigation. We also started to study polymer type systems based on the **A** pre-assembled precursor, where phase change due to an irreversible and non-destructive thermal transition is observed; the study is not sufficiently advanced to be included in this manuscript (Figure 9).

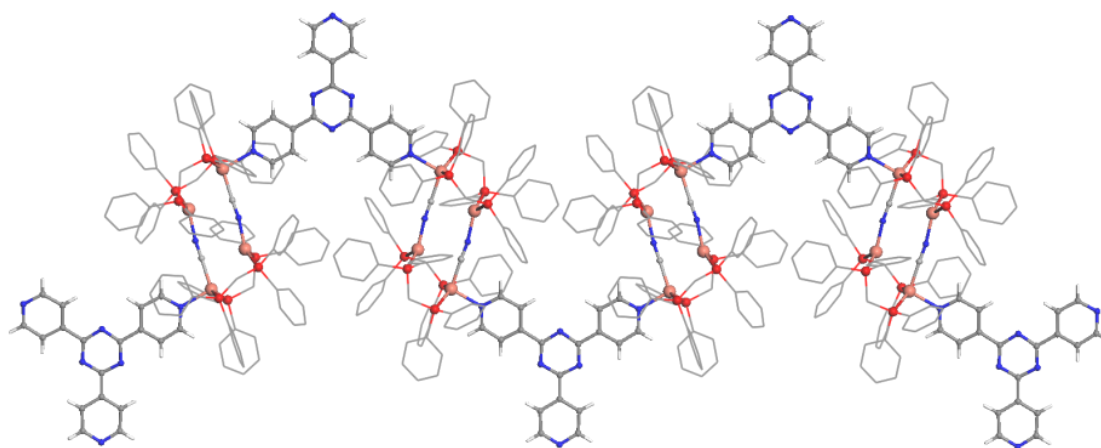


Figure 9 – Luminescent coordination polymer based of the pre-assembled **A** system. The bridging ligand is a 2,4,6-tri(4-pyridyl)-1,3,5-triazine.

¹ Lescop, C. Coordination-Driven Syntheses of Compact Supramolecular Metallacycles toward Extended Metallo-Organic Stacked Supramolecular Assemblies. *Acc. Chem. Res.* 2017, 50, 885–894. doi:10.1021/acs.accounts.6b00624.

² Lescop, C. Coordination-Driven Supramolecular Synthesis Based on Bimetallic Cu(I) Precursors: Adaptive Behavior and Luminescence. *Chem. Rec.* 2021, 21, 544–557. doi:10.1002/tcr.202000144.

³ El Sayed Moussa, M.; Evariste, S.; Wong, H.-L.; Le Bras, L.; Roiland, C.; Le Polles, L.; Le Guennic, B.; Costuas, K.; Yam, V. W.-W.; Lescop, C. A Solid State Highly Emissive Cu-i Metallacycle: Promotion of Cuprophilic Interactions at the Excited States. *Chem. Commun.* 2016, 52, 11370–11373. doi:10.1039/C6CC06613E.

⁴ Evariste, S.; Khalil, A. M.; Moussa, M. E.; Chan, A. K.-W.; Hong, E. Y.-H.; Wong, H.-L.; Le Guennic, B.; Calvez, G.; Costuas, K.; Yam, V. W.-W.; Lescop, C. Adaptive Coordination-Driven Supramolecular Syntheses toward New Polymetallic Cu(I) Luminescent Assemblies. *J. Am. Chem. Soc.* 2018, 140, 12521–12526. doi:10.1021/jacs.8b06901.

⁵ Czerwieńec, R.; Leitzl, M. J.; Homeier, H. H. H.; Yersin, H. Cu(I) Complexes – Thermally Activated Delayed Fluorescence. *Photophysical Approach and Material Design. Coord. Chem. Rev.* 2016, 325, 2–28. doi:10.1016/j.ccr.2016.06.016.

⁶ Yersin, H. *Highly Efficient OLEDs: Materials Based on Thermally Activated Delayed Fluorescence*. Wiley-VCH Verlag GmbH & Co, 2019.

Chapter I – State of the art and theoretical background

I – Introduction

I.1 – Molecular electronics, general aspects

Molecular electronics can be defined as the science domain dealing with the study and development of transport properties of electronic components constituted of molecular building blocks and of the circuits resulting of the assembly of these components.^{1,2} The concept of “molecular engineering” was first proposed by the physicist Hippel in 1956.³ This field of research is an interdisciplinary field that gathers expertise in physics, chemistry, electrical engineering, and biology (Figure 1). The main feature of molecular circuits is their nanometer range or even below. Molecular electronics can be regarded as a sub-category of nanoscience. Developments in molecular electronics often follow a bottom-up process which consists in creating a device from the association of basic fragments (atoms, ions, small molecules). It has emerged as a possible future alternative to silicon-based technology in the search of strategies for moving from microelectronics (bulk devices) to nanoelectronics by developing systems controllable at the molecular level. This domain offers the possibility to explore the electronic conductance, thermal conductance, thermoelectric effects, quantum interferences and more at the atomic scale. The involved chemistry and physics are completely controlled by quantum effects and thus can greatly diverge from bulk materials, in terms of optical, electronic or mechanical properties. Finally, it can provide tools to overcome Moore’s law tied to the conventional silicon technology. This exciting perspective makes of molecular electronics a rapidly expanding domain of nowadays research.

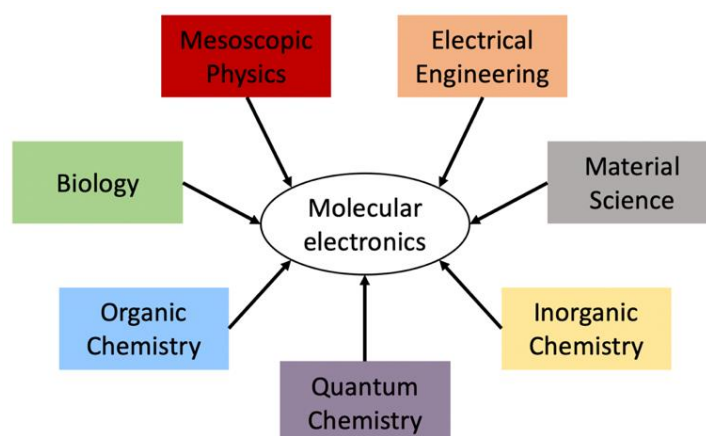


Figure 1 – Molecular electronics is an interdisciplinary field.

Among the appealing features that motivate the scientific community to explore molecular electronics, the main factors are:^{4,5}

- **Size** – The characteristic size of an electronic component is an important feature in electronics in general. Reducing the size allows to conceive less energy-demanding systems and the possibility to increase the component density in a device.
- **Self-Assembly** – In many cases, molecules can naturally create highly ordered nano-scale assembly such as self-assembled monolayers (SAMs) which are of high interest in many engineering processes, and in particular as active layer in the domain of molecular junctions.⁶
- **Chemical diversity** – The molecules can be chemically modified, which provides a high tunability of their intrinsic properties for their incorporation into functional devices. These properties can be externally and reversibly controlled in some cases, with optical,^{7,8,9,10} magnetic,¹¹ or electrical inputs¹² or with redox reactions^{13,14,15,16} allowing the switching of the molecular systems between at least two states.
- **Speed** – Even though most molecules are not good electronic conductors (nor thermal either), the time to perform operations (down to 10^{-14} s) is importantly reduced compared to silicon-based systems.⁴

Nevertheless, the use of molecules as electronic components also has disadvantages:

- **Temperature limitation** – The stability of most molecular electronic systems decreases upon temperature increase. It is highly difficult to measure current-voltage curves above room temperature or at high applied voltages (> 2 V) for most of the systems.
- **Reversibility** – The molecular junction lifetimes and current intensities are generally still insufficient for industrial applications.
- **Reproducibility** – The low reproducibility of measurements often encountered is problematic and requires at this stage a deep statistical treatment.¹⁷

I.2 – From molecular electronics to molecular junctions

The idea of using a single molecule as a rectifier came from the paper of Aviram and Ratner in 1974. In this article entitled "Molecular Rectifiers", they present a theoretical study of the electronic transport through a charge-transfer molecule containing a donor and an acceptor end-groups through which the transport would be possible in a single direction. It was only at the

end of the 90's that the measurements of current-voltage curves (I-V) were accessible. This was made possible thanks to the developments of the Scanning Tunneling Microscopy (STM), Atomic Force Microscopy (AFM) and Mechanically Controllable Break Junctions (MCBJ) notably. In these experiments, the conventional electronic devices are replaced by molecules sandwiched between electrodes to form molecular junctions. Depending on the setup, the number of molecules varies between a few hundreds to a single one. The variety of molecular junctions and associated properties is almost unlimited considering the vast number of molecular structures that chemistry affords. The challenging interdisciplinary research in the domain is devoted to target molecular systems that could replace usual bulk electronic components or even offer new unique functionalities, and to build the experimental setups and rationalize their properties.

II – Most common experimental molecular junction setups

II.1 Scanning Tunneling Microscope (STM)

The scanning tunneling microscope was invented by Binnig and Rohrer in 1981 at IBM.¹⁸ This is the first type of microscope allowing for the imaging of surfaces at the atomic level. An STM measurement consists in approaching a sharp conducting tip (few angstroms wide) very close to a conductive (modified) surface. By applying a potential difference between the tip and the surface, electrons are extracted from the tip and create a current by tunneling effect down to the substrate. This current varies exponentially with the distance (making the approach really sensitive) and thus, allows the surface to be mapped with a great precision, around 0.1 nm in lateral precision and 10 pm (0.01 nm) in depth.¹⁹ One of the most famous experiments performed in the early stage of molecular junction studies was done in 1996 by the group of Weiss. In this study, they prepared a mixed self-assembled monolayer (SAM) containing 4,4'-di(phenylene-ethynylene) benzenethiolate derivatives dispersed among saturated alkanethiol chains on an Au (111) surface and probed their electrical properties by STM (Figure 2).²⁰ From this experiment, they observed that the tunneling current intensity was higher when the tip was above a conjugated molecule compared to the non-conjugated alkyl chains covering the gold substrate.

Until now, in the field of molecular junctions, STM is still an experimental setup used, allowing for the current-voltage measurements of molecules grafted on a substrate (referred to as Scanning Tunneling Spectroscopy – STS).

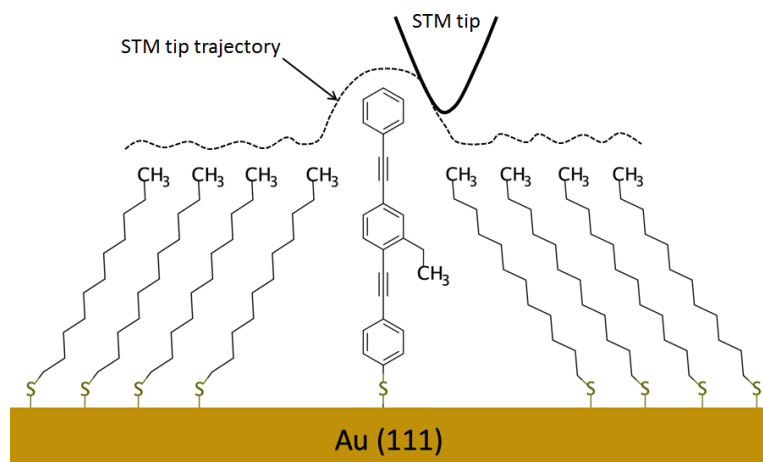


Figure 2 – Representation of the 1996 experiment of Weiss et al. Adapted from reference 20.

In another famous experiment, the group of Kubiak in 1997 achieved the first single molecule current-voltage measurement of an α,α' -xylyldithiol also on (111) gold substrate.^{21,22} They found that single molecules can exhibit exotic I-V curve with non-ohmic characteristics (Figure 3) as the voltage increases, features never observed in conventional electronics. They also showed that the interface between the molecule and the electrodes has to be critically considered as well as the Fermi level positioning.

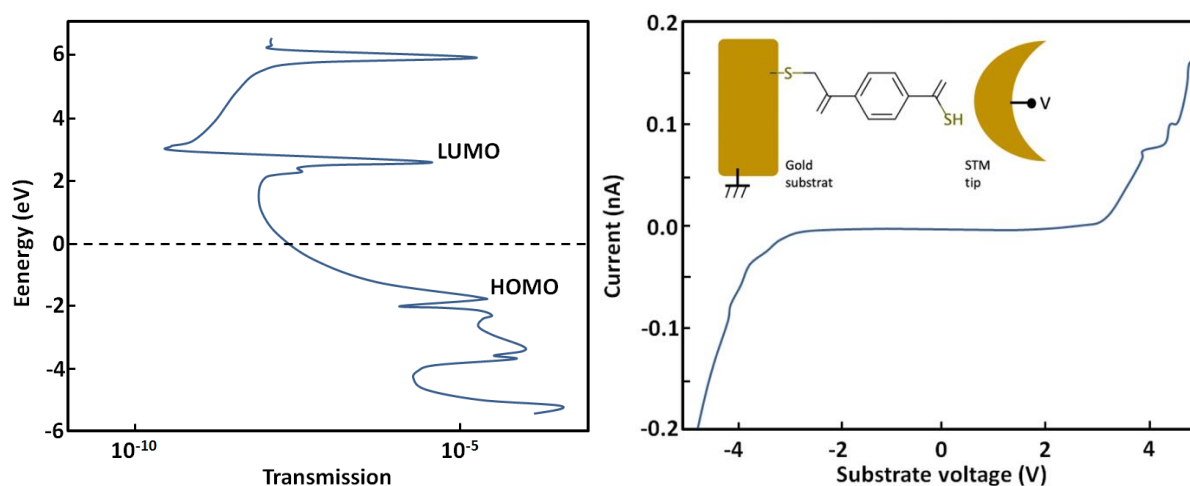


Figure 3 – Left: Calculated transmission function $\tau(E)$ through the molecule from the tip to the substrate. Right: I-V characteristics of a α,α' -xylyldithiol molecule. The insert is the schematic representation of the experiment. Adapted from reference 22.

II.2 Conductive Probe – Atomic Force Microscopy (CP-AFM)

The second important experiment to conduct I-V curve measurements is conductive probe atomic force microscope, CP-AFM (Figure 4).^{23,24,25} The atomic force microscope (AFM) was invented by Binnig et al. in 1985,²⁶ and was first modified with a conductive probe by O'Shea and coworkers in 1993.²⁷ One of the first uses of CP-AFM dates back to 1996 with the imaging of local electrical features of metallic surfaces²⁸ and in 1997 for the study of electronic transport in thin doped sexithiophene crystals.^{29,31} In this technique, the landscape of the surface is captured by measuring the deflection of an AFM cantilever with a laser and the current is measured with a current-to-voltage amplifier.³⁰ It has the advantage of having two different detection systems, an optical one for the topography and a preamplifier for the current, instead of one as in STM measurements, which allows to decorrelate the current from the topography of the surface (in STM the tunneling current is used to build the image of the surface). The main mode of CP-AFM is “contact mode” in which the voltage is kept constant and the current measured. One disadvantage compared to the STM is the tip size. It is generally several nanometers wide which induces a lateral resolution of about 10 nm (vs 0.1 nm for STM). The number of molecules coupled with the tip is thus not precisely known but can be estimated. Typically, the number of contacted molecules lies between 50 to 100 depending on the packing density and their tilt angle with the surface.

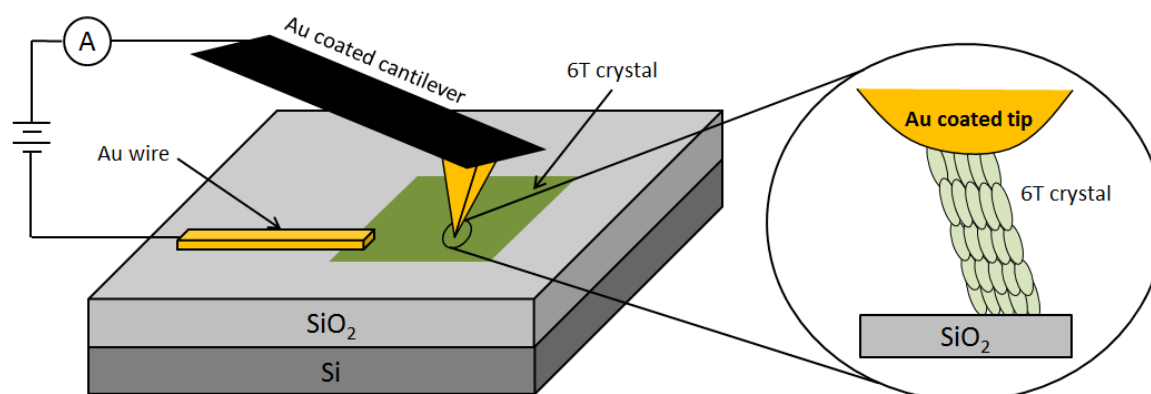


Figure 4 – Scheme of a CP-AFM experiment in which an Au-coated AFM tip is used to probe the resistance of a thin crystal of the hexathienyl molecules (6T). During a measurement, the current is recorded as a function of the applied voltage between the conducting probe and a fixed electrode. Inset shows the orientation of the 6T molecules with respect to the probe and substrate. Graphic adapted from reference 31.

This method can be used for both physisorbed and chemisorbed molecules on the tip. In general, the tip is gold-coated to allow thiol bonding for example. The contact interaction between the tip and the sample is primordial especially when saturated molecules are involved; the current can vary by 3 orders of magnitude if the molecule is chemisorbed or not, and by 2 orders of magnitude for conjugated molecules compared to saturated ones.³²

II.3 Mechanically Controllable Break Junctions (MCBJ)

The third major technique in the field of molecular electronics is MCBJ, which appeared at about the same period as the STM. In a MCBJ setup, two metallic wires are gradually separated by a gap controlled using a piezo-actuator (Figure 5), which allows to close and open the junction. The gap can be as small as one atom and can be monitored with picometer precision.³³ A wire is initially created inside the gap either by chemical etching or electromigration. When the substrate is precisely curved by the piezo-actuator, the wire breaks and molecules can spontaneously create a molecular junction inside the aperture (Figure 5).

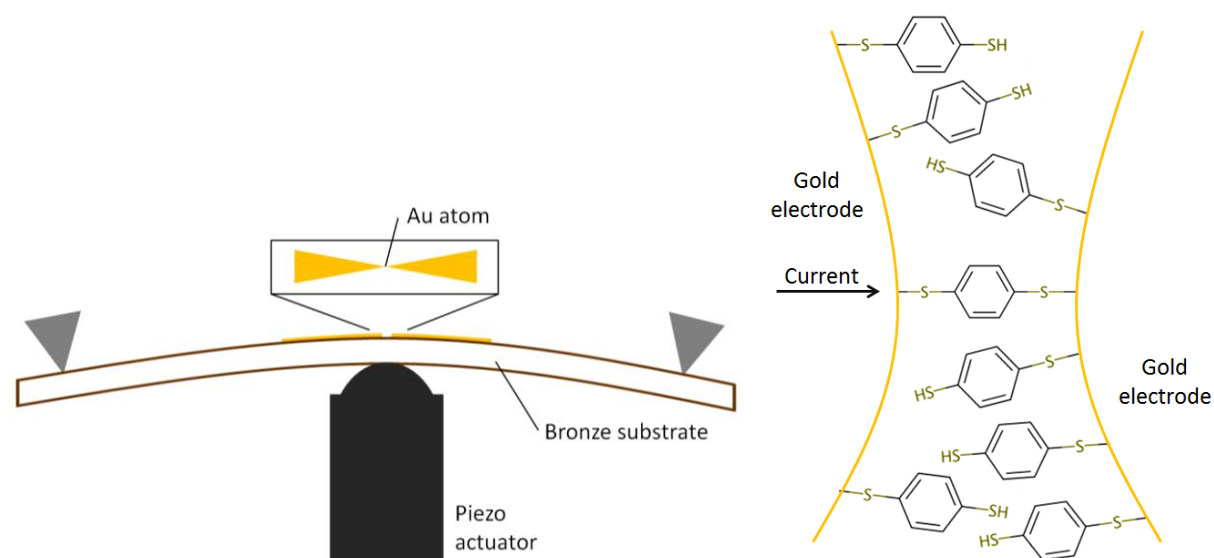


Figure 5 – Left: Simplified scheme of a MCBJ experiment. Right: scheme of benzene-1,4-dithiol molecules contacting two electrodes.

In 1997, Reed et al. measured the I-V curve of a single-molecule junction containing a benzene-1,4-dithiol molecule between gold electrodes using the MCBJ method (Figure 6).³⁴ This has the advantage compared to STM and CP-AFM to eliminate intermolecular interactions that render difficult the rationalization of the intrinsic properties of the molecules within a junction.

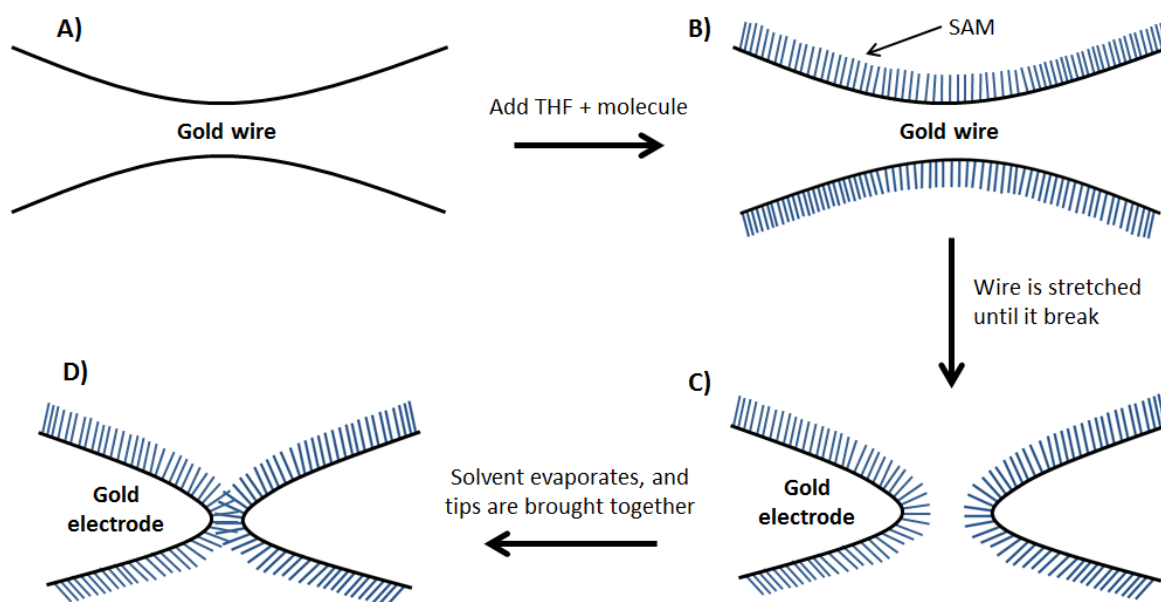


Figure 6 – Scheme of the different measurement steps: (A) initial gold wire of the break junction before breaking and tip formation. (B) addition of the benzene-1,4-dithiol, SAMs formed on the gold wire surfaces. (C) mechanical breakage of the wire in solution that produces two opposite gold contacts that are SAM-covered. (D) after solvent evaporation, the gold contacts are slowly approached until the onset of conductance is achieved. Steps (C) and (D) can be repeated numerous times for reproducibility. Graphic adapted from reference 34.

III – Theoretical background

This present section aims at introducing the general theoretical background for molecular junctions and the introduction and technicalities of thermoelectricity.

III.1 – Ohm's law

Ohm's law, applicable in the case of conducting bulk materials, stipulates that through a conductor, the transient current between two points is proportional to the electric potential across the two points. The material resistance is linked to its electrical conductivity σ as follows:^{35,5}

$$R = \frac{l}{\sigma \cdot A} \quad \text{Eq. 1}$$

with l the length of the wire (e.g. copper, iron) and A the cross-section area of the wire.

The origin of this resistivity is due to the scattering of electrons by:^{36,37}

- **Phonons** – collective vibrations (or lattice vibrations) of a bulk material around the equilibrium position of the nuclei.
- **Lattice defects** – misplaced or substituted atoms or ions which alter the periodicity of a crystalline solid. They can modify or suppress the delocalized electronic states involved in the conducting process.

These scattering events occur erratically. The mean distance that electrons travel in the material between scattering events is named the mean free path. For a metal, the mean free path is generally comprised between 10 to 50 nm at room temperature.³⁵ According to the Bose-Einstein statistic, the number of phonons increases with temperature until a certain threshold is reached. The latter is material-dependent; it is 170 K for gold using the Debye model.³⁸ The electron-phonon coupling leads to an increase in resistance and to a concomitant heating in the device. Thus, the heating of the material intensifies as the current increases.

The description of the physics linked to electrical flow in molecular-based systems does not follow the same rules. The ohmic regime does not apply mainly because:

- The resistance increases exponentially with length.
- Temperature independence of the resistance is generally measured.

- Current appears to increase non-linearly with voltage, revealing a voltage-dependence of the resistance.
- The representative mean free path for a bulk metal is higher than the length of standard molecules, which lies more in the 0.1 nm to 5 nm range (compared to the mean free path of 10 to 50 nm in a metal).

The physics in molecular junctions cannot thus be rationalized by Ohm's law. New theoretical insights were developed in the emerging community of molecular electronics to rationalize the resistivity measured in molecular junctions.

III.2 – Premise about the transport regime

The scattering events can be divided into two groups:^{39,5}

- **Inelastic diffusion** – the scatterer is not static or the electron has the possibility to interact with the internal degrees of freedom of the scatterer, which will alter the energy of the incident electron. Such inelastic scattering sources can be due to magnetic impurities, other electrons or phonons.⁴⁰
- **Elastic diffusion** – a stationary scatterer without internal degrees of freedom will conserve both the electron energy and phase. Only an alteration of its trajectory is permitted.

Both scattering events, elastic and inelastic, can be categorized with their own mean free paths. The inelastic mean free path is in the order of 20 nm for a conductor (38 nm for gold at room temperature).^{37,41} while the elastic mean free path is typically one order of magnitude smaller.^{42,43}

A molecular junction is composed of a molecule physisorbed or chemisorbed on two bulk electrodes (or more in presence of gating effects). For such a short system, inelastic scattering events are unexpected since the length of the system is in most of the cases shorter than the inelastic mean free path. In that case, the main transport regime is the phase-coherent tunneling regime.^{44,45,46} If both the elastic mean free path and the phase coherence length are larger than the molecule length, the transport is said to be ballistic, which means that the electron can cross the device without any loss of momentum. Generally, for molecular lengths greater than 5 nm, the incoherent hopping regime takes over. This regime is thermally activated (Figure 7).^{47,40}

The transport properties in molecular junctions are usually rationalized based on these assumptions.

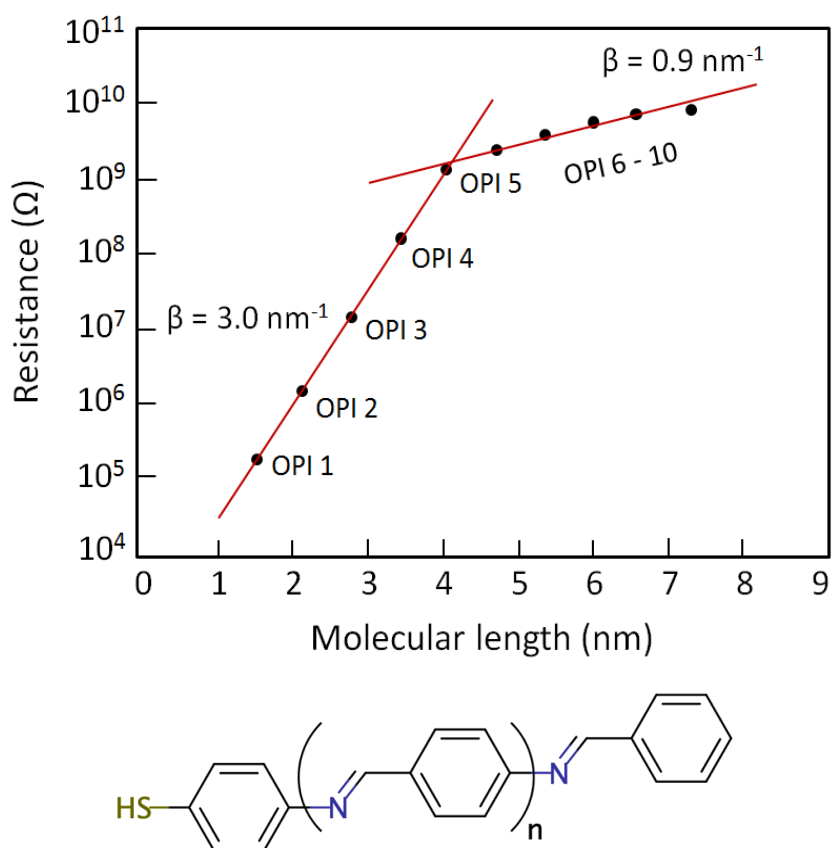


Figure 7 – Top: measurements of the resistance of different molecular wires with CP-AFM. A gold-coated tip is in contact with OPI n monolayer on a gold surface, with $n = 1-10$. The I-V traces were acquired over ± 1.5 V from OPI 3 to 10 and ± 1.0 V for OPI 1 and 2. Plot of the logarithm of the resistance (ohm) vs the molecular length (nm). Bottom: Schematic of an OPI n molecule with n ranging from 0 to 9. Adapted from reference 48.

Consequently, the main hypothesis on the transport regime and its coherence is generally valid when the molecular junction is tightly coupled to the metal electrodes, with a length that does not exceed 5 nm.^{49,50} Nevertheless, incoherent processes can still occur below this limit if the molecule is weakly coupled to the electrode (e.g. physisorption). This induces a longer crossing time of the incident electron because of the interaction with the molecule. This phenomenon is called Coulomb blockade regime.⁵¹ Indeed, the electron inside the device creates a Coulomb repulsion preventing other electrons to flow. The current-voltage shape of a Coulomb blockade resembles a staircase.⁵²

The coherent regime has some interesting particularities:^{45,5}

- Ballistic electrons are not slowed by scattering events, their speed is thus constant. They can travel at the Fermi speed ($v_{\text{Fermi}} = \sqrt{2E_{\text{F}}/m_{\text{e}}}$; $1.4 \cdot 10^6$ m/s in gold). It is one order of magnitude higher compared to the actual speed in Metal Oxide Semiconductor Field Effect Transistor (MOSFET)⁵³ of about $2 \cdot 10^5$ m/s even though the resistance of molecules is high (see Figure 1: 10^5 to 10^{10} Ω).
- The molecular resistance occurs without heating of the molecule (no inelastic interactions), thus implying no energy loss inside the molecule. Indeed, the dissipation of the energy and the Joule heating appears to occur only in the contacting bulk electrodes.^{45,54}

III.3 – Conductance is transmission

We present below the first models used to explain and rationalize the electrical properties of molecular junctions.

III.3.1 – One dimensional square barrier model

The molecule in a molecular junction can be seen as an obstacle for the current flow, where the incident electrons can be transmitted or reflected. This can be interpreted at first sight by the tunneling barrier problem in quantum mechanics. The single barrier model considers a 1-D square potential barrier of width L and of height V_0 as exemplified in Figure 8. Solving the time-independent Schrödinger's equation, the transmission probability can be determined as:^{55,5}

$$\tau(E) = \frac{J_{\text{III,transmitted}}}{J_{\text{I,incident}}} \quad \text{Eq. 2}$$

With J the current probability. I and III correspond to the regions before and after the single barrier, respectively. This implies that when an electron encounters the potential barrier, it can be either reflected or transmitted through the barrier.

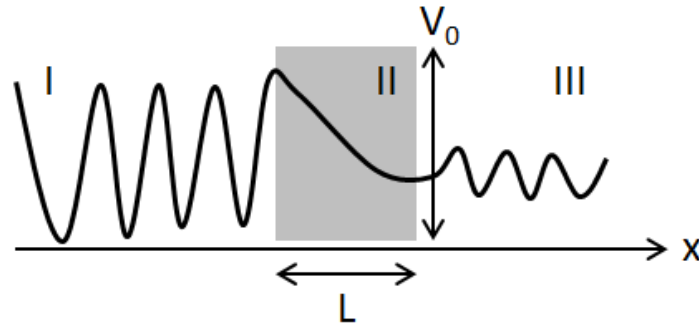


Figure 8 – Tunneling process over a 1-D barrier. An incident electron wave (I) scatter against the square barrier leading to an evanescent wave (II). If the barrier length is small enough, a certain quantity of the initial wave can be transmitted (III), implying that the associated particle has a high probability to tunnel across it.

The transmission probability $\tau(E)$ can be expressed as a function of the energy as follows:^{40,55}

$$\tau(E) = \frac{4E(V_0 - E)}{4E(V_0 - E) + V_0^2 \sinh^2(\rho_2 L)} \quad \text{Eq. 3}$$

with $\rho_2 = \frac{1}{\hbar} \sqrt{2m_e(V_0 - E)}$, and m_e the electron mass. If $\rho_2 L \gg 1$ the problem can be seen as:

$$\tau(E) \propto \exp^{-2\rho_2 L} \quad \text{Eq. 4}$$

The simplified Eq. 4 leads to a description in which an exponential decrease of the transmission is calculated with the increase of the barrier length L . This reproduces the experimental observations of an exponential increase of resistance as the molecule grows in size.

III.3.2 – One dimensional double square barrier model

A double square shaped barrier was also proposed in the literature.^{37,40,55} The resulting transmission function for this second model is displayed Figure 9. Three resonant transmission peaks are obtained echoing the transparency of the system at these energies.

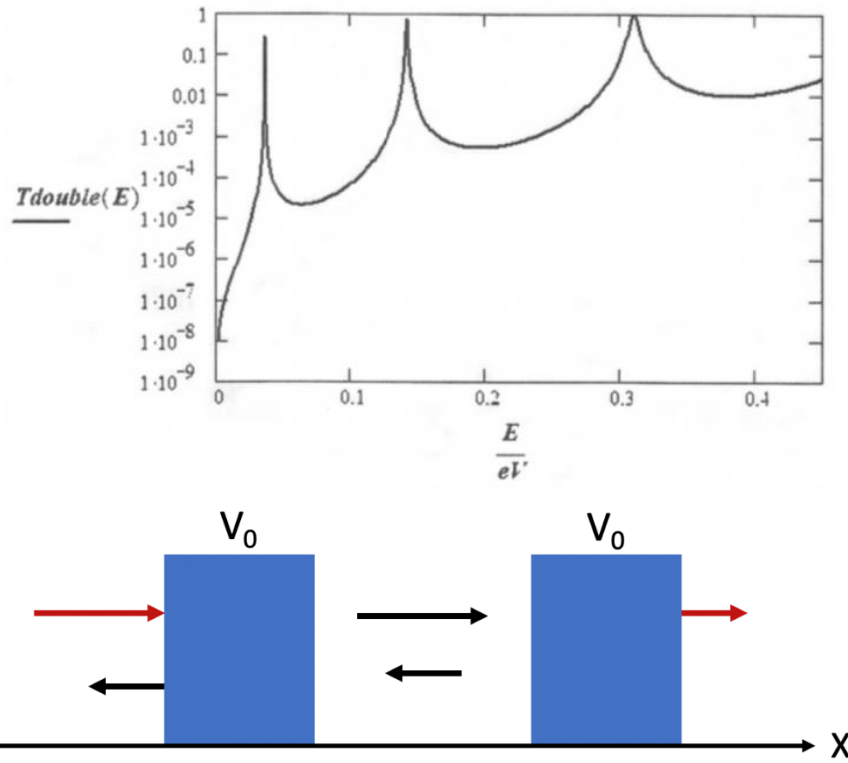


Figure 9 – Top: transmission plot of two 3 nm barriers ($L = 3$ nm) separated by 10 nm. The barrier height, $V_0 = 0.5$ eV. The transmission is only calculated for energies below V_0 . Bottom: schematic of a double squared potential barrier. An incident wave, in red, is partly transmitted or reflected (black arrow) into the central region. The transmitted wave in the central region is in turn, transmitted or reflected by the second barrier.

III.3.3 – Single resonant tunneling level

A more refined model based on a single resonant level tunneling was proposed to better reproduce the complexity of molecular junction transmission features.^{40,55} It is summarized in Figure 10. Considering two potential energy barriers, with arbitrary potential shapes (V_0 and V_0'), resolving the scattering matrices leads to the expression of the transmission $\tau(E)$ as a function of the energy:

$$\tau(E) = \frac{\tau_1 \tau_2}{1 - 2\sqrt{\mathcal{R}_1 \mathcal{R}_2} \cos(\Delta\phi) + \mathcal{R}_1 \mathcal{R}_2} \quad \text{Eq. 5}$$

where τ_1 , τ_2 , \mathcal{R}_1 and \mathcal{R}_2 are the energy dependent transmission and reflection coefficients of the first and second barrier respectively. The energy dependent phase shift is noted $\Delta\phi$.

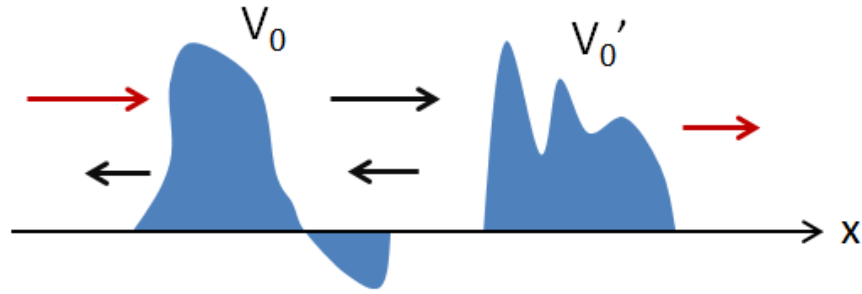


Figure 10 – The single resonant level can be represented by two separate potential barriers of arbitrary shape. V_0 and V_0' represent the corresponding potentials.

When we have: $\phi \approx 2n\pi$ and $\mathcal{R}_1, \mathcal{R}_2 \approx 1$, this leads to a resonance peak energy ϵ_0 , at which the barriers become transparent. Such singularity would not be observed if an inelastic scatterer was introduced because it would randomize the phase, meaning that the transmission across N successive barriers would go as $1/N$ instead, re-inducing an ohmic length dependency.⁵

Developing Eq. 5 around ϵ_0 (i.e. $\phi \approx 2n\pi$ and $\mathcal{R}_1, \mathcal{R}_2 \approx 1$), using a Taylor expansion to the first order and using the fact that $\sqrt{\mathcal{R}_1} = \sqrt{1 - \tau_1} \approx 1 - \tau_1/2$, one can write:⁴⁰

$$\tau(E) \approx \frac{\tau_1 \tau_2}{\left(\frac{\tau_1 + \tau_2}{2}\right)^2 + (2 - \tau_1 - \tau_2)(1 - \cos(\Delta\phi))} \quad \text{Eq. 6}$$

Applying a second order cosine expansion and a first order development of $\Delta\phi$ around the resonance energy ϵ_0 , we obtain:⁵

$$\cos(\Delta\phi(E)) \approx 1 - \frac{1}{2} \left(\frac{d\Delta\phi}{dE} \Big|_{E=\epsilon_0} \right)^2 (E - \epsilon_0)^2 \quad \text{Eq. 7}$$

Assuming that τ_i multiplied by the second order term is negligible and defining the coupling Γ as follows:⁵

$$\Gamma_i = \frac{1}{2} \left(\frac{d\Delta\phi}{dE} \right)^{-1} \tau_i \quad \text{Eq. 8}$$

the expression of the transmission $\tau(E)$ can be simplified as a Lorentzian function centered at the resonance energy, ϵ_0 , with a full width at half maximum (FWHM) of 4Γ :

$$\tau(E) = \frac{4\Gamma_1\Gamma_2}{(E - \epsilon_0)^2 + (\Gamma_1 + \Gamma_2)^2} = \frac{4\Gamma^2}{(E - \epsilon_0)^2 + 4\Gamma^2} \Big|_{\Gamma_1 = \Gamma_2} \quad \text{Eq. 9}$$

This expression is a really important equation which will be used in the next chapters of this thesis to calculate $\tau(E)$. Within this framework of the single tunneling resonant level, the coupling Γ_i is directly related to the time needed for an electron to escape the scattering region delimited by the molecular system, and is often called the “scattering rates”. It is an important quantity which is intrinsic to each molecular junction. It will be a key parameter to define the transmission properties of a molecular junction during this study. This model is one way to recover the Lorentzian shape transmission around a resonant level, but the same results can be derived using the Green’s function formalism,⁴⁰ see Figure 11 for a representation of the single level resonant using Eq. 9.

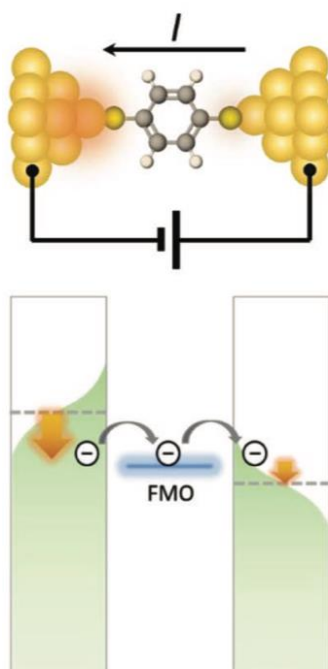


Figure 11 – Representation of a single resonant level model. The presence of the molecule, in the center of the junction, is approximated by the presence of single energy level which is the frontier molecular orbital (FMO) lying closest to the Fermi energy of the electrodes (generally the HOMO or the LUMO). Left and right electrodes are represented by electron reservoirs. If a potential difference ΔV is applied, a symmetric splitting around the zero-bias Fermi energy of $\pm \Delta V/2$ occurs (different heights in green). From reference 56.

This model is a crude simplification since a molecule is not as simple as 1-D energy barrier. Its electronic structure is composed of several occupied and unoccupied molecular orbitals (MOs). In an electronic transmission spectrum, the resonant peaks, shaped as Lorentzian functions, are

intrinsically connected to the energy position of the MOs. Each of these peaks can have different scattering rates, contingent with the ability of the electrons to flow from one end of the device to the other. This ability is mostly determined by the chemical bonding nature, and the delocalization of the orbitals between the molecule and the metal electrode which is highly sensitive to changes in the contact geometry. Undeniably, if the coupling between the molecule and the leads is strong, the passage of the electrons will be facilitated. This is why Γ_i is also called the coupling strength. Now, even if we can argue that the electronic transmission through a barrier is related to the current emerging out of a molecular junction, the exact relation between the two is not straightforward.

In 1957, Landauer demonstrated that the conductance can be perceived as electronic transmission by introducing the notion of the quantization of the conductance.^{57,58,59} In a molecular junction in which the molecule is grafted at both ends to electrodes (leads), the electrodes are considered as electron baths in equilibrium at a temperature T and with a chemical potential μ . Upon application of a bias, the electrons are injected from the electrodes to the molecule. Considering that a tunneling process occurs, it is possible to show that a relation exists between the electronic transmission and the quantized conductance.⁴⁰ Basically, considering the electrodes as one-dimensional electron gas, the directional current density J can be expressed as:

$$\begin{aligned} J_{L \rightarrow R} &= \frac{2e}{h} \int \tau(E) f_L(E, \mu_L) (1 - f_R(E, \mu_R)) \\ J_{R \rightarrow L} &= \frac{2e}{h} \int \tau(E) f_R(E, \mu_R) (1 - f_L(E, \mu_L)) \end{aligned} \quad \text{Eq. 10}$$

with L and R representing respectively the left and right electrode and $\tau(E)$ the transmission. The f_L and f_R are the Fermi-Dirac distributions, as the electron obeys the Pauli exclusion principle. The Fermi-Dirac functions write as:

$$f_{L,R} = \frac{1}{\exp\left(\frac{E - \mu_{L,R}}{k_B T_{L,R}}\right) + 1} \quad \text{Eq. 11}$$

with k_B the Boltzmann constant. Finally, the total current can be expressed as:

$$I(V) = J_{L \rightarrow R} - J_{R \rightarrow L} = \frac{2e}{h} \int_{-\infty}^{\infty} \tau(E, V) (f_L(E, \mu_L) - f_R(E, \mu_R)) dE \quad \text{Eq. 12}$$

Eq. 12 constitutes the Landauer formula. All theoretical calculated I-V curves shown in the next chapters are generated in this formalism. This equation which provides the current at each considered bias voltage is the integration of the transmission function multiplied by the difference between the left and right Fermi occupation of the electronic levels in the electrodes. The transmission function can be evaluated for example with a single resonant level (lorentzian model^{60,61}) or calculated on the basis of quantum chemical calculations, applying methods like the Green's function formalism. In that case, since the transmission is possibly voltage dependent, it has to be calculated self-consistently at each considered bias.

In fact, when a voltage bias is applied between the left and right electrodes, the chemical potentials μ_L and μ_R , are shifted symmetrically below and above the equilibrium Fermi level. This restricts the transmission spectrum to be considered in a specific bias window as shown in Figure 12. Only the transmission between the two shifted chemical potentials is integrated in the calculation of the current at the considered bias voltage.

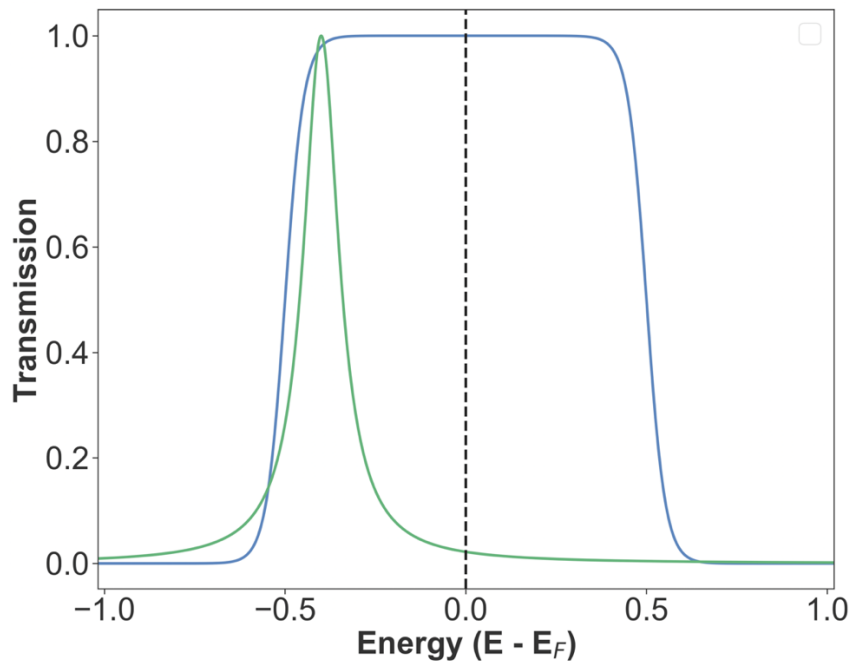


Figure 12 – The green line is the transmission probability as a function of $E - E_F$ from -1.0 eV to 1.0 eV. The E_F is the Fermi energy of the electrodes at zero bias. The blue curve represents the bias window defined by the electrodes, here $\Delta V = 1.0 V$. It corresponds to the difference between the Fermi level of the left electrode minus that of the right electrode ($f_L - f_R$). The Fermi-Dirac function is accounted for considering $T = 300 K$. The whole green portion of the transmission within this window is integrated in Eq. 12 to calculate the current at this bias voltage.

Considering $T = 0$ K and $\tau(E) = 1$, Eq. 12 which is yielding the current can be simplified as:

$$I(V) = \frac{2e^2}{h} \Delta V = 7.75 \cdot 10^{-5} \Delta V = G_0 \Delta V \quad \text{Eq. 13}$$

with G_0 the conductance quantum. The reciprocal resistance quantum is $R_0 = 12.9$ k Ω . Thus, at $\Delta V = 1.0$ V, this equation establishes that the charge current cannot be higher than 77.5 μ A in the hypothesis of a maximum of transmission around the Fermi energy. Obviously, this is the most favorable case; currents are expected to be comprised in the nA to μ A range in realistic molecular systems.

Considering a coherent ballistic regime, from the Landauer's formula, the electronic transport is built from a difference of electron current being scattered at the electrodes. This means that the created electric field can be seen as an alteration of a potential barrier shape, which will in turn change the fundamental transmission probability of the scatterer (e.g. molecule). This is what we showed using different barrier models. Another famous barrier model is the Simmons model^{62,63,64,65,66,67} Nevertheless, because the electronic structure of molecules yields a much complex electrostatic potential compared to a barrier model, the use of computational studies at the quantum level is required to access to the electrode–molecule–electrode transmission probability, which is, *a priori*, not known. This will be computed using the DFT coupled with the non-equilibrium Green's functions.

III.4 – Density functional theory (DFT) and non-equilibrium Green's functions (NEGF)

This part describes the methodologies which will be applied to calculate transmission spectra of organic and organometallic molecules employing ab initio type methods. A compromise has to be found between the precision of the results and the computational cost in order to deal with a large number of systems and additionally to provide sufficiently quantitative results to allow for the rationalization of experimental measurements; DFT appears here to be the best compromise. Contrarily to wave-function calculations which intend to solve the Schrödinger many-body equation in 3N dimensions (plus N spin degrees of freedom), with N the number of electrons, DFT essentially reduces the problem to a resolution based on the electronic density that depends only on 3 spatial coordinates to determine the properties of a many-electron system (Hohenberg and Kohn's theorems).⁶⁸ In the implementation that we use, the electrodes are considered as semi-infinite. In the directions which are perpendicular to the transport, the

periodicity is conserved, whereas along the transport direction, the scattering region (which contains the molecule) disrupts the periodicity of the metallic electrodes (Figure 13). Because this periodicity is broken, the system is referred to as "open".

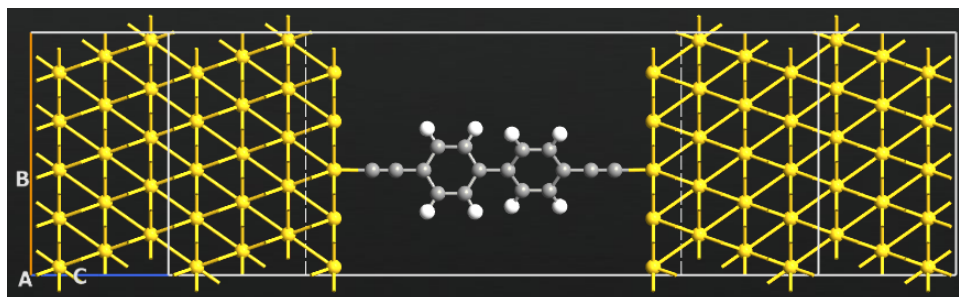


Figure 13 – Representation of a molecular junction, the directions perpendicular to the transport (A and B) are periodic, and the C direction (transport direction) is not periodic because of the scattering region (highlighted by the dotted lines).

Furthermore, from the Landauer's picture, the molecule included in the scattering region is coordinated to two infinite electrodes, with each having a different Fermi energy (or chemical potential). The system is thus out of equilibrium. The problem which rises is thus how to calculate the electronic structure of such a system and its transmission considering an open system with infinite electrodes! The solution is to employ Green's functions.⁶⁹ Introduced by Green in 1828, these functions are used to solve linear differential equations with constant coefficients. The transmission probability can be obtained from the resolution of the Green's functions.^{70,71,72,73,74,75,76} The resolution can be applied to non-equilibrium systems, which allows to calculate the transmission at different bias voltages using the Landauer's formula. This NEGF formalism was developed by Kadanoff and Baym⁷⁷ and independently by Keldysh in the early 60s.⁷⁸ In the Keldysh formalism, the electronic transmission is defined in terms of Green's function by:⁴⁰

$$\tau(E) = 4 \cdot Tr[\Gamma_L(E)G^r(E)\Gamma_R(E)G^a(E)] \quad \text{Eq. 14}$$

With Tr the trace of the transmission matrix, G^a the advanced Green function, G^r the retarded Green function, and Γ_R and Γ_L , the left and right scattering rates matrices.⁴⁰ A basic DFT/NEGF computation flowchart is presented Figure 15. Interestingly, the expression of the transmission considering a single resonant level (Lorentzian-shaped transmission) determined earlier from the last barrier model, can be derived from the NEGF formalism by considering simplifications (see reference 40, p. 201 for details).

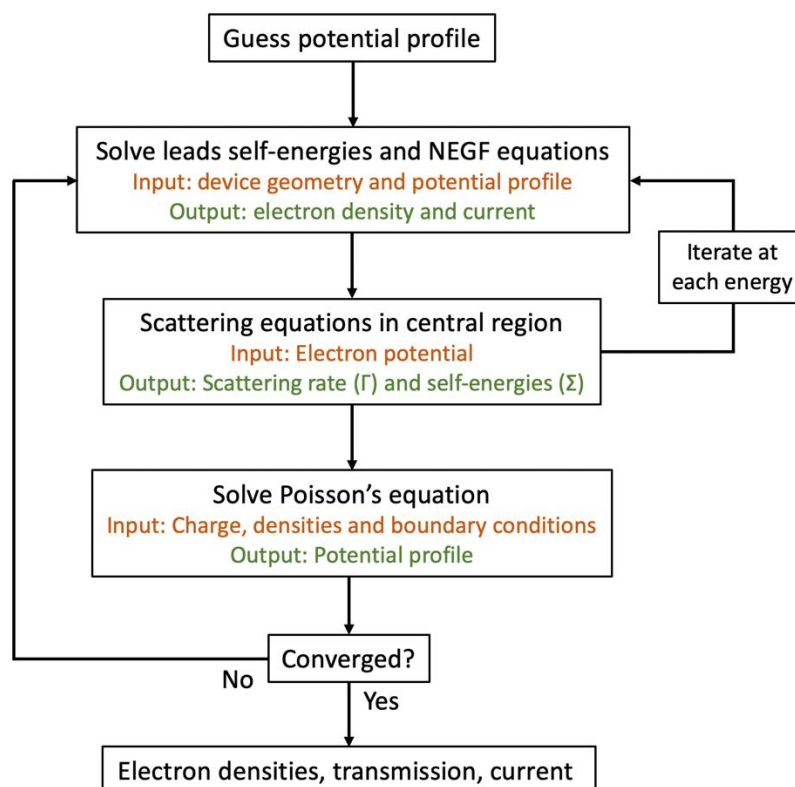


Figure 14 – Basic flowchart for the computation of transmission and current using the DFT/NEGF method. Adapted from reference 79.

The DFT coupled to the Non-Equilibrium Green's Function (DFT/NEGF) protocol is the best method to date which can resolve molecular junction systems in reasonable computational times without too much approximations. Because this method is based on DFT, it also encompasses its inherent approximations and limitations. Nevertheless, considering the I-V curves, the DFT-NEGF method can be semi-quantitative with experimental data, within one order of magnitude or less for the conductance^{80,81}, and even closer for the position of the MOs compared to the Fermi level.^{112,115} Conclusions can thus be drawn based on qualitative features of the calculated electronic transmission spectra.

III.4.1 – Computational procedure

The geometries and electronic structures of the isolated molecules were studied using the Amsterdam Density Functional package (ADF), version 2019 (vacuum, 0 K).⁸² For the periodic bulk-like systems involved in the transmission calculations (using the NEGF formalism), the Synopsys Atomistic ToolKit package (Quantum ATK 2019, 2020 and 2021 versions) was used.⁸³ The ADF calculations were performed using a TZ2P atomic basis set⁸⁴ (triple- ξ basis

set with 2 polarization functions, small frozen core) with the rev-PBE⁸⁵ exchange-correlation functional (GGA). Relativistic scalar ZORA corrections were included for all molecules. The numerical accuracy of the Becke integral was set to good ($1.1 \cdot 10^{-4}$ eV). The SCF convergence and the geometry optimization tolerance were both set to 10^{-6} a.u.

Device calculation procedure

The level of theory used was the following unless specified in the text:

Exchange correlation: GGA – revPBE (same functional as for the molecular calculations)

Basis set: Troullier–Martins type pseudopotentials (FHI); DZP (Double- ξ and 1 polarization function) for all atoms except for gold: SZP (Single- ξ and 1 polarization function).

Density-mesh cut-off: 100-125 Hartree depending on the system.

Occupation method: Fermi-Dirac with a broadening of 300 or 1000 K.

Device k-points: generally, from 5 to 10 along the A and B directions (perpendicular to the current) and between 50-150 in the C direction (transport direction).

SCF tolerance convergence: 10^{-5} a.u.

NEGF contour integrals:

- Integration method: Weighted
- Type: Semi-circle
- Integral lower bound: -50-80 eV
- Circle points: 30-40
- Real axis point density: 0.005-0.02 eV
- Real axis infinitesimal: 0.005-0.02 eV

Poisson solver:

- Fast Fourier Transform 2D or multi-grid, with periodic conditions along A and B, and boundary conditions along C (Dirichlet or Neumann).

Transmission spectrum:

- Cover bias: generally, between -2 to 2 eV relative to the Fermi energy of the electrodes.
- Infinitesimal: 10^{-6} eV
- Self-energy calculator: recursion
- k-point: between 4-10 along both A and B directions

All the k-points distributions were realized using the Monkhorst Pack grid.⁸⁶

IV – Thermoelectric properties

Thermoelectricity is the terminology assigned to describe the electricity generated by a thermoelectric effect, i.e. the difference in temperature between two sides of a material. This induces an electronic current that flows across the material and creates a voltage difference. Reversely, applying a voltage between two sides of a material generates a heat flow that creates a difference in temperature. These thermoelectric effects are at the heart of many applications like refrigeration, thermometry, or generation of electricity. Thermoelectric effects can be described by three correlated phenomena: the Seebeck, Peltier, and Thompson effects.

Seebeck effect

The first effect discovered was by Seebeck in 1821.⁸⁷ He showed that an electrical potential difference ΔV can appear when one part of a junction with two different conductors (iron and copper in Figure 1) is heated. Basically, the Seebeck effect emerges when two wires of different nature, iron and copper for example, are connected forming a thermocouple. A basic thermoelectric system is shown in Figure 15. Upon application of the temperature difference ΔT , an electrical potential difference ΔV appears and can be measured by a voltmeter.

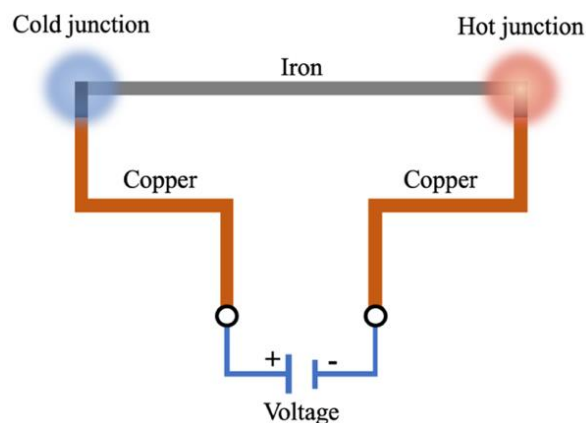


Figure 15 – Representation of a basic thermoelectric circuit, with two different conductors (iron and copper) that are connected together to make a thermocouple. To measure the voltage, a voltmeter is placed at the ends of the copper wires.

The ΔV response is proportional to the magnitude of the applied ΔT . This proportionality coefficient is called the Seebeck coefficient S . The phenomenon can be explained by considering that electrons gain energy, thus an electromotive force in the heated region and

flow to the cold part where the electrons have lower in energy, as represented in Figure 16. This creates an electrical potential difference.

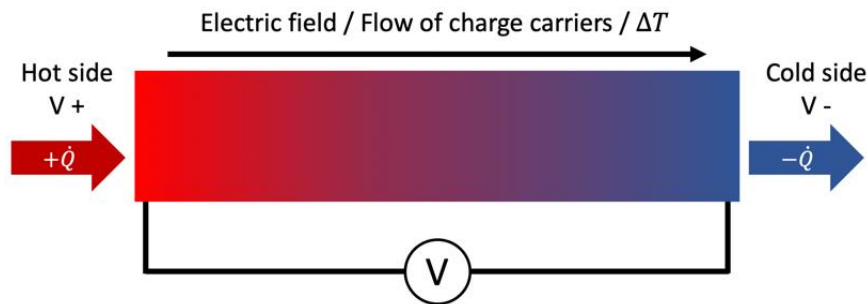


Figure 16 – Representation of the Seebeck effect, with observation of a thermovoltage with a voltmeter. With $\dot{Q} = dQ/dt$, the heat current.

Peltier effect

Peltier, a part-time physicist, observed in 1834 the second thermoelectric effect which occurs when an electrical current flow through a thermocouple.⁸⁸ It generates heating of one of the two junctions, and cooling on the other (Figure 15). These temperature changes can be reversed depending on the current direction. At that time, the correlation between the Seebeck and the Peltier effect was not established. The heating on one side of the system and cooling on the other that is generated upon application of ΔV can be explained by the conversion the energy carried by electrons into heat upon flowing across different materials.

Thomson effect

Thomson discovered in 1855 that a correlation exists between the Seebeck and Peltier effects using thermodynamic theories. From these relations, he proposed that there must exist a third thermoelectric effect, which was later called the Thomson effect; this corresponds to reversible heating or cooling when an electrical current I and a temperature gradient ΔT are applied simultaneously. Contrarily to the Seebeck and Peltier effect, the Thomson effect can be observed in a bulk material but, as of today, not in a junction configuration. Generation, emission or absorption of heat Q occur in some parts of the material.

After these discoveries, the possibilities of building thermoelectric devices for current generation, heat generation and refrigeration emerged in the scientific community. However, this was difficult to demonstrate experimentally because of the competing effects that are the

intrinsic Joule heating (heat generation induced by electrical current flow due to the collision between electrons and atoms of the conductor) and the thermal conduction (due to electrons and lattice vibrations) which greatly reduce the efficiency of such devices. The conversion effectiveness of thermoelectric generators and Peltier devices have been fully established by the work of the physicist Altenkirch in the early 1900s.^{89,90} He demonstrated that the performance of energy conversion can be increased by enhancing the electrical conductivities σ and reducing the thermal conductivities λ of the material. Nevertheless, at that time, the use of only metallic conductors did not allow to access to efficient thermoelectric systems. Actually, in 1949, a breakthrough was made in the development of a modern theory of thermoelectricity by Ioffe using the concept of figure of merit ZT .⁹¹ Ioffe endorsed and popularized the use of the semiconductors (silicon, germanium, gallium arsenide...) in thermoelectric systems to increase their performance. Nowadays, bulk materials with high thermoelectric figures of merit are doped semiconductors, some of the most famous ones are the tellurides of antimony, bismuth and lead.⁹² The research institute of Ioffe, the laboratory of semiconductors of Academy of Sciences of the USSR, has been a pioneer institution in thermoelectric research and developments leading to some of the first thermoelectric power generators and cooling devices commercially available. These scientific developments are at the origin of the democratization of the use of alloys to decrease thermal conductivity of bulk systems.

Nowadays, the research strategies to obtain efficient thermoelectric bulk materials can be synthesized as follows:

- Lowering of the thermal conductivity λ which often results in incorporating heavy elements in the materials.
- Increase of complexity in the composition and structure such as disorder and nano-structuration of the materials.
- Narrowing of the band-gap (semiconductors)
- Raising of the electrical conductivity σ to improve efficiency

IV.1 – Definitions and relationships between the thermoelectric coefficients

This section intends to provide the necessary definitions and equations related to the Seebeck coefficient, the Peltier coefficient and the figure of merit ZT and reveal their interdependence.

The Seebeck coefficient, S is defined by:

$$S = -\frac{\Delta V}{\Delta T} \quad \text{Eq. 15}$$

The Peltier coefficient of a thermocouple, π , is equal to the ratio between the rate of heating or cooling $dQ/dt = \dot{Q}$ (amount of heat transferred per unit of time) at each junction and the electrical current I :

$$\pi = \frac{\dot{Q}}{I} \quad \text{Eq. 16}$$

The second Thomson's relation expresses the Peltier coefficient in terms of the Seebeck coefficient as:⁹³

$$\pi = S \cdot T \quad \text{Eq. 17}$$

This relation correlates the Seebeck effect and the Peltier effect by the factor T which is the mean temperature of the system. This was fully demonstrated in the 1950s with the support of the Onsager reciprocal relations.⁹⁴

Finally, the figure of merit ZT which determines the efficiency of a thermoelectric system is established as follows:

$$ZT = \frac{S^2 \sigma T}{\lambda} \quad \text{Eq. 18}$$

With σ the electrical conductivity and λ the thermal conductivity. The thermal conductivity refers to the ability of a material to conduct heat. It can be divided in different contributions, the electronic thermal conductivity λ_{el} and the phononic thermal conductivity λ_{ph} .

In bulk materials, and more specifically metal, an empirical relationship between the electronic thermal conductivity and the electrical conductivity multiplied by the temperature exists and is called the Wiedemann–Franz law:^{95,96}

$$\mathcal{L} = \frac{\lambda_{el}}{\sigma \cdot T} = 2.44 \cdot 10^{-8} \text{ W} \cdot \Omega \cdot \text{K}^{-2} \quad \text{Eq. 19}$$

With \mathcal{L} the Lorentz constant.

The efficiency of heat conversion into work of a thermoelectric device is defined as the ratio between the energy provided to the external load over the heat energy absorbed at the hot junction. Indeed, in a perfect thermodynamic cycle, the efficiency η defined by the Carnot cycle (named after the French physicist Carnot in 1824) has an upper limit that a classic thermodynamic machine can achieve during the conversion of heat into work. The efficiency of a power generator, with the added figure of merit ZT , is defined as:⁹⁷

$$\eta = \frac{T_H - T_C}{T_C} \left(1 - \frac{1 + T_H/T_C}{\sqrt{1 + ZT + T_H/T_C}} \right) \quad \text{Eq. 20}$$

When ZT tends to infinity (Figure 17), one can retrieve the classic efficiency of the Carnot cycle $\eta = (T_H - T_C)/T_C$, with T_H and T_C the hot and cold temperature of each reservoir, respectively.

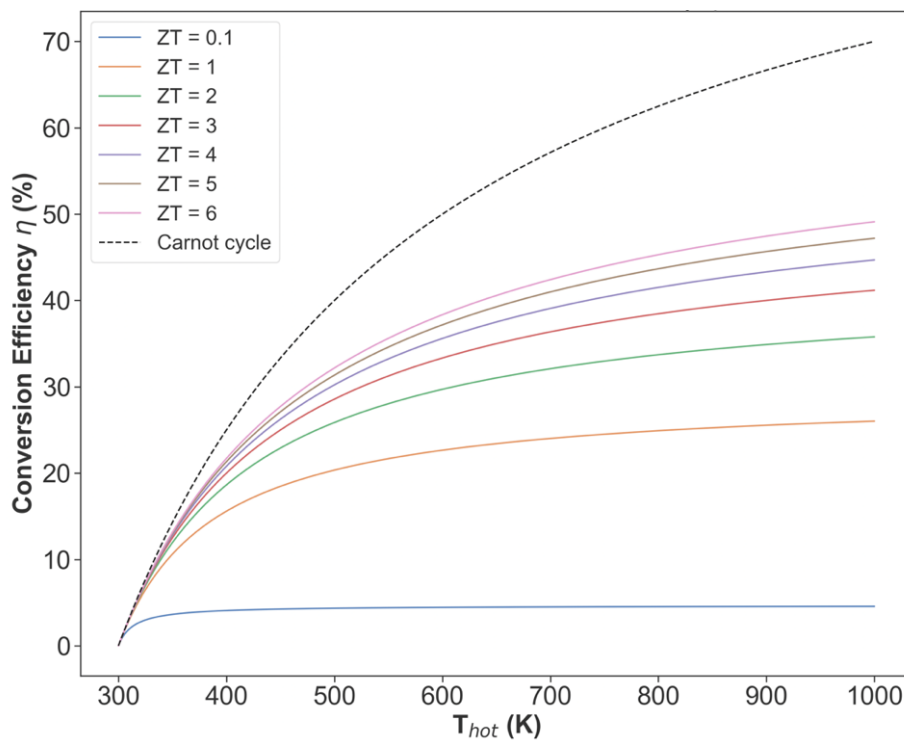


Figure 17 – Evolution of the conversion efficiency η as a function of the temperature of the hot part of the junction T_{hot} . The cold part of the junction is set at RT. The dashed line represents the theoretical Carnot cycle.

V – Thermoelectricity in molecular junctions

The ongoing research in nanotechnology is facing similar energy control issues than at the micro and macroscale. Among the different issues to be solved, one important problem concerns the heat generated by the resistance of the components of a nano-unit against the electrical current flow. It leads not only to a waste of energy but can also cause an important lowering of performance and even destruction of the nano-devices. Light irradiation, often used as external input or energy source in nano-devices, is also a cause of deterioration notably by inducing localized over-heating.⁹⁸ A straightforward approach that naturally comes to mind to prevent such deleterious effect is to exploit thermoelectric effects at the nanoscale. Besides solving these energy control problems, the development of such systems could provide thermal nano-detectors, nano-coolers or more generally nano-regulators by using their ability to transfer heat. The development of efficient thermoelectric nano-devices could also provide the conception of body implementable biosensors or monitors that need to be energetically autonomous.

The thermoelectric phenomena observed in bulk materials have been imagined to also occur at the nanoscale. This assumption came from the pioneering work of Hicks and Dresselhaus^{99,100} in 1993 which predicted that atomic wires should drastically improve the efficiency of energy conversion. This was at the origin of the intensive theoretical and experimental research developments in molecular junctions (Figure 18) built of atoms, metallic wires, molecules, quantum dots, and even biomolecules like DNA.^{101,102,103,104,105,106,107,108,109,110,111,112,113,114,115} The main feature of molecular junctions is the combination and overlap between the discrete electronic levels of the molecule energy with the continuous spectrum of energy states of the electrodes. Numerous applications using nanoscale thermoelectric systems can be envisaged, for instance: heat to voltage converters,^{116,117,118,119} local refrigerators,¹²⁰ thermal transistors,^{121,122} thermal rectifiers,^{123,124} logic gates^{125,126} and in the future, even the concept of biocompatible implementable sensors or monitors which require integrated energy sources. On the fundamental point of view, a deeper understanding of thermoelectric properties of molecular junctions could certainly provide a deeper insight into the nature and characteristics of electron and thermal transport mechanisms in these systems that will surely allow to better drive the future developments in this area.^{127,128,129,130}

Several factors play a role in the charge transport across a molecular junction and thus in its thermoelectric ability:

- The intrinsic electronic characteristics of the inserted molecule.
- The coulombic interaction between electrons.
- The constructive and destructive quantum interferences (QI) that can occur across the junction.
- The electrode vibrational properties (phonons) and their coupling with the vibrational modes of the molecule.

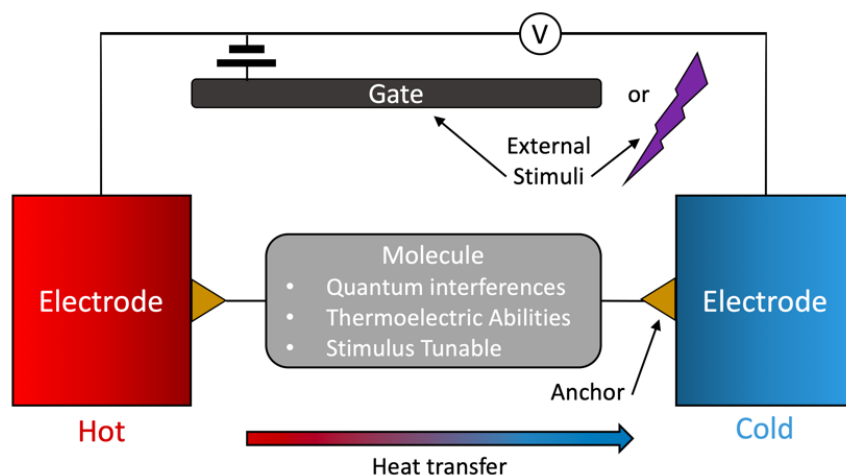


Figure 18 – Schematic of a thermoelectric molecular junction.

As stated before, applying a difference of temperature between the electrodes, ΔT , induces a current flow I of the charge carriers across the device. The nature of the charge carriers contributing to the current, electrons or holes, defines the sign of the Seebeck coefficient (Figure 19):¹²⁷

- hole transport below the Fermi level of the device, with the HOMO-like molecular level generally acting as the main transport channel (positive Seebeck coefficient).
- electron transport above the Fermi level, with the LUMO-like molecular level as the possible main transport level (negative Seebeck coefficient).

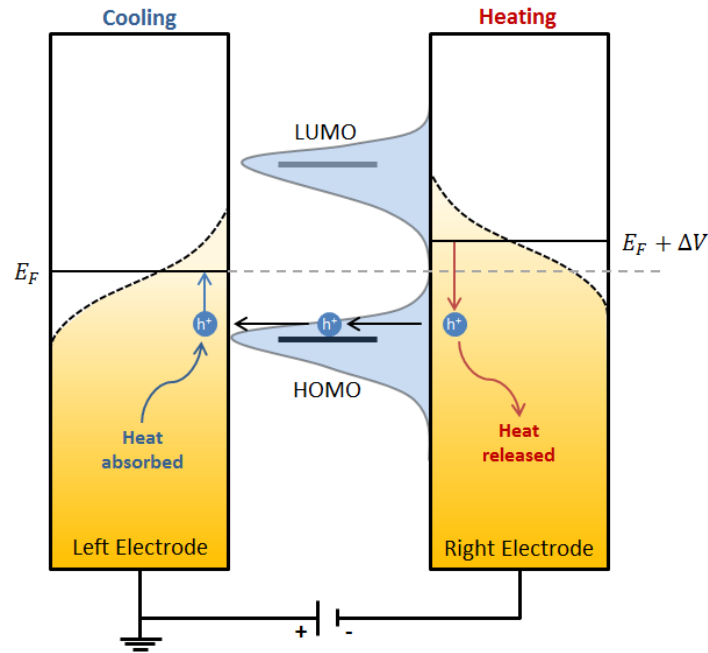


Figure 19 – Representation of the Peltier effect in a molecular junction, with generation of a net difference of temperature between the two electrodes. The transport results from the HOMO below the mean Fermi level E_F (holes as charge carriers). Applying a ΔV changes the Fermi level of the electrodes. Adapted from reference 115.

V.1 – Linear regime response formulations

In this part, the coherent thermoelectric coefficients are described within the Landauer framework. We also assume that the chemical potentials of the electrodes are equivalent to the Fermi energy $\mu \approx E_F$. In addition to these approximations, the following developments are only valid in the linear response regime i.e., by considering that the system is under a slightly out-of-equilibrium condition due to the perturbation. The linear response theory was introduced in 1957 by Kubo.¹³¹

From Eq. 12 the expression for the current $I(V)$ and the heat current in the Landauer framework are:

$$I(V, T) = \frac{2e}{h} \int_{-\infty}^{\infty} \tau(E, V) (f_L(E, \mu_L) - f_R(E, \mu_R)) dE \quad \text{Eq. 21}$$

$$Q_e(V, T) = \frac{2}{h} \int_{-\infty}^{\infty} \tau(E, V) E (f_L(E, \mu_L) - f_R(E, \mu_R)) dE \quad \text{Eq. 22}$$

Applying the linear response regime and considering a small difference of temperature $\Delta T = (T_L - T_R)$ and a small difference of potential $\Delta V = (\mu_L - \mu_R)/e$ between the electrodes, one can simplify Eq. 21 and Eq. 22 into:^{132,133}

$$I(V, T) = L_0 \Delta V + L_1 \frac{\Delta T}{T} \quad \text{Eq. 23}$$

$$Q_e(V, T) = L_1 \Delta V + L_2 \frac{\Delta T}{T} \quad \text{Eq. 24}$$

Here, L_0 refers to the linear conductance of the system divided by the quantum of conductance G_0 :

$$L_0 = G/G_0 \quad \text{with} \quad G_0 = \frac{2e^2}{h} \approx 77.46 \mu S \quad \text{Eq. 25}$$

The L_n coefficient (with $n = 0, 1, 2$) in Eq. 23 and Eq. 24 is expressed as:

$$L_n = \frac{2e}{h} \int_{-\infty}^{\infty} \tau(E) (E - \mu)^n \left(-\frac{df}{dE} \right) dE \quad \text{Eq. 26}$$

In Eq. 26, the chemical potential of the left and right electrodes, μ_L and μ_R respectively, are considered equal $\mu = \mu_L = \mu_R$; this corresponds to the system at equilibrium ($\Delta V = 0$).

V.2 – The Seebeck coefficient in the linear response regime

In this framework, considering an open circuit ($I = 0$), Eq. 23 becomes:

$$L_0 \Delta V = -\frac{L_1 \Delta T}{T} \quad \text{Eq. 27}$$

and by identification:

$$S = -\frac{1}{T} \frac{L_1}{L_0} \equiv -\frac{\Delta V}{\Delta T} \quad \text{Eq. 28}$$

This Eq. 28 will be applied to calculate the Seebeck coefficient for each studied system. The linear regime implies that $\Delta T \ll T$.

When the system is studied at low temperature, a Sommerfeld expansion³⁶ can be used to simplify Eq. 23 by removing the integral, leading to:¹²⁷

$$S_{lowT} = - \frac{\pi^2 k_B^2 T}{3|e|\tau(E)} \left. \frac{d\tau(E)}{dE} \right|_{E=E_F} \quad \text{Eq. 29}$$

From Eq. 29, it appears that the slope of the transmission at the Fermi level is essential to obtain high Seebeck coefficient. Nevertheless, this observation is not so valid upon increase of the temperature as shown in Figure 20, which displays the discrepancy between the Sommerfeld expansion (Eq. 29) and the integral form (Eq. 23) occurring between 100-150 K. In this example, at RT, the difference is about 20 $\mu\text{V/K}$ ($\sim 20\%$ error). This error is intrinsically linked to the electronic transmission's shape; thus, it can be different than the calculated 20% in Figure 20.

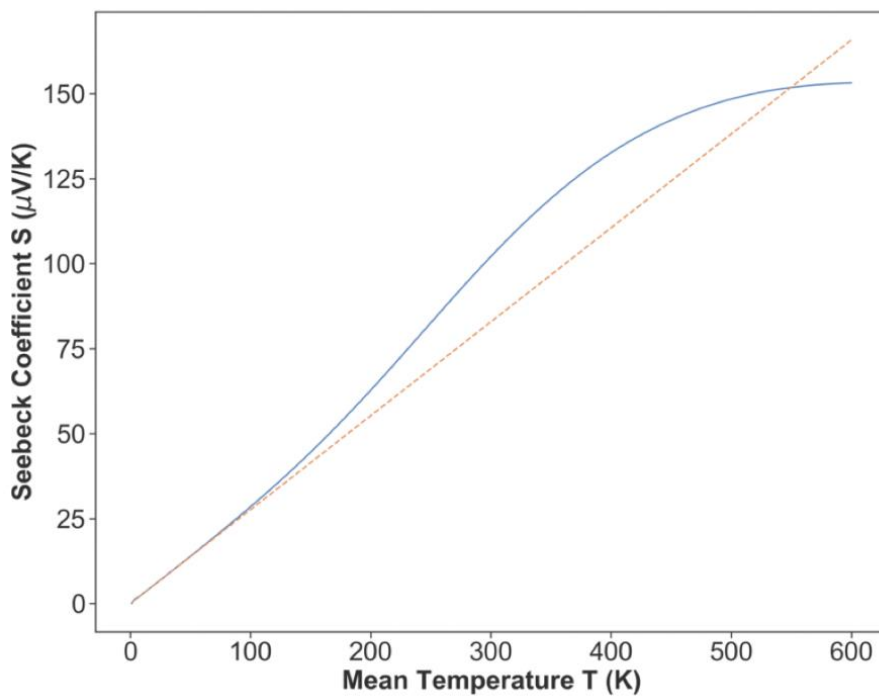


Figure 20 – Evolution of the Seebeck coefficient for the $\text{Fe}^{\text{II}}(\text{cyclam})(\text{C}_2\text{PhS})_2$ molecule (cyclam = 1,4,8,11-tetraazacyclotetradecane, see Part II, Chapter IV) as a function of the mean temperature applying Eq. 23 for the blue line and Eq. 29 for the dotted orange line.

V.3 – Calculation of the thermal conductance

For molecular systems, the use of thermal conductance is favored over thermal conductivity. The total thermal conductance can be divided into two main contributions:

- electronic thermal conductance κ_{el}
- phononic thermal conductance κ_{ph}

If only the electronic thermal conductance κ_{el} is considered ($\kappa_{ph} = 0$), using Fourier's Law of thermal conduction one can express Q_e as follows:

$$Q_e = \kappa_{el} \cdot \Delta T \quad \text{Eq. 30}$$

Using Eq. 24, Eq. 27 and Eq. 30, κ_{el} can be expressed as:

$$\kappa_{el} = \frac{1}{T} \left(L_2 - \frac{L_1^2}{L_0} \right) \quad \text{Eq. 31}$$

From Eq. 31, one can deduce that the electronic thermal conductance is dependent on the electric conductance G (because $L_0 = G/G_0$). Therefore, it can be related to the aforementioned Wiedemann-Franz Law (Eq. 19) employing conductances instead of conductivities:

$$\mathcal{L} = \frac{\kappa_{el}}{G \cdot T} \rightarrow \kappa_{el} = \mathcal{L} \cdot G \cdot T \quad \text{Eq. 32}$$

It should be noted that at the nanoscale the validity of the Wiedemann-Franz law remains an open question.^{134,135}

For the calculation of κ_{ph} , omitting the electron-phonon interactions, the phonon contribution to the heat flux Q can be expressed as:^{104,136}

$$Q_{ph} = \frac{\hbar}{2\pi} \int_0^\infty \omega \tau(\omega) [n_B(T_L) - n_B(T_R)] d\omega \quad \text{Eq. 33}$$

with n_B the Bose-Einstein distribution:

$$n_B(T) = \frac{1}{\exp\left(\frac{\hbar\omega}{k_b T_{L,R}}\right) - 1} \quad \text{Eq. 34}$$

where $\tau(\omega)$ is the transmission function for a phonon with an energy $\hbar\omega$. Using the same approach (Fourier's law of heat conduction) than for κ_{el} , one can state that $Q_{ph} = \kappa_{ph} \Delta T$, consequently, κ_{ph} can take the form:

$$\kappa_{ph} = \frac{\hbar^2}{2\pi k_b T^2} \int_0^\infty \omega^2 \tau(\omega) \frac{\exp(\hbar\omega/k_b T)}{(\exp(\hbar\omega/k_b T) - 1)^2} d\omega \quad \text{Eq. 35}$$

The phononic contribution to the total thermal conductance is present and can be substantial; in our case, we will only take a constant value of $\kappa_{ph} = 20$ pW/K, estimated from the literature (see next chapter for more details), to perform the figure of merit calculations.

V.4 – Expression of the Figure of merit (ZT)

As mentioned in the previous sections, the efficiency of the energy conversion is characterized by the dimensionless thermoelectric figure of merit ZT .¹³⁷ By introducing the electrical conductance G and the total thermal conductance κ instead of the electrical conductivity σ and thermal conductivity λ , Eq. 18 can be expressed as:

$$ZT = \frac{S^2GT}{\kappa} \quad \text{Eq. 36}$$

Finally, if only the electronic thermal conductance is considered, an "electronic" figure of merit ZT_{el} can be extracted using Eq. 27, Eq. 28 and Eq. 31:

$$ZT_{el} = \frac{L_1^2}{L_0L_2 - L_1^2} \quad \text{Eq. 37}$$

With all those keys in hand, in the next chapter we will analyze in more details the intrinsic characteristics of molecular junctions.

-
- ¹ Chau, R.; Doyle, B.; Datta, S.; Kavaliero, J.; Zhang, K. Integrated nanoelectronics for the future, *Nature Mat.* 2007, 6, 810. doi:10.1038/nmat2014.
- ² Petty, M.C.; Bryce, M.R.; Bloor, D. *Introduction to Molecular Electronics*. New York: Oxford University Press. 1995, 1–25. ISBN:0-19-521156-1.
- ³ von Hippel, A.R. Molecular engineering, *Science* 1956, 123, 315. ISBN:0262220024.
- ⁴ Heath, J.R.; Ratner, M.A. Molecular electronics, *Phys. Today* 2003, 56, 43. doi:10.1063/1.1583533.
- ⁵ van Dyck, C. *Characterization and Theoretical Design of Functional Molecular junctions*. Univ. Mons, Belgique, 2013.
- ⁶ Akkerman, H. B.; Naber, R. C. G.; Jongbloed, B.; van Hal, P. A.; Blom, P. W. M.; de Leeuw, D. M.; de Boer, B. Electron tunneling through alkanedithiol self-assembled monolayers in large-area molecular junctions. *Proc. Natl. Acad. Sci.* 2007, 104, 11161–11166. doi:10.1073/pnas.0701472104.
- ⁷ Huang, J.; Li, Q.; Ren, H.; Su, H.; Shi, Q. W.; Yang, J. Switching mechanism of photochromic diarylethene derivatives molecular junctions. *J. Chem. Phys.* 2007, 127, 094705. doi:10.1063/1.2770733.
- ⁸ Hnid, I.; Frath, D.; Sun, X.; Lafolet, F.; Lacroix, J.-C. Highly Efficient Photoswitch in Diarylethene-Based Molecular Junctions. *J. Am. Chem. Soc.* 2020, 142, 7732–7736. doi:10.1021/jacs.0c01213.
- ⁹ Battacharyya, S.; Kibel, A.; Kodis, G.; Liddell, P. A.; Gervaldo, M.; Gust, D.; Lindsay, S. Optical Modulation of Molecular Conductance. *Nano Lett.* 2011, 11, 2709–2714. doi:10.1021/nl200977c.
- ¹⁰ Martin, S.; Haiss, W.; Higgins, S. J.; Nichols, R. J. The Impact of E–Z Photo-Isomerization on Single Molecular Conductance. *Nano Lett.* 2010, 10, 2019–2023. doi:10.1021/nl9042455.
- ¹¹ Wang, Y.; Li, X.; Zheng, X.; Yang, J. Manipulation of spin and magnetic anisotropy in bilayer magnetic molecular junctions. *Phys. Chem. Chem. Phys.* 2018. doi:10.1039/c8cp05759a.
- ¹² Ke1 G.; Duan, C.; Huang, F.; Guo, X. Electrical and spin switches in single-molecule junctions. *Infomat* 2019, 2, 92–112. doi:10.1002/inf2.12068.
- ¹³ Liao, J.; Agustsson, J. S.; Wu, S.; Schönenberger, C.; Calame, M.; Leroux, Y.; Mayor, M.; Jeannin, O.; Ran, Y.-Fe.; Liu, S.-X.; Decurtins, S. Cyclic Conductance Switching in Networks of Redox-Active Molecular Junctions. *Nano Lett.* 2010, 10, 759–764. doi:10.1021/nl902000e.
- ¹⁴ Haiss, W.; van Zalinge, H.; Higgins, S. J.; Bethell, D.; Höbenreich, H.; Schiffrin, D. J.; Nichols, R. J. Redox State Dependence of Single Molecule Conductivity. *J. Am. Chem. Soc.* 2003, 125, 15294–15295. doi:10.1021/ja038214e.
- ¹⁵ Li, Z.; Pobelov, I.; Han, B.; Wandlowski, T.; Błaszczuk, A.; Mayor, M. Conductance of redox-active single molecular junctions: an electrochemical approach. *Nanotech.* 2006, 18, 044018. doi:10.1088/0957-4484/18/4/044018.
- ¹⁶ Xu, B. Q.; Li, X. L.; Xiao, X. Y.; Sakaguchi, H.; Tao, N. J. Electromechanical and Conductance Switching Properties of Single Oligothiophene Molecules. *Nano Lett.* 2005, 5, 1491–1495. doi:10.1021/nl050860j.
- ¹⁷ Ulrich, J.; Esrail, D.; Pontius, W.; Venkataraman, L.; Millar, D.; Doerrer, L. H. Variability of Conductance in Molecular Junctions. *J. Phys. Chem. B* 2006, 110, 2462–2466. doi:10.1021/jp056455y.
- ¹⁸ Binnig, G.; Rohrer, H. Scanning tunneling microscopy. *Surface Sci.* 1983, 126, 236–244. doi:10.1016/0039-6028(83)90716-1.

-
- ¹⁹ Bai, C. *Scanning tunneling microscopy and its applications*. Springer, New York, 2000. ISBN:978-3-540-65715-6.
- ²⁰ Bumm, L. A.; Arnold, J. J.; Cygan, M. T.; Dunbar, T. D.; Burgin, T. P.; Jones, L.; Weiss, P. S. Are Single Molecular Wires Conducting? *Science* 1996, 271, 1705–1707. doi:10.1126/science.271.5256.1705.
- ²¹ Andres, R. P.; Bein, T.; Dorogi, M.; Feng, S.; Henderson, J. I.; Kubiak, C. P.; Reifenger, R. Coulomb Staircase at Room Temperature in a Self-Assembled Molecular Nanostructure. *Science* 1996, 272, 1323–1325. doi:10.1126/science.272.5266.1323.
- ²² Datta, S.; Tian, W.; Hong, S.; Reifenberger, R.; Henderson, J. I.; Kubiak, C. P. Current-Voltage Characteristics of Self-Assembled Monolayers by Scanning Tunneling Microscopy. *Phys. Rev. Lett.* 1997, 79, 2530–2533. doi:10.1103/physrevlett.79.2530.
- ²³ Leatherman, G.; Durantini, E. N.; Gust, D.; Moore, T. A.; Moore, A. L.; Stone, S.; Lindsay, S. M. Carotene as a Molecular Wire: Conducting Atomic Force Microscopy. *J. Phys. Chem. B* 1999, 103, 4006–4010. doi:10.1021/jp9831278.
- ²⁴ Wold, D. J.; Frisbie, C. D. Formation of Metal–Molecule–Metal Tunnel Junctions: Microcontacts to Alkanethiol Monolayers with a Conducting AFM Tip. *JACS* 2000, 122, 2970–2971. doi:10.1021/ja994468h.
- ²⁵ Thomas, L.; Arbouch, I.; Guérin, D.; Wallart, X.; van Dyck, C.; Mélin, T.; Cornil, J.; Vuillaume, D.; Lenfant, S. Conductance Switching of Azobenzene-Based Self-Assembled Monolayers on Cobalt Probed by UHV Conductive-AFM. *Nanoscale* 2021, 13, 6977–6990. doi:10.1039/D1NR00106J.
- ²⁶ Binnig, G.; Quate, C. F.; Gerber, C. Atomic Force Microscope. *Phys. Rev. Lett.* 1986, 56, 930–933. doi:10.1103/physrevlett.56.930.
- ²⁷ Murrell, M. P.; Welland, M. E.; O’Shea, S. J.; Wong, T. M. H.; Barnes, J. R.; McKinnon, A. W.; Heyns, M.; Verhaverbeke, S. Spatially resolved electrical measurements of SiO₂ gate oxides using atomic force microscopy. *Appl. Phys. Lett.* 1993, 62, 786–788. doi:10.1063/1.108579.
- ²⁸ Houzé, F.; Meyer, R.; Schneegans, O.; Boyer, L. Imaging the local electrical properties of metal surfaces by atomic force microscopy with conducting probes. *Appl. Phys. Lett.* 1996, 69, 1975–1977. doi:10.1063/1.117179.
- ²⁹ Loiacono, M. J.; Granstrom, E. L.; Frisbie, C. D. Investigation of Charge Transport in Thin, Doped Sexithiophene Crystals by Conducting Probe Atomic Force Microscopy. *J. Phys. Chem. B* 1998, 102, 1679–1688. doi:10.1021/jp973269m.
- ³⁰ Lanza, M. *Conductive Atomic Force Microscopy*. Wiley, Berlin, 2017. ISBN:978-3-527-34091-0.
- ³¹ Kelley, T. W.; Granstrom, E.; Frisbie, C. D. Conducting Probe Atomic Force Microscopy: A Characterization Tool for Molecular Electronics. *Adv. Mat.* 1999, 11, 261–264. doi:10.1002/(sici)1521-4095(199903)11:3<261::aid-adma261>3.0.co;2-b.
- ³² Xu, B. Measurement of Single-Molecule Resistance by Repeated Formation of Molecular Junctions. *Science* 2003, 301, 1221–1223. doi:10.1126/science.1087481.
- ³³ Parks, J. J.; Champagne, A. R.; Hutchison, G. R.; Flores-Torres, S.; Abruña, H. D.; Ralph, D. C. Tuning the Kondo Effect with a Mechanically Controllable Break Junction. *Phys. Rev. Lett.* 2007, 99, 026601. doi:10.1103/physrevlett.99.026601.
- ³⁴ Reed, M. A. Conductance of a Molecular Junction. *Science* 1997, 278, 252–254. doi:10.1126/science.278.5336.252.

-
- ³⁵ Millikan, R. A.; Bishop E. S. *Elements of Electricity*, a practical discussion of the fundamental laws and phenomena of electricity and their practical applications in the business and industrial world. Am. Tech. Soc. 1917, 54.
- ³⁶ Ashcroft, N.; Mermin, N. *Solid state physics*. Science 1976.
- ³⁷ Durkam, C. *Current at the nanoscale: an introduction to nanoelectronics*. Imperial College Press 2007. doi:10.1142/P511.
- ³⁸ Debye, P. Zur Theorie der spezifischen Waerme. *Ann. Phys.* 1912, 39, 789-839. doi:10.1002/andp.19123441404.
- ³⁹ Cohen-Tannoudji C.; Diu B.; Laloë, F. *Mécanique quantique*. Hermann, 2, 1973.
- ⁴⁰ Cuevas, J. C.; Scheer, E. *Molecular Electronics: An Introduction to Theory and Experiment*, 1, World Scientific, 2011. ISBN:2301-301X.
- ⁴¹ Gall, D. Electron mean free path in elemental metals. *J. Appl. Phys.* 2016, 119, 085101. doi:10.1063/1.4942216.
- ⁴² Waser, R.; Schmid, G. *Nanotechnology: Volume 3: Information Technology I*, Nanotechnology, Wiley, 2008.
- ⁴³ Ibach, H.; Lüth, H. *Solid-State Physics: An Introduction to Principles of Materials Science*, Advanced texts in physics, Springer, 2009.
- ⁴⁴ Stern, A.; Aharonov, Y.; Imry, Y. Phase uncertainty and loss of interference: A general picture. *Phys. Rev. A* 1990, 41, 3436. doi:10.1103/PhysRevA.41.3436.
- ⁴⁵ Datta, S. *Electronic Transport in Mesoscopic Systems*, Cambridge Studies in Semiconductor Physics and Microelectronic Engineering, Cambridge University Press, 1997.
- ⁴⁶ Imry, Y. *Introduction to Mesoscopic Physics*, Mesoscopic physics and nanotechnology, Oxford University Press, USA, 1997.
- ⁴⁷ McCreery, R. L.; Yan, H.; Bergren, A. A critical perspective on molecular electronic junctions: there is plenty of room in the middle. *J. Phys. Chem. Chem. Phys.* 2013, 15, 1065, doi:10.1039/C2CP43516K.
- ⁴⁸ Ho Choi, S.; Kim, B.; Frisbie, C. D. Electrical Resistance of Long Conjugated Molecular Wires. *Science* 2008, 320, 1482–1486. doi:10.1126/science.1156538.
- ⁴⁹ Adams, D. M.; Brus, L.; Chidsey, C. E. D.; Creager, S.; Creutz, C.; Kagan, C. R.; Kamat, P. V.; Lieberman, M.; Lindsay, S.; Marcus, R. A.; Metzger, R. M.; Michel-Beyerle, M. E.; Miller, J. R.; Newton, M. D.; Rolison, D. R.; Sankey, O.; Schanze, K. S.; Yardley, J.; Zhu X. Charge transfer on the nanoscale: Current status. *J. Phys. Chem. B* 2003, 107, 6668. doi:10.1021/jp0268462.
- ⁵⁰ McCreery, R. L. Molecular Electronic Junctions. *Chem. Mat.* 2004, 16, 4477. doi:10.1021/cm049517q.
- ⁵¹ Averin, D. V.; Likharev, K. K. Coulomb blockade of single-electron tunneling, and coherent oscillations in small tunnel junctions. *J. Low Temp. Phys.* 1986, 62, 345–373. doi:10.1007/bf00683469.
- ⁵² Chang, Y.-W.; Jin, B.-Y. Theory of charge transport in molecular junctions: From Coulomb blockade to coherent tunneling. *J. Chem. Phys.* 2014, 141, 064111. doi:10.1063/1.4892058.
- ⁵³ Islam, A.; Benbakhti, B.; Kalna, K. Electron velocity decline in Si nanoscales MOSFETs with the shortening of gate length. *J. Phys.: Conf. Series* 2010, 242, 012011. doi:10.1088/1742-6596/242/1/012011.
- ⁵⁴ Datta S. *Quantum Transport: Atom to Transistor*, Cambridge University Press, 2005.
- ⁵⁵ Cohen-Tannoudji, C.; Diu, B.; and Laloë F. *Mécanique quantique*, vol. 1, Hermann, 1973,
- ⁵⁶ Wang, K.; Meyhofer, E.; Reddy, P. Thermal and Thermoelectric Properties of Molecular Junctions. *Adv. Funct. Mater.* 2019, 1904534. doi:10.1002/adfm.201904534.

-
- ⁵⁷ Landauer, R. Spatial Variation of Currents and Fields Due to Localized Scatterers in Metallic Conduction. *IBM J. R. and D.* 1957, 1, 223–231. doi:10.1147/rd.13.0223.
- ⁵⁸ Landauer, R. Electrical transport in open and closed systems. *Z. Phys. B Cond. Mat.* 1987, 68, 217. doi:10.1007/BF01304229.
- ⁵⁹ Imry Y.; Landauer, R. Conductance viewed as transmission. *Rev. Mod. Phys.* 1999, 71, S306. doi:10.1103/RevModPhys.71.S306.
- ⁶⁰ Grüter, L.; Cheng, F.; Heikkilä, T. T.; González, M. T.; Diederich, F.; Schönenberger, C.; Calame, M. Resonant tunneling through a C₆₀ molecular junction in a liquid environment. *Nanotech.* 2005, 16, 2143–2148. doi:10.1088/0957-4484/16/10/029.
- ⁶¹ Zotti, L. A.; Kirchner, T.; Cuevas, J.-C.; Pauly, F.; Huhn, T.; Scheer, E.; Erbe, A. Revealing the Role of Anchoring Groups in the Electrical Conduction Through Single-Molecule Junctions. *Small* 2010, 6, 1529–1535. doi:10.1002/sml.200902227.
- ⁶² Simmons, J. G. Low-Voltage Current-Voltage Relationship of Tunnel Junctions. *J. Appl. Phys.* 1963, 34, 238–239. doi:10.1063/1.1729081.
- ⁶³ Simmons, J. G. Generalized Thermal J-V Characteristic for the Electric Tunnel Effect. *J. Appl. Phys.* 1964, 35, 2655–2658. doi:10.1063/1.1713820.
- ⁶⁴ J. Simmons, J. G. Generalized Formula for the Electric Tunnel Effect between Similar Electrodes Separated by a Thin Insulating Film. *J. Appl. Phys.* 1963, 34, 1793–1803. doi:10.1063/1.1702682.
- ⁶⁵ Simmons, J. G. Electric Tunnel Effect between Dissimilar Electrodes Separated by a Thin Insulating Film. *J. Appl. Phys.* 1963, 34, 2581–2590. doi:10.1063/1.1729774.
- ⁶⁶ Simmons, J. G. Potential Barriers and Emission-Limited Current Flow Between Closely Spaced Parallel Metal Electrodes. *J. Appl. Phys.* 1964, 35, 2472–2481. doi:10.1063/1.1702884.
- ⁶⁷ Simmons, J. G. Low-Voltage Current-Voltage Relationship of Tunnel Junctions. *J. Appl. Phys.* 1963, 34, 238–239. doi:10.1063/1.1729081.
- ⁶⁸ Hohenberg, P.; Kohn, W. Inhomogeneous Electron Gas. *Phys. Rev.* 1964, 136, B864–B871. doi:10.1103/physrev.136.b864.
- ⁶⁹ Duffy, D. G. *Green's Functions with Applications; Studies in advanced mathematics.* Chapman & Hall, Boca Raton, Fla, 2001.
- ⁷⁰ Brandbyge, M.; Mozos, J.-L.; Ordejón, P.; Taylor, J.; Stokbro, K. Density-functional method for nonequilibrium electron transport. *J. Phys. Rev. B* 2002, 65, 165401. doi:10.1103/PhysRevB.65.165401.
- ⁷¹ Taylor, J.; Guo, H.; Wang, J. Ab initio modeling of quantum transport properties of molecular electronic devices. *J. Phys. Rev. B* 2001, 63, 245407. doi:10.1103/PhysRevB.63.245407.
- ⁷² Xue Y.; Datta, S.; Ratner M. A. First-principles based matrix Green's function approach to molecular electronic devices: general formalism. *Chem. Phys.* 2002, 281, 151. doi: 10.1016/S0301-0104(02)00446-9.
- ⁷³ Paulsson, M.; Zahid, F.; Datta, S. *Resistance of a Molecule. Nanoscience, Engineering and Technology Handbook,* CRC Press, 2002.
- ⁷⁴ Paulsson, M. Non-Equilibrium Green's Functions for Dummies: Introduction to the One Particle NEGF equations. arXiv 2002. arXiv:cond-mat/0210519.

-
- ⁷⁵ Stokbro, K.; Taylor, J.; Brandbyge, M.; Guo, H. Ab-initio Non- Equilibrium Green's Function Formalism for Calculating Electron Transport in Molecular Devices, in *Introducing Molecular Electronics*. Notes in Physics, vol. 68, 117–151, Springer Berlin Heidelberg, 2005. doi:10.1007/3-540-31514-4_5.
- ⁷⁶ Cohen, G.; Galperin, M. Green's Function Methods for Single Molecule Junctions. *J. Chem. Phys.* 2020, 152, 090901. doi:10.1063/1.5145210.
- ⁷⁷ Kadanoff, L. P.; Baym, G. *Quantum Statistical Mechanics*. WA Benjamin, Menlo Park, USA, 1962. doi:10.1201/9780429493218.
- ⁷⁸ Keldysh, L. V. Diagram technique for non-equilibrium processes. *Zh. Eksp. Teor. Fiz.* 1964, 47, 1515.
- ⁷⁹ Anantram, M. P.; Lundstrom, M. S.; Nikonov, D. E. Modeling of Nanoscale Devices. *Proc. IEEE* 2008, 96, 1511-1550. doi:10.1109/JPROC.2008.927355.
- ⁸⁰ Koentopp, M.; Chang, C.; Burke, K.; Car, R. Density functional calculations of nanoscale conductance. *J. Phys.: Cond. Mat.* 2008, 20, 083203. doi:10.1088/0953-8984/20/8/083203.
- ⁸¹ Mera, H.; Niquet, Y. M. Are Kohn-Sham Conductances Accurate? *Phys. Rev. Lett.* 2010, 105, 216408. doi:10.1103/PhysRevLett.105.216408.
- ⁸² te Velde, G.; Bickelhaupt, F.M.; Baerends, E.J.; Fonseca Guerra, C.; van Gisbergen, S. J. A.; Snijders, J.G.; Ziegler, T. Chemistry with ADF. *J. Comp. Chem.* 2001, 22, 931. doi: 10.1002/jcc.1056.
- ⁸³ a) Smidstrup, S.; Markussen, T.; Vancraeyveld, P.; Wellendorff, J.; Schneider, J.; Gunst, T.; Stokbro, K. QuantumATK: An integrated platform of electronic and atomic-scale modelling tools. *J. Phys.: Cond. Mat.* 2020, doi:10.1088/1361-648x/ab4007 b) Smidstrup, S.; Stradi, D.; Wellendorff, J.; Khomyakov, P. A.; Vej-Hansen, U. G.; Lee, M.-E.; Ghosh, T.; Jónsson, E.; Jónsson, H.; Stokbro, K. First-principles Green's-function method for surface calculations: A pseudopotential localized basis set approach. *Phys. Rev. B* 2017, 96, 195309. doi: 10.1103/PhysRevB.96.195309. c) Brandbyge, M.; Mozos, J. L.; Ordejón, P.; Taylor, J.; Stokbro, K. Density-functional method for nonequilibrium electron transport. *Phys. Rev. B* 2002, 65, 165401. doi:10.1103/PhysRevB.65.165401.
- ⁸⁴ a) van Lenthe, E.; Baerends, E. J. Optimized Slater-type basis sets for the elements 1-118. *J. Comp. Chem.* 2003, 24, 1142. doi:10.1002/jcc.10255. b) Chong, D.P.; van Lenthe, E.; van Gisbergen S. J. A.; Baerends, E. J. Even-tempered Slater-Type orbitals revisited: From Hydrogen to Krypton. *J. Comp. Chem.* 2004, 25, 1030. doi:10.1002/jcc.20030. c) Chong, D.P. Augmenting basis set for time-dependent density functional theory calculation of excitation energies: Slater-type orbitals for hydrogen to krypton. *Mol. Phys.* 2005, 103, 749. doi:10.1080/00268970412331333618.
- ⁸⁵ Zhang, Y.; Yang, W. Comment on Generalized Gradient Approximation Made Simple. *Phys. Rev. Lett.* 1998, 80, 890. doi:10.1103/PhysRevLett.80.890.
- ⁸⁶ Monkhorst, H. J.; Pack, J. D. Special points for Brillouin-zone integrations. *Phys. Rev. B* 1976, 13, 5188. doi:10.1103/PhysRevB.13.5188.
- ⁸⁷ Seebeck, T. J. Über den Magnetismus der galvanischen Kette. *Abhandlungen der Physikalischen Klasse der Königlich-Preußischen Akademie der Wissenschaften aus den Jahren 1822, 1820-1821*: 289–346.
- ⁸⁸ Peltier, J. C. A. Investigation of the heat developed by electric currents in homogeneous materials and at the junction of two different conductors. - *Ann. Chem. Phys.*, 1834.
- ⁸⁹ Altenkirch, E. Über den Nutzeffekt der Thermosäule. *Physikalische Zeitschrift* 1909, 10, 560–580.

-
- ⁹⁰ Altenkirch, E. Elektrothermische Kälteerzeugung und reversible elektrische Heizung. *Physikalische Zeitschrift*, 1911.
- ⁹¹ Vedernikov, M. V.; Jordanishvili, E. K. A. F. Ioffe and origin of modern semiconductor thermoelectric energy conversion. 17th Int. Conf. On Thermo. 1998, 1, 37–42. doi:10.1109/ICT.1998.740313.
- ⁹² Goldsmid, H. J.; Douglas, R. W. The use of semiconductors in thermoelectric refrigeration. *British J. Appl. Phys.* 1954, 5, 386. doi:10.1088/0508-3443/5/11/303.
- ⁹³ Rowe, D. M. *Thermoelectrics Handbook: Macro to Nano*. Taylor and Francis, Boca Raton, 2006. ISBN:9780849322648.
- ⁹⁴ Onsager, L. Reciprocal Relations in Irreversible Processes. I. *Phys. Rev.* 1931, 37, 405. doi:10.1103/PhysRev.37.405.
- ⁹⁵ Franz, R.; Wiedemann, G. Ueber die Wärme-Leitungsfähigkeit der Metalle. *Annalen Der Physik Und Chemie* 1853, 165, 497–531. doi:10.1002/andp.18531650802.
- ⁹⁶ Jones, W.; March, N. H. *Theoretical Solid-State Physics*. Dover Publications: New York, 1985.
- ⁹⁷ Nolas, G.; Sharp, J.; Goldsmid, H. *Thermoelectrics: Basic Principles and New Materials Developments*. Germany: Springer, 2001. ISBN:978-3-662-04569-5.
- ⁹⁸ Ceroni, P.; Credi, A.; Venturi, M. Light to investigate (read) and operate (write) molecular devices and machines. *Chem. Soc. Rev.* 2014, 43, 4068. doi:10.1039/C3CS60400D.
- ⁹⁹ Hicks, L. D.; Dresselhaus, M. S. Effect of quantum-well structures on the thermoelectric figure of merit. *Phys. Rev. B* 1993, 47, 12727. doi:10.1103/PhysRevB.47.12727.
- ¹⁰⁰ Hicks L. D.; Dresselhaus M. S. Thermoelectric figure of merit of a one-dimensional conductor. *Phys. Rev. B* 1993, 47, 16631. doi:10.1103/PhysRevB.47.16631.
- ¹⁰¹ Zimbovskaya, N. A. Seebeck effect in molecular junctions. *J. Phys.: Cond. Mat.* 2016, 28, 183002. doi:10.1088/0953-8984/28/18/183002.
- ¹⁰² Giazotto, F.; Heikkil, T. T.; Luukanen, A.; Savin, A. M.; Pekola, J. P. Opportunities for mesoscopics in thermometry and refrigeration: physics and applications. *Rev. Mod. Phys.* 2006, 78, 217. doi:10.1103/RevModPhys.78.217.
- ¹⁰³ Galperin, M.; Ratner, M. A.; Nitzan, A. Inelastic effects in molecular junction transport: scattering and self-consistent calculations for the Seebeck coefficient. *Mol. Phys.* 2008, 106, 397. doi: 10.1080/00268970701837784.
- ¹⁰⁴ Dubi, Y.; Di Ventra, M. Colloquium: Heat flow and thermoelectricity in atomic and molecular junctions *Rev. Mod. Phys.* 2001, 83 131. doi: 10.1103/RevModPhys.83.131.
- ¹⁰⁵ Zimbovskaya, N. A.; Pederson, M. R. Electron transport through molecular junctions. *Phys. Rep.* 2011, 509, 1. doi: 10.1016/j.physrep.2011.08.002.
- ¹⁰⁶ Wang, J.-S.; Agarwalla, B. K.; Li, H.; Thingna, J. Nonequilibrium Green's function method for quantum thermal transport. *Front. Phys.* 2014, 9, 673. doi:10.1007/s11467-013-0340-x.
- ¹⁰⁷ Sanchez, D.; Sothmann, B.; Jordan, A. N. Thermoelectric energy harvesting with quantum dots. *Nanotech.* 2015, 26, 032001. doi:10.1088/0957-4484/26/3/032001.
- ¹⁰⁸ Reddy, P.; Jang, S. Y.; Segalman, R. A.; Majumdar, A. Thermoelectricity in molecular junctions. *Science* 2007, 315, 1568. doi:10.1126/science.1137149.

-
- ¹⁰⁹ Baheti, K.; Malen, J. A.; Doak, P.; Reddy, P.; Jang, S.-Y.; Tilley, T. D.; Majumdar, A.; Segalman, R. A. Probing the chemistry of molecular heterojunctions using thermoelectricity *Nano Lett.* 2008, 8, 715. doi:10.1021/nl072738l.
- ¹¹⁰ Malen, J. A.; Doak, P.; Baheti, K.; Tilley, T. D.; Segalman, R. A.; Majumdar, A. Identifying the length dependence of orbital alignment and contact coupling in molecular heterojunctions *Nano Lett.* 2008, 9, 1164. doi:10.1021/nl803814f.
- ¹¹¹ Malen, J. A.; Yee, S. K.; Majumdar, A.; Segalman, R. A. Fundamentals of energy transport, energy conversion, and thermal properties in organic–inorganic heterojunctions. *Chem. Phys. Lett.* 2010, 491, 109. doi:10.1016/j.cplett.2010.03.028.
- ¹¹² Widawsky, J. R.; Darancet, P.; Neaton, J. B.; Venkataraman, L. Simultaneous determination of conductance and thermopower of single molecule junctions. *Nano Lett.* 2012, 12, 354. doi:10.1021/nl203634m.
- ¹¹³ Maciá, E. Thermoelectric power and electrical conductance of DNA based molecular junctions. *Nanotech.* 2005, 16, 254–260. doi:10.1088/0957-4484/16/5/022.
- ¹¹⁴ Widawsky, J. R.; Chen, W.; Vazquez, H.; Kim, T.; Breslow, R.; Hybertsen, M. S.; Venkataraman, L. Length dependent thermopower of highly conducting Au–C bonded single molecule junctions. *Nano Lett.* 2013, 13, 2889. doi: 10.1021/nl4012276.
- ¹¹⁵ Cui, L.; Miao, R.; Wang, K.; Thompson, D.; Zotti, L. A.; Cuevas, J. C.; Meyhofer, E.; Reddy, P. Peltier cooling in molecular junctions. *Nature Nanotech.* 2017, 13, 122-127. doi:10.1038/s41565-017-0020-z.
- ¹¹⁶ Majumdar, A. Thermoelectricity in semiconductor nanostructures. *Science* 2004, 303, 777. doi: 10.1126/science.1093164.
- ¹¹⁷ Bell, L. E. Cooling, heating, generating power, and recovering waste heat with thermoelectric systems. *Science* 2008, 321, 1457. doi:10.1126/science.1158899.
- ¹¹⁸ Rodgers, P. Nanomaterials: silicon goes thermoelectric. *Nature Nanotech.* 2008, 3, 76. doi:10.1038/nnano.2008.17.
- ¹¹⁹ Kim, K.; Jeong, W.; Lee, W.; Reddy, P. Ultra-high vacuum scanning thermal microscopy for nanometer resolution quantitative thermometry. *ACS Nano* 2012, 6, 4248. doi:10.1021/nn300774n.
- ¹²⁰ Shakouri, A. Nanoscale thermal transport and microrefrigerators on a chip. *Proc. IEEE* 2006, 94, 1613. doi:10.1109/JPROC.2006.879787.
- ¹²¹ Li, B.; Wang, L.; Casati, G. Negative differential thermal resistance and thermal transistor. *Appl. Phys. Lett.* 2006, 88, 143501. doi:10.1063/1.2191730.
- ¹²² Saira, O. P.; Meschke, M.; Giazotto, F.; Savin, A. M.; Mottonen, M.; Pekola, J. P. Heat transistor: demonstration of gate-controlled electronic refrigeration. *Phys. Rev. Lett.* 2007, 99, 027203. doi:10.1103/PhysRevLett.99.027203.
- ¹²³ Segal, D.; Nitzan, A. Spin-boson thermal rectifier. *Phys. Rev. Lett.* 2005, 94, 034301. doi:10.1103/PhysRevLett.94.034301.
- ¹²⁴ Yang, N.; Zhang, G.; Li, B. Thermal rectification in asymmetric graphene ribbons. *Appl. Phys. Lett.* 2009, 95, 033107. doi:10.1063/1.3183587.
- ¹²⁵ Wang, L.; Li, B. Thermal logic gates: computation with phonons. *Phys. Rev. Lett.* 2007, 99, 177208. doi:10.1103/PhysRevLett.99.177208.

-
- ¹²⁶ Wang, L.; Li, B. Thermal memory: a storage of phononic information. *Phys. Rev. Lett.* 2008, 101, 267203. doi:10.1103/PhysRevLett.101.267203.
- ¹²⁷ Paulsson, M.; Datta, S.; Thermoelectric effect in molecular electronics. *Phys. Rev. B* 2003, 67, 241403. doi:10.1103/PhysRevB.67.241403.
- ¹²⁸ Segal, D. Thermoelectric effect in molecular junctions: a tool for revealing transport mechanisms. *Phys. Rev. B* 2005, 72, 165426. doi:10.1103/PhysRevB.72.165426.
- ¹²⁹ Pop, E. Energy dissipation and transport in nanoscale devices. *Nano Res.* 2010, 3, 147. doi: 10.1007/s12274-010-1019-z.
- ¹³⁰ Simine, L.; Chen, W. J.; Segal, D. Can Seebeck coefficient identify quantum interference in molecular conduction? *J. Phys. Chem. C* 2015, 119, 12097. doi:10.1021/jp512648f.
- ¹³¹ Ryōgo, K. Statistical-Mechanical Theory of Irreversible Processes. I. General Theory and Simple Applications to Magnetic and Conduction Problems. *J. Phys. Soc. of Japan* 1957, 12, 570-586. doi:10.1143/JPSJ.12.570.
- ¹³² Mahan, G. D. *Many-Particle Physics, Physics of solids and liquids.* Kluwer Academic/Plenum Publishers: New York, 2000. ISBN:978-1-4757-5714-9.
- ¹³³ Cuevas, J. C.; Scheer, E. *Molecular Electronics: An Introduction to Theory and Experiment; World Scientific series in nanoscience and nanotechnology; World Scientific: Singapore; Hackensack, NJ, 2010. ISBN:978-981-4282-58-1.*
- ¹³⁴ Bürkle, M.; Asai, Y. How To Probe the Limits of the Wiedemann–Franz Law at Nanoscale. *Nano Lett.* 2018, 18, 7358–7361. doi:10.1021/acs.nanolett.8b03651.
- ¹³⁵ Gómez-Silva, G.; Ávalos-Ovando, O.; Ladrón de Guevara, M. L.; Orellana, P. A. Enhancement of Thermoelectric Efficiency and Violation of the Wiedemann-Franz Law Due to Fano Effect. *J. Appl. Phys.* 2012, 111, 053704. doi:10.1063/1.3689817.
- ¹³⁶ Mingo, N. Anharmonic phonon flow through molecular-sized junctions. *Phys. Rev. B* 2006, 74. doi:10.1103/physrevb.74.125402
- ¹³⁷ Nolas, G. S.; Sharp, J.; Goldsmid, J.; *Thermoelectrics: Basic Principles and New Materials Developments.* Springer, New York, 2001.

Chapter II – Analysis of molecular junction characteristics

I – Introduction

From an experimental point of view, the main measurements that are performed for the characterization of the transport properties of a molecular junction are the I-V curve and the conductance. In order to better evaluate and compare molecular systems, parameters are extracted from these data by applying several models and hypotheses. The two main parameters that are usually used to characterize a junction are the interfacial electronic coupling Γ , and the energy position of the first resonant peak ϵ_0 . This first part describes the different models, their approximations and limitations.

II – Methods to extract the key molecular parameters ϵ_0 and Γ

II.1 – Ultraviolet photo-electron spectroscopy

Ultraviolet photo-electron spectroscopy (UPS) consists in measuring the kinetic energy of electrons extracted from a compound upon absorption of UV photons. This is used to define the molecular orbital energies located in the valence region of the electronic structure. According to the photoelectric equation of Einstein, the kinetic energy E_c of the extracted electron is given by:¹

$$E_c = h\nu - E_b \quad \text{Eq. 1}$$

with h the Planck's constant, ν the frequency of the incoming photon, and E_b the binding energy of the electron that represents the level of energy from which it has been extracted. This technique is applied in the molecular junction field to access intrinsic characteristics (Figure 1). In that case, the molecules to be tested are deposited on a substrate (e.g., SAMs on gold) and the energy of the highest occupied molecular level, lying closest to the Fermi level of the metallic substrate can be retrieved by UPS. However, this technique does not allow for a precise estimation of the value of Γ , but it could be theoretically deduced from the broadening of the experimental peak.

This experimental technique has some drawbacks which are:

- the ϵ_0 measured is not the one characteristic of a molecular junction because the molecule is only contacted by one electrode instead of two; the actual energetic position

of ϵ_0 is expected to depend on the number of chemisorbed contacts. Nevertheless, it was theoretically^{2,3} shown that the addition of the second electrode (to create a junction) does not have a large influence on ϵ_0 , so that $\epsilon_{0-sub} \approx \epsilon_{0-junc}$, as evidenced for purely organic systems. This is mainly due to the fact that the dipole bonds are mostly independent (there is no overlap) for a long enough molecule, so that the only difference is coming from an image effect between the molecule and the metallic surface.¹⁸

- it allows to estimate the value of the HOMO of the system but not the LUMO; this implies that if the current is driven by the LUMO, the estimated ϵ_0 does not correspond to the level participating in the transport properties.
- even if we can get the HOMO's energy, there is no warranty that this level is the transporting level; indeed, it is possible that this level would be localized (on one part of the molecule) and therefore would not be a conducting level and that the delocalized levels contributing to the current would be the HOMO-1 or HOMO-2. The resolution of UPS spectra typically prevents estimating accurately the deeper-lying levels.

Inverse photoemission spectroscopy (IPES) should be carried out to estimate the LUMO energy and to be able to conclude if the current is driven or not by this level. The basic principle of IPES is to send a beam of low energy electrons which results in the population the lowest unoccupied molecular orbitals and emission of photons. The energy spectrum of the emitted photons is collected and displayed as a function of the photon counts vs incident electron energy spectrum. This technique is thus fully complementary to UPS.

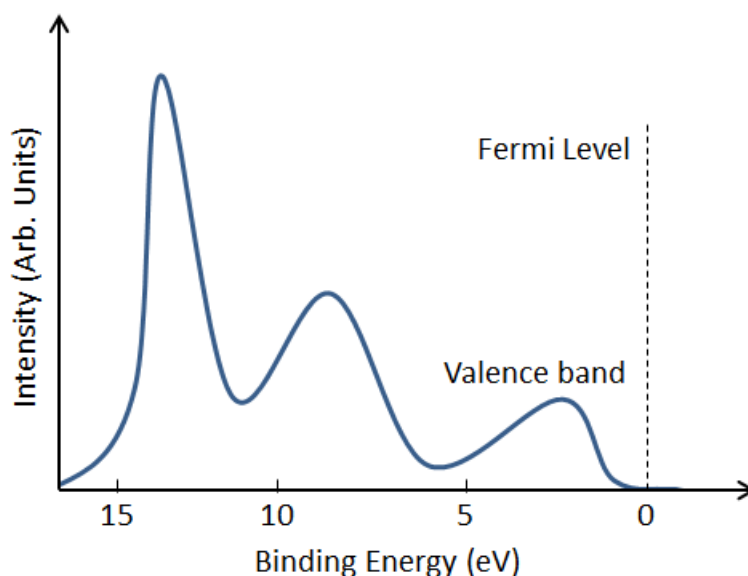


Figure 1 – Schematic representation of an UPS spectrum.

II.2 – Transition Voltage Spectroscopy

The transition voltage spectroscopy (TVS) method relies on the assumption that the offset energy of the HOMO or LUMO, ϵ_0 , can be derived from a current-voltage measurement at low bias when the resonance with the molecular level is not yet reached. To apply the TVS theory, which is based on field emission physics (Figure 2),^{4,5,6} the I-V data are plotted as:

$$\ln\left(\frac{I}{V^2}\right) = \frac{1}{V} \quad \text{Eq. 2}$$

The minimum appearing in this curve is defined as the transition voltage V_t . This method was first based on the tunneling barrier of the Simmons' model when the barrier shape was changed by the applied bias from trapezoidal to triangular.^{7,8}

To be applicable, the transport needs to match two types of regime (Table 1):

- at low voltage, a direct tunneling mechanism, with the current $I \propto V$.
- as the voltage increases, a Fowler-Nordheim (F-N) tunneling-type mechanism, leading to $I \propto V^2$.

Table 1 – Different models of coherent transport mechanisms for a molecular junction. Adapted from reference 9. With J the current density, V the bias voltage, d the barrier length, \hbar the reduced Planck's constant, m the mass of the electron, φ_B the barrier height, and T the temperature.

| Conduction mechanism | Characteristic behavior | Temperature dependence | Voltage dependence |
|---------------------------|--|--|--|
| Direct tunneling | $J \sim V \exp\left(-\frac{2d}{\hbar} \sqrt{2m\varphi_B}\right)$ | None | $I \sim V$ |
| Fowler-Nordheim tunneling | $J \sim V^2 \exp\left(-\frac{4d\sqrt{2m\varphi_B}^{3/2}}{3q\hbar V}\right)$ | None | $\ln\left(\frac{I}{V^2}\right) \sim \frac{1}{V}$ |
| Thermionic emission | $J \sim T^2 \exp\left(-\frac{\varphi_B - q\sqrt{qV/4\pi\epsilon d}}{k_b T}\right)$ | $\ln\left(\frac{I}{T^2}\right) \sim \frac{1}{T}$ | $\ln(I) \sim V^{1/2}$ |
| Hopping conduction | $J \sim V \exp\left(-\frac{\varphi_B}{k_b T}\right)$ | $\ln\left(\frac{I}{V}\right) \sim \frac{1}{T}$ | $I \sim V$ |

Later, the TVS was constructed considering the coherent transport model based on a single level.⁴ According to this model, and considering $\Gamma_L = \Gamma_R$, the relation between the transition voltage V_t and ϵ_0 is determined as:^{2,3,5,6}

$$\epsilon_0 = \frac{\sqrt{3}}{2} V_t \quad \text{Eq. 3}$$

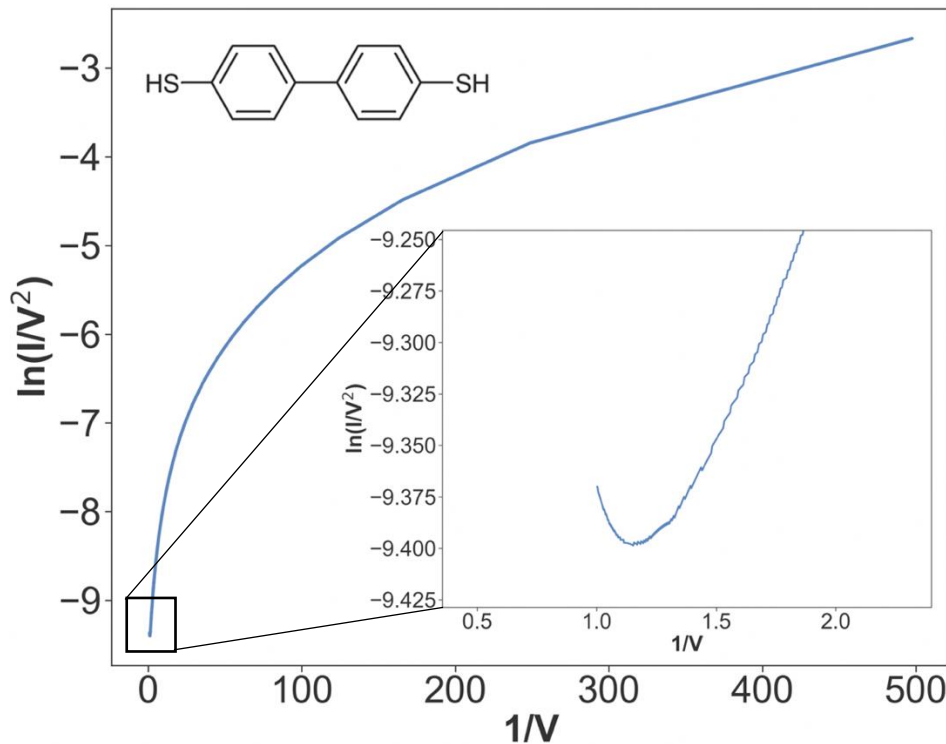


Figure 2 – F-N plot representation (Eq. 2) from the extracted data of an experimental I-V curve of a molecular junction with a biphenyl-dithiol (OPD2) molecule coupled to gold electrodes.² Inset: Zoom on the minimum of the F-N plot. The minimum of this plot is V_t , the transition voltage. Here, $V_t \approx 1.15 \text{ V}^{-1} \approx 0.87 \text{ V}$ which, using Eq. 3, leads to $|\epsilon_0| \approx 0.75 \text{ eV}$.

TVS was also studied to describe asymmetric F-N plots depending on the applied bias polarity. This induces different values for the transition voltages ($V_{t+} \neq V_{t-}$) needed to determine the energy of ϵ_0 and to quantify the asymmetric voltage division γ of the molecular junction.^{6,10}

Nevertheless, this method relies on approximations.¹¹ If the transport properties can be described by a single level model, TVS yields a quite correct estimation of the energy level position ϵ_0 if the parameter does not evolve significantly with the bias voltage. If several levels are involved in promoting the current, the applicability of TVS can be rather restricted.

II.3 – Single level model fitting

The most widely-used model to fit I-V curves is the single level model (SLM). Since the transmission as a function of energy is *a priori* not known, the hypothesis is made is that the level closest to the Fermi level of the electrodes is the only level responsible for the evolution of the current as a function of the applied voltage. In that case, the transmission has a Lorentzian shape (see Part II, Chapter I). Based on this hypothesis, the current is expressed as:

$$I(V) = \frac{2e}{h} \int_{-\infty}^{\infty} \tau(E, V) \left[f_L \left(E - \frac{eV}{2} \right) - f_R \left(E + \frac{eV}{2} \right) \right] dE \quad \text{Eq. 4}$$

with the transmission adopting a Lorentzian shape:

$$\tau(E) = \frac{4\Gamma^2}{(E - \epsilon_0)^2 + 4\Gamma^2} \Big|_{\Gamma_L=\Gamma_R} \quad \text{Eq. 5}$$

Assuming that the voltage drop is symmetrical between the two electrode interfaces of the molecular junction, in the zero-temperature limit, Eq. 4 can be solved analytically leading to:

$$I(V) = 4 \Gamma G_0 \left[\tan^{-1} \left(\frac{eV - 2\epsilon_0}{2\Gamma} \right) + \tan^{-1} \left(\frac{eV + 2\epsilon_0}{2\Gamma} \right) \right] \quad \text{Eq. 6}$$

If a system is measured at low temperature (typically $T < 50$ K), Eq. 6 is precise enough. However, at RT, it is advised to use Eq. 4 as the difference in the estimations of ϵ_0 and Γ can be in the order of 0.1 eV and few meVs respectively.

Importantly, if the transmission is not Lorentzian or if the transport peak is voltage dependent, the fit can be altered or voltage dependency has to be considered (Figure 3). When considering experimental or theoretical I-V curves with transmission shape more complex than the single level model, the applied voltage range used in the fitting is definitively a critical parameter. This is illustrated in Figure 3 by fitting an OPD2 experimental I-V curve (Au-OPD2-Au) as in the F-N plot (Figure 2), considering different voltage ranges. Both parameters evolve as a function of the selected voltage range ΔV , which represents a maximum modification of 35 % for ϵ_0 and 19 % for Γ .

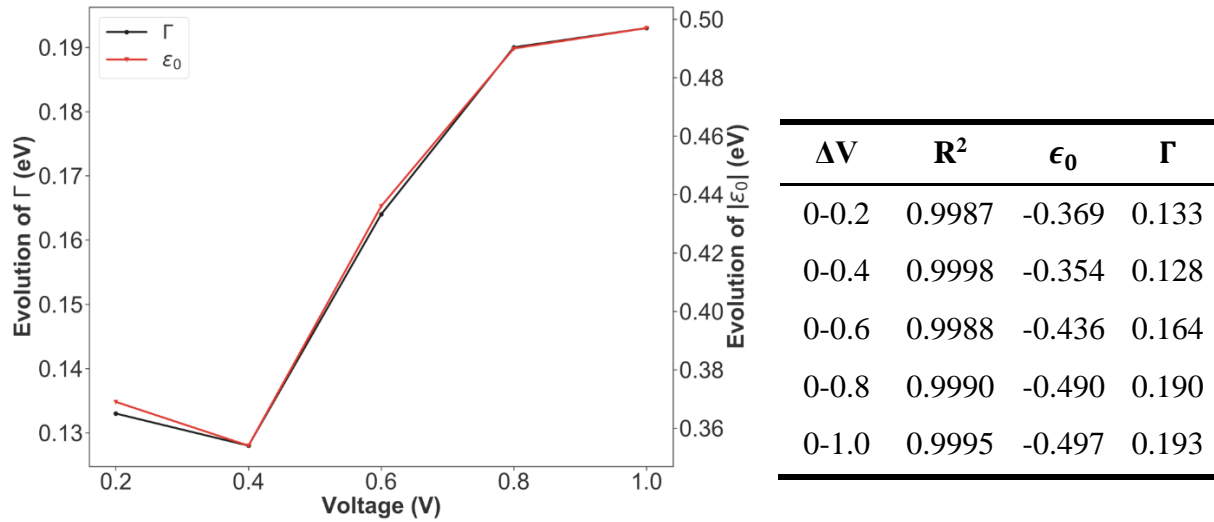


Figure 3 – Left: evolution of the absolute value of ϵ_0 and Γ in eV as a function of the integrated voltage range ΔV in volt used to fit the experimental I-V curve of the Au–OPD2–Au molecular junction.² Right: associated table that provides the R^2 (coefficient of determination) of the I-V fit (Eq. 6) and the parameters (ϵ_0 , Γ) values for each bias voltage range.

It should also be noted that by comparing the SLM and the TVS, a discrepancy arises between the two methods with the TVS yielding $|\epsilon_0| \approx 0.75 \text{ eV}$ and the SLM $|\epsilon_0(\Delta V = 1V)| \approx 0.50 \text{ eV}$.

II.4 – Modified single level model $\epsilon_0(V)$

The single level model with ϵ_0 depending on the bias voltage accounts for a Stark effect linked to the polarizability of the system. It can be described by a single level model:

$$\tau(E) = \frac{4\Gamma^2}{(E - \epsilon_0(V))^2 + 4\Gamma^2} \quad \text{Eq. 7}$$

In Eq. 7, the ϵ_0 is voltage dependent: $\epsilon_0(V) = aV^2 + bV + \epsilon_{0-init}$. $\epsilon_0(V)$ shifts as the bias voltage increases. ϵ_{0-init} corresponds to the maximum of transmission at zero bias. It can be estimated by UPS (if the conducting level is below the Fermi energy) or it can be calculated by quantum chemical calculations.

Nevertheless, if the transmission is noticeably voltage-dependent, the use of the single level model considering that $\tau(E, V = 0 \text{ V}) \approx \tau(E, V > 0.1 \text{ V})$ is not applicable as detailed in the

next section using a calculated I-V curve of Au-[Ru(TMA)(C≡C-Ph)₂S₂]-Au junction as study case.¹²

II.5 – The G+S method

In this section, we propose another method which consists in adding in the fitting procedure to estimate the energy level alignment or interfacial electronic coupling (parameters ϵ_0 and Γ , respectively), the use of the linear conductance and the Seebeck coefficient.¹²

The field of molecular electronics aims at developing functional nano-electronic devices by inserting molecules between two metallic electrodes. The I-V curves of such devices can be measured by several techniques such as CP-AFM for SAMs or MCBJ for single molecules.^{13,14,15,16} Fitting the I-V curves of molecular junctions by simple analytical models is often done to extract relevant molecular parameters, i. e. ϵ_0 and Γ , to build up useful property-relationships. However, such models can suffer from severe limitations in some cases and hence provide unreliable molecular parameters. This is illustrated here by extracting key molecular parameters by fitting computed voltage-dependent transmission spectra and by comparing them to the values obtained by fitting the calculated I-V curves with a typical Lorentzian model used in the literature. Doing so, we observe a large discrepancy between the two sets of values which warns us about the risks of using simple fitting expressions. Interestingly, we demonstrate that the quality of the fit can be improved by imposing the low bias conductance and Seebeck coefficient of the junction to be recovered in the fitting procedure.

Although UPS is typically used to infer the position of the HOMO electronic level with respect to the Fermi level of a substrate in a SAM configuration, the relative position of the electronic levels is expected to be different in a molecular junction configuration (due to additional interfacial electronic coupling, built-in fields¹⁷ and image charge effects when a second electrode is introduced).¹⁸

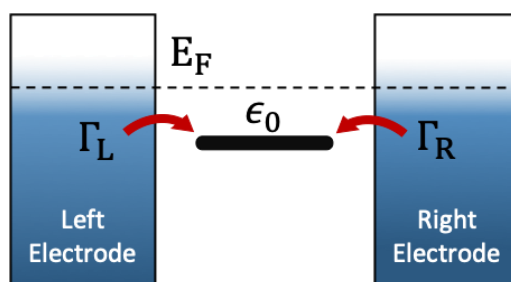


Figure 4 – Simplified scheme featuring a single transporting molecular level of energy ϵ_0 (here the HOMO) coupled by a coupling strength Γ_R to the right electrode and Γ_L with the left electrode. The Fermi energy (E_F) is represented by the dashed line.

At the present stage, ϵ_0 and Γ parameters are mostly deduced by fitting experimental I-V curves, considering that the electronic transmission at the origin of the current is of Breit–Wigner resonance type (Lorentzian-type shape); this model considers a single molecular level (generally the HOMO or LUMO of the molecule) at the energy ϵ_0 coupled to the electronic states of the electrodes (Figure 4).¹⁹ The full width at half maximum of this Lorentzian reflects the amplitude of the electronic coupling Γ . The Lorentzian-type expression of the electronic transmission $\tau(E)$ at a given energy E is expressed as:

$$\tau(E) = \frac{4\Gamma_L\Gamma_R}{(E - \epsilon_0)^2 + (\Gamma_L + \Gamma_R)^2} \quad \text{Eq. 8}$$

In the case of symmetric contacts between the molecule and the two electrodes, Γ_L and Γ_R are equal ($\Gamma_L = \Gamma_R = \Gamma$) leading to the simplified expression:

$$\tau(E) = \frac{4\Gamma^2}{(E - \epsilon_0)^2 + 4\Gamma^2} \quad \text{Eq. 9}$$

It is important to stress that this model suffers from severe limitations in considering that only one molecular transporting level is present close to the Fermi level, as evidenced theoretically by Neaton and co-workers.²⁰ Using the DFT + Σ (i.e., static self-energy correction) formalism, some junctions show electronic transmissions which deviate importantly from a Lorentzian-shape curve. The single-level model is indeed expected to break down for molecules displaying several close-lying energy levels in the transmission window. A second important hypothesis of this fitting model is to consider that the molecular parameters Γ and ϵ_0 are bias voltage independent. In reality, and depending on how the applied voltage drops across the molecule, the level^{19-g)} energy may be bias-dependent. Recent calculations clearly demonstrated that Γ is a bias dependent parameter.²¹ Moreover, this model does not account for the typical decrease in the intensity of the transmission peak with increasing bias. Finally, if there are several molecules in the junctions, the total transmission is not simply the sum of the transmission spectrum of the individual molecules so that a prefactor accounting for cooperative effects should be introduced. Accordingly, we will only focus on single-molecule junctions in the following. Despite its significant restrictions, this model has been widely exploited by

experimentalists to shed light on the electronic structure of molecular junctions and to establish relationships between the I-V characteristics and the electronic structure of the molecular junction. In this context, we aim at addressing the reliability of this analytical procedure using quantum chemistry (QC) as a tool able to provide in parallel I-V curves that can be fitted using the same models as previously described in literature and the actual calculated electronic parameters of a single molecule junction based on calculated transmission functions. This allows us to evaluate the accuracy of the fitting models in recovering a correct amplitude for the two parameters using I-V curves in comparison to the values calculated independently. It is important to emphasize at this stage that the scientific evidences given below are not dependent on the level of theory used. The present work highlights that much care has to be taken while using the single-level fitting procedure to extract the physical characteristics of a molecular junction.

In order to exemplify the problems that can arise from I-V curve fittings using this single-level model, we choose to evaluate the transmission properties of the trans-Ru(TMA)(C≡C-C₆H₄-SH)₂ molecule (TMA = 1,5,9,13-tetramethyl-1,5,9,13-tetraaza-cyclo-hexadecane) grafted to gold electrodes. This system has been chosen as study case for several reasons. First, it is a symmetric molecular junction in which the metallic center Ru(II) is coordinated in a trans arrangement to conjugated (thiol)aryl-acetylide organic linkers. The rest of the central metal coordination sphere is completed by a tetra-chelating ligand via nitrogen atoms (Figure 5).

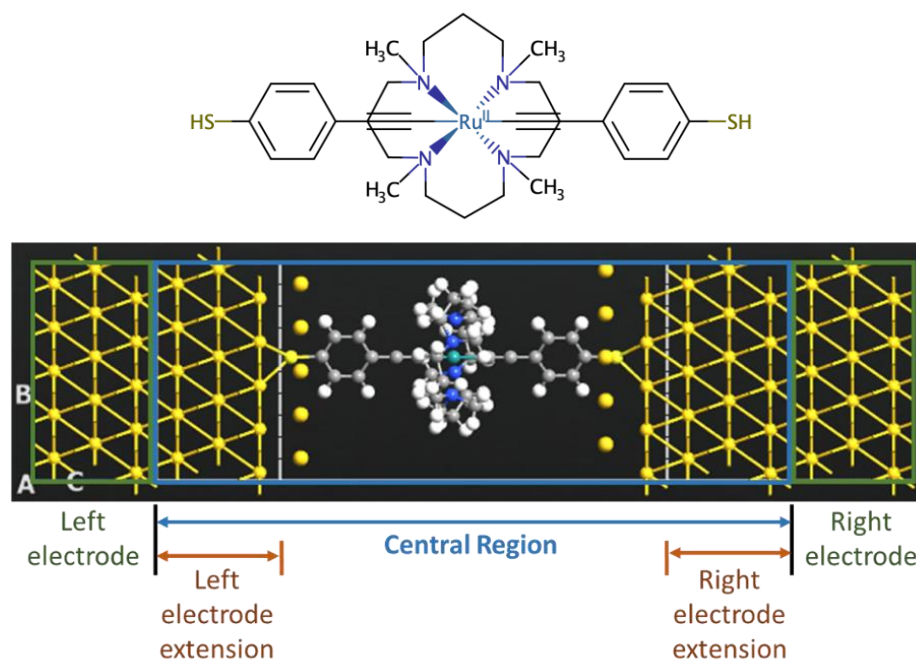


Figure 5 – Top: chemical structure of $\text{trans-Ru(TMA)(C}\equiv\text{C-C}_6\text{H}_4\text{-SH)}_2$ (TMA = 1,5,9,13-tetramethyl-1,5,9,13-tetraazacyclohexadecane). Bottom: Representation of the junction (electrode–molecule–electrode) built with QuantumATK.²⁶ The sulfur atoms are anchored in the hollow position on the (111) surface of gold. We use ghost atoms on top of the gold surface (represented by the yellow spheres) to obtain a better electronic description of the surface.²²

This pseudo-octahedral environment stabilizes the metal center to fulfill the 18-electron rule conferring a high thermodynamic stability to the system. As lots of organometallic complexes, it displays a weak oxidation potential in comparison to most organic conjugated molecules,²³ a feature which promotes molecular levels close to the Fermi energy of the electrodes. Since this system is known in its molecular form²⁴ and closely-related molecular junctions have been successfully investigated experimentally by us and others²⁵, it is highly suitable to experimental investigations. It has been chosen as case study among a large series of candidates that we have been screening since its calculated transmission properties show a high transmission peak close to the Fermi level with a quasi-Lorentzian shape, as required for this study.

The molecular junction is built by grafting the molecule to two gold electrodes via sulfur–gold bonds on the hollow site of the gold (111) surface (Figure 5). The transmission spectra and I-V curves have been simulated in the coherent regime at the DFT/NEGF level using the ATK package software from Synopsys.²⁶ The calculated transmission spectrum given in Figure 7 (right) at zero bias ($\Delta V = 0.0$ V) displays a Lorentzian peak centered at $\epsilon_0 = -0.21$ eV below the Fermi level. A very narrow peak (hence not contributing to the current) is also found at ϵ_1

= -0.40 eV and is associated to other states involving the molecular backbone (Figure 6).²⁷ Nonetheless, the main transmission peak can be accurately fitted by a single level as shown below.

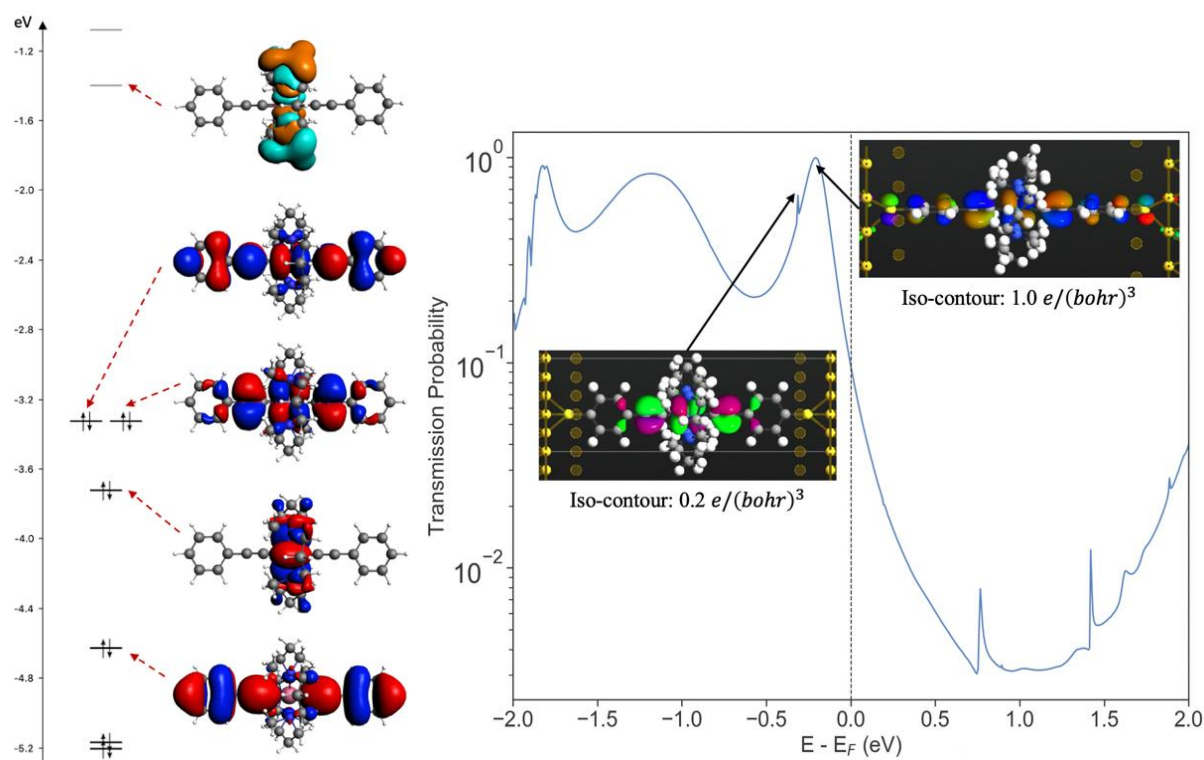


Figure 6 – Left: Molecular orbital diagram of the isolated molecule $\text{trans-Ru(TMA)(C}\equiv\text{C-C}_6\text{H}_5)_2$; Iso-contour plots of the highest occupied molecular orbitals (MO).^{28,29} Calculations and MO plots were obtained using ADF 2019; Slater basis set: TZ2P, small frozen core; Functional revPBE; Iso-contours: $\pm 0.01 \text{ (e/bohr}^3)^{-1/2}$ Right: Transmission spectrum of the molecular junction at 0.0 V; representation of two transmission eigenstates.

The Landauer formula used to estimate the current is given in Eq. 10, where $\mu_{L,R}$ is the chemical potential of the left (L) and right (R) electrode, T the temperature, k_B the Boltzmann constant, and $f_{L,R}$ is the Fermi–Dirac function:

$$I(V) = \tau(E, V) [f_L(E, \mu_L) - f_R(E, \mu_R)] dE;$$

$$f_{L,R} = \frac{1}{\frac{\exp(E - \mu_{L,R})}{k_B T} + 1} \quad \text{Eq. 10}$$

In the following, we will also refer to the Seebeck coefficient S and the conductance G . S corresponds to the bias that can be generated by a difference of temperature between the two

electrodes ($S = -\Delta V/\Delta T$)^{19a),30,31,32,33} S has been measured for many molecular junctions.^{34,35} This parameter can be calculated using the transmission spectrum at zero bias (in the linear regime approximation) and is formally defined at zero current I . A simplification of the current equation (Eq. 10) can thus be done leading to Eq. 11 (see Part II, Chapter I, section 2). In this expression, the L_n terms are incorporating integrals of the Fermi–Dirac function at equilibrium (f_{eq}) (Eq. 12 and Eq. 13) which describes the distribution of electrons/holes over energy states in the electrodes.^{30,31,32,33}

$$S = -\frac{1}{T} \frac{L_1}{L_0} \quad \text{Eq. 11}$$

$$L_n = -\frac{2e}{h} \int \tau(E, V) (E - \mu_{eq})^n \frac{\partial f_{eq}}{\partial E} dE \quad \text{Eq. 12}$$

$$f_{eq} = \frac{1}{\frac{\exp(E - \mu_{eq})}{k_B T} + 1} \quad \text{Eq. 13}$$

The conductance G is calculated within the linear regime approximation as:

$$G = L_0 G_0 \quad \text{Eq. 14}$$

with G_0 the quantum of conductance (77.48 mS). The coupling (Γ) and the energy (ϵ_0) can be deduced in the single-level approximation directly from each calculated transmission spectrum by fitting the peak closest to the Fermi level by a Breit-Wigner function. The obtained values can be considered as benchmark reference values for this study since they are directly issued from the DFT/NEGF transmission calculations (labelled later as Γ_t and ϵ_{0-t}). One couple of values Γ_t and ϵ_{0-t} is thus obtained at each voltage (Table 2).

Table 2 – Γ_τ (eV), $\epsilon_{0-\tau}$ (eV), S ($\mu\text{V}/\text{K}$) and G (G/G_0) obtained by application of the single-level method to fit $\tau(E)$ at each applied voltage (V). The average values of the different parameters in the bias interval between 0.0 and 0.2 eV and between 0.0 and 1.0 V are the values reported in Table 3.

| V | Γ_τ | $\epsilon_{0-\tau}$ | S_τ | G_τ/G_0 |
|-----|---------------|---------------------|----------|--------------|
| 0.0 | 0.034 | -0.214 | 88 | 0.114 |
| 0.1 | 0.034 | -0.221 | 87 | 0.114 |
| 0.2 | 0.034 | -0.234 | 83 | 0.116 |
| 0.3 | 0.035 | -0.259 | 78 | 0.120 |
| 0.4 | 0.035 | -0.281 | 72 | 0.127 |

| | | | | |
|---------------|-------|--------|----|-------|
| 0.5 | 0.036 | -0.310 | 66 | 0.135 |
| 0.6 | 0.037 | -0.337 | 60 | 0.143 |
| 0.7 | 0.039 | -0.358 | 56 | 0.151 |
| 0.8 | 0.040 | -0.381 | 52 | 0.156 |
| 0.9 | 0.043 | -0.402 | 50 | 0.159 |
| 1.0 | 0.046 | -0.429 | 49 | 0.159 |
| [0 - 0.2] av. | 0.034 | -0.223 | 86 | 0.115 |
| [0 - 1.0] av. | 0.038 | -0.311 | 67 | 0.136 |

The Γ_t and ϵ_{0-t} values given in Table 3 for several ranges of bias are the averaged values over the considered voltage range. The calculated I/V curve of the Au-[Ru(TMA)(C≡C-C₆H₄-S)₂]-Au junction has been generated from calculated transmission spectra from 0.0 to 1.0 V by voltage steps of 0.1 V. It is represented in Figure 7a. The physical characteristics of the molecular junction can be now deduced by a fitting procedure of the I-V curve, using the single-level model to obtain Γ_{I-V} and ϵ_{0-I-V} (Eq. 9).

Table 3 – Γ (eV), ϵ_0 (eV), S (μ V/K) and G (G/G_0) obtained by: a) application of the single-level method to fit $\tau(E)$ at each applied voltage (see Table 2); we report here the values averaged over the voltage range; b) fitting of the I/V curve, c) by adding G and S to the fitting procedure. The percentage errors are given in Table S2.

| Bias voltage range (V) | | 0.0 – 0.1 | 0.0 – 0.2 | 0.0 – 1.0 |
|----------------------------------|-----------------------|-----------|-----------|-----------|
| a) Fit of $\tau(E)$ | Γ_τ | 0.034 | 0.034 | 0.038 |
| | $\epsilon_{0-\tau}$ | -0.214 | -0.223 | -0.311 |
| | G_τ/G_0 | 0.114 | 0.115 | 0.136 |
| | S_τ | 88 | 86 | 67 |
| b) Fit of I/V curve (Eq. 3) | $\Gamma_{I/V}$ | 0.169 | 0.105 | 0.165 |
| | $\epsilon_{0-I/V}$ | -0.947 | -0.590 | -0.863 |
| | $G_{I/V}/G_0$ | 0.114 | 0.114 | 0.129 |
| | $S_{I/V}$ | 14 | 23 | 15 |
| c) Fit using the "G+S" procedure | Γ^{G+S} | 0.031 | - | - |
| | ϵ_{0-}^{G+S} | -0.189 | - | - |
| | G^{G+S}/G_0 | 0.113 | - | - |
| | S^{G+S} | 88 | - | - |

This was done using several voltage ranges in the I-V curve: (i) from 0 to 100 meV, a range of bias in which the current is proportional to the bias (linear regime); the transmission properties are slightly changed within this small potential window (no noticeable energy shift of ϵ_0 or Γ);

(ii) in a larger voltage window ranging from 0 to 200 meV; (iii) for the total calculated I-V curve (from 0 to 1 V). The results of these fits are given in Table 3 together with the reference values Γ_t and ϵ_{0-t} previously obtained. Although the three I-V curves fits are of very good accuracy ($R^2 \approx 1$), the associated values $\epsilon_{0_{I-V}}$ strongly deviate from ϵ_{0-t} , whatever the bias range considered.

Table 4 – Percentage error of Γ (eV), ϵ_0 (eV), S ($\mu\text{V}/\text{K}$) and G/G_0 obtained by a) the fitting of the I/V curve (I/V) and b) by adding G and S to the fitting procedure (“G+S”) (see Table 3) with respect to the reference values Γ_τ , $\epsilon_{0-\tau}$, S_τ , G_τ/G_0 respectively.

a)

| ΔV | R^2 | $\Gamma_{I/V}$ % error | $\epsilon_{0-I/V}$ % error | $S_{I/V}$ % error | $G_{I/V}/G_0$ % error |
|------------|-------|---------------------------|-------------------------------|----------------------|--------------------------|
| 0-1.0 | 0.997 | 340.0 | 177.1 | 77.8 | 5.1 |
| 0-0.2 | 1.000 | 208.4 | 164.4 | 73.7 | 0.9 |
| 0-0.1 | 1.000 | 398.6 | 335.6 | 84.2 | 0.0 |

b)

| $\Gamma^{\text{“G+S”}}$ % error | $\epsilon_{0-\text{“G+S”}}$ % error | $S^{\text{“G+S”}}$ % error | $G^{\text{“G+S”}}/G_0$ % error |
|------------------------------------|--|-------------------------------|-----------------------------------|
| 8.6 | 13.2 | 0.9 | 0.9 |

The Γ_{I-V} values are at least doubled compared to Γ_t . As expected, the conductance Γ_{I-V} is close to the reference value since it is the fitted quantity. Interestingly, there is an order of magnitude difference between the Seebeck coefficient estimated from the different fitting ranges (S_{I-V}) and the reference one (S_t) (Table 3). The high quality of the I-V curve fits highly contrasts with the poor description of some of the molecular junction properties (ϵ_0 , Γ and S). In the framework of the transition voltage spectroscopy, ϵ_0 can also be estimated in principle as the minimum value in an I/V versus $\ln(I/V^2)$ plot.^{5,6} This approach is not expected to provide reliable trends when the transmission peak is noticeably shifted with the bias voltage (Figure 8). However, in the case of weakly polarizable organic systems, such as oligophenylene derivatives (Figure 9), the procedure based on the I/V versus $\ln(I/V^2)$ plot to evaluate ϵ_0 is applicable.^{2,3}

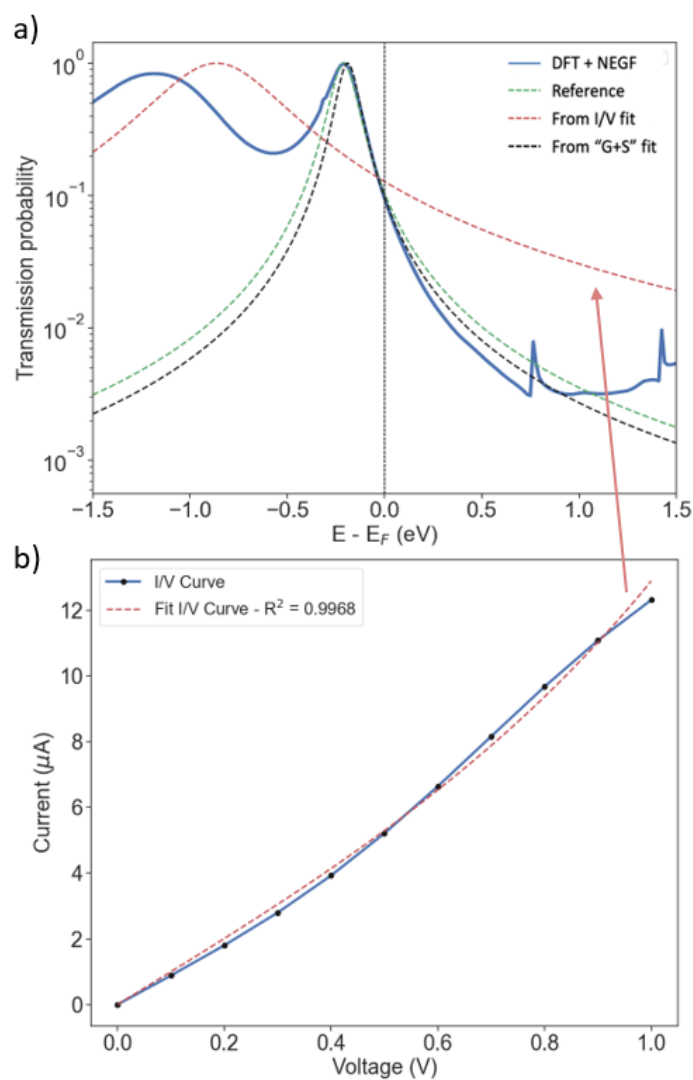


Figure 7 – a) Calculated transmission spectrum at zero bias; Lorentzian curves generated from the transmission curve, the I-V and the “G+S” fits are given in dotted green, red and black lines respectively; see Figure 8 with bias voltages up to 1.0 V. b) I-V curve obtained from transmission calculations (steps of 0.1 V) and fit of the I-V curve.

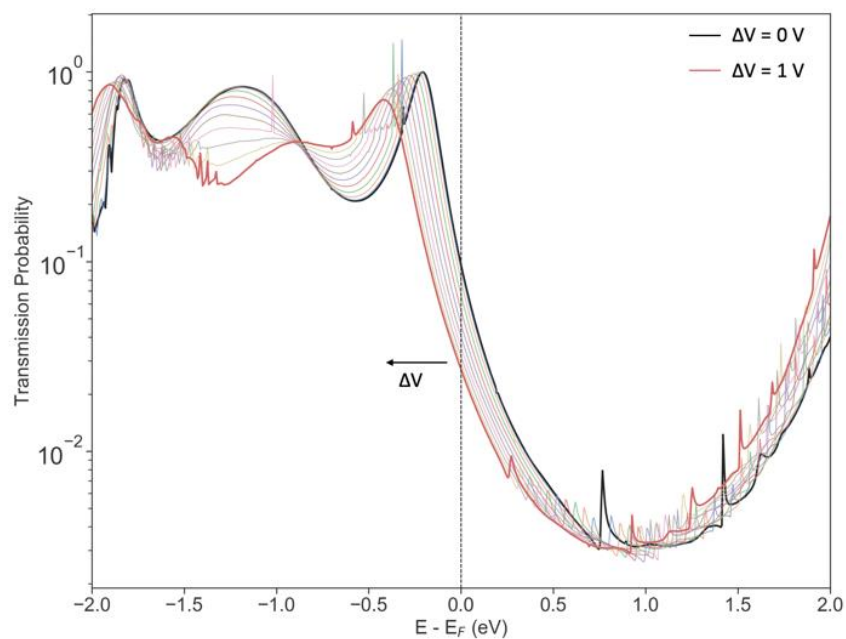


Figure 8 – Calculated transmission spectra of the Au-*trans*-Ru(TMA)(C≡C-C₆H₄S)₂-Au junction at biases ranging from 0.0 to 1.0 V by steps of 0.1 V.

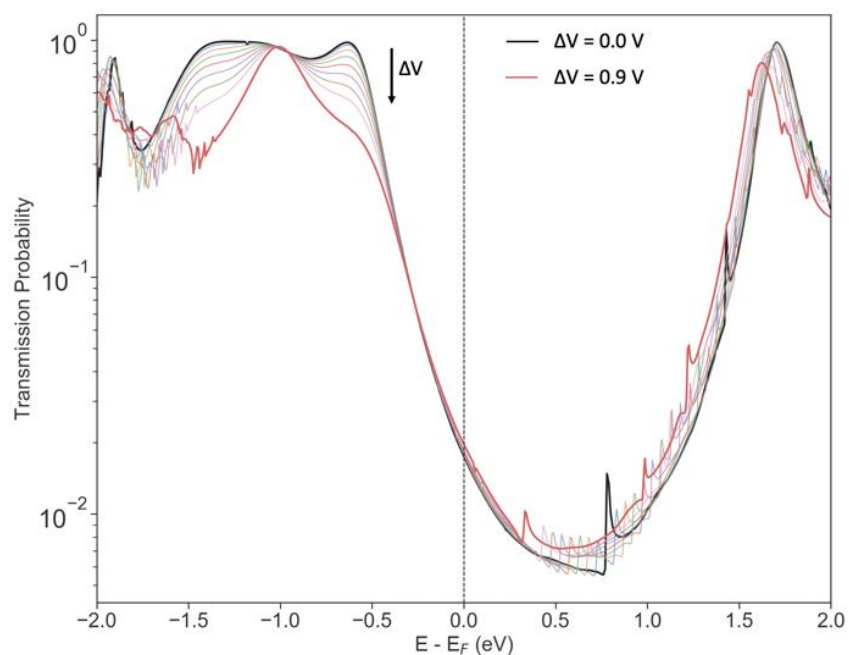


Figure 9 – Calculated transmission spectra of an Au-oligo(phenylene-ethynylene)-Au junction at biases ranging from 0 to 0.9 V by steps of 0.1 V, as obtained using the same computational approach.

Deviations are expected for a large integration voltage window due to the fact that ϵ_0 and Γ are bias dependent properties (Figure 8).

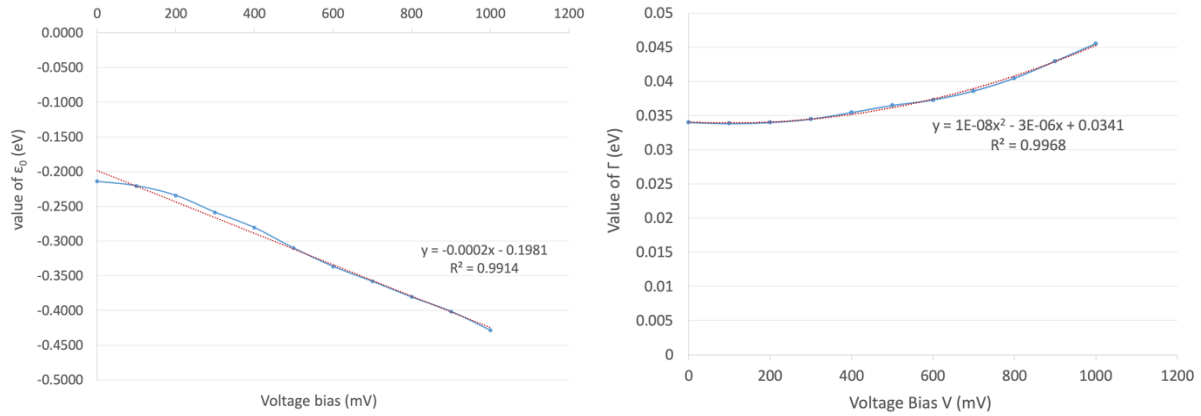


Figure 10 – Evolution of $\epsilon_{0-\tau}$, and Γ_τ (in eV) as a function of the applied bias V (in mV) based on the fitting of the transmission peak. Left: $\epsilon_{0-\tau}$ vs voltage. Right: Γ_τ vs voltage.

The calculated $\epsilon_{0-\tau}$ varies indeed linearly with the bias ($\epsilon_{0-\tau}$ (V) = $-2.0 \cdot 10^{-4} - 0.198$ V) with $R^2 = 0.9914$), and Γ_τ follows a second order polynomial progression with the voltage change (Γ_τ (V) = $1.4 \cdot 10^{-8} V^2 - 2.9 \cdot 10^{-6} V + 3.4 \cdot 10^{-2}$ with $R^2 = 0.9968$). Such evolutions revealed in this example are totally omitted in the single-model treatment. It surely induces a failure in obtaining the correct physical properties of a system when using a too large bias voltage window. On the other hand, if the fitting range is too small ($|eV| < \epsilon_{0-\tau}$), the I-V curves are mainly linear and no meaningful values of the two parameters can be inferred.

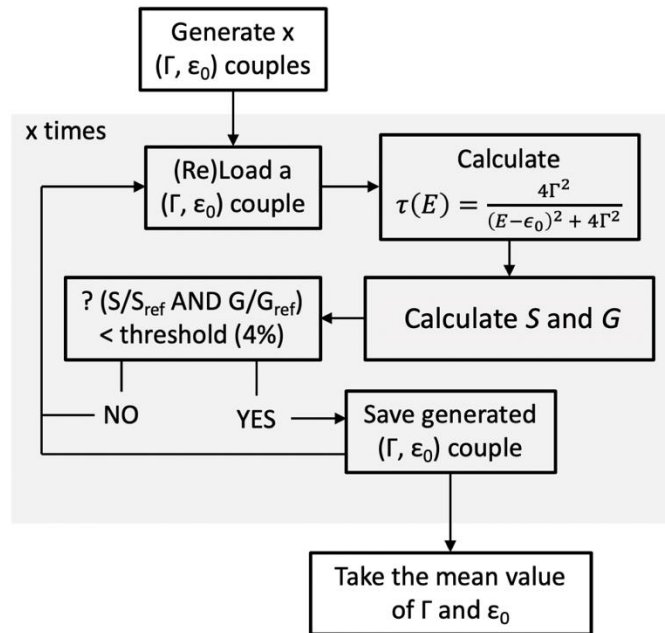


Figure 11 – Workflow for the calculation of G_τ/G_0 and S_τ which yields the (Γ, ϵ_0) couple within the “G+S” method. Γ ranges from 0.01 to 0.1 eV and ϵ_0 range from -2 to 0 eV.

A major improvement can be obtained by imposing both the low bias conductance and the Seebeck coefficient of the junction to be recovered with a chosen accuracy (here above 95 %). The procedure adopted is explained in Figure 11. This procedure is referred as the “G+S” method in Table 3. Doing so, the differences against the reference values of ϵ_0 and Γ are strongly reduced, with the right order of magnitude recovered at low bias (Table 3 and Figure 7a). This improvement can be rationalized by highlighting that in the I-V fit procedure, a perfect Lorentzian-type shape of the transmission is assumed. Thus, the more the system deviates from it, the more ϵ_0 and Γ have probabilities to be erroneous even though $R^2 \approx 1$. Imposing the constraint of also recovering S introduces a tolerance to the deviation from a perfect Lorentzian-shape that significantly improves the extracted parameters. Importantly, although the physical meaning of the parameters is improved, the corresponding I-V curve is apparently less satisfactory, with an R^2 that significantly deviates from 1. This relates to the fact that deviations are appearing when the linear regime approximation becomes irrelevant, i.e. at higher bias (Figure 12). The “G+S” procedure can be applied to experimental I-V curves (see Table 5 for applications to data reported in reference 36).

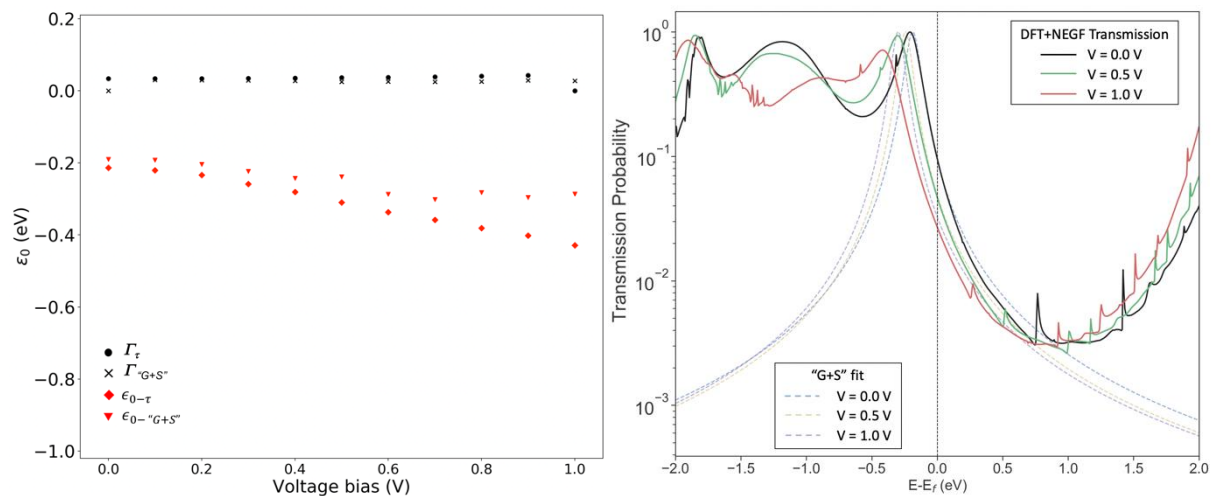


Figure 12 – Left: plot of $\Gamma_{\text{G+S}}$ and $\epsilon_{0-\text{G+S}}$ values calculated when including in the fit the conductance G from the relation $G = I/V$ and the Seebeck S at each voltage. Right: representation of the Lorentzian curves constructed using the previous results for three voltage ranges. The DFT/NEGF calculated transmissions at comparable voltages are shown in solid lines for comparison.

Table 5 – The experimental G and S values, G_{exp}/G_0 and S_{exp} , are extracted from reference 36 for three different Au–molecule–Au junctions: bi-phenyl and tri-phenyl (with thiol anchoring) and bipyridine (N-gold coordination). The value of $\epsilon_{0\text{-theo}}$ is taken from the same article and corresponds to calculations performed at the DFT+ Σ level. The values "I/V" and "G+S" are obtained by applying the procedures described in the main text to the experimental data (I/V curves, G_{exp}/G_0 and S_{exp}). Interestingly, the "G+S" method in green gives results closer to the experimental data (in blue) and closer to $\epsilon_{0\text{-theo}}$ for the tri-phenyl and bi-pyridine systems. For the bi-phenyl case, the system can be well described with the fitting of the I/V curve only, and give similar results as the "G+S" method, pointing to a quasi-lorentzian shape of the transmission, in agreement with computational studies published in the same article.

| Junction | S_{exp} | G_{exp}/G_0 | $\epsilon_{0\text{-theo}}$ | $S_{I/V}$ | $G_{I/V}/G_0$ | $\epsilon_{0\text{-I/V}}$ | $\Gamma_{I/V}$ | S_{G+S} | G_{G+S}/G_0 | $\epsilon_{0\text{-G+S}}$ | Γ_{G+S} |
|-------------|------------------|----------------------|----------------------------|-----------|---------------|---------------------------|----------------|-----------|---------------|---------------------------|----------------|
| bi-phenyl | 13 | 4.90E-3 | -1.5 | 13 | 5.10E-3 | -1.18 | 0.042 | 13 | 5.20E-3 | -1.1 | 0.039 |
| tri-phenyl | 16 | 1.65E-4 | -1.2 | 27 | 1.69E-4 | -0.57 | 0.003 | 16 | 1.68E-4 | -0.9 | 0.006 |
| bi-pyridine | -7 | 1.10E-3 | 2.0 | -22 | 1.20E-4 | 0.67 | 0.011 | -7 | 1.10E-3 | 2.1 | 0.035 |

Restricting the fitting to small voltage segments of the I-V curve could be seen as an alternative since the ϵ_0 and Γ are not supposed to significantly change in each bias window. As shown in Figure 13, this procedure fails in reproducing the right bias dependence of the transmission spectra.

In conclusion, we have demonstrated that using a Breit–Wigner resonance type model to fit experimental or calculated I-V curves to get an insight into the electronic and transmission properties of molecular junctions can lead to significant errors in the evaluation of the molecular parameters ϵ_0 and Γ . We have shown that the correct position and width of the Lorentzian resonance cannot be reconstructed from the fitted values, even for a case study which presents a quasi-ideal transmission peak shape. The level of accuracy of the fitting procedure in the description of the physics has been strongly improved when considering simultaneously the conductance and the Seebeck coefficient of the junction that are both accessible experimental parameters.³⁴

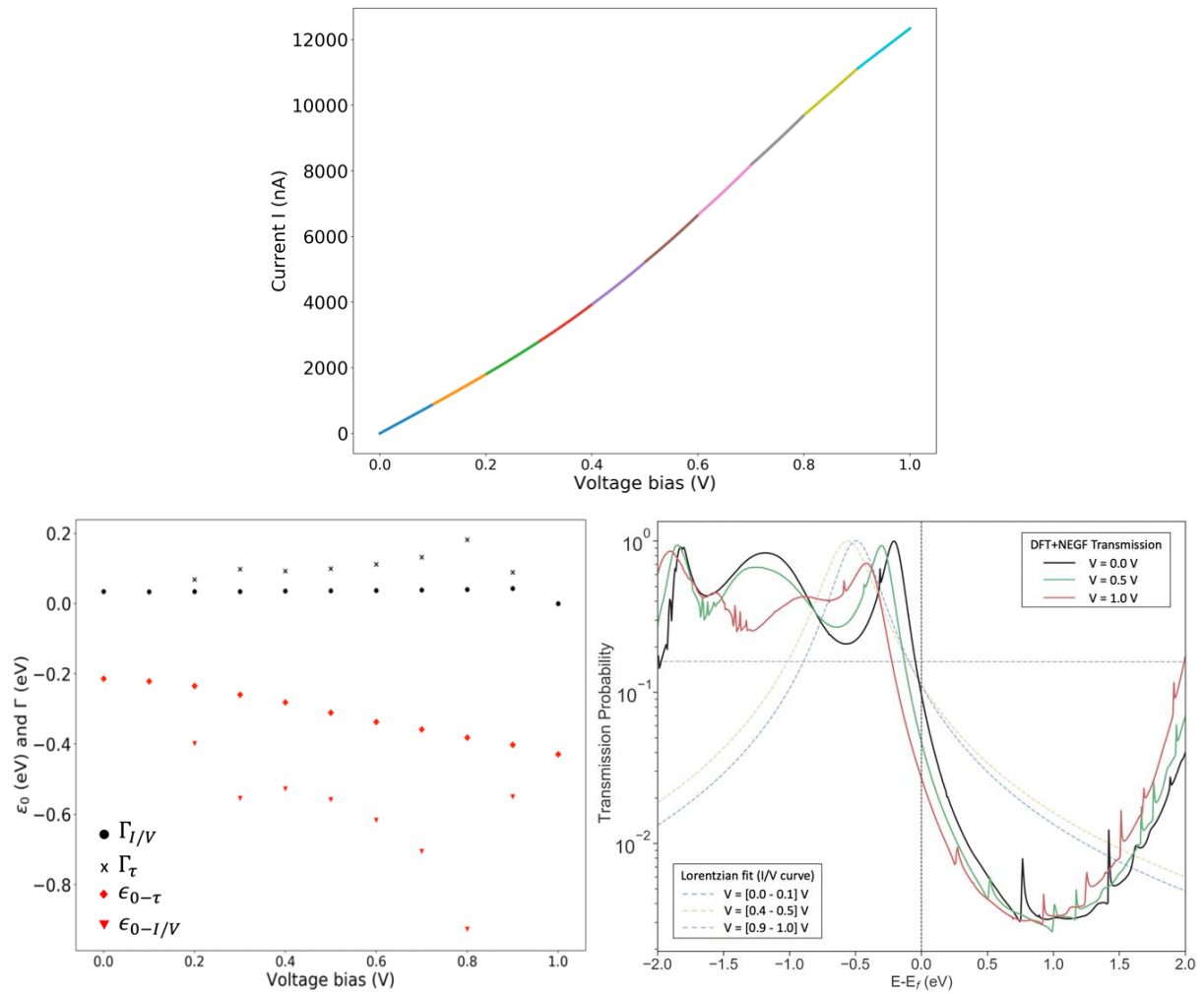


Figure 13 – Top: visualization by color segment of the 100 mV parts of the I/V curve used for the integration to extract $\Gamma_{I/V}$ and $\epsilon_{0-I/V}$. Bottom left: plot of the resulting $\Gamma_{I/V}$, $\epsilon_{0-I/V}$ values as a function of the lower value of the bias voltage range. Bottom right: representation of the Lorentzian curves constructed using the previous results for three voltage ranges (the fit did not converge in the range $V = [0.9 - 1.0]$ V). DFT/NEGF calculated transmissions at comparable voltages are depicted as solid lines for comparison.

The “G+S” method allows to determine the ϵ_{0-init} with quite good precision compared to the single level model for fits done at low voltage. Applying this modified single level model, we can retrieve the displacement of $\epsilon_0(V)$. The reliability of the traditionally done Lorentzian fitting procedures can be improved by measuring the Seebeck coefficient in combination with the conductance.

III – Transmission and thermoelectric junctions

One of the main questions to be addressed in this thesis is to determine the type of transmission desirable to get better thermoelectric properties. To do so, we have tested different types of theoretical transmission that could be accessible with molecular junctions and evaluate the corresponding thermoelectric properties.

III.1 – Phononic thermal conductance κ_{ph}

The phononic thermal conductance κ_{ph} has been both experimentally and theoretically obtained^{36,37,38,39,40,41,42,43} for different types of molecular junctions. Different ranges of values that have been published in the literature for κ_{ph} are summarized in Table 6.

Table 6 – Typical range of phononic thermal conductance κ_{ph} in pW/K issued from different references, both theoretically and experimentally.

| Ref | Type | Molecules | Coordination | Electrode | κ_{ph} |
|-----|------------|---------------------------------|--------------|-----------|---------------|
| 36 | Experiment | Alkane chains | S | Au | 12 – 30 |
| 38 | Theory | Alkane chains – (H and F) | S, N | Au | 12 – 45 |
| 39 | Theory | Alkane chains | - | - | 20 – 130 |
| 40 | Theory | Benzenediamine | N | Au | 25 |
| 41 | Theory | Fullerene | C | Au | 7.0 – 46.3 |
| 42 | Theory | Oligoynes and Alkanes | S | Au | 5.6 – 33.4 |
| 43 | Experiment | Oligo (phenylene ethynylene) | S | Au | 20 ± 6 |

The common feature between all these studies is that κ_{ph} decreases as the size of the molecule increases. In this thesis, we will consider quite rigid organic and organometallic molecules ranging from 1.5 to 3.0 nm for which a reduction of κ_{ph} is expected compared to small molecules (< 1.2 nm). Since the denominator in the equation to calculate ZT depends both on the electronic and phononic thermal conductance, we will consider $\kappa_{ph} = 20$ pW/K to simulate our ZT in the next chapters.

Indeed, if only the electronic thermal conductance without the phonon contribution is taken to calculate ZT , i.e. the electronic Figure of Merit ZT_{el} , non-realistic values can be obtained. For

example, taking $S = 500 \mu\text{V/K}$, $G/G_0 = 10^{-6}$, $\kappa_{el} = 10^{-15} \text{ pW/K}$, $T = 300 \text{ K}$, gives $ZT_{el} = 5.8$ where as $ZT = 3.10^{-4}$ using $\kappa_{ph} = 20 \text{ pW/K}$, leading to a ratio between both Figures of Merit of 2.10^4 . In fact, in all the systems where $\kappa_{el} \ll \kappa_{ph}$ and κ_{ph} is neglected, $ZT_{el} \gg ZT$.

III.2 – Lorentzian shape transmission

Considering that the molecule electronic transmission is driven by a single level chemisorbed to the electrodes, different ϵ_0 and Γ couples could be tentatively tried to evaluate which thermoelectric properties would prevail at RT, as shown Figure 14.

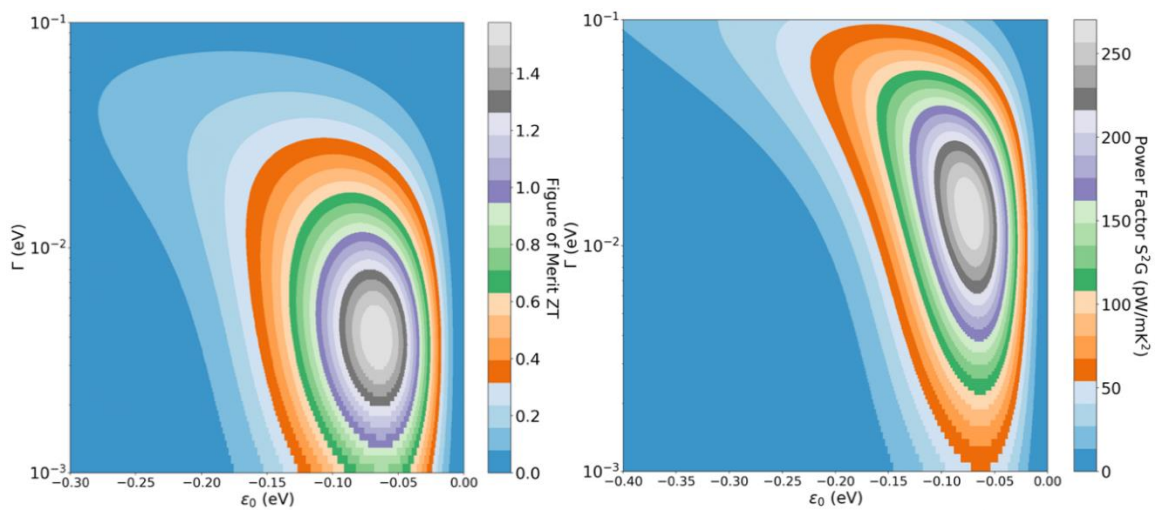


Figure 14 – Evolution of the Figure of Merit ZT and the power factor S^2G as a function of ϵ_0 and Γ . Left: evolution of ZT . Right: evolution of S^2G .

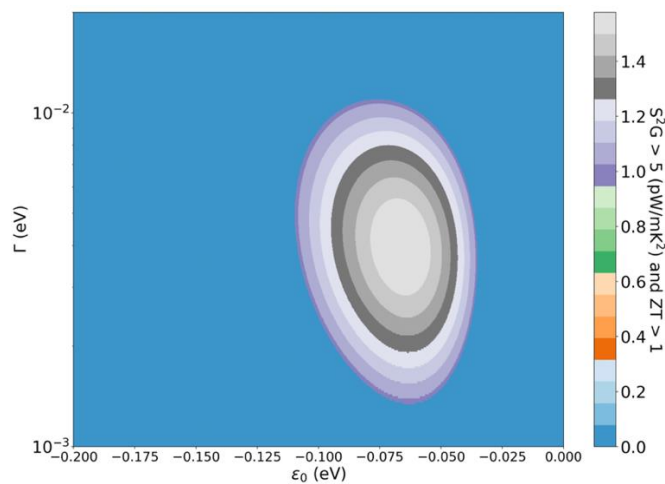


Figure 15 – Colored area corresponding to (ϵ_0, Γ) couples that lead to $S^2G > 5 \text{ pW/mK}^2$ and $ZT > 1$, the condition being not satisfied in the blue areas. The coloring is based on the ZT values.

In the case of a single Lorentzian shape transmission, the possible (ϵ_0, Γ) couples giving a Figure of Merit $ZT > 1$ and a thermopower $S^2G > 5$ pW/mK² are contained between -0.11 and -0.04 eV for ϵ_0 and between 1 meV and 10 meV for Γ (Figure 15), the best ZT being ≈ 1.6 ($\kappa_{ph} = 20$ pW/K). This simulation can conclude that an electronic transmission having a shape close to a single Lorentzian will not induce high thermoelectric efficiency.

III.3 – Lorentzian shape transmission and Fano resonance

The second type of theoretical transmission shape discussed here is a Lorentzian shape coupled with a Fano resonance. A Fano resonance is a type of quantum interference^{44,45,46} (QI). The expression of the electronic transmission from a single level model with a QI reads:⁴⁷

$$\tau(E) = \frac{4\Gamma^2}{\left(E - \epsilon_0 - \frac{V^2}{E - \epsilon_1}\right)^2 + 4\Gamma^2} \quad \text{Eq. 15}$$

With V the coupling between the first transporting state ϵ_0 and the localized state ϵ_1 responsible for the quantum interference.

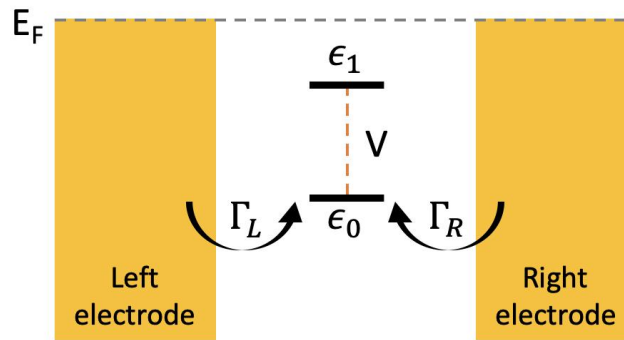


Figure 16 – Schematic model of a molecular junction with a side group, as considered in this study. A molecule consisting of two fragments is coupled between two electrodes. The energies of the transporting level of the two fragments are labelled ϵ_0 and ϵ_1 . The transfer integral or coupling between them is set to V . $\Gamma_{L,R}$ represents the coupling strength between fragment 0 and the electrodes while fragment 1 is not (weakly) coupled to them.

It has been intuited that a Fano resonance near the Fermi level could drastically increase thermoelectric properties. This assumption result from the definition of the Seebeck coefficient in the low temperature limit:

$$S_{lowT} = - \frac{\pi^2 k_B^2 T}{3|e|\tau(E)} \left. \frac{d\tau(E)}{dE} \right|_{E=E_F} \quad \text{Eq. 16}$$

Indeed, the slope of the transmission at the Fermi level is important, but this is only predominant at low temperature; as T increases up to RT, the complete integrated version of Eq. 16 is necessary (see Part II, Chapter I, Eq. 28). By nature, a Fano resonance is energetically narrow and thus this feature does not change the thermoelectric properties, as evidenced in Figure 17.

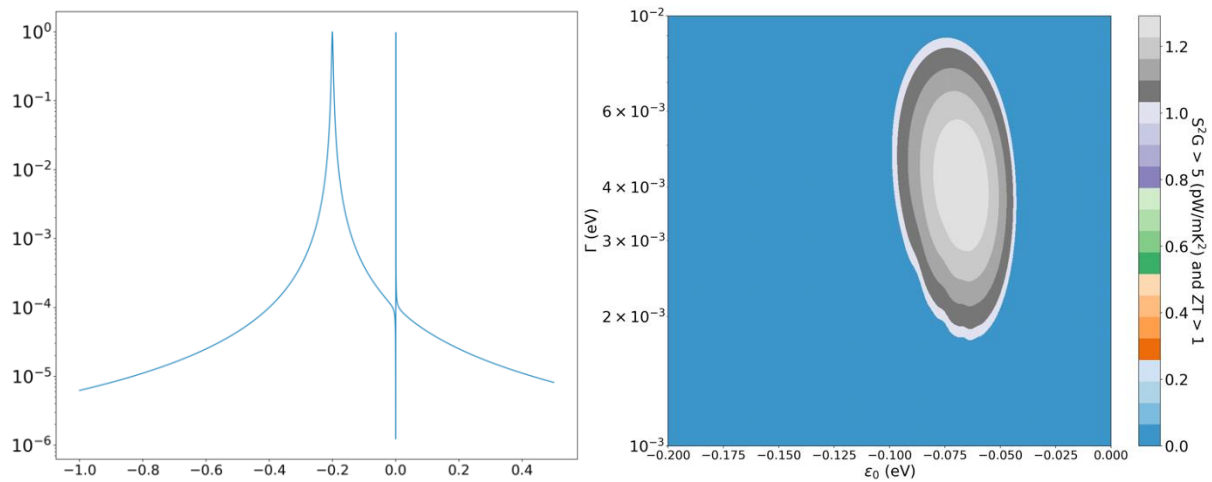


Figure 17 – Left: representation of a transmission created with Eq. 15. The parameters are $\epsilon_0 = -0.20$ eV, $V^2 = 10^{-4}$ eV² and $\epsilon_1 = -0.02$ eV. Right: values of (ϵ_0, Γ) couples for which the thermopower $S^2G > 5$ pW/mK² and the Figure of Merit $ZT > 1$. The blue zone represents all the (ϵ_0, Γ) couples which do not satisfy the above conditions.

Indeed, even with a Fano resonance quasi perfectly placed compared to the Fermi level, the influence on the thermoelectrics properties are barely noticeable. Changing reasonably the coupling value V or the position of the level ϵ_1 hardly change this conclusion. A huge Fano resonance which has maximum and minimum sufficiently energetically spaced can moderately influence the thermoelectrics values but less than the QI effect presented below.

III.4 – Lorentzian shape transmission and anti-resonance

In this model, we also consider a two-level model having an anti-resonance as QI in the transmission function instead of a Fano resonance. This can be created also using equation Eq. 15 but considering a larger coupling $V > 0.01$ eV.

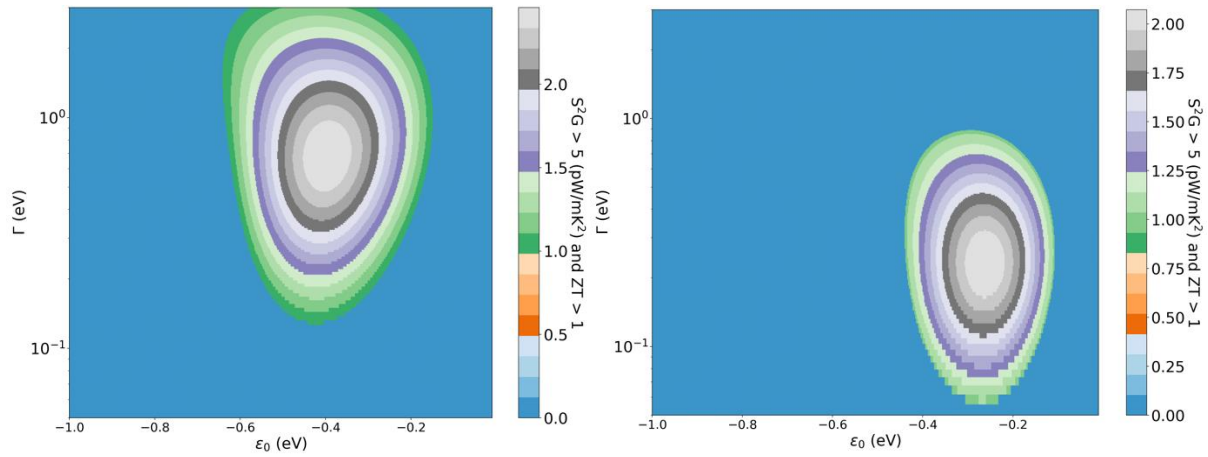


Figure 18 – Representation of the obtained values of (ϵ_0, Γ) couples for which the thermopower $S^2G > 5 \text{ pW/mK}^2$ and the Figure of Merit $ZT > 1$. The blue zone represents all the (ϵ_0, Γ) couples which do not satisfy the above conditions. Left: coupling $V^2 = 3 \text{ eV}^2$ and $\epsilon_1 = 0.1 \text{ eV}$. Right: coupling $V^2 = 3 \text{ eV}^2$ and $\epsilon_1 = 0.2 \text{ eV}$.

Inspection of Figure 18 shows that ZT is enhanced in presence of anti-resonance, reaching up to 3 (left graph of Figure 18). In this example, ϵ_0 validates the conditions between -0.62 and -0.10 eV (compared to -0.11 and -0.04 eV in the simple Lorentzian shape). Moreover, in Figure 18, we only modified the energetic position of the ϵ_1 level, though changing the coupling V also changes the thermoelectric properties. Consequently, the possibilities to obtain interesting thermoelectric properties are enhanced if anti-resonances are present close to the Fermi level.

It should be noted that using Eq. 8 with high value of coupling V , the energy of the maximum of the transmission peak does not corresponds to the ϵ_0 of the junction without QI (or when the coupling V is small) and is actually given by the following expression accounting for the coupling between the two levels.

$$\epsilon_{bond,anti} = \frac{\epsilon_0 + \epsilon_1 \pm \sqrt{(\epsilon_0 - \epsilon_1)^2 + 4V^2}}{2} \quad \text{Eq. 17}$$

IV – Transmission study: an overview on OPE molecules

In this part of the thesis, we intend to explore the nature of the factors potentially responsible for discrepancies between experimental and theoretical data based on DFT/NEGF calculations. To do so, we investigate the change in transmission with modifications of the electrode shape and the geometry of the coordination at the anchoring site.

In order to compare the DFT/NEGF calculations to experimental results, the influence of the shape of the electrode and the contact geometry in the simulation on the transmission is an important factor to consider. The selection of benzenedithiol (BDT), biphenyldithiol (BPDT), the oligo-phenyl-ethynyl-dithiol (OPE2), and (phenyl-ethynyl-dithiol)-anthracene (OPE5) in Figure 19 as test molecules was motivated first by the fact that experimental and computational studies were available.^{48,36,2,3} Secondly, the UPS measurements of OPE2 and OPE5 junctions shows that the deduced ϵ_0 are shifted by 0.32 V, a noticeable value that simulation should recover (Table 7). Since the theoretical model is built to promote structural configurations maximizing the conductance, only the highest experimental conductance values were taken for comparison purpose; in the cases where the conductance was obtained by both the MCBJ and STM methods, a mean value of the highest conductance was chosen.

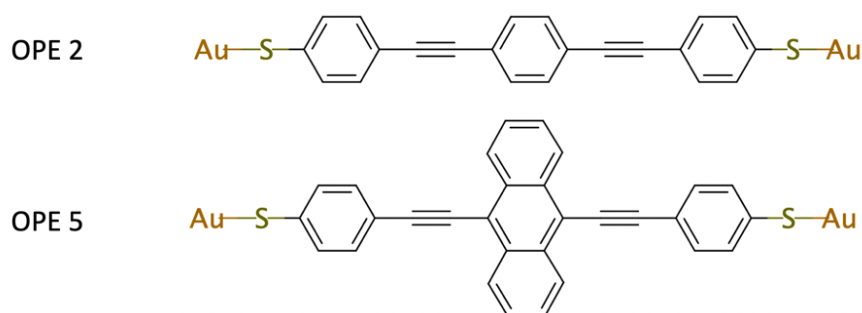


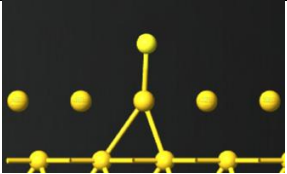
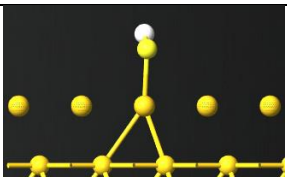
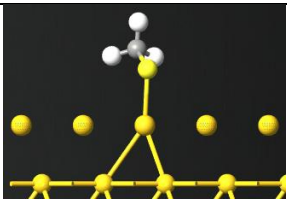
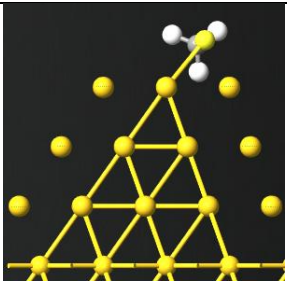
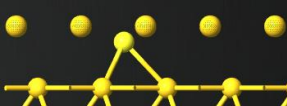
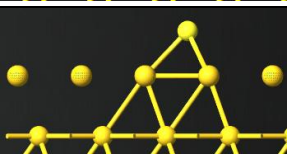
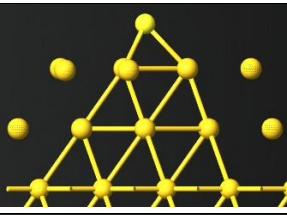
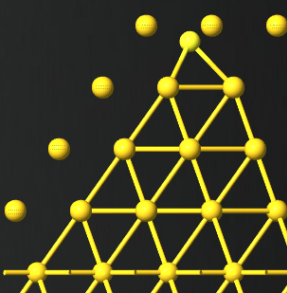
Figure 19 – Chemical structures of OPE2 and OPE5 investigated from reference 48.

Table 7 – UPS experimental data for the extraction of ϵ_0 , conductance, and UV-Vis gap for different OPE derivatives. Adapted from reference 48.

| Molecules | UPS ϵ_0 (eV) | G/G ₀ | UV-Vis gap (eV) |
|-----------|-----------------------|------------------|-----------------|
| OPE2 | -0.81 | 1.55E-04 | 3.38 |
| OPE5 | -0.49 | 4.75E-04 | 2.53 |

We have first considered different shapes of electrode, and different anchoring geometries between the sulfur and the gold substrate. Their shapes are described in Table 8.

Table 8 – The different electrode shapes and anchoring geometries considered in this study.

| Name | Schematic representation | Au-S: Top coordination |
|-----------|---|---|
| #1-top |  | Gold adatom coordinated to a sulfur atom in top position. |
| #2-top |  | Gold adatom coordinated to a sulfur atom in top position with H still coordinated to S. |
| #3-top |  | Gold adatom coordinated to a sulfur atom in top position with CH ₃ still coordinated to S. |
| #4-top |  | Gold tip (size 2) coordinated to a sulfur atom in top position with CH ₃ still coordinated to S. |
| Name | Schematic representation | Au-S: Hollow coordination |
| #1-hollow |  | Flat gold electrode coordinated to a sulfur atom in hollow position. |
| #2-hollow |  | Gold tip (size 1) coordinated to a sulfur atom in hollow position. |
| #3-hollow |  | Gold tip (size 2) coordinated to a sulfur atom in hollow position. |
| #4-hollow |  | Gold tip (size 3) coordinated to a sulfur atom in hollow position. |

The #1-top geometry coordination (first entry, Table 8) was the configuration chosen in the computational study in reference 48. The calculated transmissions are shown in Figure 13. For these molecular junctions in which the sulfur terminal atom is in top coordination with the gold electrodes (#1-top / #1-top), the HOMO is inevitably pinned close to the Fermi level. Its energy (compared to E_F) is only marginally affected by the nature of the molecule. We illustrate this pinning effect in Figure 20 for BDT, BPDT and OPE2.

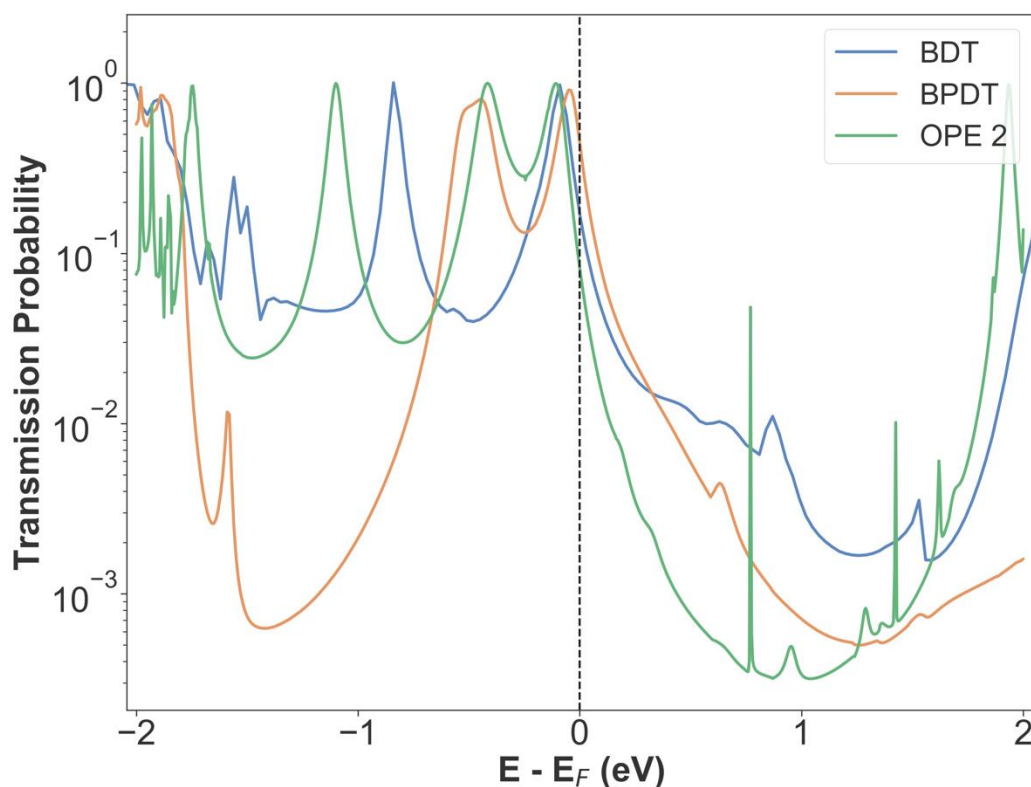


Figure 20 – Calculated electronic transmission spectra of a benzenedithiol (BDT), biphenyldithiol (BPDT) and an oligo(phenylene ethynylene) (OPE2) with the sulfur atoms coordinated to the gold surface in (#1-top / #1-top) anchoring configuration. All these chain-like molecules are lying perpendicularly to the gold substrates.

In their combined experimental and computational study, Kaliginedi and coworkers⁴⁸ did calculate the same (#1-top / #1-top) configuration and also the mixed arrangement #1-top on one side of the molecule and #1-hollow on the other side (see Table 8). In order to evaluate the influence of the adatom on the results, a third arrangement in which both ending sulfurs are bonded in a top configuration to one gold atom of each gold (111) surface (flat electrodes) has been considered, i.e., T/T configuration. Figure 21 reports their results. The transmission for the (#1-top / #1-top) fully matches with our results (see Figure 20) and the calculation for which

only one contact is in #1-top position and the other in #1-hollow lead also to a pinning of the transmission peak close to the Fermi energy. The comparison between the transmission curves (#1-top / #1-top) and (T/T) allows to conclude that the effect of the gold adatom is mainly found in the strength of the coupling (weaker coupling for #1-top / #1-top than T/T) but the influence on the position of the peak is weak.

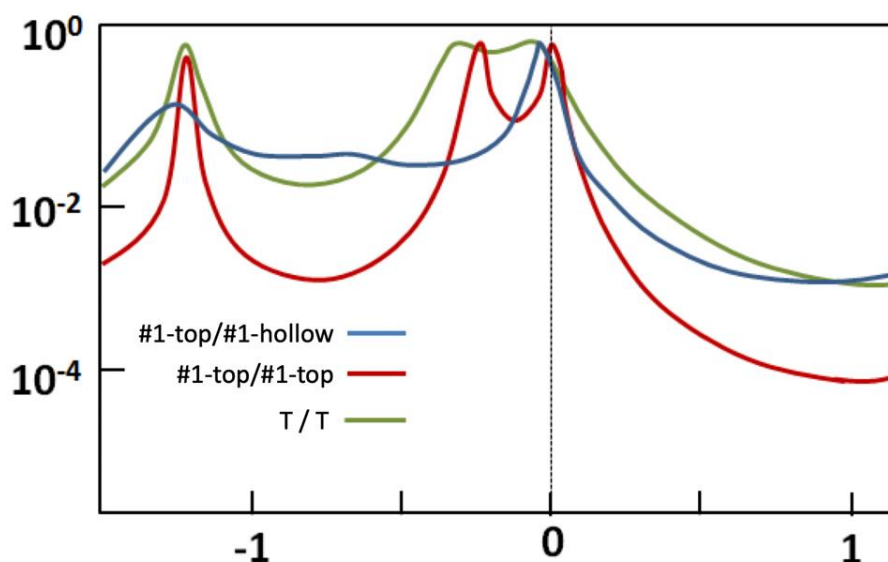


Figure 21 – Effect of the coupling configuration on the transmission of an OPE2. Adapted from reference 48. See Table 5 and text for the labelling.

To overcome this apparent problem, a lot of computational studies are considering the sulfur atom also bonded to a hydrogen atom or a methyl group.^{49,50} We thus investigated those configurations together with the enlargement of the tip shape of the electrodes as listed in Table 8. These results are reported in Table 9 for the case study molecules OPE2 and OPE5. For the OPE2 system in hollow coordination, the device with the gold tip configuration (#3-hollow) yields the best match with UPS measurements with $\epsilon_0(\text{UPS}) = -0.81$ eV and $\epsilon_0(\#3\text{-hollow}) = -0.80$ eV. The conductance ratio between #3-hollow and the experimental value is 25 with $G_{\#3\text{-hollow}}/G_0 = 3.83\text{E-}3$ and $G_{\text{exp}}/G_0 = 1.55\text{E-}04$. In all top configurations, the values of the calculated ϵ_0 are far from the UPS values, but the conductance values are closer to the experimental data (the ratios are 8.5, 3.9 and 10.4 for #2-top, #3-top, #4-top respectively). For the OPE5 system the same conclusions can be reached; the #3-hollow coordination scheme is the closest to UPS experiment with $\epsilon_0(\text{UPS}) = -0.49$ eV and $\epsilon_0(\#3\text{-hollow}) = -0.49$ eV, but with a conductance ratio about 18 times greater for the theoretical approach ($G_{\#3\text{-hollow}}/G_0 = 8.42\text{E-}3$ and $G_{\text{exp}}/G_0 =$

4.75E-04). In top position, the calculated ϵ_0 are also far from UPS measurements, but the conductance are better matching the experimental values with ratios of 3.5 and 1.1.

Table 9 – Theoretical data extracted from the transmission spectra. the ϵ_0 is in eV, G/G_0 the conductance, “LUMO” corresponds to the LUMO energy position compared to the Fermi level in eV. The HOMO-LUMO gap (H-L gap) in eV, S the Seebeck coefficient in $\mu\text{V/K}$. On the right are collected the different ratios compared to the experimental data listed in Table 7.

| Position | ϵ_0 | G/G_0 | LUMO | H-L Gap | S | ϵ_0 Ratio | G/G_0 Ratio | Gap ratio |
|-----------|--------------|----------|------|---------|-------|-----------------------|------------------|--------------|
| OPE2 | | | | | | | | |
| #1-top | - | - | - | - | - | - | - | - |
| #2-top | -1.24 | 1.31E-03 | 1.09 | 2.34 | -6.3 | 1.5 | 8.5 | 0.7 |
| #3-top | -1.37 | 6.04E-04 | 0.96 | 2.33 | -16.6 | 1.7 | 3.9 | 0.7 |
| #4-top | -1.70 | 1.62E-03 | 0.68 | 2.38 | -39.9 | 2.1 | 10.4 | 0.7 |
| #1-hollow | -0.64 | 1.81E-02 | 1.70 | 2.35 | 30.8 | 0.8 | 116.6 | 0.7 |
| #2-hollow | -0.73 | 4.16E-03 | 1.50 | 2.23 | 7.5 | 0.9 | 26.8 | 0.7 |
| #3-hollow | -0.80 | 3.83E-03 | 1.45 | 2.25 | 6.7 | 1.0 | 24.7 | 0.7 |
| #4-hollow | -0.73 | 4.40E-03 | 1.57 | 2.29 | 13.8 | 0.9 | 28.4 | 0.7 |
| OPE5 | | | | | | | | |
| #2-top | -0.75 | 1.66E-03 | 0.75 | 1.50 | -8.0 | 1.5 | 3.5 | 0.6 |
| #3-top | -0.77 | 5.44E-04 | 0.73 | 1.50 | -12.7 | 1.6 | 1.1 | 0.6 |
| #1-hollow | -0.33 | 4.29E-02 | 1.21 | 1.55 | 49.7 | 0.7 | 90.3 | 0.6 |
| #2-hollow | -0.44 | 9.57E-03 | 1.09 | 1.53 | 17.9 | 0.9 | 20.1 | 0.6 |
| #3-hollow | -0.49 | 8.42E-03 | 1.04 | 1.53 | 15.0 | 1.0 | 17.7 | 0.6 |
| #4-hollow | -0.42 | 9.85E-03 | 1.10 | 1.53 | 25.3 | 0.9 | 20.7 | 0.6 |

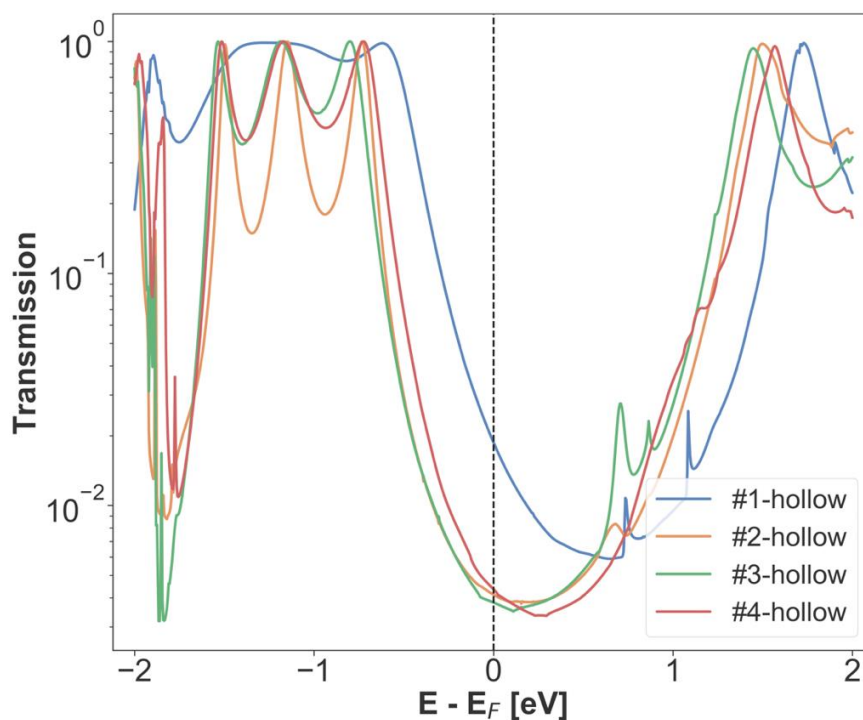


Figure 22 – Transmission spectra of the OPE2 molecule with the sulfur coordinated in hollow position. #1-hollow in blue, #2-hollow in orange, #3-hollow in green and #4-hollow in red.

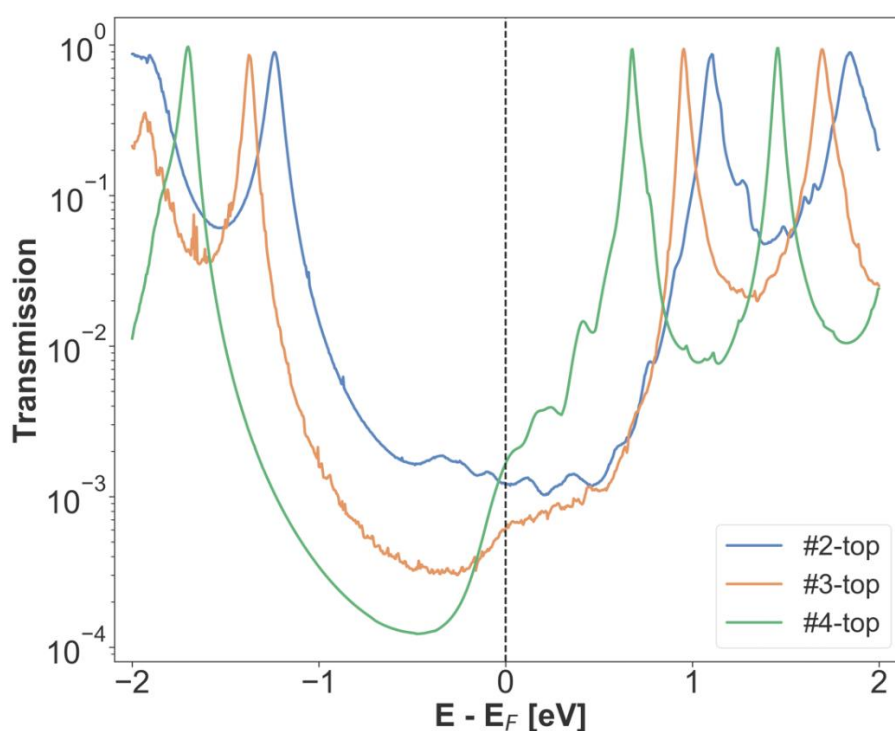


Figure 23 – Transmission spectra of the OPE2 with the sulfur in top position with either an H or a CH_3 bonded to it. #2-top in blue and #3-top in orange. The #4-top in green is with an additional gold tip and a CH_3 bonded to the sulfur atoms.

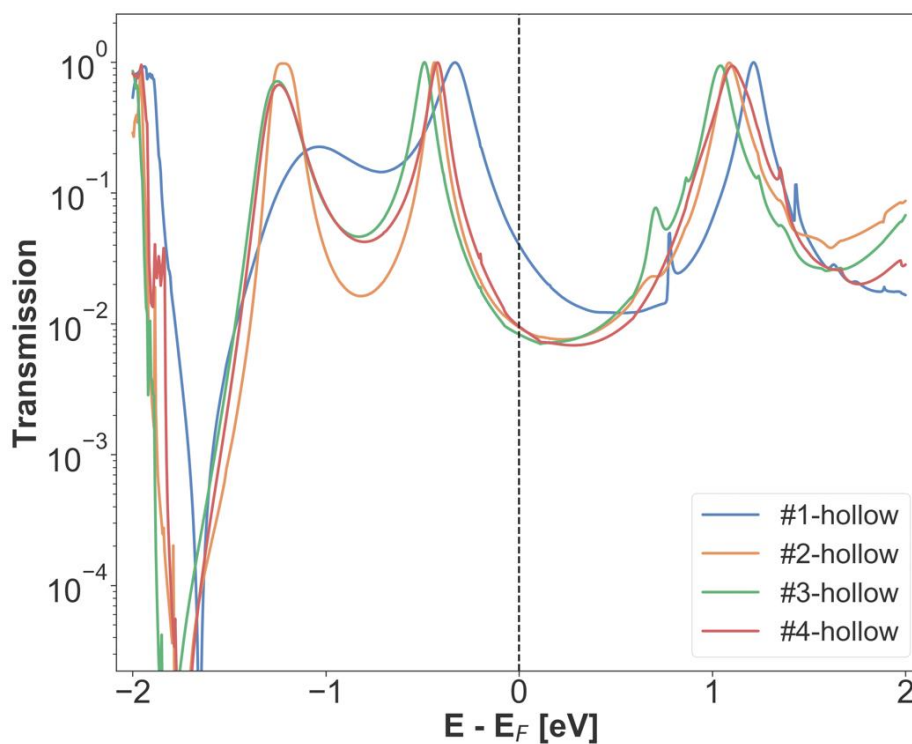


Figure 24 – Transmission spectra of the OPE5 molecule with the sulfur coordinated in hollow position. #1-hollow in blue, #2-hollow in orange, #3-hollow in green and #4-hollow in red.

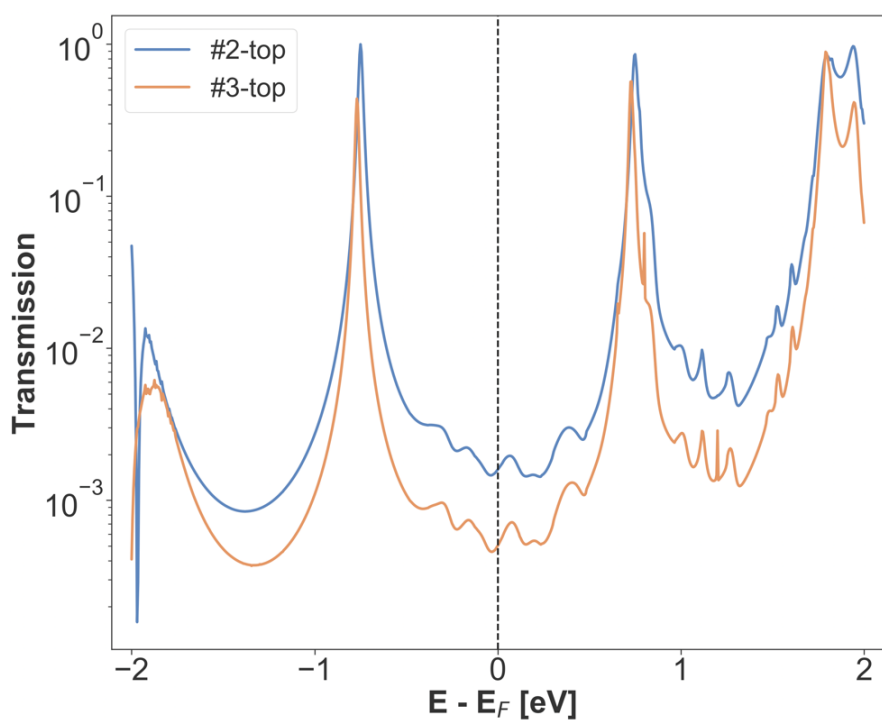


Figure 25 – Transmission spectra of the OPE5 with the sulfur in top position with either an H or a CH_3 bonded to it. #2-top in blue and #3-top in orange.

From this analysis, several observations can be done:

- it is possible that the molecular configurations in an UPS measurement (made on SAMs) does not match the configuration in a junction (made by CP-AFM or MCBJ). This could be one explanation for the discrepancy between hollow configurations, giving ϵ_0 values in agreement with UPS measurements and top configurations (with H or CH₃), giving close values for the conductance but not for ϵ_0 .
- another possible explanation of the discrepancy is that the experimental conductance values of molecular junctions are obtained from statistical data. Thus, the retrieved conductance is due to an average of several configurations for the anchoring group. A statistical study is thus necessary to fully rationalize the experimental data.
- the influence of the DFT functional could be an important point for the values obtained before. We tested this in #3-hollow configuration for OPE2. The results are shown in Figure 26.

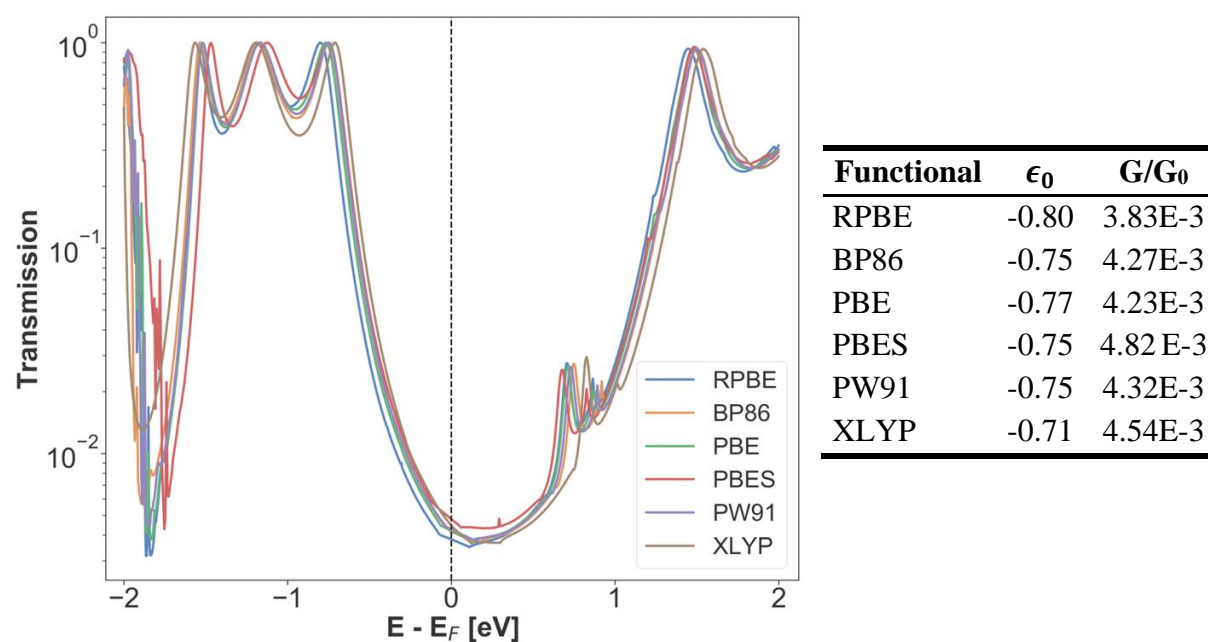


Figure 26 – Left: transmission spectra for the OPE2 in #3-hollow coordination for different types of GGA functional available in Quantum ATK. Right: table of ϵ_0 and G/G_0 for each tested GGA functional.

The recent update of QuantumATK (June 2021) provides a new hybrid-GGA functional available for molecular transport calculations: HSE06. Using this new functional, we calculated the transmission of the OPE2 molecule, as described by the #1-hollow coordination, and found the same ϵ_0 value as for the #3-hollow system, without adding the hollow gold tip (Figure 27).

The results are thus indeed functional-dependent but the role of the diversity of configurations in the experimental results is surely also important. Considering that our goal is first to enhance the thermoelectric properties by chemical engineering, we intentionally restrict our calculations to the hollow-configuration which yields the best comparison with experiment (for ϵ_0 at least).

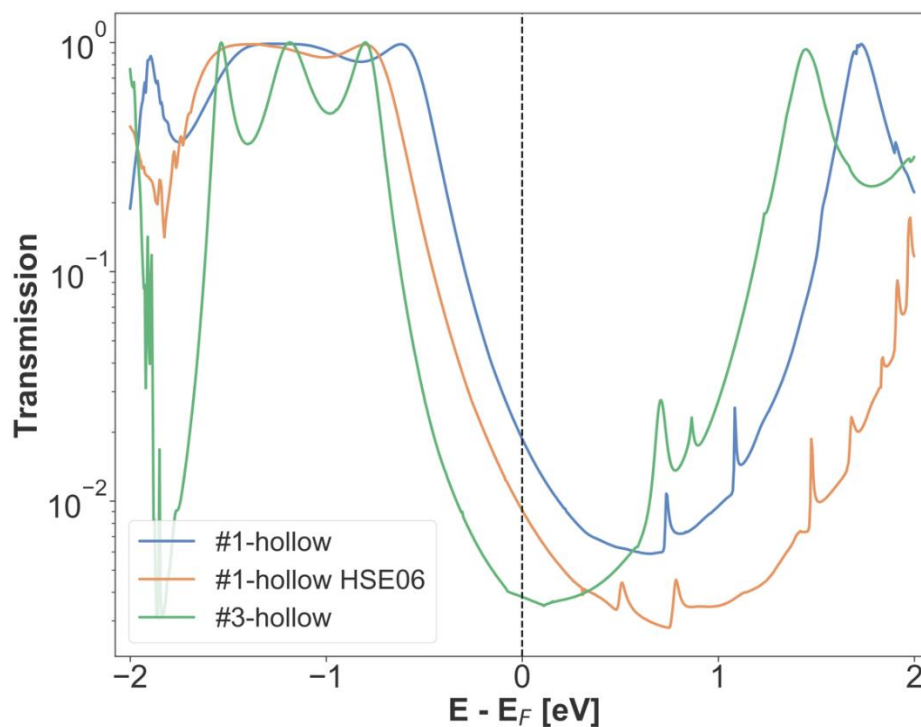


Figure 27 – Comparison of transmission spectra for the OPE2 molecule in #1-hollow configuration with revPBE functional and HSE06 and in #3-hollow configuration (revPBE functional).

-
- ¹ Hüfner, S. Photoelectron Spectroscopy: Principles and Applications. Springer, 2003. ISBN:3-540-41802-4.
- ² Xie, Z.; Bâldea, I.; Smith, C. E.; Wu, Y.; Frisbie, C. D. Experimental and Theoretical Analysis of Nanotransport in Oligophenylene Dithiol Junctions as a Function of Molecular Length and Contact Work Function. *ACS Nano* 2015, 9, 8022–8036. doi:10.1021/acsnano.5b01629.
- ³ Xie, Z.; Bâldea, I.; Frisbie, C. D. Determination of Energy-Level Alignment in Molecular Tunnel Junctions by Transport and Spectroscopy: Self-Consistency for the Case of Oligophenylene Thiols and Dithiols on Ag, Au, and Pt Electrodes. *J. Am. Chem. Soc.* 2019, 141, 3670–3681. doi:10.1021/jacs.8b13370.
- ⁴ Huisman, E. H.; Guédon, C. M.; van Wees, B. J.; van der Molen, S. J. Interpretation of Transition Voltage Spectroscopy. *Nano Lett.* 2009, 9, 3909–3913. doi:10.1021/nl9021094.
- ⁵ Bâldea, I. Revealing Molecular Orbital Gating by Transition Voltage Spectroscopy. *Chem. Phys.* 2010, 377, 15–20. doi:10.1016/j.chemphys.2010.08.009.
- ⁶ Bâldea, I. Ambipolar Transition Voltage Spectroscopy: Analytical Results and Experimental Agreement. *Phys. Rev. B* 2012, 85, 035442. doi:10.1103/PhysRevB.85.035442.
- ⁷ Beebe, J. M.; Kim, B.; Gadzuk, J. W.; Frisbie, C. D.; Kushmerick, J. G. Transition from Direct Tunneling to Field Emission in Metal-Molecule-Metal Junctions. *Phys. Rev. Lett.* 2006, 97, 026801.
- ⁸ Beebe, J. M.; Kim, B.; Frisbie, C. D.; Kushmerick, J. G. Measuring Relative Barrier Heights in Molecular Electronic Junctions with Transition Voltage Spectroscopy. *ACS Nano* 2008, 2, 827. doi:10.1021/nm700424u.
- ⁹ Cuevas, J. C.; Scheer, E. *Molecular Electronics, an introduction to theory and experiments*, 2nd edition, Table 13.1, page 383, World scientific, 2016. ISBN:978-981-3226-02-9
- ¹⁰ Mirjani, F.; Thijssen, J. M.; van der Molen, S. J. Advantages and Limitations of Transition Voltage Spectroscopy: A Theoretical Analysis. *Phys. Rev. B* 2011, 84, 115402. doi:10.1103/PhysRevB.84.115402.
- ¹¹ Chen, J.; Markussen, T.; Thygesen, K. S. Quantifying Transition Voltage Spectroscopy of Molecular Junctions: Ab Initio Calculations. *Phys. Rev. B* 2010, 82, 121412. doi:10.1103/PhysRevB.82.121412.
- ¹² Delmas, V.; Diez-Cabanes, V.; van Dyck, C.; Scheer, E.; Costuas, K.; Cornil, J. On the Reliability of Acquiring Molecular Junction Parameters by Lorentzian Fitting of I/V Curves. *Phys. Chem. Chem. Phys.* 2020, 22, 26702–26706. doi:10.1039/D0CP05372D.
- ¹³ Wold, D. J.; Frisbie, C. D. Fabrication and Characterization of Metal–Molecule–Metal Junctions by Conducting Probe Atomic Force Microscopy. *JACS* 2001, 123, 5549–5556. doi: 10.1021/ja0101532.
- ¹⁴ Samorì, P. *STM and AFM Studies on (Bio)Molecular Systems: Unravelling the Nanoworld*. Springer Berlin Heidelberg, Vol. 285: Berlin, Heidelberg, 2008.
- ¹⁵ Hong, W.; Valkenier, H.; Mészáros, G.; Manrique, D. Z.; Mishchenko, A.; Putz, A.; García, P. M.; Lambert, C. J.; Hummelen J. C.; Wandlowski, T. An MCBJ case study: The influence of π -conjugation on the single-molecule conductance at a solid/liquid interface. *Beilstein J. Nanotechnol.* 2011, 2, 699–713. Doi:10.3762/bjnano.2.76.
- ¹⁶ Wang, L.; Wang, L.; Zhang L.; Xiang, D. Advance of Mechanically Controllable Break Junction for Molecular Electronics. *Top Curr. Chem. (Z)* 2017, 375, 61. doi: 10.1007/s41061-017-0149-0.
- ¹⁷ Van Dyck C.; Bergren, A. Large Built-In Fields Control the Electronic Properties of Nanoscale Molecular Devices with Dipolar Structures. *J. Adv. Electron. Mater.* 2018, 4, 1700656. doi:10.1002/aelm.201700656.

- ¹⁸ Diez-Cabanes, V.; Gonzalez, S. R.; Osella, S.; Cornil, D.; Van Dyck, C.; Cornil, J. Energy Level Alignment at Interfaces Between Au (111) and Thiolated Oligophenylenes of Increasing Chain Size: Theoretical Evidence of Pinning Effects. *Adv. Theo. Sim.* 2018, 1, 1700020. doi: 10.1002/adts.201700020.
- ¹⁹ a) Huisman, E. H.; Guédon, C. M.; van Wees, B. J.; van der Molen, S. J. Interpretation of Transition Voltage Spectroscopy. *Nano Lett.* 2009, 9, 3909–3913. doi:10.1021/nl9021094. b) Briechle, B. M.; Kim, Y.; Ehrenreich, P.; Erbe, A.; Sysoiev, D.; Huhn, T.; Groth U.; Scheer, E. Current–voltage characteristics of single-molecule diarylethene junctions measured with adjustable gold electrodes in solution. *J. Nanotech.* 2012, 3, 798–808. doi:10.3762/bjnano.3.89. d) Xie, Z.; Bâldea, I.; Smith, C. E.; Wu Y.; Frisbie, C. D. Experimental and Theoretical Analysis of Nanotransport in Oligophenylene Dithiol Junctions as a Function of Molecular Length and Contact Work Function. *ACS Nano* 2015, 9, 8022–8036. doi:10.1021/acsnano.5b01629. e) Isshiki, Y.; Matsuzawa, Y.; Fujii S.; Kiguchi, M. Investigation on Single-Molecule Junctions Based on Current–Voltage Characteristics. *Micromachines* 2018, 9, 67. doi:10.3390/mi9020067. f) Xie, Z.; Bâldea I.; Frisbie, C. D. Determination of Energy-Level Alignment in Molecular Tunnel Junctions by Transport and Spectroscopy: Self-Consistency for the Case of Oligophenylene Thiols and Dithiols on Ag, Au, and Pt Electrodes. *J. Am. Chem. Soc.* 2019, 141, 3670–3681. doi:10.1021/jacs.8b13370.
- ²⁰ Quek, S. Y.; Choi, H. J.; Louie S. G.; Neaton, J. B. Thermopower of Amine–Gold-Linked Aromatic Molecular Junctions from First Principles. *ACS Nano* 2011, 5, 551–557. doi:10.1021/nn102604g.
- ²¹ Liu Z.-F.; Neaton, J. B. Voltage Dependence of Molecule–Electrode Coupling in Biased Molecular Junctions. *J. Phys. Chem. C* 2017, 121, 21136–21144. doi:10.1021/acs.jpcc.7b05567.
- ²² Smidstrup, S.; Stradi, D.; Wellendorff, J.; Khomyakov, P. A.; Vej-Hansen, U. G.; Lee, Maeng E.; Ghosh, T.; Jónsson, E.; Jónsson, H.; Stokbro, K. First-principles Green's-function method for surface calculations. *Phys. Rev. B*, 2017, 96, 195309. doi:10.1103/PhysRevB.96.195309.
- ²³ Costuas K.; Rigaut, S. Polynuclear carbon-rich organometallic complexes: clarification of the role of the bridging ligand in the redox properties. *Dalton Trans.* 2011, 40, 5643–5658. doi: 10.1039/C0DT01388A.
- ²⁴ a) Wong, C.-Y.; Lee, F.-W.; Che, C.-M.; Cheng, Y. F.; Phillips, D. L.; Zhu, N. Spectroscopic Studies and Structures of trans-Ruthenium(II) and Ruthenium(III) Bis(cyanide) Complexes Supported by a Tetradentate Macrocyclic Tertiary Amine Ligand. *Inorg. Chem.* 2008, 47, 10308–10316. doi:10.1021/ic800743a. b) Doro, F. G.; Ferreira, K. Q.; da Rocha, Z. N.; Caramori, G. F.; Gomes A. J.; Tfouni, E. The versatile ruthenium(II/III) tetraazamacrocyclic complexes and their nitrosyl derivatives. *Coord. Chem. Rev.* 2016, 306, 652–677. doi:10.1016/j.ccr.2015.03.021.
- ²⁵ a) Meng, F.; Hervault, Y.-M.; Norel, L.; Costuas, K.; van Dyck, C.; Geskin, V.; Cornil, J.; Hng, H. H.; Rigaut, S.; Chen, X. Photo-modulable molecular transport junctions based on organometallic molecular wires. *Chem. Sci.* 2012, 3, 3113–3118. doi:10.1039/C2SC20323E. b) Milan, D. C.; Vezzoli, A.; Planje I. J.; Low, P. J. Metal bis(acetylide) complex molecular wires: concepts and design strategies. *Dalton Trans.* 2018, 47, 14125–14138. doi:10.1039/C8DT02103A.
- ²⁶ QuantumATK Q-2019.12 Synopsys. <https://www.synopsys.com/silicon/quantumatk.html>.
- ²⁷ a) Porod, W.; Shao Z.; Lent, C. S. Resonance-antiresonance line shape for transmission in quantum waveguides with resonantly coupled cavities. *Phys. Rev. B* 1993, 48, 8495–8498. doi:10.1103/PhysRevB.48.8495. b) Göres, J.; Goldhaber-Gordon, D.; Heemeyer, S.; Kastner, M. A.; Shtrikman, H.; Mahalu D.; U. Meirav. Fano resonances in electronic transport through a single-electron transistor. *Phys. Rev. B* 2000, 62, 2188–2194. c) Lambert, C. J.

Basic concepts of quantum interference and electron transport in single-molecule electronics. *Chem. Soc. Rev.* 2015, 44, 875–888. doi:10.1039/C4CS00203B.

²⁸ te Velde, G.; Bickelhaupt, F. M.; Baerends, E. J.; Fonseca Guerra, C.; van Gisbergen, S. J.; A.; Snijders, J. G.; Ziegler, T. Chemistry with ADF. *J. Comp. Chem.* 2001, 22, 931. doi:10.1002/jcc.1056.

²⁹ ADF 2019, SCM, Theoretical Chemistry, Vrije Universiteit, Amsterdam, Netherlands, <http://www.scm.com>.

³⁰ Paulsson M.; Datta, S. Thermoelectric effect in molecular electronics. *Phys. Rev. B* 2003, 67, 241403. doi:10.1103/PhysRevB.67.241403.

³¹ Reddy, P.; Jang, S.-Y.; Segalman R. A.; Majumdar, A. Thermoelectricity in Molecular Junctions. *Science* 2007, 315, 1568-1571. doi:10.1126/science.1137149.

³² Zimbovskaya, N. A. *Transport Properties of Molecular Junctions*. Springer tracts in modern physics. Springer: New York, 2013.

³³ Zimbovskaya, N. A. Seebeck effect in molecular junctions. *J. Phys.: Cond. Mat.* 2016, 28, 183002. doi:10.1088/0953-8984/28/18/183002.

³⁴ Widawsky, J. R.; Darancet, P.; Neaton, J. B.; Venkataraman, L. Simultaneous Determination of Conductance and Thermopower of Single Molecule Junctions. *Nano Lett.* 2012, 12, 354–358. doi:10.1021/nl203634m.

³⁵ Cui, L.; Miao, R.; Wang, K.; Thompson, D.; Zotti, L. A.; Cuevas, J. C.; Meyhofer, E.; Reddy, P. Peltier cooling in molecular junctions. *Nature Nanotech.* 2018, 13, 122–127. doi:10.1038/s41565-017-0036-4.

³⁶ Cui, L.; Hur, S.; Akbar, Z. A.; Klöckner, J. C.; Jeong, W.; Pauly, F.; Jang, S.-Y.; Reddy, P.; Meyhofer, E. Thermal Conductance of Single-Molecule Junctions. *Nature* 2019, 572, 628–633. doi:10.1038/s41586-019-1420-z

³⁷ Wang, K.; Meyhofer, E.; Reddy, P. Thermal and Thermoelectric Properties of Molecular Junctions. *Adv. Funct. Mater.* 2019, 1904534. doi:10.1002/adfm.201904534.

³⁸ Klöckner, J. C.; Bürkle, M.; Cuevas, J. C.; Pauly, F. Length dependence of the thermal conductance of alkane-based single-molecule junctions: An ab initio study. *Phys. Rev. B* 2016, 94. doi:10.1103/physrevb.94.205425.

³⁹ Segal, D.; Nitzan, A.; Hänggi, P. Thermal Conductance through Molecular Wires. *J. Chem. Phys.* 2003, 119, 6840–6855. doi:10.1063/1.1603211.

⁴⁰ Klöckner, J. C.; Cuevas, J. C.; Pauly, F. Tuning the Thermal Conductance of Molecular Junctions with Interference Effects. *Phys. Rev. B* 2017, 96, 245419. doi:10.1103/PhysRevB.96.245419.

⁴¹ Klöckner, J. C.; Siebler, R.; Cuevas, J. C.; Pauly, F. Thermal Conductance and Thermoelectric Figure of Merit of C₆₀-Based Single-Molecule Junctions: Electrons, Phonons, and Photons. *Phys. Rev. B* 2017, 95, 245404. doi:10.1103/PhysRevB.95.245404.

⁴² Sadeghi, H.; Sangtarash, S.; Lambert, C. J. Oligoynes Molecular Junctions for Efficient Room Temperature Thermoelectric Power Generation. *Nano Lett.* 2015, 15, 7467–7472. doi:10.1021/acs.nanolett.5b03033

⁴³ Mosso, N.; Sadeghi, H.; Gemma, A.; Sangtarash, S.; Drechsler, U.; Lambert, C.; Gotsmann, B. Thermal Transport through Single-Molecule Junctions. *Nano Lett.* 2019, 9b02089. doi: 10.1021/acs.nanolett.9b02089.

⁴⁴ Göres, J.; Goldhaber-Gordon, D.; Heemeyer, S.; Kastner, M. A.; Shtrikman, H.; Mahalu, D.; Meirav, U. Fano Resonances in Electronic Transport through a Single-Electron Transistor. *Phys. Rev. B* 2000, 62, 2188–2194. doi:10.1103/PhysRevB.62.2188.

-
- ⁴⁵ Porod, W.; Shao, Z.; Lent, C. S. Resonance-Antiresonance Line Shape for Transmission in Quantum Waveguides with Resonantly Coupled Cavities. *Phys. Rev. B* 1993, 48, 8495–8498. doi:10.1103/PhysRevB.48.8495.
- ⁴⁶ Papadopoulos, T. A.; Grace, I. M.; Lambert, C. J. Control of Electron Transport through Fano Resonances in Molecular Wires. *Phys. Rev. B* 2006, 74. doi:10.1103/PhysRevB.74.193306.
- ⁴⁷ Nozaki, D.; Sevincli, H.; Avdoshenko, S. M.; Gutierrez, R.; Cuniberti, G. Control of Quantum Interference in Molecular Junctions: Understanding the Origin of Fano and Anti- Resonances. *J. Phys.: Conf. Series* 2013, 427, 012013. doi:10.1088/1742-6596/427/1/012013.
- ⁴⁸ Kaliginedi, V.; Moreno-García, P.; Valkenier, H.; Hong, W.; García-Suárez, V. M.; Buitter, P.; Otten, J. L. H.; Hummelen, J. C.; Lambert, C. J.; Wandlowski, T. Correlations between Molecular Structure and Single-Junction Conductance: A Case Study with Oligo (Phenylene-Ethynylene)-Type Wires. *J. AM. Chem. Soc.* 2012, 134, 5262–5275. doi: 10.1021/ja211555x.
- ⁴⁹ Wang, K.; Vezzoli, A.; Grace, I. M.; McLaughlin, M.; Nichols, R. J.; Xu, B.; Lambert, C. J.; Higgins, S. J. Charge Transfer Complexation Boosts Molecular Conductance through Fermi Level Pinning. *Chem. Sci.* 2019, 10, 2396–2403. doi:10.1039/C8SC04199G.
- ⁵⁰ Camarasa-Gomez, M.; Hernangomez-Perez, D.; Inkpen, M. S.; Lovat, G.; Fung, E.-D.; Roy, X.; Venkataraman, L. Evers, F. Mechanically-tunable Quantum Interference in Ferrocene-based Single-Molecule Junctions. *Nano Lett.* 2020, 20, 6381-6386. doi:10.1021/acs.nanolett.0c01956

Chapter III – Study of OPAn molecular junctions

I – Introduction

Among the different projects on molecular junctions involving our team, the group of Rigaut "organometallic and catalysis" at the ISCR in Rennes and the group of Scheer in the Physics Department in the University of Konstanz, a study on anchoring group has been devoted to (Au-C) covalent bonds in MCBJ's at low temperature. Indeed, in order to study in-depth, the electronic and magnetic transport properties and other physical properties of functional molecules, the ability to form single-molecule junctions which are stable and robust at low temperature and in vacuum are also of particular interest for choosing suitable end-groups. Thiols (-SH),¹ amines (-NH₂),^{2,3} cyanides (-CN),⁴ pyridines⁵ are among the most commonly used end-groups for their coupling strengths and known contact geometries. Recently, there has been surge of interest in establishing direct gold carbon (Au-C) covalent bonds to achieve more robust and highly conducting molecular junctions.^{6,7,8,9,10,11} Initial studies with Au-C bonded single-molecule junctions were observed by Venkataraman's group on methylene terminated oligophenyls and polymethylene chains which shows near resonant transport and enhanced conductance compared to other end-groups.⁷ Hong *et al.* characterized the (oligo)-phenylene-ethynylene (OPE) derivatives using Raman scattering¹¹ and Arasu *et al.* proposed bipodal platforms based on biphenylene with two Au-C bonds which shows very stable and interesting electronical properties of Au-C anchoring scheme.¹²

The experimental fabrication of the junction from a solution is the critical step. For the creation of direct Au-C bond, one possibility is to functionalize the molecule with the highly toxic SnMe₃ group which cleaves off on contact with Au electrodes.^{6,7,13} The *in situ* cleavage of trimethylsilyl group attached to alkynyl moiety using tetrabutylammonium fluoride is an alternative.¹¹ Recently, another binding mechanism based on alkynyls forming direct Au-C bonds without the need for any precursor was reported.¹⁴ So far, all these experiments have been performed in solution at room temperature. The characterization with photoemission spectroscopy has shown that it is also possible to form Au-C bonds in ultrahigh vacuum conditions.¹⁵ Sheer's and Rigaut's groups have been collaborating to fabricate and characterize single-molecule junctions with direct Au-C covalent σ bonds at low temperature (4.2 K) under vacuum conditions. The computational studies were performed to give some insights for the interpretation of the experimental results.

The three studied oligophenyl-diethynyl molecules with alkynyl end-groups, OPA_n ($n = 2, 3, 4$) where n represents the number of phenyl units, are shown in Figure 1. They have been synthesized in the group of Rigaut. The MCBJs, which were fabricated by Scheer and coworkers are robust and the results are reproducible over several weeks at $T = 4.2$ K which allows to carry advanced physical characterization among which inelastic electron tunneling spectroscopy (IETS). Although IETS observations are known for several other anchoring groups,^{16,17,18} an experimental characterization of the vibrational modes from single-molecule junctions with Au-C linkers were still unknown before this work. This chapter presents the main experimental results obtained by our collaborators. We performed quantum chemical calculations at the density functional theory (DFT level) for the isolated molecules and tight-binding density functional theory (DFTB) level for both isolated and gold-coordinated molecules.

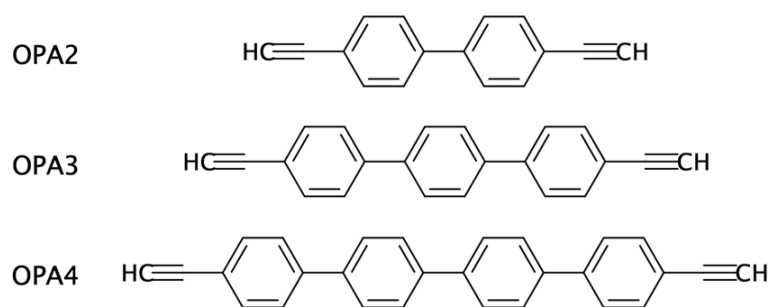


Figure 1 – The bare oligophenyl-diethynyl molecules with alkynyl end-groups (OPA_n) used in this study. Number of phenyl rings $n = 2, 3, 4$.

II – Experimental data and characterization by Rigaut's and Scheer's groups

The group of Scheer prepared the OPA_n molecule solutions with DCM as solvent under nitrogen atmosphere to make single molecule junctions with the MCBJ technique (see Part II, Chapter I). The yield of molecular junctions formed with low concentrations was very small, as seen in Figure 2. In contact with the gold electrodes, the hydrogen atoms at the outer ends of the molecules cleave off to form direct Au-C bonds.¹⁹ This method avoids the use of any additional precursor which could leave non-desired groups in the solution. Electrical transport measurements were carried out at 4.2 K. First, they opened and closed the samples to form Au contacts and molecule junctions repeatedly. The conductance $G = I/V$ was measured at fixed bias voltage across the junctions. The evolution of G is evaluated as a function of displacement between the gold electrodes. From these data, 1-D conductance histograms can be created.

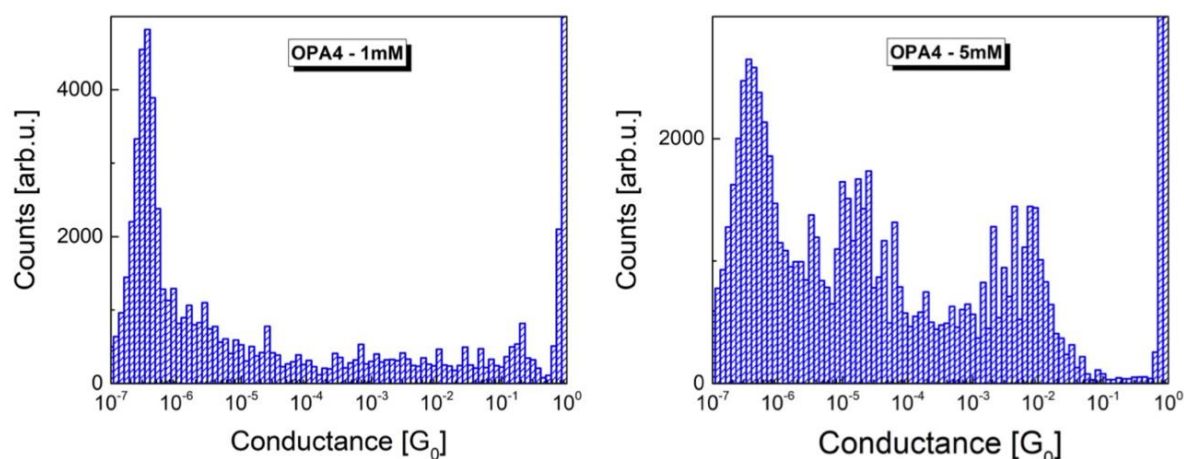


Figure 2 – Example highlighting the difficulty to obtain molecular junctions with low concentration (left, 1 mM) compared to higher concentration (right, 5mM) for OPA4 molecules.

Figure 3 shows representative traces obtained for each device. The noise floor of the conductance measurement is below $10^{-6} G_0$. Au single-atom contacts form on every opening trace, as confirmed by the plateau formation at $1 G_0$. After the Au-Au contacts breaks, several conductance plateaus at different G for the different molecules are observed and are attributed to the formation of molecular junctions. The length of plateaus should increase with molecular length but exceptions are found in this study. Upon further stretching of the junctions, their conductance finally drops to noise level indicating the breaking of the junction. The theoretical lengths of fully stretched Au-OPAn-Au junctions are 1.2, 1.6 and 2.1 nm, for $n = 2, 3$, and 4, respectively.¹⁴ It should be noted that the uncertainty in the determination of the plateau length in the MCBJ method is about 30 %.²⁰ In addition, they study the IET spectra of individual junctions by using a lock-in technique in a bias range from -300 mV to 300 mV and an AC modulation voltage of 3 mV.

III – Results and analysis

Figure 3 shows representative opening traces and corresponding 1-D histograms obtained from 300-500 traces measured at a bias voltage of 100 mV. In these histograms, the maxima are labeled HC for high conductance and LC for low conductance. The histogram of OPA2 has one conductance shoulder (HC) around $1.5 \cdot 10^{-4} G_0$ and another (LC) at around $2.1 \cdot 10^{-5} G_0$ (Figure 2b). The majority of OPA2 opening traces has flat plateaus near $10^{-4} G_0$ with a length of 0.2-0.5 nm. Slanted plateaus of length up to 1.5 nm starting above $10^{-4} G_0$ and decreasing upon

stretching are also observed. The latter can be attributed to the presence of dimerized OPA2 systems in the junctions (OPA2-OPA2) resulting of alkyne homo-coupling and the possibility of having a part of the molecule lying over the electrode surfaces, as sometimes observed for long molecules.^{21,22,23}

The OPA3 shows pronounced flat plateaus around $10^{-4} G_0$ of length 0.6 to 1 nm as shown in Figure 2c, corresponding to a single OPA3 bridged molecule. The conductance at OPA3 molecular plateaus is slightly higher than that of OPA2, which agrees with the reported room temperature studies.¹⁴ The OPA3 histogram has a HC close to $2 \cdot 10^{-4} G_0$ and the probability of stretched junctions extends until a LC of $10^{-5} G_0$ (Figure 2d).

OPA4 exhibits five different kinds of molecular traces in contrast to OPA2 and OPA3. Figure 2e shows the frequently observed traces for OPA4 which are based on observed conductance, plateau length and probability of formation:

- Type I – long plateaus up to 1.5 nm and conductance between $10^{-2} G_0$ and $10^{-3} G_0$.
- Type II – longer plateaus up to 2 nm with a conductance around $10^{-5} G_0$.
- Type III – flat plateaus at higher ($10^{-3} G_0$) and lower conductance ($10^{-5} G_0$) with plateau length around 0.5 nm.
- Type: IV – Slanted plateaus starting at lower conductance ($10^{-4} G_0$). Very short lengths, less than 0.5 nm
- Type V – Slanted plateaus starting at higher conductance ($10^{-2} G_0$). Very short lengths, less than 0.5 nm

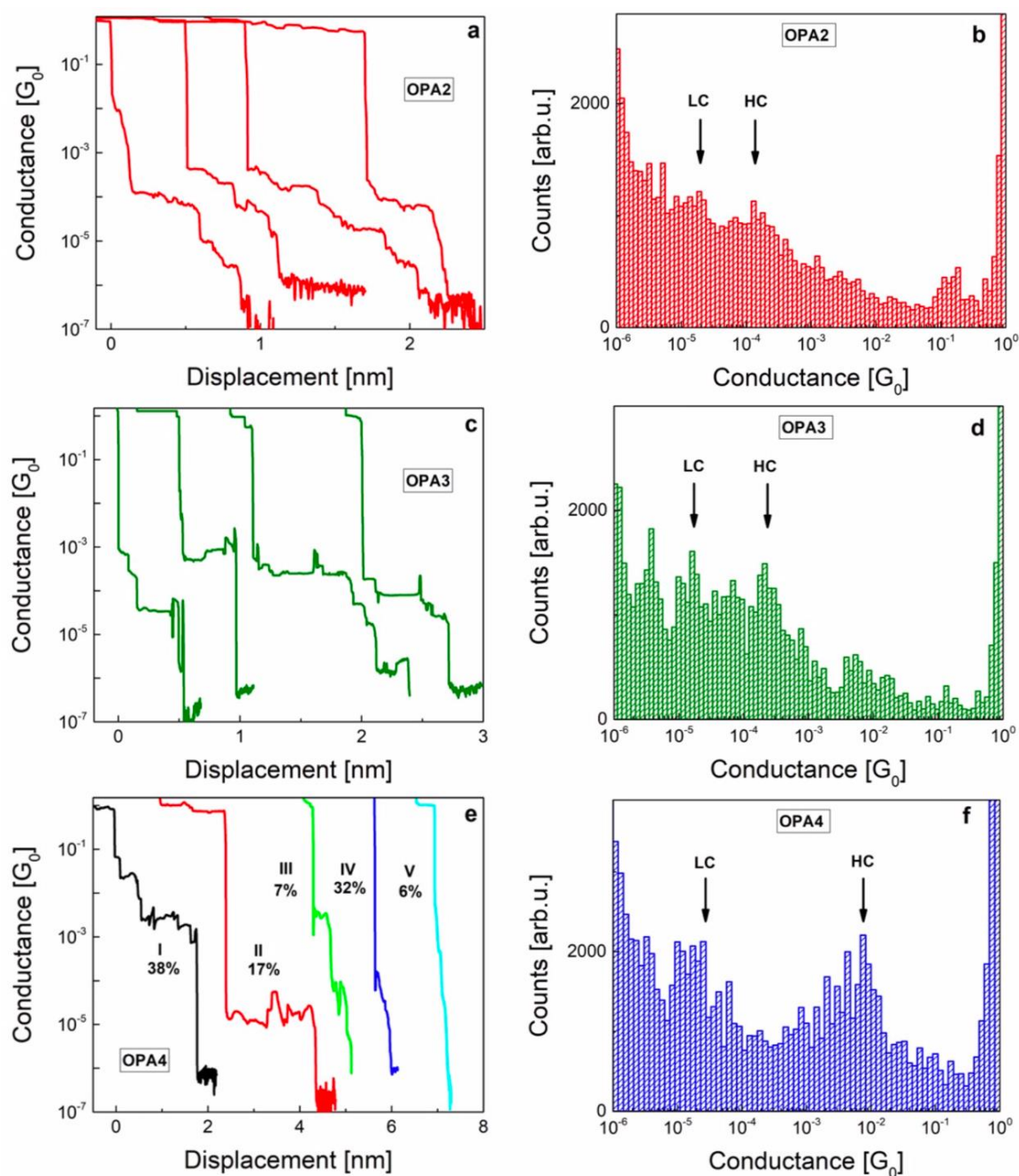


Figure 3 – Examples of opening traces with molecular plateaus and 1-D histograms observed for OPA2 (a, b), OPA3 (c, d) and OPA4 (e, f) respectively with an applied bias voltage of 100 mV. Displacement is measured as the inter-electrode distance upon stretching the junction. Maxima of histograms are labelled as HC and LC for higher and lower conductance respectively. The probability of each type of traces observed from the OPA4 molecule is also shown.

To confirm the traces, OPA4 measurement on multiple samples and statistical evaluation were carried out by the group of E. Scheer. The molecular junction (OPA4) yield creation was 32 %.

The majority of traces falls into Type I with 38 % probability and Type II with 17 %, which agrees with the molecular junction conductance found in previous studies at ambient conditions.¹⁴ The possibility of parallel π - π stacking of the molecules could give rise to Type I traces.²⁴ Type IV with 32 % can be associated with junctions chemically bonded to only one electrode. Type III 7 % and Type V 6 %, indicate that some molecular junctions could not be well connected to the electrodes and breaks apart easily upon stretching, resulting in short plateau lengths.

An increase in conductance (HC case) as the number of phenyl groups increases is found, which is in contradiction with the usual trend of exponential decay of conductance with molecular length for hydrocarbon molecules in off-resonant transport.²⁵ However, a non-exponential, but still decreasing conductance with length was previously found by another group for OPA_n junctions in room temperature conditions.¹⁴ The authors noted a pronounced variation of the most probable conductance based on the concentration of the solution, suggesting that the formation of molecular junctions connected in parallel might play a role. The strength of the experimental MCBJ setup at low temperature is to allow to provide further evidence for Au-C coordinated molecular junctions by analyzing the IET spectrum.

The IET spectrum is defined as d^2I/dV^2 normalized with the differential conductance dI/dV to compare spectra gathered from junctions with different conductance. The spectra were measured over a fixed bias range of -300 mV to 300 mV and symmetrized using the formula $y = [f(x) - f(-x)]/2$, to suppress contributions that might arise from conductance fluctuations or other phenomena since an IET spectrum is supposed to be symmetric.²⁶ The IETS for OPA3 and OPA4 junctions with conductance around $10^{-3} G_0$ were performed. In the case of OPA2, the IET spectrum was numerically derived from the dI/dV curve of a HC junction due to the limited lock-in sensitivity in this conductance range. Figure 4 compares experimental and symmetrized IETS from 0 - 300 mV for each OPA_n molecule. Previous studies of surface enhanced Raman characterizations on molecular systems involving Au-C covalent bonds determined the Au-C stretch to lie around 46-52 mV.^{11,27} Later, Giuseppe et al. using first principle simulations of IETS in metal-molecule junctions, found a signature of the Au-C stretch vibration mode near 60-70 mV.²⁸ The OPA_n devices show bands around 60-75 mV, which we attribute to the vibrations of Au-C bond. The C \equiv C stretching mode is also observed in all molecular junctions around 250-270 mV as shown in Figure 4.¹¹ Typical Au phonon mode near 10-20 mV,²⁹ ring breathing near 140-160 mV and typical ring vibrations at 190-220 mV

in all molecules were also observed.^{30,31,32} The strong signature of Au-C and C≡C vibration modes provides a direct evidence of stable Au-C coordinated molecular junction.

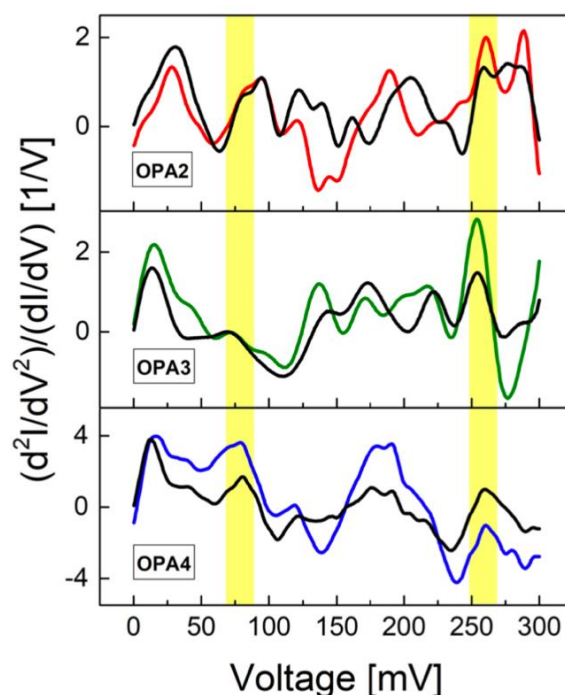


Figure 4 – Experimental inelastic electron tunneling spectra (IETS) for OPA2, OPA3 and OPA4 with red, green and blue curves respectively. Symmetrized IETS spectra calculated for each molecular junction with $y = [f(x) - f(-x)]/2$ in black lines. The yellow regions indicate the typical energies of Au-C vibrations (60-75 mV) and C≡C stretching mode (250-275 mV).

IV – Computational study

IV.1 – Computational Details

Molecular geometry optimizations of the OPA systems were performed applying the density functional theory method (DFT with the revPBE functional using a Slater TZ2P atomic basis set with a small frozen core), as implemented in the SCM ADF suite of program.³³ Analytical vibrational frequency calculations were performed, including the calculation of the infrared and Raman intensities; the calculated frequencies ensure that all geometries correspond to a minimum on the potential energy surface. The densities of vibrational states were also plotted by using a Gaussian broadening for each vibrational state (with a FWHM = 3 meV).

The simulation of the vibrational properties of the Au-molecule-Au junctions and mono-coordinated Au-molecule systems were simulated by an Au₃ cluster model using the self-consistent-charge density functional tight-binding method (SCC-DFTB) using the DFTB+, 20.1 code.³⁴ Additional calculations showed no sensible changes in the vibrational property results when increasing the cluster size up to Au₁₃. The parameter sets “mio” and “auorg” were used. The geometry optimizations were converged imposing a force criterion of 1.10^{-5} a.u. In all cases, no imaginary frequencies were found ensuring that all geometries correspond to a minimum of the potential energy surface (MODES procedure). The densities of vibrational states were obtained by using a Gaussian broadening for each vibrational state (FWHM = 3 meV).

The calculations of the transport properties of the molecular junctions were performed by coupling the DFT with the NEGF approach, as implemented in the QuantumATK 2020 package.³⁵ The geometries obtained for the isolated molecules were used to build the molecular devices. The distance between the terminal carbon and the flat gold surface was set at 1.97 Å in a top position (optimized distance obtained with the DFTB calculations with the cluster model). The semi-infinite gold electrodes were cleaved in the (111) direction. Ghost atoms were added near the gold surface which is used to add basis sets to better depict the surfaces. The ATK computational details used are: GGA RevPBE exchange-correlation functional; FHI atomic basis set double-zeta plus polarization for C and H and single-zeta polarized basis for Au; SCF accuracy tolerance of 1.10^{-5} Hartree; Density mesh cut-off 100 Hartree; $5 \times 5 \times 75$ k-points (along the a, b, and c directions, with c the transport direction) using the Monkhorst-Pack grid; Weighted semi-circle method with integral lower bound of 1.85 Hartree and 50 circle points; Fast Fourier transform 2-D Poisson solver. The zero-bias transmission spectra were simulated by calculating 801 points between -2.0 eV and 2.0 eV (Fermi energy located at 0.0 eV), with 5×5 k-points in the a and b direction.

IV.2 – Computational Results

In order to get a theoretical insight into the understanding of the IETS spectra, quantum-chemical calculations at the density functional theory (DFT level) for the isolated molecules and tight-binding density functional theory (DFTB) level for both isolated and gold-coordinated molecules were performed.

DFT phonon calculations of the entire molecular junctions could not be performed because of excessive memory requirements. In Figure 5 is represented the DFT simulated density of vibrational states for the OPA2, OPA3 and OPA4 bare molecules with their simulated infrared and Raman spectra. The vibrational mode frequencies are in good agreements with the experimental data. The calculated $C\equiv C$ stretching mode is at 265 meV for the three compounds, and the IR $C\equiv C$ experimental frequency is at 261 meV for OPA2 and OPA3.^{40,36}

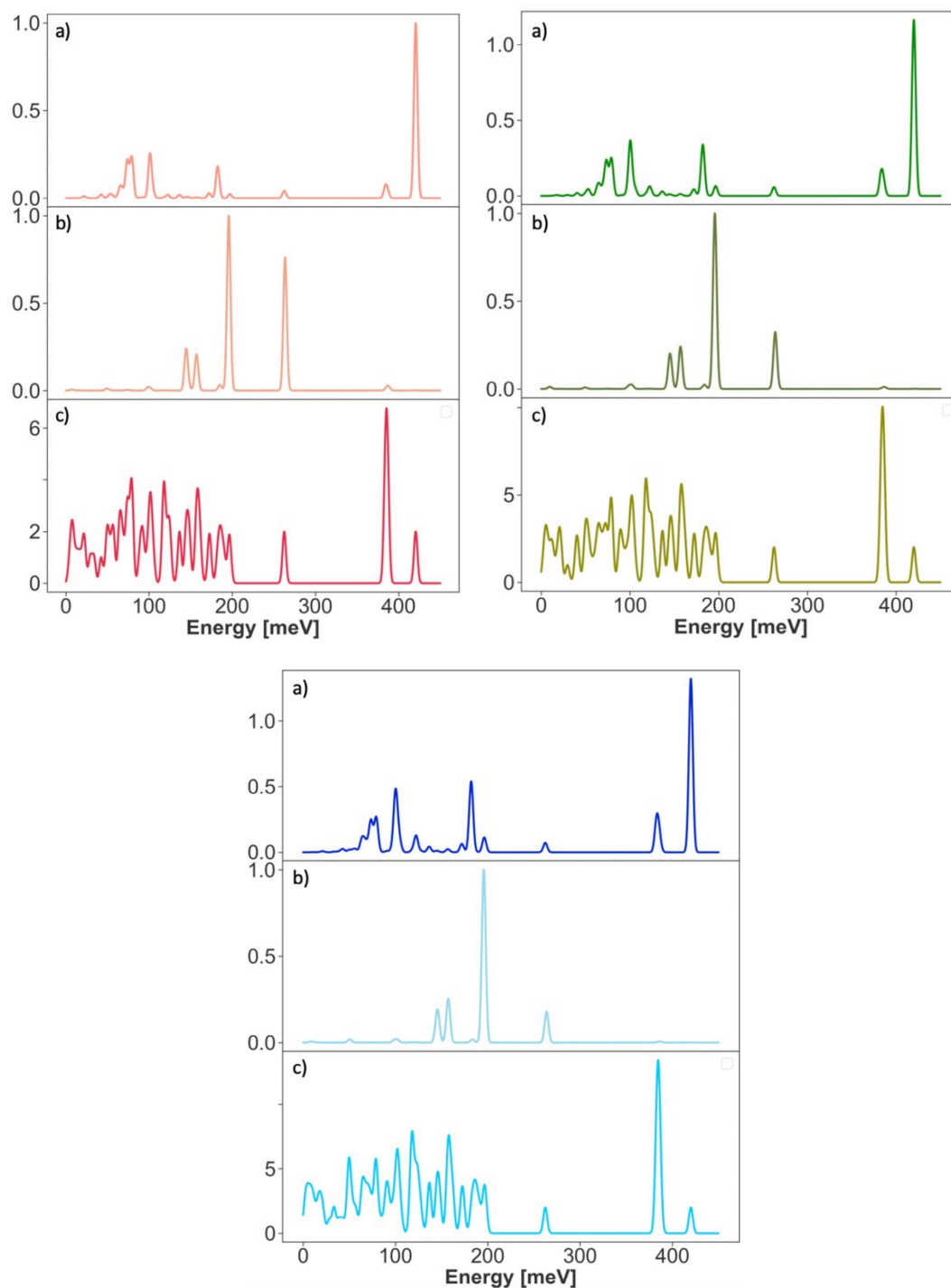
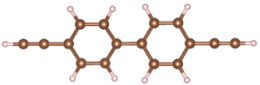
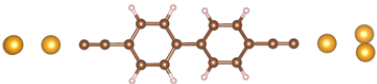
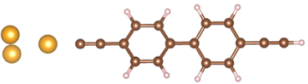
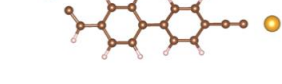
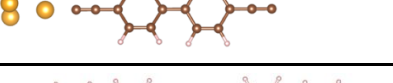
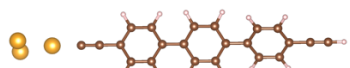
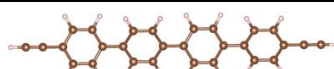


Figure 5 – Vibrational study for the OPA2 (top left), OPA3 (top right) and OPA4 (bottom) molecules at the DFT level. a) Calculated IR normalized intensity. b) Calculated normalized Raman intensity. c) Calculated vibrational density of states.

The DFTB calculations on the DFTB optimized structure overestimate by 18 meV this vibrational mode mainly because of the change in interatomic distances; nevertheless, the overall density of the vibrational state spectra is in really good agreement between DFT and DFTB results, as shown in Table 1.

Table 1 – DFTB calculated energies of characteristic vibrational modes (meV) and their localization for OPA2, OPA2-OPA2, OPA3 and OPA4 molecules (DFT energies are given in parentheses) and coordinated to two Au₃ clusters at both ends (A), or coordinated to one Au₃ cluster (B). For OPA2, different coordination scenarios were added (see text).

| | Coordination | Mol. length (nm) | Au-C | C≡C | C=C-H |
|---------------------|---|------------------|------|------------|-------|
| OPA2 |  | 1.46 | - | 283 (265) | - |
| OPA2-A |  | 1.24 | 38 | 275 | - |
| OPA2-B |  | 1.35 | 26 | 275 283 | - |
| OPA2-C |  | 1.39 | 43 | 249 | - |
| OPA2-D |  | 1.16 | 43 | - | 220 |
| OPA2-E |  | 1.21 | 48 | 275 | 219 |
| OPA2-F |  | 1.25 | 27 | 274 267 | - |
| (OPA2) ₂ |  | 2.84 | - | 283 | - |

| | | | | | | |
|------------------------|---|------|----------|------------|-----|--|
| | | | | | 290 | |
| (OPA2) ₂ -A |  | 3.02 | 42 | 275 290 | - | |
| OPA3 |  | 1.90 | - | 283 (265) | | |
| OPA3-A |  | 1.68 | 40 | 275 | - | |
| OPA3-B |  | 1.78 | 37. 3 | 275 283 | - | |
| OPA4 |  | 2.32 | - | 283 (265) | - | |
| OPA4-A |  | 2.11 | 38 | 275 | - | |
| OPA4-B |  | 2.21 | 36. 5 | 275 283 | - | |

This gives us confidence in the qualitative trends which can be obtained by the tight binding DFT approach. The vibrational study was extended to gold-coordinated molecules by employing a cluster-type model, i.e., by coordinating the terminal carbon atoms to Au₃ gold clusters. The geometries of the OPA2, OPA3 and OPA4 backbone were fully optimized at the DFTB level. Additionally to a carbon-gold coordination at both ends of the molecule (A), a single coordination to one of the electrodes was also considered (B). Alternative scenarios were considered for OPA2: arrangement in which the terminal hydrogen does not leave upon binding (C); the same arrangement considering that hydrogen migration occurs to the adjacent carbons (D); a non-symmetrical configuration with case A on one side and case C on the other side (E); single gold-coordination as in case B but considering that the terminal hydrogen would have been removed during the process.

The vibrational signature of the Au-C-(molecule) binding is calculated in the range 30-50 meV for the whole series; this is a value probably underestimated (due to the cluster-type model) but in line with the IETS results and reference 11 and 27 reinforcing the chemical anchoring scheme. It has to be noted that these low-energy vibrational modes are a collective motion of atoms involving gold atoms and most of the carbon atoms of the molecules. The results in Table 1 reveal that the triple C≡C bond vibrational modes are lowered by roughly 10 meV when the terminal carbon is substituted by Au₃ (OPAn-A). This Au₃-C≡C vibrational signature is found

at roughly 275 meV for these symmetrical systems. The calculated density of vibrational modes of the OPA2-A system reported in Figure 5 reveals that this peak is well-separated from the rest of the vibrational modes (same result for OPA3-A and OPA4-A). The IETS spectra show effectively this signature for the HC regime junctions. Interestingly, the IETS of OPA2 in this region show at least two peaks (Figure 4). Several scenarios were intended to explain this feature. First, only one end of the molecule was chemically anchored (case B and F). In the same energy region, their vibrational signatures are made of two distinct vibrational C≡C modes separated by less than 10 meV. The presence of the (C≡)C-H stretching above 400 meV as shown in Figure 6 would permit us to discriminate between the two configurations but this part of the IETS spectrum cannot be accessed because of experimental stability issues. Nevertheless, since the IETS were done on the HC regime junctions, the calculated substantial drop in the conductance for single-gold-coordinated systems rule out these possibilities (see below).

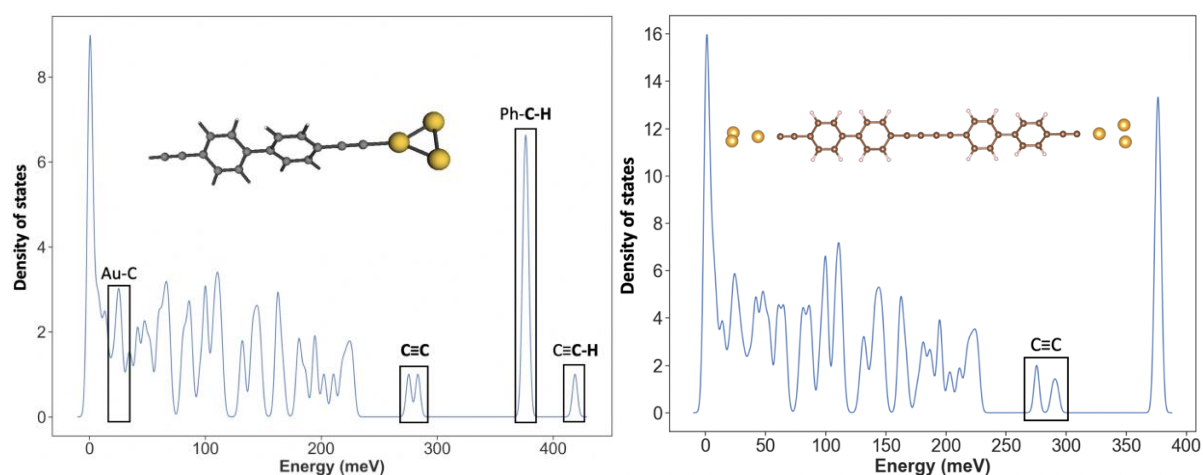


Figure 6 – DFTB vibrational density of states of OPA2-B (left) and (OPA2)₂-A (right).

In a recent paper, van der Zant *et al.* reported ambient condition MCBJs measurements of the OPAn series and suggested a sp^2 -hybridized carbon to explain the unusual ordering in conductance when increasing the number of phenyl groups such as the presence of two distinct high-count conducting behavior.¹⁴ We performed the vibrational study of the arrangement C, D and E to study this possibility (Table 1). Doing so, the vibrational signature of a C≡C around 275 meV disappears and the C=C vibrational modes is lower in energy, 250 meV in case (C) and down to 220 meV for case (D) and (E) (in the same region as the phenyl vibrational region). This result does not satisfactorily explain the IETS measurements.

Considering that some opening traces that show plateaus which are larger than OPA2 (Figure 3a) can suggest the presence of longer molecules, we investigated the possibility of the presence of a dimer OPA2-OPA2 resulting from C-C coupling. This reaction was observed experimentally for OPA3 by Klappenberger and co-workers by covalent homocoupling of terminal alkynes on Ag(111) metallic surfaces.⁴⁰ Gold is also able to induce the same reaction as recently reported for phenylacetylene homo-coupling.³⁷ The (OPA2)₂ vibrational signature in the region around 275 meV is made of two distinct peaks separated by 15 meV and are due to the terminal vibrational motion of the C≡C and the C≡C-C≡C central units of the molecule. This could explain the more structured IETS peaks for OPA2 measurements.

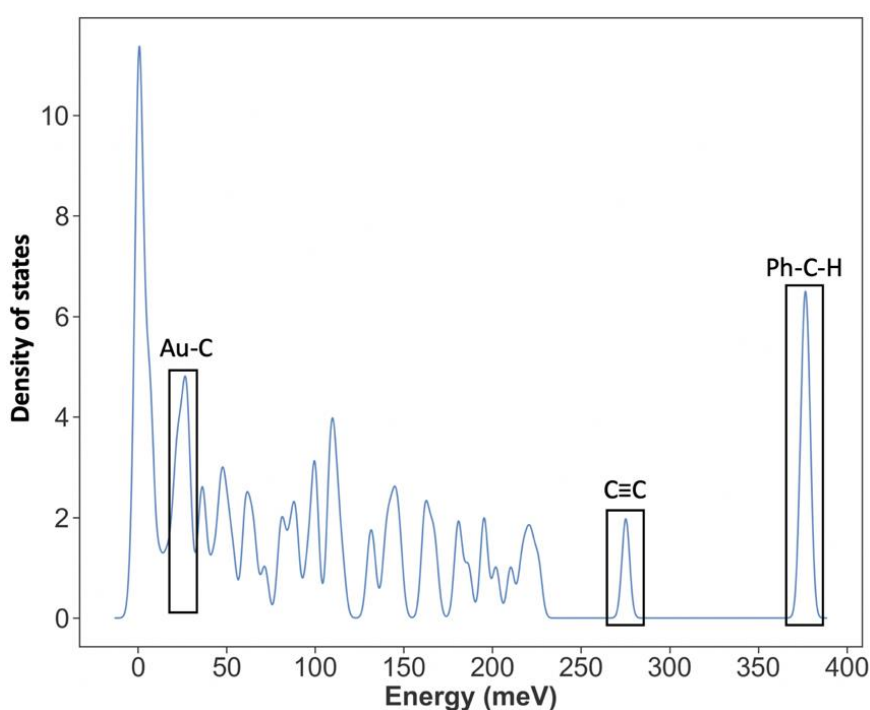


Figure 7 – DFTB-calculated density of vibrational states for the Au₃-OPA2-Au₃ system.

Transmission spectra of Au-OPAn-Au junctions were calculated at the DFT/NEGF level (see Part II, Chapter I for computational details). In case of chemical anchoring, the terminal carbon has been positioned in top coordination mode on (111) cleaved gold electrode surface (Figure 8). The corresponding transmission spectra are given in Figure 9.

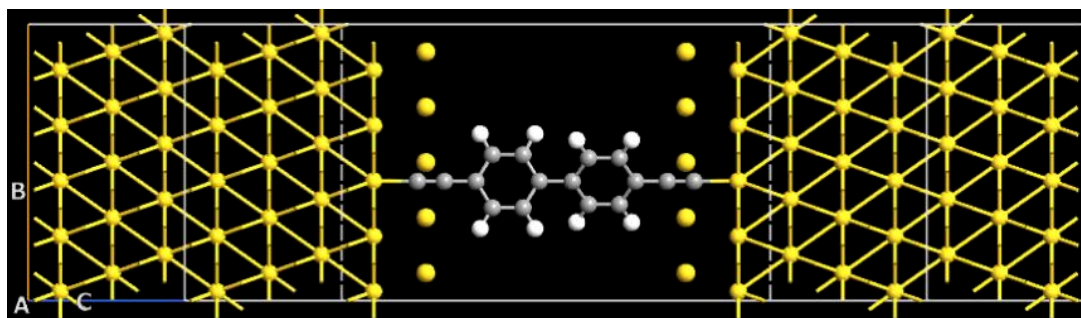


Figure 8 – Representation of the OPA2-A molecular device as simulated in Quantum ATK 2020. The yellow spheres above the gold surfaces represent ghost atoms.

The calculated conductance are about 2 orders of magnitude higher than the experimental high conductance peak for the symmetric OPA2, OPA3 and OPA4 junctions as expected for this level of theory with this most stable coordination.³⁸ The calculated evolution of $\log(G/G_0)$ with increasing number of phenyl rings is shown in Figure 10. The calculated exponential decay $\beta = 1.05$ is in line with the usual exponential decay reported in literature. This value is 1.58 for the parent oligophenyl dithiol junctions.³⁹ The OPA2-OPA2 junction was also added to the series and turns out to have a conductance value intermediate between OPA3 and OPA4. Considering that some of the experimental opening traces associated with high conductance peak plateau over more than 2 nm, one plausible explanation is presence of dimerized OPA2 systems in the junctions (OPA2-OPA2) resulting of alkyne homocoupling. For the junctions in which OPA2-OPA2 molecules would be trapped, the possibility of having a part of the molecule lying over the electrode surface, as sometimes observed for long molecules, could explain opening traces in which a regular decrease of conductance is measured with the displacement.

The large panel of conductance measured for OPA2 reveals a large variety of molecular junction types in which OPA2-A is in competition with $(\text{OPA2})_2$. Such dimerization is surely occurring for OPA3, as already shown experimentally,⁴⁰ and for OPA4; however, the resulting length of the dimeric systems, especially for OPA4 diminishes their probability to form molecular junctions via the present MCBJ method.

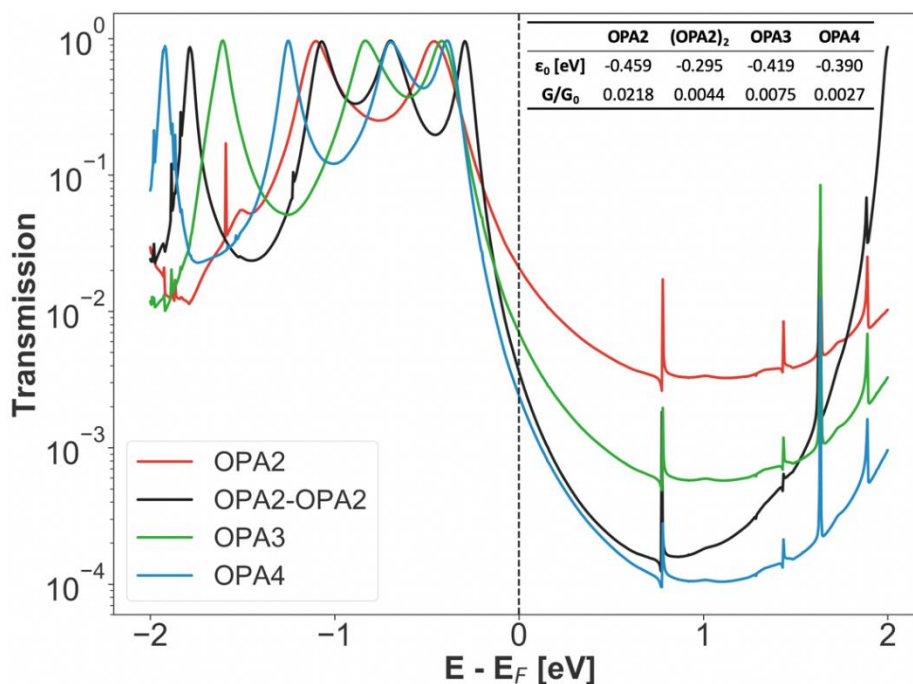


Figure 9 – Transmission spectra of OPA2, OPA3 and OPA4 at zero bias. ϵ_0 given in eV is the energetic position of the main peak responsible for the conductance of the system with respect to the Fermi energy, G/G_0 is the conductance.

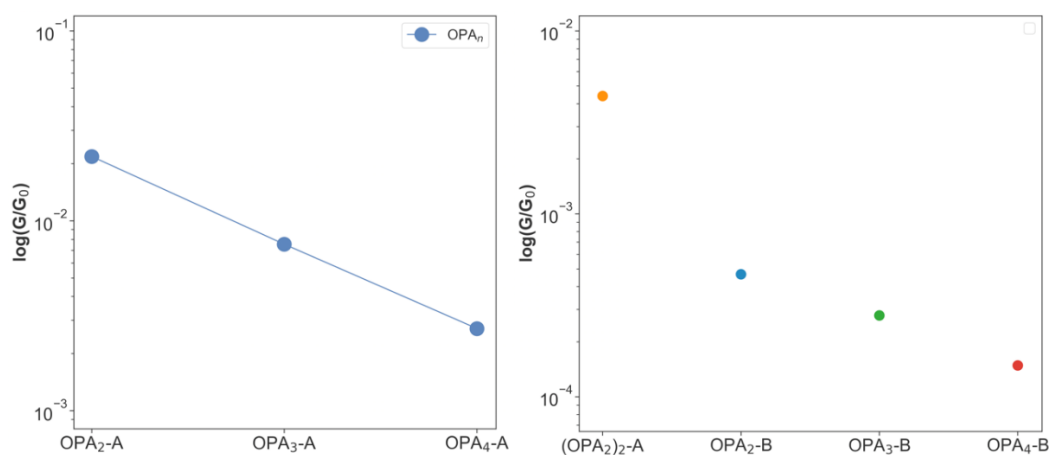


Figure 10 – Log (G/G_0) as a function of the number of phenyl rings in the OPAn molecules with an exponential decay factor $\beta = 1.05$ (left) and for the scenarios OPAn-B and $(OPA2)_2$ -A (see Table 1).

For the B scenario, only one side of the molecule is covalently coordinated to the electrode (the other side is at van der Waals distance with $H-Au = 2.86 \text{ \AA}$). The transmission difference between the A and B scenario is given in Figure 11. The ϵ_0 is quite similar between both cases, but the conductance diminishes by about 2 orders of magnitude (from 10^{-2} to 10^{-4} , see Table 2)

when going from A to B. In the B case, $\log(G/G_0)$ evolves as a function of the number of phenyl rings with $\beta = 0.57$.

Table 2 – Comparison of the linear conductance G/G_0 of the OPAn-A and OPAn-B molecules, as calculated with the (DFT+NEGF method).

| Name | G/G_0 | Name | G/G_0 | A/B Ratio |
|--------|---------|--------|---------|-----------|
| OPA2-A | 0.0218 | OPA2-B | 0.0005 | 44 |
| OPA3-A | 0.0075 | OPA3-B | 0.0003 | 25 |
| OPA4-A | 0.0027 | OPA4-B | 0.0002 | 14 |

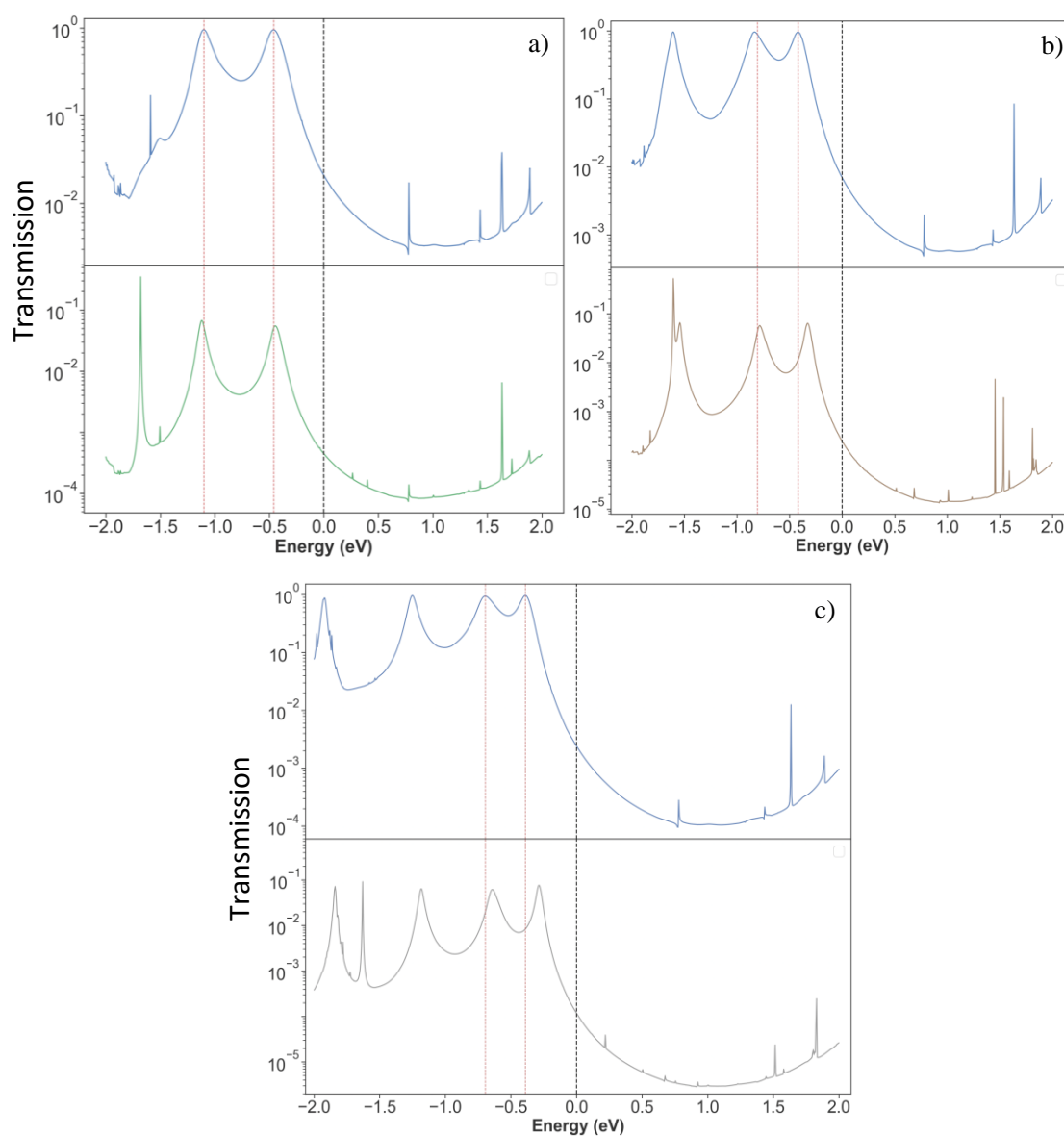


Figure 11 – Transmission spectra for each OPAn-A and OPAn-B system. Top: transmission when both sides of the molecule are connected to the Au surface of the electrodes. Bottom: transmission when only one side is connected to the surface with the other side at the van der

Waals distance H-Au = 2.86 Å. a) OPA2-A and OPA2-B, b) OPA3-A and OPA3-B and c) OPA4-A and OPA4-B.

V – Conclusions

This cooperative work allows us demonstrating that single molecular junctions presenting direct Au-C covalent bonding can be fabricated in situ. Interestingly, the study of the conventional conductance histograms reveals several peaks for all molecules corresponding to different binding configurations. The IETS and detailed phonon mode analysis accessed with DFT calculations revealed the presence of the Au-C vibration mode and the signature of the C≡C band, providing further evidence to our analysis. This shows that the Au-C linking scheme is suitable for the formation of molecular wires as platform for functional molecular devices also at low temperature. The study clearly establishes that although all three molecules belong to the same class of molecular wires with the same end-groups, the formed junctions can be quite different in geometry and in formation yield. Our analysis also demonstrates the importance of the combination of complementary measurement techniques to elucidate the actual nature of the molecular junctions.

-
- ¹ Huang, Z.; Chen, F.; Bennett, P. A.; Tao, N. Single molecule junctions formed via Au-thiol contact: Stability and breakdown mechanism. *J. Am. Chem. Soc.* 2007, 129, 13225-13231. doi:10.1021/ja074456t.
- ² Venkataraman, L.; Klare, J. E.; Tam, I. W.; Nuckolls, C.; Hybertsen, M. S.; Steigerwald, M. L. Single-molecule circuits with well-defined molecular conductance. *Nano Lett.* 2006, 6, 458-462. doi:10.1021/nl052373+.
- ³ Quek, S. Y.; Venkataraman, L.; Choi, H. J.; Louie, S. G.; Hybertsen, M. S.; Neaton, J. B. Amine - Gold linked single-molecule circuits: Experiment and theory. *Nano Lett.* 2007, 7, 3477-3482. doi:10.1021/nl072058i.
- ⁴ Zotti, L. A.; Kirchner, T.; Cuevas, J. C.; Pauly, F.; Huhn, T.; Scheer, E.; Erbe, A. Revealing the role of anchoring groups in the electrical conduction through single-molecule junctions. *Small* 2010, 6, 1529-1535. doi:10.1002/sml.200902227.
- ⁵ Tam, S. E.; Parks, J. J.; Shum, W. W.; Zhong, W. Y.; Santiago-Berrios, M.; Zheng, X.; Yang, W.; Chan, G.; Abruna, D. H.; Ralph, C. D. Single-molecule conductance of pyridine terminated dithienylethene switch molecules. *ACS Nano* 2011, 5, 6, 5115-5123. doi:10.1021/nn201199b.
- ⁶ Cheng, Z. L.; Skouta, R.; Vasquez, H.; Widawsky, J.R.; Schneebeli, S.; Chen, W.; Hybertsen, M.S.; Breslow, R.; Venkataraman, L. In situ formation of highly conducting covalent Au-C contacts for single-molecule junctions. *Nature Nanotech.* 2011, 6, 353-357. doi:10.1038/nnano.2011.66.
- ⁷ Chen, W.; Widawsky, J.R.; Vasquez, H.; Schneebeli, S.; Hybertsen, M. S.; Breslow, R.; Venkataraman, L.; Highly conducting π -conjugated molecular junctions covalently bonded to gold electrodes. *J. Am. Chem. Soc.* 2011, 133, 17160-170163. doi:10.1021/ja208020j.
- ⁸ Widawsky, J. R.; Chen W.; Vasquez H.; Kim T.; Breslow R.; Hybertsen, M. S.; Venkataraman, L. Length-dependent thermopower of highly conducting Au-C bonded single molecule junctions. *Nano Lett.* 2013, 13, 2889-2994. doi:10.1021/nl4012276.
- ⁹ Pla-Vilanova, P.; Aragonés, A. C.; Ciampi, S.; Sanz, F.; Darwish, N.; Diez-Perez, I. The spontaneous formation of single-molecule junctions via terminal alkynes. *Nanotech.* 2015, 26, 381001. doi:10.1088/0957-4484/26/38/381001.
- ¹⁰ Ricci, A. M.; Calvo, E. J.; Martin, S.; Nichols, R. J. Electrochemical scanning tunneling spectroscopy of redox-active molecules bound by Au-C bonds. *J. Am. Chem. Soc.* 2010, 132, 2494-2495. doi:10.1021/ja907867b.
- ¹¹ Hong, W.; Li, H.; Liu, S. X.; Fu, Y.; Li, J.; Kaliginedi, V.; Decurtins, S.; Wandlowski, T. Trimethylsilyl-terminated oligo(phenylene ethynylene): An approach to single-molecule junctions with covalent Au-C σ -bonds. *J. Am. Chem. Soc.* 2012, 134, 19425-19431. doi:10.1021/ja307544w.
- ¹² Arasu, N. P.; Vasquez, H. Direct Au-C contacts based on biphenylene for single molecule circuits. *Phys. Chem. Chem. Phys.* 2018, 20, 10378. doi:10.1039/C8CP00613J.
- ¹³ Schwarz, F.; Kastlunger, G.; Lissel, F.; Riel, H.; Venkateshan, K.; Berke, H.; Stadler, R.; Lortscher, E. High-Conductive Organometallic Molecular Wires with Delocalized Electron Systems Strongly Coupled to Metal Electrodes. *Nano Lett.* 2014, 14, 10, 5932-5940. doi:10.1021/nl5029045.
- ¹⁴ Olavarria-Contreras, I. J.; Perrin, M. L.; Chen, Z.; Klyatskaya, S.; Ruben, M.; van der Zant, H. S. J. C–Au Covalently Bonded Molecular Junctions Using Nonprotected Alkynyl Anchoring Groups. *J. Am. Chem. Soc.* 2016, 138, 8465–8469. doi:10.1021/jacs.6b03383.

- ¹⁵ Batra, A.; Kladnik, G.; Gorjizadeh, N.; Meisner, J.; Steigerwald, M.; Nuckolls, C.; Quek, S. Y.; Cvetko, De.; Morgante, A.; Venkataraman, L. Trimethyltin-Mediated Covalent Gold–Carbon Bond Formation. *J. Am. Chem. Soc.* 2014, 136, 12556–12559. doi:10.1021/ja5061406.
- ¹⁶ Kim, Y.; Song, H.; Strigl, F.; Pernau, H.-F.; Lee, T.; Scheer, E. Conductance and vibrational states of single-molecule junctions controlled by mechanical stretching and material variation. *Phys. Rev. Lett.* 2011, 106, 196804. doi:10.1103/PhysRevLett.106.196804.
- ¹⁷ Kushmerick, J. G.; Lazorcik, J.; Patterson, C.H.; Shashidhar, R.; Vibronic Contributions to Charge Transport Across Molecular Junctions. *Nano Lett.* 2004, 4, 4, 639–642. doi:10.1021/nl049871n.
- ¹⁸ Kim, Y.; Hellmuth, T. J.; Burkle, M.; Pauly, F.; Scheer, E. Characteristics of amine-ended and thiol-ended alkane single-molecule junctions revealed by inelastic electron tunneling spectroscopy. *ACS Nano* 2011, 5, 4104–4111. doi:10.1021/nn200759s.
- ¹⁹ Maity, P.; Takano, S.; Yamazoe, S.; Wakabayashi, T.; Tsukuda, T. Binding motif of terminal alkynes on gold clusters. *J. Am. Chem. Soc.* 2013, 135, 9450–9457. doi:10.1021/ja401798z.
- ²⁰ Metzger, R. M. Unimolecular Electronics. *Chem. Rev.* 2015, 115, 5056. doi:10.1021/cr500459d.
- ²¹ Martin, S.; Grace, I.; Bryce, M. R.; Wang, C.; Jitchati, R.; Batsanov, A. S.; Higgins, S. J.; Lambert, C. J.; Nichols, R. J. Identifying Diversity in Nanoscale Electrical Break Junctions. *J. Am. Chem. Soc.* 2010, 132, 9157–9164. doi:10.1021/ja103327f.
- ²² Cirera, B.; Zhang, Y. Q.; Björk, J.; Klyatskaya, S.; Chen, Z.; Ruben, M.; Barth, J. V.; Klappenberger, F. Synthesis of Extended Graphdiyne Wires by Vicinal Surface Templating. *Nano Lett.* 2014, 14, 1891–1897. doi:10.1021/nl4046747.
- ²³ Mohammadparast, F.; Dadgar, A. P.; Tirumala, R. T. A.; Mohammad, S.; Topal, C. O.; Kalkan, A. K.; Andiappan, M. C-C Coupling Reactions Catalyzed by Gold Nanoparticles: Evidence for Substrate-Mediated Leaching of Surface Atoms Using Localized Surface Plasmon Resonance Spectroscopy. *J. Phys. Chem. C* 2019, 123, 11539–11545. doi:10.1021/acs.jpcc.8b12453.
- ²⁴ Fu, T.; Smith, S.; Camarasa-Gomez, M.; Yu, X.; Xue, J.; Nuckolls, C.; Evers, F.; Venkataraman, L.; Wei, S. Enhanced Coupling through π -Stacking in Imidazole-Based Molecular Junctions. *Chem. Sci.* 2019, 10, 9998–10002. doi:10.1039/c9sc03760h.
- ²⁵ Quek, S. Y.; Choi, H. J.; Louie, S. G.; Neaton, J. B. Length Dependence of Conductance in Aromatic Single-Molecule Junctions. *Nano Lett.* 2009, 9, 3949–3953. doi:10.1021/nl9021336.
- ²⁶ Scheer, E.; Cuevas, J. C. *Molecular Electronics: An Introduction to Theory and Experiment.* World Scientific, 2017. ISBN:978-981-3226-02-9.
- ²⁷ Laurentius, L.; Stoyanov, S. R.; Gusarov, S.; Kovalenko, A.; Du, R.; Lopinski, G. P.; McDermott, M. T. Diazonium-Derived Aryl Films on Gold Nanoparticles: Evidence for a Carbon-Gold Covalent Bond. *ACS Nano* 2011, 5, 4219–4227. doi:10.1021/nn201110r.
- ²⁸ Foti, G.; Vazquez, H.; Sanchez-Portal, D.; Arnau, A.; Frederiksen, T. Identifying Highly Conducting Au-C Links through Inelastic Electron Tunneling Spectroscopy. *J. Phys. Chem. C* 2014, 118, 27106–27112. doi:10.1021/jp5077824.
- ²⁹ Frederiksen, T.; Paulsson, M.; Brandbyge, M.; Jauho, A. P. Inelastic Transport Theory from First Principles: Methodology and Application to Nanoscale Devices. *Phys. Rev. B* 2007, 75, 1–22. doi:10.1103/PhysRevB.75.205413.

- ³⁰ Arroyo, C. R.; Frederiksen, T.; Rubio-Bollinger, G.; Velez, M.; Arnau, A.; Sanchez-Portal, D.; Agraït, N. Characterization of Single-Molecule Pentanedithiol Junctions by Inelastic Electron Tunneling Spectroscopy and First-Principles Calculations. *Phys. Rev. B* 2010, 81, 4–8. doi:10.1103/PhysRevB.81.075405.
- ³¹ Kula, M.; Jiang, J.; Luo, Y. Probing Molecule-Metal Bonding in Molecular Junctions by Inelastic Electron Tunneling Spectroscopy. *Nano Lett.* 2006, 6, 1693–1698. doi:10.1021/nl060951w.
- ³² Paulsson, M.; Frederiksen, T.; Brandbyge, M. Inelastic Transport through Molecules: Comparing First-Principles Calculations to Experiments. *Nano Lett.* 2006, 6, 258–262. doi:10.1021/nl052224r.
- ³³ ADF 2019, SCM, Theoretical Chemistry, Vrije Universiteit, Amsterdam, The Netherlands, <http://www.scm.com>.
- ³⁴ a) Elstner, M.; Porezag, D.; Jungnickel, G.; Elsner, J.; Haugk, M.; Frauenheim, T.; Suhai, S.; Seifert, G. Self-consistent-charge density-functional tight-binding method for simulations of complex materials properties. *Phys. Rev. B* 1998, 58, 7260–7268. doi:10.1103/PhysRevB.58.7260. b) Hourahine, B.; Aradi, B.; Blum, V.; Bonafe, F.; Buccheri, A.; Camacho, C.; Cevallos, C.; Deshayes, M.Y.; Dumitrică, T.; Dominguez, A.; Ehlert, S.; Elstner, M.; van der Heide, T.; Hermann, J.; Irle, S.; Kranz, J.J.; Köhler, C.; Kowalczyk, T.; Kubăr, T.; Lee, I.S.; Lutsker, V.; Maurer, R.J.; Min, S.K.; Mitchell, I.; Negre, C.; Niehaus, T.A.; Niklasson, N.; Page, A.J.; Pecchia, A.; Penazzi, G.; Persson, M.P.; Řezáč, J.; Sanchez, C. G.; Sternberg, M.; Stohr, M.; Stuckenberg, F.; Tkatchenko, A.; Yu, V.W.-Z.; Frauenheim, T. DFTB+, a software package for efficient approximate density functional theory based atomistic simulations, *J. Chem. Phys.* 2020, 152, 124101. doi:10.1063/1.5143190.
- ³⁵ QuantumATK Q-2020 Synopsys. <https://www.synopsys.com/silicon/quantumatk.html>.
- ³⁶ Liu, L.; Liu, Z.; Xu, W.; Xu, H.; Zhang, D.-Q.; Zhu, D. B. Syntheses, optical and electrochemical properties of 4,4'-bis-[2-(3,4-dibutyl-2-thienylethynyl)] biphenyl and its oligomers. *Tetrahedron* 2005, 61, 3813–3817. doi:10.1016/j.tet.2005.01.133.
- ³⁷ Mohammadparast, F.; Dadgar, A. P.; Tirumala, R. T. A.; Mohammad, S.; Topal, C. O.; Kalkan, A. K.; Andiappan, M. C–C Coupling Reactions Catalyzed by Gold Nanoparticles: Evidence for Substrate-Mediated Leaching of Surface Atoms Using Localized Surface Plasmon Resonance Spectroscopy. *J. Phys. Chem. C* 2019, 123, 11539–11545. doi:10.1021/acs.jpcc.8b12453
- ³⁸ a) Kanuru, V. K.; Kyriakou, G.; Beaumont, S. K.; Papageorgiou, A. C.; Watson, D. J.; Lambert, R. M. Sonogashira Coupling on an Extended Gold Surface in Vacuo: Reaction of Phenylacetylene with Iodobenzene on Au(111). *J. Am. Chem. Soc.* 2010, 132, 8081–8086. doi:10.1021/ja1011542. b) Sánchez-Sánchez, C.; Yubero, F.; González-Elipe, A. R.; Feria, L.; Sanz, J. F.; Lambert, R. M. The Flexible Surface Revisited: Adsorbate-Induced Reconstruction, Homocoupling, and Sonogashira Cross-Coupling on the Au(100) Surface. *J. Phys. Chem. C* 2014, 118, 11677–11684. doi:10.1021/jp501321u. c) Sanchez-Sanchez, C.; Orozco, N.; Holgado, J. P.; Beaumont, S. K.; Kyriakou, G.; Watson, D. J.; Lambert, R. M. Sonogashira Cross-Coupling and Homocoupling on a Silver Surface: Chlorobenzene and Phenylacetylene on Ag(100). *J. Am. Chem. Soc.* 2015, 137, 940–947. doi:10.1021/ja5115584.
- ³⁹ Xie, Z.; Bâldea, I.; Smith, C. E.; Wu, Y.; Frisbie, C. D. Experimental and Theoretical Analysis of Nanotransport in Oligophenylene Dithiol Junctions as a Function of Molecular Length and Contact Work Function. *ACS Nano* 2015, 9, 8022–8036. doi:10.1021/acs.nano.5b01629.
- ⁴⁰ Cirera, B.; Zhang, Y.-Q.; Björk, J.; Klyatskaya, S.; Chen, Z.; Ruben, M.; Barthe, J. V.; Klappenberger, F. Synthesis of Extended Graphdiyne Wires by Vicinal Surface Templating. *Nano Lett.* 2014, 14, 1891–1897. doi:10.1021/nl4046747

Chapter IV – Organometallic systems to improve thermoelectric properties

I – Introduction

This second chapter deals with organometallic wires that have been considered to date mostly as conducting molecules, as rectifiers, or for spintronics applications.¹ A great advantage of organometallic complexes is that they are easily adaptable to target desired electronic properties and that they can handle concomitantly several properties (photophysical, redox, magnetic...). The combination of metal atom(s), ancillary ligands, organic conjugated linkers, and anchoring groups offers a vast range of possibilities which can be further modulated by adding functional groups. Moreover, electronic levels associated with the main backbone and pending ligands can couple to generate QI effects, ideally in the vicinity of the Fermi level of the electrodes. A theoretical guidance is clearly necessary to discriminate the best systems among the really large number of chemical compositions. This research is done in collaboration with experimental physicists and chemists to have a comprehensive study that combines computational investigations, synthesis and measurements. The synthesis and characterization of target molecules are done by the group "organometallic and catalysis" in ISCR (OMC). The fabrication and characterization of the molecular devices are done in parallel on single-molecule junctions in the group of Scheer at the University of Konstanz (UKON) and on SAM-based junctions in the group of Vuillaume at the "Institut d'électronique, de microélectronique et de nanotechnologie" (IEMN). The purpose of studying SAM configuration is to assess the possible impact of intermolecular interactions (cooperative effects) on the electrical and TE properties. The comparison between simulations and experimental results is expected to help identifying the factors to be improved in the subsequent molecular design protocol. A target goal would be to obtain thermopower-enhanced molecular units combining high conductance and high Seebeck coefficient. A power generation efficiency of 25 % is an optimum value for most applications.

The field of molecular thermoelectrics has been incredibly productive over the last ten years.² The feasibility and potentiality of molecular modules to achieve thermoelectric effects were demonstrated in 2007.³ Several important milestones have been achieved since then, especially at the experimental level by the first measurements of phonon conductance and of Peltier

cooling in molecular junctions.^{2f} A large part of the investigations has been carried out on main group molecular systems in line with the ongoing work in the closely related domains of molecular electronics.⁴ So far, promising, carbon-, silicon- and more recently bio-based devices are all showing the same experimental drawback: high S but low G and consequently low ZT . For example, Solomon *et al.* reported recently the largest thermopower measured to date for a bicyclo-octasilane junction ($S = 970 \mu\text{V/K}$),⁵ i.e., thirty times higher than the C_{60} dimer representing the best molecular system ever measured before.⁶ Unfortunately, its ZT is very weak ($\sim 10^{-2}$) because of really low conductance values. Large enough G is undeniably necessary to allow for a substantial quantity of converted energy, thus to improve the power factor (S^2G). Nevertheless, κ_{el} increases in parallel to G at the detriment of ZT . A subtle balancing must be found in the search of ideal electronic features and necessitates robust predictive protocols. The present efforts to improve TE properties of molecular devices have been focused on the chemical engineering of the molecular backbone to directly impact the conducting properties G and $\tau(E)$.

The choice of organometallic wires which is to date almost unexplored in thermoelectrics⁷ is based on the previous experimental results obtained by OMC and those of other groups that demonstrate that organometallic MJ can be formed. They are sufficiently robust and show enhanced conducting properties compared to organic wires of similar length and rigidity.^{8,9} This is notably the case for electron-rich systems incorporating transition metal (TM) atoms of group VIII (such as Fe and Ru) in the conjugated backbone. In such systems, the participation of the metal atom in the highest occupied MOs induces a lowering of the oxidation potentials and thus a closest proximity to the Fermi energy. Additionally, MOs similar to the conjugated MOs in the electronic structures of pure organic conjugated wires, and responsible for charge transport are also present in these systems. They are fully delocalized over the molecule and are coupled to the electrodes near the Fermi energy. They present an antibonding character between the metal d orbitals and the p orbitals of the neighboring carbon atoms.^{11,12}

The main strategy proposed to date to enhance thermoelectric properties has been to add pendant units connected to a conjugated organic wire though with limited possibilities of modifications. This increases also typically to a large extent the steric hindrance, which is detrimental to device fabrication.^{3a} On the positive side, this induces QI by a partial electronic confinement over the lateral substituent which creates an abrupt decrease in the electronic transmission near the Fermi level that can, in certain conditions, boost the thermoelectric

properties. Here, instead of introducing additional groups to induce QI, we took advantages of molecular levels already present in the organometallic MJs, i.e. metal-centered and ligand-centered levels. A second strategy, to be combined with the first one, is to conceive multiple-path wires that yield constructive or destructive QI effects due to the phase differences between the multiple conduction pathways.^{5,10} This theoretical concept has been fully demonstrated experimentally and can be transposed to organometallic wires.^{5,11}

Remote control of the thermoelectric properties to alter the electronic conductance is also achievable. Indeed, if the electronic transmission is significantly lowered, the thermoelectric properties will concomitantly decrease. In that respect, external stimuli, such as light,^{12,13} mechanical force,¹⁴ magnetic field,¹⁵ electrical field,¹⁶ and electrochemical potential,¹⁷ have already been used to change the conductance of molecular devices. This is thus directly transferable to TE organometallic molecular devices.

Introducing metal atoms in the conjugated path or in its vicinity allows to:

- Expand the possibilities of structural and electronic modulation compared to organic systems in view of the huge diversity of metal and ligand combinations.
- Benefit from the inherent properties of the transition metals (redox, magnetic, optical).
- Increase easily the number of functionalities by ligand modifications or incorporation of additional chemical functions.



Figure 1 – The general structure of the target organometallic wires.

We have concentrated our efforts on organo-ruthenium and organo-iron systems. They have been shown to engender much better conducting properties than the rest of the transition metals.^{9,18} The good overlap and energetic alignment between Ru and Fe orbitals and carbon atomic orbitals allows to keep the electronic delocalization when the metal centers are incorporated in organic conjugated wires and to decrease the redox potentials. The long-term plan would be to investigate the different systems shown in Figure 2. This family of platforms already exists and exhibits various ligand substitution schemes. In this thesis, we will concentrate on case studies in order to better target the factors that drive the properties for future

developments. The quantum-chemical calculations are done at the DFT level using a GGA functional, triple- ξ atomic basis sets with two polarization functions. The same functional is used for the DFT/NEGF calculations for sake of coherence.

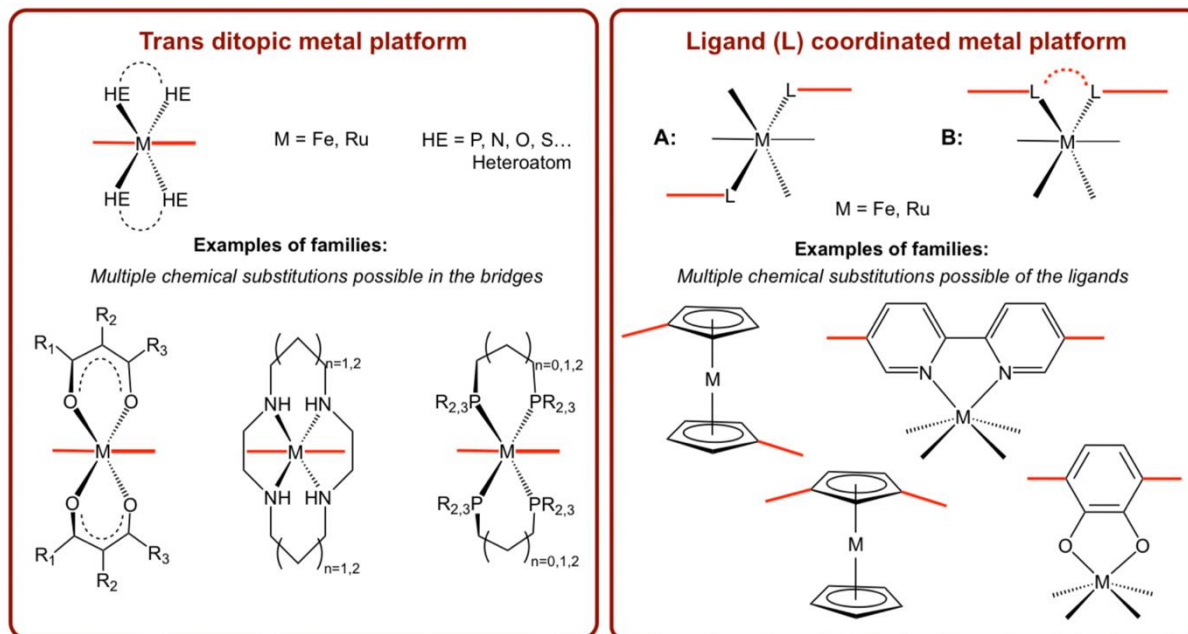


Figure 2 – Structures of candidate organometallic wires

Many possibilities exist for the choice of the conjugated spacers. Some are generating competition among the conducting paths that are creating QI in the transmission, and hence possibilities of TE enhancement. A lot of organic units can be combined to create conjugated linkers of varying nature and length, see Figure 3. The anchoring group also plays an important role notably in defining the strength of the interfacial coupling (Γ), and has thus an impact on the transmission $\tau(E)$. In this study, we deliberately concentrate our efforts on thiol-gold anchoring which provides a warranty of success on the experimental point of view.

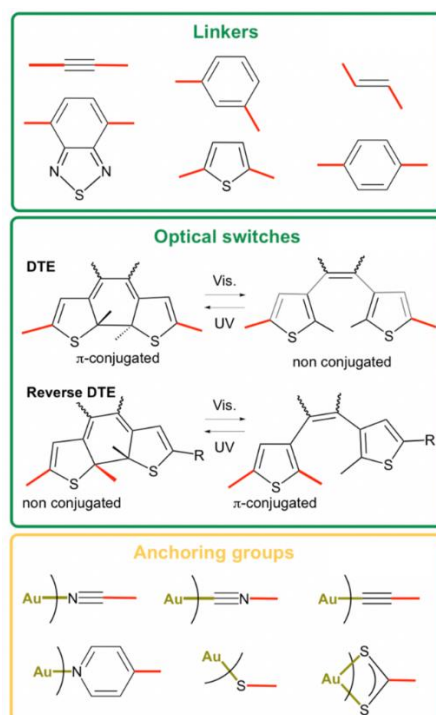


Figure 3 – Typical linkers, optical switches and anchoring groups involved in the candidate organometallic wires.

Calculations in which both the atoms of the organometallic compound and those of the electrodes are treated explicitly at a quantum level can constitute a heavy computational cost, even for DFT. To circumvent this issue, we study the possibility of using a Density Functional Tight-Binding (DFTB) method that consists in an approximate and parameterized DFT scheme (see Part II, Chapter VI). DFTB methods allow to run calculations with costs reduced by two orders of magnitude compared to DFT.

II – Functionalization of the $\text{Fe}^{\text{II}}(\text{cyclam})(\text{C}_2\text{Ph-S})_2$ system

Our first case study system is a $\text{Fe}^{\text{II}}(\text{cyclam})(\text{C}_2\text{Ph})_2$ molecule (with cyclam = 1,4,8,11-tetraazacyclotetradecane) which could be described as a three-phenyl oligo(phenylene-ethynylene), OPE3, in which the central phenyl is replaced by an iron center chelated by a cyclam ligand (see Figure 4). We applied different types of chemical modifications on the cyclam and the phenyl groups of this initial system, Fe-bare, to evaluate the degree of tuning of the electronic transmission depending on the added/modified chemical groups. The studied systems, that have been chosen to screen different possible modifications, are named Fe-methoxy, Fe-fluorine, Fe-benzene and Fe- CH_2COOH and are described in Figure 4.

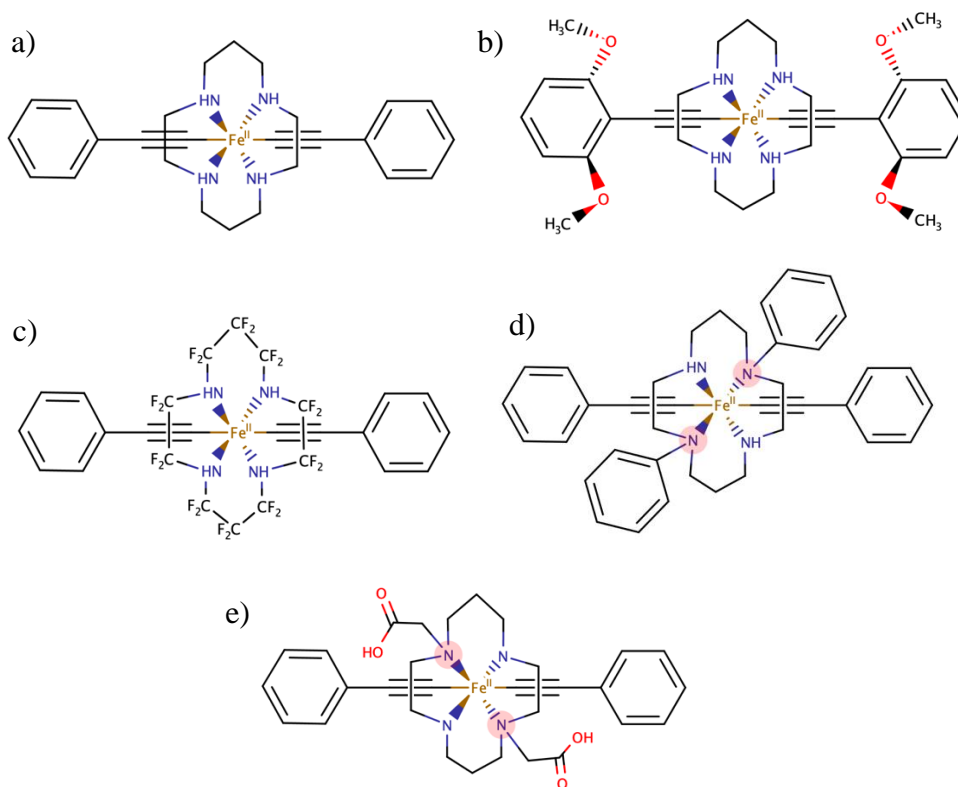


Figure 4 – Chemical structures of the molecules used to test different functionalization schemes: a) Fe-bare. b) Fe-methoxy c) Fe-fluorine d) Fe-benzene and e) Fe-CH₂COOH.

In this first part, two levels of methodology were used: molecular DFT calculations on cluster models and DFT/NEGF in junction configurations. Indeed, since one of the goals of this work is to perform at the end a chemical design to target molecular junctions presenting enhanced thermoelectric properties, numerous simulations need to be done. We thus investigated the reliability of DFT clusters models which are much less resource-demanding to account for some electronic features that could be used to determine the systems to be investigated more deeply.

II.1 – Description of the transport properties using Au₁₃ cluster-type molecular model compared with junction DFT/NEGF calculations

The cluster-model used to mimic a junction configuration consists in replacing the gold semi-infinite electrodes by clusters of several gold atoms. After a preliminary study in which different sizes and coordination modes were investigated, Au₃ clusters have been chosen since this allows recovering geometric and electronic features of the reference DFT junction-type simulations. Indeed, if the cluster size is smaller the ordering of the last occupied molecule-centered and gold-centered levels is reversed compared with the reference DFT junction-type simulations. The odd number of gold atoms allows to form a thiol contact with the molecule

without charging the total system. Finally, the triangular faces of the Au₁₃ gold cluster give access to hollow coordination for the anchoring of the sulfur atoms.¹⁹

The electronic structures of the five compounds sketched in Figure 4 in a junction-like cluster configuration are given in Figure 5. In these molecular calculations, the Fermi level is approximated to the energy of the last occupied gold-centered levels (in yellow, Figure 5). The molecular levels in blue (Figure 5) are those containing a high contribution of iron d orbitals (see Table 1).

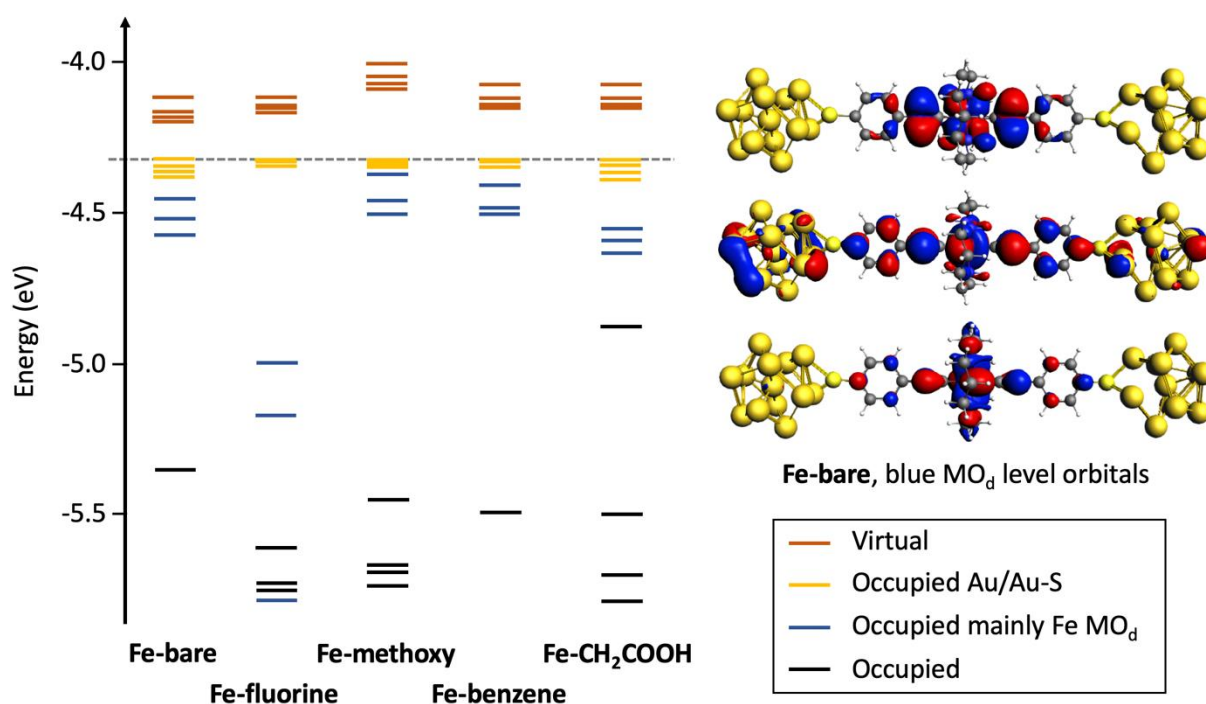


Figure 5 – Left: DFT MO energetic diagram of the 5 systems with Au₁₃ gold clusters coordinated by a thiol group in the hollow position. Right: Representation of the 3 orbitals with the largest iron d character for the Fe-bare cluster. Coloring of the levels: brown = virtual gold-centered MOs, yellow = occupied gold- or gold-thiol-based levels, blue = occupied MOs presenting a predominant d iron contribution (MO_d), black = other occupied MOs.

Table 1 – Description of the MO_d energy levels: $\Delta E(\text{MO}_d\text{-MO}_{\text{Au}})$ is the energy difference in eV between the gold levels and the Fe-centered MO_d; main atomic contributions are also given (> 3 %).

| $\Delta E(\text{MO}_d\text{-MO}_{\text{Au}})$ (eV) | Atomic character | | | |
|---|------------------|-------------------|------------|-------------|
| | Fe | Linker Σ C | Σ S | Σ Au |
| Fe-bare | | | | |

| | | | | | | | |
|-------------------------|------|------|---|------|-----------------|--------|----------------------|
| MO _d 1 | 0.12 | 75 % | 3d _{yz} | 20 % | 1p _y | | |
| MO _d 2 | 0.19 | 42 % | 3d _{xz} | 15 % | 1p _x | | 3 % 2s |
| | | 20 % | 3d _{x²-y²} | | | | |
| MO _d 3 | 0.24 | 70 % | 3d _{x²-y²} | 03 % | 1p _x | | |
| | | 11 % | 3d _{xz} | | | | |
| | | 03 % | 3d _{xy} | | | | |
| Fe-fluorine | | | | | | | |
| MO _d 1 | 0.66 | 33 % | 3d _{xz} | 20 % | 1p _x | | |
| | | 20 % | 3d _{z²} | | | | |
| | | 07 % | 3d _{xy} | | | | |
| MO _d 2 | 0.84 | 56 % | 3d _{yz} | 21 % | 1p _y | | |
| | | 10 % | 3d _{xz} | 03 % | 1p _x | | |
| | | 03 % | 3d _{xy} | | | | |
| MO _d 3 | 1.45 | 30 % | 3d _{xy} | | | 3 % 2p | 3 % 5d _{xz} |
| | | 23 % | 3d _{x²-y²} | | | | |
| | | 10 % | 3d _{xz} | | | | |
| | | 04 % | 3d _{yz} | | | | |
| Fe-methoxy | | | | | | | |
| MO _d 1 | 0.04 | 58 % | 3d _{xz} | 15 % | 1p _y | | |
| | | 13 % | 3d _{yz} | 03 % | 1p _x | | |
| | | 03 % | 3d _{xy} | | | | |
| MO _d 2 | 0.12 | 35 % | 3d _{xz} | 08 % | 1p _x | | 3 % 2s |
| | | 12 % | 3d _{yz} | | | | |
| | | 10 % | 3d _{xy} | | | | |
| | | 05 % | 3d _{x²-y²} | | | | |
| | | 03 % | 3d _{z²} | | | | |
| MO _d 3 | 0.17 | 40 % | 3d _{xy} | 03 % | 1p _x | | |
| | | 37 % | 3d _{x²-y²} | | | | |
| | | 04 % | 3d _{xz} | | | | |
| Fe-benzene | | | | | | | |
| MO _d 1 | 0.08 | 45 % | 3d _{xz} | | | | |
| | | 25 % | 3d _{yz} | | | | |
| | | 04 % | 3d _{x²-y²} | | | | |
| MO _d 2 | 0.15 | 66 % | 3d _{z²} | 17 % | 1p _y | | |
| | | 09 % | 3d _{x²-y²} | | | | |
| | | 04 % | 3d _{xy} | | | | |
| | | 03 % | 3d _{xz} | | | | |
| | | 03 % | 3d _{yz} | | | | |
| MO _d 3 | 0.17 | 33 % | 3d _{x²-y²} | 08 % | 1p _z | | |
| | | 23 % | 3d _{xz} | | | | |
| | | 06 % | 3d _{xy} | | | | |
| | | 03 % | 3d _{z²} | | | | |
| Fe-CH ₂ COOH | | | | | | | |

| | | | | | | |
|-------------------|------|------------------------------|---|--------------|------------------------------------|--|
| MO _d 1 | 0.22 | 34 % 17 % 10 % 15 % | 3d _{yz} 3d _{x²-y²} 3d _{xy} 3d _{xz} | 04 % 03 % | 1p _y 1p _x | |
| MO _d 2 | 0.26 | 46 % 10 % 09 % 04 % | 3d _{xz} 3d _{yz} 3d _{z²} 3d _{xy} | 09 % | 1p _x | |
| MO _d 3 | 0.31 | 44 % 26 % 07 % | 3d _{xy} 3d _{yz} 3d _{x²-y²} | 10 % | 1p _y | |

The analysis of the MO_d levels in terms of atomic orbital participation given in Table 1 reveals in all cases that two of these three MOs are strongly metal centered and poorly delocalized over the conjugated path. We will show later that these orbital shapes are at the origin of Fano resonances. The difference in energy between the MO_d and the last Au-centered MOs which are associated to the Fermi energy of the model junctions can vary importantly depending on the chemical modification performed (Table 1). Considering Fe-bare as the reference system, the fluorination of the methyl groups of the cyclam importantly stabilizes these levels (by up to 0.54 eV). This substitution by electron-withdrawing atoms is detrimental to the conductance. The substitution of the hydrogen atoms on the amine is limited from a synthetic point of view to few possibilities (phenyl, carboxylate). The effect on the electronic structure is more limited but the MO_d Fe-Phenyl get slightly closer to the MO_{Au} levels. Another possibility to reach this is to modify the organic linker notably by adding electron donating groups (OMe here). It has effectively the same effect.

To evaluate the reliability of this cluster-type model, DFT/NEGF calculations were performed on the molecular junction configurations incorporating the same molecules. The computed transmissions as well as the main transmission eigenstates for the Fe-bare case are shown in Figure 6. The latter are obtained as eigenstates of the transmission matrix defined by, as implemented in QuantumATK:

$$g_{n,m} = \sum_k t_{nk} t_{km}^\dagger \quad \text{Eq. 1}$$

where t_{nk} is the transmission amplitude from the Bloch state ψ_n in the left electrode to the Bloch state ψ_k in the right electrode (Bloch's states are Schrödinger's equation solutions in a

periodic potential described as plane waves).²⁰ The transmission eigenstates are obtained by propagating the linear combination of Bloch states:

$$\sum_n e_{\alpha,n} \psi_n \quad \text{Eq. 2}$$

And by finding the $e_{\alpha,n}$ that diagonalize the transmission matrix $\mathcal{G}_{n,m}$, (i.e. the eigenstates) leading to:

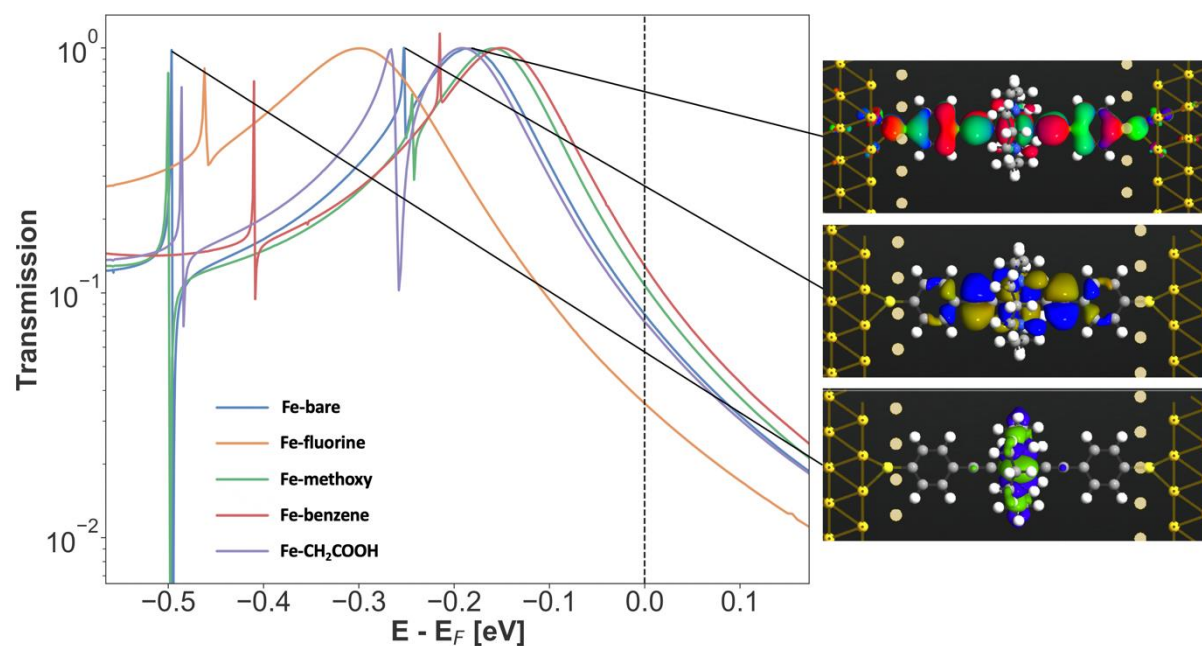
$$\sum_m \mathcal{G}_{n,m} e_{\alpha,n} = \lambda_\alpha e_{\alpha,n} \quad \text{Eq. 3}$$

with λ_α the transmission eigenvalue.

These eigenstates are highly comparable to the Au₁₃-Fe-bare-Au₁₃ MO_d shown in Figure 4. The comparison between the relative energies of the MO_d (Table 1) and the energy of the main transmission states given in Figure 6 allows us to conclude that the cluster model is reproducing qualitatively the main features:

- The ordering is globally the same. For the systems in which the difference between the energies of the MO_d was small, an inversion can be found (Fe-methoxy and Fe-benzene).
- The eigenvalues have the same order of magnitude but the differences are much reduced in the DFT/NEGF scheme (range of energy: 0.04 to 0.66 eV vs 0.15 to 0.30 eV).
- A noticeable discrepancy is the ordering of the highest two MO_d corresponding to a transport level and a localized one.

The device calculation confirmed that Fe-fluorine junction has a transmission main peak too far from the Fermi energy to promote a current at moderate bias voltage. For all the other systems, all transport levels which have a substantial metal character and are strongly coupled to the electrodes are really close to one another in each system (with a variation by less than 50 meV). This could be interpreted as a pinning effect in the system, as shown previously in the literature, notably for organic systems.^{21,22,23}



| $E - E_F$ | Molecular level 1 | Molecular level 2 | Molecular level 3 |
|-------------------------|-------------------|-------------------|-------------------|
| Fe-bare | 0.19 | 0.25 | 0.50 |
| Fe-methoxy | 0.16 | 0.24 | 0.50 |
| Fe-fluorine | 0.30 | 0.46 | < 1.00 |
| Fe-benzene | 0.15 | 0.21 | 0.41 |
| Fe-CH ₂ COOH | 0.19 | 0.26 | 0.49 |

Figure 6 – Top left: computed transmission of the five systems at the DFT/NGEF level. Top right: main transmission eigenstates of the Fe-bare device. Bottom: energy difference in eV between the Fermi level and the main molecular-based transmission states.

We can thus conclude that the Au₁₃ cluster-type model applied to a series of compounds provides electronic structure data that give qualitative trends on their transport properties. Even though not quantitative, it allows to exclude systems in a prospective study and thus limit the number of DFT/NEGF calculations to be performed. It is also interesting for large molecular systems for which the cost of DFT/NEGF calculations can become prohibitive.

II.2 – Thermoelectric properties

The key electronic and thermoelectric parameters extracted from the calculated transmission at zero bias are collected in Table 2. The ZT was calculated considering the thermal phononic κ_{ph} contribution at 20 pW/K. The thermoelectric properties are moderately affected by the chemical modifications performed except for Fe-fluorine whose conductance is really weak compared to

the others. For instance, excluding Fe-fluorine from the comparison, the ZT ranges between 0.256 for Fe-bare to 0.337 for Fe-benzene while the Seebeck coefficient S ranges from 102 $\mu\text{V/K}$ for Fe-bare to 108 $\mu\text{V/K}$ for Fe-methoxy.

Table 2 – Electronic and thermoelectric parameters for the five systems presented in Figure 4 extracted from the computed transmission at zero bias (DFT/NEGF level). S is the Seebeck coefficient in $\mu\text{V/K}$, S^2G the thermopower in pW/mK^2 , G/G_0 the ratio of conductance over the quantum of conductance G_0 , κ_{el} the electronic thermal conductance in pW/K , Q_{cal} the maximum power that can be extracted from one electrode (Peltier effect) in pW and V_p the voltage in mV at which Q_{cal} occurs.

| System | ZT | ZT_{el} | S | S^2G | G/G_0 | κ_{el} | Q_{cal} | V_p |
|-------------------------|-------|-----------|-----|--------|---------|---------------|-----------|-------|
| Fe-bare | 0.256 | 0.324 | 102 | 82 | 0.1021 | 76 | 4037 | -35.0 |
| Fe-methoxy | 0.321 | 0.387 | 108 | 126 | 0.1391 | 97 | 6207 | -37.4 |
| Fe-fluorine | 0.098 | 0.166 | 72 | 16 | 0.0397 | 29 | 742 | -23.0 |
| Fe-benzene | 0.337 | 0.398 | 107 | 147 | 0.1670 | 111 | 7245 | -36.6 |
| Fe-CH ₂ COOH | 0.235 | 0.301 | 99 | 71 | 0.0940 | 71 | 3466 | -33.6 |

These results clearly reveal that substitutions that only alter the energy of the conducting levels and their atomic contributions will not provide sufficient changes to really modify the thermoelectric properties. Alternative routes need to be evaluated, notably the presence of quantum interferences in the transmission features as mentioned in the introduction.

III – Influence of meta/para thiol coordination on transmission properties

Among the different possibilities to generate QIs, multiple-path transmission is a possibility that has fully been demonstrated.^{11a)} We have investigated role of the meta and para coordination of the phenyl groups of the linkers in the organometallic framework, to assess whether QI can be created and what is the impact on the thermoelectric properties. The Fe-bare system was used as case study. Three coordination modes have been tested:

- para-para: both thiols are in para coordination with respect to the external phenyl rings (pp).
- para-meta: one thiol is in meta configuration and the other one in para (pm).
- meta-meta: both thiols are in meta coordination with respect to the phenyl rings (mm).

The electronic transmissions and the transmission eigenstates of the pp-Fe-bare, pm-Fe-bare and mm-Fe-bare are given in Figure 7. The main impact of changing the para-para linkage to the meta-meta coordination mm-Fe-bare is a decrease of the coupling strength (Γ) between the molecular orbitals (notably ϵ_0) and the gold surface, resulting into an important depletion of the device conductance from 0.1021 to 0.0026 G/G_0 . The pm-Fe-bare system shows a mixed behavior with the principal peak of transmission exhibiting a larger coupling than for the mm-Fe-bare system but smaller than for the pp-Fe-bare. We do retrieve the same eigenstate shapes in the three molecular junctions. The study of the thermoelectric properties depicted in Table 3 reveals that the mm-Fe-bare system yields a high Seebeck coefficient with $S = 346 \mu\text{V/K}$, and $ZT_{el} = 4.5$ which is high. Nevertheless, as stated before, it is important to include as well the thermal phonon conductance to have a complete picture. As shown earlier, κ_{ph} is typically on the order of a few pW/K. The global ZT would be 0.357 by considering $\kappa_{ph} = 20 \text{ pW/K}$ which is an estimation based on literature (see Part II, Chapter I and Chapter II). The system would be quite interesting with a non-negligible thermopower $S^2G = 26 \text{ pW/mK}^2$ if the real κ_{ph} turns out to be smaller.

The conjugated organic linkers play thus a crucial role in inducing QI that importantly modifies the thermoelectric properties. Nevertheless, if the conductance is too small the ZT and the S^2G thermopower are not improved even though the Seebeck coefficient is importantly increased (102 to 346 $\mu\text{V/K}$) in that study. The nature of the metal center(s) and its coordination to the linkers are also of high importance in the molecular design.

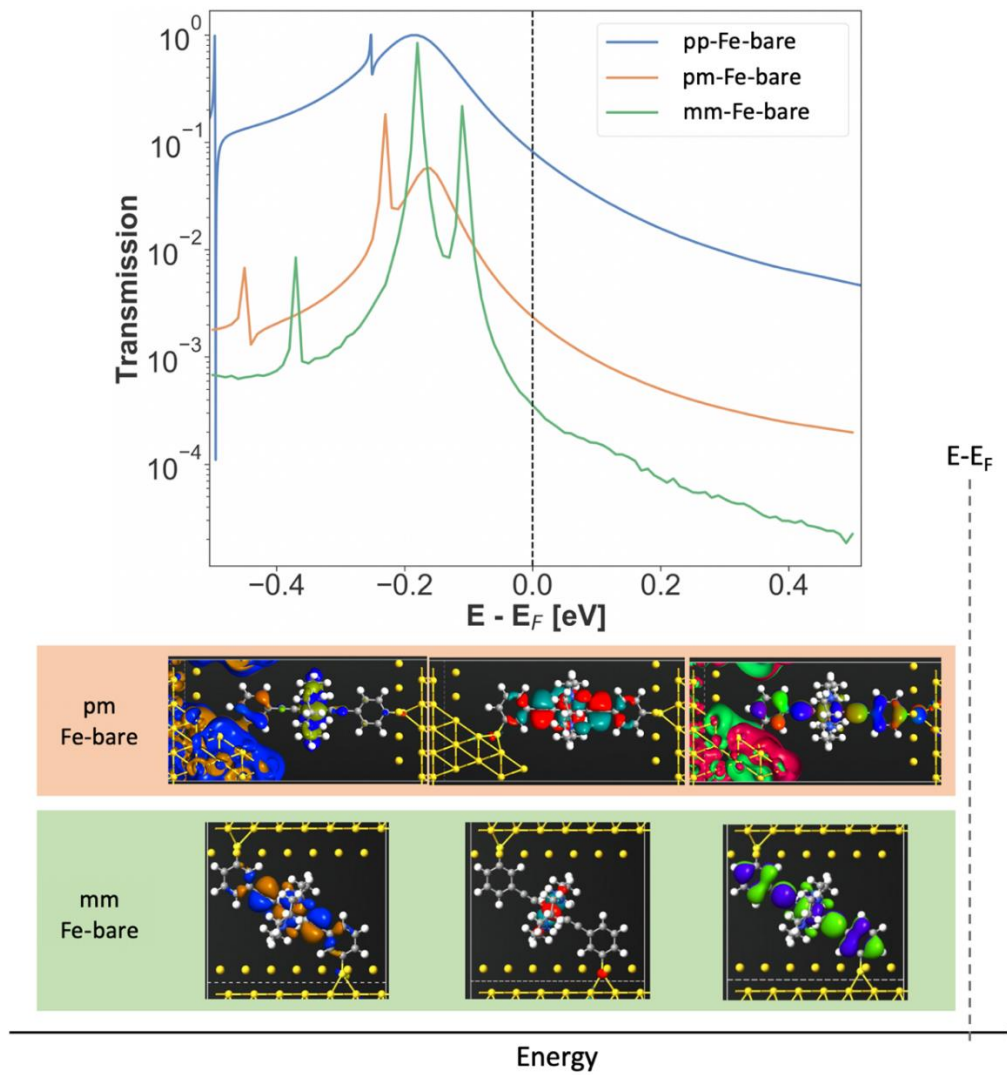


Figure 7 – Top: computed electronic transmissions for the three different coordination modes: pp-Fe-bare, pm-Fe-bare and mm-Fe-bare. Bottom: transmission eigenstates of the three main peaks below the Fermi level of the pm-Fe-bare and mm-Fe-bare systems. The main transmission eigenstates of the pp-Fe-bare systems are shown Figure 6.

Table 3 – Electronic and thermoelectrics data for pp-Fe-bare, pm-Fe-bare and mm-Fe-bare from their computed transmission spectrum at zero bias. Estimation of ZT with $\kappa_{ph} = 20$ pW/K. Seebeck coefficient S in $\mu\text{V/K}$, S^2G the thermopower in pW/mK^2 , G/G_0 is the reduced conductance. Q_{cal} in pW, and V_p in mV.

| System | ZT | ZT_{el} | S | S^2G | G/G_0 | κ_{el} | Q_{cal} | V_p |
|------------|-------|-----------|-----|--------|---------|---------------|-----------|-------|
| pp-Fe-bare | 0.256 | 0.324 | 102 | 82 | 0.1021 | 76 | 4037 | -35 |
| pm-Fe-bare | 0.059 | 0.458 | 133 | 5 | 0.0033 | 3 | 243 | -52 |
| mm-Fe-bare | 0.340 | 4.523 | 346 | 25 | 0.0026 | 2 | 3412 | -191 |

IV – Screening of organometallic systems and their transmission

We have thus screened different coordination metal structure, with different ligands, one anchoring group (thiol), and different coordination modes (meta and para). The results are detailed below as a function of the nature of the metal ligands. For each junction containing thiol anchoring, the sulfur is in hollow coordination with respect to the gold electrodes.

IV.1 – Metallocene molecular systems

Ferrocene-containing molecular junctions: coordination to the electrodes via the same ligand

Since its discovery in 1952,²⁴ the Ferrocene (Fc) has been used in a really large variety of domains because of its interesting redox, donor, chelating properties notably. It has been studied in covalent molecular junctions both theoretically and experimentally with different linkers and anchoring groups.^{25,26,27,28,29,30} These studies highlight the important role of the conformation and of the path of transmissions. To the best of our knowledge the phenyl-ethynyl linker with a thiol anchoring has never been investigated. The organometallic configurations that have been studied up to now present covalent ethynyl-metal bonds with the phenyl-ethynyl linker. The ferrocene incorporation is different since the coordination to the linkers is done via its cyclopentadienyl (Cp) groups. Conformational considerations were investigated by Camarasa-Gómez and coworkers.²⁸

The role of meta and para configurations of the linker-anchoring groups was also investigated. First, the configurations in which the two linkers are substituting the same Cp group of the ferrocene were considered (Figure 8). In that configuration, the metallic center is lying out of the conjugated path. The associated transmission spectrum is displayed in Figure 9. The features of the transmission spectrum of the para systems are really far from the single-level model lorentzian-shape transmission. A really similar transmission feature was indeed calculated by Camarasa-Gómez and coworkers for a phenyl-thiol linker.²⁸ It consists in two parts:

- at $E-E_F = -0.54$ eV: Fano resonance. The associated transmission eigenstates $n^{\circ}3$ and $n^{\circ}4$ in Figure 9 is mainly due confinement on the ferrocene itself. The transmission pathways are also represented Figure 9, bottom image. The transmission pathways correspond to the casting of the transmission coefficients into local bond contributions. The local bond contribution can be positive and negative. A negative value means that the electron is back scattered along the local bond. The direction of the arrows shows the flow of the electrons.³¹ We can see here a lot of scattering and back scattering around

the ferrocene.

- between 0.5 eV and E_F : a sharp anti-resonance indicative of destructive QI is observed and suppresses the transmission around E_F (transmission probability $\sim 10^{-4}$ at the Fermi level). The transmission eigenstates n° 6 to 9 represented in Figure 9 show that this is resulting from a partial delocalization over the left part of the molecule including the (C \equiv C-Ph) linker cyclopentadienyl ending by Fe d orbitals.

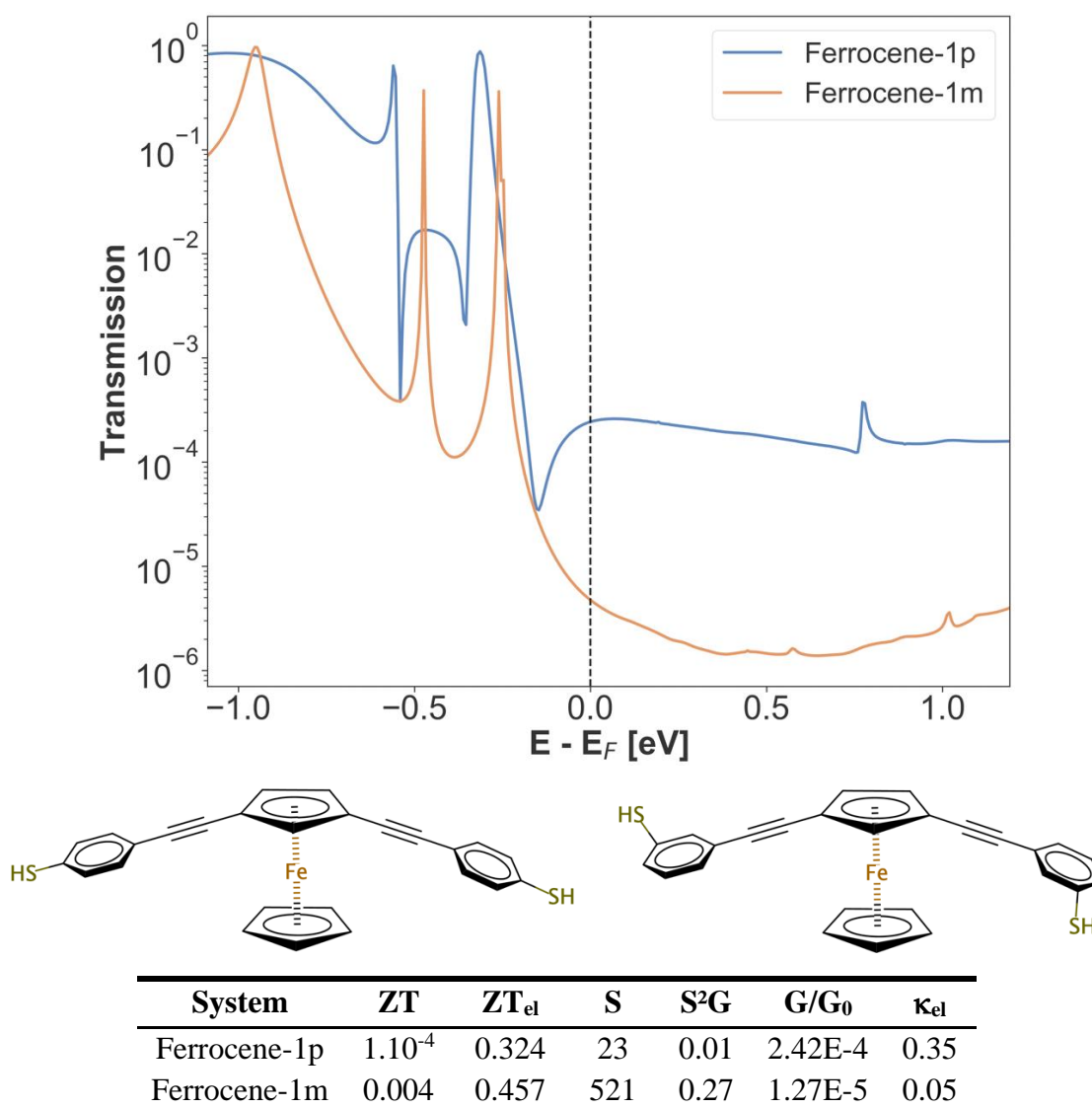


Figure 8 – Top: transmission spectra of both meta and para ferrocene systems with the metal lying out of the main conjugated path. Middle: chemical structure of the molecules, left: Ferrocene-1p and right: Ferrocene-1m. Bottom: Calculated thermo (electric) properties of the two junctions.

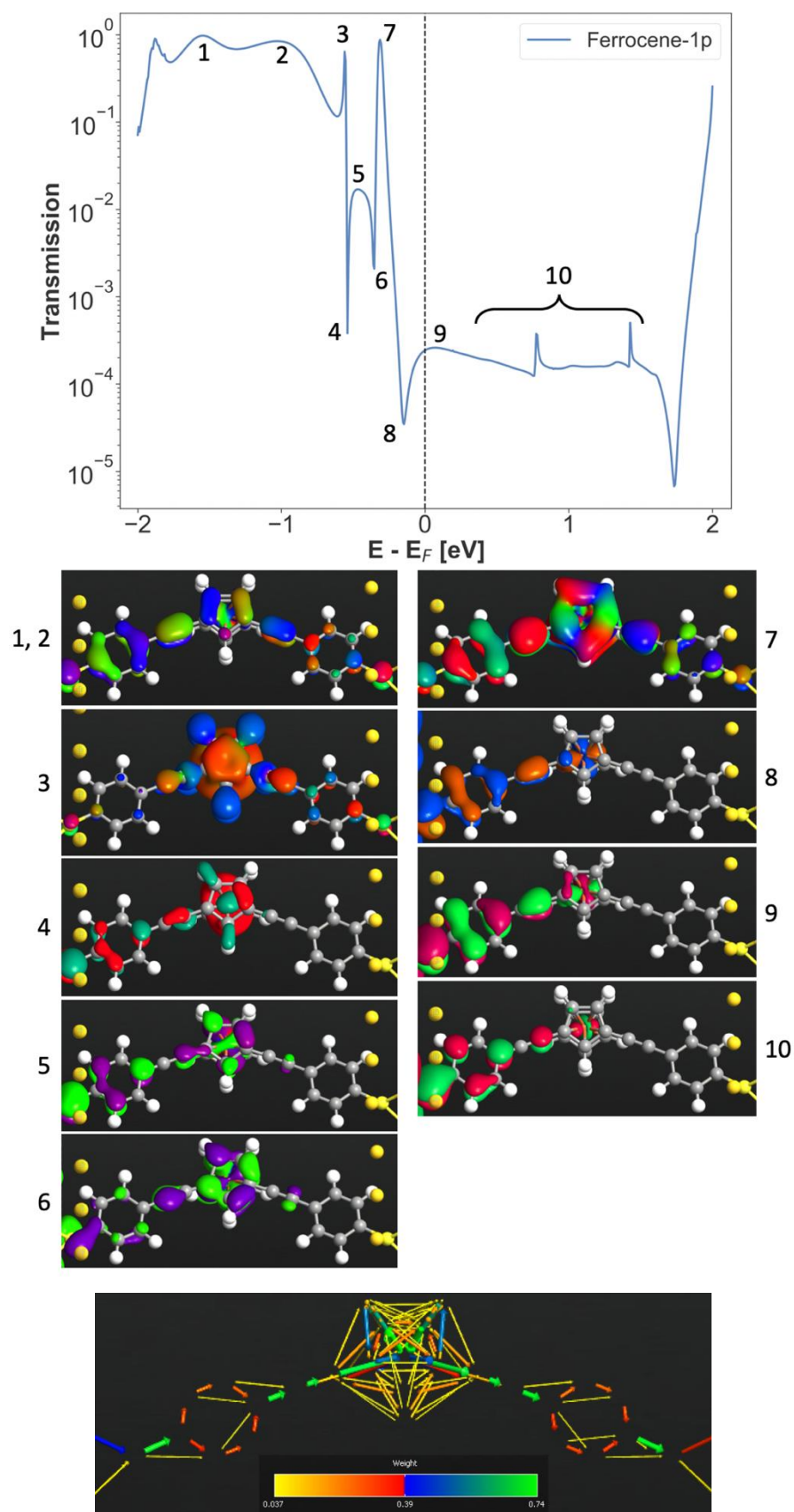


Figure 9 – Transmission and selected transmission eigenstates of the Ferrocene-1p. Bottom: transmission pathways of the Fano resonance at $E - E_F = -0.54$ eV (see text for more details).

Considering that the calculated Fermi level is not perfectly accurate in DFT, we have shifted the energy of the Fermi level to evaluate the range of thermoelectric values that could be expected. A similar study was performed by Lambert *et al.* recently.³² The thermoelectric properties calculated as a function of this energy shift are represented in Figure 10. This procedure can also be seen as a simplified simulation of the impact upon gating the junction.

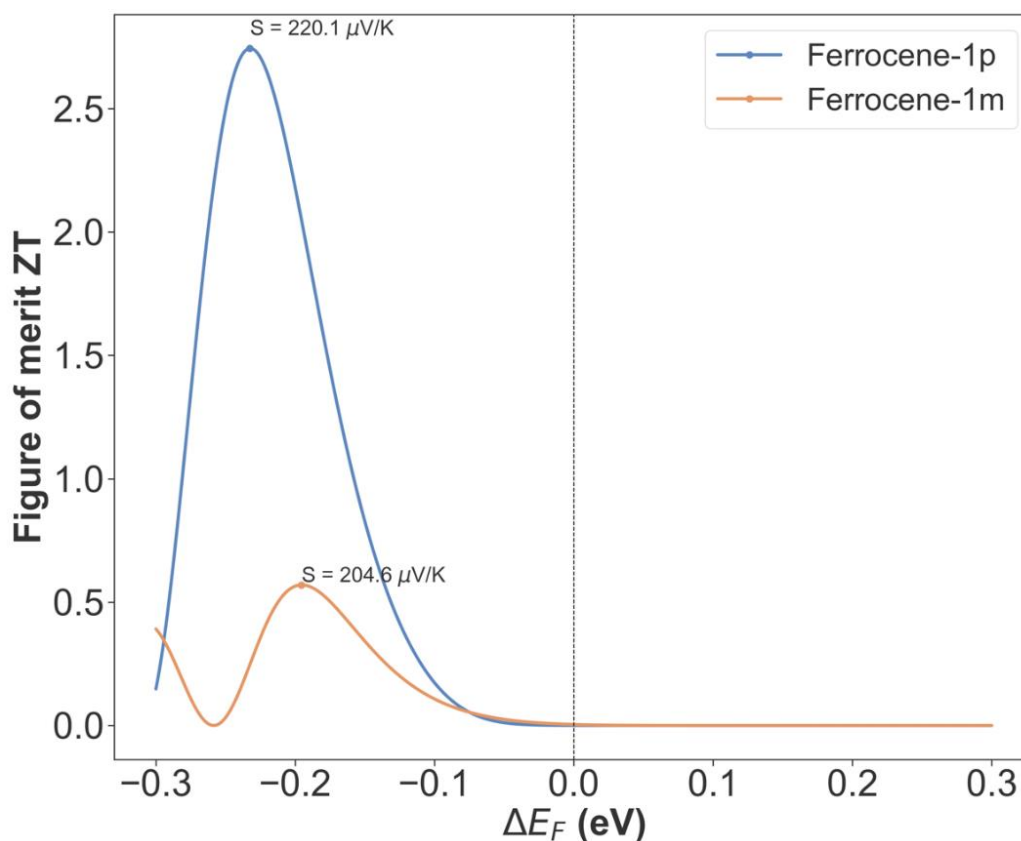


Figure 10 – Evolution of the figure of merit ZT as a function of the variation of the Fermi energy ΔE for both systems with $\Delta E_{\max} = \pm 0.3$ eV. The Seebeck coefficient is only reported for the best value of the respective ZT .

The Ferrocene-1p system displays interesting thermoelectric properties with a modification of $\Delta E \approx -0.23$ eV, see Figure 10. The calculations yield $ZT_{1p} = 2.74$ ($ZT_{el-1p} = 10.43$) and a maximum for the meta coordination with $\Delta E \approx -0.19$ eV; $ZT_{1m} = 0.56$ ($ZT_{el-1m} = 58.06$).

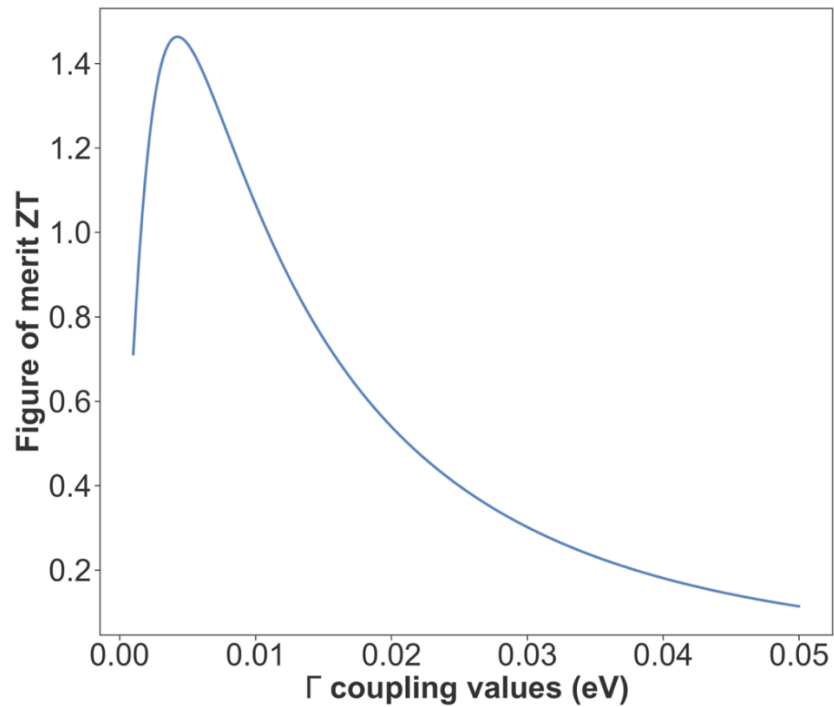


Figure 11 – Evolution of ZT as a function of the coupling strength considering a Lorentzian simulated with $\epsilon_{0-model} = -0.082$ eV, which correspond to the calculated $\epsilon_{0-1p-optimized}$ of the ferrocene-1p shifted by $\Delta E = -0.23$ eV from Figure 9. The variation of Γ (considering $\Gamma_L = \Gamma_R$) ranges between 1 meV and 50 meV.

Considering that the Fermi energy lies at the optimal value for ZT , we computed next the ZT values for only a single resonant level with a Lorentzian shape to understand the role of the anti-resonance in the thermoelectric properties of Ferrocene-1p. We made the hypothesis that $\epsilon_{0-model} = \epsilon_{0-1p-optimized} = -0.082$ eV (corresponding to a shift $\Delta E = -0.23$ eV). Because the anti-resonance is expected to modify the coupling strength of the transporting level, we tested different Γ values ranging from 1 meV to 50 meV. The resulting evolution of ZT is shown Figure 11. The best ZT that is obtained by this process in which no anti-resonance is taken into account is 1.4. The value obtained with the computed transmission of Ferrocene-1p is $ZT = 2.74$. This demonstrates that anti-resonance can be beneficial to the enhancement of the thermoelectric properties compared to a single Lorentzian shape transmission.

Ferrocene-containing molecular junctions: coordination of electrodes to each ligand

The Fc can be incorporated into the molecular junction via its Cp ligands. In the precedent study, the phenyl-ethynyl linkers were coordinated to the same Cp ligand of the Fe. In this part, we investigate the case in which each electrode is coordinated to a different Cp, as represented in Figure 12. The calculated transmissions are given in Figure 12 for the para and meta coordination of the thiol group on the phenyl groups. In these configurations, the conjugated pathway encompasses the metal center; the systems are referred to as Ferrocene-2p and Ferrocene-2m for the para-para and meta-meta coordination, respectively.

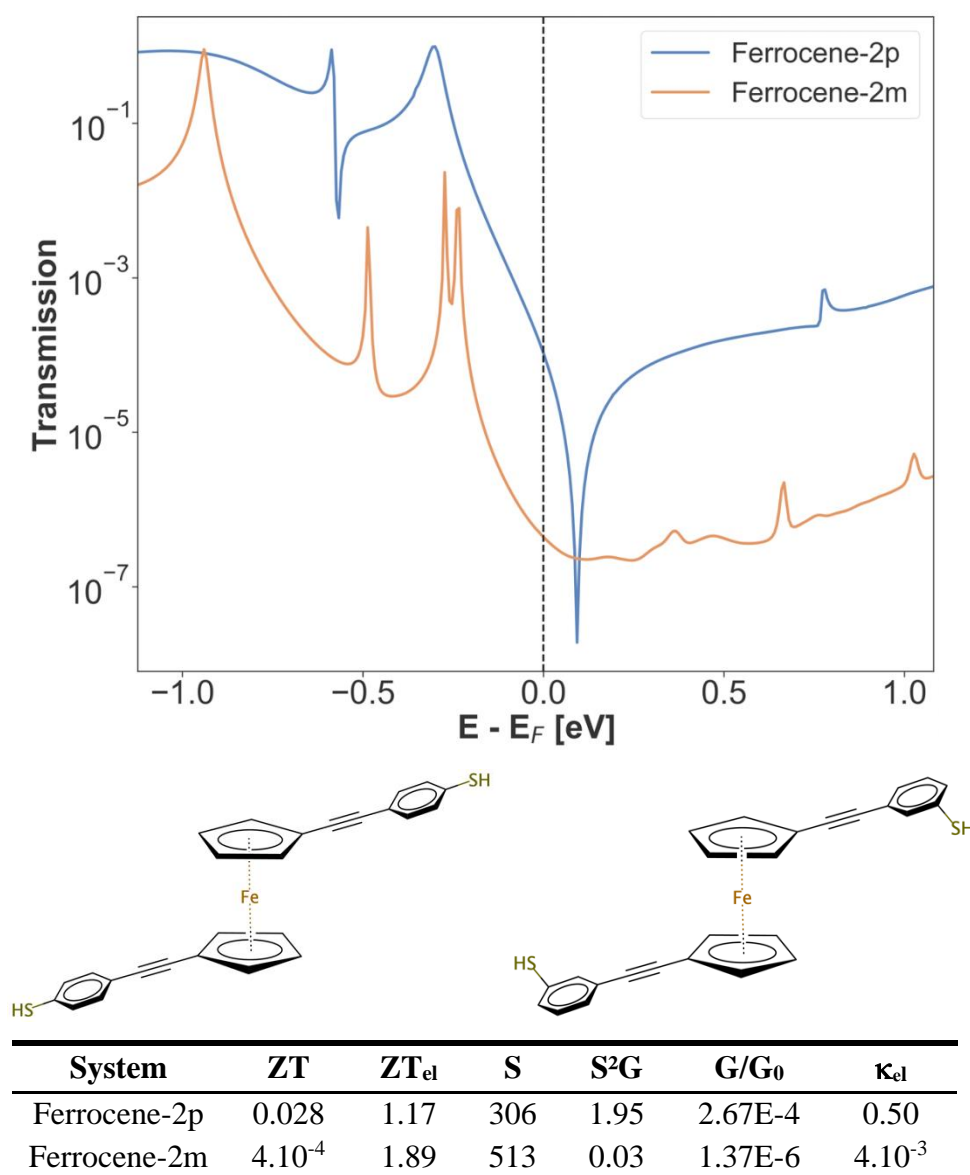


Figure 12 – Top: Transmission spectra of both the meta and para ferrocene systems with the metal incorporated in the main conjugated path. Middle: chemical structure of the molecules,

left: Ferrocene-2p and right: Ferrocene-2m. Bottom: associated thermoelectric properties of the two junctions.

The transmission spectra are similar to their counterpart Ferrocene-1p and Ferrocene-1m. The extraction of the thermoelectric values leads to ZT of 0.028 and $4 \cdot 10^{-4}$ respectively (Figure 12). The inclusion of the Fe metal in the conjugated path moderately increases the thermoelectric features compared to the previous compounds in which the conjugated path was settled through the same Cp ligand. The main differences are:

- For the Ferrocene-2p, the main resonant peak is broader, and the anti-resonance lies above the Fermi level compared to Ferrocene-1p.
- For the Ferrocene-2m, the overall conductance and transmission maxima are much smaller compared to the Ferrocene-1m ($G_{1m}/G_0 = 1.27 \cdot 10^{-5}$ and $G_{2m}/G_0 = 1.37 \cdot 10^{-6}$), and the transmission maximum of the main transport level drops from $\tau_{1m} = 0.360$ to $\tau_{2m} = 0.008$).

As shown Figure 13, the variation of the Fermi level ΔE to account for the limitations of DFT has less impact compared to Ferrocene-1p and Ferrocene-1m. The maximum of ZT is $ZT_{2p} = 1.74$ compared to $ZT_{1p} = 2.74$.

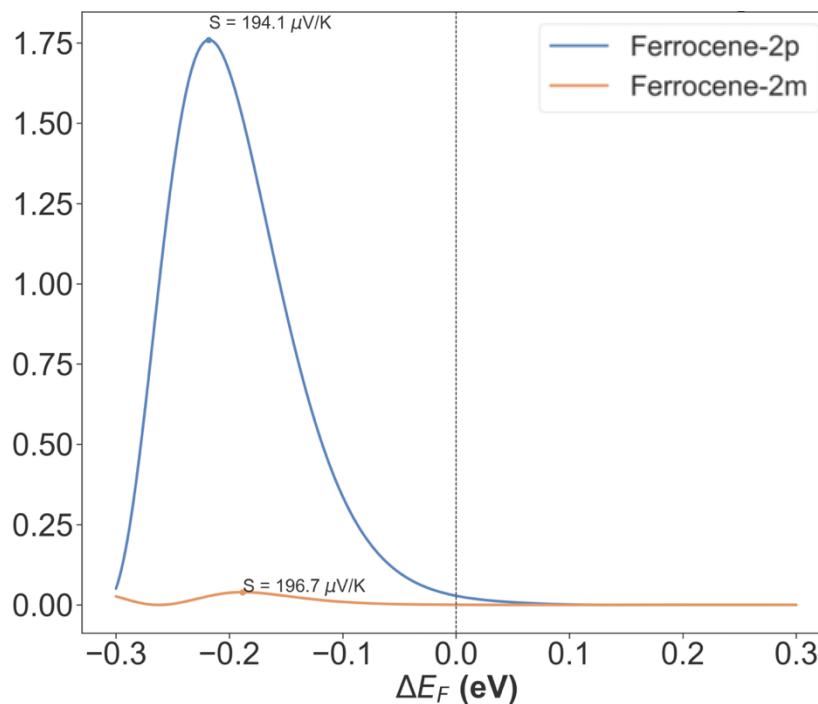
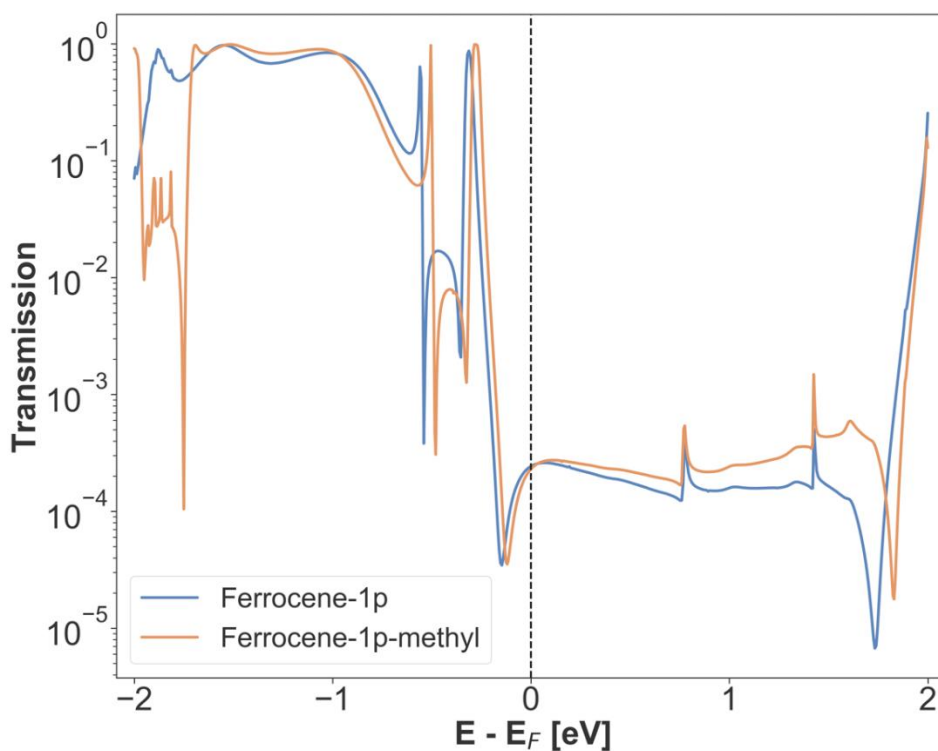


Figure 13 – Evolution of the figure of merit ZT as a function of the variation of the Fermi level energy ΔE for both systems with $\Delta E_{\max} = \pm 0.3$ eV. The Seebeck coefficient is only reported for the best value of the respective ZT .

The incorporation of the metal directly into the conjugated path does not appear as a breakthrough strategy to improve the thermoelectric properties. In the next section, the functionalization of the Cp ring will be investigated in the search of means to enhance thermoelectric properties.

Ferrocene-containing molecular junctions: functionalization of the Cp rings

As seen earlier, the functionalization of the $\text{Fe}(\text{cyclam})(\text{C}\equiv\text{C}-\text{Ph})_2$ systems were not conclusive for tuning the electronic transmission. Since the electronic scheme is quite different in Fc-junctions, chemical modifications are suspected to induce a different response. We choose to investigate this issue using the most promising system as reference, i.e. Ferrocene-1p. The hydrogen atoms of the Cp ligands have been substituted by methyl groups (Ferrocene-1p-methyl, representation in Figure 14). The expected consequence is to lead to a more electron-rich metal center (thus more easily oxidizable) and thus to shift the main transport peak closer to the Fermi level while keeping the anti-resonance features in the transmission. The resulting transmission is shown in Figure 14.



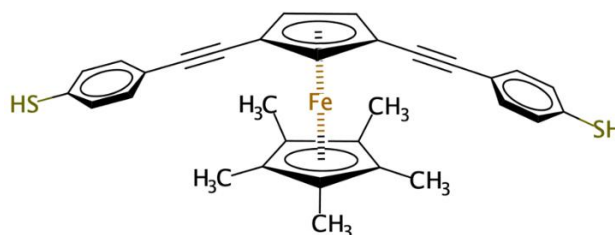


Figure 14 – Comparison of the transmission spectrum upon methyl substitution of Ferrocene-1p. Top: transmission of Ferrocene-1p and Ferrocene-1p-methyl. Bottom: representation of the Ferrocene-1p substituted by 5 methyl group.

Interestingly, even if the electronic structure of the isolated systems shows a destabilization of the HOMOs upon introduction of the methyl groups, the incorporation in the junction almost completely annihilates this molecular feature due to a pinning effect, as seen in Figure 14. Another possibility to shift the transmission peaks closer to the Fermi level is to apply an external electrostatic field. This is investigated in the next section.

Electrostatic gating of the Ferrocene-1p-methyl system

A dielectric gate, positioned to induce an electric field perpendicular to the transport direction through the molecular junction, was introduced in the computational model (Figure 16). Other gate positioning could be implemented but this one corresponds to experimental setups.^{33,34} The expected result is to induce an energy shift the molecular-centered levels closer to the Fermi level to enhance the thermoelectric properties. The Ferrocene-1p-methyl which is the compound whose transmission peak lies closer to the Fermi level was used as test molecule. Upon a negative increase in the gate voltage, the main transmission peak is effectively displaced toward the Fermi level, from -0.28 eV to -0.16 eV. Interestingly, this is associated with a decrease of transmission for this peak, from $\tau = 0.99$ to $\tau = 0.62$ upon a gating variation from 0.0 V to -2.0 V. In contrast, the second part of the anti-resonance which introduces a depletion close to the Fermi level is very moderately affected by the gating with an associated shift from -0.12 eV to -0.10 eV, with the gate set at 0.0 V and -2.0 V, respectively.

The inversion of the electric field orientation (positive gating) has a stronger effect on the main transmission peak which shifts from -0.28 eV to -1.06 eV for 0.0 V to $+2.0$ V gating, respectively; this is accompanied by a slight decrease in its transmission probability ($\tau_{-2.0V} = 0.62$ and $\tau_{+2.0V} = 0.66$). Contrarily to the negative gating, the energy of the depletion of the anti-resonance moves significantly from -0.12 eV at a gating of 0.0 V to -0.88 eV at $+2.0$ V.

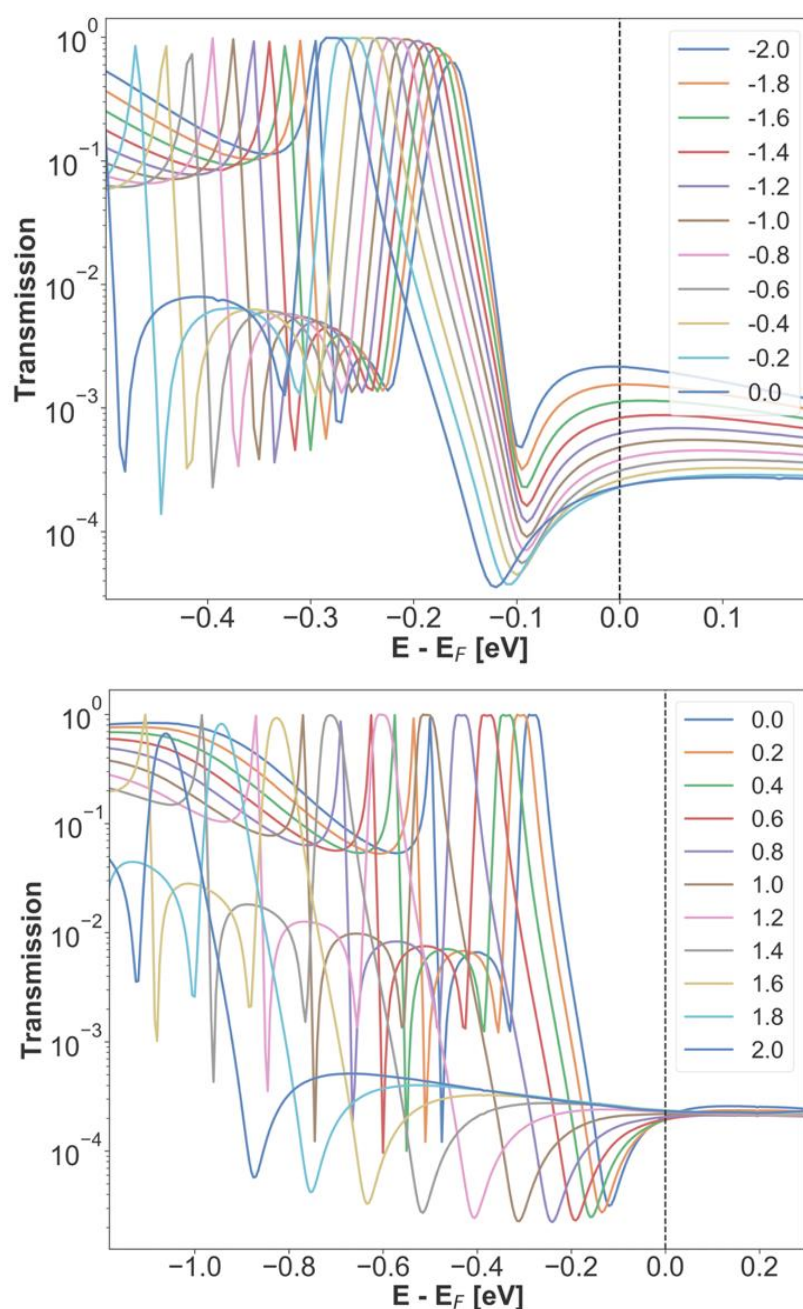


Figure 15 – Electronic transmission shifts of the Ferrocene-1p-methyl as a function of the applied gate voltage, from -2.0 V to +2.0 V.

The impact of an external gate voltage on the Ferrocene-1p-methyl appears to only marginally shift the main transport level closest to the Fermi level. Nevertheless, these small changes associated with the change in transmission maxima are imparting the thermoelectric descriptors. The evolution of ZT and Seebeck coefficient is plotted in Figure 15 as a function of gate voltage. This graphical representation allows to visualize the decorrelation between the maximum in the Figure of merit and that of the Seebeck coefficient.

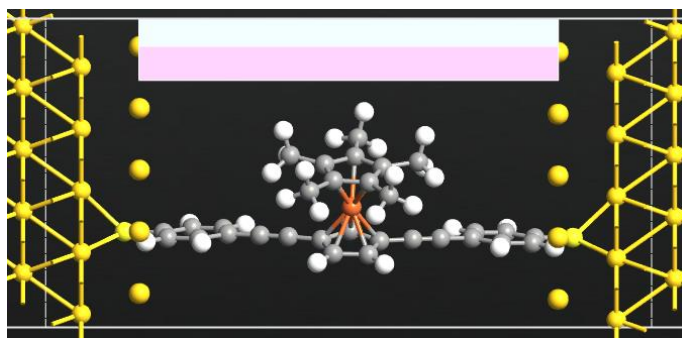


Figure 16 – Representation of a dielectric gate perpendicular to the electrode in QuantumATK. The white part is the metallic surface and the pink one is the dielectric with $\epsilon_r = 4$ (silicon dioxide permittivity).³⁵ This is the representation of a Single-Molecule Field Effect Transistor (FET).

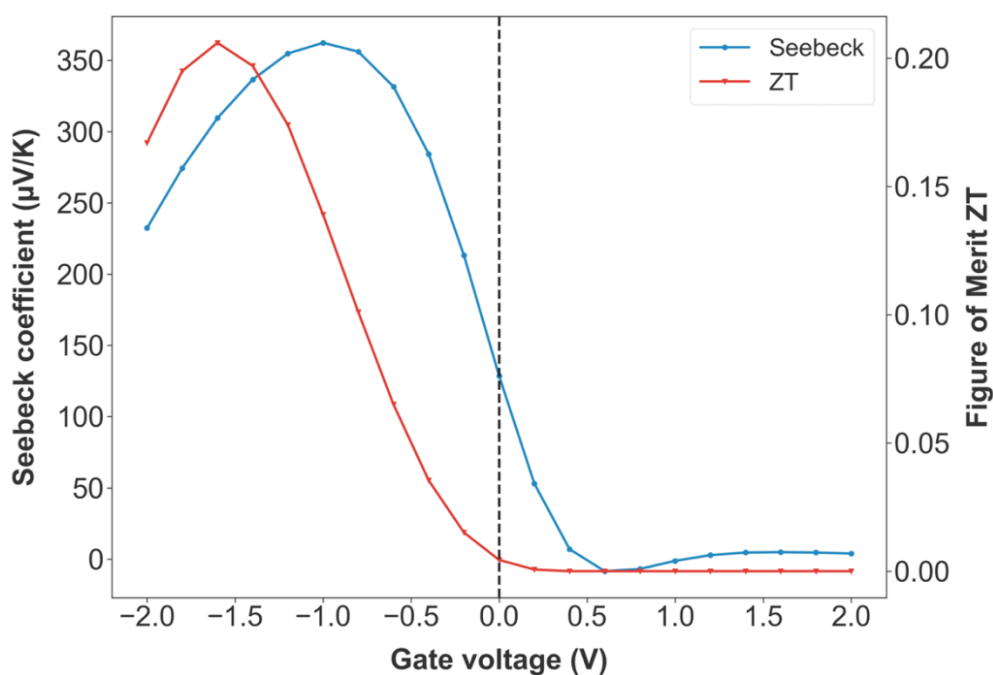
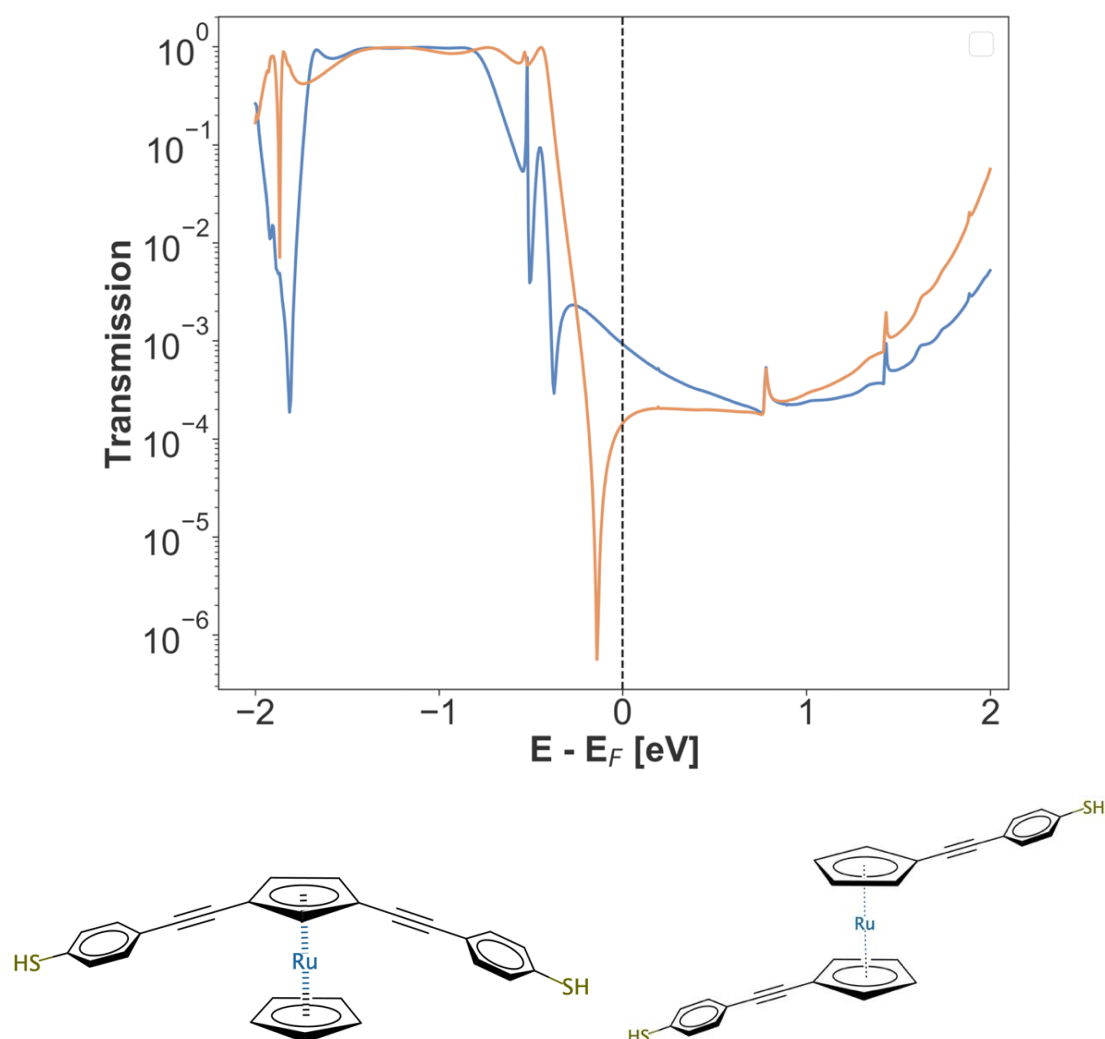


Figure 17 – Evolution of ZT ($\kappa_{ph} = 20$ pW/K) in red and of the Seebeck coefficient ($\mu\text{V/K}$) in blue of Ferrocene-1p-methyl as a function of the applied gate voltage (V).

Ruthenocene-containing molecular junctions: Ruthenocene-1p and Ruthenocene-2p

A similar study was performed on ruthenocene-containing systems (ruthenocene = RuCp_2 ,³⁶ see Figure 18 for the representation of the complete molecule) to evaluate the impact of the nature of the metal. Ruthenocene is presenting an irreversible oxidation 0.41 V beyond the ferrocene oxidation.³⁷ It thus appears interesting to assess whether this change would also be cancelled via pinning effects as observed introducing substituents. The electronic transmissions

of the ruthenocene derivatives are comparable to the ferrocene analogues; the peaks and depletion region are shifted slightly away from the Fermi level. With $\epsilon_{0Ru-1p} = -0.45$ eV, i.e., -0.14 eV compared to the ferrocene-1p ($\epsilon_0 = -0.31$ eV), its transmission peak is also reduced from $\tau_{Fe1p} = 0.87$ to $\tau_{Ru1p} = 0.09$. For $\epsilon_{0Ru-2p} = -0.45$ eV, i.e., -0.15 eV compared to the ferrocene-2p ($\epsilon_0 = -0.30$ eV) while the intensity of the transmission peak is the same.



| System | ZT_{el} | ZT | S ($\mu\text{V}/\text{K}$) | S^2G (pW/mK^2) | G/G_0 | κ_{el} (pW/K) |
|----------------|-----------|--------|------------------------------|------------------------------------|---------|--|
| Ruthenocene-1p | 0.0341 | 0.0015 | 29 | 0.103 | 0.0015 | 0.9 |
| Ruthenocene-2p | 0.0139 | 0.0005 | 18 | 0.038 | 0.0014 | 0.8 |

Figure 18 – Top: transmission spectra of both para ruthenocene systems with and without the metal in the main conjugated path. Middle: chemical structure of the molecules, left: Ruthenocene-1p and right: Ruthenocene-2p. Bottom: Thermoelectric properties of the two junctions.

Other variants of these ruthenocene-containing systems were tested by performing functionalization of the cyclopentadienyl with 5 or 8 methyl groups, but none of these modifications were particularly interesting in terms of electronic and thermoelectric properties or transmission shapes compared to the ferrocene ones.

IV.2 Study of the modification of the linker using Ru(TMA)(C≡C-Ph)₂ as metal moiety

For further molecular design of efficient thermoelectric molecular junctions, the role and the influence of the linkers need to be evaluated. In the preliminary studies performed to identify synthesizable candidates for molecular junction fabrication, the Ru(TMA)X₂ (with TMA = 1,5,9,13-tetramethyl-1,5,9,13-tetraazacyclo-hexadecane) and X representing different type of linkers shown Figure 19 have been identified as systems of interest. The study of the linker influence on the thermoelectric properties was thus performed taking Ru(TMA) as common central group that allows to shift the transmission peaks quite close to the Fermi energy.

The calculated Seebeck coefficients are reported in Figure 20. A first conclusion is that the meta coordination of the thiol group gives higher values in all cases. This can be explained by the fact that meta coordination implies two competitive conductive paths and weaker coupling ($\Gamma_{\text{para}} < \Gamma_{\text{meta}}$) with the electrodes that both modify the shape of the transmission at the Fermi energy. The derivative and therefore the slope of the transmission is larger than for para thiol coordination, inducing an increase in the Seebeck coefficient. An important element to highlight is the high sensitivity of the Seebeck coefficient to slight changes in energy as revealed by the error bars shown in Figure 20 (considering $\Delta E = \pm 0.2$ eV). B-m (biphenyl) and C-m (Ph-C≡C-Ph) are the most interesting systems in terms of Seebeck coefficient.

The Figure of Merit (Figure 21) does not behave accordingly with the Seebeck coefficients as already highlighted before. Indeed, larger ZT are found for the para thiol coordination in contrast to the trends observed for the Seebeck coefficient. The E system is an exception with $ZT_{\text{E-m}} > ZT_{\text{E-p}}$. This conclusion is notably due to the added $k_{\text{ph}} = 20$ pW/K (added for the meta and the para systems). Compared to the Seebeck coefficient, the energetic position of the ϵ_0 in all the systems is far from being attractive to get interesting values for the Figure of Merit.

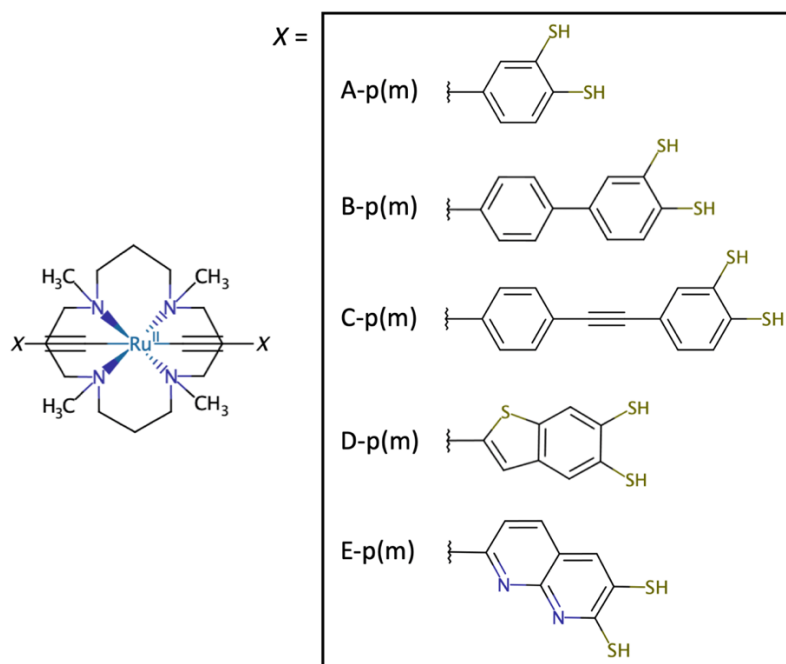


Figure 19 – Chemical structures of the tested molecules: $[\text{Ru}(\text{TMA})\text{X}_2]$, with TMA = 1,5,9,13-tetramethyl-1,5,9,13-tetraazacyclo-hexadecane and X corresponding to the different types of organic linker sketched.

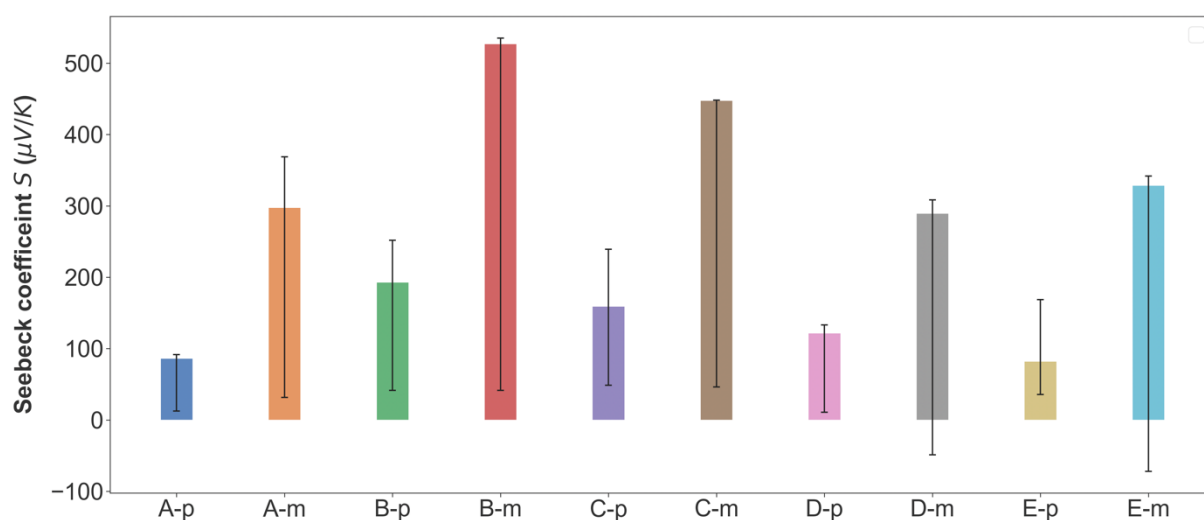


Figure 20 – Seebeck coefficient ($\mu\text{V}/\text{K}$) as a function of the different linkers, in meta (m) or para (p) coordination. The error bar represents the variation of the Seebeck coefficient considering $\Delta E_{\text{F}} = \pm 0.2 \text{ eV}$.

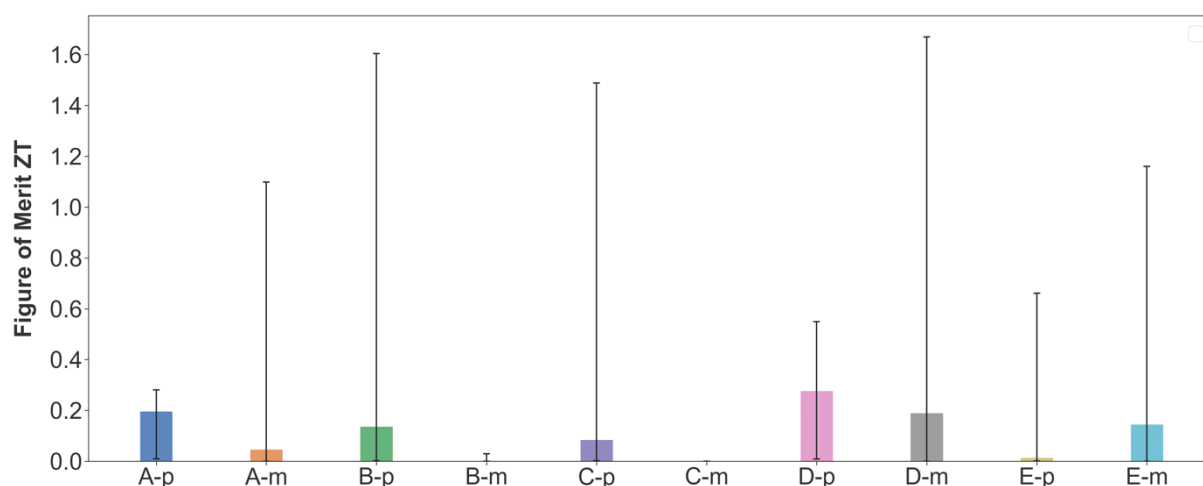


Figure 21 – Figure of merit ZT as a function of the different linkers, in meta (m) or para (p) coordination. The error bar represents the variation of ZT considering $\Delta E_F = \pm 0.2$ eV.

The different results gathered in this chapter reveal several factors that can be modified to design coordination complexes showing increased thermoelectric properties in molecular junction configuration on the basis of study cases. The chemical substitutions performed in organic linkers or ancillary ligands to introduce more donor or acceptor groups does not lead to important modifications of the electronic transmission. This can nevertheless be an advantage in the context of a fine tuning of the electronic transmission. The second design idea based on the creation of quantum interference in the transmission spectrum has been tested by modifying the coordination of the sulfur anchor to the phenyl end groups of the linker from para to meta position. This configuration turns out to reduce the global conductance but an increase of the Seebeck coefficient is noted in all studied cases. Unfortunately, the associated Figure of merit ZT is concomitantly significantly reduced. This is mostly due to the reduction of the overlap between the gold and the thiol-molecule molecular levels. Alternatively, derivatives of ferrocene and ruthenocene have been designed to evaluate the “T-shaped” molecule configuration that reveals to be able to induce QI in organic systems. In the studied coordination complexes, QI of anti-resonance and Fano resonance types have been calculated leading to interesting features in the transmission pattern, which could improve the thermoelectric properties. The ability of an external gating to modify the properties of the electronic transmission has been tested on these systems and has shown to provide interesting enhancement of the calculated thermoelectric values. These results are demonstrating the potentiality of ferrocene-like systems to induce very interesting and potentially addressable thermoelectric molecular junctions in transistor type configuration for example.

The next chapter is focused on the comparison between the experimental data obtained by our collaborators and the theoretical computation performed on the **Fe-cyclam** and the **Ru-dppe** molecular junctions to rationalize the electronic properties and to assess the precision of the computational method.

- ¹ a) Tanaka, Y.; Kiguchi, M.; Akita, M. Inorganic and Organometallic Molecular Wires for Single-Molecule Devices. *Chem. Eur. J.* 2017, 23, 4741. doi:10.1002/chem.201604812. b) Chen, X.; Roemer, M.; Yuan, L.; Du, W.; Thompson, D.; del Barco, E.; Nijhuis C. A. Molecular diodes with rectification ratios exceeding 10^5 driven by electrostatic interactions. *Nature Nanotech.* 2017, 12, 797. doi:10.1038/nnano.2017.110.
- ² a) Lambert, C. J. Basic concepts of quantum interference and electron transport in single-molecule electronics. *Chem. Soc. Rev.* 2015, 44, 875. doi:10.1039/C4CS00203B. b) Zimbovskaya, N. A. Seebeck effect in molecular junctions. *J. Phys.: Cond. Mat.* 2016, 28, 183002. doi:10.1088/0953-8984/28/18/183002. c) Rincón-García, L.; Evangeli, C.; Rubio-Bollinger, G.; Agraït N. Thermopower measurements in molecular junctions. *Chem. Soc. Rev.* 2016, 45, 4285. doi:10.1039/C6CS00141F. d) Moth-Poulsen, K. Handbook of Single-Molecule Electronics. Pan Stanford Publishing Pte. Ltd: Boca Raton, 299, 2016. ISBN:9814463396. e) Longji, C.; Ruijiao, M.; Chang J.; Meyhofer, E.; Pramod, R. Perspective: Thermal and thermoelectric transport in molecular junctions. *J. Chem. Phys.* 2017, 146, 092201. doi:10.1063/1.4976982. f) Park, S.; Kang, H.; Yoon, H.-J. Structure–thermopower relationships in molecular thermoelectrics. *J. Mater. Chem. A* 2019, 7, 14419. doi:10.1039/C9TA03358K. g) Wang, K.; Meyhofer, E.; Reddy, P. Thermal and Thermoelectric Properties of Molecular Junctions. *Adv. Funct. Mater.* 2020, 1904534. doi:10.1002/adfm.201904534.
- ³ Reddy, P.; Jang, S.-Y.; Segalman, R. A.; Majumdar, A. Thermoelectricity in Molecular Junctions. *Science* 2007, 315, 1568. doi:10.1126/science.1137149.
- ⁴ Zeng, Y.-J.; Wu, D.; Cao, X.-H.; Zhou, W.-X.; Tang, L.-M.; Chen, K.-Q. Nanoscale Organic Thermoelectric Materials: Measurement, Theoretical Models, and Optimization Strategies. *Adv. Funct. Mater.* 2020, 30, 1903873. doi:10.1002/adfm.201903873.
- ⁵ a) Garner, M. H.; Li, H.; Chen, Y.; Su, T. A.; Shangguan, Z.; Paley, D. W.; Liu, T.; Ng, F.; Li, H.; Xiao, S.; Nuckolls, C.; Venkataraman L.; Solomon, G. C. Comprehensive suppression of single-molecule conductance using destructive σ -interference. *Nature* 2018, 558, 415. doi:10.1038/s41586-018-0197-9. b) Garner, M. H.; Li, H.; Neupane, M.; Zou, Q.; Liu, T.; Su, T. A.; Shangguan, Z.; Paley, D. W.; Ng, F.; Xiao, S.; Nuckolls, C.; Venkataraman L.; Solomon, G. C. Permethylated Introducing Destructive Quantum Interference in Saturated Silanes. *J. Am. Chem. Soc.* 2019, 141, 15471. doi:10.1021/jacs.9b06965.
- ⁶ Rincón-García, L.; Ismael, A. K.; Evangeli, C.; Grace, L.; Rubio-Bollinger, G.; Porfirakis, K.; Agraït, N.; Lambert, C. J. Molecular design and control of fullerene-based bi-thermoelectric materials. *Nature Mat.* 2016, 15, 289. doi:10.1038/nmat4487.
- ⁷ Naher, M.; Milan, D. C.; Al-Owaedi, O. A.; Planje, I. J.; Bock, S.; Hurtado-Gallego, J.; Batante, P.; Abd Dawood, Z. M.; Rincón-García, L.; Rubio-Bollinger, G.; Higgins, S. J.; Agraït, N.; Lambert, C. J.; Nichols, R. J.; Low, P. J. Molecular Structure–(Thermo)electric Property Relationships in Single-Molecule Junctions and Comparisons with Single- and Multiple-Parameter Models. *J. Am. Chem. Soc.* 2021, 143, 3817. doi:10.1021/jacs.0c11605.
- ⁸ a) Luo, L.; Benameur, A.; Brignou, P.; Choi, S. H.; Rigaut, S.; Frisbie C. J. Length and Temperature Dependent Conduction of Ruthenium-Containing Redox-Active Molecular Wires. *J. Phys. Chem. C* 2011, 115, 19955. doi:10.1021/jp207336v. b) Meng, F. Hervault, Y.-M.; Norel, L.; Costuas, K.; Van Dyck, C.; Geskin, V.; Cornil, J.; Hng, H. H.; Rigaut, S.; Chen, X. Photo-modulable molecular transport junctions based on organometallic molecular wires. *Chem. Sci.* 2012, 3, 3113. doi:10.1039/C2SC20323E. c) Rigaut, S. Metal complexes in molecular

junctions. *Dalton Trans.* 2013, 42, 15859. doi:10.1039/C3DT51487K. d) Meng, F.; Hervault, Y.-M.; Shao, Q.; Hu, B.; Norel, L.; Rigaut, S. Orthogonally modulated molecular transport junctions for resettable electronic logic gates. *Nature Com.* 2014, 5, 3023. doi:10.1038/ncomms4023.

⁹ a) Schwarz, F.; Kastlunger, G.; Lissel, F.; Egler-Lucas, C.; Semenov, S. N.; Ventkatesan, K.; Berke, H.; Stadler, R.; Lörtscher E. Field-induced conductance switching by charge-state alternation in organometallic single-molecule junctions. *Nature Nanotech.* 2016, 11, 170. doi:10.1038/nnano.2015.255. b) Schwarz, F.; Kastlunger, G.; Lissel, F.; Riel, H.; Ventkatesan, k.; Berke, H.; Stadler, R.; Lörtscher E. High-Conductive Organometallic Molecular Wires with Delocalized Electron Systems Strongly Coupled to Metal Electrodes. *Nano Lett.* 2014, 14, 5932. doi:10.1021/nl5029045.

¹⁰ O'Driscoll, L.; Bryce, M. B. Extended curly arrow rules to rationalize and predict structural effects on quantum interference in molecular junctions. *Nanoscale* 2021, 13, 1103. doi:10.1030/d0nr07819k

¹¹ a) Arroyo, C. R.; Tarkuc, S.; Frisenda, R.; Seldenthuis, J. S.; Woerde, C. H. M.; Eelkema, R.; Grozema, F.; van der Zant, H. J. S. Signatures of Quantum Interference Effects on Charge Transport Through a Single Benzene Ring. *Angew. Chem. Int. Ed.* 2013, 52, 315. doi:10.1002/anie.201207667. b) Huang, B.; Liu, X.; Yuan, Y.; Hong, Z.-W.; Zheng, J.-F.; Pei, L.-Q.; Shao, Y.; Li, J.-F.; Zhou, X.-S.; Chen, J.-Z.; Jin, S.; Mao, B.-W. Controlling and Observing Sharp-Valleyed Quantum Interference Effect in Single Molecular Junctions. *J. Am. Chem. Soc.* 2018, 140, 17685. doi:10.1021/jacs.8b1045.

c) Liu, J.; Huang, X.; Wang, F.; Hong, W. Quantum Interference Effects in Charge Transport through Single-Molecule Junctions: Detection, Manipulation, and Application. *Acc. Chem. Res.* 2019, 52, 151. doi:10.1021/acs.accounts.8b00429.

¹² a) Kronemeijer, A. J.; Akkerman, H.; Kudernac, T.; van Wees, B.; Feringa, B.; Blom, P.; de Boer, B. Reversible Conductance Switching in Molecular Devices. *Adv. Mat.* 2008, 20, 1467. doi:10.1002/adma.200800053. b) Uchida, K.; Yamanoi, Y.; Yonezawa, T.; Nishihara, H. Reversible On/Off Conductance Switching of Single Diarylethene Immobilized on a Silicon Surface. *J. Am. Chem. Soc.* 2011, 133, 9239. doi:10.1021/ja203269t. c) Ikeda, M.; Tanifuji, N.; Yamaguchi, H.; Irie, M.; Matsuda, I. Photoswitching of conductance of diarylethene-Au nanoparticle network. *Chem. Comm.* 2007, 1355. doi:10.1039/B617246F. d) Tsai, C.-S.; Wang, J.-K.; Skodje, R.; Lin, J.-C. A Single Molecule View of Bistilbene Photoisomerization on a Surface Using Scanning Tunneling Microscopy. *J. Am. Chem. Soc.* 2005, 127, 10788. doi:10.1021/ja052448b. e) Comstock, M.; Levy, N.; Kirakosian, A.; Cho, J.; Lauterwasser, F.; Harvey, J.; Strubbe, D.; Frechet, J.; Trauner, D.; Louie, S.; Crommie M. Reversible Photomechanical Switching of Individual Engineered Molecules at a Metallic Surface. *Phys. Rev. Lett.* 2007, 99, 038301. doi:10.1103/PhysRevLett.99.038301. f) Del Valle, M.; Gutierrez, R.; Tejedor, C. Cuniberti Tuning the conductance of a molecular switch. *Nature Nanotech.* 2007, 2, 176. doi:10.1038/nnano.2007.38. g) Katsonis, N.; Kudernac, T.; Walko, M.; van der Molen, S. J.; van Wees, B. J.; Feringa B. L. Reversible Conductance Switching of Single Diarylethenes on a Gold Surface. *Adv. Mater.* 2006, 18, 1397. doi:10.1002/adma.200600210. h) Kudernac, T.; Katsonis, N.; Browne, W.; Feringa B. Nano-electronic switches: Light-induced switching of the conductance of molecular systems. *J. Mater. Chem.* 2009, 19, 7168. doi:10.1039/B902009H. i) Tam, E.; Parks, J.; Shum, W.; Zhong, Y.-W.; Santiago-Berrios, M.; Zhang, X.; Yang, W.; Chan, G.; Abruña, H.; Ralph, D.; Single-Molecule Conductance of Pyridine-Terminated Dithienylethene Switch Molecules. *ACS Nano*, 2011, 5, 5115. doi:10.1021/nn201199b. j) Aradhya, S.; Meisner, J.; Krikorian, M.; Ahn, S.; Parameswaran, R.; Steigerwald, M.; Nuckolls, C.; Venkataraman, L. Dissecting Contact Mechanics from

Quantum Interference in Single-Molecule Junctions of Stilbene Derivatives. *Nano Lett.* 2012, 12, 1643. doi:10.1021/nl2045815.

¹³ a) Pace, G.; Ferri, V.; Grave, C.; Elbing, M.; von Hanisch, C.; Zharnikov, M.; Mayor, M.; Rampi, M. A.; Samori, P. Cooperative light-induced molecular movements of highly ordered azobenzene self-assembled monolayers. *Proc. Natl. Acad. Sci. U.S.A.* 2007, 104, 9937. doi:10.1073/pnas.0703748104. b) Smaali, K.; Lenfant, S.; Karpe, S.; Ocafrain, M.; Blanchard, P.; Deresmes, D.; Godey, S.; Rochefort, A.; Roncali, J.; Vuillaume, D. High On–Off Conductance Switching Ratio in Optically-Driven Self-Assembled Conjugated Molecular Systems. *ACS Nano* 2010, 4, 2411. doi:10.1021/nn100295x.

¹⁴ a) Pobelov, I.; Li, Z.; Wandlowski, T. Electrolyte Gating in Redox-Active Tunneling Junctions-An Electrochemical STM Approach. *J. Am. Chem. Soc.* 2008, 130, 16045. doi:10.1021/ja8054194. b) Kim, Y.; Song, H.; Strigl, F.; Pernau, H.-F.; Lee, T.; Scheer, E. Conductance and Vibrational States of Single-Molecule Junctions Controlled by Mechanical Stretching and Material Variation. *Phys. Rev. Lett.* 2011, 106, 196804. doi:10.1103/PhysRevLett.106.196804.

¹⁵ a) Pasupathy, A.; Bialczak, R.; Martinek, J.; Grose, J.; Donev, L.; McEuen, P.; Ralph, D. The Kondo Effect in the Presence of Ferromagnetism. *Science* 2004, 306, 86. doi:10.1126/science.1102068. b) Cho, W. J.; Cho, Y.; Min, S. K.; Kim, W. Y.; Kim, K. S. Chromium Porphyrin Arrays as Spintronic Devices. *J. Am. Chem. Soc.* 2011, 133, 9364. doi:10.1021/ja111565w.

¹⁶ a) Collier, C.; Mattersteig, G.; Wong, E.; Luo, Y.; Beverly, K.; Sampaio, J.; Raymo, F.; Stoddart, J. F. A [2]Catenane-Based Solid State Electronically Reconfigurable Switch. *Health Science* 2000, 289, 1172. doi:10.1126/science.289.5482.1172. b) Kubatkin, S.; Danilov, A.; Hjort, M.; Cornil, J.; Bredas, J.-L.; Stuhr-Hansen, N.; Hedegard, P.; Bjørnholm, T. Single-electron transistor of a single organic molecule with access to several redox states. *Nature* 2003, 425, 698. doi:10.1038/nature02010. c) Song, H.; Kim, Y.; Jang, Y. H.; Jeong, H.; Reed, M.; Lee, T. Observation of molecular orbital gating. *Nature* 2009, 462, 1039. doi:10.1038/nature08639.

¹⁷ a) Xu, B.; Li, X.; Xiao, X.; Sakaguchi, H.; Tao, N. Electromechanical and Conductance Switching Properties of Single Oligothiophene Molecules. *Nano Lett.* 2005, 5, 1491. doi:10.1021/nl050860j. b) Díez-Pérez, I.; Li, Z.; Guo, S.; Madden, C.; Huang, H.; Che, Y.; Yang, X.; Zang, L.; Tao, N. Ambipolar Transport in an Electrochemically Gated Single-Molecule Field-Effect Transistor. *ACS Nano* 2012, 6, 7044. doi:10.1021/nn302090t. c) He, J.; Fu, Q.; Lindsay, S.; Cizek, J.; Tour, J. Electrochemical Origin of Voltage-Controlled Molecular Conductance Switching. *J. Am. Chem. Soc.* 2006, 128, 14828. doi:10.1021/ja0635433. d) Li, Z.; Liu, Y.; Mertens, S.; Pobelov, I.; Wandlowski, T. From Redox Gating to Quantized Charging. *J. Am. Chem. Soc.* 2010, 132, 8187. doi:10.1021/ja102754n. e) Janin, M.; Ghilane, J.; Lacroix J.-C. When Electron Transfer Meets Electron Transport in Redox-Active Molecular Nanojunctions. *J. Am. Chem. Soc.* 2013, 135, 2108. doi:10.1021/ja3122125.

¹⁸ Tanaka, Y.; Kato, Y.; Tada, T.; Fujii, S.; Kiguchi, M.; Akita, M. “Doping” of Polyyne with an Organometallic Fragment Leads to Highly Conductive Metallapolyne Molecular Wire. *J. Am. Chem. Soc.* 2018, 140, 10080. doi:10.1021/jacs.8b04484.

¹⁹ Gam, F.; Paez-Hernandez, D.; Arratia-Perez, R.; Liu, C. W.; Kahlal, S.; Saillard, J.-Y.; Muñoz-Castro, A. Coinage Metal Superatomic Cores: Insights into Their Intrinsic Stability and Optical Properties from Relativistic DFT Calculations. *Chem. Euro. J.* 2017, 23, 11330–11337. doi:10.1002/chem.201701673.

²⁰ Kittel, C. *Introduction to Solid State Physics*. Wiley, 1996. ISBN:0-471-14286-7.

- ²¹ Van Dyck, C.; Geskin, V.; Kronemeijer, A. J.; de Leeuw, D. M.; Cornil, J. Impact of Derivatization on Electron Transmission through Dithienylethene-Based Photoswitches in Molecular Junctions. *Phys. Chem. Chem. Phys.* 2013, 15, 4392. doi:10.1039/c3cp44132f.
- ²² Van Dyck, C.; Geskin, V.; Cornil, J. Fermi Level Pinning and Orbital Polarization Effects in Molecular Junctions: The Role of Metal Induced Gap States. *Adv. Func. Mater.* 2014, 24, 6154–6165. doi:10.1002/adfm.201400809.
- ²³ Diez-Cabanes, V.; Gonzalez, S. R.; Osella, S.; Cornil, D.; Van Dyck, C.; Cornil, J. Energy Level Alignment at Interfaces Between Au (111) and Thiolated Oligophenylenes of Increasing Chain Size: Theoretical Evidence of Pinning Effects. *Adv. Theo. Sim.* 2018, 1, 1700020. doi:10.1002/adts.201700020.
- ²⁴ Werner, H. At Least 60 Years of Ferrocene: The Discovery and Rediscovery of the Sandwich Complexes. *Angew. Chem. Int. Ed.* 2012, 51, 6052–6058. doi:10.1002/anie.201201598.
- ²⁵ Takaloo, A. V.; Sadeghi, H. Quantum Interference Enhanced Thermoelectricity in Ferrocene Based Molecular Junctions. *J. Nano. Nanotech.* 2019, 19, 7452–7455. doi:10.1166/jnn.2019.16622
- ²⁶ Kanthasamy, K.; Ring, M.; Nettelroth, D.; Tegenkamp, C.; Butenschön, H.; Pauly, F.; Pfnür, H. Charge Transport through Ferrocene 1,1'-Diamine Single-Molecule Junctions. *Small* 2016, 12, 4849–4856. doi:10.1002/sml.201601051.
- ²⁷ Yuan, S.; Wang, S.; Kong, Z.; Xu, Z.; Yang, L.; Wang, D.; Ling, Q.; Wang, Y. Theoretical Studies of the Spin-Dependent Electronic Transport Properties in Ethynyl-Terminated Ferrocene Molecular Junctions. *Micromachines* 2018, 9, 95. doi:10.3390/mi9030095.
- ²⁸ Camarasa-Gomez, M.; Hernangomez-Perez, D.; Inkpen, M. S.; Lovat, G.; Fung, E.-D.; Roy, X.; Venkataraman, L.; Evers, F. Mechanically-tunable Quantum Interference in Ferrocene-based Single-Molecule Junctions. *Nano Lett.* 2020, 20, 6381–6386. doi:10.1021/acs.nanolett.0c01956.
- ²⁹ Sun, Y.-Y.; Peng, Z.-L.; Hou, R.; Liang, J.-H.; Zheng, J.-F.; Zhou, X.-Y.; Mao, B.-W. Enhancing electron transport in molecular wires by insertion of a ferrocene center. *Phys. Chem. Chem. Phys.* 2014, 16, 2260. doi:10.1039/c3cp53269k.
- ³⁰ Yuan, Y.; Yan, J.-F.; Lin, D.-Q.; Mao, B.-W.; Yuan, Y.-F. Ferrocene-Alkynyl Conjugated Molecular Wires: Synthesis, Characterization, and Conductance Properties. *Chem. Euro. J.* 2018, 24, 3545–3555. doi:10.1002/chem.201705176.
- ³¹ Solomon, G. C.; Herrmann, C.; Hansen, T.; Mujica, V.; Ratner, M. A. Exploring local currents in molecular junctions. *Nat. Chem.* 2010, 2, 223–228. doi:10.1038/nchem.546.
- ³² Noori, M.; Sadeghi, H.; Lambert, C. J. High-Performance Thermoelectricity in Edge-over-Edge Zinc-Porphyrin Molecular Wires. *Nanoscale* 2017, 9, 5299–5304. doi:10.1039/C6NR09598D.
- ³³ Zhou, P.; Zheng, J.; Han, T.; Chen, L.; Cao, W.; Zhu, Y.; Zhou, D.; Li, R.; Tian, Y.; Liu, Z.; Liu, J.; Hong, W. Electrostatic Gating of Single-Molecule Junctions Based on the STM-BJ Technique. *Nanoscale* 2021, 13, 7600–7605. doi:10.1039/D1NR00157D.
- ³⁴ Spivak, M.; de Graaf, C.; Arcisauskaitė, V.; López, X. Gating the Conductance of Extended Metal Atom Chains: A Computational Analysis of $\text{Ru}_3(\text{Dpa})_4(\text{NCS})_2$ and $[\text{Ru}_3(\text{Npa})_4(\text{NCS})_2]$. *Phys. Chem. Chem. Phys.* 2021, 23, 14836–14844. doi:10.1039/D1CP02429A.
- ³⁵ Gray, P. R.; Hurst, P. J.; Lewis, S. H.; Meyer, R. G. *Analysis and Design of Analog Integrated Circuits*. Wiley, 40, 2009. ISBN:978-0-470-24599-6.

³⁶ Wilkinson, G. The Preparation and Some Properties of Ruthenocene and Ruthenocinium Salts. *J. Am. Chem. Soc.* 1952, 74, 6146–6147. doi:10.1021/ja01143a538.

³⁷ Swarts, J. C.; Nafady, A.; Roudebush, J. H.; Trupia, S.; Geiger, W. E. One-Electron Oxidation of Ruthenocene: Reactions of the Ruthenocenium Ion in Gentle Electrolyte Media. *Inorg. Chem.* 2009, 48, 2156–2165. doi:10.1021/ic802105b.

Chapter V – Computational study of iron- and ruthenium-based molecular junctions: comparison to experimental measurements

I – Introduction

In order to better predict the (thermo) electronic properties using computational approaches to perform molecular design and obtain molecular junctions with enhanced thermoelectric properties, the evaluation of the inconsistencies between computational and experimental results is compulsory. In collaboration with our experimental collaborators, i.e., Rigaut's group for the synthesis and the characterization of the molecules, Vuillaume's group for the SAMs fabrication and physical characterization (CP-AFM, UPS and XPS), and Scheer's group for the MCBJs study at low temperature, we have started a combined computational and experimental study of molecular junctions incorporating two different organometallic compounds.

The two molecules that are represented in Figure 1 have been chosen for a set of reasons. The Ru molecule which will be called **Ru-dppe** has been studied by the group of S. Rigaut over the last two decades for its conducting properties. Since their pioneering work with the group of Frisbie,^{1,12} the Ru(dppe)₂ unit has been integrated in several molecular junctions.^{2,3,4,5,6,7,8} In most of the cases, the Ru(dppe)₂ containing wires are giving higher conductance than organic conjugated wires of comparable length. It is one of the most studied organometallic molecular junctions to date and can thus be considered as a case study.

The prospective computational early work done in the group revealed that the Fe(cyclam)(C≡C-Ph-S-)₂, noted **Fe-cyclam**, as a neutral molecule (iron formally in +II oxidation state) presents a really interesting Seebeck coefficient of 100 μV/K at 300 K while having a theoretical conductance of about 0.1 G/G₀. Interestingly, at the molecular level, the most stable species is the magnetic cationic one in which the iron is in the +III oxidation state. The synthesis of this organometallic platform is well described in the literature. The same linker (phenyl-ethynyl) and the same anchoring (thiol) have been chosen because they are commonly used, well-mastered on an experimental point of view, and for sake of comparison.

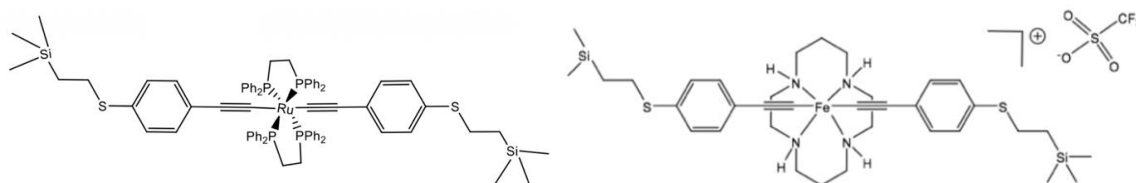


Figure 1 – Schematic representation of the $\text{Ru}(\text{dppe})_2(\text{C}\equiv\text{C}-\text{Ph}-\text{S}(\text{EDMS}))_2$ and $\text{Fe}(\text{cyclam})(\text{C}\equiv\text{C}-\text{Ph}-\text{S}(\text{EDMS}))_2$ molecules - dppe = diphenyl-diphosphino-ethane; cyclam = 1,4,8,11-tetraazacyclotetradecane; EDMS = ethyl(dimethyl)silane (protecting group).

II – Ru-dppe molecular junction: experimental studies

II.1 – Single molecule junction (MCBJ) measurements, first batch of measurements – Group of E. Scheer

The **Ru-dppe** substituted by EDMS protecting groups, as shown in Figure 1, was synthesized by the group of Rigaut (ISCR, Rennes). The MCBJs were fabricated by dropping a THF solution of **Ru-dppe** (1 mM) to which tetra-*n*-butyl ammonium fluoride (TBAF) was added to remove the EDMS protecting groups. The solvent was evaporated in a nitrogen atmosphere. The electrical contacts were made using copper wire on gold electrodes with conducting silver paint. A full description of the setup and description is available in reference 9.

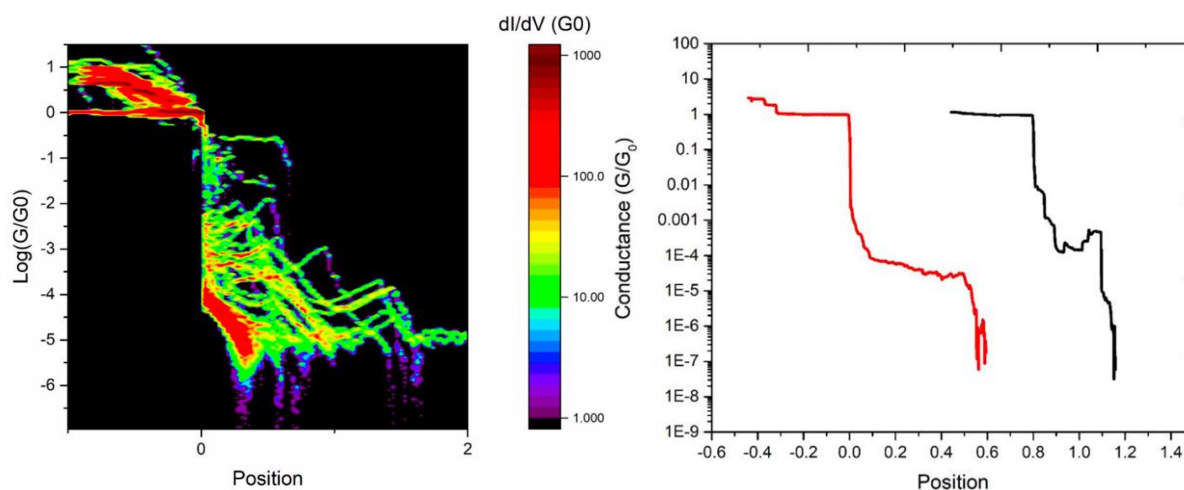


Figure 2 – Left: 2-D conductance histograms of the **Ru-dppe** device. Right: two typical selected traces. The x axis “position” is in nm.

The 2-D conductance histogram measured at 4.2 K shown in Figure 2 is mainly built of traces from 1.5 to 2 nm in length, in agreement with the molecular length (~ 2.14 nm between the ending S atoms). Two types of traces are extracted in the right part of Figure 2. The **Ru-dppe**

MCBJs are thus sufficiently stable to be characterized at low temperature. Yet, the configurations in which the molecular wires are spread in between the two electrodes are not only high conductance (HC) configurations. A typical HC I-V curve is shown in the left part of Figure 3. Four independent voltage I-V curves measurements at positive bias are given on the right side of Figure 3. These curves are uncommon and not constituted of a linear part followed by a quadratic evolution, which is the typical profiles that are encountered in most molecular junctions.^{10,11,12} The linear conductance extracted from these curves give a conductance G_{HC} of about $4.9 \cdot 10^{-3} G_0$. The SLM procedure was tentatively applied to get the key parameters ϵ_0 and Γ but it failed even in the linear regime. The TVS method was also unsuccessful to estimate ϵ_0 since no minimum could be found as shown in Figure 4.

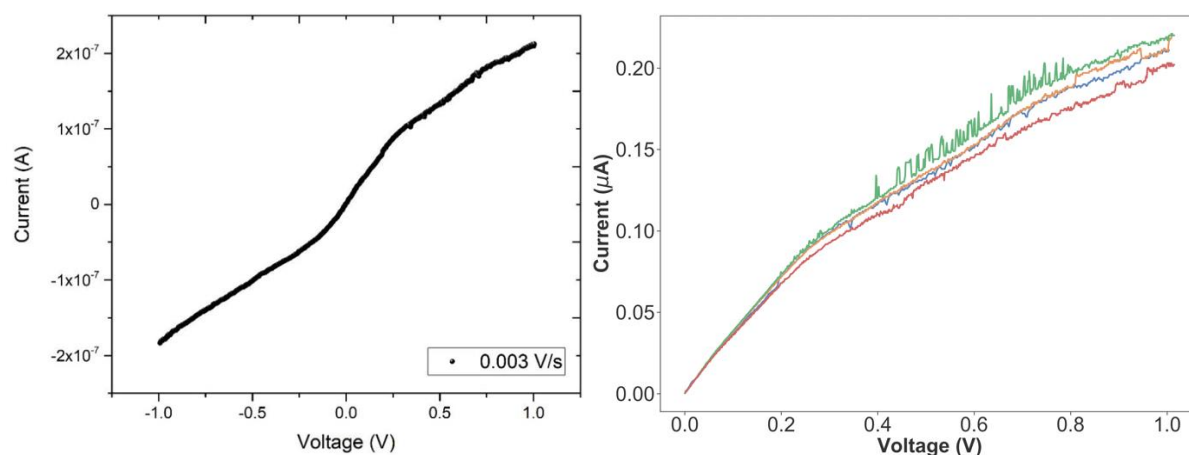


Figure 3 – Left: typical HC current-voltage curve of the Au–Ru-dppe–Au device measured by Scheer’s group at a sweeping rate of 0.003 V/s. Right: representation of 4 independent HC I-V curves at positive bias.

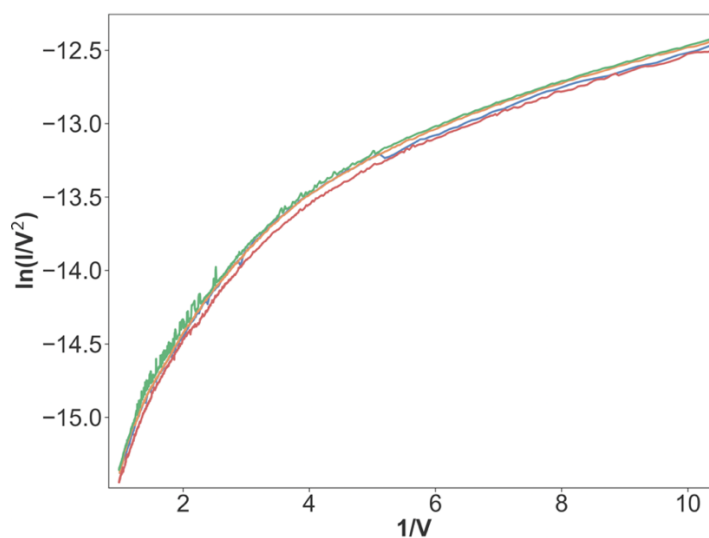


Figure 4 – F-N plot issued from the I-V curves shown from the right of Figure 3.

The rationalization of the experimental data from this first batch is hampered by the fact that the SLM and the TVS models are not applicable. We attempt to use a modified version of the SLM model in which ϵ_0 is voltage dependent. Since many initial ($\epsilon_{0\text{-init}}$, Γ) couples could be used to potentially fit the data, the choice of the initial values is based on other experimental data. Indeed, $\epsilon_{0\text{-init}}$ and Γ were estimated to -0.30 eV and 11 meV respectively on the basis of two other experimental characterizations: SLM fits of the **Ru-dppe** SAM measurements of Vuillaume's group (described below), and of the data obtained by Frisbie *et al.* in reference 13 for the parent system $\text{Ru}(\text{dppe})_2(\text{C}\equiv\text{C-Ph}-(\text{CH}_2)_2\text{S})_2$ (Figure 5). The resulting fit is shown Figure 6. It is important to stress that this model does not account for a variation of Γ with the bias neither consider the possible diminution of the maximum of transmission probability as the voltage increases (due for example to the polarization of the electronic cloud of the molecule). Using these values as a starting point, the corresponding fitting of the **Ru-dppe** gave the voltage dependence $|\epsilon_0(V)| = 0.10V^2 + 0.28V + 0.30$ (Figure 6).

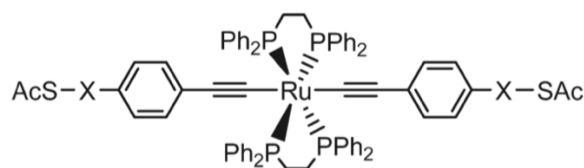


Figure 5 – Scheme of the molecule used to estimate $\epsilon_{0\text{-init}}$ and Γ from reference 13 for $X = (\text{CH}_2)_2$.

The $\epsilon_{0\text{-final}}$ of -0.68 eV is more than twice the value at zero bias ($\epsilon_{0\text{-init}} = -0.30$ eV). As said previously, this is certainly exaggerated by the fact that the possible bias voltage dependency of Γ and the reduction of transmission as the bias ΔV increases were not considered. Unfortunately, this could not be accounted for since it results in an increase of the quantity of parameters that lead to an overfitting of the data.

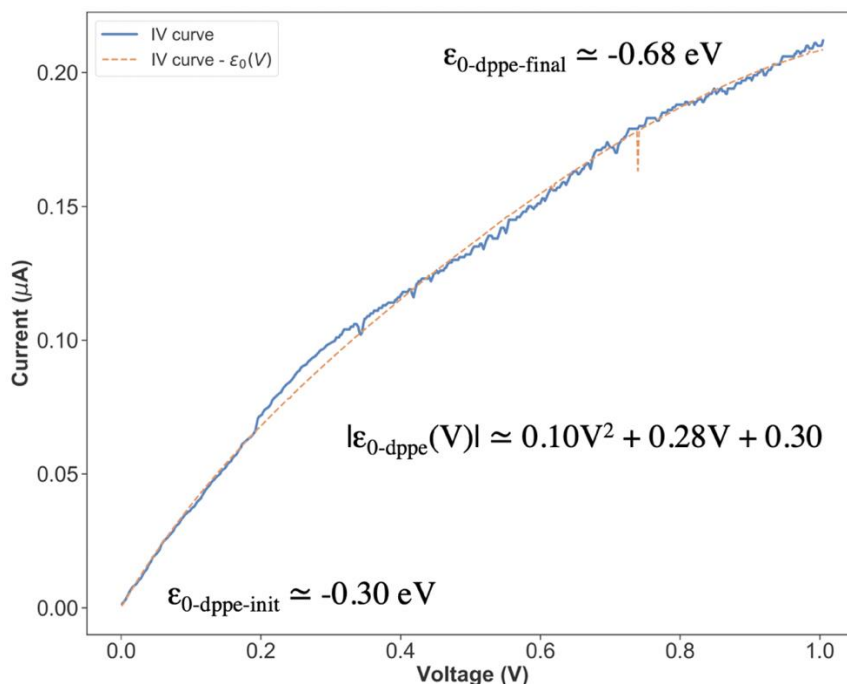


Figure 6 – Modified SLM fit on a typical **Ru-dppe** I-V curve. The parameters are $\epsilon_{0-init} = -0.30$ eV, $\Gamma = 11$ meV. The $\epsilon_{0-final}(\Delta V = 1.0 \text{ V}) = -0.68$ eV.

II.2 – Single molecule junction (MCBJ) measurements, second batch of measurements – Group of E. Scheer

A second series of measurements was performed on a second batch of **Ru-dppe** MCBJ. The main results are displayed in Figure 7. Interestingly, they were quite different both in the I-V curve shapes and in the repartition of the conductance values. In the 2-D histograms, the displacements associated to HC are smaller with maximum traces of 1.2 nm long. This is importantly reduced compared to the first batch and the theoretical size of the molecule (~2 nm). A substantial number of conductance traces are associated to a lower conductance (LC) close to $G_{LC} \approx 2.10^{-5} G_0$ whereas the high conductance, $G_{HC} \approx 2.10^{-3} G_0$, has the same order of magnitude as for the first batch ($G_{HC} \approx 4.9.10^{-3} G_0$). Selected I-V curves are extracted in Figure 8. Different contacts between the molecule and the gold electrodes can explain the important difference in the I-V curves between the two batches of measurements. This could be also due to a possible degradation of the solid-state powder. A new series of measurements is definitely needed to tackle these apparent discrepancies.

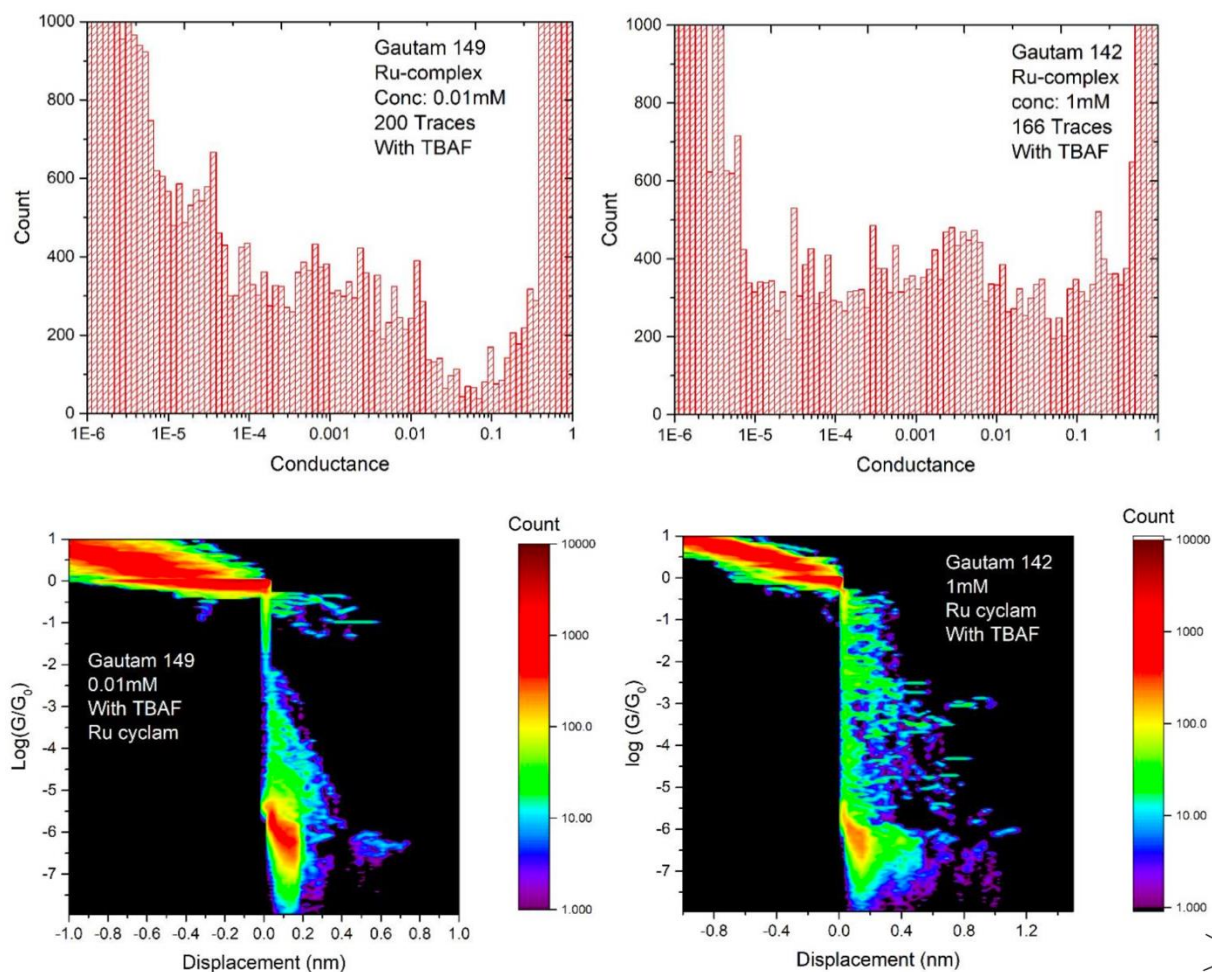


Figure 7 – Top: count histograms for two separate measurements. Bottom: two 2-D conductance histograms of the **Ru-dppe** system from the second batch of molecules.

Furthermore, the fact that some of the I-V curves (Figure 8) are not symmetrical in regard to the voltage polarity is not expected for a symmetrical molecule (both in terms of anchoring and conjugated backbone). In the negative bias part, the shapes of the I-V curves of Type-1, Type-2 and Type-3 displayed in Figure 8 are similar to profiles found in presence of Kondo effect or Coulomb blockade regime which would implies at least one weak interfacial coupling.¹⁴

We performed the fitting (SLM and TVS) procedures for the positive and negative bias for each type of I-V curve presented in Figure 8, and their results are displayed in Table 1.

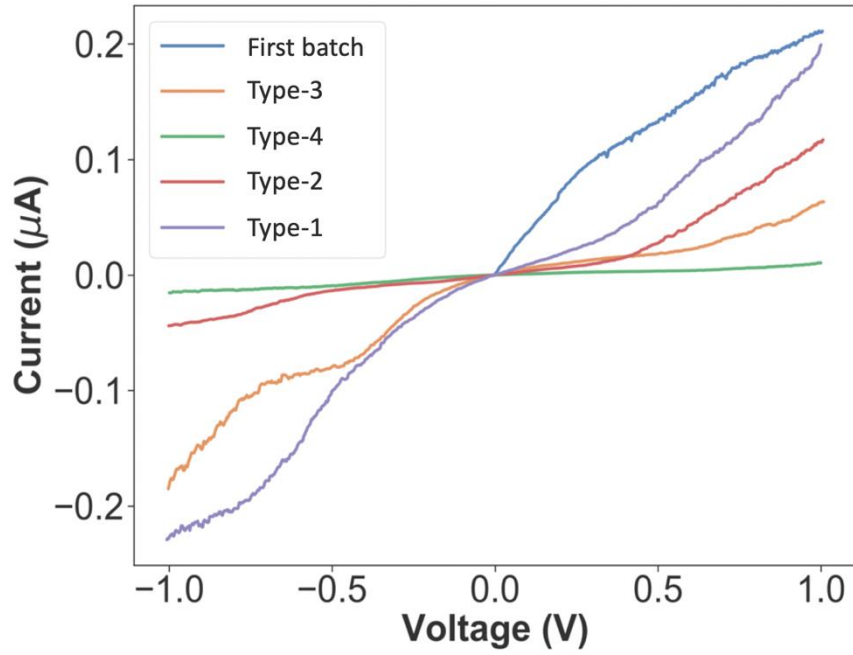


Figure 8 – Selection of typical I-V curves of the second batch of **Ru-dppe** MCBJ characterizations. Type-1: purple, Type-2: red curve, Type-3: orange curve, Type-4: green curve. A typical trace of the HC case in the first batch of measurements is given in blue for sake of comparison.

Table 1 – Summary of the parameters obtained by applying an SLM fit and TVS procedure on the four different types of I-V curves shown Figure 8. The missing values are due to failure of the SLM methods to fit the experimental data or when no minimum was found in the TVS graph. Note that when the SLM fit is performed in the 0 to 1.0 V range, only the higher bias part of the I-V curve (from ~ 0.5 V to 1.0 V) is correctly fitted. A second fit was thus performed in a smaller bias range (0.0 to ± 0.5 V).

| Method | SLM | | | | | | TVS | |
|-------------------------------------|--------------|----------|--------------|----------|--------------|----------|--------------|--------------|
| | 0 – 1.0 | | 0 – 0.5 | | 0 – -0.5 | | 0 – 1.0 | 0 – -1.0 |
| ϵ_0 in eV; Γ in meV | ϵ_0 | Γ | ϵ_0 | Γ | ϵ_0 | Γ | ϵ_0 | ϵ_0 |
| Type-1 ($1.16 \cdot 10^{-3}$) | -0.77 | 15.1 | -0.59 | 10.0 | -0.30 | 5.9 | -0.84 | - |
| Type-2 ($4.27 \cdot 10^{-4}$) | - | - | -0.34 | 3.2 | - | - | -0.33 | -0.50 |
| Type-3 ($7.61 \cdot 10^{-4}$) | -0.75 | 7.9 | - | - | -0.24 | 3.8 | -0.65 | - |
| Type-4 ($1.13 \cdot 10^{-4}$) | -0.81 | 3.6 | - | - | -0.30 | 1.9 | -0.67 | - |

The TVS applied to the negative bias part only gives a minimum for the Type-2 curve with $|\epsilon_0| = 0.50$ V. For the positive bias, the $|\epsilon_0|$ values extracted from TVS are quite different. They are

equal to 0.33 eV and 0.84 eV for Type-1 and Type-2 respectively, while TVS applied to Type-3 and Type-4 lead to similar $|\epsilon_0|$ values, 0.65 and 0.67 eV, respectively.

The SLM fit was first applied in the negative bias up to $\Delta V_{\max} = -0.5$ V since it failed for larger ranges of voltage bias. For the Type-1, Type 3 and Type 4 curves, the SLM gives similar ϵ_0 with $\epsilon_{0-mean} (\Delta V_{\max} = -0.5 \text{ V}) = -0.28 \pm 0.04$ eV.

For the positive bias, the SLM fits from 0 to 1.0 V lead to homogeneous results with $\epsilon_{0-mean} = -0.78 \pm 0.03$ eV for Type-1, Type-3 and Type-4 (no fit possible in Type-2). Interestingly, these fits poorly recover the I-V curves below 0.5 V bias but match very well above this threshold. This can be indicative that the transmission is modified upon bias voltage increase (e.g. due to polarization effects).

It appears interesting to only fit the I-V curves up to 0.5 V. In that case, -0.59 eV and -0.34 eV are found for ϵ_0 for Type-1 and Type-2 respectively. This is indeed in favor of a modification of the transmission feature upon application of the voltage.

II.3 – CP-AFM on Ru-dppe junctions (SAMs on Au substrate) – Group of D. Vuillaume

The SAMs were prepared by Vuillaume's group following a standard procedure. The I-V characteristics (back and forth) were measured at each point of a 10×10 grid with a pitch of 100 nm. About 200 I-V traces were recorded for each dataset. They repeated the measurements at several locations on the SAMs with different cantilever load forces (10-34 nN). The sweep voltage speeds ranged from 0.04 to 4.0 V/s. Importantly, the tip of the AFM cantilever is made of an alloy of Pt/Ir.

The SAM thickness determined by ellipsometry is 1.5 nm. A theoretical value of ~ 2.1 nm is obtained considering that the EDMS groups are removed in the fabrication process. The thickness is moderately smaller compared to the theoretical value. The molecule main axis is probably tilted from the surface normal. Indeed, a tilting angle of 40° from the surface normal would induce a thickness of 1.5 nm. Another possibility could be a mixing between coordinated molecules (height ~ 2.1 nm) and molecules lying on the substrate (height ~ 0.8 nm, i.e., thickness of the dppe ligand around the ruthenium atom).

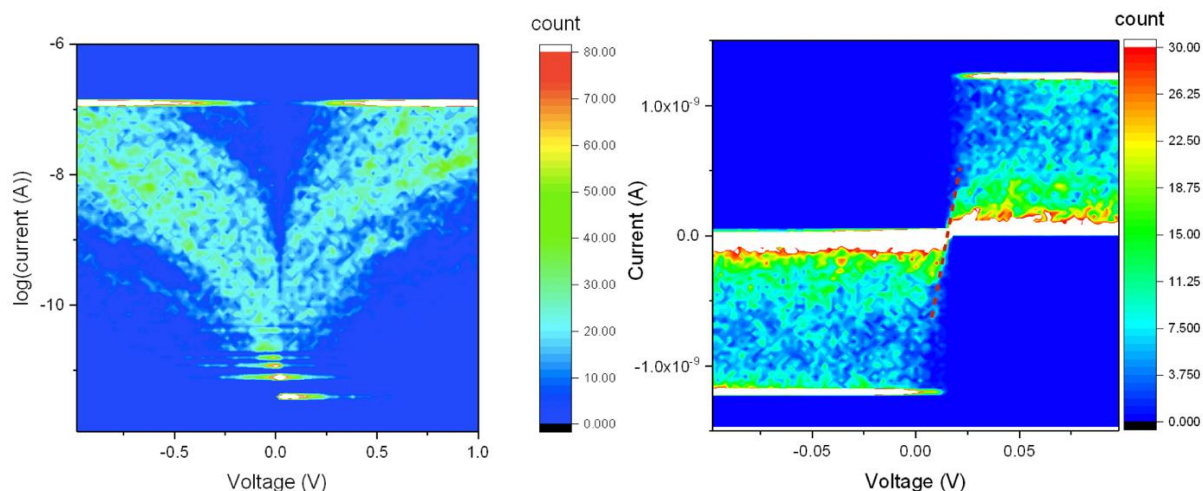


Figure 9 – CP-AFM on **Ru-dppe** SAMs. Left: I-V traces. Right: estimated maximum linear conductance extracted from the I-V curves with $G_{HC} \approx 1.29 \cdot 10^{-3} G_0$.

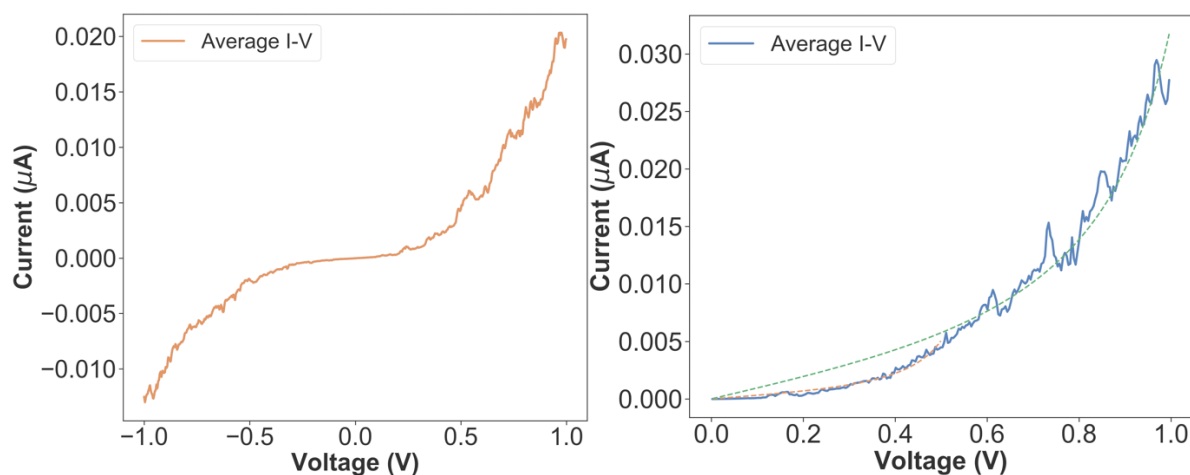


Figure 10 – CP-AFM on **Ru-dppe** SAMs. Left: averaged I-V curve from the data of Figure 9. Right: SLM fit of the positive bias part of the averaged I-V curve. Orange dotted curve: fit of the I-V from 0 to 0.5 V; Green dotted curve: fit of the I-V from 0 to 1.0 V.

The I-V curves obtained for this system are shown in Figure 9. The dataset presents a quite large dispersion. The maximum conductance was estimated from this data at $\sim 1.3 \cdot 10^{-3} G_0$. The molecular parameters ϵ_0 and Γ were estimated from the averaged I-V curve (Figure 10) using the SLM method: $\epsilon_0 = -0.32$ eV and $\Gamma = 0.89$ meV in the bias range from 0 to 0.5 V. The fit performed in the 0 to 1.0 V bias range is poor in the small voltage region, as shown in Figure 10. Because the tip is not made of gold, the coupling values of the two electrodes are different ($\Gamma_L \neq \Gamma_R$). If this is considered in the fits, the obtained couplings are $\Gamma_L = 0.81$ meV and $\Gamma_R = 0.98$ meV.

The extraction of ϵ_0 from TVS done by the group of Vuillaume is complicated by the important noise (see Figure 11). The value $\epsilon_0(\text{TVS}) = -0.18 \pm 0.07$ eV emerges from a majority of the TVS showing a minimum. The dispersion of the TVS curves minima was also plotted, as shown in Figure 11. They also applied the SLM (up to 0.5 V) on a hundred of I-V curves to obtain a more statistical analysis leading to $\epsilon_0(\text{SLM}) = -0.32 \pm 0.06$ eV. The two methods are using the same dataset to normally extract the same molecular parameter ϵ_0 . The discrepancy in the results suggests that the hypotheses and approximations are not equivalent and lead to a different descriptor.

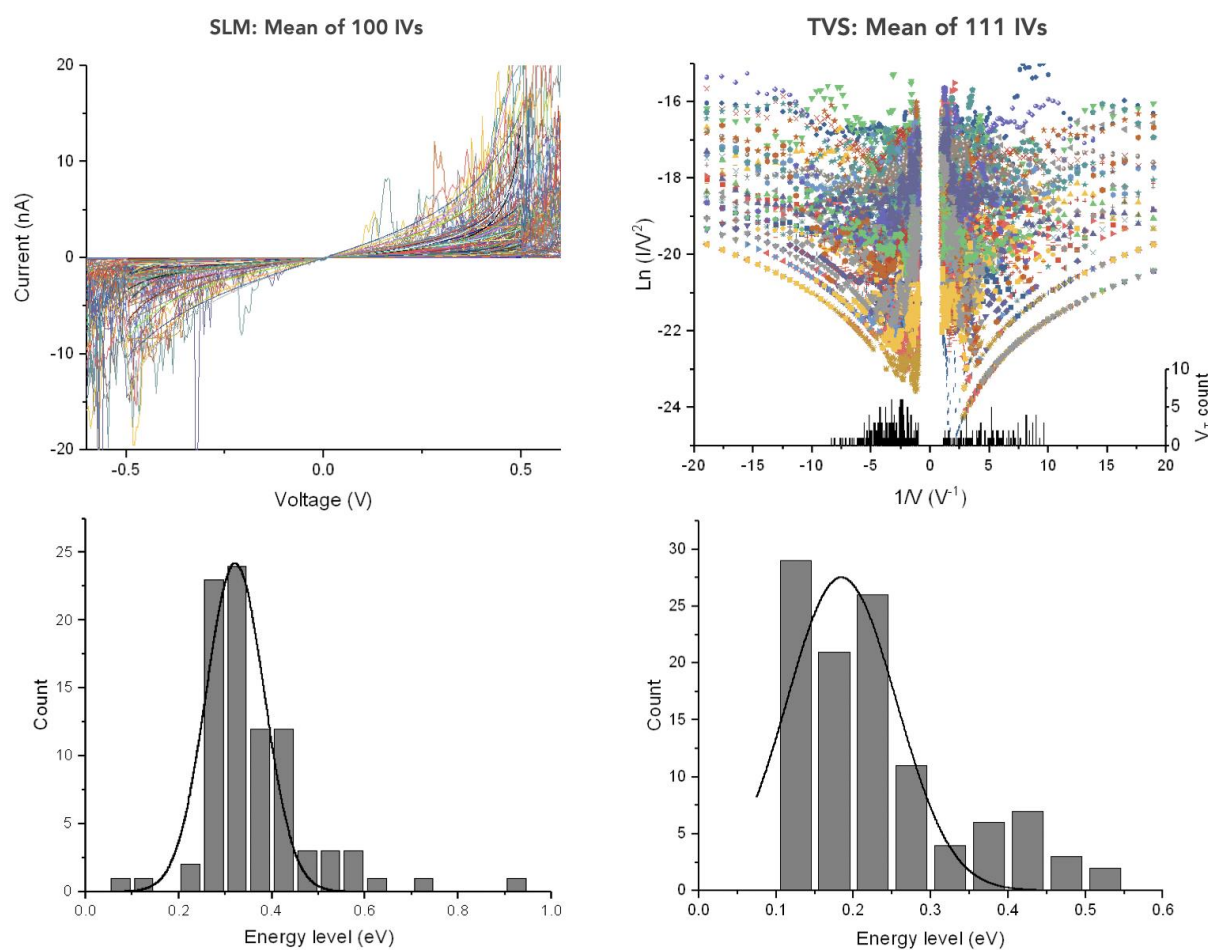


Figure 11 – **Ru-dppe** SAM I-V curves and extracted data by Vuillaume's team. Statistical values of ϵ_0 , using both the SLM and TVS approaches on a hundred of I-V curves. This yield: $\epsilon_0(\text{SLM}) = -0.32 \pm 0.06$ eV and $\epsilon_0(\text{TVS}) = -0.18 \pm 0.07$ eV.

UPS and XPS measurements were also performed by the group of Vuillaume using another batch of **Ru-dppe** SAMs. The SAMs were prepared by impregnating an Au substrate with a 20/80 THF-EtOH solution of **Ru-dppe** for 2 days in a glove box away from light. Then, the

substrate was washed by a THF/EtOH solution under ultrasound. It was shown that in these conditions, the thiol deprotection occurs spontaneously on gold without using TBAF. The thickness of the SAM measured by ellipsometry is $d = 0.8$ nm. Interestingly, it matches with the expected height for **Ru-dppe** molecules lying on the gold surface, as stated earlier. This warns us to take the following results cautiously. The XPS analysis did not detect silicon signals corroborating the absence of EDMS. The presence of an N_{1s} signature was detected but rationalized by traces of ammonium salts coming from the synthesis. The P_{2p} and Ru_{3p} are not detected but published results of parent systems showed that they are extremely weak and could be hidden in the background.¹ The UPS measurements shown in Figure 12 allows to extract a "HOMO energy" (-0.34 eV) which is normally directly linked to ϵ_0 . Even though the thickness of the SAM is smaller than expected, this ϵ_0 (UPS) value is in adequacy with the value extracted from the statistical average of hundred I-V curves with the SLM fitting (ϵ_0 (SLM) = -0.32 ± 0.06 eV). As a reminder, the comparison between both methods should be pondered by an added image effect.

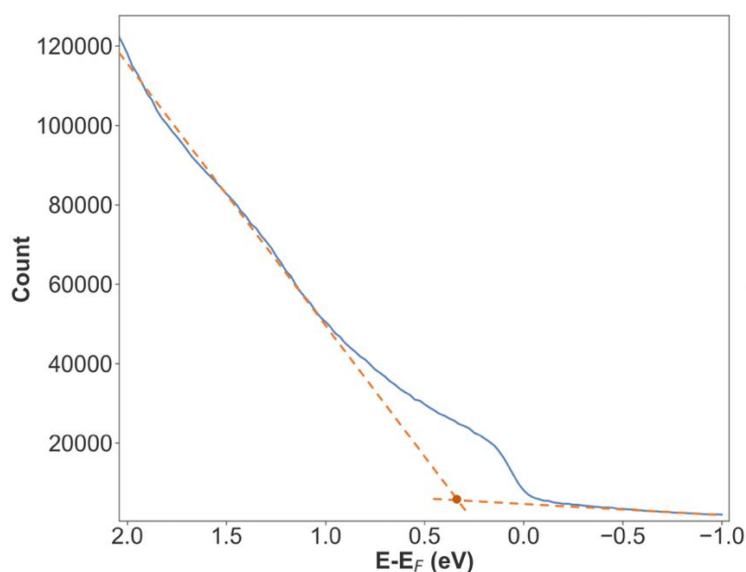


Figure 12 – UPS measurements (blue curve with binding energies relative to the Fermi energy of the gold substrate) for the **Ru-dppe** molecule SAM. ϵ_0 is estimated at -0.34 eV (orange dot).

III – Fe-cyclam molecular junctions: experimental studies

III.1 – Single molecule junction (MCBJ) measurements, first batch of measurements – Group of E. Scheer

The same procedure as described for the **Ru-dppe** system was applied by the group of Scheer to study the conducting properties of **Fe-cyclam**-based MCBJ. In that case, different concentrations of solutions were used, from 0.05 to 0.5 mM, as summarized in Table 2.

Table 2 – Main conductance peaks at a bias voltage of 100 mV of **Fe-cyclam** MCBJ as a function of the concentration of the solution used to prepared the MCBJs.

| Concentration (mM) | Main conductance peak (G/G ₀) | Counts |
|--------------------|---|--------------------|
| 0.05 | 10^{-6} ; 2.10^{-5} ; 10^{-4} ; 2.10^{-3} | 800; 200; 300; 200 |
| 0.1 (Sample 1) | 10^{-6} ; 10^{-4} (wide) | 1400; 500 |
| 0.1 (Sample 2) | 10^{-6} ; 2.10^{-4} (wide) | 1000; 1200 |
| 0.1 (Sample 3) | 10^{-6} | 1000 |
| 0.5 | 10^{-6} ; 10^{-4} to 10^{-2} (wide) | 1000; 1750; 1250 |

The measured conductance is spread between 10^{-6} G/G₀ to 10^{-2} G/G₀ with a main occurrence at of 10^{-4} G/G₀. Two series of I-V curves were measured, one from 0.0 V to 1.0 V and another from 0.0 V to 0.3 V (Figure 13).

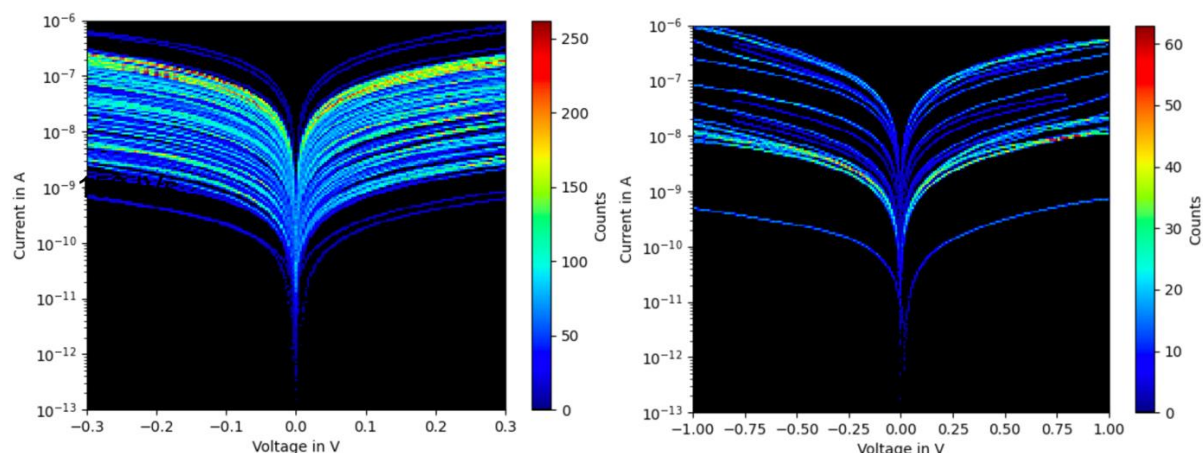


Figure 13 – Current-voltage curves of the **Fe-cyclam** system using the MCBJ technique: Left: from -0.3 to 0.3 V, 223 I-Vs. Right: from -1.0 V to 1.0 V, 25 I-Vs.

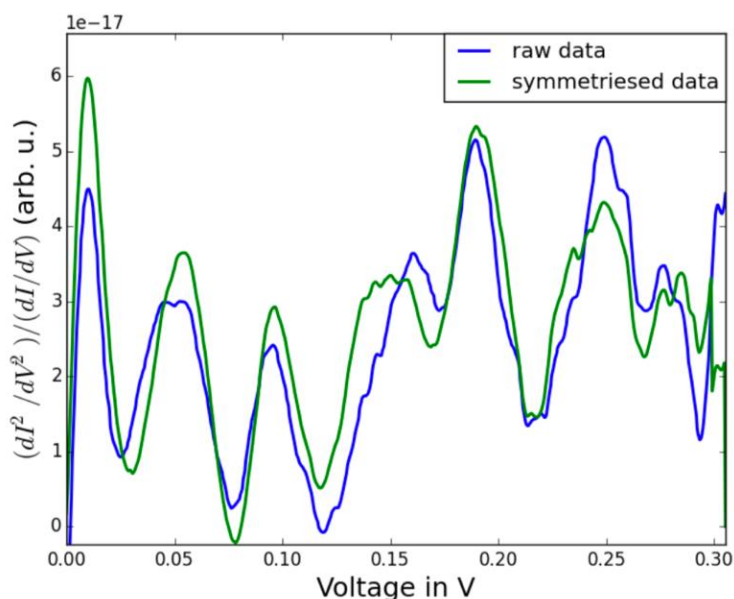


Figure 14 – Experimental IETS spectra obtained from one of the most representative conductance ($\sim 10^{-4}$ G/G₀) I-V curve.

The IETS shown Figure 14 was realized on one of the representative conductance **Fe-cyclam** MCBJ ($\sim 10^{-4}$ G/G₀). The IETS peaks are associated to specific vibrations in which the molecular signature can be extracted.^{15,16,17} This technique is used to check that a single molecular junction is formed. The peaks below 20 mV are corresponding to Au bulk phonon modes.^{18,19} The peaks in the 27-33 meV region are signature of Au-S vibrations.^{20,21} By comparison with the vibrational properties of the isolated **Fe-cyclam** molecule, the peak at 100-110 mV can be attributed to molecular vibrations.²² The C≡C vibrations are situated between 250-270 meV.^{18,23} These results demonstrate that the **Fe-cyclam** is grafted to at least on electrode of the junction in this particular case.

The SLM method was applied to a sample of the high conductance I-V curves, i.e., with a conductance of $3.1 \cdot 10^{-4}$ G₀. The resulting ϵ_0 and Γ are given in Figure 15. Since the curve is symmetrical only the positive bias was fitted. Depending on the integration range (0-0.5 V or 0-1.0 V), as it was the case for the **Ru-dppe** molecule, the energetic position ϵ_0 and the coupling strength Γ are modified (with $\epsilon_0 = -0.53$ eV, $\Gamma = 4.7$ meV and $\epsilon_0 = -0.70$ eV, $\Gamma = 6.6$ meV for 0 to 0.5 V and 0 to 1.0 V, respectively).

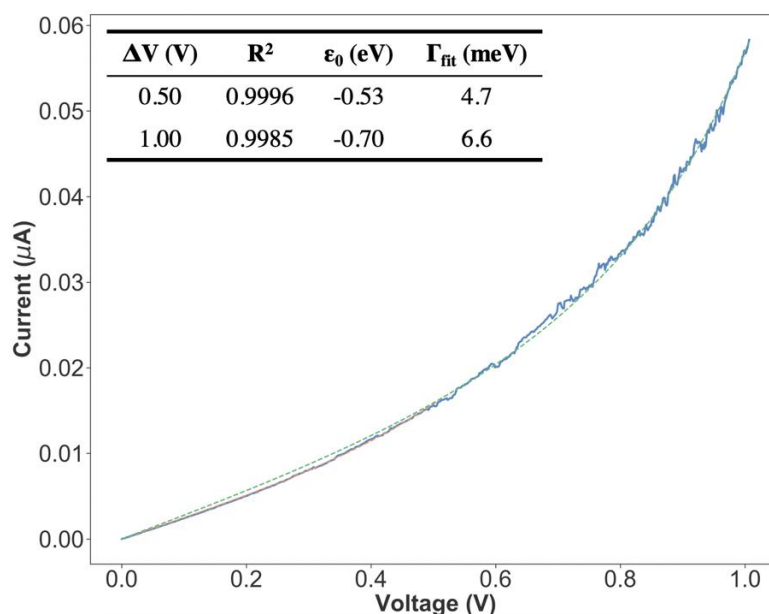


Figure 15 – Fit of a representative high conductance I-V curve using the SLM model. The green dotted line corresponds to the fit between 0 to 1.0 V and the orange one is the fit from 0 to 0.5 V.

III.2 – CP-AFM on Fe-cyclam junctions (SAM on Au substrate) – Group of D. Vuillaume

The same procedure as for **Ru-dppe** was applied for the **Fe-cyclam**. The SAM thickness obtained by ellipsometry is $d = 1.8$ nm (theoretically ~ 2 nm without the EDMS protection groups). The thickness appears to be more in adequacy with a molecule grafted approximately perpendicularly to the substrate. The tilting angle to get $d = 1.8$ nm is 33° normal to the surface.

The I-V curves obtained for this system are displayed in Figure 16. The maximum conductance could be estimated at $G_{\text{HC}} = 6.4 \cdot 10^{-6} G_0$ (about 200 times lower than **Ru-dppe**). From the averaged I-V curve (Figure 17), using the SLM, the molecular parameters ϵ_0 and Γ were estimated at: $\epsilon_0(0 - 0.5 \text{ V}) = -0.49$ eV and $\Gamma_{\text{mean}}(0 - 0.5 \text{ V}) = 0.6$ meV. For $\Delta V = 1.0$ V, the fitting is also pretty good and gives $\epsilon_0(0 - 1.0 \text{ V}) = -0.72$ eV and $\Gamma_{\text{mean}}(0 - 1.0 \text{ V}) = 1.0$ meV. Using the TVS approach, $|\epsilon_0|$ can be approximated to 0.65 eV. In Figure 18 reports the corresponding dispersions from the SLM (for 0 - 0.5 V) and TVS models; a hundred of I-V curves was analyzed to provide a statistical average of ϵ_0 , leading to $\epsilon_0(\text{SLM}) = -0.76 \pm 0.18$ eV and $\epsilon_0(\text{TVS}) = -0.70 \pm 0.16$ eV. For this molecule, both methods overlap although the variation is much more significant than for the **Ru-dppe** molecule.

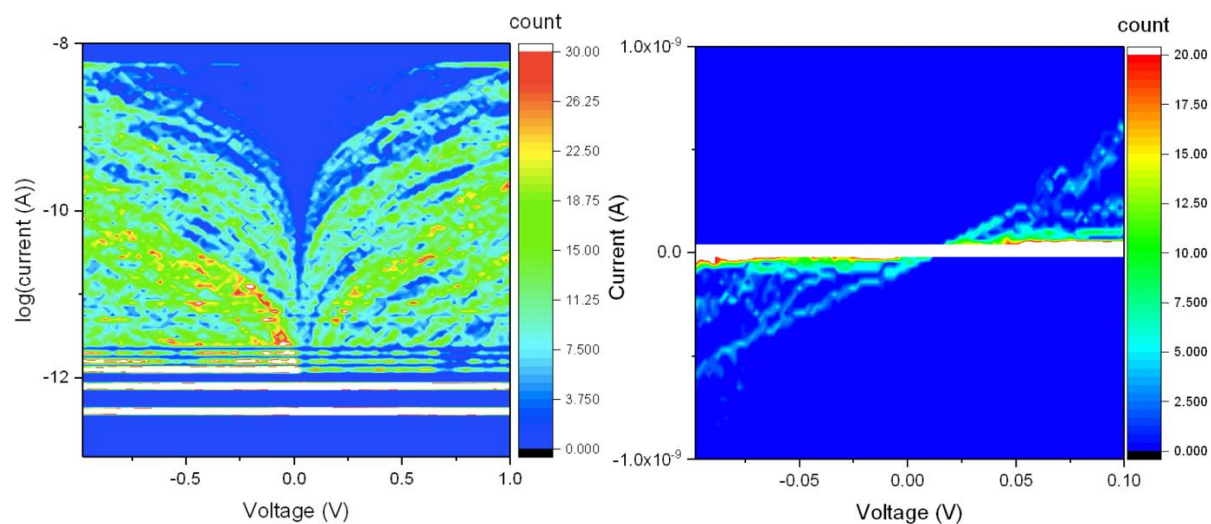


Figure 16 – Left: I-V traces exhibiting a large dispersion of the current. Right: estimated maximum linear conductance from the I-V curves with $G_{\text{HC}} \approx 6.4 \cdot 10^{-6} G_0$.

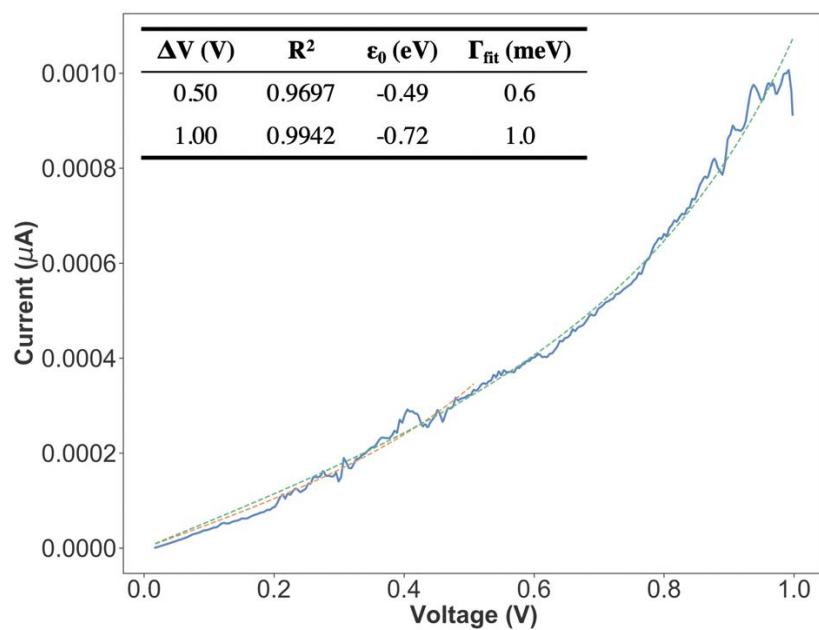


Figure 17 – CP-AFM on **Fe-cyclam** SAM. SLM fit of the positive bias part of the averaged I-V curve. Orange dotted curve: fit of the I-V from 0.0 to 0.5 V; Green dotted curve: fit of the I-V from 0.0 to 1.0 V

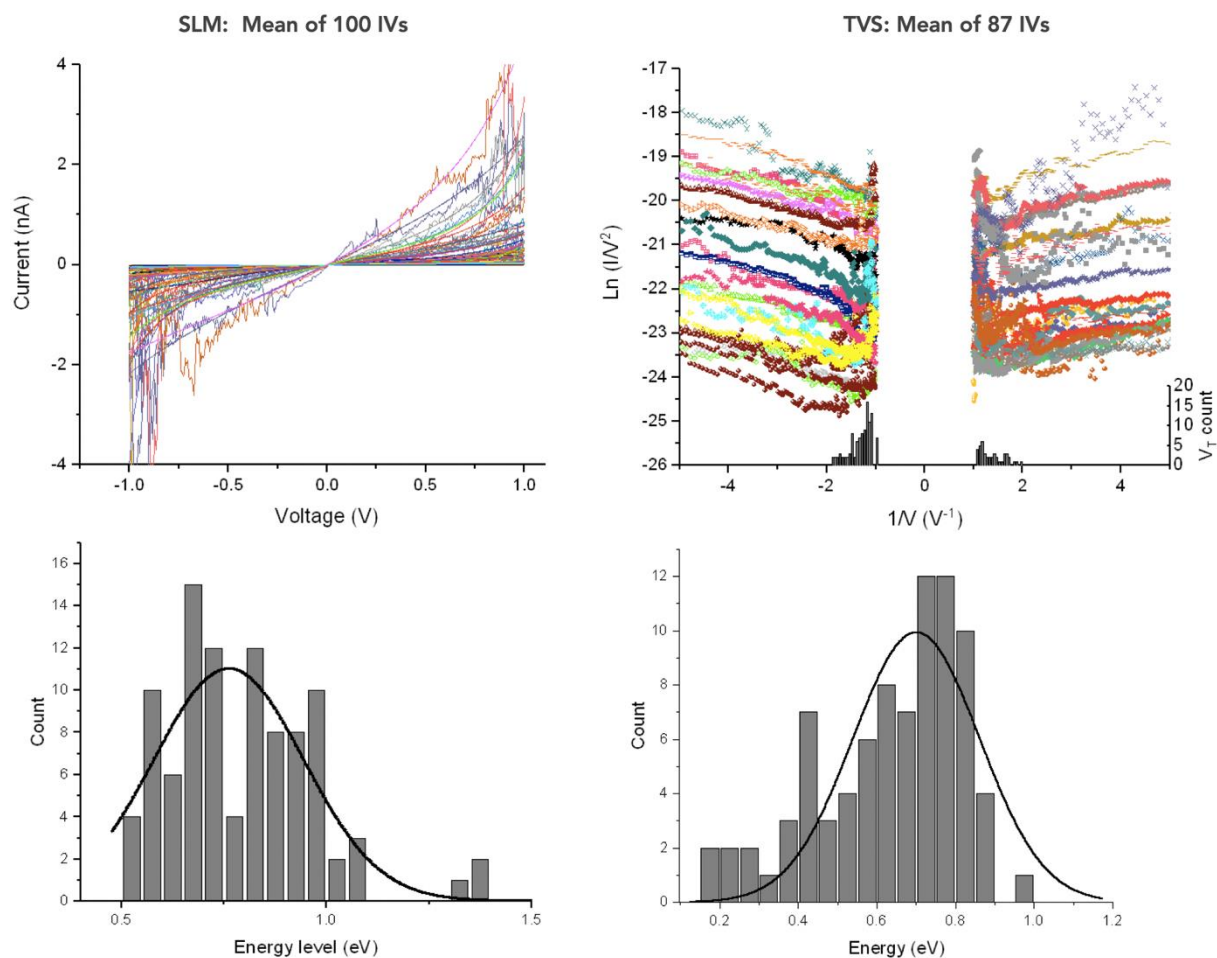


Figure 18 – Fe-cyclam SAM I-V curves and extracted data by Vuillaume's team. Statistical values of ϵ_0 , using both the SLM and TVS method on a hundred of I-V curves leading to $\epsilon_0(\text{SLM}) = -0.76 \pm 0.18$ eV and $\epsilon_0(\text{TVS}) = -0.70 \pm 0.16$ eV.

UPS and XPS measurements were also performed as for **Ru-dppe** SAM. The XPS does not detect any feature which would indicate the presence of the CF_3SO_3^- counter ion (absence of F_{1s} and oxidized sulfur SO_x). The EDMS group was also not observed (no Si traces). For this new sample, the measured SAM thickness is $d = 3$ nm. It could be indicative of molecules lying on the molecular monolayer, thus not grafted to the gold substrate. The XPS and UPS data have to be taken with a grain of salt and further experiments would need to be done to confirm the present data. The UPS measurements point to $\epsilon_0 = -0.73$ eV (Figure 19).

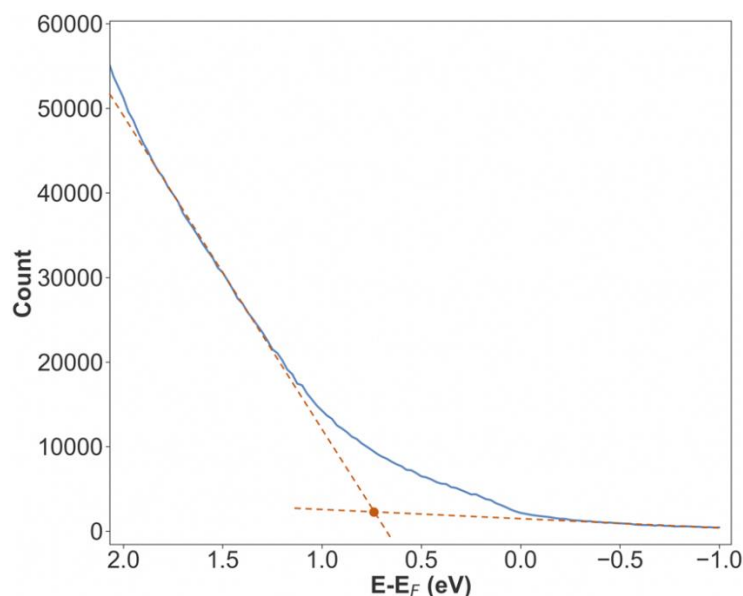


Figure 19 – UPS measurements (blue curve with binding energies relative to the Fermi energy of the gold substrate) for the **Fe-cyclam** molecule. ϵ_0 is estimated at -0.73 eV (orange dotted lines).

IV – Comparison of the I-V characteristics between the two sets of experimental data

For **Ru-dppe**, the first batch of MCBJ measurements performed at low temperature by Scheer and coworkers are leading to quite different characteristics of the conducting properties compared to the SAM configuration studied by Vuillaume and collaborators. The conductance is also much lower for the SAM setup compared to the single molecule junction configuration, a feature that is often found but not fully understood to date.^{24,25,26,27} In order to facilitate the comparison, current has been normalized in the next figures. Interestingly, this rescaling of the I-V curves shown in Figure 20 reveals really similar behaviors between the second batch of MCBJ measurements and SAM characterizations of the **Ru-dppe** system. The agreement is particularly good for the red IV-curve (Type-2 curve), whereas the deviations observed for the green and purple curve, associated to different values of ϵ_0 , are certainly due to different junction geometries (Part II, Chapter II). The curvature of the I-V curves is indeed mainly governed by the position of ϵ_0 (and with Γ predominant in the current intensity).

A good agreement between MCBJ and CP-AFM is also found for the **Fe-cyclam** system in Figure 20, right. Indeed, both SLM fit showed that ϵ_0 ($0 - 1.0$ V) ≈ -0.70 eV.

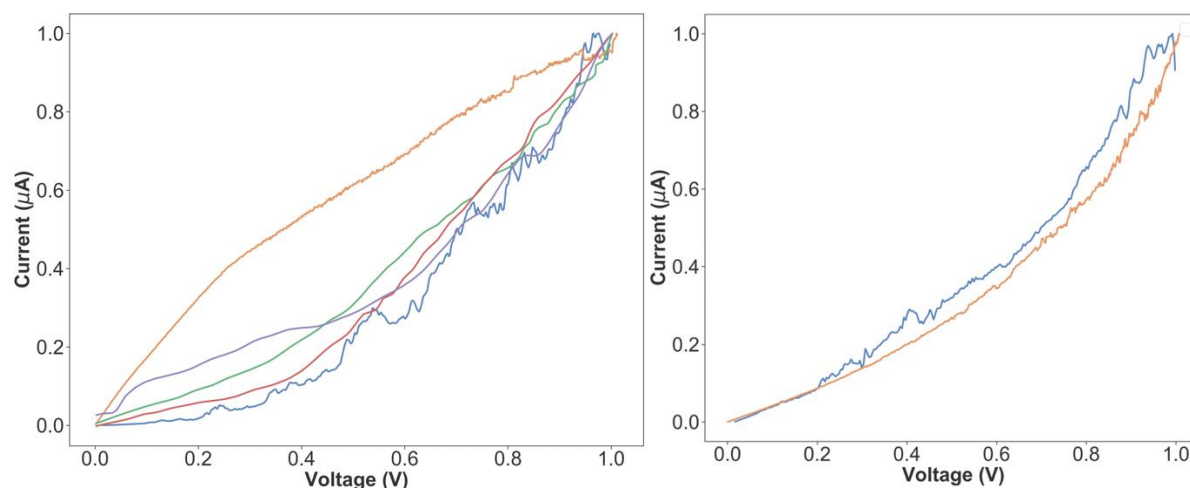


Figure 20 – Normalized current I-V curves. Left: **Ru-dppe** system; CP-AFM in blue, first batch MCBJ in orange, second MCBJ batch in red, purple, and green. Right: **Fe-cyclam** system; CP-AFM in blue, MCBJ in orange.

V – Computational study of the Ru-dppe and Fe-cyclam junctions

Computational details

The geometries of the molecular systems were optimized in gas phase using the ADF program, with the GGA-revPBE functional, a TZ2P basis set, and ZORA relativistic correction (see Part II, Chapter I, section III.4.1). The cluster model using Au₁₃ was applied at the same level of theory (see Part II, Chapter III). The transmissions of the junctions were calculated with the thiol anchoring in hollow coordination modes (#1-hollow and #3-hollow) on gold electrodes (see Part II, Chapter II) at the DFT/NEGF level using the QuantumATK package software from Synopsys (see Part II, Chapter I). The hybrid-GGA HSE06 functional has been implemented in the recent update QuantumATK 2021 and was tested for the zero-bias transmission.

V.1 – Ru-dppe system

The DFT MO energy diagrams of the isolated **Ru-dppe** molecule (with hydrogen as terminal group) and cluster model are represented in Figure 21. A substantial HOMO-LUMO gap of 2.10 eV in the **Ru-dppe** molecular electronic structure reflects the good thermodynamic stability of the compound. Among the highest occupied orbitals, the HOMO and HOMO-1 present a delocalization along the conjugated path with the participation of the Ru d atomic orbitals. The **Ru-dppe** cluster model allows to predict that the conducting levels should be quite close to the Fermi level (0.40 eV below the gold states).

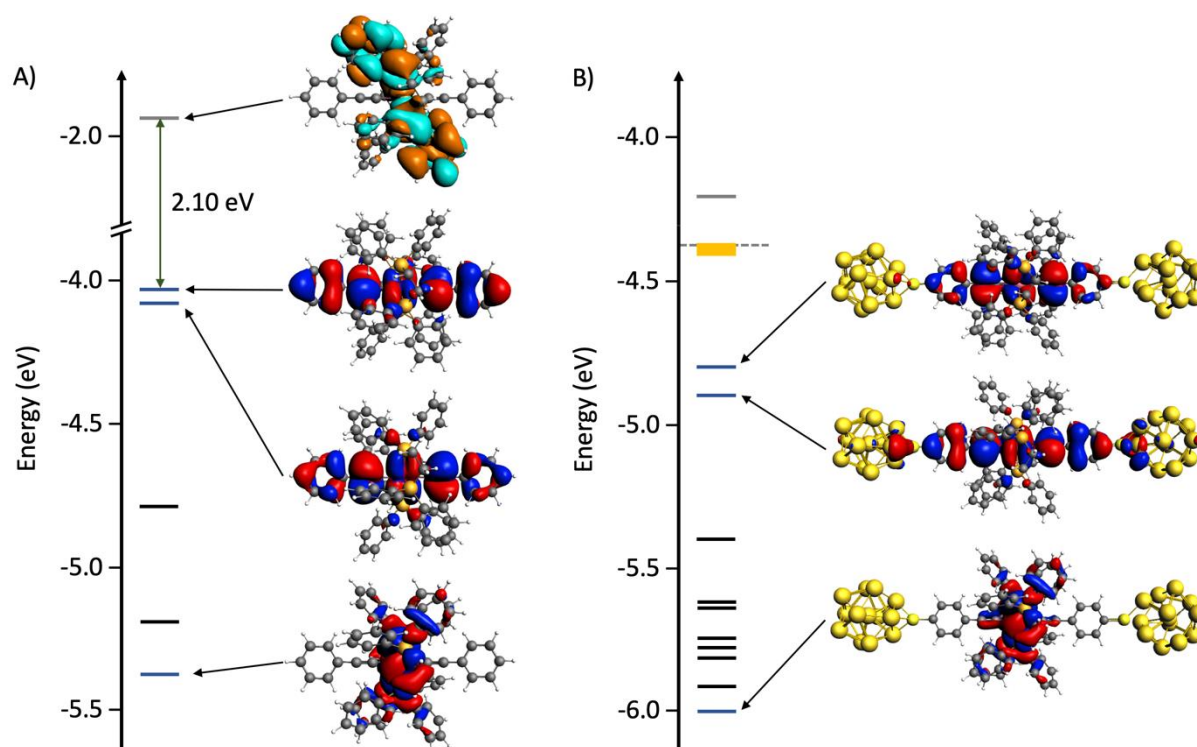


Figure 21 – A) DFT MO energy diagram of the bare **Ru-dppe** molecule. B) DFT MO energy diagram of the functionalized **Ru-dppe** molecule with two Au₁₃ gold clusters (cluster model). Coloring of the levels: yellow = occupied gold levels, blue = occupied MOs presenting a predominant *d* iron contribution (MO_d), black = other occupied MOs, grey = unoccupied levels.

DFT/NEGF calculations were performed for the molecular junction incorporating a single **Ru-dppe** molecule. The computed transmissions are shown in Figure 22. The position of the main transport peak ϵ_0 is at -0.23 eV for the two DFT functionals used, whereas the QI feature and a second transport peak shifts depending on the functional. The conductance is $8.8 \cdot 10^{-2} G_0$ with revPBE and $9.9 \cdot 10^{-2} G_0$ with the hybrid HSE06. Compared to the different experimental data, the theoretical conductance is 19 times higher compared to the MCBJ first batch, and between a factor 80-800 depending on the I-V curve type for the second batch. One of the main reason added to the fact that the method is not fully quantitative is that the only conductance calculated is obtained for an ideal configuration with flat electrodes (#1-hollow). The experimental junctions that are measured are surely made of a large number of configurations as shown by the statistical gaussian shape of the results. The comparison of the computational conductance results with the SAM experiments is worst, as expected. If an additivity of the individual molecular conductance is assumed (in the SAM experiments, about 80-100 molecules are considered to be trapped between the AFM tip and the substrate), the ratio would be between 5700-7200. The **Ru-dppe** molecular junction characteristics (ϵ_0 and Γ) are the following:

- MCBJ: the mean value of ϵ_0 using the SLM up to $\Delta V = 0.5$ V when applicable gives $\epsilon_{0\text{-mean}} = -0.29$ eV and $\Gamma_{\text{mean}} = 3.86$ meV (see Table 1).
- CP-AFM (SAM): SLM with $\epsilon_0 = -0.32 \pm 0.06$ eV and $\Gamma = 0.89$ meV for a selected I-V curve.
- DFT/NEGF: the fit of the transmission gives $\epsilon_0 = -0.23$ eV and $\Gamma = 37$ meV

Remarkably, even though the coupling and thus conductance in the computational study is one order of magnitude higher, the value of ϵ_0 is in reasonable agreement with both experimental series of measurements. This agreement is also found for junctions with organic conjugated molecules. Furthermore, the use of the #3-hollow binding configuration (i.e., adding a specific hollow tip) for the gold electrodes shape enhances the concordance between experiment and theory, as shown in Part II, Chapter II on the OPE-derivatives. It was not applied here due to the excessive size of the system. Nevertheless, a computational study reproducing quantitatively the experimental results would necessitate molecular dynamic calculations to gather a statistical bench of coordination geometries (different arrangements of the gold electrodes would also need to be considered).

The construction of a precise DFT/NEGF I-V curve requires to calculate the transmission at each bias voltage (considering that $\tau(E, V = 0 \text{ V}) \neq \tau(E, V > 0.1 \text{ V})$). Because of the important size of the system, this could not be performed for **Ru-dppe**. We only computed three additional transmission spectra at 0.2, 0.6 and 0.8 V, using the revPBE functional (Figure 23) in order to at least evaluate the degree of evolution of the transmission properties upon bias. The normalized I-V curves with the computational results and the experimental ones are displayed in Figure 23, up to 0.8 V. Considering, three values for only one junction geometric configuration is clearly not sufficient to reproduce experimental I-V curves.

The calculated transmission is hardly modified between 0 and 0.2 V while higher voltages do shift the energy position of the main conducting peak, expand its FWHM and decrease its transmission probability.

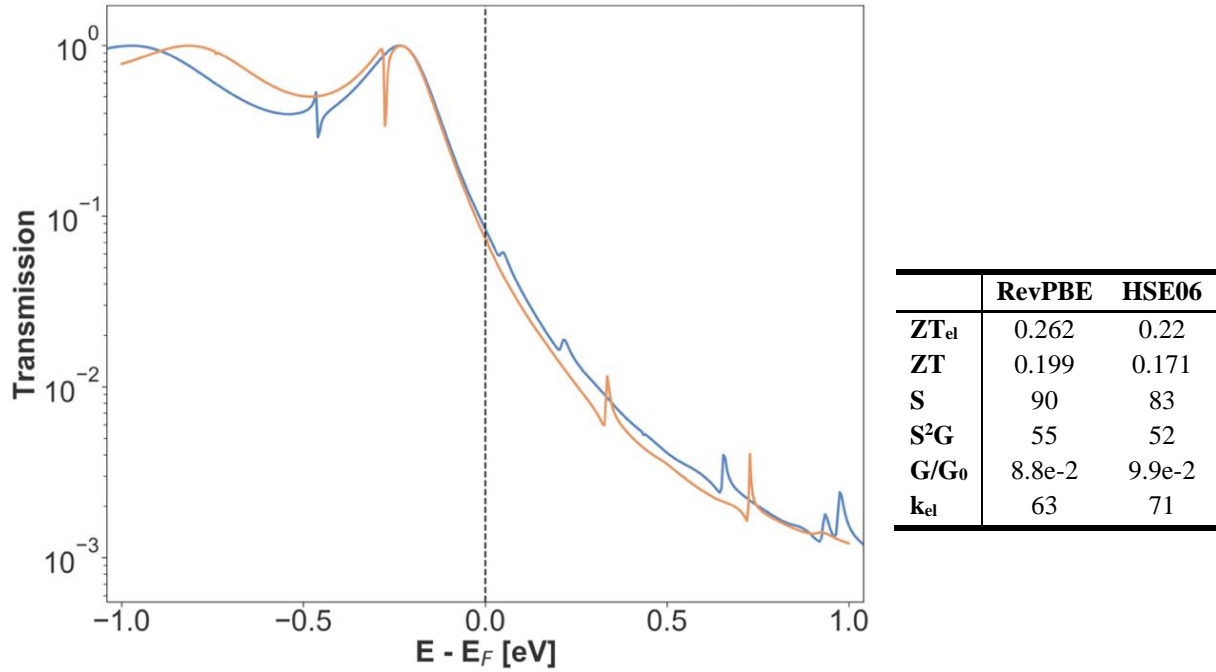


Figure 22 – Zero bias transmission of the **Ru-dppe** junction calculated at the DFT revPBE level in blue and DFT HSE06 level in orange. Main (thermo)electric characteristics.

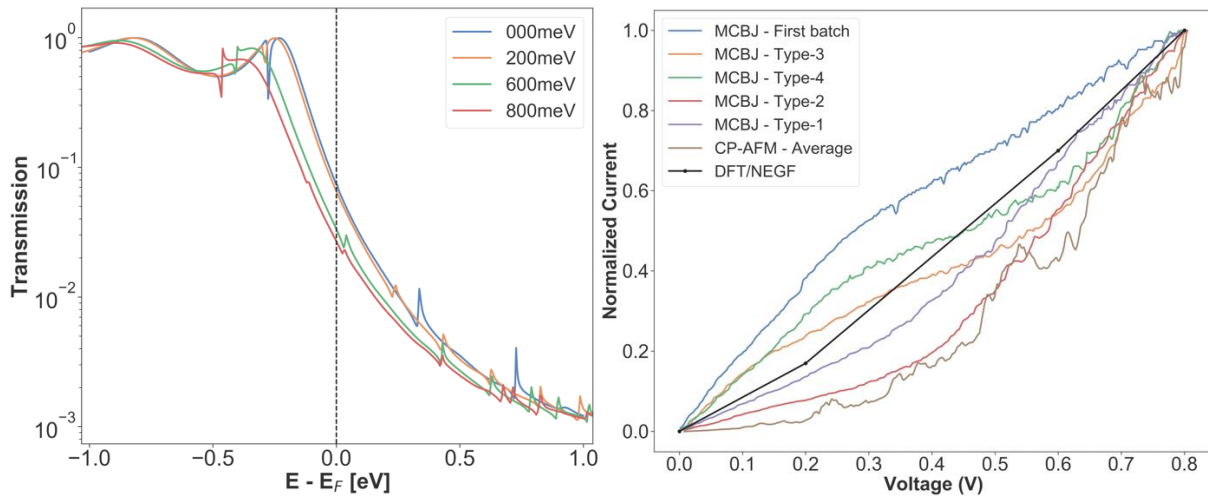


Figure 23 – Left: DFT/NEGF transmission as a function of the applied bias to the **Ru-dppe** junction (revPBE). Right: experimental and computational normalized I-V curves up to 0.8 V.

The computed thermoelectric properties of the **Ru-dppe** junction given in Figure 22 yield quite high Seebeck values ($\sim 85 \mu\text{V/K}$) but the conductance is too high to generate an interesting thermoelectric system (because it induces a high κ_{el} and thus low ZT value). Indeed, even when considering a variation of the Fermi level energy (ΔE_{Fermi}) either to account for the computational inaccuracy, or to simulate a gating effect, the maximum Figure of Merit is expected to be 0.30 with an $\Delta E_{\text{Fermi}} = -0.10 \text{ eV}$.

V.2 – Fe-cyclam system

The **Fe-cyclam** molecules are stable as cations in which the formal oxidation degree of the iron is +III and are thus associated to a counter-ion (**Fe^{III}-cyclam**). They therefore present an open-shell electronic structure and are thus magnetic with one unpaired electron. Because the molecule is easily reduced,²⁸ we performed calculations for both oxidation states (+II and +III). The DFT molecular study of **Fe^{II}-cyclam** (unsubstituted and cluster Au₁₃ model) has been described in Part II, Chapter III. The transmissions of the **Fe^{II}-cyclam** junction have been calculated at the DFT/NEGF level with a thiol end group in hollow coordination. Two configurations of electrode have been implemented: flat gold electrode #1-hollow and, #3-hollow tip as described in Part II, Chapter II. The influence of the functional on the results was also tested. These results are reported in

Figure 24.

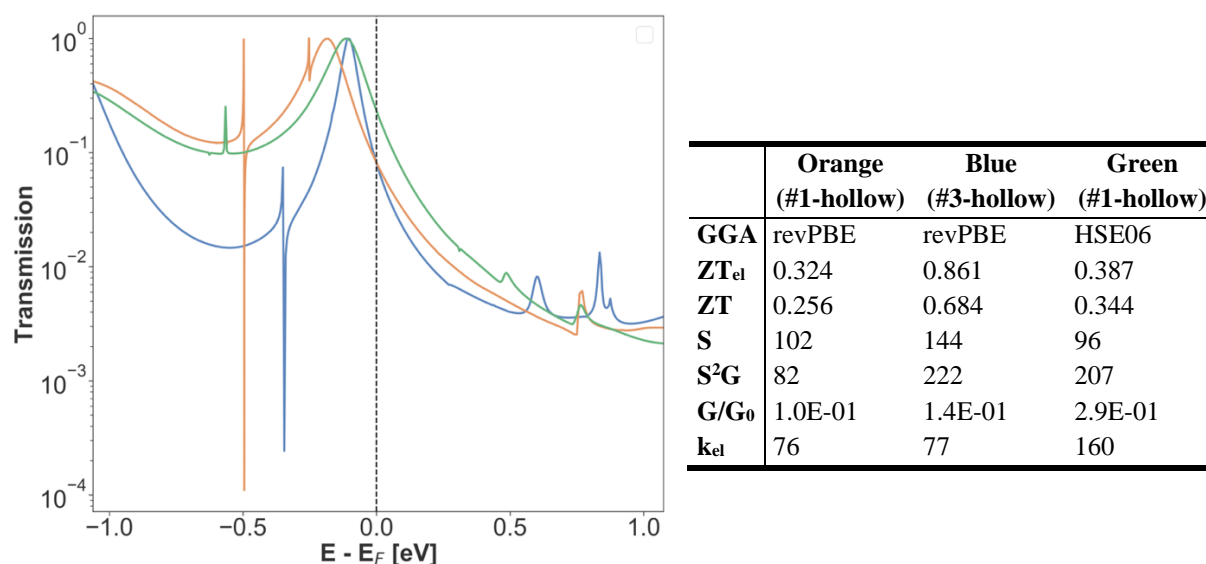


Figure 24 – Zero bias DFT/NEGF transmissions of the **Fe^{II}-cyclam**. Blue: #3-hollow electrode configuration, revPBE GGA functional; Green: #1-hollow electrode configuration, HSE06 hybrid functional; Orange: #1-hollow electrode configuration, revPBE GGA functional.

Contrarily to the **Ru-dppe** system, the change from revPBE GGA functional to the HSE06 hybrid functional modifies the energetic position of ϵ_0 but only slightly the electronic coupling Γ . The ϵ_0 value obtained with the #3-hollow tip is equivalent to the value given by the HSE06 hybrid functional with the #1-hollow geometry, but Γ is different. Thus, by applying the #3-hollow model, we have fashioned a pseudo-correction of the revPBE functional on ϵ_0 which has the consequence to over-corrects the coupling Γ and consequently the conductance.

Whatever the model, the calculated conductance is one order of magnitude higher than for **Ru-dppe**. In both sets of experimental data (MCBJ and CP-AFM), the conductance of the **Ru-dppe** junction is systematically more conductive than that of **Fe-cyclam**. The oxidation state of the **Fe-cyclam** molecular system certainly plays an important role when considering that the **Fe^{III}-cyclam** is more stable at the molecular level. The process of incorporation in the junction might partially modify this oxidation state. For instance, XPS measurements reveal that the counterion is not present after the immobilization of the molecule on gold and the electrodes can play the role of electron reservoirs. Thus, both oxidation states should be investigated.

The **Fe^{III}-cyclam** was studied as isolated cationic radical molecule and substituted by Au₁₃. The corresponding MO energy diagrams are given in Figure 25. The open-shell electronic structure of **Fe^{III}-cyclam** presents some similarities with **Fe^{II}-cyclam**, with the set of alpha and beta spin-orbitals (SO) highly similar but with energies shifted upward with one electron less for the beta SOs, and on the contrary, stabilized for the alpha SOs. The highest conducting SO of beta type is much closer to the pseudo Fermi energy in the cluster-model calculations.

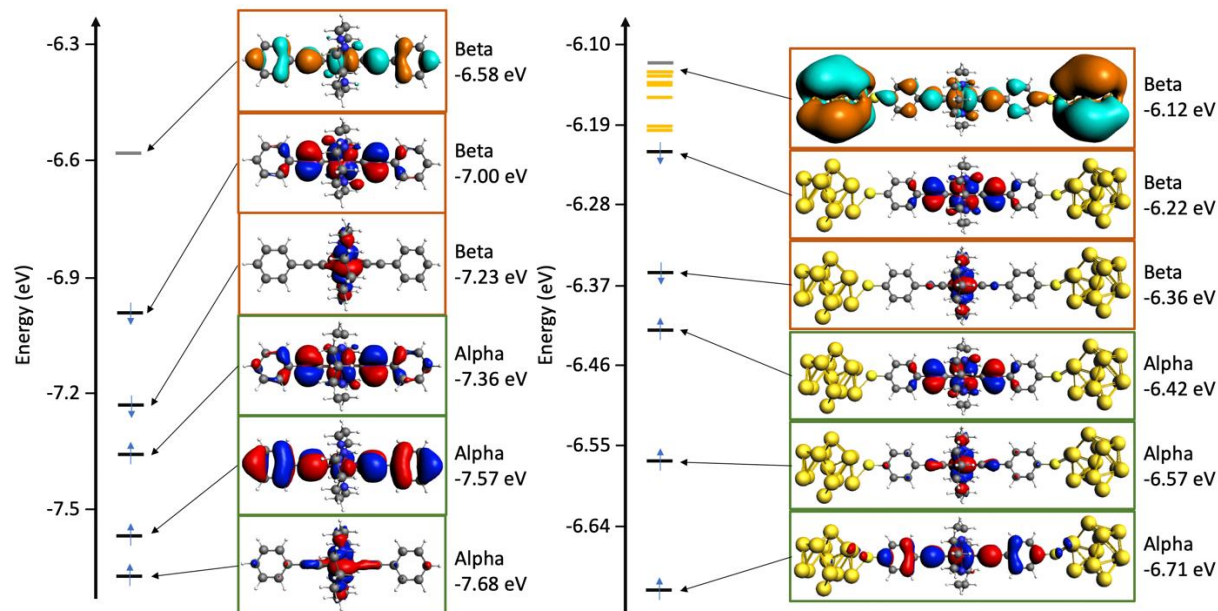


Figure 25 – Left: DFT SO energy diagram of the bare **Fe^{III}-cyclam** molecule. Right: DFT SO energy diagram of the functionalized **Fe^{III}-cyclam** molecule with two Au₁₃ gold cluster (cluster-model). Coloring of the levels: yellow = occupied gold levels, blue = occupied SOs presenting a predominant *d* iron contribution (SO_d), black = other occupied SOs, grey = unoccupied levels.

The implementation of the DFT/NEGF protocol implies the actual charge distribution is the result of the electronic density of the central region reaching equilibrium with the gold electrodes, meaning that one cannot impose a charge to the system. Several computational strategies can be used to obtain an oxidized electronic configuration of the central molecule. A counter-ion can be added in the cell. We performed several simulations in which a chlorine counterion was positioned at different places in the central region of the junction to observe the impact of its position on the transmission shape. Indeed, the Cl^- position has an influence on the transmission as shown in Figure 26 (red circles). These features are due to an undesired overlap of the electronic density between the chlorine anion and the **Fe-cyclam** molecule.

The retained Cl^- position, avoiding interactions with **Fe-cyclam**, is distant from the closest molecule atom by 6 Å and the corresponding transmission and main transmission eigenstates are shown in Figure 27 (procedure B1 of Table 3). All systems containing a chlorine atom were treated with this configuration. In the B1 calculation, chlorine is negatively charged (-0.38 e, Table 3, B1 entry) but this is not sufficient to confer a cationic character to the **Fe-cyclam**. Indeed, the Mulliken atomic charge is almost identical to the **Fe^{II}-cyclam** calculation (A entry in Table 3), and the spin polarization is only of 0.5 electron between the spin up and spin down population (instead of 1). In this B1 scenario, the main transmission peak of the alpha spin is $\epsilon_{0-\alpha} = -0.67$ eV and beta spin $\epsilon_{0-\beta} = 0.01$ eV which is basically pinned on the Fermi level (Figure 27). The alpha spin transmission is consistent with the experimental UPS and SLM values ($\epsilon_0 = -0.73$ eV), but this is the beta spin main transmission peak which is responsible for the main transmission path and leads to a huge conductance of 0.66 G_0 . Both experimental setups are revealing that the **Fe-cyclam** conductance is much lower than that of **Ru-dppe**. The electronic configuration A (**Fe^{II}-cyclam**) and B1 are thus not reproducing the experimental data.

Because the introduction a Cl^- anion appeared insufficient to induce an oxidation of the molecular part, the application of an “atomic shift” appears necessary. We applied different values of atomic shift on the iron and/or chlorine atom to modify the initial electronic repartition. The results of the different tested protocols are summarized in Table 3 (B2, C, E1, E2, E3, and E4). The A, B1 and B2 systems were calculated with the #1-hollow flat electrodes, and all of the others with the #3-hollow tip electrodes. The atomic shift is introduced by adding a negative and/or a positive electronic potential term to the Hamiltonian of the central region.

The use of these atomic shifts imposed to increase the size of the scattering region. The three gold slabs on each side of the junction (“+3 GS” in Table 3) were added to guarantee the charge neutrality and convergence of the global system. χ corresponds to a scaled initial spin state (ranging from 0 to 1, with 1 the highest spin state and 0 the lowest) of the considered atom.

In Table 3, in the C and D protocols we try to only gate either the Fe (+1 eV) or the Cl⁻ (-1 eV). When only the Cl⁻ is gated (C), the corresponding $\epsilon_{0-\alpha}$ and $\epsilon_{0-\beta}$ were not modified compared to the B1 system, only the charge on the Cl atom was increased (-0.5 e). Interestingly, the gating of the Fe on the D system leads to modifications of both main transmission peaks when the system does not contain a chlorine ion. $\epsilon_{0-\beta}$ is not pinned to the Fermi energy anymore.

When applying the E1, E2, E3 and E4 protocols, we tried different atomic gating (except in E3 in which only the initial scaled spin state χ was increased from 0.20 to 0.75). Overall the E1 approach appears to be the best compromise.

The only difference between the B2 and the E1 system, is the electrodes shape (#1-hollow and #3-hollow, respectively) and the values of $\epsilon_{0-\alpha}$ and $\epsilon_{0-\beta}$ are almost equivalent. The transmission features and the values of $\epsilon_{0-\alpha}$ and $\epsilon_{0-\beta}$ that are provided by E1 are difficult to validate without further experimental inputs to determine the oxidation state(s) of the Fe atom for instance. Figure 28 represents the transmission spectrum generated with the E1 protocol. The main problem with the addition of an “atomic gating” is that the chosen E1 protocol leads to a Fano resonance at the Fermi level, and a mixing of the transmission eigenstates compared to the non-atomic shifted B1 system (Figure 27).

We thus recently investigated an alternative approach which is to apply a gating perpendicularly (as already shown in Part II, Chapter III) to the transmission direction to gradually oxidize the molecule. The transmission spectra obtained using a positive voltage on the gate (2, 3, and 4 V) are displayed in Figure 29. The transmissions are not spin polarized anymore since we retrieve the **Fe^{II}-(cyclam)** oxidation state.

Because of time constraints, we could not proceed to test further gating values, but it seems plausible that only a small perturbation could modify the oxidation state of the junctions. This would completely change their conductance values and I-V curves. This behavior could be traced back to the larger variation of ϵ_0 and Γ from the SLM fits of Vuillaume’s group compared to **Ru-dppe**.

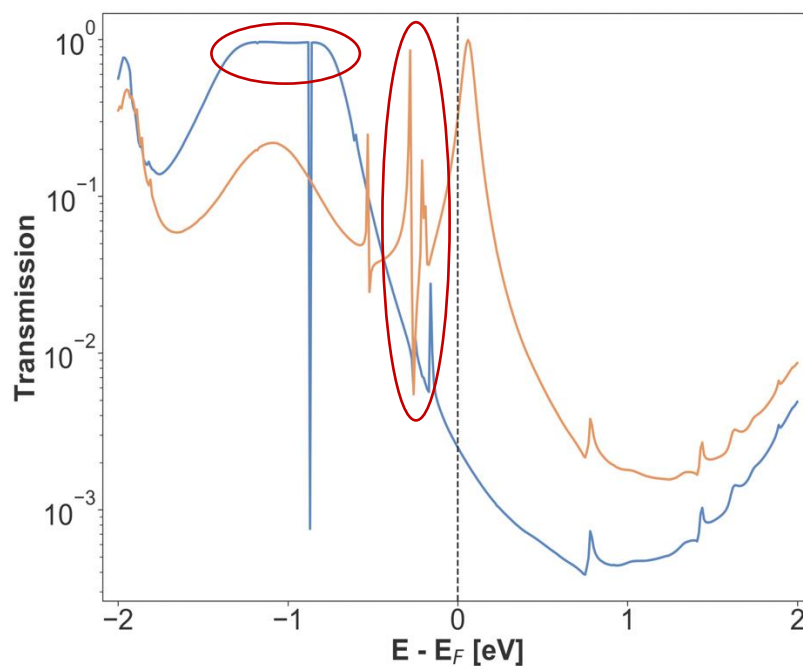


Figure 26 – DFT/NEGF zero-bias transmission of **Fe-cyclam** junction with the Cl^- counter-ion inducing perturbations in the transmission shapes (red circles). Blue curve: spin down transmission; Orange curve: spin up transmission.

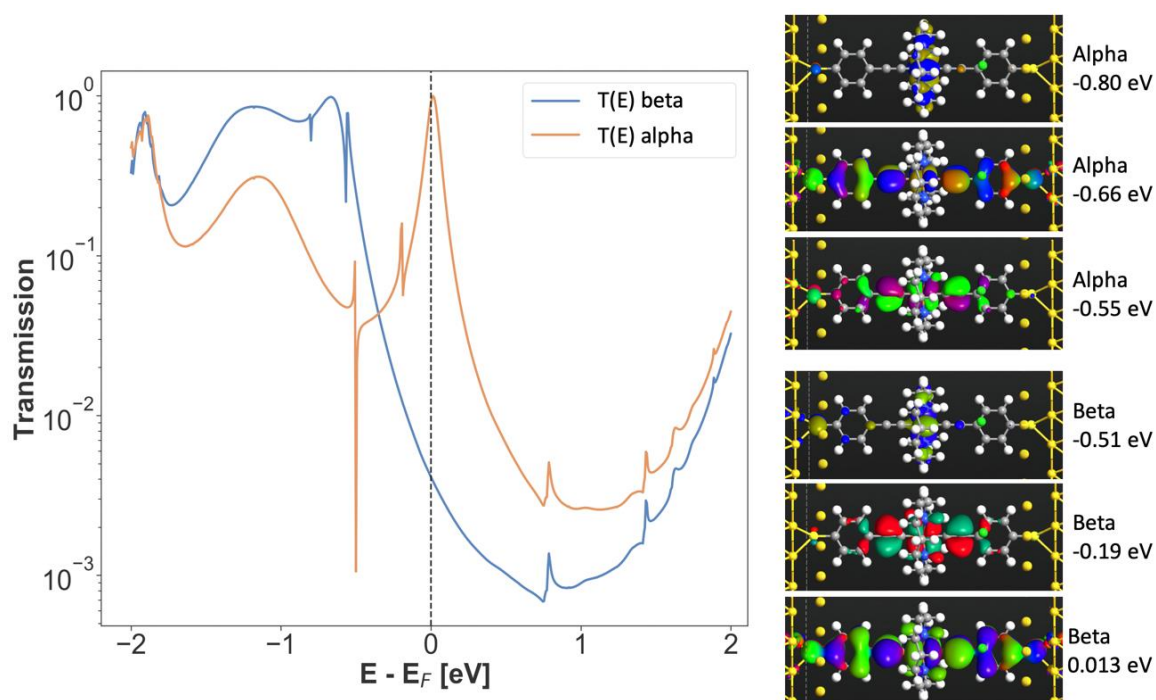


Figure 27 – Left: DFT/NEGF zero-bias transmission of **Fe-cyclam** junction following the procedure B1 of Table 3. Blue curve: spin down (β) transmission; Orange curve: spin up (α) transmission. Right: main transmission eigenstates.

Table 3 – Main calculation results applying different computational protocols used to calculate the transmission of the **Fe-cyclam** junction at the DFT/NEGF level. χ and χ_C are the scaled initial spin state ratio applied to the iron atom and the two carbon atoms coordinated to the iron atom respectively. "+ 3 GS" consists in adding three additional gold slabs (on each side) to the central region to ensure the charge neutrality of the device. $\epsilon_{0-\alpha}$ and $\epsilon_{0-\beta}$ in eV are the spin up and spin down energies of the main transmission peaks, respectively. μ_S is the spin magnetic moment in Bohr magneton. A is the **Fe^{II}-cyclam** junction configuration. A, B1 and B2 were calculated with the #1-hollow flat electrodes configuration while the #3-hollow tip configuration was used for the other calculations.

| | Atomic gating | | Fe electrons (3d + 4s) | | | Mulliken charges (e) | | | | | | Transmission | | Comments |
|----|---------------|------|---------------------------|------------------------------|-------|----------------------|-------|------|-------|-------|---------|-----------------------|----------------------|-------------------------|
| | Fe | Cl | \uparrow & \downarrow | $\uparrow\text{-}\downarrow$ | Total | Fe | Cl | Mol. | Au | Tot. | μ_S | $\epsilon_{0-\alpha}$ | $\epsilon_{0-\beta}$ | |
| A | - | - | 8.02 | 0.00 | 8.02 | -0.02 | / | 1.41 | -1.43 | -0.02 | / | -0.19 | | Unpolarized |
| B1 | - | - | 4.28 3.74 | 0.54 | 8.02 | -0.02 | -0.38 | 1.67 | -1.31 | -0.02 | 0.60 | -0.67 | 0.01 | $\chi = 0.20$ |
| B2 | 1.0 | -1.0 | 2.53 3.17 | -0.63 | 5.70 | 2.30 | -0.37 | 1.17 | -1.22 | -0.04 | -0.65 | -0.78 | -0.50 | + 3 GS $\chi = 0.20$ |
| C | - | -1.0 | 4.25 3.77 | 0.48 | 8.02 | -0.02 | -0.50 | 0.75 | -0.28 | -0.03 | 0.52 | -0.61 | -0.02 | + 3 GS $\chi = 0.20$ |
| D | 1.0 | - | 3.07 2.64 | 0.44 | 5.71 | 2.29 | / | 0.53 | -0.56 | -0.03 | 0.45 | -0.87 | -0.51 | + 3 GS $\chi = 0.20$ |

Continuation of **Table 3**.

| | Gating | | Fe electrons (3d + 4s) | | | Mulliken charges (e) | | | | | | Transmission | | Comments |
|----|--------|-----------------|------------------------|------|-------|----------------------|-----------------|------|-------|-------|---------|-----------------------|----------------------|-------------------------|
| | Fe | Cl ⁻ | ↑ & ↓ | ↑-↓ | Total | Fe | Cl ⁻ | Mol. | Au | Tot. | μ_S | $\epsilon_{0-\alpha}$ | $\epsilon_{0-\beta}$ | |
| E1 | 1.0 | -1.0 | 3.12 2.59 | 0.53 | 5.71 | 2.29 | -0.40 | 0.31 | -0.34 | -0.03 | 0.53 | -0.70 | -0.48 | + 3 GS $\chi = 0.20$ |
| E2 | 0.5 | -1.5 | 3.65 3.20 | 0.45 | 6.85 | 1.15 | -0.40 | 0.29 | -0.32 | -0.03 | 0.46 | -0.48 | -0.24 | + 3 GS $\chi = 0.20$ |
| E3 | 1.0 | -1.0 | 3.12 2.59 | 0.53 | 5.71 | 2.29 | -0.40 | 0.31 | -0.34 | -0.03 | 0.53 | -0.70 | -0.48 | + 3 GS $\chi = 0.75$ |
| E4 | 1.5 | -1.0 | 3.69 2.33 | 1.36 | 6.02 | 1.98 | -0.25 | 0.04 | -0.08 | -0.04 | 1.69 | -0.25 | -0.47 0.14 | + 3 GS $\chi = 0.20$ |

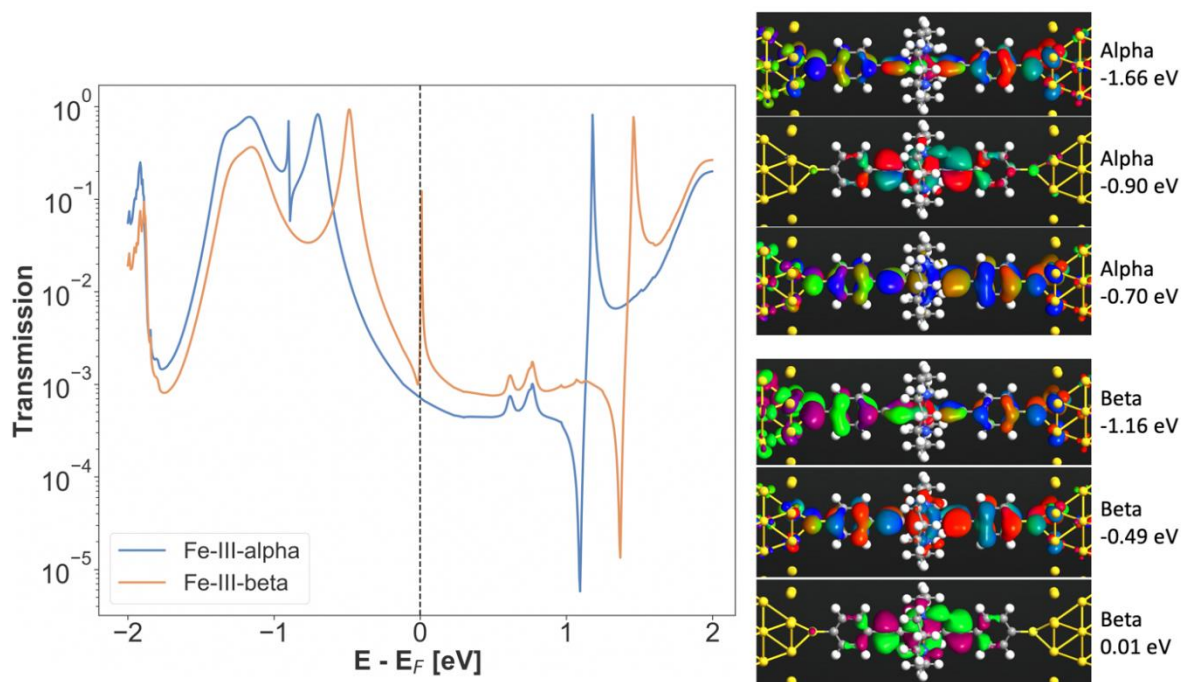


Figure 28 – Left: DFT/NEGF zero-bias transmission of the **Fe-cyclam** junction following the E1 protocol. Blue curve: spin down transmission; Orange curve: spin up transmission. Right: main transmission eigenstates.

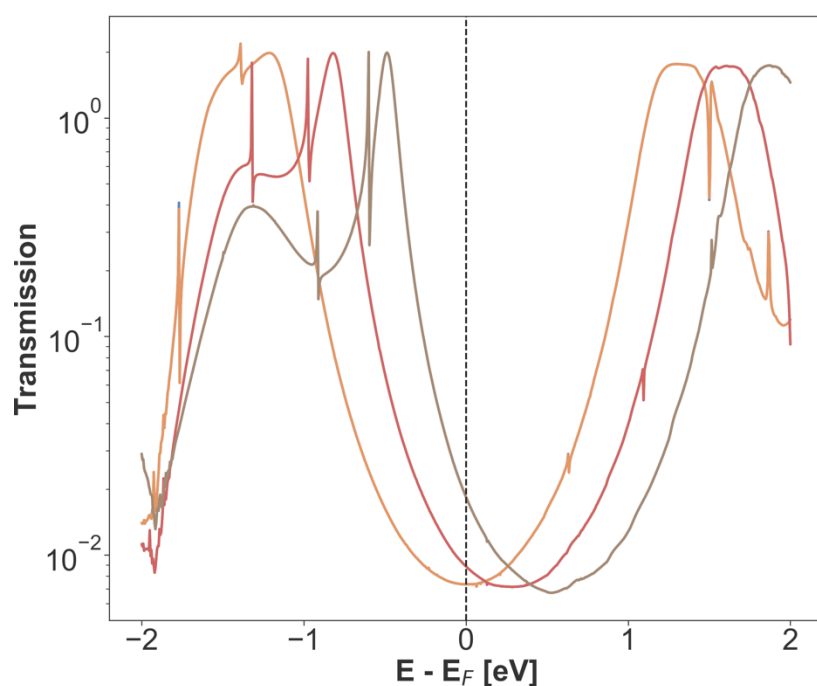


Figure 29 – DFT/NEGF zero-bias transmission of the **Fe-cyclam** junction with 3 different gate voltages: orange 4 V, red, 3V and grey 2 V. The transmissions are not spin polarized anymore.

VI – Conclusions

In this chapter, the objective was to compare experimental and computational results for junctions containing organometallic complexes. The first input of our study relates to the tests made for extracting the molecular junction characteristics from the experimental results. The SLM appears to be applicable in a restricted range of voltages for these organometallic systems in which at least two transmission regimes appear to be operative. The lack of reproducibility and the important dispersion in the experimental results are revealing that multiple configurations are involved, a feature not considered for the moment in our simulations. Additionally, the comparison between the SAM and MCBJ measurements are revealing that the conducting features in SAM are not the simple addition of the property of the molecules incorporated in the junction.

In order to further perform predictions on the basis of computationally assisted molecular modeling to find systems presenting enhanced thermoelectric properties, a qualitative compatibility has to be at least attained between calculations and experiments on organometallic series. The computational study of the **Ru-dppe** led to quite satisfying results for two of the three series of measurements performed. The variation of the experimental results implies to be cautious before providing definitive conclusions. For the **Fe-cyclam** system, the question to be solved on both the experimental and computational point of views, is to know if the open-shell radical character of the molecule is kept in the junction configuration. We have implemented a set of protocols to access different electronic configurations. A first set of XPS measurements performed in the group of Vuillaume is showing that the signatures of Fe^{II} and Fe^{III} are detected. These results open interesting perspectives on the computational point of view and the enlargement of the configurational space of the junctions accessed via molecular dynamics simulations (MD) for instance would be of high interest. In the following part, the ability of TB-DFT to describe the geometry and the electronic features of metal containing systems has been investigated. This low-cost method is indeed well adapted to MD calculations. The thermal conductance of the junctions started to be studied in the group of Vuillaume. They are currently analyzing these results in order to correlate the results to the intrinsic properties of individual molecular junctions.

-
- ¹ Kim, B.; Beebe, J. M.; Olivier, C.; Rigaut, S.; Touchard, D.; Kushmerick, J. G.; Zhu, X.-Y.; Frisbie, C. D. Temperature and Length Dependence of Charge Transport in Redox-Active Molecular Wires Incorporating Ruthenium(II) Bis(σ -Arylacetylide) Complexes. *J. Phys. Chem. C* 2007, 111, 7521–7526. doi:10.1021/jp068824b.
- ² Sugimoto, K.; Tanaka, Y.; Fujii, S.; Tada, T.; Kiguchi, M.; Akita, M. Organometallic Molecular Wires as Versatile Modules for Energy-Level Alignment of the Metal–Molecule–Metal Junction. *Chem. Comm.* 2016, 52, 5796–5799. doi:10.1039/C6CC01705C.
- ³ Tanaka, Y.; Kato, Y.; Tada, T.; Fujii, S.; Kiguchi, M.; Akita, M. “Doping” of Polyynes with an Organometallic Fragment Leads to Highly Conductive Metallapolyne Molecular Wire. *J. Am. Chem. Soc.* 2018, 140, 10080–10084. doi:10.1021/jacs.8b04484.
- ⁴ Tanaka, Y.; Kato, Y.; Sugimoto, K.; Kawano, R.; Tada, T.; Fujii, S.; Kiguchi, M.; Akita, M. Single-Molecule Junctions of Multinuclear Organometallic Wires: Long-Range Carrier Transport Brought about by Metal–Metal Interaction. *Chem. Sci.* 2021, 12, 4338–4344. doi:10.1039/D0SC06613C.
- ⁵ Bock, S.; Al-Owaedi, O. A.; Eaves, S. G.; Milan, D. C.; Lemmer, M.; Skelton, B. W.; Osorio, H. M.; Nichols, R. J.; Higgins, S. J.; Cea, P.; Long, N. J.; Albrecht, T.; Martín, S.; Lambert, C. J.; Low, P. J. Single-Molecule Conductance Studies of Organometallic Complexes Bearing 3-Thienyl Contacting Groups. *Chem. Eur. J.* 2017, 23, 2133–2143. doi:10.1002/chem.201604565.
- ⁶ Naher, M.; Milan, D. C.; Al-Owaedi, O. A.; Planje, I. J.; Bock, S.; Hurtado-Gallego, J.; Bastante, P.; Abd Dawood, Z. M.; Rincón-García, L.; Rubio-Bollinger, G.; Higgins, S. J.; Agraït, N.; Lambert, C. J.; Nichols, R. J.; Low, P. J. Molecular Structure–(Thermo)Electric Property Relationships in Single-Molecule Junctions and Comparisons with Single- and Multiple-Parameter Models. *J. Am. Chem. Soc.* 2021, 143, 3817–3829. doi:10.1021/jacs.0c11605.
- ⁷ Zhang, L.-Y.; Duan, P.; Wang, J.-Y.; Zhang, Q.-C.; Chen, Z.-N. Ruthenium(II) as Conductive Promoter To Alleviate Conductance Attenuation in Oligoynyl Chains. *J. Phys. Chem. C* 2019, 123, 5282–5288. doi:10.1021/acs.jpcc.9b00148.
- ⁸ Schwarz, F.; Kastlunger, G.; Lissel, F.; Egler-Lucas, C.; Semenov, S. N.; Venkatesan, K.; Berke, H.; Stadler, R.; Lörtscher, E. Field-Induced Conductance Switching by Charge-State Alternation in Organometallic Single-Molecule Junctions. *Nature Nanotech.* 2016, 11, 170–176. doi:10.1038/nnano.2015.255.
- ⁹ Scheer, E.; Cuevas, J. C. *Molecular Electronics: An Introduction to Theory and Experiment* (2nd Edition). World Scientific Pub, 2017.
- ¹⁰ Xie, Z.; Bâldea, I.; Smith, C. E.; Wu, Y.; Frisbie, C. D. Experimental and Theoretical Analysis of Nanotransport in Oligophenylene Dithiol Junctions as a Function of Molecular Length and Contact Work Function. *ACS Nano* 2015, 9, 8022–8036. doi:10.1021/acsnano.5b01629.
- ¹¹ Xie, Z.; Bâldea, I.; Frisbie, C. D. Determination of Energy-Level Alignment in Molecular Tunnel Junctions by Transport and Spectroscopy: Self-Consistency for the Case of Oligophenylene Thiols and Dithiols on Ag, Au, and Pt Electrodes. *J. Am. Chem. Soc.* 2019, 141, 3670–3681. doi:10.1021/jacs.8b13370.
- ¹² Briechele, B. M.; Kim, Y.; Ehrenreich, P.; Erbe, A.; Sysoiev, D.; Huhn, T.; Groth, U.; Scheer, E. Current–Voltage Characteristics of Single-Molecule Diarylethene Junctions Measured with Adjustable Gold Electrodes in Solution. *Beilstein J. Nanotechnol.* 2012, 3, 798–808. doi:10.3762/bjnano.3.89.

- ¹³ Luo, L.; Benameur, A.; Brignou, P.; Choi, S. H.; Rigaut, S.; Frisbie, C. D. Length and Temperature Dependent Conduction of Ruthenium-Containing Redox-Active Molecular Wires. *J. Phys. Chem. C* 2011, 115, 19955–19961. doi:10.1021/jp207336v.
- ¹⁴ Cuevas, J. C.; Scheer, E. *Molecular Electronics: An Introduction to Theory and Experiment*. World Scientific: Singapore, Hackensack, NJ, 2010.
- ¹⁵ Kula, M.; Jiang, J.; Luo, Y. Probing Molecule–Metal Bonding in Molecular Junctions by Inelastic Electron Tunneling Spectroscopy. *Nano Lett.* 2006, 6, 1693–1698. doi:10.1021/nl060951w.
- ¹⁶ Troisi, A.; Ratner, M. A. Molecular Signatures in the Transport Properties of Molecular Wire Junctions: What Makes a Junction “Molecular”? *Small* 2006, 2, 172–181. doi:10.1002/smll.200500201.
- ¹⁷ Smit, R. H. M.; Noat, Y.; Untiedt, C.; Lang, N. D.; van Hemert, M. C.; van Ruitenbeek, J. M. Measurement of the conductance of a hydrogen molecule. *Nature* 2002, 419, 906–909. doi:10.1038/nature01103.
- ¹⁸ Hong, W.; Li, H.; Liu, S. X.; Fu, Y.; Li, J.; Kaliginedi, V.; Decurtins, S.; Wandlowski, T. Trimethylsilyl-terminated oligo(phenylene ethynylene)s: An approach to single-molecule junctions with covalent Au-C σ -bonds. *J. Am. Chem. Soc.* 2012, 134, 19425–19431.
- ¹⁹ Fu T.; Smith S.; Camarasa-Gomez M.; Yu X.; Xue J.; Nuckolls C.; Evers F.; Venkataraman L.; Wei S.; Enhanced coupling through p-stacking in imidazole-based molecular junctions. *Chem. Sci.* 2019, 10, 9998–10002.
- ²⁰ Kudelski, A. Characterization of thiolate-based mono- and bilayers by vibrational spectroscopy: A review. *Vib. Spectro.* 2005, 39, 200–213. doi:10.1016/j.vibspec.2005.03.005.
- ²¹ Bürgi, T. Properties of the gold–sulphur interface: from self-assembled monolayers to clusters. *Nanoscale* 2015, 7, 15553–15567. doi:10.1039/c5nr03497c
- ²² Vasconcellos, L. C.; Oliveira, C. P.; Castellano, E. E.; Ellena, J.; Moreira, Í. S. Structure and properties of iron–cyclam complex of 2-aminophenol. *Polyhedron* 2001, 20, 493–499. doi:10.1016/s0277-5387(00)00621-5.
- ²³ Kushmerick J. G.; Lazorcik J.; Patterson C.H.; Shashidhar R.; Vibronic Contributions to Charge Transport Across Molecular Junctions. *Nano Lett.* 2004, 4, 4, 639–642.
- ²⁴ Selzer, Y.; Cai, L.; Cabassi, M. A.; Yao, Y.; Tour, J. M.; Mayer, T. S.; Allara, D. L. Effect of Local Environment on Molecular Conduction: Isolated Molecule versus Self-Assembled Monolayer. *Nano Letters* 2005, 5, 61–65. doi:10.1021/nl048372j.
- ²⁵ Dubi, Y. Dynamical coupling and negative differential resistance from interactions across the molecule-electrode interface in molecular junctions. *J. Chem. Phys.* 2013, 139, 154710. doi:10.1063/1.4825157.
- ²⁶ Landau, A.; Kronik, L.; Nitzan, A. Cooperative Effects in Molecular Conduction. *J. Comp. and Theo. Nano.* 2008, 4, 535–544. doi:10.1166/jctn.2008.2496.
- ²⁷ Dubi, Y. Transport Through Self-Assembled Monolayer Molecular Junctions: Role of In-Plane Dephasing. *J. Phys. Chem. C* 201, 118, 21119–21127. doi:10.1021/jp503887p.
- ²⁸ Cao, Z.; Forrest, W. P.; Gao, Y.; Fanwick, P. E.; Ren, T. Trans-[Fe(cyclam)(C₂R)₂]⁺: A New Family of Iron(III) Bis-Alkynyl Compounds. *Organometallics* 2012, 31, 6199–6206. doi:10.1021/om300515r.

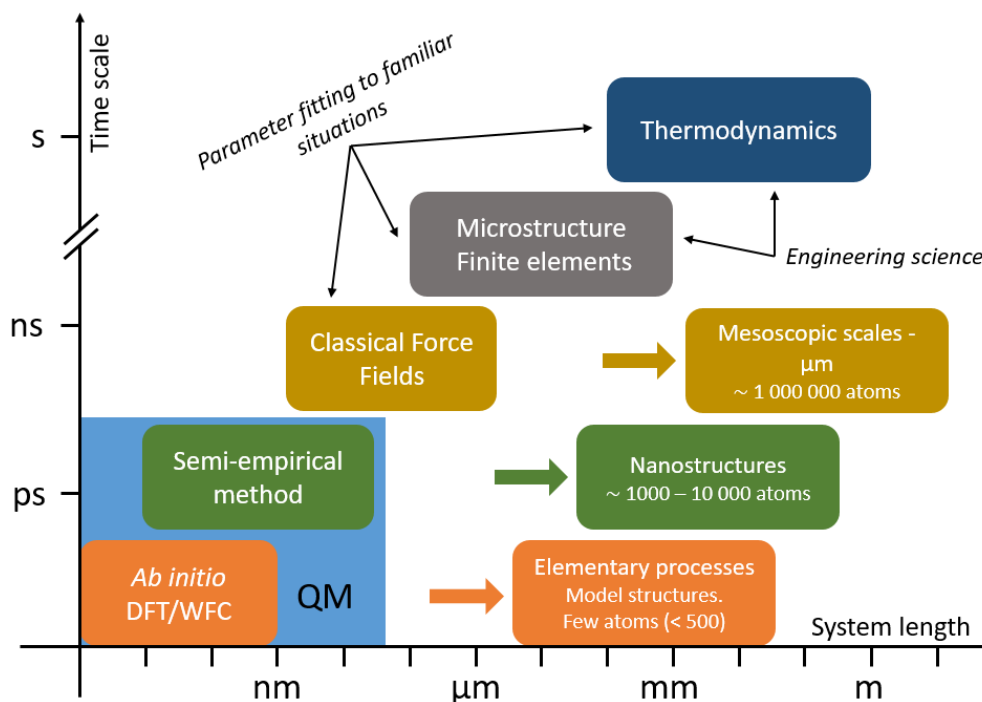
Chapter VI – A Tight Binding approach as a prospective method

I – Introduction

In this chapter we try to evaluate whether the use of rapid methods, such as tight binding (TB) approaches could have enough precision to allow us: i) to study organometallic-based molecular junctions for a large-scale sampling of many different molecules which could lead to the discovery of interesting electrical or thermoelectric properties, and ii) to test several anchor/molecule geometries (with a total geometry optimization of the junction, i.e. electrodes and molecules) and perform a statistical study of the relevant parameters (e.g. conductance, Seebeck coefficient, ZT). To do so, three TB methods were tested, DFTB2, DFTB3 and GFN2-xTB. A sample test of 51 simple systems containing transition metals was used.

II – Tight-binding methods

DFT is nowadays one of the most popular and versatile technique to calculate the physical and chemical features of various types of chemical systems (molecules, metallic clusters and periodic bulks and surfaces). It can be used as a cheaper alternative to highly accurate wave function-based methods (CASSCF, RASSCF), which are built from Hartree-Fock (with an exact exchange) and include electron correlation. Despite the constant increase in the computing power (memory/processors) available, there is still a need to calculate the properties of large systems composed of hundreds to thousands of atoms, for which even DFT may face computing resource limitations. In Scheme 1 is represented the different families of methods at the theoretician's disposal, depending on the time scale and the system size under study. The classical force field (FF) methods involved in molecular mechanics and dynamics (dark-yellow in Scheme 1), are several orders of magnitude faster than DFT, allowing to deal with millions of atoms and to trail their dynamics up to the nanosecond scale. It contains a large number of empirical parameters and can be very precise for well-parameterized systems but suffer from transferability when changing too much the chemical nature of the systems. More importantly, molecular mechanics and dynamics do not consider any quantum effects, preventing the access to the electronic structure of the systems.



Scheme 1 – Graph showing the type of methods that can be used depending on the size of the system and the time scale. Adapted from reference 1.

The semi-empirical quantum approaches (SE) are located between the *ab initio* and FF methods in this theoretical landscape (green in Scheme 1). They can be up to three orders of magnitude faster than DFT but remain more demanding than FF. Historically, they usually contain a smaller number of element-specific parameters than in FF frameworks. Generally, these parameters are also more transferable, as they are less dependent on the chemical nature of the systems. The major advantage of SE methods is that they can tackle almost all quantum effects described by DFT, HF or post-HF methods. The SE methods can be divided into two main families. The first is based on an approximation of the HF theory by neglecting and parameterizing some two-electron integrals (for instance via the Zero Differential Overlap approximation, ZDO^{2,3}) which leads to the neglect of diatomic differential overlap (NDDO^{4,5}) methods (MNDO,⁶ AM1,^{7,8} PM3⁹). The second family of SE method is often, called “Tight-Binding (TB)”^{10,11} methods which represent a DFT counterpart to HF-SE methods, and are based on the same integral neglecting/parameterization philosophy.

The two SE approaches that we will investigate in this chapter are DFT-based TB methods, namely the “Density-Functional Tight-Binding” (DFTB) and the “xTB” models. Both schemes are based on the use of a minimal valence atomic orbitals (AOs) basis set.^{11,12}

II.1 – Density Functional Tight Binding (DFTB)

DFTB appears in the 90's under the impulsion of Seifert, Frauenheim, Eschrig and coworkers.¹³ The principle is to use minimal a basis set (“tight”) including valence orbitals only (“binding”). The idea is to pre-calculate DFT integrals (which represent the DFTB parametrizations) to accelerate the calculations compared to DFT. The resources needed to do a quantum-chemical calculation can be reduced by more than two orders of magnitude. Its parametrization is less empirical because it relies on DFT calculations. In contrast to the main SE methods, electron correlation is included in DFTB through DFT and is not parametrized. It also inherits all the DFT weaknesses, which are the delocalization error and the static correlation error.¹⁴

In DFTB, to converge the energy of a system, the notion of self-consistent field (SCF) is replaced by the concept of Self-Consistent Charges (SCC). Indeed, the DFTB energy is obtained as a Taylor expansion of the total Kohn-Sham DFT energy around a reference density (sum of the density of neutral atoms in the system); the changes in density in the non-zeroth terms accounting for potential charge transfers in the real molecule, are replaced by changes in atomic Mulliken charges. The total energy is expressed as:

$$E_{\text{tot}} = E_{\text{orb}} + E_{\text{SCC}} + E_{\text{rep}} \quad \text{Eq. 1}$$

With E_{orb} , the electronic or orbital energy, E_{rep} , the tabulated repulsion energy, and E_{SCC} , the self-consistent charge term.

The three terms in Eq. 1 can be explained as follows:

- **E_{orb}** – it represents the sum of the atomic densities between all pairs of atoms A and B present in the molecule. It is composed of two-center integrals. The integral calculations are based on the nature of the A and B atoms and their distance (related to the Hamiltonian H and the overlap matrix S, as in the extended Hückel theory). These are DFT pre-calculated integrals.
- **E_{SCC}** – the total density is not the simple sum of the atomic densities (E_{orb}). The charges (and the density) are self-coherently related to the total energy using an E_{SCC} term which corresponds to a second-order Taylor expansion of the KS density functional for the total energy for the DFTB2 and up to the third order for DFTB3 with respect to the variation in the Mulliken atomic charges. The atomic Hubbard

parameters U_a (or “chemical hardness”) and its derivative U_a^d (calculated with DFT) are given as parameters to drive this SCC contribution for DFTB2 and DFTB3 respectively.

- **E_{rep}** – it contains the effects overlooked by the various approximations (the most important being the missing core electrons). It is a two-body contribution and this parametrization process is the most time consuming. Typically, one has to determine for every pair of atoms in the targeted system the total energy E_{tot} as a function of the bond distance R for specific bonds using high level DFT or ab initio methods. An example is given in Figure 2 for the repulsion function for the Au-S interaction.

In addition, it is possible to adjust the AOs confinement radii r_0 (usually, several times the covalent radius) to compensate the approximation of “atom-like” potential (otherwise, the AOs would be too diffuse) in order to further match the desired application. Noteworthy, none of the parameterization step necessitates experimental data, as they are all based on DFT reference calculations.

The resolution of the total energy E_{tot} is done self-consistently by the resolution of the KS equation based on a variational principle, leading to the molecular orbitals of the system. The major drawback of this TB method is, like most parameter-based method, the need of explicit parameterization for each type of atom pair (E_{orb}), leading to numerous information to register. As a consequence, a fraction of the periodic table is covered by DFTB parametrization to date, and thus limits the molecules and applications to those including the parameters available for atoms and atom pairs (for example, no parametrization for a lot of transition metals).

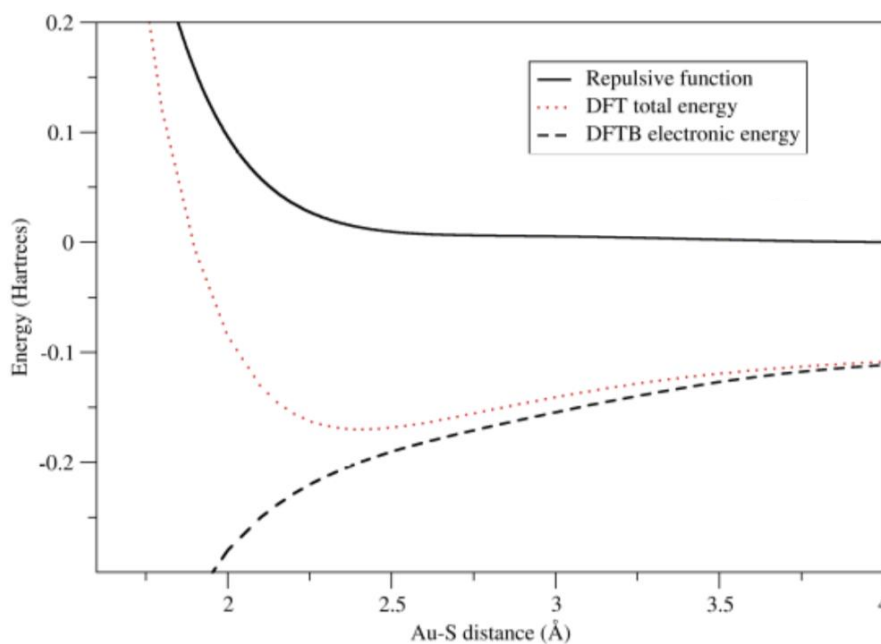


Figure 2 – Representation of the Au-S repulsion function for the calculation of E_{rep} .

Once parameterized, the DFTB model can be used to perform single point calculations, geometry optimizations or frequency calculations. Spin polarization¹⁵ can be included to treat open-shell systems and Time-dependent DFTB¹⁶ (TD-DFTB) can be used to explore excited-state properties. Solvent effects can also be described through a polarizable continuum model (PCM)¹⁷, as well as long-range interactions with empirical dispersion terms.¹⁸ The methods are implemented in several codes like DFTB+,¹⁹ Gaussian,²⁰ ADF²¹ or QuantumATK.²² In our study, we will use the DFTB+ program. Table 1 gathers the most used sets of parameters available in DFTB. The number of available parameters sets remains quite small compared to FF methods, and most of these parameters (for instance, the “trans3d” set for transition metals) have not been thoroughly tested. This definitely represents one of the main obstacles preventing more applications of the DFTB method to study materials of experimental interest.

Table 1 – Selection of parameter sets available in DFTB.²³

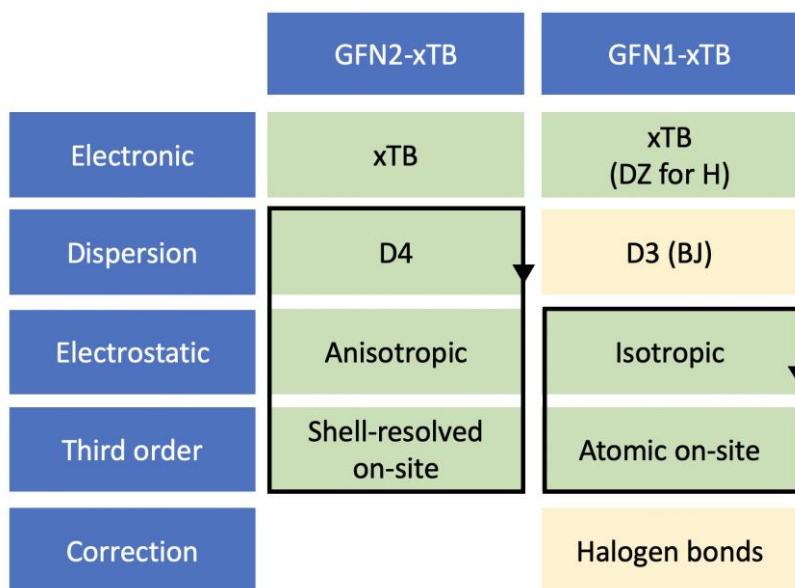
| Set | Elements | Description |
|-----------------------|--|--|
| mio ^{24,25} | H - C - N - O - S - P | Organic and bio molecules |
| auorg ²⁵ | Au – (H, C, N, O, S) | Gold-thiolate compounds |
| halorg ²⁶ | (F, Cl, Br, I) – (C, N, O, H) | Halogens and organic atoms |
| trans3d ²⁷ | (Sc, Ti, Fe, Co, Ni) – (H, C, N, O) | Few transition metals, but only with H, C, N and O atoms, for bio systems. |
| znorg ²⁸ | Zn – (C, H, N, O, S) | Zn bulk, ZnO bulk, ZnO surfaces, ZnO with |

| | | |
|---------------------|----------------------|--|
| | | organic molecules |
| tiorg ²⁹ | Ti – (C, H, N, O, S) | Ti bulk, TiO ₂ bulk, TiO ₂ surfaces, TiO ₂ with organic molecules |

Biological systems interacting with surfaces or at interface with solid materials have been modeled in this framework.^{30,31,32,33} The use of fast TB method is also interesting in terms of electron dynamics or TD-DFT calculations.^{34,35} The Auorg set has also been extensively studied with organic molecules^{36,37,38,39} and used to model gold electrodes in the case of charge transport.⁴⁰

II.2 – Extended tight-binding method (xTB)

The Geometry, Frequency, Noncovalent, eXtended TB (GFN-xTB)⁴¹ method is another type of DFT-based SE method designed to reproduce ground-state properties of molecules. GFN-xTB (see Scheme 2 for a listing of the xTB models) roughly uses the same approximations for the definition of the Hamiltonian and the electronic energy as DFTB⁴² but its parametrization does rely on pair of atoms. Indeed, the parametrization used in GFN-xTB is based on element specific and empirical fitting allowing covering most of the periodic table (up to $Z = 86$, Radon). The semi-empirical parameters are largely global and element-specific. As an example, for each of the second-row elements (from boron to fluorine), 11 different parameters are specified: two atomic energy levels (the 2s and 2p), their respective AO exponents, two chemical hardnesses (for the definition of chemical hardness in DFT see reference 43), two electronic repulsion factors, two off-diagonal Hamiltonian polynomial factors, and one atomic-shell charge scaling parameter. The parameters are extracted using reference data produced by hybrid DFT computations.⁴⁴ One advantage over DFTB2 is that all the transition metals are parametrized. It is also implemented in various software such as AMS,⁴⁵ CP2K,⁴⁶ Cuby4,⁴⁷ Entos,⁴⁸ ORCA,⁴⁹ or TeraChem.⁵⁰



Scheme 2 – A glance over the two GFN methods (GFN1 and GFN2) with their main characteristics. Green squares designate quantum description. Pale yellow ones describe a classical or semi-classical picture. The parts surrounded by arrows are treated self-consistently. Adapted from reference 13. D3 (BJ)⁵¹ and D4⁵² correspond to Grimme *et al.* empirical dispersion.

The GFN2-xTB formalism is the most widely used xTB version. Just like DFTB methods, the xTB formalism is derived from the Kohn-Sham DFT equations. The total energy in xTB is expressed as follows:⁴¹

$$E_{tot} = E_0^H + \Delta E^H + E_{XC}^{LDA} + E_C^{NL} \quad \text{Eq. 2}$$

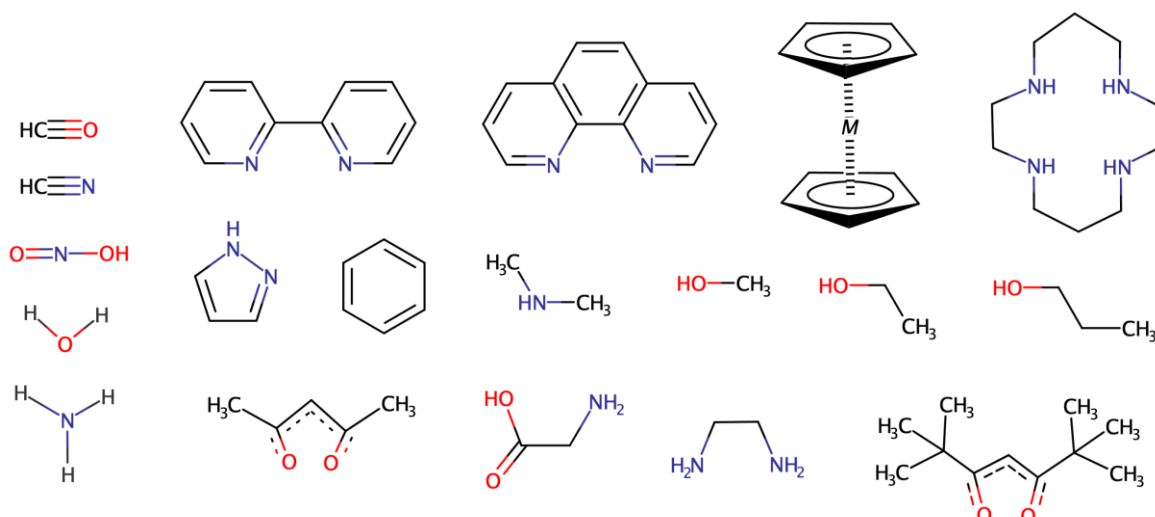
with E_0^H the energy at the reference density (which is the sum of the neutral atoms densities) ρ_0 , ΔE^H is the Hartree energy difference associated to $\Delta\rho$ which is the difference between the reference density ρ_0 and the converged density ρ ($\rho = \rho_0 + \Delta\rho$), E_{XC}^{LDA} is the semi-local exchange-correlation energy and E_C^{NL} is the non-local correlation energy. The wavefunctions are formulated in terms of a partially polarized minimal valence atomic basis set, consisting of Gaussian-type (GTO) functions. The atomic orbitals (AOs) are optimized during the parameterization and are tied to a specific GFN-xTB version. The molecular orbitals (MOs) are expanded as a linear combination of AOs. Just like in DFTB, the xTB methods employ a non-orthogonal basis which is different from Hartree–Fock-based semi empirical methods. The total energy is Taylor expanded around the reference density. The GFN2-xTB truncates

this expansion after the third-order term.²⁵² It is important to note that this method is formulated in a spin-restricted way. The spatial molecular orbitals are identical for α (up) and β (down) electrons. This treatment, even for open-shell systems, is rooted in the fact that no spin-dependent terms are present in the GFN2-xTB Hamiltonian. This can lead to improper energetic splitting for states of different multiplicity, implying that GFN2-xTB Hamiltonian will always favor the low-spin configurations.⁴¹

As for DFTB, xTB has been applied to biologic⁵³ and organometallic⁵⁴ systems and used for studies of electronic spectra of large systems,⁵⁵ conformer generation,⁵⁶ electron ionization,⁵⁷ redox potential⁵⁸ or vibrational frequencies.^{59,60}

III – Application to transition metal complexes

In the following section, we aim at assessing the ability of the DFTB and xTB method to describe molecular junctions based on transition metal complexes. As a first step, this section is dedicated to the quantification of the accuracy of the TB description of isolated metal complexes at the molecular level. To do so, we selected a set of 51 representative complexes. We used quite small molecules containing one transition metal center among the following: iron, nickel, cobalt, zinc, copper and titanium. For each metal, different types of ligand (Scheme 3) were tested.



Scheme 3 – Set of organic ligands used to build the set of complexes.

The assessment of TB method accuracy is based on a comparison of metal-ligand distances and electronic structures, notably the HOMO-LUMO gaps and the shapes of the molecular orbitals with the corresponding DFT results and experimental data. The DFTB2 was tested using the parameter sets: “mio”, “trans3d”, “znorg”, and “tiorg” (Table 1). We will also study the performance of the DFTB3 implementation, for the complexes for which the parameterization was available (i.e, Ni,⁶¹ Zn^{62,63} and Cu⁶⁴). The xTB results were obtained using the GFN2-xTB version of the formalism.

DFTB calculations were conducted using the DFTB+ software⁶⁵ and xTB calculations using the standalone version of the program.⁶⁶ The DFT results were obtained with the Amsterdam Density Functional program (ADF) using a TZ2P basis set, a small frozen core and the PBE GGA functional. This DFT scheme is selected as a relevant reference because it is analogous to the DFT framework used in the DFTB parameterization.¹ The metal-ligand distance references are either issued from experimental crystallographic information or from a high computational level method like coupled cluster (CC) taken from the literature.

In order to rationalize more easily the performance of the TB methods, we decomposed our benchmark study in two steps: i) an in-depth comparison between TB and DFT/CC/exp values for six relevant complexes encompassing various types of ligands and metallic centers and ii) a more general and statistical analysis of the TB accuracy for the set of 51 different complexes.

III.1 In-depth study of selected complexes

The different results for the handpicked complexes are presented in Table 1. We selected, among the 51 systems, three Fe coordination complexes with different type of anchoring for the ligand: $[\text{Fe}(\text{bipy})_3]^{2+}$ (nitrogen coordination), $[\text{Fe}(\text{H}_2\text{O})_6]^{2+}$ (oxygen coordination) and $[\text{Fe}(\text{CO})_6]^{2+}$ (carbon coordination). In parallel, we considered three tri-phenanthroline-based complexes encompassing different metallic centers: $[\text{M}(\text{phen})_3]^{2+}$ with $\text{M} = \text{Fe}, \text{Ni}$ and Co . These six complexes are pseudo-octahedral compounds. For each system, we computed the metal-ligand distance ($d_{\text{M-L}}$), the molecular orbitals (HOMO-1, HOMO, LUMO, LUMO+1), their energy level diagram and compared the results to DFT calculations and to an external reference.

Table 2 – Metal-ligand distance (d_{M-L}), HOMO-LUMO (HL) gap and spin state of the molecules at different levels of theory. The Spin state column is the most stable spin state from the external reference. The last column is the most stable spin state in the considered level of theory. A positive ΔE HS/LS means that the LS state is more stable.

| Method | d_{M-L} (Å) | HL gap (eV) | Spin state | Most stable spin state (ΔE HS/LS in eV) |
|--|----------------|--------------|------------|--|
| [Fe(bipy)₃]²⁺ | | | | |
| Ref ⁶⁷ | 1.980 | - | - | - |
| DFT | 1.969 (-0.011) | 1.63 | | S = 0 (+1.457) |
| DFTB2 | 2.038 (+0.058) | 1.46 (-0.17) | S = 0 | S = 2 (-0.082) |
| xTB | 1.914 (-0.066) | 1.47 (-0.16) | | S = 0 (+3.129) |
| [Fe(H₂O)₆]²⁺ | | | | |
| Ref ^{68,69} | 2.165 | - | - | - |
| DFT | 2.165 (+0.000) | 0.40 | | S = 2 (-1.110) |
| DFTB2 | 2.207 (+0.042) | 0.07 (-0.34) | S = 2 | S = 0 (+0.408) |
| xTB | 2.350 (+0.185) | 8.48 (+8.08) | | S = 0 (+1.605) |
| [Fe(CO)₆]²⁺ | | | | |
| Ref ^{68,69} | 1.949 | - | - | - |
| DFT | 1.889 (-0.060) | 4.65 | | S = 0 (+3.767) |
| DFTB2 | 2.146 (+0.197) | 2.48 (-2.18) | S = 0 | S = 0 (+0.762) |
| xTB | 1.858 (-0.091) | 4.10 (-0.55) | | S = 0 (+4.979) |
| [Fe(phen)₃]²⁺ | | | | |
| Ref ⁶⁷ | 1.975 | - | - | - |
| DFT | 1.976 (+0.001) | 1.69 | | S = 0 (+1.310) |
| DFTB2 | 2.051 (+0.076) | 1.54 (-0.15) | S = 0 | S = 2 (-0.299) |
| xTB | 1.934 (-0.041) | 1.50 (-0.19) | | S = 0 (+3.075) |
| [Ni(phen)₃]²⁺ | | | | |
| Ref ^{70,71,72} | 2.106 | - | - | - |
| DFT | 2.114 (+0.008) | 2.01 | | - |
| DFTB2 | 2.177 (+0.071) | 0.93 (-1.08) | S = 1 | - |
| DFTB3 | 2.097 (-0.009) | 0.28 (-1.73) | | - |
| xTB | 2.104 (-0.002) | 1.30 (-0.71) | | - |
| [Co(phen)₃]³⁺ | | | | |
| Ref ^{73,74} | 1.942 | - | - | - |
| DFT | 1.968 (+0.026) | 2.31 | | HS not converged |
| DFTB2 | 1.967 (+0.025) | 2.98 (+0.67) | S = 0 | S = 0 (+3.320) |
| xTB | 1.946 (+0.004) | 2.51 (+0.20) | | S = 0 (+3.510) |

III.1.1 – Spin states of the complexes

To perform the geometry optimizations at each level of theory, we used the most stable spin state either based on DFT or reference. Table 1 presents such computed spin states. For the selected Fe complexes, the LS state ($S = 0$) is the most stable for $[\text{Fe}(\text{bipy})_3]^{2+}$ at the reference level. The DFTB2 method results in an inversion of stabilization of the HS state ($S = 2$) over the LS state, by 0.082 eV. On the contrary, the xTB method favors the LS state by 3.129 eV. For $[\text{Fe}(\text{H}_2\text{O})_6]^{2+}$, found as a HS state ($S = 2$) with DFT and reference calculation, both DFTB2 and xTB values result in a more stable LS state ($S = 0$) by +0.408 eV and +1.605 eV, respectively. $[\text{Fe}(\text{CO})_6]^{2+}$ is found to be a low spin state ($S = 0$) in the reference calculations, and in the TB methods also by 0.762 eV and 4.979 eV, respectively. Overall, for these different Fe-based complexes, the TB methods are not consistently able to retrieve the correct spin state of the system. Especially, as enounced in the introduction, the xTB method always greatly over-stabilizes the LS state in all cases.

These tendencies are similar when changing the metal in the sub-series of phenanthroline-based complexes. For $[\text{Fe}(\text{phen})_3]^{2+}$, the DFTB2 calculation results in an energy inversion toward the HS state compared to references, with a ΔE HS/LS of -0.299 eV, while the xTB method stabilizes the LS state by 3.075 eV. For the $[\text{Ni}(\text{phen})_3]^{2+}$, the system was only considered as a d^8 configuration, with $S = 1$. For $[\text{Co}(\text{phen})_3]^{3+}$, both TB methods correctly find the LS state as the most stable, by a significant energy of 3.320 eV and 3.510 eV for DFTB2 and xTB, respectively.

III.1.2 – Study of the metal-ligand distances

For the sub-series of Fe complexes, $[\text{Fe}(\text{bipy})_3]^{2+}$, $[\text{Fe}(\text{CO})_6]^{2+}$ and $[\text{Fe}(\text{H}_2\text{O})_6]^{2+}$, DFT is able to retrieve metal ligand distances in close agreement with our references (experimental values for $[\text{Fe}(\text{bipy})_3]^{2+}$ and CCSD(T) calculations for $[\text{Fe}(\text{CO})_6]^{2+}$ and $[\text{Fe}(\text{H}_2\text{O})_6]^{2+}$) with -0.011 Å, +0.000 Å and -0.060 Å deviations, respectively (Table 2)). DFTB2 returns $d_{\text{M-L}}$ values systematically and sometimes drastically larger than our reference with +0.058 Å, +0.042 Å and +0.197 Å of difference for $[\text{Fe}(\text{bipy})_3]^{2+}$, $[\text{Fe}(\text{H}_2\text{O})_6]^{2+}$ and $[\text{Fe}(\text{CO})_6]^{2+}$, respectively. Regarding xTB, the magnitude of the $d_{\text{M-L}}$ deviations is similar to those obtained in DFTB2, but the distances are either underestimated or overestimated depending on the complex. For xTB, the high spin system $[\text{Fe}(\text{H}_2\text{O})_6]^{2+}$ is the less accurately reproduced, as expected.

For the second sub-series composed of $[\text{Fe}(\text{phen})_3]^{2+}$, $[\text{Ni}(\text{phen})_3]^{2+}$ and $[\text{Co}(\text{phen})_3]^{3+}$ complexes, the performance of DFTB2 remains acceptable, with no distances dramatically overestimated: deviations of +0.076 Å, +0.071 Å and +0.025 Å are respectively obtained. The xTB calculations return shorter distances for $[\text{Fe}(\text{phen})_3]^{2+}$ and $[\text{Ni}(\text{phen})_3]^{2+}$ with -0.041 Å and -0.002 Å deviations, and a slightly longer average distance for the Cobalt system with +0.004 Å.

Overall, for the description of the metal-ligand distances, it is clear that the xTB method is more accurate than DFTB2 for which a systematic overestimation of these values is observed. For complexes, this deviation is too large (around 0.2 Å) and clearly problematic. Noteworthy, for $[\text{Ni}(\text{phen})_3]^{2+}$, DFTB3 calculations are possible, and yield a strongly improved $d_{\text{M-L}}$ value.

III.1.3 – Electronic structures

In the following, the DFT electronic structures are used as reference. The HOMO-LUMO electronic gaps for the different complexes calculated with DFT and DFTB2/xTB methods are compared in Table 2. This value appears to be extremely sensitive to the approximations made in the TB models, and the deviations are also extremely dependent on the complex nature. For DFTB2, the largest deviations are found in the case of the $[\text{Fe}(\text{CO})_6]^{2+}$ complex (deviation of -2.177 eV) and $[\text{Ni}(\text{phen})_3]^{2+}$ (-1.076 eV) while the gap values for $[\text{Fe}(\text{bipy})_3]^{2+}$ and $[\text{Fe}(\text{phen})_3]^{2+}$ complexes are for instance more accurately reproduced (within 0.2 eV only). For $[\text{Ni}(\text{phen})_3]^{2+}$, using a DFTB3 does not reduce this error. The xTB method shows in general electronic gaps in better agreement with DFT than DFTB2 for closed-shell systems, but open-shell systems like $[\text{Fe}(\text{H}_2\text{O})_6]^{2+}$ remain problematic.

Figure 4 and Figure 5 present the energy level diagrams of the different complexes, with a comparison between DFT and TB frontier molecular orbitals. In most cases, the topology of the last occupied (HOMO and HOMO-1) and first unoccupied (LUMO and LUMO+1) are roughly retrieved by both DFTB2 and xTB. However, discrepancies appear in the relative weight of the metal and ligands in the orbital for some complexes, as well as inversions in the orbital ordering in some cases. For example, for the $[\text{Fe}(\text{phen})_3]^{2+}$, both TB methods have MOs in good agreement with DFT. In contrast, the xTB MOs of $[\text{Ni}(\text{phen})_3]^{2+}$ are quite different from DFT MOs (no metal contribution of the virtual LUMO and LUMO+1 for

example). Finally, some complexes like $[\text{Fe}(\text{H}_2\text{O})_6]^{2+}$ show inverted orbitals where the DFTB2 SOMO corresponds to the SOMO-2 of DFT.

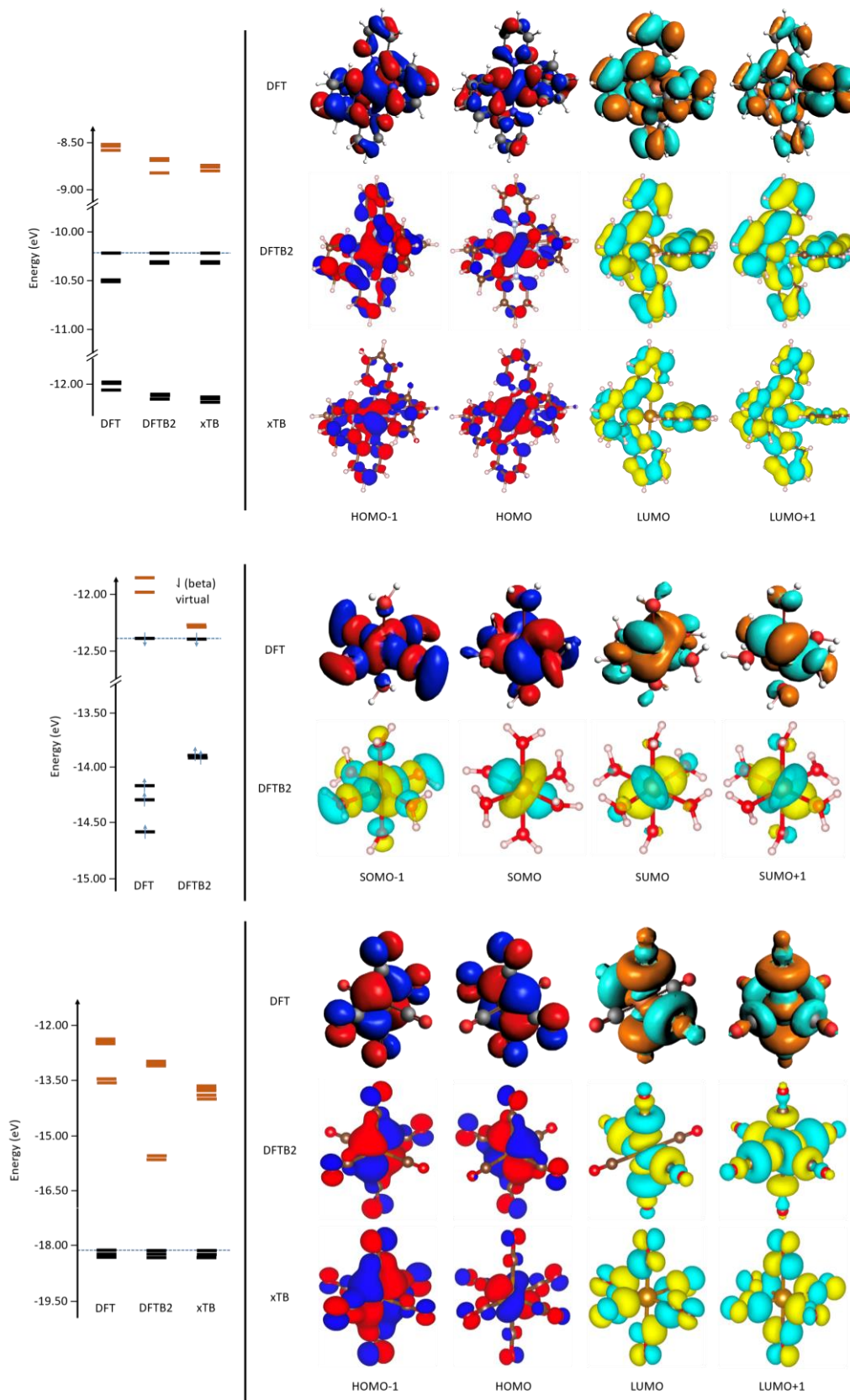


Figure 4 – Molecular orbital diagram at different levels of theory for: $[\text{Fe}(\text{bipy})_3]^{2+}$ (top), $[\text{Fe}(\text{H}_2\text{O})_6]^{2+}$ (middle), and $[\text{Fe}(\text{CO})_6]^{2+}$ (bottom). Occupied levels in black; Empty levels in orange. The HOMOs were aligned for sake of clarity. Iso-values is 0.05 e/bohr^3 .

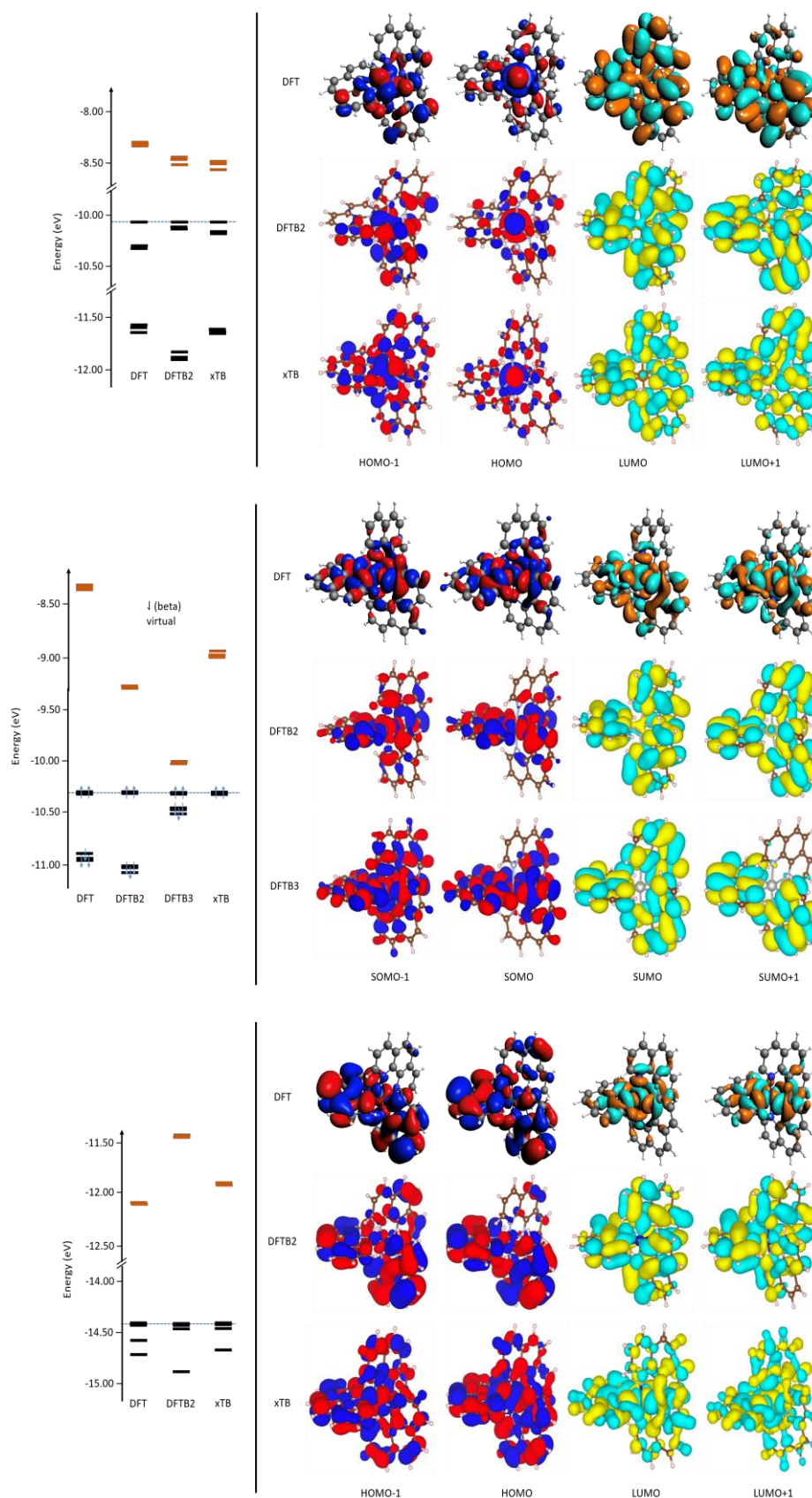


Figure 5 – Molecular orbital diagram at different levels of theory for: $[\text{Fe}(\text{phen})_3]^{2+}$ (top), $[\text{Ni}(\text{phen})_3]^{2+}$ (middle), and $[\text{Co}(\text{phen})_3]^{2+}$ (bottom). Occupied levels in black; Empty levels in orange. The HOMOs were aligned for sake of clarity. Iso-values is 0.05 e/bohr^3 .

III.1.4 – Overview of the comparisons

Figure 6 summarizes the computed values obtained for the three Fe complexes encompassing different ligands. The electronic gaps provided by the DFTB2 and xTB methods are found always to be lower than the DFT values, and the magnitude of the deviation appears to be system-dependent. For the $d_{\text{M-L}}$ distance, DFTB2 tends to systematically overestimate the $d_{\text{M-L}}$ distance compared to the reference and DFT, while the xTB method returns lower $d_{\text{M-L}}$ values in all cases. These different deviations are clearly non-negligible for the Fe complexes.

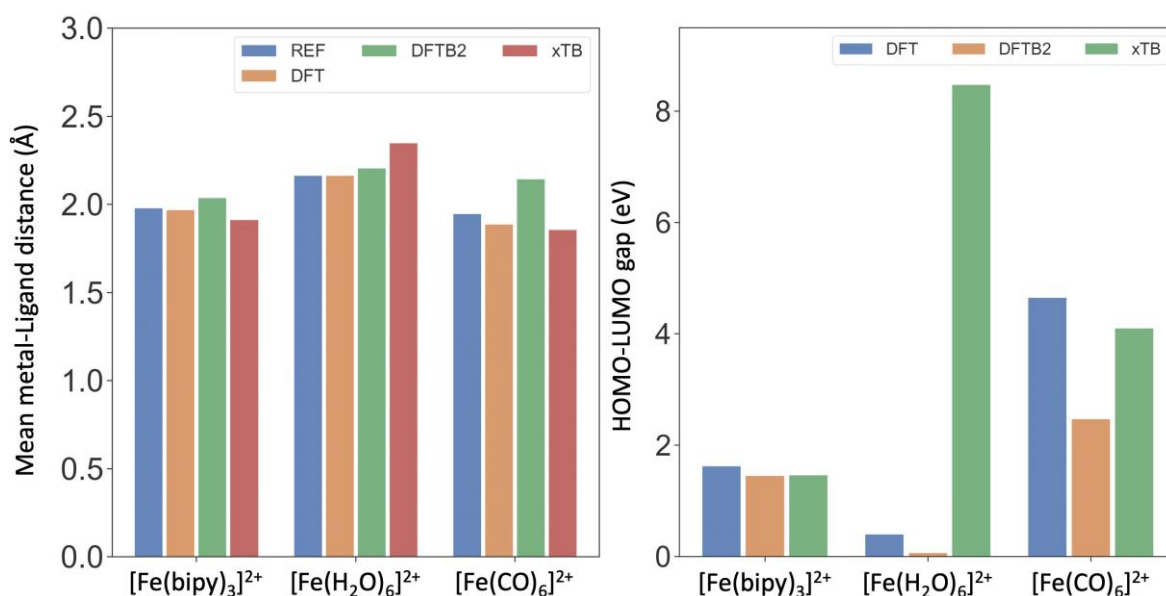


Figure 6 – Summary of the reference and computed metal-ligand distances and the HOMO-LUMO gaps obtained for three indicated Fe complexes.

Figure 7 summarizes the values obtained for phenanthroline-based complexes coordinated to different metals. The electronic gaps obtained with DFTB2 and xTB methods are lower than those obtained in DFT in the case of the Fe and Ni complexes, but higher for the Co complex. The magnitude of the deviation appears to be metal-dependent. For the $d_{\text{M-L}}$ distance DFTB2 tends to systematically overestimate the $d_{\text{M-L}}$ distance compared to the reference and to DFT while the xTB method returns lower $d_{\text{M-L}}$ values except for $[\text{Co}(\text{phen})_3]^{3+}$. Clearly, some of these deviations are dramatic and prevent the use of TB methods for such metallic complexes.

However, the magnitude of the errors is highly system-dependent and the small batch of complexes considered in this study does not allow to draw clear conclusions. In the following, we will then attempt at drawing a more general and statistical description of the TB methods accuracy.

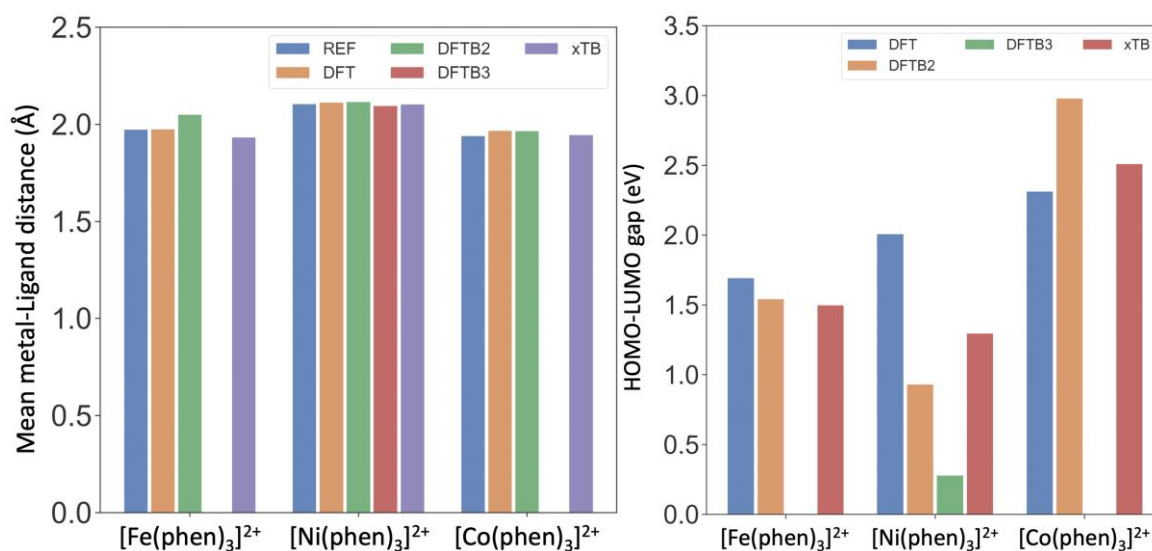


Figure 7 – Summary of the reference and computed metal-ligand distances and the HOMO-LUMO gaps obtained for three indicated phenanthroline complexes.

IV – General statistics on the performance of the TB methods

The results obtained for the 51 studied complexes are gathered in Table S1 and S2, in the annexes. The calculated (DFT and DFTB2/DFTB3/xTB) metal-ligand distances (d_{M-L}) are given in Table S1, and the HOMO-LUMO gap in Table S2. External reference values (experimental or CC calculations) are not considered in this step since they are not always available.

Figure 8 displays the variations of d_{M-L} (Δd_{M-L}) among all TB methods and DFT. Globally, the xTB distances are smaller than the DFT ones, and the magnitude of the error is not particularly metal-dependent. Only two systems, [Fe(C₅H₅)₂] and [Zn(Ph)₂], behave reversely with deviation of +0.117 Å and +0.103 Å, respectively. Nonetheless, the TB geometry optimizations of cobalt complexes (in orange) lead to the closest distances to the DFT values compared to the other metals.

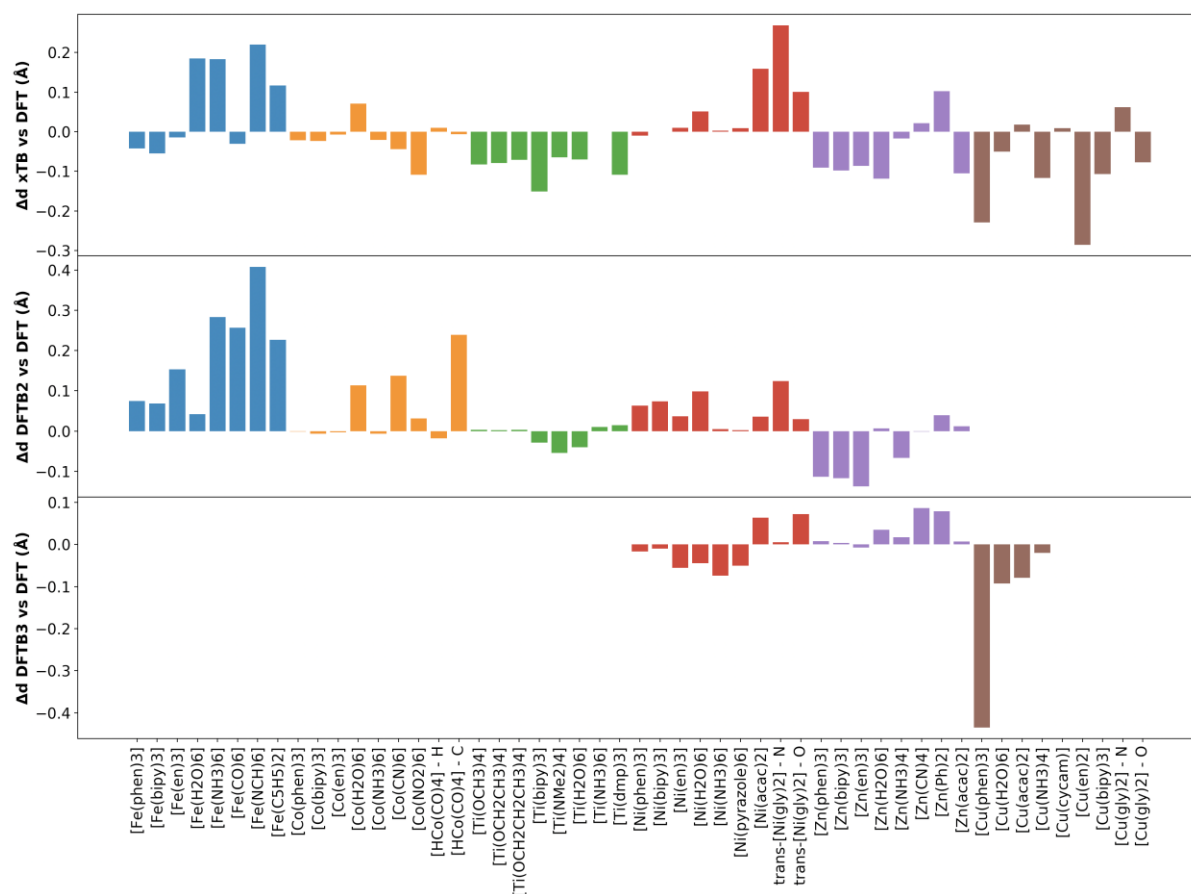


Figure 8 – Δd_{M-L} , which is the difference between the metal-ligand distance obtained with the considered TB method (top: xTB, middle: DFTB2 and bottom: DFTB3) and DFT for each system. The graphs are grouped by metal and colored as following: blue is Fe, orange is Co, green is Ti, red is Ni, Zn is purple and brown is Cu.

Twelve systems exhibit distance deviations to DFT of less than $\pm 0.005 \text{ \AA}$. The DFTB2 data are displayed in the middle of Figure 8. Compared to the xTB values, the deviations appear to be more metal dependent, with the Fe complexes being the least accurately described (e.g., $\text{Fe}(\text{NCH})_6$ with a $+0.408 \text{ \AA}$ error). Overall, 21 complexes present distances with a deviation to DFT smaller than $\pm 0.005 \text{ \AA}$. The deviations are presented at the bottom of Figure 8. One should note that fewer parameters are accessible for this formalism, thus the quantity of data compiled is reduced to only 21 Ni, Zn or Cu complexes. 50 % of these 21 systems are leading to DFTB3 distance deviation below the $\pm 0.005 \text{ \AA}$ threshold. The least accurately described system standing out in the graph is the $\text{Cu}(\text{phen})_3$ with a -0.435 \AA of deviation.

In Figure 9 represents the deviations in the HOMO-LUMO gap (ΔHL) compared to DFT. For xTB, the ΔHL values are in the majority of cases positive, but can range from -1 eV to almost +2 eV. Large discrepancies are found depending on the type of ligands when considering the

same metal. Overall, there is no metal exhibiting smaller ΔHL values than the others. Only twelve complexes present ΔHL values less than ± 0.250 eV. The DFTB2 deviations are presented in the middle of Figure 9. This shows when considering the metal dependency that the Ti complexes are the best described. Deviations for all Ni complexes are almost similar, except for the Ni(acac)₂ system. For DFTB2, twelve systems present ΔHL values with a deviation smaller than ± 0.250 eV. Globally, the extrema in ΔHL are higher for the DFTB2 method compared to xTB. Finally, the deviations for the DFTB3 method, in the bottom of Figure 9, show no clear trend with only four systems exhibiting ΔHL values below ± 0.250 eV. The main conclusion is that the HL gaps of the copper complexes lie the closest to the DFT values.

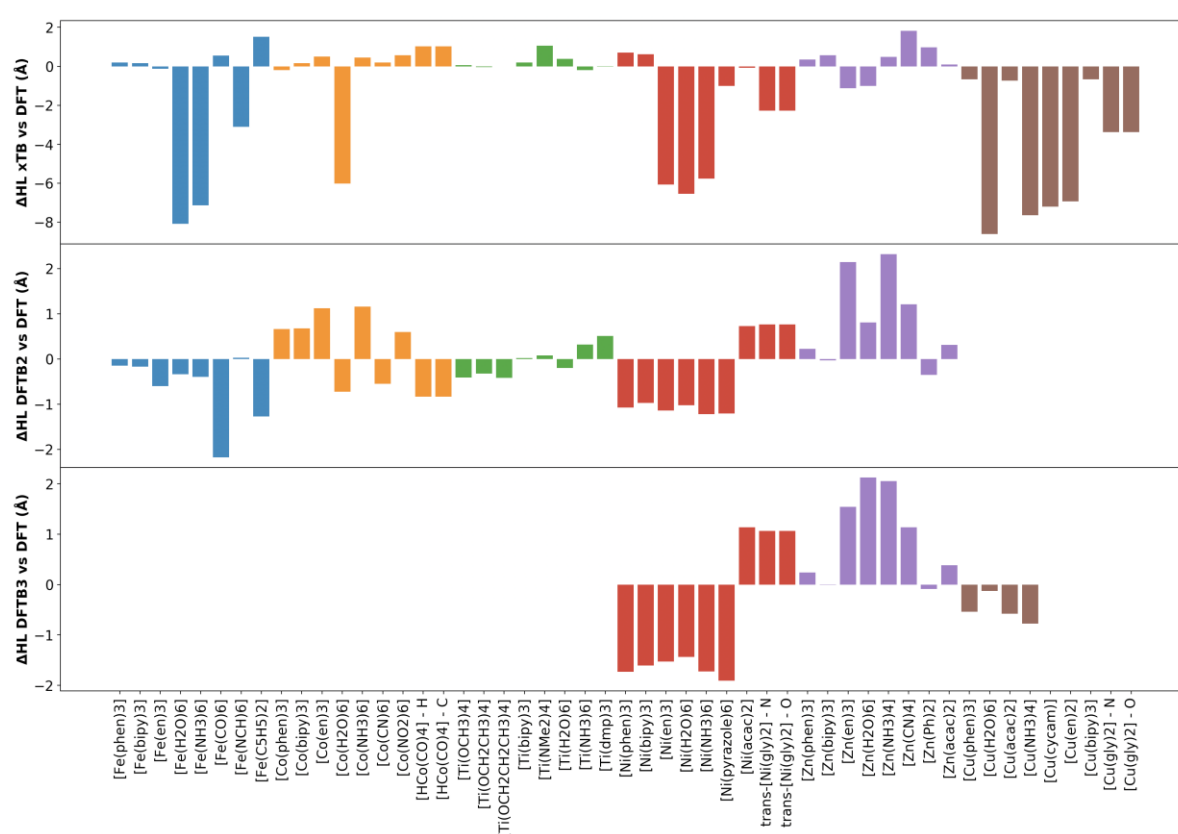


Figure 9 – Representation of ΔHL , which is the difference between HOMO-LUMO gap obtained with the considered TB method (top: xTB, middle: DFTB2 and bottom: DFTB3) and DFT. The graphs are grouped by metal and colored as following: blue is Fe, orange is Ni, green is Zn, red is Co, Ti is purple and brown is Cu.

We collect in Table 3 and Table 4 the mean, the absolute mean, the mean squared error (MSE) and the mean absolute deviation around the mean value (MAD) of the d_{M-L} and the HL gap values compared to DFT.

The MSE and MAD are defined as:

$$MSE = \frac{1}{n} \sum_{i=1}^n (x_{i-TB} - x_{i-DFT})^2 \quad \text{Eq. 1}$$

$$MAD = \frac{1}{n} \sum_{i=1}^n |x_{i-TB} - m(x_{TB})| \quad \text{Eq. 2}$$

with x_{i-TB} the value of the parameter for complex i for the tight binding method, x_{i-DFT} the corresponding value for complex i for DFT, n is the size of the sample (i.e. the number of tested molecules) and $m(x_{TB})$ the mean value of parameter for the TB method considered.

Table 3 – d_{M-L} mean, absolute mean, mean squared error (MSE) and mean absolute deviation around the mean value (MAD) for each method compared to DFT. All-systems (closed-shell and open-shell) or only closed-shell systems are considered in this analysis.

| Method | Descriptor | Mean (Å) | Mean (Å) | MSE (Å ²) | MAD (Å) |
|--------|---------------------------------|----------|-----------|-----------------------|---------|
| xTB | Δd_{M-L} (closed-shell) | -0.045 | 0.062 | 0.006 | 0.047 |
| | Δd_{M-L} (all-systems) | -0.015 | 0.078 | 0.011 | 0.076 |
| DFTB2 | Δd_{M-L} (closed-shell) | 0.011 | 0.054 | 0.007 | 0.070 |
| | Δd_{M-L} (all-systems) | 0.043 | 0.073 | 0.013 | 0.076 |
| DFTB3 | Δd_{M-L} (closed-shell) | 0.028 | 0.030 | 0.002 | 0.053 |
| | Δd_{M-L} (all-systems) | -0.024 | 0.060 | 0.012 | 0.063 |

Table 4 – HL gap mean, absolute mean, mean squared error (MSE) and mean absolute deviation around the mean value (MAD) for each method compared to DFT. All-systems (closed-shell and open-shell) or only close-shell systems are considered in this analysis.

| Method | Descriptor | Mean (eV) | Mean (eV) | MSE (eV ²) | MAD (eV) |
|--------|----------------------------|-----------|------------|------------------------|----------|
| xTB | ΔHL (closed-shell) | 0.332 | 0.525 | 0.506 | 1.832 |
| | ΔHL (all-systems) | -1.499 | 2.037 | 10.929 | 2.426 |
| DFTB2 | ΔHL (closed-shell) | 0.279 | 0.693 | 0.899 | 0.705 |
| | ΔHL (all-systems) | -0.049 | 0.728 | 0.865 | 0.724 |
| DFTB3 | ΔHL (closed-shell) | 0.545 | 0.878 | 1.350 | 0.878 |
| | ΔHL (all-systems) | -0.062 | 1.085 | 1.618 | 1.082 |

One tendency appears clearly from the study of Table 3: having open-shell systems in the analysis increases the MSE and MAD values for each of the TB approach. The MSE is the

lowest for the DFTB3 method with $+0.002 \text{ \AA}^2$ (only closed-shell systems) followed closely by DFTB2 with $+0.006 \text{ \AA}^2$ and xTB with $+0.007 \text{ \AA}^2$. The TB methods are, overall, similarly accurate for closed-shell complexes. Adding of the open-shell systems in the analysis roughly doubles the MSE for DFTB2 and xTB with MSE of $+0.011 \text{ \AA}^2$ and $+0.013 \text{ \AA}^2$, respectively. DFTB3 accuracy is six times lower when considering open-shell systems with a MSE value of $+0.012 \text{ \AA}^2$.

Table 4 details the error on the HL gaps. The xTB method is totally inaccurate upon addition of the open-shell systems in the set of molecules, with the MSE increasing from $+0.506 \text{ eV}^2$ to $+10.929 \text{ eV}^2$. The DFTB2 and DFTB3 are more suited than xTB to describe open-shell systems. Upon inclusion of open-shell systems the MSE for the DFTB2 method is modified from $+0.899 \text{ eV}^2$ to $+0.865 \text{ eV}^2$ and for DFTB3 the MSE increases from $+1.350 \text{ eV}^2$ to $+1.618 \text{ eV}^2$. The xTB is the closest to DFT for closed-shell systems only, and DFTB3 is the farthest. Overall, obtaining a HL gap value close to DFT HL gap appears to be a real bottleneck for all TB methods, regardless of the ligand and the metal considered.

IV – Conclusions and perspectives

This chapter aimed at assessing the ability of several Tight-Binding DFT-based computational schemes to describe the geometry and electronic structure of transition metal complexes. In particular the metal-ligand distances, electronic gap and the nature of the molecular orbitals were thoroughly studied for a series of 51 complexes and compared to reference data. For an application targeting transmission calculations, and with the idea of improving the electric and/or thermoelectric properties using a fast sampling of various organometallic molecules, the output is rather negative. Indeed, TB approaches in their present forms are not consistently accurate and the errors returned are extremely system dependent (ligand and metal), which may impede further screening studies. Nevertheless, we present in Figure 10 a first application of DFTB2 on two systems of interest for molecular junctions: $\text{Fe}(\text{cyclam})(\text{C}\equiv\text{CPh}_2)_2(\text{SH})_2$ and $\text{Ferrocene}(\text{C}\equiv\text{CPh}_2)_2(\text{SH})_2$ (both tested in previous chapters). It can be seen from the molecular orbital diagram that some frontier orbitals are inverted compared to DFT for both molecules. This would change the transmission spectra and therefore the properties of the junction. The HL gaps are also different implying that the MOs alignment of the molecule with gold might be really different between the TB method and DFT. Finally, after making a single-point calculation on the $\text{Au}_{13}\text{-Fe}(\text{cyclam})(\text{C}\equiv\text{C-Ph-S})_2\text{-Au}_{13}$ cluster geometry, we noticed that the *d* occupied MOs of the iron were located above the

gold, (see Part II, Chapter III on the Au₁₃ cluster for more details) so that an incorrect ordering of the gold orbitals and MOs is obtained. We thus tend to conclude that none of the tested TB methods can be used, even qualitatively, at the present stage to perform a screening on metallic-containing molecules. An essential improvement of the DFTB2 method encompasses necessarily the redefinition of the metallic parameter sets, specifically for targeted organometallics molecules. It is a time-consuming procedure but once finished, would permit a real breakthrough to alleviate the technological barrier that is limiting the development of molecular electronics by allowing the testing of larger molecules and polymetallic systems. Fast device optimization (i.e., concomitant optimization of the electrodes and the molecules) would allow us to consider statistically different anchoring geometries, and hence to provide a more realist comparison with experimental data in terms of conductance, thermoelectric properties and I-V curves.

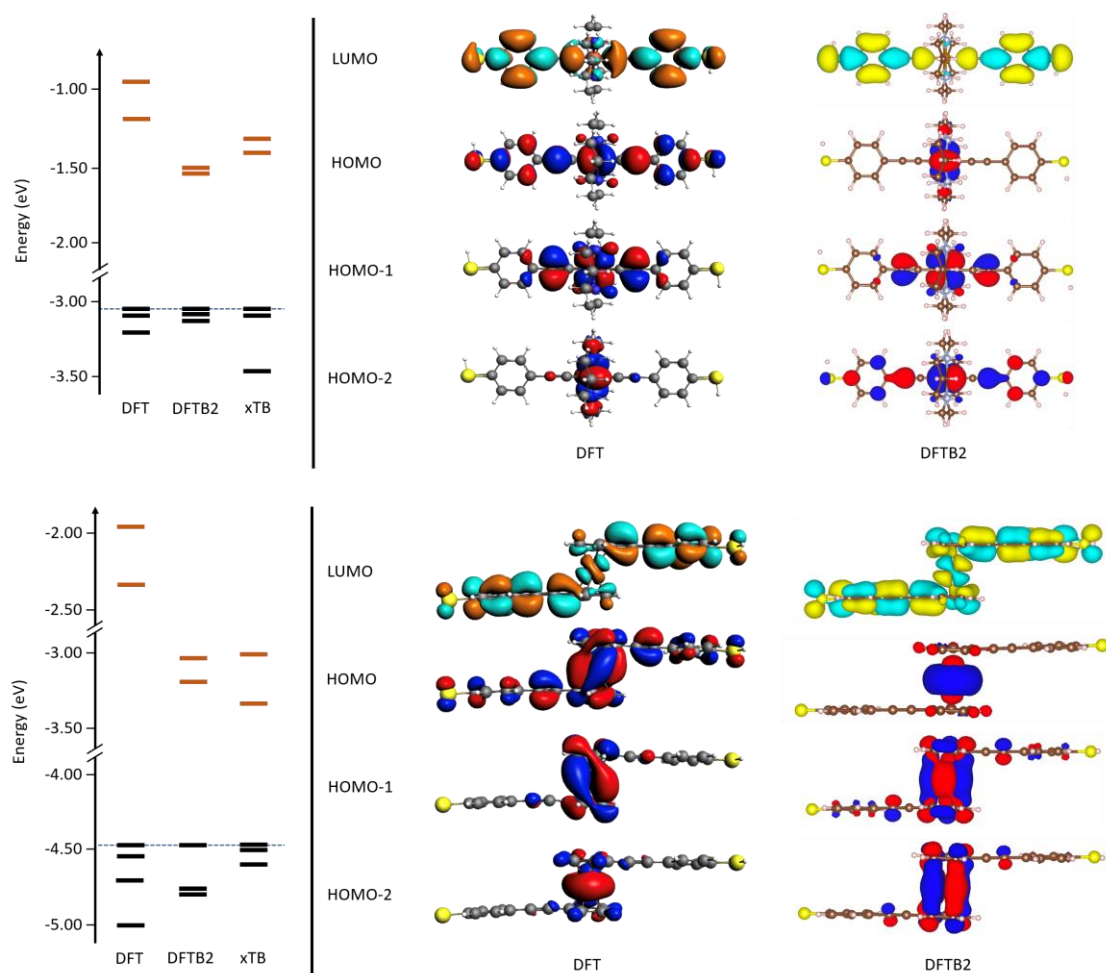


Figure 10 – Top) Fe(cyclam)(C≡C-Ph-SH)₂ and bottom) Ferrocene(C≡C-Ph-SH)₂ MOs energy diagram with the different methods. The HOMOs are aligned for sake of clarity. Right: frontier molecular orbitals obtained in DFT and DFTB2.

-
- ¹ Aradi, B. DFTB, method, implementation, parametrization. ISCS 2011, Shanghai.
- ² Pople, J. A. Electron interaction in unsaturated hydrocarbons. *Trans. Faraday Soc.* 1953, 49, 1375.
- ³ Fischer-Hjalmars, I. Zero Differential Overlap in ϕ -Electron Theories. *Adv. Quant. Chem.* 1966, 25-46. doi:10.1016/s0065-3276(08)60071-4.
- ⁴ Pople, J. A. Approximate Self-Consistent Molecular Orbital Theory. I. Invariant Procedures. *J. Chem. Phys.* 1965, 43, S129. doi: 10.1063/1.1701475.
- ⁵ Hofmann, H.-J.; Birner, P. Success of the NDDO method to predict conformations in conjugated systems. *Chem. Phys. Lett.* 1976, 37, 608-610. doi:10.1016/0009-2614(76)85049-x.
- ⁶ Ground states of molecules. 38. The MNDO method. Approximations and parameters. *J. Am. Chem. Soc.* 1977. doi:10.1021/ja00457a004.
- ⁷ Dewar, M. J. S.; Zoebisch, E. G.; Healy, E. F.; Stewart, J. J. P. Development and use of quantum mechanical molecular models. 76. AM1: a new general-purpose quantum mechanical molecular model. *J. Am. Chem. Soc.* 1985, 107, 3902–3909. doi:10.1021/ja00299a024.
- ⁸ Jakalian, A.; Bush, B. L.; Jack, D. B.; Bayly, C. I. Fast, efficient generation of high-quality atomic charges. AM1-BCC model: I. Method. *J. Comp. Chem.* 2000, 21, 132–146. doi:10.1002/(sici)1096-987x(20000130)21:2<132::aid-jcc5>3.0.co;2-p.
- ⁹ Stewart, J. J. P. Optimization of parameters for semiempirical methods I. Method. *J. Comp. Chem.* 1989, 10, 209–220. doi:10.1002/jcc.540100208.
- ¹⁰ Goringe, C M; Bowler, D R; Hernández, E. Tight-binding modelling of materials. *Rep. Prog. Phys.* 1997, 60, 1447–1512. doi:10.1088/0034-4885/60/12/001.
- ¹¹ Elstner, M.; Seifert, G. Density functional tight binding. *Phil. Trans. of the RSA: Math., Phys. Eng. Sci.* 2014, 372, 20120483–20120483. doi:10.1098/rsta.2012.0483.
- ¹² Seifert, G.; Eschrig, H.; Bieger, W. Eine approximative Variante des LCAO – $X\alpha$ Verfahrens. *Z. Phys. Chem.* 1986, 267, 529–539.
- ¹³ Porezag, D.; Frauenheim, T.; Köhler, T.; Seifert, G.; Kaschner, R. Construction of tight-binding-like potentials on the basis of density-functional theory: Application to carbon. *Phys. Rev. B* 1995, 51, 12947–12957. doi:10.1103/physrevb.51.12947.
- ¹⁴ Cohen, A. J.; Mori-Sanchez, P.; Yang, W. Insights into Current Limitations of Density Functional Theory. *Science* 2008, 321, 792–794. doi:10.1126/science.1158722.
- ¹⁵ Zheng, G.; Witek, H. A.; Bobadova-Parvanova, P.; Irle, S.; Musaeu, D. G.; Prabhakar, R.; Frauenheim, T. Parameter Calibration of Transition-Metal Elements for the Spin-Polarized Self-Consistent-Charge Density-Functional Tight-Binding (DFTB) Method: Sc, Ti, Fe, Co, and Ni. *J. Chem. Theo. Comp.* 2007, 3, 1349–1367. doi:10.1021/ct600312f.
- ¹⁶ Niehaus, T. A.; Suhai, S.; Della Sala, F.; Lugli, P.; Elstner, M.; Seifert, G.; Frauenheim, T. Tight-binding approach to time-dependent density-functional response theory. *Phys. Rev. B* 2001, 63. doi:10.1103/physrevb.63.085108.
- ¹⁷ Mennucci, B. Polarizable continuum model. *Wiley Interdisciplinary Reviews: Comp. Mol. Science* 2012, 2, 386–404. doi:10.1002/wcms.1086.

- ¹⁸ Brandenburg, J. G.; Grimme, S. Accurate Modeling of Organic Molecular Crystals by Dispersion-Corrected Density Functional Tight Binding (DFTB). *J. Phys. Chem. Lett.* 2014, 5, 1785–1789. doi:10.1021/jz500755u.
- ¹⁹ Hourahine, B.; Aradi, B.; Blum, V.; Bonafé, F.; Buccheri, A.; Camacho, C.; Cevallos, C.; Deshayé, M. Y.; Dumitrica, T.; Dominguez, A.; Ehlert, S.; Elstner, M.; van der Heide, T.; Hermann, J.; Irle, S.; Kranz, J. J.; Köhler, C.; Kowalczyk, T.; Kubar, T.; Lee, I. S.; Lutsker, V.; Maurer, R. J.; Min, S. K.; Mitchell, I.; Negre, C.; Niehaus, T. A.; Niklasson, A. M. N.; Page, A. J.; Pecchia, A.; Penazzi, G.; Persson, M. P.; Rezác, J.; Sánchez, C. G.; Sternberg, M.; Stöhr, M.; Stuckenberg, F.; Tkatchenko, A.; Yu, V. W.-z.; Frauenheim, T. DFTB+, a software package for efficient approximate density functional theory based atomistic simulations. *J. Chem. Phys.* 2020, 152, 124101. doi:10.1063/1.5143190.
- ²⁰ Guishan, Z.; Marcus, L.; Jacek, J.; Thom, V.; Michael, J. F.; Keiji, M. Implementation and benchmark tests of the DFTB method and its application in the ONIOM method. *Int. J. Quant. Chem.* 2009, 109, 1841–1854. doi:10.1002/qua.22002.
- ²¹ Yakovlev, A.; Philippsen, P.; Borini, S.; Rüger, R.; Oliveira, A. F.; de Reus, M.; Asl, M. G.; McCormack, D.; Patchkovskii, S.; Heine, T. ADF DFTB 2016, SCM. Theoretical Chemistry, Vrije Universiteit, Amsterdam.
- ²² Stokbro, K.; Petersen, D. E.; Smidstrup, S.; Blom, A.; Ipsen, M.; Kaasbjerg, K. Semi-empirical model for nanoscale device simulations. *Phys. Rev. B* 2010, 82, 075420. doi: 10.1103/PhysRevB.82.075420.
- ²³ <https://dftb.org/parameters/download>
- ²⁴ Gaus, M.; Cui, Q.; Elstner, M. DFTB3: Extension of the Self-Consistent-Charge Density-Functional Tight-Binding Method (SCC-DFTB). *J. Chem. Theo. Comp.* 2011, 7, 931–948. doi:10.1021/ct100684s.
- ²⁵ Elstner, M.; Porezag, D.; Jungnickel, G.; Elsner, J.; Haugk, M.; Frauenheim, T.; Suhai, S.; Seifert, G. Self-consistent-charge density-functional tight-binding method for simulations of complex materials properties. *Phys. Rev. B* 1998, 58, 7260–7268. doi:10.1103/physrevb.58.7260.
- ²⁶ Niehaus, T. A.; Elstner, M.; Frauenheim, T.; Suhai, S. Application of an approximate density-functional method to sulfur containing compounds. *J. Mol. Struct.: Theochem* 2001, 541, 185–194. doi:10.1016/s0166-1280(00)00762-4.
- ²⁷ Zheng, G.; Witek, H. A.; Bobadova-Parvanova, P.; Irle, S.; Musaeu, D. G.; Prabhakar, R.; Morokuma, K.; Lundberg, M.; Elstner, M.; Kohler, C.; Frauenheim, T. *J. Chem. Theory and Comput.* Parameter calibration of transition-metal elements for the spin-polarized self-consistent-charge density-functional tight-binding (DFTB) method: Sc, Ti, Fe, Co, and Ni. 2007,3 ,1349-136.
- ²⁸ Moreira, N. H.; Dolgonos, G.; Aradi, B.; da Rosa, A. L.; Frauenheim, T. Toward an Accurate Density-Functional Tight-Binding Description of Zinc-Containing Compounds. *J. Chem. Theo. Comp.* 2009, 5, 605–614. doi:10.1021/ct800455a.
- ²⁹ Dolgonos, G.; Aradi, B.; Moreira, N. H.; Frauenheim, T. An Improved Self-Consistent-Charge Density-Functional Tight-Binding (SCC-DFTB) Set of Parameters for Simulation of Bulk and Molecular Systems Involving Titanium. *J. Chem. Theo. Comp.* 2010, 6, 266–278. doi:10.1021/ct900422c.
- ³⁰ Sellì, D.; Fazio, G.; Seifert, G.; Di Valentin, C. Water Multilayers on TiO₂ (101) Anatase Surface: Assessment of a DFTB-Based Method. *J. Chem. Theo. Comput.* 2017, 13, 3862–3873. doi:10.1021/acs.jctc.7b00479.
- ³¹ Naumov, V.; Loginova, A.; Avdoshin, A.; Ignatov, S.; Mayorov, A.; Aradi, B.; Frauenheim, T. Structural, electronic, and thermodynamic properties of TiO₂/organic clusters: performance of DFTB method with different parameter sets. *Int. J. Quant. Chem.* 2020. doi:10.1002/qua.26427.

- ³² Chen, Y.; Liu, M.; Chen, J.; Li, Y.; Zhao, C.; Mu, X. A density functional based tight binding (DFTB+) study on the sulfidization-amine flotation mechanism of smithsonite. *Appl. Surface Sci.* 2018, 458, 454–463. doi:10.1016/j.apsusc.2018.07.014.
- ³³ Hu, H.; Lu, Z.; Elstner, M.; Hermans, J.; Yang, W. Simulating Water with the Self-Consistent-Charge Density Functional Tight Binding Method: From Molecular Clusters to the Liquid State. *J. Phys. Chem. A* 2007, 111, 5685–5691. doi:10.1021/jp070308d.
- ³⁴ Stojanović, L.; Aziz, S. G.; Hilal, R. H.; Plasser, F.; Niehaus, T. A.; Barbatti, M. Nonadiabatic Dynamics of Cycloparaphenylenes with TD-DFTB Surface Hopping. *J. Comp. Theo. Chem.* 2017, 13, 5846–5860. doi:10.1021/acs.jctc.7b01000.
- ³⁵ Maity, S.; Bold, B. M.; Prajapati, J. D.; Sokolov, M.; Kubař, T.; Elstner, M.; Kleinekathöfer, U. DFTB/MM Molecular Dynamics Simulations of the FMO Light-Harvesting Complex. *J. Phys. Chem. Letters* 2020, 11, 8660–8667. doi:10.1021/acs.jpcllett.0c02526.
- ³⁶ Fihey, A.; Hettich, C.; Touzeau, J.; Maurel, F.; Perrier, A.; Köhler, C.; Aradi, B.; Frauenheim, T. SCC-DFTB parameters for simulating hybrid gold-thiolates compounds. *J. Comp. Chem.* 2015, 36, 2075–2087. doi:10.1002/jcc.24046.
- ³⁷ Tandiana, R.; Brun, E.; Sicard-Roselli, C.; Domin, D.; Van-Oanha, N.-T.; Clavaguérab, C. Probing the structural properties of the water solvation shell around gold nanoparticles: A computational study. *J. Chem. Phys.* 2021, 154, 044706. doi:10.1063/5.0037551.
- ³⁸ Domínguez-Castro, A.; Lien-Medrano, C. R.; Maghrebi, K.; Messaoudi, S.; Frauenheim, T.; Fihey, A. Photoinduced charge-transfer in chromophore-labeled gold nanoclusters: quantum evidence of the critical role of ligands and vibronic couplings. *Nanoscale* 2021, 13, 6786. doi:10.1039/d1nr00213a.
- ³⁹ Vuong, V. Q.; Madridejos, J. M. L.; Aradi, B.; Sumpter, B. G.; Metha, G. F.; Irle, S. Density-functional tight-binding for phosphine stabilized nanoscale gold clusters. *Chem. Science* 2020, 11, 13113–13128. doi:10.1039/D0SC04514D.
- ⁴⁰ Tebikachew, B. E.; Li, H. B.; Pirrotta, A.; Börjesson, K.; Solomon, G. C.; Hihath, J.; Moth-Poulsen, K. Effect of Ring Strain on the Charge Transport of a Robust Norbornadiene–Quadricyclane-Based Molecular Photoswitch. *J. Phys. Chem. C* 2017, 121(13), 7094–7100. doi:10.1021/acs.jpcc.7b00319.
- ⁴¹ a) C. Bannwarth, E. Caldeweyher, S. Ehlert, A. Hansen, P. Pracht, J. Seibert, S. Spicher, S. Grimme *WIREs Comput. Mol. Sci.*, 2020, 11, e01493. DOI: 10.1002/wcms.1493. b) S. Grimme, C. Bannwarth, P. Shushkov, *J. Chem. Theory Comput.*, 2017, 13, 1989–2009. DOI: 10.1021/acs.jctc.7b00118. c) C. Bannwarth, S. Ehlert and S. Grimme., *J. Chem. Theory Comput.*, 2019, 15, 1652–1671. DOI: 10.1021/acs.jctc.8b01176. d) P. Pracht, E. Caldeweyher, S. Ehlert, S. Grimme, *ChemRxiv*, 2019. doi:10.26434/chemrxiv.8326202.v1.
- ⁴² Gaus, M.; Cui, Q.; Elstner, M. DFTB3: Extension of the self-consistent-charge density-functional tight-binding method (SCC-DFTB). *J. Chem. Theory Comp.* 2011, 7, 931–948. Doi: Gaus, M., Cui, Q., & Elstner, M. (2011). DFTB3: Extension of the Self-Consistent-Charge Density-Functional Tight-Binding Method (SCC-DFTB). *Journal of Chemical Theory and Computation*, 7(4), 931–948. doi:10.1021/ct100684s.
- ⁴³ Makov, G. Chemical Hardness in Density Functional Theory. *J. Phys. Chem* 1995, 99, 9337–9339. doi:10.1021/j100023a006.
- ⁴⁴ Grimme, S.; Bannwarth, C.; Shushkov, P. A Robust and Accurate Tight-Binding Quantum Chemical Method for Structures, Vibrational Frequencies, and Noncovalent Interactions of Large Molecular Systems Parametrized

for All spd-Block Elements ($Z = 1-86$). *J. Chem. Theory Comput.* 2017, 13, 1989–2009. doi:10.1021/acs.jctc.7b00118.

⁴⁵ Ruger R, Franchini M, Trnka T, et al. AMS 2019.3, SCM, Theoretical Chemistry. Amsterdam, The Netherlands: Vrije Universiteit <http://www.scm.com>.

⁴⁶ T. D. Kuhne, M. Iannuzzi, M. D. Ben, V. V. Rybkin, P. Seewald, F. Stein, T. Laino, R. Z. Khaliullin, O. Schutt, F. Schiffmann, D. Golze, J. Wilhelm, S. Chulkov, M. H. Bani-Hashemian, V. Weber, U. Borstnik, M. Taillefumier, A. S. Jakobovits, A. Lazzaro, H. Pabst, T. Muller, R. Schade, M. Guidon, S. Andermatt, N. Holmberg, G. K. Schenter, A. Hehn, A. Bussy, F. Belleflamme, G. Tabacchi, A. Glob, M. Lass, I. Bethune, C. J. Mundy, C. Plessl, M. Watkins, J. VandeVondele, M. Krack, and J. Hutter. Cp2k: An electronic structure and molecular dynamics software package – Quickstep: Efficient and accurate electronic structure calculations; 2020.

⁴⁷ ezac, J. Cuby: An integrative framework for computational chemistry. *J. Comp. Chem.* 2016, 37, 1230–1237. doi:10.1002/jcc.24312.

⁴⁸ Manby, F.; Miller, T.; Bygrave, P.; Ding, F.; Dresselhaus, T.; Batista-Romero, F.; Buccheri, A.; Bungey, C.; Lee, S.; Meli, R.; Miyamoto, K.; Steinmann, C.; Tsuchiya, T.; Welborn, M.; Wiles, T.; Williams, Z. entos: A quantum molecular simulation package. 2019

⁴⁹ Neese, F. The ORCA program system. *WIREs Comp. Mol Sci.* 2012, 2, 73–78.

⁵⁰ Seritan, S.; Bannwarth, C.; Fales, B. S. Hohenstein, E.; Kokkila-Schumacher, S.; Luehr, N.; Snyder Jr, J.; Song, S.; Titov, A.; Ufimtsev, I.; Martınez, T. TeraChem: Accelerating electronic structure and ab initio molecular dynamics with graphical processing units. *J. Chem. Phys.* 2020, 152, 224110. doi:10.1063/5.0007615.

⁵¹ Grimme, S.; Antony, J.; Ehrlich, S.; Krieg, H. A consistent and accurate ab initio parametrization of density functional dispersion correction (DFT-D) for the 94 elements H-Pu. *J. Chem. Phys.* 2010, 132, 154104. doi:10.1063/1.3382344.

⁵² Caldeweyher, E.; Bannwarth, C.; Grimme, S. Extension of the D3 dispersion coefficient model. *J. Chem. Phys.* 2017, 147, 034112. doi:10.1063/1.4993215

⁵³ Schmitz, S.; Seibert, J.; Ostermeir, K.; Hansen, A.; Goller, A. H.; Grimme, S. Quantum Chemical Calculation of Molecular and Periodic Peptide and Protein Structures. *J. Phys. Chem. B* 2020, 124, 3636–3646. doi:10.1021/acs.jpcc.0c00549.

⁵⁴ Bursch, M.; Neugebauer, H.; Grimme, S. Structure Optimization of Large Transition-Metal Complexes with Extended Tight-Binding Methods. *Angew. Chem. Int. Ed.* 2019, 58, 11078–11087. doi:10.1002/anie.201904021.

⁵⁵ Grimme, S.; Bannwarth, C. Ultra-fast computation of electronic spectra for large systems by tight-binding based simplified Tamm-Dancoff approximation (sTDA-xTB). *The Journal of Chemical Physics* 2016, 145, 054103. doi:10.1063/1.4959605.

⁵⁶ Grimme, S.; Bannwarth, C.; Dohm, S.; Hansen, A.; Pisarek, J.; Pracht, P.; Seibert, J.; Neese, F. Fully Automated Quantum-Chemistry-Based Computation of Spin-Spin-Coupled Nuclear Magnetic Resonance Spectra. *Angewandte Chemie Int. Ed.* 2017, 56, 14763–14769. doi:10.1002/anie.201708266.

⁵⁷ Koopman, J.; Grimme, S. Calculation of Electron Ionization Mass Spectra with Semi-empirical GFNn-xTB Methods. *ACS Omega* 2019. doi:10.1021/acsomega.9b02011.

- ⁵⁸ Neugebauer, H.; Bohle, F.; Bursch, M.; Hansen, A.; Grimme, S. Benchmark Study of Electrochemical Redox Potentials Calculated with Semiempirical and DFT Methods. *J. Phys. Chem. A* 2020, 124, 7166–7176. doi:10.1021/acs.jpca.0c05052.
- ⁵⁹ Katsyuba, S. A.; Spicher, S.; Gerasimova, T. P.; Grimme, S. Fast and Accurate Quantum Chemical Modeling of Infrared Spectra of Condensed-Phase Systems. *J. Phys. Chem. B* 2020. doi:10.1021/acs.jpbc.0c05857.
- ⁶⁰ Spicher, S.; Grimme, S. Single-Point Hessian Calculations for Improved Vibrational Frequencies and Rigid-Rotor-Harmonic-Oscillator Thermodynamics. *J. Comp. Theo. Chem.* 2021, 17. doi: 10.1021/acs.jctc.0c01306.
- ⁶¹ Vujović, M.; Huynh, M.; Steiner, S.; Garcia-Fernandez, P.; Elstner, M.; Cui, Q.; Gruden, M. Exploring the applicability of density functional tight binding to transition metal ions. Parameterization for nickel with the spin-polarized DFTB3 model. *J. Comp. Chem.* 2018. doi:10.1002/jcc.25614.
- ⁶² Gaus, M.; Goetz, A.; Elstner, M. Parametrization and Benchmark of DFTB3 for Organic Molecules. *J. Chem. Theo. Comp.* 2012, 9, 338–354. doi:10.1021/ct300849w.
- ⁶³ Lu, X.; Gaus, M.; Elstner, M.; Cui, Q. Parametrization of DFTB3/3OB for Magnesium and Zinc for Chemical and Biological Applications. *J. Phys. Chem. B* 2014, 119, 1062–1082. doi:10.1021/jp506557r.
- ⁶⁴ Bruschi, M.; Bertini, L.; Bonačić-Koutecký, V.; De Gioia, L.; Mitrić, R.; Zampella, G.; Fantucci, P. Speciation of Copper–Peptide Complexes in Water Solution Using DFTB and DFT Approaches: Case of the [Cu(HGGG)(Py)] Complex. *J. Phys. Chem. B* 2012, 116, 6250–6260. doi:10.1021/jp210409c.
- ⁶⁵ Hourahine, B.; Aradi, B.; Blum, V.; Bonafé, F.; Buccheri, A.; Camacho, C.; Cevallos C.; Deshayé, M. Y.; Dumitrică T.; Dominguez, A.; Ehlert, S.; Elstner, M.; van der Heide, T.; Hermann, J.; Irle, S.; Kranz, J. J.; Köhler, C.; Kowalczyk, T.; Kubař, T.; Lee, I. S.; Lutsker, V.; Maurer, R. J.; Min, S. K.; Mitchell, I.; Negre, C.; Niehaus, T. A.; Niklasson, A. M. N.; Page, A. J.; Pecchia, A.; Penazzi, G.; Persson, M. P.; Řezáč, J.; Sánchez, C. G.; Sternberg, M.; Stöhr, M.; Stuckenberg, F.; Tkatchenko, A.; Yu, V. W.-z.; Frauenheim, T. DFTB+, a software package for efficient approximate density functional theory based atomistic simulations. *J. Chem. Phys.* 2020, 152, 124101. doi: 10.1063/1.5143190.
- ⁶⁶ Bannwarth, C.; Caldeweyher, E.; Ehlert, S.; Hansen, A.; Pracht, P.; Seibert, J.; Spicher, S.; Grimme, S. Extended tight-binding quantum chemistry methods. *WIREs Comput. Mol. Sci.* 2020, 11, e01493. doi:10.1002/wcms.1493.
- ⁶⁷ Rafiei, S.; Chiniforoshan, H.; Khoshgoftarmanesh, A. H.; Ghasemi, S.; Notash, B. Synthesis and crystal structure of tris (1,10 phenanthroline)-iron(II)tetra(4-Nitro-phenyl-urea) bis chloride, [Fe(phen)₃][Cl₂·L₄] chelates and evaluation of their efficacy as iron source for tomato in nutrient solution culture. *Plant Growth Reg.* 2014, 75, 123–132. doi:10.1007/s10725-014-9937-5.
- ⁶⁸ Song, S.; Kim, M.-C.; Sim, E.; Benali, A.; Heinonen, O.; Burke, K. Benchmarks and Reliable DFT Results for Spin Gaps of Small Ligand Fe(II) Complexes. *J. Comp. Theo. Chem.* 2018, 14, 2304–2311. doi:10.1021/acs.jctc.7b01196.
- ⁶⁹ Alipour, M.; Izadkhast, T. Appraising Spin-State Energetics in Transition Metal Complexes Using Double-Hybrid Models: Accountability of SOS0-PBESCAN0-2(a) as a Promising Paradigm. *Phys. Chem. Chem. Phys.* 2020, 22, 9388–9404. doi:10.1039/D0CP00807A.
- ⁷⁰ Hughes, T. F.; Friesner, R. A. Correcting Systematic Errors in DFT Spin-Splitting Energetics for Transition Metal Complexes. *J. Comp. Theo. Chem.* 2011, 7, 19–32. doi:10.1021/ct100359x.

⁷¹ Suescun, L.; Mombrú, A. W.; Mariezcurrena, R. A. Tris(1,10-Phenanthroline)Nickel(II) Dinitrate Thiourea Monohydrate. *Acta Crystallogr. C Cryst Struct. Comm.* 1999, 55, 1991–1993. doi:10.1107/S0108270199011312.

⁷² Androš, L.; Matković-Čalogović, D.; Planinić, P. A series of compounds containing various (oxalato)tantalate(V) complex anions – synthesis, properties and the mixed-metal oxide formation via thermal decomposition. *Cryst. Eng. Comm.* 2013, 15, 533–543. doi:10.1039/c2ce26391b.

⁷³ Warten, R. M. L.; Öhrström, L.; Opiteck, G. J.; Shang, M.; & Lappin, A. G. The oxidation of [Co(edta)]²⁻ by [Co(phen)₃]³⁺. *Inorganica Chimica Acta* 1994, 225, 75–82. doi:10.1016/0020-1693(94)04032-x.

⁷⁴ Sharma, R. P.; Singh, A.; Brandão, P.; Felix, V.; Venugopalan, P. Second sphere coordination in binding of fluoroanions: Synthesis, spectroscopic characterization and single crystal X-ray structure determination of [Co(phen)₃](BF₄)₃·H₂O and [Co(phen)₃](PF₆)₃·CH₃COCH₃. *J. Mol. Struct.* 2009, 920, 119–127. doi:10.1016/j.molstruc.2008.10.036.

Conclusion and perspectives

In the first part of the manuscript dealing with copper (I) luminescent complexes, a theoretical approach based on (TD-)DFT employing a relatively small atomic basis set and the PBE0 hybrid functional was used to rationalize the photophysical properties of large polynuclear systems, namely Cu_6CN_2 and Cu_8CN_4 . The comparison between the computed and experimental data are in good agreement. The occurrence of a TADF process for Cu_6CN_2 is notably strongly supported by the computational study which reveals that considering the constraints imposed by the crystal packing reduces the energy between the first singlet and triplet excited states. The calculated emission wavelengths are also well reproduced. The calculations also point out the role of the Cu-Cu interactions which is enhanced upon excitation, hence favoring the spin-orbit coupling. *A contrario*, the computational results obtained for the smaller systems $[\text{Cu}_2(\text{dppa})_3]^{2+}$ and $[\text{Cu}_2(\text{dppm})_3]^{2+}$ are revealing a more complex energy ordering and coupling of the excited states that render difficult to draw firm conclusions. For $[\text{Cu}_2(\text{dppa})_3]^{2+}$, the hydrogen bonding between the $[\text{Cu}_2(\text{dppa})_3]^{2+}$ and its counter-ion (either PF_6^- or BF_4^-) and more globally the crystal packing should be considered in our computational study.

Several points should be addressed in future studies to circumvent these problems:

- The crystallization of the $[\text{Cu}_2(\text{dppa})_3]^{2+}$ with non-interacting counter-ion and a non-coordinating solvent will certainly lead to better agreement between the experimental and computational approach.
- As seen in Chapter II, several ISC routes are possible which indicates that the experimental study of the influence of the excitation wavelength used to realize the emission spectra can be interesting to perform to better understand these systems.
- The use of a more accurate computational approach would be necessary to access to more reliable energies and better evaluate the different competing processes.

Other multi-nuclear copper (I) systems are currently under investigation and were thus not presented in the manuscript, notably a polymeric version of the Cu_4CN_2 system using several types of organic linker like the 2,4,6-tri-4-pyridyl-1,3,5-triazine, bypyridine-33' or 1,3-di(4-pyridyl)propane (Figure 1). These systems have interesting luminescent properties. Indeed, in the polymeric form, a yellow luminescence is created; by different mechanisms (e.g., mechanochromic or heating), the polymer can undergo structural changes leading to a blue

emission, which is highly similar to that observed for Cu_4CN_2 complex. By pouring a drop of solvent (dichloromethane) on the powder, a yellow emission is recovered. The computational study that was performed to date concerns the bonding dissociation energy of the pyridyl ligands to the copper to analyze the possible dissociation processes occurring in this system (concomitantly or not). The computation of the different excited states of the isolated units should help to rationalize the optical properties of such systems.

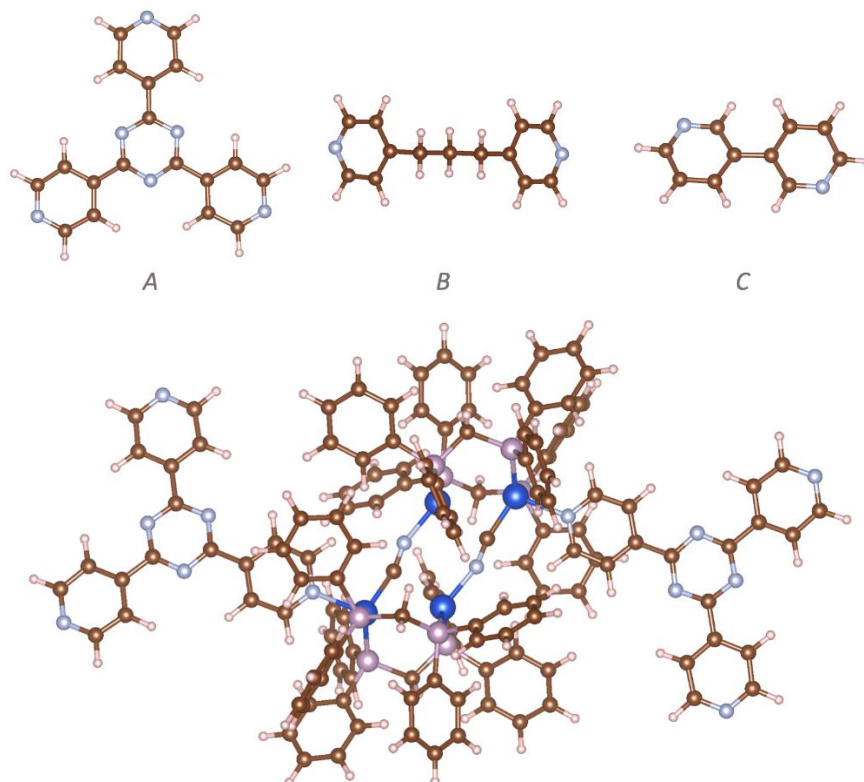


Figure 1 – Top: type of organic linker used in the polymeric Cu_4CN_2 system. **A** = 2,4,6-tri-4-pyridyl-1,3,5-triazine, **B** = bipyridine-3,3' and **C** = 1,3-di(4-pyridyl)propane. Bottom: representation of the polymeric Cu_4CN_2 unit with the **A** linker.

The second part of this manuscript is devoted to molecular junctions. The different rationalizing schemes and methodologies in the field are given in the first chapter. The DFT/NEGF computational approach was applied to study the different molecular junctions. The main goal of this part of the manuscript is to identify the transmission features that can enhance thermoelectric properties, to compare and give insights to rationalize the experimental results, and to evaluate the potential of transition metal containing molecules for thermoelectric properties. Several factors were evaluated:

- As shown in Chapter II, the presence of anti-resonance in the transmission peak close to the Fermi level enhances the thermoelectric properties compared to a classic Lorentzian-shaped transmission. Fano resonances have almost no effect at RT. The ferrocene-derivatives display such QI, leading to interesting thermoelectric properties if the main transport level can be adjusted to lie closer to the Fermi level, using an external gate for example.
- The nature of the metal is utterly important. Chromium, cobalt, platinum, molybdenum and manganese metal-containing systems were also studied without yielding interesting results. The coordination complexes incorporating iron and ruthenium were those for which the best properties were calculated.
- The coordination of the sulfur anchor in the meta position of the terminal phenyl group of the linker does not create Fano nor anti-resonance interferences contrarily to what is reported in literature for organic molecular junctions. The “T-shaped” molecular systems are promising alternatives.

Several limitations and possible solutions concerning the computational approach were also discussed:

- The Fermi level position accuracy compared to the first occupied and unoccupied molecular levels is clearly functional and basis set dependent. Using more sophisticated functionals like the screened hybrid-GGA HSE06 (recently available in QuantumATK 2021) can certainly enhance the quantitative agreement between experiments and computations. Modified DFT methods like DFT+ Σ which includes static corrections to the Kohn–Sham energy levels built on many-electron calculations can also help to better reproduce the conductance of organic molecules, as reported by Quek *et al.* for systems with a nitrogen anchoring group.¹
- The geometries of the electrode greatly influence the position of the different molecular levels (even when using the same anchoring group and a similar hollow coordination). The use of a statistical approach to consider the diversity of junctions observed in experimental conditions is highly desirable.
- Charged systems are complex to simulate using the DFT/NEGF tools.
- The electrical conductance is always overestimated compared to experimental data. This is certainly due to several factors, the dominant one being that only the best

possible molecular junctions are typically computed. For a better comparison, the dispersal of the experimental junction types should be accounted for (see above).

- The use of semi-empirical tight-binding methods (DFTB or GFN2-xTB) was evaluated as way to give access to this statistical approach needed to better compare theory with experiment. Our results show that, to date, it is not reliable for transition metal-containing systems.
- In this study, the lack of applicable methodology to evaluate the thermal phonon conductance at the theoretical level for the systems studied in the manuscript is damageable since ZT would be better evaluated. Indeed, we employed a value of 20 pW/K for the thermal phonon conductance on the basis of experimental evaluations. The actual value might be smaller, especially when the rigidity and the length of the molecules increase.

The use of DFT as computational tool allowed us to rationalize at a semi-quantitative level the optical properties of copper (I) complexes of different sizes revealing the complexity of the multiple competitive processes that could occur after excitation. Even though more sophisticated tools would be need to access precisely to the de-excitation cascade, these calculations are giving valuable information on the nature of the excitation, the geometrical and electronic changes of the first excited states allowing to rationalize the TADF-like behavior measured experimentally.

DFT coupled with NEGF has also proven to be an interesting and comprehensive tool to perform a molecular design of organometallic junction in the aim of enhancing thermoelectric properties. The systems which has been identified in this manuscript by computational means are presenting rich electronic transmission features that give rise to appealing perspective in this emerging field. This study also reveals the need of faster computational tools that would allow to simulate the large diversity of geometries that are observed experimentally in order to simulate and therefore interpret and predict the properties of experimental molecular junctions.

¹ Quek, S. Y.; Khoo, K. H. Predictive DFT-Based Approaches to Charge and Spin Transport in Single-Molecule Junctions and Two-Dimensional Materials: Successes and Challenges. *Acc. Chem. Res.* 2014, 47, 3250–3257. doi:10.1021/ar4002526.

Part II – Chapter VI – Tight Binding as a prospecting method

Table S1 – d_{M-L} values for the different complexes obtained with all the methods. The charge of the complex is given, along with the most stable spin state of the system.

| Complex | Charge | Spin state | d_{M-L} (DFT) | d_{M-L} (xTB) | d_{M-L} (DFTB2) | d_{M-L} (DFTB3) |
|--|--------|------------|-----------------|-----------------|-------------------|-------------------|
| [Fe(phen) ₃] | +2 | 0 | 1.976 | 1.934 | 2.051 | - |
| [Fe(bipy) ₃] | +2 | 0 | 1.969 | 1.914 | 2.038 | - |
| [Fe(en) ₃] | +2 | 0 | 2.052 | 2.038 | 2.205 | - |
| [Fe(H ₂ O) ₆] | +2 | 2 | 2.165 | 2.350 | 2.207 | - |
| [Fe(NH ₃) ₆] | +2 | 2 | 2.273 | 2.456 | 2.556 | - |
| [Fe(CO) ₆] | +2 | 0 | 1.889 | 1.858 | 2.146 | - |
| [Fe(NCH) ₆] | +2 | 2 | 2.150 | 2.370 | 2.558 | - |
| [Fe(C ₅ H ₅) ₂] | 0 | 0 | 2.044 | 2.161 | 2.271 | - |
| [Ni(phen) ₃] | +2 | 1 | 2.114 | 2.104 | 2.177 | 2.097 |
| [Ni(bipy) ₃] | +2 | 1 | 2.102 | 2.102 | 2.176 | 2.092 |
| [Ni(en) ₃] | +2 | 1 | 2.175 | 2.185 | 2.212 | 2.119 |
| [Ni(H ₂ O) ₆] | +2 | 1 | 2.078 | 2.130 | 2.177 | 2.033 |
| [Ni(NH ₃) ₆] | +2 | 1 | 2.185 | 2.188 | 2.190 | 2.111 |
| [Ni(pyrazole) ₆] | +2 | 1 | 2.139 | 2.148 | 2.141 | 2.088 |
| [Ni(acac) ₂] | 0 | 1 | 1.848 | 2.007 | 1.884 | 1.911 |
| trans-[Ni(gly) ₂]-N | 0 | 1 | 1.903 | 2.171 | - | 1.908 |
| trans-[Ni(gly) ₂]-O | 0 | 1 | 1.840 | 1.941 | - | 1.912 |
| [Zn(phen) ₃] | +2 | 0 | 2.210 | 2.119 | 2.096 | 2.218 |
| [Zn(bipy) ₃] | +2 | 0 | 2.208 | 2.111 | 2.092 | 2.212 |
| [Zn(en) ₃] | +2 | 0 | 2.264 | 2.178 | 2.127 | 2.256 |
| [Zn(H ₂ O) ₆] | +2 | 0 | 2.122 | 2.004 | 2.129 | 2.157 |
| [Zn(NH ₃) ₄] | +2 | 0 | 2.074 | 2.057 | 2.007 | 2.091 |
| [Zn(CN) ₄] | +2 | 0 | 2.048 | 2.070 | 2.047 | 2.134 |
| [Zn(Ph) ₂] | 0 | 0 | 1.925 | 2.028 | 1.965 | 2.004 |
| [Zn(acac) ₂] | 0 | 0 | 1.965 | 1.860 | 1.977 | 1.972 |
| [Co(phen) ₃] | +3 | 0 | 1.968 | 1.946 | 1.967 | - |
| [Co(bipy) ₃] | +3 | 0 | 1.962 | 1.938 | 1.955 | - |

| | | | | | | |
|---|----|-----|-------|-------|-------|-------|
| [Co(en) ₃] | +3 | 0 | 2.012 | 2.005 | 2.009 | - |
| [Co(H ₂ O) ₆] | +2 | 3/2 | 2.097 | 2.168 | 2.210 | - |
| [Co(NH ₃) ₆] | +3 | 0 | 2.022 | 2.001 | 2.015 | - |
| [Co(CN) ₆] | -3 | 0 | 1.911 | 1.868 | 2.049 | - |
| [Co(NO ₂) ₆] | -3 | 0 | 2.011 | 1.902 | 2.042 | - |
| [HCo(CO) ₄]-H | 0 | 0 | 1.483 | 1.493 | - | - |
| [HCo(CO) ₄]-C | 0 | 0 | 1.781 | 1.775 | - | - |
| [Ti(OCH ₃) ₄] | 0 | 0 | 1.816 | 1.734 | 1.819 | - |
| [Ti(OCH ₂ CH ₃) ₄] | 0 | 0 | 1.820 | 1.741 | 1.821 | - |
| [Ti(OCH ₂ CH ₂ CH ₃) ₄] | 0 | 0 | 1.815 | 1.744 | 1.819 | - |
| [Ti(bipy) ₃] | 0 | 0 | 2.116 | 1.966 | 2.088 | - |
| [Ti(NMe ₂) ₄] | 0 | 0 | 1.928 | 1.863 | 1.874 | - |
| [Ti(H ₂ O) ₆] | +3 | 1/2 | 2.095 | 2.026 | 2.055 | - |
| [Ti(NH ₃) ₆] | +4 | 0 | 2.211 | 2.210 | 2.221 | - |
| [Ti(dmp) ₃] | 0 | 0 | 1.974 | 1.865 | 1.988 | - |
| [Cu(phen) ₃] | +2 | 1/2 | 2.194 | 1.965 | - | 1.759 |
| [Cu(bipy) ₃] | +2 | 1/2 | 2.069 | 1.963 | - | - |
| [Cu(H ₂ O) ₆] | +2 | 1/2 | 2.015 | 1.965 | - | 1.922 |
| [Cu(cyclam)] | +2 | 1/2 | 2.049 | 2.059 | - | - |
| [Cu(acac) ₂] | 0 | 1/2 | 1.942 | 1.961 | - | 1.863 |
| [Cu(gly) ₂]-N | 0 | 1/2 | 2.073 | 2.135 | - | - |
| [Cu(gly) ₂]-O | 0 | 1/2 | 1.916 | 1.838 | | - |
| [Cu(en) ₂] | 0 | 1/2 | 2.128 | 1.842 | | - |
| [Cu(NH ₃) ₄] | +2 | 1/2 | 2.059 | 1.942 | | 2.039 |

Table S2 – HOMO-LUMO gap, in eV, for the different systems obtained with all the methods.

| Complex | DFT | DFTB2 | xTB | DFTB3 |
|--|------------|--------------|------------|--------------|
| [Fe(phen) ₃] | 1.694 | 1.543 | 1.500 | - |
| [Fe(bipy) ₃] | 1.625 | 1.457 | 1.459 | - |
| [Fe(en) ₃] | 2.215 | 1.615 | 2.340 | - |
| [Fe(H ₂ O) ₆] | 0.402 | 0.065 | 8.480 | - |
| [Fe(NH ₃) ₆] | 0.396 | 0.001 | 7.523 | - |
| [Fe(CO) ₆] | 4.654 | 2.477 | 4.103 | - |
| [Fe(NCH) ₆] | 0.361 | 0.388 | 3.463 | - |
| [Fe(C ₅ H ₅) ₂] | 2.886 | 1.612 | 1.362 | - |
| [Ni(phen) ₃] | 2.009 | 0.933 | 1.298 | 0.280 |
| [Ni(bipy) ₃] | 1.900 | 0.929 | 1.288 | 0.291 |
| [Ni(en) ₃] | 2.060 | 0.916 | 8.132 | 0.532 |
| [Ni(H ₂ O) ₆] | 2.089 | 1.068 | 8.624 | 0.651 |
| [Ni(NH ₃) ₆] | 2.218 | 0.998 | 7.970 | 0.494 |
| [Ni(pyrazole) ₆] | 2.209 | 1.000 | 3.209 | 0.300 |
| [Ni(acac) ₂] | 1.623 | 2.353 | 1.694 | 2.760 |
| trans-[Ni(gly) ₂]-N | 1.720 | - | 3.991 | 2.782 |
| trans-[Ni(gly) ₂]-O | 1.720 | - | 3.991 | 2.782 |
| [Zn(phen) ₃] | 3.135 | 3.362 | 2.779 | 3.376 |
| [Zn(bipy) ₃] | 3.362 | 3.334 | 2.796 | 3.365 |
| [Zn(en) ₃] | 5.281 | 7.422 | 6.400 | 6.822 |
| [Zn(H ₂ O) ₆] | 6.653 | 7.459 | 7.662 | 8.774 |
| [Zn(NH ₃) ₄] | 7.147 | 9.466 | 6.657 | 9.201 |
| [Zn(CN) ₄] | 6.398 | 7.611 | 4.572 | 7.531 |
| [Zn(Ph) ₂] | 4.377 | 4.025 | 3.399 | 4.288 |
| [Zn(acac) ₂] | 3.377 | 3.690 | 3.287 | 3.762 |
| [Co(phen) ₃] | 2.314 | 2.980 | 2.512 | - |
| [Co(bipy) ₃] | 2.676 | 3.352 | 2.514 | - |
| [Co(en) ₃] | 2.659 | 3.781 | 2.151 | - |
| [Co(H ₂ O) ₆] | 0.836 | 0.110 | 6.844 | - |
| [Co(NH ₃) ₆] | 2.628 | 3.785 | 2.183 | - |

| | | | | |
|---|-------|-------|-------|-------|
| [Co(CN) ₆] | 4.155 | 3.604 | 3.951 | - |
| [Co(NO ₂) ₆] | 2.670 | 3.264 | 2.107 | - |
| [HCo(CO) ₄]-H | 4.086 | - | 3.052 | - |
| [HCo(CO) ₄]-C | 4.086 | - | 3.052 | - |
| [Ti(OCH ₃) ₄] | 4.205 | 3.793 | 4.151 | - |
| [Ti(OCH ₂ CH ₃) ₄] | 4.352 | 4.026 | 4.392 | - |
| [Ti(OCH ₂ CH ₂ CH ₃) ₄] | 4.081 | 3.666 | 4.081 | - |
| [Ti(bipy) ₃] | 0.557 | 0.575 | 0.354 | - |
| [Ti(NMe ₂) ₄] | 3.044 | 3.121 | 1.991 | - |
| [Ti(H ₂ O) ₆] | 0.626 | 0.426 | 0.248 | - |
| [Ti(NH ₃) ₆] | 2.674 | 2.992 | 2.863 | - |
| [Ti(dmp) ₃] | 0.510 | 1.016 | 0.532 | - |
| [Cu(phen) ₃] | 0.781 | - | 1.443 | 0.241 |
| [Cu(bipy) ₃] | 0.794 | - | 1.452 | - |
| [Cu(H ₂ O) ₆] | 0.578 | - | 9.173 | 0.450 |
| [Cu(cyclam)] | 0.888 | - | 8.089 | - |
| [Cu(acac) ₂] | 1.024 | - | 1.759 | 0.447 |
| [Cu(gly) ₂]-N | 0.891 | - | 4.271 | - |
| [Cu(gly) ₂]-O | 0.891 | - | 4.271 | - |
| [Cu(en) ₂] | 0.250 | - | 7.176 | - |
| [Cu(NH ₃) ₄] | 1.114 | | 8.761 | 0.342 |

Titre : Élaboration in silico de systèmes moléculaires pour la fabrication de dispositifs en nano- et opto-électronique.

Mots clés : chimie de coordination, jonction moléculaire, chimie computationnelle

Résumé : Les travaux de chimie computationnelle développés dans cette thèse ont concerné deux axes de recherche. La première partie concerne l'étude théorique de complexes de cuivre(I) polynucléaires luminescents. Le deuxième chapitre s'attèle à rendre compte des résultats expérimentaux obtenus par C. Lescop et collaborateurs (ISCR - INSA Rennes) pour des dimères de cuivre pontés par trois diphosphines. Différents niveaux de calculs sont testés afin de quantifier la précision des résultats. Le chapitre suivant rassemble l'étude de composés métallacycliques apparentés comprenant respectivement 6 et 8 atomes de cuivre. Ces études montrent l'importance de la réorganisation géométrique des états excités et des interactions intermoléculaires à l'état solide.

La deuxième partie de cette thèse vise à appor-

ter un appui théorique au développement des dispositifs moléculaires à haute performances thermoélectriques. Le premier chapitre rend compte de l'état de l'art et des facteurs influençant la variation des propriétés thermoélectriques. Les chapitres II et III présentent les outils théoriques disponibles pour l'études des propriétés de transmission de jonctions moléculaires et de leurs caractéristiques thermoélectriques. Les atouts des composés organométalliques à induire des propriétés thermoélectriques sont traités dans le chapitre IV et V. Une augmentation sensible de la conductance et des coefficients de Seebeck est calculée. Un design moléculaire computationnel implique l'utilisation de méthodes peu coûteuses. Les méthodes "density functional tight-binding" sont évaluées à cette fin dans le dernier chapitre.

Title: In silico elaboration of molecular systems for the fabrication of nano- and opto-electronic devices.

Keywords: coordination chemistry, molecular junction, computational chemistry

Abstract: The computational studies developed in this thesis are divided in two research projects. The first part concerns a theoretical study of luminescent polynuclear copper (I) complexes. The second chapter reports computational results that are compared to experimental data obtained by C. Lescop and collaborators (ISCR - INSA Rennes) for copper dimers bridged by three diphosphines. Different levels of calculations are tested in order to quantify the accuracy of the results. The following chapter brings together the study of related metallacyclic compounds comprising respectively 6 and 8 copper atoms. These studies show the importance of the geometric reorganization of excited states and intermolecular interactions in the solid state.

The second part of this thesis aims at providing

a theoretical support to the development of molecular devices presenting high thermoelectric performance. The first chapter reports on the state of the art and the factors influencing the variation of thermoelectric properties. Chapters II and III present the theoretical tools available for the study of the transmission properties of molecular junctions and their thermoelectric characteristics. The advantages of organometallic compounds in inducing thermoelectric properties are treated in chapters IV and V. A significant increase in conductance and Seebeck coefficients is calculated. A computational molecular design implies the use of cheap computational methods. The density functional tight-binding methods are evaluated for this purpose in the last chapter.

Résumé

L'équipe de Chimie Théorique Inorganique (CTI) de l'Institut des Sciences Chimiques de Rennes (ISCR) est un groupe de recherche regroupant des chercheurs du CNRS, de l'Université de Rennes 1 et de l'école supérieure des sciences chimique de Rennes (ENSCR). Le groupe de recherche utilise des outils de chimie computationnelle pour rationaliser les propriétés structurales et physiques des molécules et du solide. Ses thèmes de recherche portent sur les : i) architectures complexes (i.e. gros clusters atomiques, verres) (axe 1), ii) matériaux solides pour l'énergie (axe 2), et iii) systèmes moléculaires multifonctionnels pour l'optoélectronique, la spintronique et le magnétisme (axe 3). Le présent projet s'inscrit dans l'axe de recherche 3 et vise à contribuer au développement des technologies en électronique moléculaire, optoélectronique ou spintronique utilisant une approche quantique computationnelle. L'intérêt principal de ces dispositifs est de fournir un rendement élevé à l'échelle nanométrique, ce qui est en accord avec les défis environnementaux d'aujourd'hui. Les systèmes moléculaires ont démontré leurs potentiels dans différents secteurs comme le stockage de données, les technologies de l'information, la médecine, ou encore l'énergie. Le projet de recherche de thèse présenté dans ce manuscrit est consacré à deux applications qui tirent parti des molécules contenant des métaux de transition : l'éclairage à bas coût et la récupération d'énergie (chaleur) ou d'électricité à l'échelle nanométrique (thermoélectricité). Pour la première application, les travaux se sont centrés sur des molécules contenant des atomes de cuivre. Ce sont des systèmes attrayants en raison de leurs propriétés physico-chimiques, disponibilité, faible toxicité et de leurs faibles coûts. L'objectif général est de proposer une alternative aux systèmes contenant des métaux lourds et des lanthanides qui sont les plus couramment développés pour la création de diodes électroluminescentes phosphorescente (PhOLED), ou pour des applications d'éclairage. Ce sont des composés plus toxiques, plus rares et donc chers. L'étude computationnelle qui est présentée dans ce manuscrit s'appuie sur des résultats expérimentaux obtenus dans l'équipe de Lescop de l'ISCR (Rennes) et permet de rationaliser les propriétés optiques de ces systèmes contenant du cuivre (I) en utilisant la théorie de la fonctionnelle de la densité (DFT). Pour la deuxième application, à savoir la récupération d'énergie à l'échelle nanométrique, les travaux se sont focalisés sur la conception de jonctions moléculaires *in-silico* pour des applications en nano-thermoélectricité dans le but de récupérer et de convertir l'énergie dissipée dans des nano-dispositifs en électricité. Cette partie de la thèse a été développée en collaboration avec différents collaborateurs expérimentalistes : l'équipe de recherche de Rigaut à l'ISCR (Rennes), l'équipe de recherche de Scheer de l'université de Constance (Allemagne), et enfin l'équipe de recherche de Vuillaume (Lille).

La première partie porte sur l'étude computationnelle de complexes luminescents multi-nucléaires de cuivre (I) et est divisée en trois chapitres. Le premier développe les différents concepts de base de la luminescence

des molécules, notamment le mécanisme de fluorescence retardée activée thermiquement (TADF) ainsi que l'intérêt d'utiliser des molécules contenant des métaux de transition (notamment les systèmes contenant du cuivre). Cette description est suivie d'une présentation de la chimie supramoléculaire induite par coordination développée par Lescop et ses collègues pour synthétiser des complexes multi-nucléaires innovants de cuivre (I). La procédure de calcul employée pour simuler et interpréter les comportements photo-physiques de certains de ces systèmes s'appuie sur la DFT pour laquelle le choix de la fonctionnelle et les bases de fonctions atomiques sont expliqués sur la base de la littérature. Le deuxième chapitre est consacré à l'étude de deux complexes di-nucléaires, $[\text{Cu}_2(\text{X})_3]^{2+}$ avec X correspondant à des ligands diphosphines (dppa, dppm). Ces systèmes permettent d'évaluer l'influence de la taille des fonctions de base atomiques et la non prise en compte des effets relativistes sur la précision des résultats. Le chapitre III vise à rationaliser les propriétés photo-physiques de deux complexes de cuivre (I) beaucoup plus gros : un complexe hexa-nucléaire et un complexe octa-nucléaire en utilisant la même méthodologie de calcul que précédemment. Les propriétés photo-physiques de ces systèmes polynucléaires formant des métallacycles $[\text{Cu}_6\text{CN}_2]$ et $[\text{Cu}_8\text{CN}_4]$ ont été étudiées. La comparaison entre les calculs et les données expérimentales sont en bon accord. L'occurrence d'un processus TADF pour $[\text{Cu}_6\text{CN}_2]$ est fortement soutenue par l'étude computationnelle qui révèle que compte tenu des contraintes imposées par l'arrangement cristallin conduit à limiter la différence d'énergie entre le premier état singulet et le premier état triplet excité. Les longueurs d'onde d'émission calculées sont également bien reproduites. Les calculs mettent en évidence le renforcement des interactions Cu--Cu lors de l'excitation, favorisant alors un couplage spin-orbite. Les résultats de calcul obtenus pour les systèmes plus petits $[\text{Cu}_2(\text{dppa})_3]^{2+}$ et $[\text{Cu}_2(\text{dppm})_3]^{2+}$ décrits dans le chapitre II montrent une concentration importante d'états excités à basse énergie ce qui complexifie la rationalisation par rapport aux systèmes $[\text{Cu}_6\text{CN}_2]$ et $[\text{Cu}_8\text{CN}_4]$. En effet, la précision de la méthode de calcul devient décisive pour la fiabilité des interprétations. Enfin, l'étude montre aussi des interactions intramoléculaires telles que de la liaison hydrogène entre $[\text{Cu}_2(\text{dppa})_3]^{2+}$ et les contre-ions (PF_6^- ou BF_4^-) présente dans l'arrangement cristallin, modifient les propriétés optiques du système.

La seconde partie de la thèse concerne l'étude de jonctions moléculaires contenant des métaux de transition. Les propriétés thermoélectriques de systèmes de coordination dans des jonctions moléculaires y sont évaluées avec comme objectif final de concevoir des jonctions moléculaires efficaces en termes de propriétés thermoélectriques. La thermoélectricité est la capacité qu'a un système à convertir un gradient thermique en un courant électrique (effet Seebeck), ou inversement (effet Peltier). Le premier chapitre est une introduction à l'électronique moléculaire et les équipements expérimentaux utilisés pour caractériser des jonctions moléculaires. Cette section est suivie par une description des bases théoriques utilisées par la suite pour étudier et évaluer le transport électronique. Ce chapitre se termine par l'introduction des concepts

théoriques permettant de rationaliser le transport thermoélectrique dans des jonctions moléculaires. Le deuxième chapitre introduit des paramètres permettant la comparaison entre les données expérimentales obtenues à partir des courbes courant-tension (courbes I-V) de jonctions moléculaires en utilisant différents modèles (modèle à niveau unique, « transition voltage spectroscopy », modèle à deux niveaux...) et des mesures additionnelles telles que la spectroscopie photoélectronique UV. Les différents termes de la conductance thermique phononique (κ_{ph}) – termes intervenant dans les grandeurs physiques thermoélectriques – sont aussi expliqués et quantifiés. Enfin, la présence d'interférence quantique (IQ) sur des transmissions théoriques est abordée. L'existence de résonances Fano n'ont pas d'effet visible à température ambiante sur les propriétés thermoélectriques, en revanche la présence d'anti-résonance dans le pic de transmission le plus proche du niveau de Fermi peut améliorer les propriétés thermoélectriques par rapport à une transmission théorique de forme Lorentzienne. La présence d'anti-résonance est une caractéristique recherchée dans les chapitres suivants. Les calculs de transmission électronique de différentes jonctions moléculaires étudiées dans les chapitres III, IV et V sont réalisés en utilisant l'approche DFT couplé avec le formalisme des fonctions de Green hors équilibre (NEGF). Le chapitre III rassemble des données expérimentales obtenues par le groupe de Scheer sur les systèmes organiques, à savoir la jonction Au | oligophényl-diéthynyle | Au, dont les groupes d'ancrage sont des alcynyles (Au-C) - OPAn ($n = 2, 3, 4$), où n est le nombre d'unités phényles. Deux approches computationnelles (DFT/NEGF et DFTB) ont été utilisées pour rationaliser les propriétés électroniques, analyser le potentiel de la liaison Au-C à très basse température (4 K) et d'étudier les différents types jonctions possibles. L'objectif principal du chapitre IV est d'évaluer le potentiel de différents systèmes moléculaires comprenant des métaux de transition pour obtenir des propriétés thermoélectriques intéressantes. La nature du métal est très importante et l'étude montre que parmi les complexes de coordination étudiés ce sont ceux qui incorporent des atomes de fer et de ruthénium qui présentent les meilleures caractéristiques. Les dérivés du ferrocène présentent des anti-résonances conduisant à des propriétés thermoélectriques intéressantes dans le cas où le niveau de transport principal peut être ajusté à l'aide d'une grille de tension pour se rapprocher du niveau de Fermi. Pour un espaceur comprenant un cycle phényle terminal auquel est coordonné le groupement d'ancrage (ici un atome de soufre) en position méta, les calculs montrent qu'il n'existe pas d'interférence Fano ni d'anti-résonance contrairement à ce qui est rapportés dans la littérature pour des jonctions moléculaires purement organiques. Les simulations montrent que les molécules en forme de « T » sont aussi une alternative prometteuse. Plusieurs limitations concernant l'approche computationnelle utilisée ont également été discutées : la différence d'énergie entre le niveau de Fermi et le premier niveau occupé ou inoccupé du système est clairement dépendant de la fonctionnelle. L'utilisation d'une fonctionnelle hybride tel que la GGA HSE06 (récemment disponible dans QuantumATK 2021) semble améliorer l'accord quantitatif entre expériences et calculs. Une méthode DFT modifiée tel que la DFT+ Σ comprenant des corrections statiques pour les

niveaux d'énergie Kohn-Sham peut également aider à mieux reproduire la conductance des molécules organiques, comme le rapportent Quek *et al.* pour des systèmes liés par un atome d'azote aux électrodes. La géométrie de l'électrode influence grandement la position des différents niveaux moléculaires par rapport au niveau de Fermi. L'utilisation d'une approche statistique pour considérer la diversité des jonctions observées dans les conditions expérimentales est hautement souhaitable. Les systèmes chargés sont complexes à simuler à l'aide des outils DFT/NEGF. La conductance est toujours surestimée par rapport aux données expérimentales ; ceci est certainement dû à plusieurs facteurs, le principal étant que seules les meilleures jonctions moléculaires possibles sont calculées. Pour une meilleure comparaison, la dispersion des types de jonctions expérimentales doit être prise en compte. Le chapitre V rassemble les données expérimentales obtenues par nos collaborateurs sur des jonctions organométalliques dans différentes configurations et conditions expérimentales. Sur cette base, une analyse des propriétés conductrices des jonctions et une comparaison avec les données expérimentales sont apportées. Elles révèlent un besoin de concevoir des méthodes de calcul plus rapides capables de mieux prendre en considération la diversité des géométries des jonctions révélées par la dispersion de la conduction observée dans les mesures expérimentales. L'utilisation de méthodes semi-empiriques a été évaluée dans la chapitre VI comme moyen de donner accès à cette approche statistique nécessaire pour mieux comparer la théorie avec l'expérience. La théorie de la fonctionnelle de la densité à liaison forte (DFTB, GFN2-xTB) qui a été utilisée avec succès dans des systèmes biologiques est évaluée pour des systèmes de coordinations. Cette étude montre que les paramètres disponibles pour les métaux de transition ne sont pas suffisamment fiables pour modéliser de nouveaux systèmes.

L'utilisation de la DFT comme outil de calcul nous a permis de rationaliser à un niveau semi-quantitatif les propriétés optiques de complexes de cuivre (I) de différentes tailles illustrant la complexité de plusieurs processus compétitifs qui peuvent se produire après excitation. Même si l'utilisation d'outils plus sophistiqués serait nécessaire pour accéder formellement au chemin de désexcitation, ces calculs donnent des informations sur la nature de l'excitation, la géométrie et les changements électroniques des premiers états excités permettant de rationaliser un comportement de type TADF mesuré expérimentalement. Enfin la DFT/NEGF s'est également avéré être un outil intéressant et complet pour cibler des jonctions organométalliques dont les propriétés thermoélectriques sont exacerbées. Les systèmes qui ont été identifiés *in silico* dans ce manuscrit présentent de bonnes caractéristiques de transmission qui donnent lieu à des perspectives attrayantes dans ce domaine émergent. Cette étude révèle également le besoin d'outils de calcul plus rapides qui permettraient de simuler la grande diversité de géométries observées expérimentalement afin de simuler, d'interpréter et de prédire les propriétés des jonctions moléculaires obtenues expérimentalement.